Improving Performance of Buildings in Very High-Seismic Regions

Volume 1 – Methods, Findings, and Recommendations

FEMA P-2343 / March 2024

FEMA

nehrp

FEMA P-2343 / March 2024

Improving Performance of Buildings in Very High-Seismic Regions – Volume 1

Prepared by
APPLIED TECHNOLOGY COUNCIL
201 Redwood Shores Parkway, Suite 240
Redwood City, California 94065
www.ATCouncil.org

Prepared for
FEDERAL EMERGENCY MANAGEMENT AGENCY
Mai (Mike) Tong, Project Officer
Robert D. Hanson, Technical Advisor
Washington, D.C.

APPLIED TECHNOLOGY COUNCIL
Jon A. Heintz, Project Executive
Justin Moresco, Project Manager

PROJECT TECHNICAL COMMITTEE
Charles A. Kircher (Project Tech. Director)
Jeffrey W. Berman
James R. Harris
John Hooper
Weichiang Pang

WORKING GROUP MEMBERS
Bibek Bhardwaj
Addie Lederman
Dimitrios Lignos
Sereen Majdalaweyh
Uzochukwu D. Uwaoma

PROJECT REVIEW PANEL
Russell Berkowitz
Kelly Cobeen*
Gregory Deierlein
Andre Filiatrault
Emily Guglielmo
Devin Huber
Phil Line
James O. Malley
Bob Pekelnicky

*ATC Board Representative

FEMA

Notice

Any opinions, findings, conclusions, or recommendations expressed in this publication do not necessarily reflect the views of the Applied Technology Council (ATC), the Department of Homeland Security (DHS), or the Federal Emergency Management Agency (FEMA). Additionally, neither ATC, DHS, FEMA, nor any of their employees, makes any warranty, expressed or implied, nor assumes any legal liability or responsibility for the accuracy, completeness, or usefulness of any information, product, or process included in this publication. Users of information from this publication assume all liability arising from such use.

Cover photograph: Partially collapsed 15-story building caused by the 1999 Chi-Chi/Nantou, Taiwan Earthquake (image credit: NOAA National Geophysical Data Center, NOAA/NCEI).

This document is the first of a two-part set.

Appendix H through Appendix K can be found in FEMA P-2343, Volume 2.

Foreword

Twelve States and Territories—California, Washington, Oregon, Utah, Puerto Rico, Nevada, Alaska, South Carolina, Hawaii, Guam, Missouri, and Tennessee—have over 42.9 million people and 13.3 million buildings in very high-seismic regions. Some recent studies show buildings designed for very high-seismic regions, while in compliance with national building codes and standards, may still be subject to higher probability of collapse and not meet the code-prescribed performance criteria. The FEMA National Earthquake Hazards Reduction Program (NEHRP) supported a problem-focused study to investigate the issue. This report provides technical resources to address the potentially high collapse risk for buildings in very high-seismic regions.

The study examined building overstrength, a factor of influence to building seismic performance, and conducted analysis of selected archetype buildings that represent typical designs for very high-seismic regions. A similar trend of rising collapse risk is observed across all building models for very high-seismic regions despite differences of archetype height, overstrength, construction material, building displacement capacity, and hysteretic behavior. In further evaluation of the analysis results, it is found that a primary cause of the trend is due to increasing displacement demand from higher ground motions against displacement capacity of a building that is not increasable. Building period and site soil condition are two major influencing factors to the trend. The report summarizes the findings and recommendations to help reduce the impact of the issue for new building design.

FEMA is grateful to the Applied Technology Council (ATC), the Project Technical Committee, and the Project Review Panel for their great effort and endeavor to discover the trend of the issue and develop feasible remedies for consideration and implementation in national standards and building codes. Appreciation is extended to the project workshop participants for providing additional suggestions, to the American Institute of Steel Construction (AISC) for developing detailed archetype designs for in-depth evaluation, and to the U.S. Geological Survey (USGS) for seismic hazard data and exposure of very high-seismic risk for the nation. Although the study is limited in scope and time, the findings and recommendations are significant. Hopefully, they will help make people living in communities with very high-seismic hazard safer in future earthquakes.

National Earthquake Hazards Reduction Program

Federal Emergency Management Agency

Preface

Recent analytical studies of modern code-conforming buildings have found that the risk of collapse in an earthquake increases with the intensity of the ground motions despite the seismic-force-resisting system of the building being designed for proportionally stronger shaking. In addition, some systems had predicted collapse probabilities given risk-targeted Maximum Considered Earthquake (MCE_R) ground motions that exceeded the 10% reliability objective for Risk Category II structures that is defined in national model codes and seismic design standards. If these analytical predictions are valid, it means that the goal of acceptable collapse performance for all modern code-confirming structural systems—regardless of site seismicity—is not being achieved. Concern about the collapse safety of buildings in very high-seismic regions is the impetus for this report.

In 2019, the Applied Technology Council (ATC) was awarded the first in a series of task orders under contract HSFE60-17-D-0002 with the Federal Emergency Management Agency (FEMA) to investigate "Improving Seismic Performance for New Buildings in Very High Seismic Regions," designated the ATC-154 Project. The purpose of this project was to quantify and validate the seismic collapse performance of buildings in very high-seismic regions designed in accordance with current requirements of ASCE/SEI 7, *Minimum Design Loads and Associated Criteria for Buildings and Other Structures*. The project also sought to identify weaknesses in current code provisions and design standards for buildings in very high-seismic regions and to provide recommendations for conceptual code changes to seismic codes and standards, as well as for future studies.

ATC is indebted to the leadership of Charlie Kircher, Project Technical Director, and to the other members of the ATC-154 project team for their efforts in developing this report. The Project Technical Committee, consisting of Jeff Berman, Jim Harris, John Hooper, and Weichiang Pang, managed and performed the technical development effort. Bibek Bhardwaj and Sereen Majdalaweyh assisted in the wood light-frame numerical modeling, and Addie Lederman, Dimitrios Lignos, and Uzo Uwaoma assisted in the numerical modeling of non-wood systems. The Project Review Panel, consisting of Russ Berkowitz, Kelly Cobeen, Greg Deierlein, Andre Filiatrault, Emily Guglielmo, Devin Huber, Phil Line, Jim Malley, and Bob Pekelnicky, provided technical review and advice at key stages of the work. Andre Filiatrault provided significant input and review for the wood light-frame modeling.

ATC would like to thank Nicolas Luco, Kishor Jaiswal, Sanaz Rezaeian, and Ken Rukstales of the U.S. Geological Survey, Jesse Rozelle of FEMA, and Doug Bausch of NiyamIT Inc. for providing seismic hazard and inventory data that were used to investigate the potential scope of very high-seismic regions. ATC also would like to thank Yasmin Chaudhry of the AISC Steel Solutions Center for preparing designs of steel special moment resisting frame archetypes.

ATC gratefully acknowledges Mike Tong (FEMA Project Officer) and Bob Hanson (FEMA Technical Advisor) for their input and guidance in the preparation of this report, and Ginevra Rojahn and Kiran Khan who provided ATC report production services. The names and affiliations of all who contributed to this report, including those who participated in the review workshop held August 11, 2022, in the San Francisco Bay Area, are provided in the list of Project Participants at the end of this report.

Justin Moresco
ATC Director of Projects

Jon A. Heintz
ATC Executive Director

Executive Summary

Recent analytical studies of modern code-conforming buildings have found that the risk of building collapse in an earthquake increases with the intensity of the ground motions despite the seismic-force-resisting system being designed for proportionally stronger shaking. Further, in very high-seismic (VHS) regions, such as those relatively close to an active fault, predicted collapse probabilities given risk-targeted Maximum Considered Earthquake (MCE_R) ground motions were found to exceed the 10% reliability objective for Risk Category II structures that is defined in national model codes and seismic design standards. If these analytical predictions are valid, modern code-conforming structural systems may not be achieving an acceptably low seismic risk of collapse for buildings located in VHS regions. Concern about the collapse safety of buildings in VHS regions is the impetus for this report.

This report documents the issues, approaches, analyses, findings, and conclusions of an investigation that sought to quantify and validate the seismic collapse performance of buildings in VHS regions. The report also presents recommendations for conceptual code changes and future studies based on the findings and conclusions. For this work, VHS regions are defined by ground-motion intensities greater than the strongest level of shaking required for evaluation of a new structural system proposed for incorporation into ASCE/SEI 7 or for evaluation of an alternative structural system as permitted by ASCE/SEI 7. That strongest level of shaking is defined by FEMA P-695, referred to therein as Seismic Design Category (SDC) D_{max}, and has a short-period MCE_R response spectral acceleration, S_{MS}, of 1.5g and a 1-second MCE_R response spectral acceleration, S_{M1}, of 0.9g. VHS regions are found across the United States, constituting areas with about 42.9 million people and about 11% of U.S. buildings representing $7.5 trillion in replacement costs.

Four structural systems were selected for study: (1) wood light-frame walls with wood structural panel sheathing (wood), (2) steel buckling restrained braced frames (BRBFs), (3) steel special moment resisting frames (SMFs), and (4) reinforced concrete ductile coupled walls (DCW). The selected systems are common for new construction in VHS regions for a wide range of occupancies.

Prior studies identified building overstrength, Ω, as an important factor influencing the trend of increased computed collapse probabilities for systems designed and evaluated for VHS ground motions. Consistent with FEMA P-695, overstrength is defined as an archetype model's maximum base shear from a pushover curve divided by its design base shear ($\Omega = V_{max}/V$). Thus, two sets of technical studies were conducted. One set investigated the expected ranges of building overstrength for the selected systems. These studies considered, where appropriate, contributions from elements not considered part of the seismic-force-resisting system (e.g., gravity frames, partitions) and related overstrength as a function of S_{MT}, which is the value of MCE_R response spectral acceleration at the code-based fundamental period, T, for a given archetype model. The second set of technical studies investigated the computed collapse performance of the selected systems using building archetypes representing current design and construction practices for Risk Category II and IV structures.

Two-dimensional, nonlinear, multi-degree-of-freedom (MDOF) models were developed for the wood archetypes, and equivalent single-degree-of-freedom (eSDOF) nonlinear models were developed for the non-wood archetypes. Simplified models were used in order to reduce the computational demands of nonlinear response history analyses and increase the number of models that could be analyzed. eSDOF models of non-wood systems were created based on the nonlinear MDOF models and analysis results of prior research studies. Different from a traditional SDOF model, an eSDOF model translates the detailed model's collapse failure mode, system pushover curve, period, and force and displacement relation into a nonlinear single-degree-of-freedom model. eSDOF models were calibrated to match the corresponding MDOF model performance. This innovative analysis method was shown to accurately represent the MDOF model collapse performance trends.

For each system, MDOF or eSDOF models were developed for large numbers of archetypes of varying height (or number of stories), strength, and displacement capacity, reflecting the full range of expected values for these parameters that are likely to occur in modern low-rise and mid-rise buildings. The archetypes encompassed a broad range of strengths representative of different designs for MCE_R response spectral accelerations spanning moderate seismic regions (e.g., S_{MS} = 0.75g) to the strongest level of expected ground motions in regions of very high seismicity (e.g., S_{MS} = 3.0g). Importantly, the vast majority of the modeled archetypes (except those used for calibration or validation) are representative of designs but were not actually designed. This innovative approach enabled the investigation of about 800 archetype models of the four systems.

The archetype models then were used to calculate collapse probabilities given MCE_R ground motions in accordance with the methods of FEMA P-695, with some noted adaptations. For example, in order to calculate a more accurate view of performance, the models included contributions from elements not considered part of the seismic-force-resisting system (e.g., gravity frames). The extensive data on collapse performance that were generated enabled the creation of "collapse surfaces," which describe the interaction of the two primary building response properties, strength and displacement capacity, that govern earthquake collapse performance for a given structural system and height. Collapse surfaces illuminate the trends in collapse performance with increasing S_{MT} for a given structural system and height.

KEY FINDINGS

The analytical results show that the probabilities of collapse given S_{MT} increase as a function of MCE_R ground motions across all investigated structural systems, despite the design strengths for the structural systems increasing proportionally for stronger shaking as is currently required by national codes and design standards. The trend of rising probability of collapse in VHS regions was found across all investigated structural systems regardless of differences in archetype height, overstrength, displacement capacity, and hysteretic behavior. The trend suggests that seismic design strength in VHS regions may need to be increased above those required by current national codes and design standards in order to meet the ASCE/SEI 7 performance criterion of no more than 10% probability of collapse given MCE_R ground motions.

Several factors were investigated to help explain the cause of the trend of increasing collapse risk in VHS regions. The original hypothesis of the project was that overstrength was the major factor influencing the trend. However, further investigations found the major factor to be limited collapse displacement capacity. Displacement demand increases with S_{MT}, but displacement capacity for a given structural system does not. For example, all the BRBF archetypes have displacement capacities of about 9.5% to 10% (measured as the median story drift of the governing story at incipient collapse). This is caused by inherent limits in the displacement capacity of a given structural system at the peak in the response curve, P-delta effects, and non-simulated failure assumptions of the same archetype at different strengths. Therefore, despite increased design strength for a building in a VHS region, the corresponding increased displacement demand on the structural system still exceeds its displacement capacity, causing a rise in collapse risk.

RECOMMENDATIONS

The report provides a series of recommendations for conceptual changes to ASCE/SEI 7. Due to many practical limitations, increasing the displacement capacity of structural systems qualified for use where ground motions are very high would be challenging and require extensive system-specific study and perhaps significant changes to engineering practice. However, increasing required design strength in ASCE/SEI 7 beyond current proportional increases with S_{MT} is a practical solution that could help reduce collapse risk to meet desired performance. The conceptual changes to ASCE/SEI 7 put forward include, but are not limited to, increasing the design base shear in VHS regions, such as by adopting a load amplification factor for the seismic response coefficient, C_S, increasing the seismic importance factor, I_e, for Risk Category IV structures, and refining the response modification coefficient, R, on a system-by-system basis while considering its constituent parts, where one part is related to total system ductility and damping and another part is related to system overstrength. Key limitations and assumptions related to the analytical work are highlighted, and these should be considered when developing any future code changes. The report presents frameworks for code changes, recognizing the details of any changes would need to be determined by code change committees in light of the key limitations and assumptions of this investigation.

The report also recognizes that if nothing is done to address the trend of increasing collapse risk in VHS regions, the decision is de facto to revise the uniform ASCE/SEI 7 performance criterion to accept higher probabilities of collapse for VHS regions.

Several topics for futures studies are documented. These include the need for additional collapse studies for systems designed for VHS ground motions and using detailed nonlinear models. These collapse studies would ideally be informed by the development of improved component backbone curves for nonlinear response from actual ground motions. As has been documented in other studies, there is a need for an update to FEMA P-695, including a re-evaluation of the spectral shape factor and ground motions used for collapse evaluations. The boundary for SDC E and SDC F structures should be reviewed, as should the benchmark buildings in ASCE/SEI 41 in light of the findings of this investigation.

Table of Contents

Volume 1

Volume 2

List of Figures

Volume 1

Volume 2

List of Tables

Volume 1

Volume 2

Chapter 1: Introduction

1.1 Background and Purpose

This report documents the approaches, analyses, findings, conclusions, and recommendations for technical studies conducted in a multi-year project titled, "Improving Seismic Performance for New Buildings in Very High Seismic Risk Regions." At the time this work began, commercial and multi-family residential buildings were designed in accordance with ASCE/SEI 7-16, *Minimum Design Loads and Associated Criteria for Buildings and Other Structures* (ASCE, 2016), which was adopted by reference in the 2018 edition of the *International Building Code* (IBC) (ICC, 2018). The current version of this standard is ASCE/SEI 7-22 (ASCE, 2022), which has been proposed for adoption by the 2024 edition of the IBC.

Design seismic loads in ASCE/SEI 7-22 are based on risk-targeted maximum considered earthquake (MCE_R) ground motions, which were introduced in FEMA P-750, *NEHRP Recommended Seismic Provisions for New Buildings and Other Structures* (FEMA, 2009a). Buildings designed and constructed in accordance with national model codes and seismic design standards (e.g., ASCE/SEI 7-22) are expected to meet general seismic performance targets, which are described in terms of not exceeding a specified probability of collapse given MCE_R ground motions. A collapse probability of no more than 10 percent, given MCE_R ground motions, is the anticipated "reliability" in ASCE/SEI 7-22 (Table 1.3-2) for Risk Category II structures, which constitute the vast majority of all buildings. Given MCE_R ground motions, collapse probabilities of no more than 5 percent for Risk Category III and no more than 2.5 percent for Risk Category IV structures are also defined in Table 1.3-2. Further, the use of MCE_R ground motions in building design is intended to provide a reasonable assurance of seismic performance for all buildings—regardless of site seismicity, building period, seismic-force-resisting system or other characteristic—designed in accordance with the governing building code.

The report series FEMA P-2139, *Short-Period Building Collapse Performance and Recommendations for Improving Seismic Design* (FEMA, 2020), documented analytical studies of archetypes of various seismic-force-resisting systems that were designed for values of short-period MCE_R spectral response acceleration adjusted for site class effects, S_{MS} = 2.25g, as well as archetypes designed for values of S_{MS} = 1.5g. FEMA P-2139 referred to these ground motions as "very high seismic" and "high seismic," respectively. The analytical results indicated that short-period buildings in very high-seismic hazard regions (i.e., S_{MS} = 2.25g) have a significantly increased probability of collapse given MCE_R ground motions relative to short-period buildings in high-seismic hazard regions (i.e., S_{MS} = 1.5g), even when the seismic-force-resisting system is designed for proportionally larger (in this case, 50 percent greater) seismic forces. For example, the very high-seismic commercial occupancy archetypes with wood light-frame systems had computed collapse probabilities given MCE_R ground motions that increased between 53 percent and 160 percent relative to high-seismic archetypes. In addition, the FEMA P-2139 multi-family dwelling and commercial occupancy archetypes of wood light-frame systems and the commercial occupancy archetypes of steel special concentrically braced

frame (SCBF) systems designed and evaluated for very high-seismic forces had computed collapse probabilities given MCE_R ground motions that often exceeded the 10 percent collapse-safety objective of ASCE/SEI 7 for Risk Category II structures. Furthermore, analytical studies documented in Appendix A of FEMA P-695, *Quantification of Building Seismic Performance Factors* (FEMA, 2009b), also showed a substantial increase in probability of collapse for reinforced concrete archetypes designed and evaluated for seismic forces greater than $S_{MS} = 1.5g$.

FEMA P-2139 identified archetype overstrength, Ω, as an important factor influencing the trend of increased computed collapse probabilities for systems designed and evaluated for very high-seismic ground motions. Consistent with FEMA P-695, FEMA P-2139 defined overstrength to be an archetype model's maximum base shear from a pushover curve divided by its design base shear ($\Omega = V_{max}/V$). The overstrength for very high-seismic archetypes in the FEMA P-2139 analytical studies was consistently less than the overstrength for the same archetypes designed for high-seismic ground motions.

The purpose of the work documented in this report is to quantify and validate the seismic collapse performance of buildings in very high-seismic hazard regions designed in accordance with current ASCE/SEI 7 requirements. The focus is on identifying and quantifying "generic" trends in the seismic collapse performance of buildings in very high-seismic hazard regions, not on providing data for other purposes, such as to re-evaluate the values of Response Modification Coefficients, *R*, of specific seismic -force-resisting systems (SFRSs). The project also sought to identify weaknesses in current code provisions and design standards for buildings in very high-seismic regions and to provide recommendations for conceptual code changes to seismic codes and standards, as well as for future studies.

1.2 Regions of Very High Seismicity

For this work, very high-seismic (VHS) regions are defined by ground-motion intensity greater than the strongest level of shaking required by FEMA P-695 for evaluation of a new seismic-force-resisting system proposed for incorporation into Table 12.2-1 of ASCE/SEI 7-22 or for evaluation of an alternative structural system as permitted by Section 12.2.1.1 of ASCE/SEI 7-22. The strongest level of shaking required by FEMA P-695, referred to therein as Seismic Design Category (SDC) D_{max}, has a short-period Maximum Considered Earthquake (MCE) spectral acceleration of $S_{MS} = 1.5g$ (i.e., $S_{MS} = F_a S_S = 1.0 \times 1.5g$) and a 1-second MCE spectral acceleration of $S_{M1} = 0.9g$ (i.e., $S_{M1} = F_v S_1 = 1.5 \times 0.6g$) of ASCE/SEI 7-05, assuming a default condition of Site Class D. ASCE/SEI 7-05, *Minimum Design Loads for Buildings and Other Structures* (ASCE, 2005), was the current version of ASCE/SEI 7 when the FEMA P-695 methodology was developed in 2009. The ground-motion criteria of FEMA P-695 intentionally exclude buildings at sites in regions of very high seismicity (i.e., $S_{MS} > 1.5g$ or $S_{M1} > 0.9g$) by implicitly accepting greater risk for these buildings (Section 5.2.2, FEMA P-695). The focus of this investigation is on understanding and quantifying the increased "risk" of building collapse in these VHS regions.

Figure 1-1 is a map of U.S. states and territories with regions of very high seismicity (i.e., $S_{MS} > 1.5g$ or $S_{M1} > 0.9g$) shaded in red. Seismicity is defined using the ASCE/SEI 7-22 ground motions and assuming default site conditions, which for ASCE/SEI 7-22 is taken as the maximum response of Site Classes C, CD, and D.

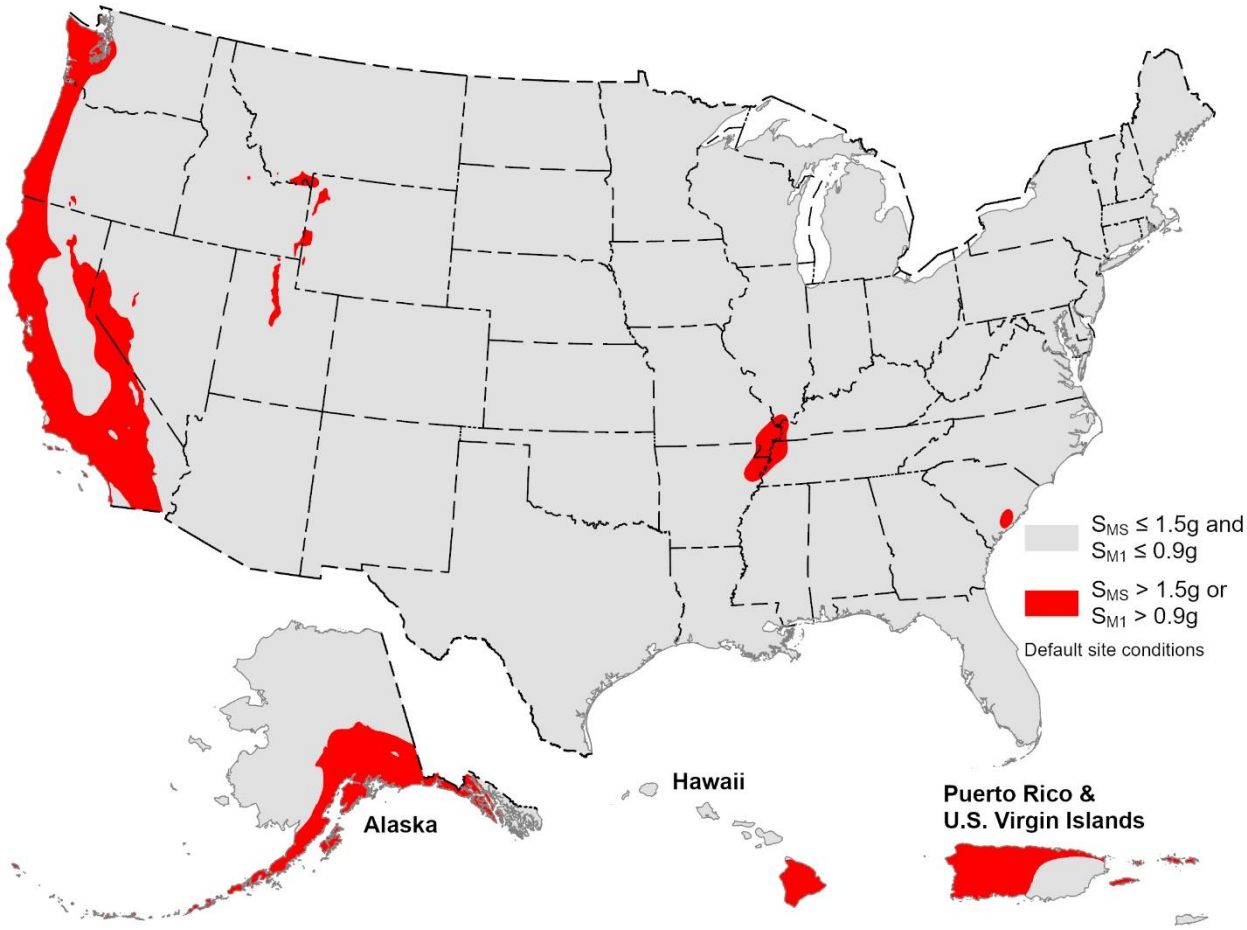

Figure 1-1 Map of U.S. states and territories showing areas of very high seismicity ($S_{MS} > 1.5g$ or $S_{M1} > 0.9g$) using ASCE/SEI 7-22 ground motions assuming default site conditions (image credit: USGS).

ASCE/SEI 7 response spectral intensities changed for default site conditions between ASCE/SEI 7-05 (i.e., the ground motions referenced by FEMA P-695) and ASCE/SEI 7-22, where values for the latter are greater over all periods (see Section 6.1 for more details). However, this investigation uses the FEMA P-695 SDC D_{max} response spectrum to define the boundary between high-seismic and very high-seismic ground motions because these are the highest ground motions required by ASCE/SEI 7-22 for evaluation of a new seismic-force-resisting system. As will be seen in future chapters, the definition of the very high-seismic boundary is primarily used in this report to help establish a baseline ground-motion spectrum that can be referenced and compared against. Furthermore, because the intent of this investigation is to understand and quantify the increased risk

of building collapse in regions of very high seismicity, a large range of seismicity extending from much lower to much higher values than the boundary is considered. It should be noted that regions of very high seismicity include, and are larger than, near-fault regions as defined by the ASCE/SEI 7-22 Deterministic Lower Limit (DLL) response spectrum.

The definition of very high seismicity in this report should not be confused with the ASCE/SEI 7 definition of SDC E or SDC F. Structures are assigned these seismic design categories when they are located where the 1-second mapped spectral response acceleration parameter, S_1, is greater than or equal to 0.75g (ASCE/SEI 7 Section 11.6). Risk Category I, II, or III structures are assigned to SDC E, and Risk Category IV structures are assigned to SDC F. The definition of very high-seismic ground motions used in this report is more comprehensive than the ASCE/SEI 7 definition of SDC E or SDC F because this report's definition: (1) considers both short-period and 1-second spectral response acceleration values; (2) uses spectral accelerations that are adjusted for site effects by assuming the default site condition; and (3) includes 1-second spectral accelerations less than $S_1 = 0.75$g (i.e., as low as $S_1 = 0.6$g).

1.3 Potential Scope of the Problem

Observations of building performance in past earthquakes consistently show trends of much worse damage and loss in areas where the ground shaking is very strong. For example, the 1995 Kobe earthquake in Japan is notable because buildings close to the fault rupture (within 5 km, or 3.1 miles) were subjected to very strong ground shaking and experienced collapse rates greater than 20%, whereas the collapse rate was only about 1.2% for all buildings located greater than 5 km from fault rupture collapsed (FEMA, 2020).

Most buildings that collapsed in the 1995 Kobe earthquake were older (pre-1981) construction, whereas modern construction sustained less structural damage and had much lower collapse rates. For example, newer (1982–1994) Japanese wood-frame buildings performed relatively well considering the strength of the ground motions. In the Nada Ward of Kobe City, where median short-period (0.3-second) spectral accelerations were about 2.0g, about 16 percent of newer wood-frame buildings were heavily damaged, whereas in this same ward, about 57 percent of all older (pre-1981) wood-frame buildings were heavily damaged (FEMA, 2020).

Observations of building damage from the 1995 Kobe earthquake and other non-U.S. earthquakes where ground motions were very strong are not directly applicable since construction is different from that in the United States. Conversely, observations of building damage in the 1994 Northridge earthquake and other U.S. earthquakes are of limited value since ground motions rarely exceeded those of the boundary between high and very high seismicity (e.g., 1.5g at short periods). In summary, there is not sufficient historical earthquake data to reliably quantify the increased risk of collapse for U.S. buildings designed and subjected to very high-seismic ground motions relative to buildings designed and subjected to lower seismicity levels. However, it is possible to quantify the population and building exposure in regions of very high seismicity, providing a measure for the potential scope of the problem.

Table 1-1 and Table 1-2 present estimates of population and building exposure (number, occupancy, and value of buildings) in VHS regions throughout all U.S. states and territories. Table 1-1 presents the data using the short-period criterion ($S_{MS} > 1.5g$) for very high seismicity, and Table 1-2 presents the data using the 1-second criterion ($S_{M1} > 0.9g$). Similar to Figure 1-1, seismicity is defined using the ASCE/SEI 7-22 ground motions and assuming default site conditions. More information about assumptions and sources of data are in Appendix A, which also presents population and building exposure binned by more discrete values of S_{MS} and S_{M1}.

About 42.9 million people live or work in regions of very high seismicity (defined by $S_{M1} > 0.9g$), and about 11% of U.S. buildings, representing $7.5 trillion in replacement costs, are in regions of very high seismicity (defined by $S_{M1} > 0.9g$). These figures are slightly less when the VHS boundary is defined by $S_{MS} > 1.5g$. Two-thirds of the U.S. building replacement costs in VHS regions are residential, and one-third is non-residential. The three West Coast states of California, Oregon, and Washington account for 84% of the U.S. population and 80% (by number) of the U.S. building exposure that are in regions of very high seismicity. California is the major driver, accounting for 30.7 million of the 42.9 million people in VHS regions. However, other states and territories with notable VHS exposure include Utah, Puerto Rico, Nevada, Alaska, South Carolina, Hawaii, Guam, Missouri, and Tennessee. In some cases, the percentage of the population in VHS regions is significant even outside of the West Coast. For example, Utah, Puerto Rico, and Alaska all have about 70% of their population in VHS regions. See Appendix A for more details.

Table 1-1 Population, Number of Buildings, and Building Replacement Value for all U.S. States and Territories Binned by Values of Short-Period MCE_R Response Spectral Acceleration, S_{MS}, of ASCE/SEI 7-22

ASCE/ SEI 7-22 S_{MS} Bins	Population (in millions)	Distribution of Buildings		Replacement Value ($ in billions)		
		Number (in millions)	Percent	Residential Buildings	Non-Res. Buildings	All Buildings
All	335.1	124.5	100%	39,898	22,477	62,375
≤ 1.5g	295.6	112.4	90%	35,309	20,084	55,393
> 1.5g	39.4	12.1	10%	4,590	2,392	6,982

Table 1-2 Population, Number of Buildings, and Building Replacement Value for all U.S. States and Territories Binned by Values of 1-second MCE_R Response Spectral Acceleration, S_{M1}, of ASCE/SEI 7-22

ASCE/ SEI 7-22 S_{M1} Bins	Population (in millions)	Distribution of Buildings		Replacement Value ($ in billions)		
		Number (in millions)	Percent	Residential Buildings	Non-Res. Buildings	All Buildings
All	335.1	124.5	100%	39,898	22,477	62,375
≤ 0.9g	292.2	111.2	89%	34,904	19,931	54,835
> 0.9g	42.9	13.3	11%	4,995	2,546	7,540

1.4 Approach and Scope of Studies

Four seismic-force-resisting systems were selected for study: (1) wood light-frame walls with wood structural panel sheathing (wood), (2) steel buckling restrained braced frames (BRBFs), (3) steel special moment resisting frames (SMFs), and (4) reinforced concrete ductile coupled walls (DCW). The selected systems are common for new construction in very high-seismic hazard regions for a wide range of occupancies.

Two sets of technical studies were conducted. One set, which is documented in Chapter 2, investigated the expected ranges of building overstrength ($\Omega = V_{max}/V$) for the selected systems designed to current codes and standards for Risk Category II and IV structures. These studies considered, where appropriate, contributions from elements not considered part of the seismic-force-resisting system (e.g., gravity frames, partitions), and related overstrength as a function of S_{MT}, which is the value of MCE_R response spectral acceleration at the code-based fundamental period, T, for a given archetype model.

The second set of technical studies investigated the computed collapse performance of the selected systems using building archetypes representing modern design and construction practices for Risk Category II and IV structures. Archetype configurations representing structure only (i.e., no nonstructural elements), commercial, and multi-family dwelling occupancies were investigated for wood systems. All archetypes of the non-wood systems represent commercial occupancies.

Two-dimensional, nonlinear, multi-degree-of-freedom (MDOF) models were used for the wood archetypes, and equivalent single-degree-of-freedom (eSDOF) nonlinear models were used for the non-wood archetypes. These simplified models, which were calibrated against more detailed models that were developed from a variety of prior research studies. Simplified models were used in order to reduce the computational demands of nonlinear time history analyses and increase the number of individual models that could be analyzed. A validation study for the eSDOF models of the steel SMF system was conducted that involved developing detailed archetype designs and two-dimensional MDOF models.

eSDOF models of non-wood systems were created based on the nonlinear MDOF models and analysis results of prior research studies. Different from traditional SDOF models, an eSDOF model translates the detailed model's collapse failure mode, system pushover curve, period, and force and displacement relation into a nonlinear single-degree-of-freedom model. The eSDOF model is then calibrated to match the corresponding MDOF model performance. This method is shown to accurately represent the MDOF model collapse performance trends.

For each system, numerical models were developed for large numbers of archetypes of varying height (or number of stories), strength, and displacement capacity, reflecting the full range of expected values for these parameters that are likely to occur in modern low-rise and mid-rise buildings. The archetypes encompassed a broad range of strengths representative of different designs for MCE_R response spectral accelerations spanning moderate seismic regions (e.g., S_{MS} = 0.75g) to the strongest level of expected ground motions in regions of very high seismicity (e.g., S_{MS} = 3.0g). Importantly, the vast majority of the modeled archetypes (except those used for calibration or validation) are representative of designs but were not actually designed, as is described in more detail in Chapter 3. This innovative approach enabled the investigation of about 800 archetype models of the four SFRSs.

The archetype models were used to calculate collapse probabilities given MCE_R ground motions in accordance with the methods of FEMA P-695, with some noted adaptations. For example, in order to calculate a more realistic view of performance, the analyses include contributions from elements not considered part of the SFRS (e.g., gravity frames), whereas FEMA P-695 strictly speaking only requires analysis of the SFRS. The FEMA P-695 Far-Field record set was the primary record set used by this study for collapse evaluations; however, the FEMA P-695 Near-Field record set also was used to analyze the wood multi-family dwelling archetypes. Both sets contain strong-motion records from earthquake sources that are typical of shallow crustal events in California and other Western U.S. locations.

The technical studies provide extensive data for determining the differences in the expected seismic collapse performance of buildings designed and subjected to a range of ground motions, including the strongest level of ground motions in regions of very high seismicity. These data, which are summarized in Chapter 6, are the basis for recommendations for conceptual changes to seismic design codes and standards, as well as for future studies, presented in Chapter 7.

1.5 Organization and Content

This report describes the results of analytical studies that investigated the seismic collapse performance of buildings in very high-seismic hazard regions. The focus is on identifying and quantifying generic collapse trends, not on providing data for other purposes, such as to re-evaluate the values of *R* of specific SFRSs.

Chapter 2 presents the expected ranges of building overstrength for selected systems designed to current codes and standards for Risk Category II and IV structures.

Chapter 3 documents the procedures followed for conducting the analytical studies.

Chapter 4 presents model development and collapse results for the wood archetypes.

Chapter 5 presents model development and collapse results for non-wood archetypes.

Chapter 6 summarizes results of the Chapter 4 and Chapter 5 collapse evaluations and develops trends of increased collapse risk in VHS regions.

Chapter 7 provides recommendations for seismic code changes and future study.

Appendix A documents the work done to quantify population and building exposure in VHS regions.

Appendix B provides background information for the Chapter 2 overstrength study.

Appendix C summarizes the analytical procedures of Chapter 3 in a succinct step-by-step guide.

Appendix D provides background information about the process for developing the wood MDOF models used in Chapter 4.

Appendix E provides background information about the process for developing non-wood eSDOF models used in Chapter 5.

Appendix F provides background information about model development and results for the steel SMF validation study that is presented in Chapter 5.

Appendix G provides background information about the capacity spectrum method and examples of its use. This method is introduced in Chapter 6 as a way to help explain the computed trends in collapse performance.

Appendix H presents detailed collapse results for the wood models.

Appendix I presents detailed collapse results for the BRBF models.

Appendix J presents detailed collapse results for the steel SMF models.

Appendix K presents detailed collapse results for the DCW models.

References and a list of project participants are provided at the end of the report.

Chapter 2: Building Overstrength

2.1 Introduction

Total strength and total displacement capacity were found to be the most important parameters influencing the collapse performance of the high-seismic baseline archetypes studied in previous research efforts (FEMA, 2020). Total strength is more than the minimum required strength defined in seismic design standards. It generally includes the expected strength of the defined seismic force-resisting system (SFRS) and contributions from elements that are not part of the SFRS. The ratio of total to required strength is referred to as overstrength and is the focus of the material presented in this chapter.

The purpose of this chapter is to identify and quantify sources of building overstrength. Building overstrength is considered a major contributing factor for seismic performance of buildings. ASCE/SEI 7 requires SFRS design to provide minimum strength to achieve the intended seismic safety performance criteria. The quantification of building overstrength is provided for the four systems being investigated, as described in Chapter 1. Building overstrength comes from several sources in addition to the SFRS, and the contributions from these other sources vary depending on several factors, such as the use of the building.

Similar to overstrength, total displacement capacity, which is another major factor influencing system building seismic performance, can be beneficially influenced by sources outside the SFRS, and the results associated with this type of increase in displacement capacity are also described in this chapter. However, the quantification of total displacement capacity is defined in the collapse analysis modeling described in Chapter 4 and Chapter 5.

A portion of overstrength comes from design factors, linear analysis, capacity-design based details, conservative bias in the nominal strength of components of the SFRS, and strain-hardening. Additional overstrength includes contributions from the non-SFRS structure (gravity system), nonstructural components (e.g., partitions) and architectural configuration (e.g., where walls serve architectural and structural function).

Overstrength is defined as the ratio of total strength to required strength, as follows:

$$\Omega = V_{max}/V \tag{2-1}$$

where:

V_{max} is the pushover strength, or for some systems, the peak strength in the cyclic envelope, and

V is the design base shear (required strength) taken from ASCE/SEI 7 Section 12.8 and equals C_sW

Although this simple expression is unchanged, details of determining C_S and the values of ground motion parameters have changed since the development of the FEMA P-695 methodology (see Chapter 6 for a discussion of how design ground motion parameters have changed).

In this context, the term overstrength refers to real strength greater than the design strength and not to the design overstrength factor, Ω_0, defined in Chapter 11 of ASCE/SEI 7, which is used to estimate maximum demands on elements that are required to remain essentially elastic. Values of Ω can be smaller or larger than those of Ω_0.

There are circumstances in which the strength or stiffness of non-SFRS elements changes the behavior in undesirable ways. For example, the inclusion of partial height masonry infill walls in a concrete moment frame system does increase the overall strength, but it has been shown to reduce the deformation capacity by inducing shear failure of the columns of the moment frame. Such behavior is controlled by deformation compatibility requirements in the seismic design standard and is not given further consideration here.

The FEMA P-2139 study found that the sources and the amount of overstrength varied between different types of buildings. In this study, building overstrength is characterized as coming from several sources, including:

- The SFRS—this is the difference between the expected SFRS strength and the minimum required design strength,
- Gravity System, both its inherent strength and its effect on the SFRS performance,
- Nonstructural Building Components—mainly derived from full height partitions, and in light frame construction, additional sheathings and finishes on all walls, and
- Architectural configuration overstrength—occurs when the provided SFRS is more than is required due to other design constraints, such as masonry walls between classrooms in a school building.

All these contributions vary with the type of SFRS and with building occupancy, and this chapter does not explore all building types. For example, single story stiff wall, flexible diaphragm buildings would require additional considerations, but that is beyond the scope of this study.

The required strength goes up with increasing ground motion intensity, and for systems controlled by strength, the expected strength of the SFRS goes up in proportion. For systems controlled by drift, the increase in SFRS strength can be even more. The gravity system contribution to strength does not go up with increasing ground motion intensity, thus this contribution to the ratio decreases with increasing ground motion. Similarly, nonstructural building components strength does not go up with increasing ground motion intensity. In some SRFS (mainly light-frame wood buildings), the nonstructural building components strength contribution decreases with increasing ground motion intensity since some nonstructural building components are replaced by SFRS components. In all systems considered, the nonstructural contribution to overstrength decreases with increasing ground

motion. Similarly, architectural configuration overstrength does not go up with increasing ground motion intensity, and thus the contribution due to architectural configuration decreases with increasing ground motion intensity.

For strength-controlled designs the overstrength ratio considering all the constituents goes down with increasing ground motion intensity. For drift-controlled systems, this is not necessarily true.

There are also circumstances where the strength and stiffness of non-SFRS elements change the SFRS behavior in desirable ways without significantly increasing the peak resistance of the building as a whole. For example, by vertically distributing the SFRS yielding to more stories, the deformation capacity of the SFRS increases. The V_{max} value for the SFRS pushover can remain nearly unchanged, but, due to distributing the yielding to more floors, the displacement of the structure as a whole beyond peak resistance increases. This effect is most pronounced in stiff SFRS that tend to concentrate their yielding over only a few floors. Specific examples include Special Concentrically Braced Frames (SCBF) and Buckling-Restrained Braced Frames (BRBF). An example of this effect for a BRBF follows.

Figure 2-1 shows the pushover result for a 9-story BRBF archetype derived from data by Ochoa (2017) (see Chapter 5 for more details). BRBF9-1 shows the pushover result for the archetype with the BRBF columns oriented in their weak axis. BRBF9-2 shows the pushover result for the archetype with the BRBF columns oriented in their strong axis, which results in an increase in the deformation capacity of the system. BRBF9-3 shows the pushover result for the archetype with the BRBF columns oriented in their weak axis and including the gravity columns, which results in an even larger increase in deformation capacity of the system. The resulting increase in displacement capacity here exceeds 100%, while the increase in V_{max} is only about 5%.

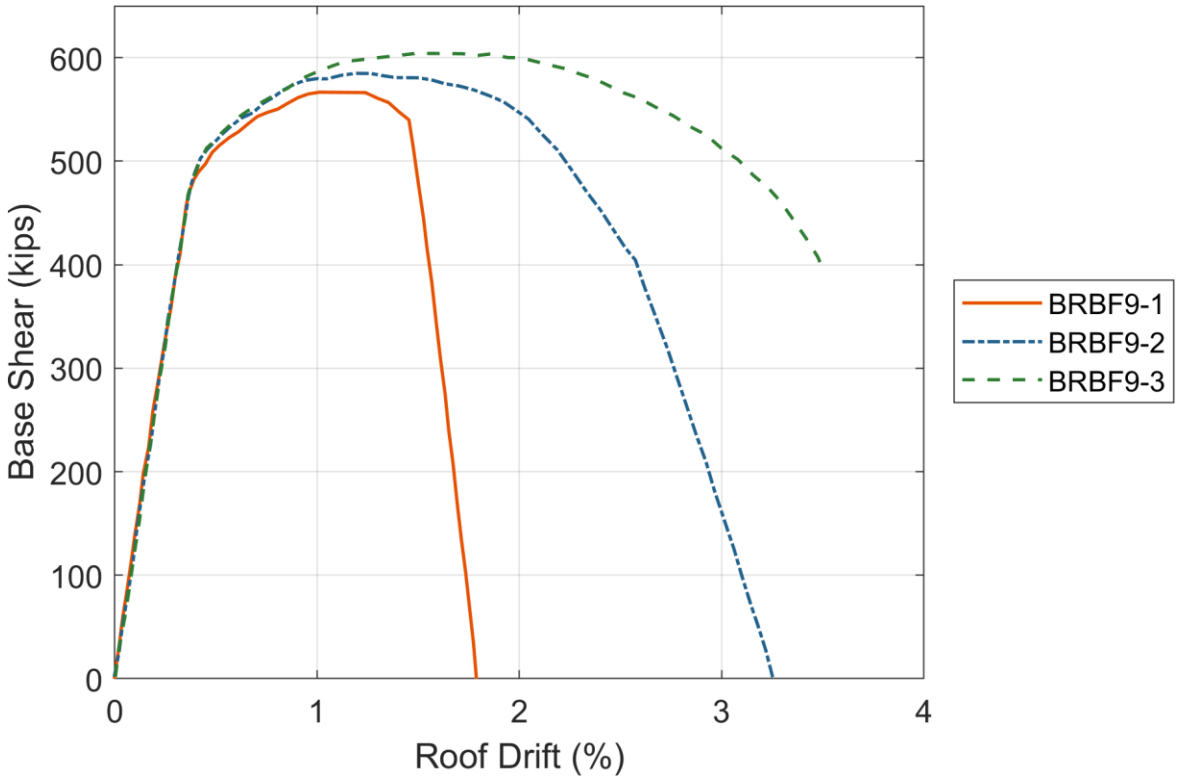

Figure 2-1 9-Story BRBF pushover curves derived from data by Ochoa (2017).

In such systems the beneficial effect on displacement is not captured by Ω, but Chapters 4 and 5 include this effect in the development of their backbone envelopes.

2.2 Overview and Approach

In this section, a general treatment of SFRS, gravity system, nonstructural, and architectural configuration is developed. Depending on the particular SFRS, the strengths from sources outside the SFRS itself can sometimes be more conveniently treated by combining sources.

2.2.1 Seismic Force-Resisting System Overstrength

SFRS overstrength can come from a variety of sources. The basic SFRS overstrength is given by the following:

$$\text{SFRS Overstrength} = \text{bias in design} \times (1/\varphi) \times (\text{expected/nominal strength}) \quad (2\text{-}2)$$

where φ is the resistance factor from the material standards and varies by SFRS.

The range for most systems is approximately 1.25-2.5. Factors affecting this range are described below. Bias in design is affected by several factors including:

- Design conservatism (e.g., conservatism to cover contingencies late in design versus "tight" design),
- Constraints on geometric layout (e.g., vertical alignment of light frame walls from story to story, or minimum sizes of stairwells and elevator shafts in low rise shear wall buildings),
- Constraints on member proportions (e.g., catalogue of available sizes that meet detailing limitations, which was shown to be significant in low rise SCBF in FEMA P-2139-4), and
- Capacity-limited design approaches. AISC 341 Capacity Limited Design approach results in stronger, and frequently stiffer, members outside the "fuse" resulting in additional overstrength from these members (e.g., columns in SCBF and BRBF).

Going from the required strength to the nominal strength ($1/\varphi$) is the first step in estimating the expected strength. Values of φ can vary from 0.9 to 0.5. Thus, this factor can be significant.

Nominal strength definitions are generally simplified versions of true best estimates, and they are also generally based on specified material properties, rather than expected material properties. Both differences can be significant.

Other factors affecting SFRS overstrength include the following:

- SFRS governed by minimum base shear equations

  In very high-seismic sites, the minimum base shear equations (ASCE/SEI 7 Eq. 12.8-6 and 12.8-7) governs when:

  - $T >$ ~2.5 s for response modification factor, $R = 8$
  - $T >$ ~3.2 s for $R = 5$ or 6

  The multi-period spectra approach in ASCE/SEI 7-22 influences the period at which these minimum base shear equations become effective. See Appendix B.4 for more details on this issue.

- SFRS governed by wind loads

  Studies indicated overstrength from wind is not an issue in very high seismic hazard sites for buildings being considered (buildings with periods resulting in the seismic base shear not being governed by the minimum base shear equations). See Appendix B.3 for more detail on this issue. It is possible that Risk Category IV buildings in the most tornado-prone regions could be an exception, but this was not studied.

- SFRS governed by drift

Experience shows that steel SMF are governed by drift resulting in increased building overstrength, with overstrength values reaching 2 in some situations, and even more for buildings assigned to Risk Category (RC) IV. Overstrength due to the drift-controlled nature of steel SMF are discussed in Section 2.4 and includes the results of a 9-story, three-dimensional archetype that was designed for varying seismic hazard regions. Overstrength results of the same 9-story archetype designed to RC II and RC IV criteria are discussed in Section 2.7. The design of BRBF and tall wood light-frame buildings assigned to RC IV can also be controlled by drift. The extra overstrength for drift control in RC IV buildings with these last two systems is not quantified in this study.

- Analysis method (Response Spectrum Analysis (RSA) vs. Equivalent Lateral Force (ELF)) used in design process.

  Studies based on ASCE/SEI 7-05 and ASCE/SEI 7-10 indicate that ELF design could increase overstrength by a factor of 1.5-2 for some systems and especially for those that are drift controlled. This range is reduced to approximately 1.2 to 1.7 with the change in ASCE/SEI 7-16 that requires RSA design base shears be scaled to 100% of the ELF base shear.

Previous research (NIST GCR-10-917-20) examined the relative importance of ductility and overstrength as constituents of an overall value for *R*. Figure 2-2 is a plot from that study; the vertical axis is an estimate of the portion of the *R* factor that can be attributed to displacement ductility, while the horizontal axis is the overall *R* factor that would deliver a 10 percent probability of collapse at the MCE_R demand for the archetype studied. The radial lines are the horizontal axis divided by the vertical axis. The various archetype results indicate a range of SFRS overstrength (R_O in the Figure 2-2, denoted as Ω in this report) for a variety of systems.

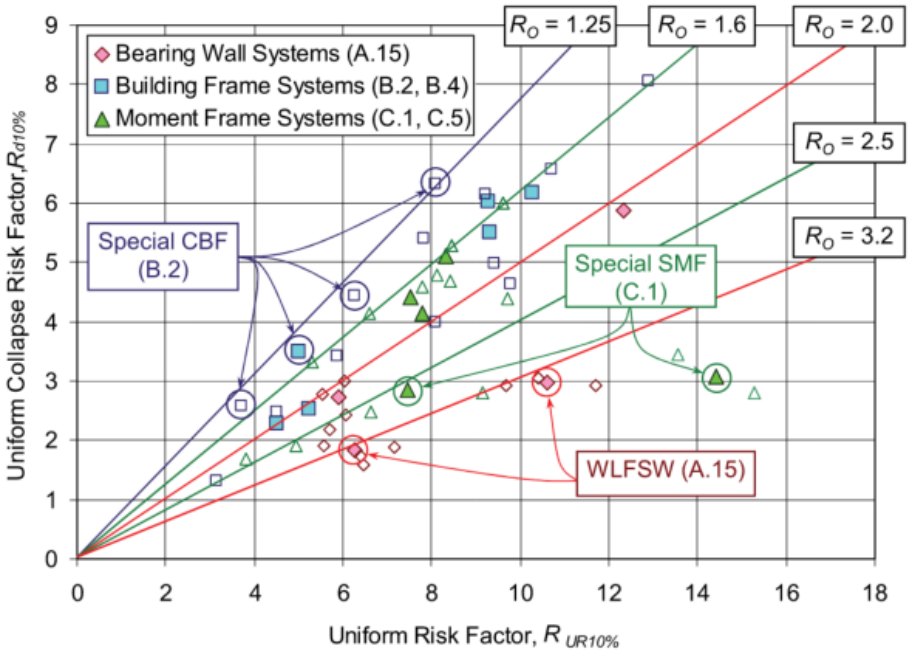

Figure 2-2 Overstrength factors (R_O) from NIST GCR-10-017-20.

Below are the recommended lower-bound Ω values from that study by system.

- Bearing Wall Systems:
  - Wood light-frame shear wall with low aspect ratio (WLFSW, A.15): $\Omega = 2.0$
  - WLFSW with high aspect ratio: $\Omega = 3.2$

  The change in the nominal strengths and the resistance factor φ in the 2021 edition of the wood design standard (SDPWS) does affect these values, because the design strength did not change.
- Building Frame Systems:
  - Special SCBF (B.2): $\Omega = 1.25$
  - Special Reinforced Concrete Shear Wall (RCSW) (B.4): $\Omega = 1.6$
- Moment Frame Systems:
  - Special SMF (C.1): $\Omega = 2.5$
  - Special Reinforced Concrete Moment Frame (RCMF) (C.5): $\Omega = 1.6$

Specific values for overstrength are provided for each system evaluated in this study and are informed by these lower-bound values and are based on more analysis than the factors shown in Figure 2-2.

2.2.2 Gravity System Overstrength

Gravity system overstrength generally refers to the moment-resisting frame action of beams or slabs and columns that are not part of the SFRS, and thus it varies by material and gravity system. For the two predominant concrete floor systems, beam-and-slab and flat slab, the gravity system overstrength can range from 0.1 to over 2, particularly when considering both frame-wall interaction and outrigger action. For steel gravity systems, the gravity system overstrength is affected by framing direction (short vs long), style of beam-to-columns connections and the presence of a composite concrete and steel deck. For wood light frame systems, the contribution of non-SFRS load bearing walls is governed by the sheathing. The contribution of beam and post frame action is not considered herein.

In addition to the moment frame action of the gravity framing systems just described, gravity columns alone can have an important effect on system overstrength, provided the columns are continuous. As noted previously for the BRBF example, the contribution of such columns to the maximum strength of the structure (V_{max}) may be small, but the columns can increase the overall displacement capacity, including the displacement at collapse.

2.2.3 Nonstructural Building Components Overstrength

Nonstructural building component overstrength generally comes from the following:

- Nonstructural full height partition walls,
- Masonry veneer over concrete masonry unit (CMU) walls, depending somewhat on the connections (ties), and
- Infill in frames (generally not present in new buildings).

Overstrength of light-frame buildings (wood and cold-formed steel) is strongly affected by sheathing materials on all walls: SFRS walls, bearing walls, non-bearing exterior walls, and nonstructural partition walls. Gypsum wallboard (GWB) is used as the interior finish over shear panels or bracing. Exterior sheathings include exterior rated GWB, fiberboard, and structural wood panels, usually covered with exterior finish materials, such as stucco, which can make significant contributions to overstrength.

Light-frame-building overstrength includes increases in rocking (wall overturning) resistance provided by perpendicular walls acting as flanges. For a given building type and exterior finish material, the strength from these sheathings is relatively constant regardless of ground motion intensity or number of stories, thus the overstrength ratio goes down with increasing ground motion and with increasing stories because the required design strength goes up in both cases. In some

circumstances the strength from nonstructural sheathings can actually decrease with increasing ground motion demand (e.g., where exterior nonstructural sheathing under the finish is replaced by sheathing panels designed as part of the SFRS).

Exterior cladding and sheathing on interior partitions generally do not provide much overstrength in steel and concrete framed buildings. In part this is due to weak or non-existent connection at the top of partitions. Steel moment frame systems are an exception, in that full-height partitions at shafts, restrooms, and fire-rated corridors can make measurable contributions. Architectural precast concrete cladding is not considered in this study; it is usually isolated in a fashion that it provides no racking resistance.

2.2.4 Architectural Configuration Overstrength

Architectural configuration overstrength occurs when the provided SFRS is more than is required due to other design constraints (e.g., acoustic separation, fire resistance). This occurs mainly in SFRS comprised of wall systems. Generally, the unit strength of such walls is designed to material-specific minimum values, but since the length of the walls is more than is required to meet the design force level, the resulting SFRS overstrength can be quite large. Building occupancy affects the potential additional SFRS overstrength. While some occupancies can provide this additional SFRS, others are likely not to as indicated in Table 2-1.

Table 2-1 Building Occupancies Effect on Architectural Configuration Overstrength

Occupancies Providing Additional SFRS Architectural Configuration Overstrength	Occupancies Not Providing Additional SFRS Architectural Configuration Overstrength
Classroom	Offices
Hotel	Retail
Warehouses/Big Box Retail	Hospitals
Some residential	Life Science Labs

2.2.5 Results

Overstrength recommendations for the purpose of this study are developed on a system-by-system basis in the following sections.

- Section 2.3 Light-Frame Buildings
- Section 2.4 Steel Special Moment Frames Buildings
- Section 2.5 Steel Buckling-Restrained Braced Frames Buildings
- Section 2.6 Reinforced Concrete Ductile Coupled Walls Buildings

2.3 Light-Frame Building Overstrength

Light-frame construction has the potential for significant overstrength from the various sheathing and finish materials applied to the walls, depending on the occupancy and architectural style. Wood light-frame buildings are the focus in this study, but the non-SFRS wall sheathing contributions are expected to be very similar for cold-formed steel light frame buildings of the same type of occupancy. The SFRS overstrength for steel light-frame systems has not been reviewed, and there is no expectation that it will be the same as found for wood light-frame.

2.3.1 Wood Light-Frame SFRS Overstrength

The 2021 edition of the AWC NDS Special Design Provisions for Wind and Seismic (SDPWS) have raised the nominal strengths and lowered the design resistance factors, but the design strengths have not changed substantially. The bias of expected strength over nominal strength is now 1.07, and the resistance factor is 0.5. The bias in design strength provided over design strength required is real and inherently tends to go up in the upper stories of multistory light-frame buildings. Previous studies (FEMA, 2020) have demonstrated that the collapse mechanism in wood light-frame buildings is essentially always in the first story. That study included several designs of archetypical multi-unit residential (MFD) and commercial (COM) buildings. Taking the four-story designs from that study, the design bias in the first story was 1.05 for MFD and 1.14 for COM; the mean for the combined set was 1.10.

Given those numbers, the expected overstrength in the SFRS itself is calculated thus:

$$OS_{SFRS} = (1.07/0.5) \times 1.1 = 2.35$$

There is the distinct possibility that wood light-frame buildings taller than four stories will have additional SFRS overstrength due to the drift requirements in ASCE/SEI 7. The drift limit in ASCE/SEI 7, for low rise Risk Category II buildings, is 0.025 times the story height, but that limit drops to 0.020 for five stories and taller. The most significant contribution to drift in wood shear panels is the combination of nail slip and shear strain in the sheathing. Axial tension and compression in the end posts is the next most significant contribution to drift. These values are not constant for all design possibilities. The nail slip and shear strain drift of OSB sheathing is quite different than that for plywood sheathing. For a reasonable mix of thicknesses, nail size, and nail spacing, the drift ratio of OSB sheathing ranges from 0.9% to 1.3%, with an average of 1.1%. For the same mix, the drift ratio of plywood ranges from 1.5% to 2.6%, with an average of 1.9% (all values include the C_d factor of 4). A reasonable approximation of the drift due to flexure (strain in the end posts) is 0.25%. The basis of these drift estimates due to shear and flexure is in Appendix B. The estimates are based upon walls with a height to length ratio of 1; drifts are much higher for narrow panels, but once that ratio drops below 0.5 the design capacity is reduced, essentially to compensate for the drift issue. If full height steel tension rods are used, the flexural contribution to drift can easily double. Therefore, it is very conceivable that taller wood light frame buildings, especially over four stories, will have additional SFRS overstrength if they are designed:

- with plywood rather than OSB,
- with 10d nails at close spacing, and
- with a preponderance of height to length ratios less than 1.

On average, there will be no additional strength in the SFRS due to drift requirements.

There is variability in all the contributions to SFRS overstrength. Laboratory test data does not show large variability, but the conditions in a lab are much more carefully controlled than actual construction. There is not much data on the strength of in-place construction. In the studies behind the development of load and resistance factor design provisions (NBS SP577), a coefficient of variation of 0.18 was used for the calibration examples, derived from data for the flexural strength of glued-laminated beams. Nailed wood shear panels are assembled at the construction site, not in a factory. Even though the inherent variability of nails is less than natural or engineered lumber, the overall variability of as-built shear walls is very likely higher than that for glu-lam lumber.

One could attempt to infer a coefficient of variation from the resistance factors in SDPWS. If the target reliability for a strength failure under wind were actually in line with the objectives in Chapter 1 of ASCE/SEI 7 (e.g., a 50-year reliability index of 3.0), the resistance factor for wind of 0.8 would imply a coefficient of variation under 0.15. On the other hand, the resistance factor of 0.5 for seismic loads would imply a coefficient of variation over 0.35. That low resistance factor is undoubtedly driven more by the uncertainty in inelastic response than variation in peak strength. Given the paucity of data and the fact that the objective here is to establish first a central trend and second a reasonable range, a round value of 0.2 is adopted for a coefficient of variation in the SFRS overstrength for wood shear walls. This value includes the contribution from design overstrength, which itself is smaller than the as-built variability, as well as being statistically independent.

Figure 2-3 shows the central trend and recommended range of SFRS overstrength, which does not vary with ground motion intensity nor with type of occupancy.

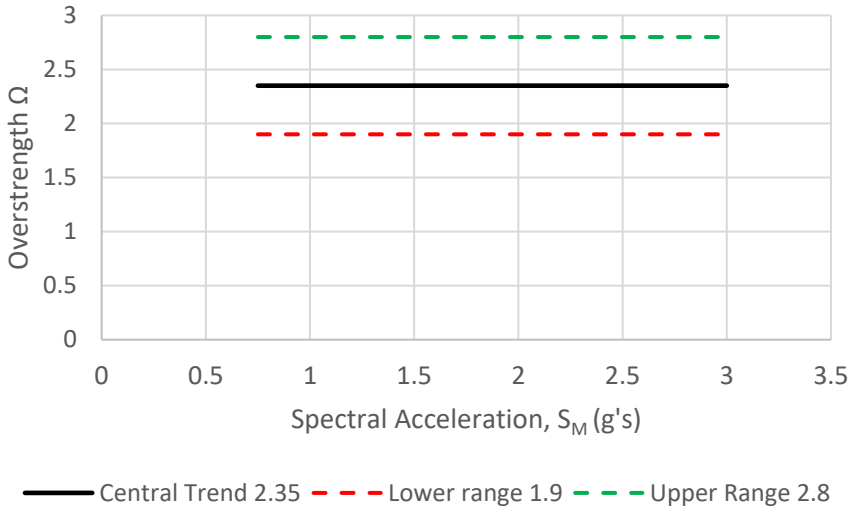

Figure 2-3 Wood light-frame SFRS overstrength.

2.3.2 Wood Light-Frame Overstrength from non-SFRS Sheathings and Finishes

Sheathing on light framing provides resistance to racking. Since the development of light framing in the 19th century, there have been many variations in sheathing materials and configurations. Currently popular sheathings include:

- Gypsum wallboard (GWB) on all interior surfaces as a base for paint and other finishes, almost to the exclusion of any other material,
- GWB, OSB, plywood, or fiberboard on the exterior face of exterior walls, usually as a base for a finish, and
- Some currently popular exterior finishes, such as stucco, can also provide racking resistance.

The primary variation in GWB is the thickness, with ½" being used where fire resistance is not required and 5/8" being generally used where fire resistance is required. Double layers are sometimes used for improved acoustic separation or for a higher degree of fire resistance. Another variation is that the attachment of the GWB to the framing is sometimes indirect, via acoustic isolation strips of very light gage cold-formed steel (referred to as resilient channels). The peak strengths of gypsum wallboard used in this study are (refer to Appendix B for more detail):

- 200 pounds per lineal foot (plf) for one layer of ½" GWB directly applied,
- 250 plf for 5/8" GWB directly applied, and

- 250 plf for a double layer of 5/8" GWB attached to resilient channels.

There are significant variations in finish materials applied to the exterior face of exterior walls. Stucco is currently the most popular finish, by a wide margin. (For the purpose of this study, synthetic stone and thin brick embedded in mortar is essentially the same as stucco.) In the past stucco was applied to the framing with no sheathing beneath, only a moisture barrier, such as asphalt paper, but several decades ago some type of board sheathing was applied to the framing before the stucco. In recent years OSB has been the underlayment of choice for most buildings because it is cost effective.

Additional exterior finish materials include horizontal board siding, plywood panels that serve as both sheathing and finish, various types of particle and cement boards, and metal panels. Many of these alternate materials are used as accents, and where they are so used, it is typically above the first story. The strength values used in this study for exterior finish are:

- 1000 plf for stucco, and

- 200 plf for horizontal board siding.

The peak strengths of the nonstructural materials cannot be added directly to the peak strength of the designed shear walls. The basic rule for evaluation of capacity of combined materials is to reduce them by 50%. While that is an appropriately conservative rule for evaluation purposes, it is unduly conservative for the purpose of this study. Figure 2-4 shows backbone curves used for the response history analysis of shear panels with multiple materials. Notice that GWB and stucco reach peak strengths at smaller story drift ratios than the structural wood panels, whereas the horizontal board siding reaches its peak at a much larger story drift ratio. Figure 2-5 shows that the shear wall panels do maintain a relatively higher peak strength over a larger range of drifts than indicated in Figure 2-4. Therefore, the previously cited peak strengths of GWB and stucco are multiplied by 0.9 for the purpose of estimating an overall overstrength for the building. The strength of horizontal wood siding is not adjusted.

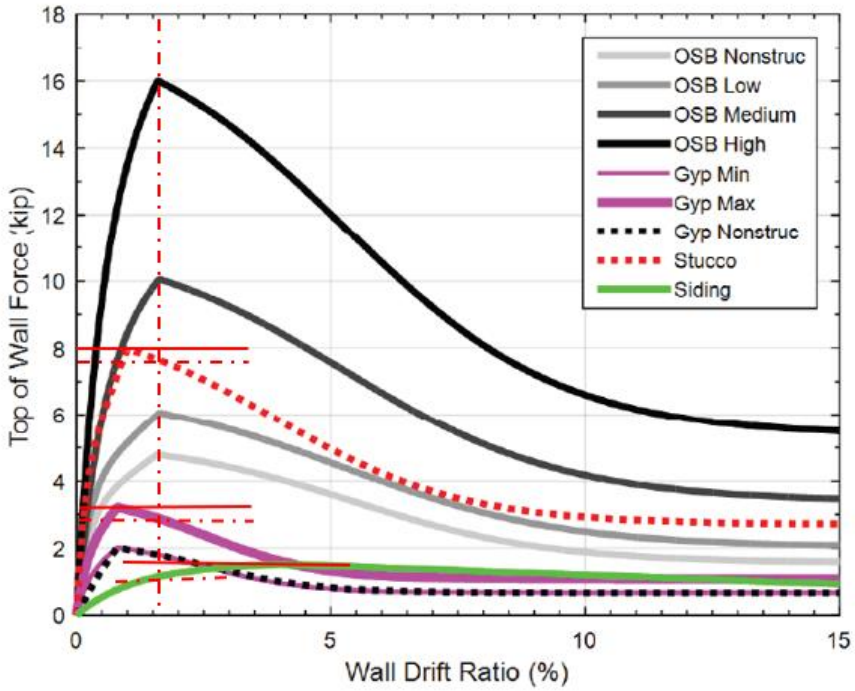

Figure 2-4 **Demonstration of addition of post-peak strengths of non-SFRS sheathings to peak of SRFS sheathing (adaption of Figure 2-2 from FEMA 2139-2, developed for 8 ft long by 10 ft high panels and showing residual capacity developed in that study).**

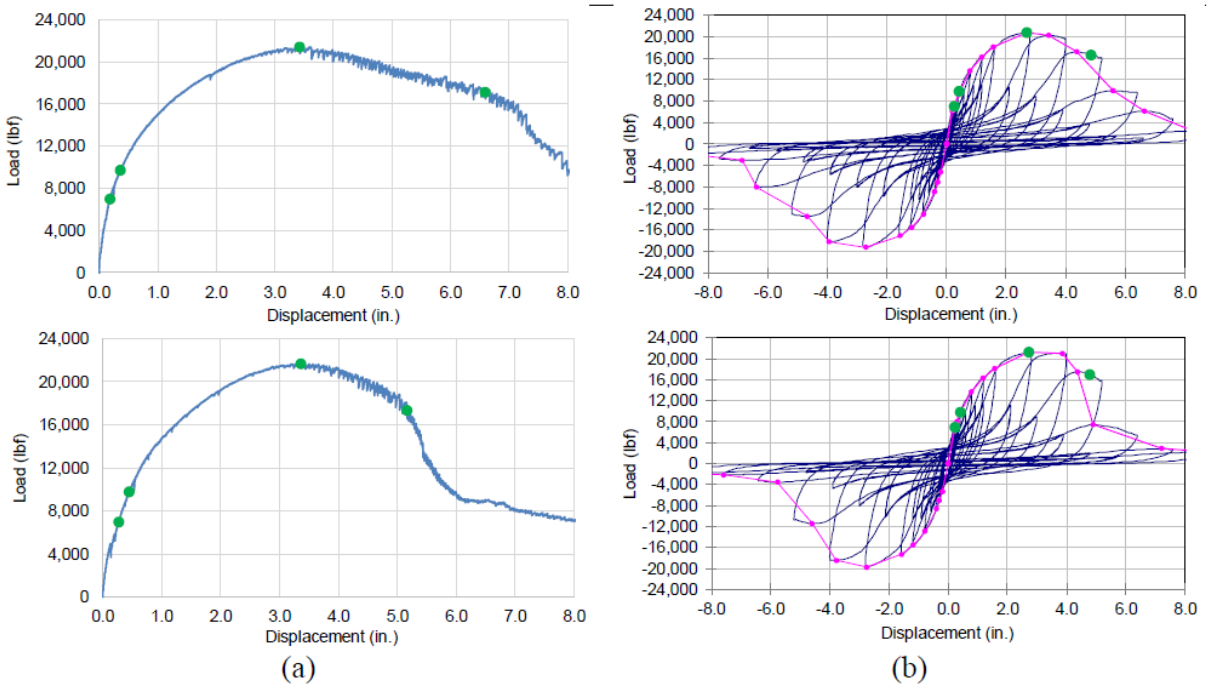

Figure 2-5 **Monotonic and cyclic response of OSB shear walls with 10d nails @ 2 in. o.c. (Line et al., 2019).**

2.3.3 Common Functional Types of Wood Light-Frame Buildings

The most common uses for wood light frame construction are:

- Single family detached houses,
- Single family attached houses (row houses),
- Multi-family apartment buildings,
- Single story commercial buildings, and
- Multi-story commercial buildings.

The majority of single-family houses, detached or attached, are one- and two-story buildings. Based on prior studies (FEMA, 2020), one- and two-story residential buildings have generally performed well in prior strong ground shaking, and thus are not a focus for this study. Multi-family apartment buildings of wood light frame construction have found increasing popularity in recent years and are a principal focus of this study. Single story commercial buildings can take many forms; common occupancies include retail stores, restaurants, and service shops (e.g., repair garages, tire stores). Multi-story commercial buildings are frequently used for multi-tenant office buildings. Apartment buildings are referenced by the acronym MFD, and commercial buildings by COM.

2.3.4 Overstrength for Wood Light Frame Apartment Buildings

A survey of 33 apartment units in 9 projects located in California, Utah, Colorado, and Virginia has been conducted to develop quantities for estimating the strength contributed by non-SFRS sheathing on interior walls and partitions in apartment buildings. The data recorded included the floor area, the length and width of the units, and the lengths of interior partitions in each direction within each unit. The amount of openings in the exterior walls was also recorded for two buildings. In reviewing projects for the survey, it was decided to exclude projects designed as loft style apartments. Loft style apartments generally have tall ceilings and few partitions that extend from floor to ceiling; they are a distinct minority of modern apartments. Their behavior will simply be different than the single-story flat style of apartments that are included in this study.

Table 2-2 shows a summary of data for the interior walls. It includes the sum of walls in both directions, which can include both nonstructural partitions as well as interior bearing walls. It does not include any walls around the perimeter of the apartment unit.

Table 2-2 Summary of Data for Interior Walls, Flat Style Apartments

Quantity	Area of Unit, sf	Lineal Feet of Interior Walls per 100 sf Area
Mean	939	6.82
Median	914	6.67
Std Dev	329	1.64
CoV	0.35	0.24
Max	1518	11.25
Min	384	3.44

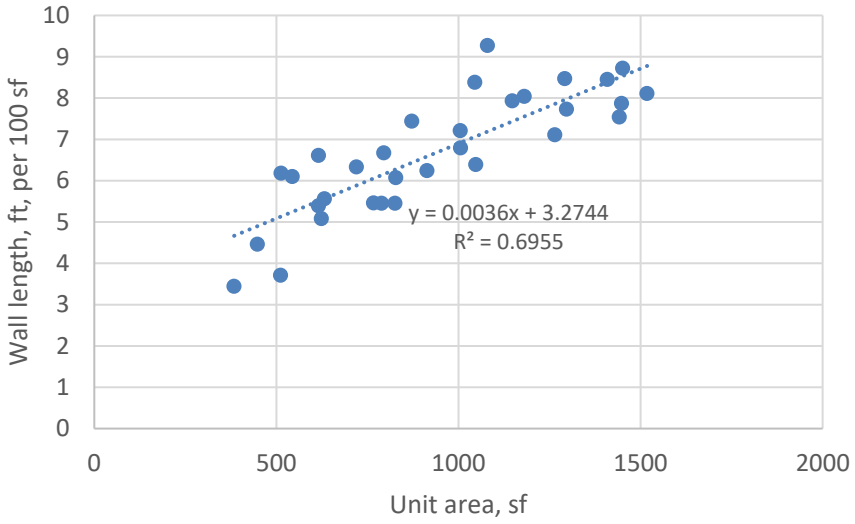

Figure 2-6 Length of interior walls vs area of unit.

The data show a definite correlation between the size of the unit and the ratio of length of interior partitions to floor area; Figure 2-6 summarizes that relation. The smallest apartments tend to be studio apartments, which have the smallest amount of interior walls. The smaller units tend to have a bias toward more interior walls perpendicular to the long direction of the unit, but that tendency diminishes in larger units, and it tends to disappear when considering the amalgamation of several units in a story. Therefore, in this study the interior walls are considered to be uniformly divided between the two principal directions for a building.

It is then convenient to express the strength provided by sheathings on interior walls as the product of the strength of the wall multiplied by half the length of wall per unit of area. For example, at the mean size of unit, the best fit relation predicts 6.7 lineal feet of wall per 100 square feet of floor. Using the strength for ½" GWB on each face, discounted by 10% for deformation compatibility, and dividing the result equally in each of two directions results in a strength of 12 pounds per square foot

of floor area. This can be related to design demand by multiplying the seismic weight per square foot by the short period spectral design acceleration and dividing by the design *R* factor. Thus, for a two-story building located where $S_{DS} = 1.0$ and with seismic weights at the roof of 25 psf and at the second floor of 45 psf, the design demand is $(25 + 45) \times 1.0/6.5 = 10.8$ psf and the overstrength ratio provided by the interior walls alone is 1.1 (i.e., 12/10.8), which would be added directly to the overstrength ratio provided by the SFRS. This contribution clearly decreases with each additional story. Before considering variability in this contribution, it is worthwhile examining the contribution by the walls around the perimeter of each unit.

To rationally approach the contribution of the unit perimeter, it is necessary to construct archetypical floor plans. Figure 2-7 shows such a plan for a building with eight units per floor. The archetype allows computations for the contributions of exterior walls, demising walls (party walls), and corridor walls with consideration of the effect of the ratio of unit depth to width and the number of units per story. The total perimeter length is related to the square root of the unit floor area and the aspect ratio. Thus, the ratio of the length of perimeter wall divided by the unit area decreases as the floor area of the unit goes up. This trend is opposite to the trend for interior walls, for which the contribution goes up with increasing unit area.

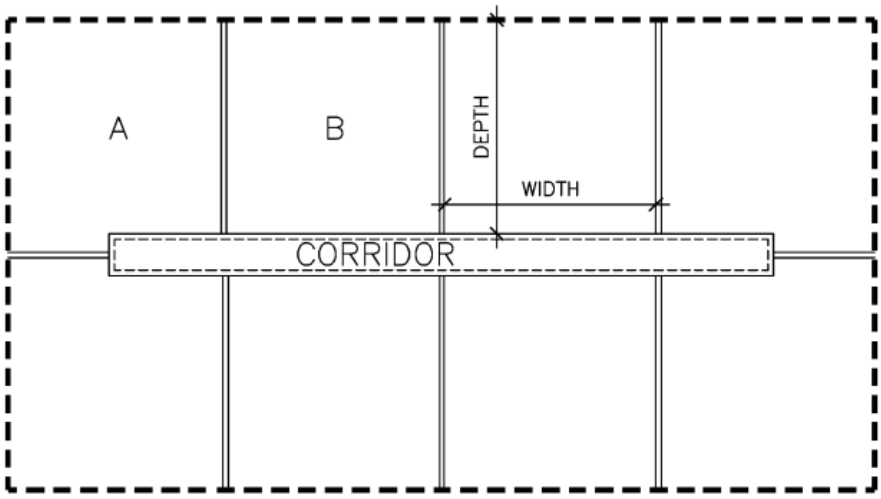

Figure 2-7 MFD archetype adopted for estimation of non-SFRS walls (the number of units per story can vary).

The corridor walls included 5/8" GWB directly applied to one face and two layers of 5/8" GWB applied to resilient channels on the opposite face, which is a common detail for acoustic separation and fire resistance. A single four-foot opening is created for access to each unit. The party walls can be either a wall with staggered studs and 5/8" GWB directly applied to each face or a set of two parallel walls with 5/8" GWB facing each unit and no sheathing within the interstitial space. For either type, the lateral strength contribution is the same: a single layer of 5/8" GWB for the full length of the party wall for the unit. The exterior wall has 5/8" GWB on its interior face. The most common case for the exterior face is stucco over 7/16" OSB with minimum nailing, which is the strongest

assembly. A weak assembly of horizontal board siding over the same OSB is also given consideration.

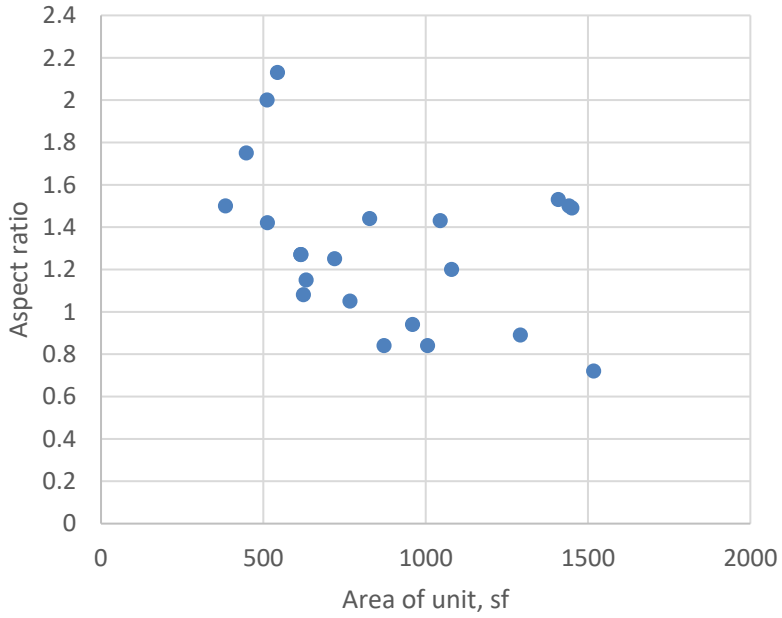

Figure 2-8 Depth to length ratio of unit vs area of unit.

Figure 2-8 shows a scatter gram of unit aspect ratio versus unit floor area. The small units were studio apartments, and no building studied was predominantly that type of unit. If units smaller than 600 sf are excluded, there is no discernable pattern, thus no relation between aspect ratio and unit size is included in this study. The mean value for the aspect ratio is 1.3 and the coefficient of variation is 0.28.

One additional set of data is necessary to estimate the contribution of the unit perimeter walls: the amount of openings (mostly windows and doors) in the exterior walls. The amount of opening is quantified as the total horizontal length of openings divided by the total horizontal perimeter, not the ratio of areas. Based upon a more detailed study of two buildings, one of which included parking garage doors along most of the length of one side of the first story, it was decided to use 50% open (horizontal length, not area) as the central value with a range of 30% to 70%.

For a building with 12 units per story, using the mean value for unit area, unit aspect ratio, and fraction of exterior openings, the contribution from corridor walls is 5.6 psf, from party walls is 7.1 psf, and from exterior walls with stucco is 18.1 psf, giving a total of 30.8 psf. If the exterior were board siding, the total drops to 23.5 psf. Figure 2-9 shows the contributions from interior and perimeter walls, and their sum, for the expected values for aspect ratio, units per story, and exterior openings. Figure 2-10 and Figure 2-11 show that variations in the number of units per story and unit the aspect ratio do not cause important changes in the total resistance from non-SFRS components. Figure 2-12 and Figure 2-13 show that the fraction of exterior openings is a result in significant

variation in non-SFRS resistance, but somewhat less so for the weaker exterior wall assembly. (More detail regarding all the survey data and the computations based on the archetypes is included in Appendix B).

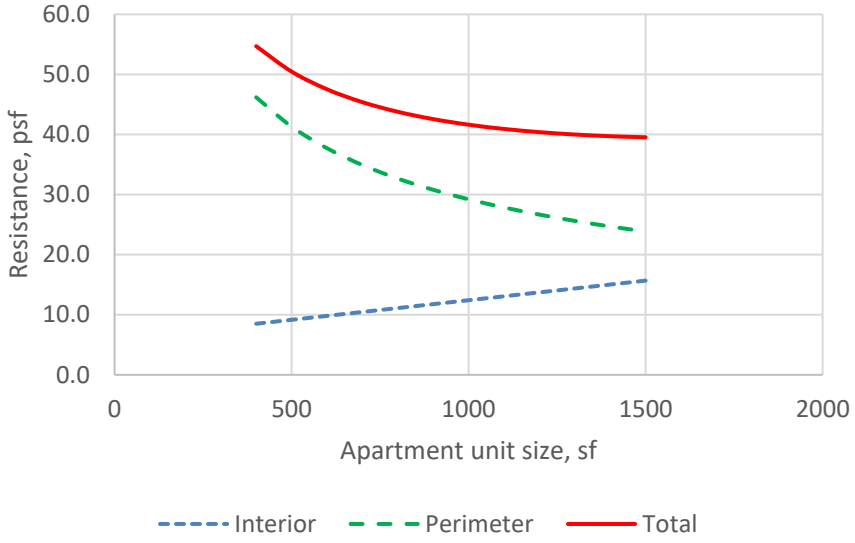

Figure 2-9 **Resistance from non-SFRS walls versus unit size, at expected values for aspect ratio, units per story, and fraction of openings in exterior walls.**

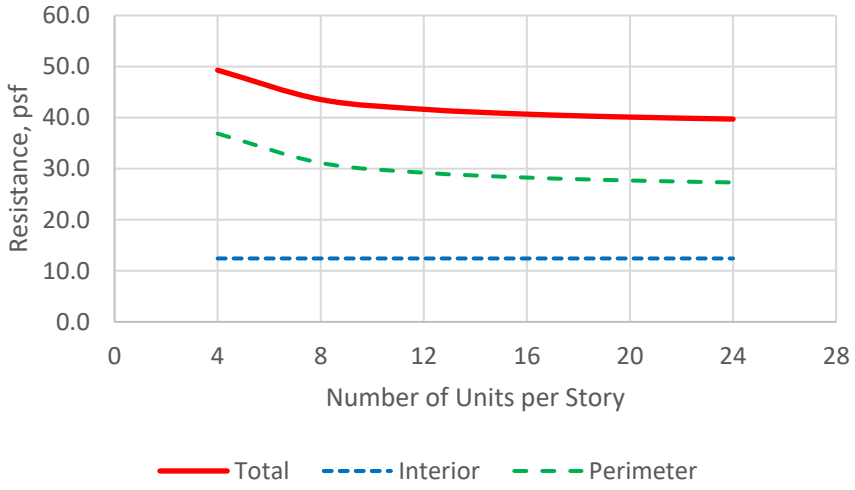

Figure 2-10 **Resistance from non-SFRS walls versus number of units per story, at expected values for area of unit, aspect ratio, and fraction of openings in exterior walls.**

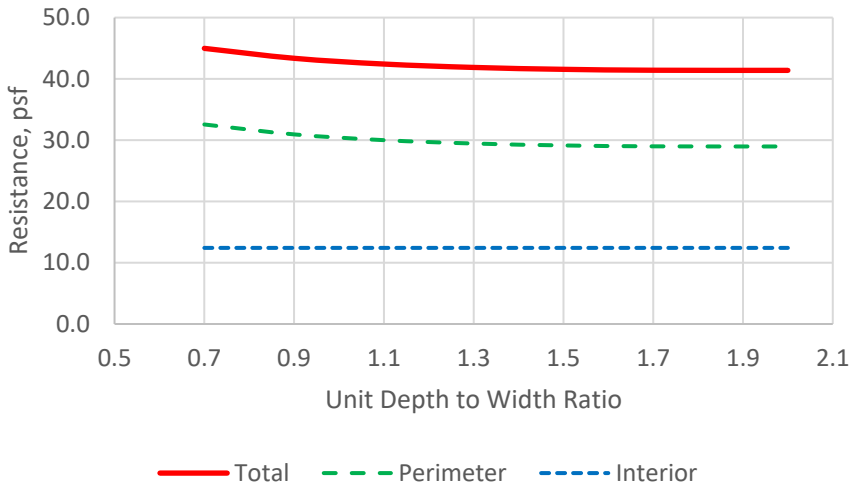

Figure 2-11 **Resistance from non-SFRS walls versus aspect ratio, at expected values for area of unit, units per story, and fraction of openings in exterior walls.**

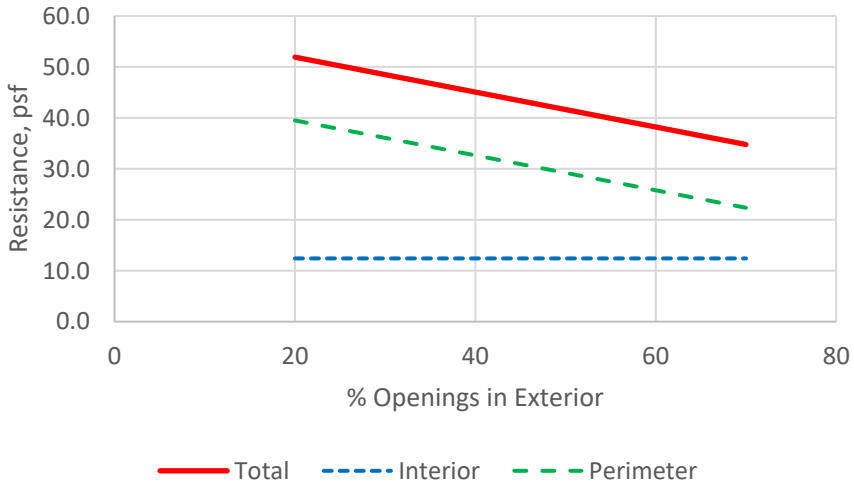

Figure 2-12 **Resistance from non-SFRS walls versus percent openings in exterior, at expected values for area of unit, unit depth to width ratio, and units per story.**

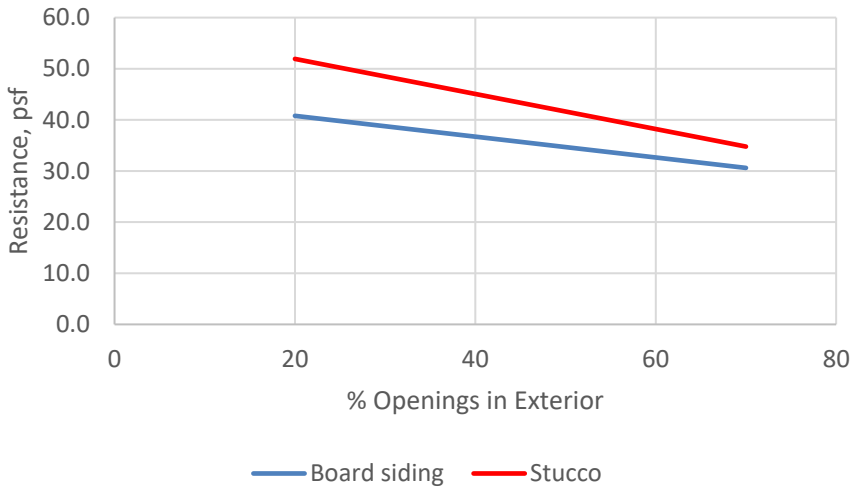

Figure 2-13 Resistance from non-SFRS walls considering type of exterior finish.

Table 2-3 shows the variability of the non-SFRS strength recommended for use in this study.

Table 2-3 Variability in Non-SFRS Resistance (psf), MFD

Parameter	Central	Low	High	Rough CoV
Unit area	42	39	50	0.13
Units/story	42	40	48	0.10
Unit aspect ratio	42	42	45	0.04
%Openings w/ stucco	42	35	48	0.15
%Openings w/ siding	37	35	40	0.07

The variabilities in Table 2-3 all pale in comparison to the likely variation in actual capacity of any given wall in comparison to the modeled expected value. The variability is inevitably higher than that for the SFRS shear walls, where 0.20 is used for the coefficient of variation (CoV). Therefore, the values in the table are rounded to a central value of 40 psf and a CoV of 0.25.

Figure 2-14 shows the total overstrength ratio (both SFRS and non-SFRS) as a function of the short period MCE_R response spectral acceleration and the number of stories in the building, using the central values. (The horizontal axis is labeled S_M; the light-frame buildings are all low rise, so the period is short enough that the design spectral acceleration does not vary with the period, therefore S_M is S_{MS}.) Figure 2-15 shows the same chart but truncated to improve readability. Figure 2-16 shows the recommended variation to consider for a three-story building.

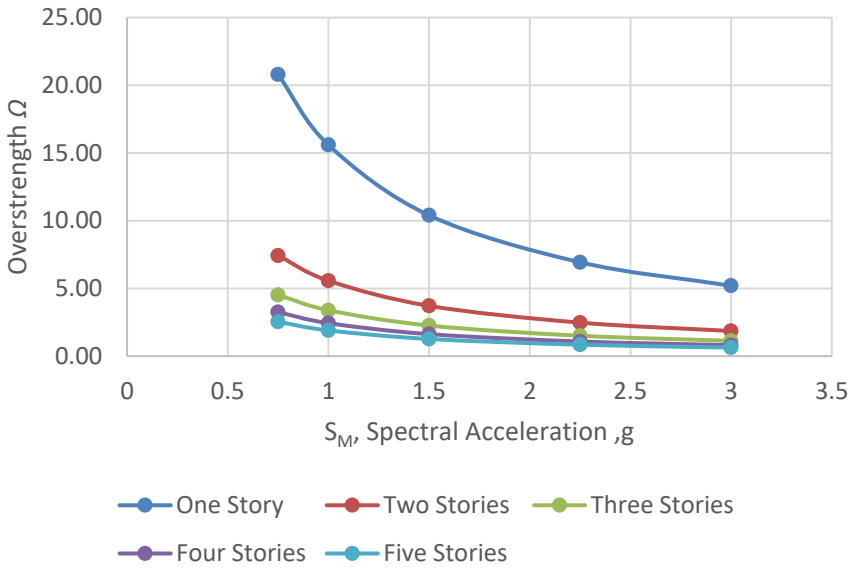

Figure 2-14 MFD non-SFRS overstrength ratios, central trend.

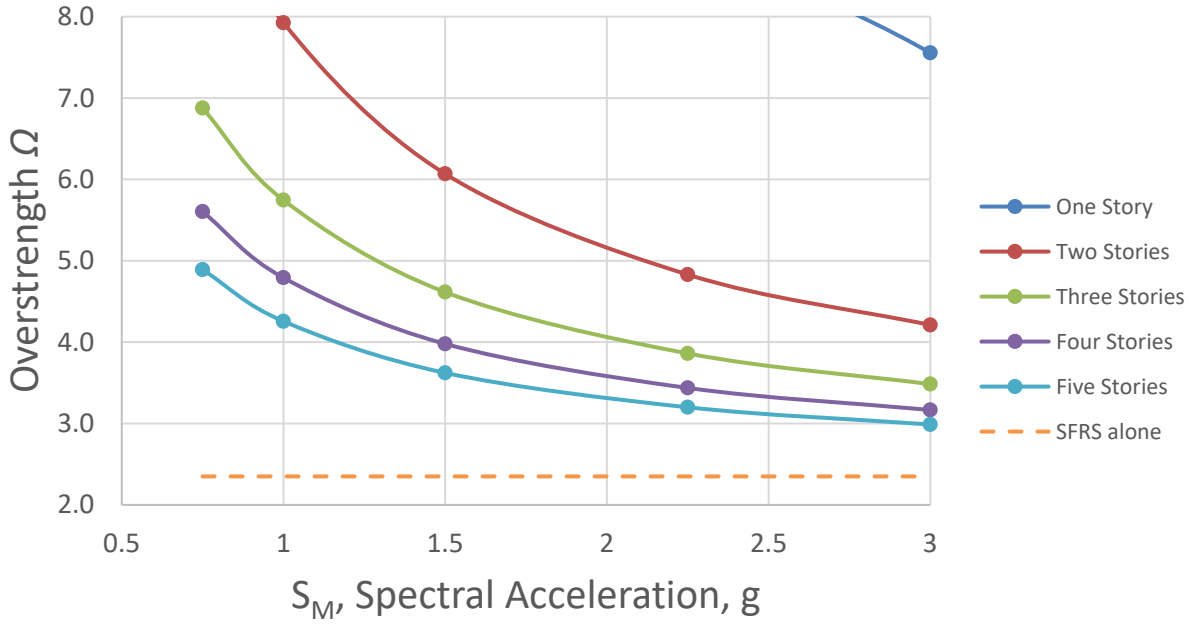

Figure 2-15 MFD total overstrength ratios, central trend, truncated.

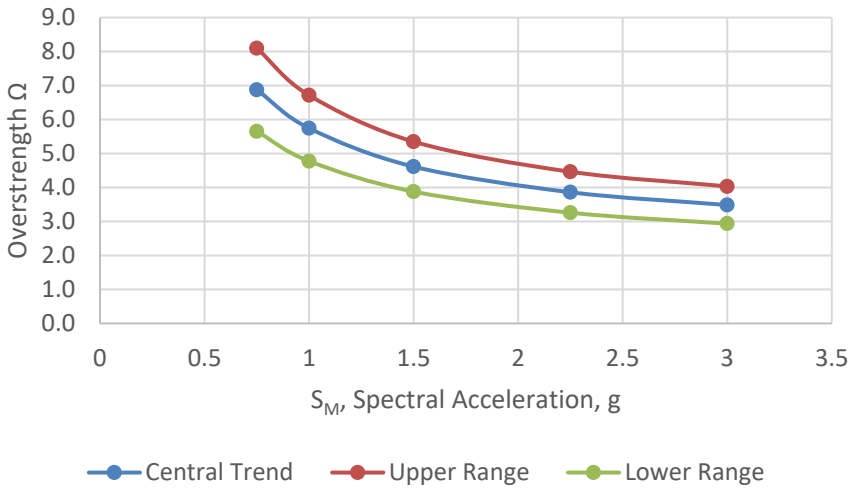

Figure 2-16 MFD overstrength, 3 story, with variability.

The overstrength ratios decrease with increasing spectral acceleration. At extremely large accelerations, the ratio asymptotically approaches the value for the SFRS alone, shown in Figure 2-3.

2.3.5 Overstrength for Wood Light Frame Commercial Buildings

Multistory wood light frame commercial buildings are usually used for office occupancies. There are far fewer of such buildings than there are multi-unit residential. It is believed that such buildings are most frequently multi-tenant buildings. Therefore, there are certain similarities with the multi-unit residential buildings. The following assumptions are made for the purposes of this study:

- Partitions within a unit are laterally braced by the ceiling, which is suspended from the structure, rather than being directly applied to the structure. Therefore, interior partitions do not contribute to lateral force resistance.
- The corridor and party walls do connect to the structure (due to fire and smoke requirements, as well as acoustic separation), and therefore they contribute to lateral force resistance in the same fashion as in the multi-unit residential building.
- The exterior walls have the same basic construction and variations as the multi-unit residential building.
- The generic floor plan adopted for the multi-unit residential building is a satisfactory representation for a multi-tenant office building. The average number of units per story ranges from 4 to 8 units
- The average size of a unit is 2000 square feet, and the average aspect ratio is 1.0.
- The seismic weight per unit area is the same as the multi-unit residential building.

These assumptions yield the following results:

- Length of perimeter walls (corridor, demising, exterior) is 8.9 lineal feet per 100 square feet of floor area, and
- The lateral force resistance for a floor plan with four units per story is 26.1 psf, while the lateral force resistance with eight units per story is 22.5 psf.

From these assumptions, a central trend for non-SFRS resistance is 25 psf with a CoV of 0.4. (The CoV for the non-SFRS overstrength was arbitrarily increased from 0.25 for the multi-unit residential to 0.4 based upon the lack of data from real projects. The effect of this decision on the total uncertainty is muted by the 0.2 CoV used for the SFRS overstrength for both types of buildings.) The overstrength of the SFRS is identical to that for the multi-unit residential. Figure 2-17 shows the central trend for the total overstrength (see subsequent text for explanation of the values for the one-story COM building), and Figure 2-18 shows the variability for the three-story archetype.

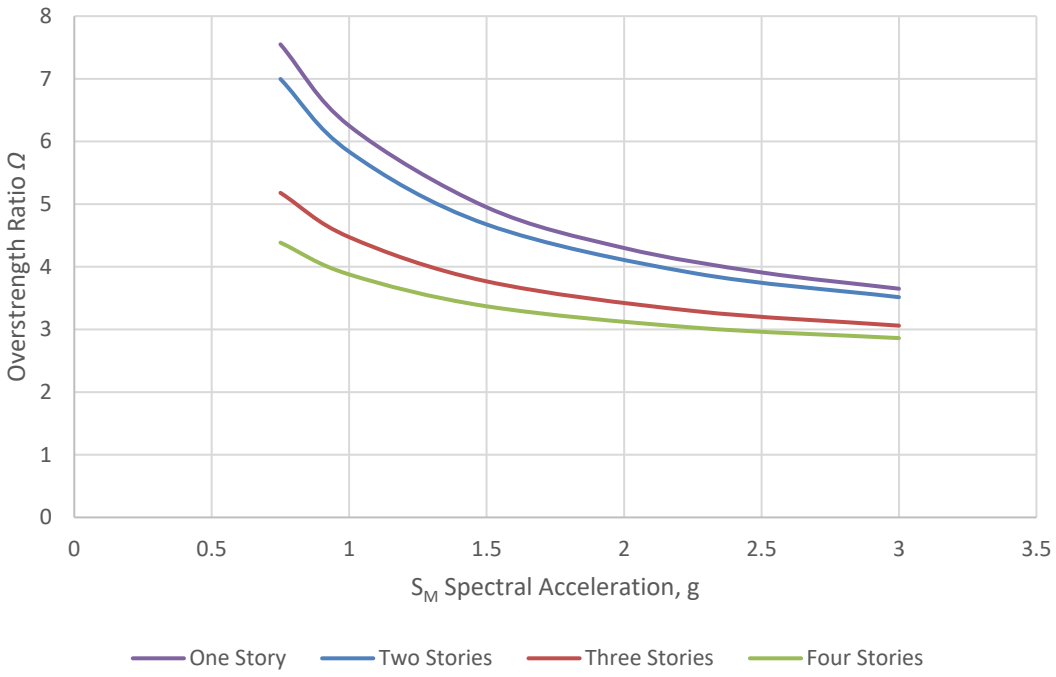

Figure 2-17 Total overstrength ratio for multi-story wood light frame commercial buildings, central trend.

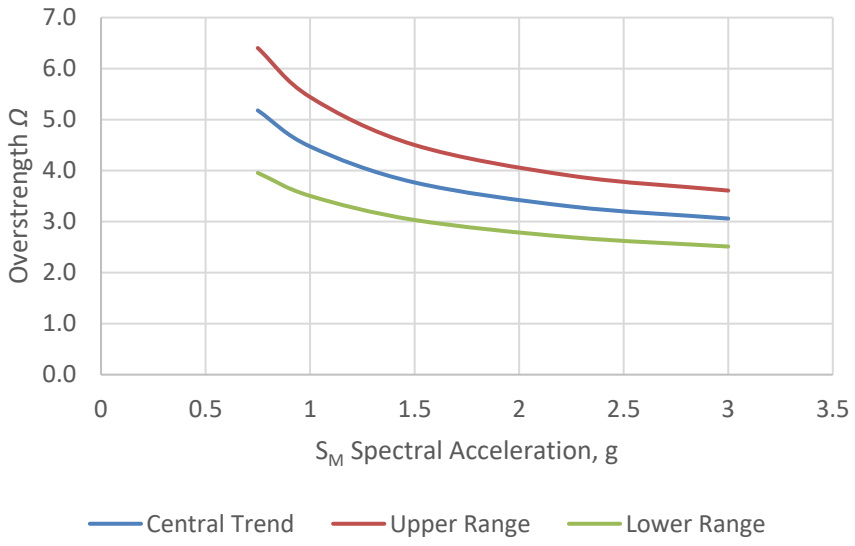

Figure 2-18 Three story commercial building overstrength, with variability.

Wood light frame construction is frequently used for one story commercial buildings, but the nature of occupancies served varies greatly. It is believed that retail, restaurant, and service occupancies are much more common than multi-tenant office occupancy for such buildings, and therefore, there are far fewer non-SFRS walls of any type. It is quite common for such buildings to have extensive glass on the exterior and for the only interior non-SFRS walls to be for restrooms and separation of public spaces from "back-of-the-house" spaces. Without going into extensive detail, the amount of interior walls could easily be in the range of one to two lineal feet per 100 square feet of floor area. There will also be a contribution from non-SFRS sheathings on the SFRS walls. Based on judgment a central trend of the non-SFRS resistance for the one-story commercial building is set at 10 psf times the floor area, with a CoV of 0.5. Given that the seismic weight of the roof is less than that for the typical floor, the contribution to overstrength is actually not reduced from the multi-story building as much as the pure ratio of the numbers. Using 25 psf as a value for the seismic weight of the one-story building, the non-SFRS contribution to Ω is $2.6/S_{DS}$. This is added to the SFRS overstrength (from Figure 2-3) to achieve the total overstrength ratio, shown in Figure 2-19. The variabilities of SFRS and non-SFRS are added directly, which is a conservative approach, but the confidence in the data for the non-SFRS is quite low.

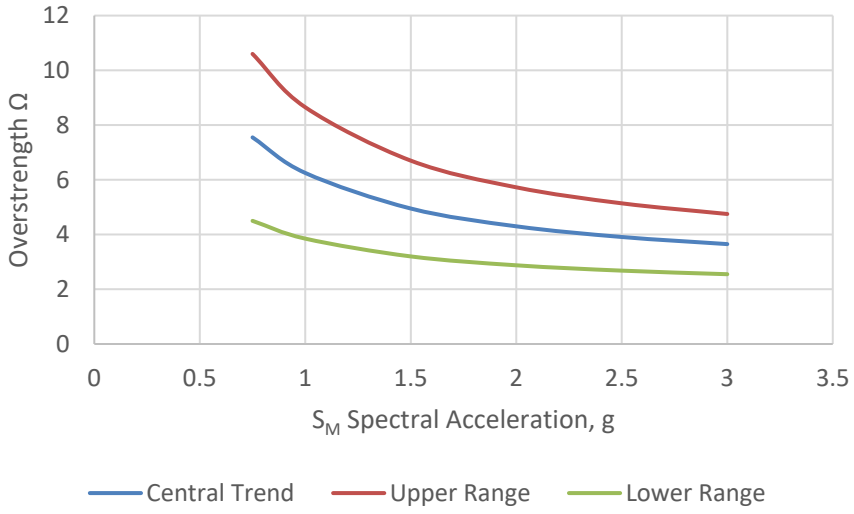

Figure 2-19 One story wood light frame commercial building overstrength, with variability.

2.4 Steel Special Moment Frame Buildings

For steel SMF buildings, overstrength comes from the SFRS and the gravity system. The SRFS overstrength, as defined previously, is given below:

$$\text{SFRS Overstrength} = \text{Bias in design} \times (1/\varphi) \times (\text{expected/nominal})$$

The bias in the design portion of the SFRS overstrength comes from several sources as discussed below. Member proportioning for SMF buildings influences the resulting bias in design and consists of the following:

- Column vs. beam size selection,
- Sizing columns to eliminate the need for doubler plates, and
- Location of column and beam size transitions/splices.

Two studies (NIST GCR-10-917-8 and ATC-63-2/3) proportioned the members independently for a 4-story and 12-story archetype. The resulting overstrength difference for the 4-story archetype was minimal but varied by 40% for the 12-story archetype, suggesting a range of overstrength variation of at least 1.0 to 1.4 based solely on member proportioning.

SMF buildings are typically drift-controlled. Member sizes are generally increased beyond what is required to meet the strength requirements of ASCE/SEI 7 to meet the drift requirements. Member proportioning for drift results in a broad bias in design range.

The analysis method used in the design process, as noted previously, has a large influence in the results, especially for drift-controlled SMF buildings.

Five previous studies evaluated the performance of SMF for a range of archetypes and provided values of the archetype's overstrength. These studies included the biases due to member proportioning, the drift-controlled nature of SMF, and analysis procedures (ELF and RSA) used in the design process. Although both results are shown, given that the majority of SMF designs utilize RSA procedures, the resulting recommendations are based on the RSA results. The study by Elkady and Lignos also included the effect of composite action of the concrete slab and steel beams in the SFRS, the results for which are used to adjust the SFRS overstrength values as noted below. The results of each of these studies are summarized below.

These studies all included archetypes tall enough that the design strength was controlled by the ASCE/SEI 7 minimum base shear equation. For the purpose of examining overstrength, archetypes taller than 12 stories were excluded (at 12 stories, the minimum base shear for a system with $R = 8$ is about one-third more than the period-based design spectrum, and by 20 stories, the factor is about 2).

Elkady and Lignos reported SFRS overstrength values for a perimeter frame with reduced beam section (RBS) connections for 2-, 4-, 8-, 12- and 20-story archetypes. The archetypes were designed using RSA procedures. The study also evaluated the effect of composite behavior of the beams in the SFRS as well as the effect of the gravity framing system considering both non-composite steel beams and composite beams. The effects of gravity framing overstrength is discussed later in this chapter. The resulting SFRS overstrength values are summarized in Table 2-4. The average incremental increase in overstrength due composite behavior of the beams in the SFRS is 0.4. Except where noted otherwise, the additional studies referenced in this section did not include the effect of composite action on the peak strength of the frame. Thus, the incremental increase in overstrength from Elkady and Lignos is added to the resulting recommended SFRS overstrength shown later in this section. It would be expected that the addition for the composite effect would diminish for taller buildings, due to use of deeper beams, but taller buildings are excluded from this study.

Table 2-4 SFRS Overstrength Results from Elkady and Lignos

No. of Stories	Non-composite Steel Beam SFRS Ω	Composite Beam SFRS Ω
2	3.0	3.5
4	1.8	2.0
8	2.6	3.1
12	2.1	2.5

FEMA P-2012 reported SFRS overstrength values for a perimeter frame with RBS connections for 3-, 9-, 20-story archetypes. The 3-story and 9-story archetypes are used as the basis for determining the collapses surfaces shown in Chapter 5. Both ELF and RSA procedures were evaluated. In ASCE/SEI 7-16, a change was made to scale the RSA base shear to 100% of the ELF base shear. Still, the RSA overstrength values will be lower than the ELF overstrength values due to the resulting

RSA drifts being smaller than those calculated using the ELF procedure since there is no period limit when determining drifts. The resulting member sizes for drift-controlled SMF will be smaller for RSA-designed buildings than for ELF-designed buildings, resulting in the lower overstrength values.

In addition, sizing columns to eliminate the need for doubler plates was evaluated. The change in overstrength by eliminating doubler plates was minimal. The resulting overstrength results are summarized in Table 2-5.

Table 2-5 SFRS Overstrength Results from FEMA P-2012

No. of Stories	ELF-Based Ω	RSA-Based Ω
3	4.7	2.5
9	4.2	1.8

NIST GCR 12-917-8 reported SFRS overstrength values for a perimeter frame with RBS connections for 1-, 2-, 4-, 8-, 12-, and 20-story archetypes. The 20-story archetypes are not included since their design was controlled by the ASCE/SEI 7 minimum base shear equation. Both ELF and RSA procedures were evaluated. The resulting overstrength values are summarized in Table 2-6.

Table 2-6 SFRS Overstrength Results from NIST GCR 12-917-8

No. of Stories	ELF-Based Ω	RSA-Based Ω
1	4.6	5.5
2	3.7	3.9
4	2.9	2.2
8	Not Provided	3.3
12	Not Provided	2.7

Kim and Han (2020) reported SFRS overstrength values for a perimeter frame with RBS connections for 4-, 8-, 12- and 16-story archetypes. The 16-story archetypes are not included since their design was controlled by the ASCE/SEI 7 minimum base shear equation. Both ELF and RSA procedures were evaluated. The resulting overstrength values are summarized in Table 2-7.

Table 2-7 SFRS Overstrength Results from Kim and Han (2020)

No. of Stories	ELF-Based Ω	RSA-Based Ω
4	2.7	2.1
8	2.6	1.9
12	1.9	1.4

Flores et al. (2014) reported SFRS overstrength values for a perimeter frame with RBS connections for 2-, 4- and 8-story archetypes. The archetypes were designed using RSA procedures. The resulting SFRS overstrength values are summarized in Table 2-8. The study also evaluated the effect of the gravity framing system on the overall overstrength of the archetypes, which is discussed later in this chapter.

Table 2-8 SFRS Overstrength Results from Flores et al. (2014)

No. of Stories	RSA-Based Ω
2	3.9
4	2.3
8	3.3

Using the RSA-based Ω results from Tables 2-4 through Table 2-8, the overstrength values for the 3-story and 9-story archetypes without consideration for composite behavior are summarized in Table 2-9.

Table 2-9 SFRS Overstrength Values for 3-story and 9-story Archetypes without Consideration for Composite Behavior

	High Seismic		
No. of Stories	Lower	Upper	Central
3	1.9	3.5	2.7
9	1.7	3.1	2.4

Including the incremental increase in overstrength due to the composite behavior of beams in the SFRS of 0.4 from Elkady and Lignos results in the recommended SFRS overstrength values for the 3-story and 9-story archetypes shown in Table 2-10.

Table 2-10 Recommended SFRS Overstrength Values for 3-story and 9-story Archetypes

No. of Stories	High Seismic		
	Lower	Upper	Central
3	2.3	3.9	3.1
9	2.1	3.5	2.8

Given the resulting overstrength values for the 3-story and 9-story archetypes are so similar, it is recommended that the final values be made independent of the number of stories.

The studies reviewed for steel SMF cited in this chapter did not evaluate changes in SFRS overstrength associated with increasing seismic design levels. To assess whether the overstrength values change with increasing seismic design level, a 9-story, three-dimensional archetype was developed using the office floor plan shown in Figure 2-26. Summary information regarding the archetype is presented in Chapter 5 with detailed information presented in Appendix F. Three designs were performed to interrogate the difference in performance for High D (S_{DS} = 1.0 and S_{D1} = 0.6), Very High Seismic (S_{DS} = 1.5 and S_{D1} = 1.2), and Ultra High Seismic (S_{DS} =2.0 and S_{D1} = 1.8) seismic design levels. It should be noted that increases in S_{DS} and S_{D1} between each seismic design level are not uniform due to differences in the spectral shape at default site conditions in ASCE/SEI 7-22. Thus, the S_{D1} ratios, relative to High D, for Very High Seismic and Ultra High Seismic are 2 and 3, rather than 1.5 and 2.0 for S_{DS}. However, since steel SMF are drift controlled, these increases did not necessarily result in similar increases in overstrength. The purpose of performing these designs was to make this assessment and to determine whether overstrength does, indeed, change with design level. The resulting SFRS overstrength values were 2.5, 3.8, and 4.1, respectively.

This analysis included the effect of composite action in the SFRS connections and the resistance of the gravity system. Therefore, the numbers cannot be directly compared with the prior tabulations. The composite action effect on overstrength would decrease for higher ground motions, because the added strength is a smaller portion of the strength where the beams are larger. The gravity system effect remains constant, and thus becomes a smaller addition to the overstrength ratio for larger ground motions. The substantial net increase in overstrength observed in this study comes from the fact that the stronger structures have shorter periods, which increases the spectral acceleration at which the drift checks are made. In fact, the period for the design based on Ultra High D ground motions was less than $C_u T_a$. Based on this work, the recommended values in Table 2-10, including the relative results between lower, upper and central values, are extended to produce the final recommended SFRS overstrength values for steel SMF shown in Table 2-11.

Table 2-11 Final Recommended SFRS Overstrength Values for Steel SMF in High D, Very High Seismic, and Ultra High Seismic Regions

Design Level	Lower	Upper	Central
High D	2.0	3.8	2.8
Very High Seismic	2.3	4.1	3.2
Ultra High Seismic	2.6	4.4	3.6

The recommended SFRS overstrength results from the five studies are compared to the results from eleven concept design examples prepared by Mission Viejo, California-based SidePlate Systems below. Nine of the concept design examples used their proprietary connection and two were designed using prequalified Welded Unreinforced Flange (WUF) beam and Reduced Beam Section (RBS) connections. The results for the design examples are shown in Table 2-12.

Table 2-12 Concept Design Results from SidePlate

Example No.	Location	No. of Stories	Occupancy	Connection Type	Max. Beam DCR	Avg. Beam DCR	Max. Col DCR	Avg. Col DCR
1	San Francisco, CA	2	Airport	WUF	0.61	0.40	0.40	0.24
2	Walnut Creek, CA	2	School	SP	0.82	0.59	0.50	0.36
3	Walnut Creek, CA	2	School	SP	0.52	0.54	0.37	0.22
4	Pleasanton, CA	3	Office	SP	0.71	0.52	0.80	0.42
5	Huntington Beach, CA	3	School	SP	0.74	0.56	0.52	0.34
6	San Diego, CA	4	Airport	RBS	0.98	0.75	0.79	0.50
7	San Diego, CA	4	Airport	SP	0.98	0.81	0.76	0.48
8	San Diego, CA	4	Airport	SP	0.97	0.79	0.89	0.52
9	San Diego, CA	4	Airport	SP	0.90	0.73	0.70	0.42
10	Irvine, CA	6	Hospital	SP	0.99	0.70	0.86	0.30
11	Bellevue, WA	17	Office	SP	0.96	0.82	0.64	0.41

As the results indicate, the maximum demand-to-capacity ratios (DCR) are typically controlled by the beams, and the average DCR are also controlled by the beams, which is consistent with the strong column-weak beam design approach for SMF. The statistical results are shown in Table 2-13.

Table 2-13 Summary of DCR from SidePlate Concept Designs

	Max. Beam DCR	Avg. Beam DCR	Max. Col DCR	Avg. Col DCR
Median	0.90	0.70	0.70	0.41
Mean	0.83	0.66	0.66	0.38
Standard Deviation	0.16	0.13	0.18	0.10

The reciprocal of the average beam and column DCRs provides the SFRS overstrength values shown in Table 2-14.

Table 2-14 SFRS Overstrength Estimate from SidePlate Concept Designs

Beams	Columns
1.5	2.6

The beam values represent a lower-bound estimate of the overstrength whereas the column values represent an upper-bound estimate. The beam values are based on the beam end that reaches a DCR of 1.0. For SMF beams with no gravity load, which is only a hypothetical case since all beams support some gravity load, the other end of the beam would also have a DCR of 1.0. For beams with gravity load, the end where gravity loads and seismic moments are additive will plastify first, while the other end will plastify at higher seismic demand due to the counteracting effects of gravity. The resulting overstrength could therefore exceed 2.

The lower-bound beam overstrength value is based on linear elastic design and does not include the following adjustments that are needed to estimate nonlinear pushover results and the associated overstrength value.

- AISC 341 φ factor is 0.9 for design limit states controlled by flexure.
- The expected/nominal values are based on R_y, which defines the ratio of expected yield stress to the specified minimum yield stress. For the typical materials used in SMFs (ASTM A992 and ASTM A913), the value of R_y is 1.1
- Additional strength comes from the strain-hardening of the steel members, particularly in the hinge locations in the beams. A reasonable strain-hardening ratio, R_{sh}, is on the order of 1.07.

The resulting recommended expected/nominal values are given in Table 2-15.

Table 2-15 Recommended Expected/Nominal Values

High Seismic		
Lower	**Upper**	**Central**
1.2	1.4	1.3

Adjusting the overstrength values for beams and columns shown in Table 2-14 by the central value shown in Table 2-15 and modifying this result by including the incremental increase in overstrength due to the composite behavior of beams in the SFRS of 0.4 from Elkady and Lignos results in the SFRS overstrength values shown in Table 2-16. The lower-bound beam overstrength value exceeds the final recommended SFRS overstrength lower value of 2.0 shown in Table 2-11 while the column upper-bound overstrength value is the same as the upper value of 3.6 in Table 2-11. The trends and ranges from the five cited reports and the SidePlate concept designs are similar suggesting the recommended overstrength SFRS results listed in Table 2-11 are appropriate.

Table 2-16 Adjusted Overstrength Results from SidePlate Concept Designs

Beams	Columns
2.4	3.8

The above results do not incorporate the contribution of the gravity framing system, which needs to be added to obtain the overall building overstrength. Gravity framing system overstrength studies for steel SMF are limited. However, a previous study (ATC-63-2/3) evaluated the seismic performance of 4-story and 12-story SMF archetypes and included the effects of the gravity framing system. The typical floor plan is shown in Figure 2-20.

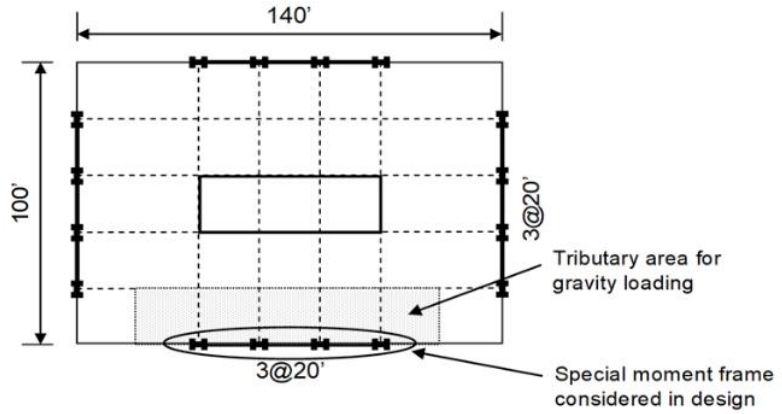

Figure 2-2 Typical floor plan configuration of steel building archetypes

Figure 2-20 4-Story archetype floor and framing plan from ATC-63-2/3.

Figure 2-21 shows an increase in V_{max} of 35% to 38% depending on gravity framing system direction for the 4-story archetype. V_d in the denominator of the vertical axis is the required strength V.

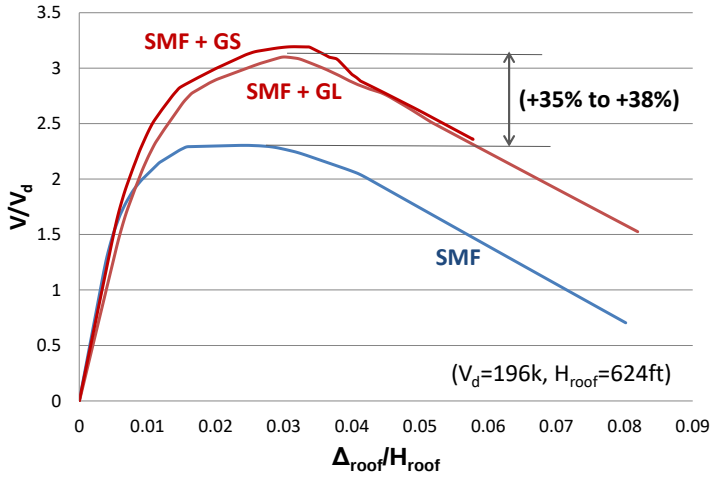

Figure 2-21 Pushover curve for the 4-story archetype from ATC-63-2/3. GS represents gravity framing in the short direction and GL represents gravity framing in the long direction. SMF denotes the SFRS acting alone.

The resulting gravity framing system contribution increased the overstrength by 1.4 and 1.2 for the 4-story and 12-story archetypes, respectively, as shown in Table 2-17.

Table 2-17 Gravity System Contribution to Overstrength for the 4-Story and 12-Story Archetypes from ATC-63-2/3

Archetype Design ID Number	Gravity System	Overstrength
4SMF1	None	2.30
4SMF2	GL	3.10
4SMF3	GS	3.17
4SMF1-C	None	2.31
4SMF2-C	GL	3.10
12SMF1	None	3.71
12SMF2	GL	4.44
12SMF3	GS	4.32

In the development of the pushover envelopes for SMF, Chapter 5 uses the results for the 3-story and 9-story archetypes from FEMA P-2012. While these analyses were very detailed, the associated gravity framing system was not included in the archetype. As noted above, Flores, Charney, and Lopez-Garcia studied the effect of the gravity system on SMF for 2-story, 4-story, and 8-story archetypes. The 4-story and 8-story are close in height to the 3-story and 9-story archetypes and are

used to assess, along with the results above from ATC-63-2/3, the effect of the gravity framing system on the SMF.

Figure 2-22 shows the contribution of the gravity columns only from Flores, Charney, and Lopez-Garcia. The gravity beam-to-column connections were taken as having zero stiffness and strength, so all the influence of the gravity columns are based on their moment of inertia alone, acting essentially as spines that help to vertically distribute the nonlinear behavior in the SFRS. The increase in the peak pushover strength, V_{max}, is essentially zero. However, the displacement capacity is increased with the inclusion of the gravity columns. This increase in displacement capacity is included in the pushover envelope curves evaluated in Chapter 5.

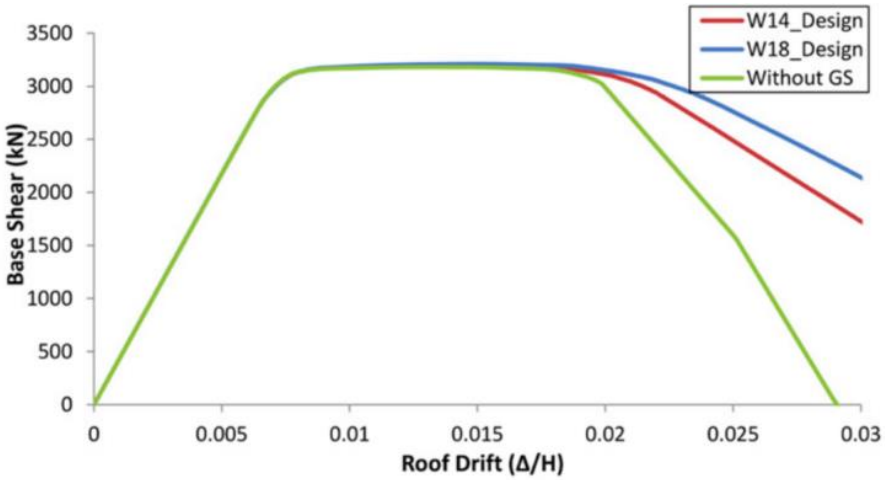

Figure 2-22 8-Story Pushover Curve Comparison with and without Gravity System (GS) Spines from Flores et al. (2014).

Figure 2-23 and Figure 2-24 show the pushover curves for the 4-story and 8-story archetypes assuming 35% of the gravity beam strength, which is a reasonable approximation of the beam-to-column connection capacity for a composite gravity framing system. The resulting increase in V_{max} for all the gravity system modeling approaches shown in the figures relative to the SMF acting alone (black line on the figures) is consistent with the results from the ATC-63-2/3 study regarding the contribution of gravity framing system to overall system overstrength.

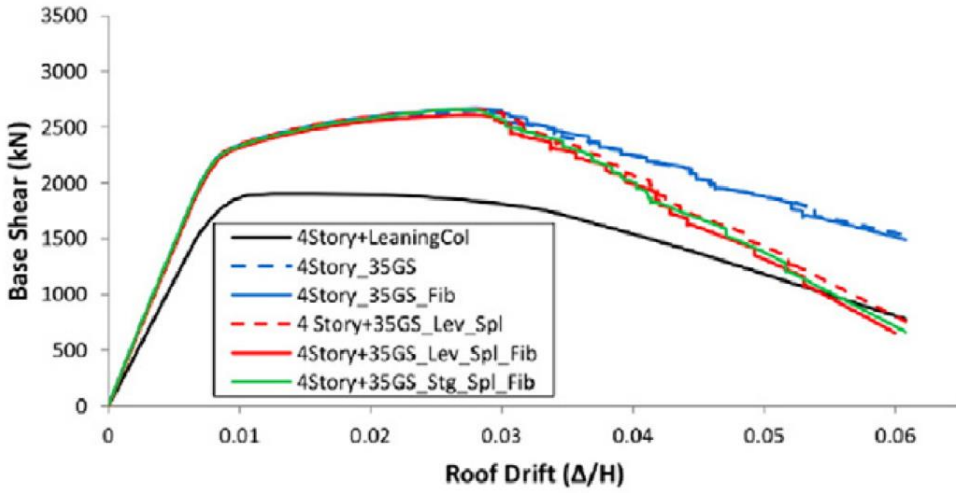

Figure 2-23 4-Story pushover curve assuming 35% of gravity beam strength from Flores et al. (2014).

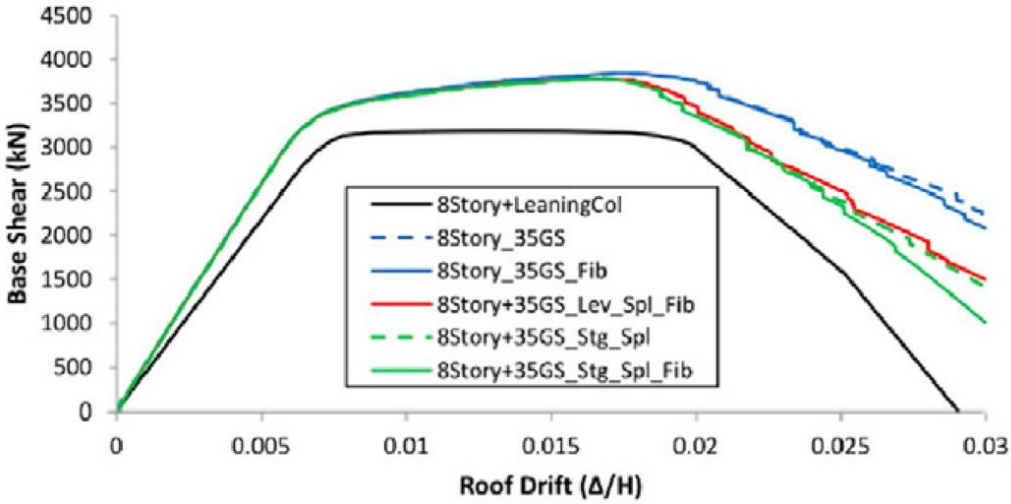

Figure 2-24 8-Story pushover curve assuming 35% of gravity beam strength from Flores et al. (2014).

To quantify the overstrength contribution from gravity framing systems, two archetype floor framing plans were evaluated. The first is the floor framing plan from Flores et al. (2014) (Figure 2-25). A second-floor framing plan was also developed to represent a typical office floor and show the lower trend for the overstrength contribution from gravity framing systems (Figure 2-26).

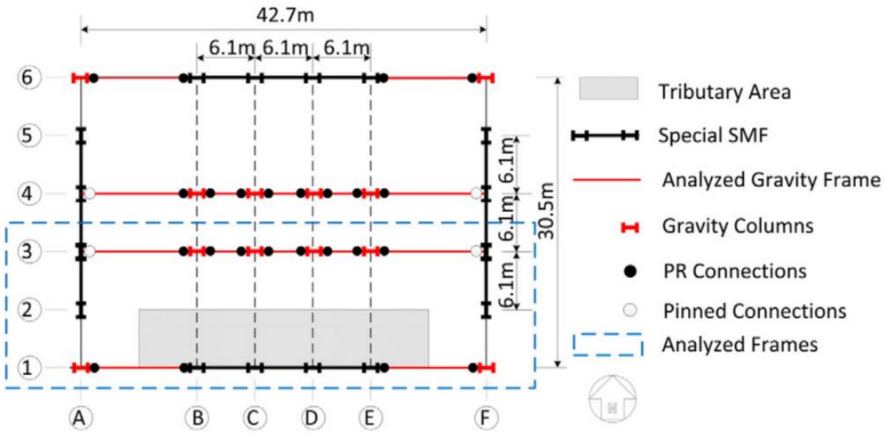

Figure 2-25 Archetype 1: floor framing plan from Flores et al. (2014)

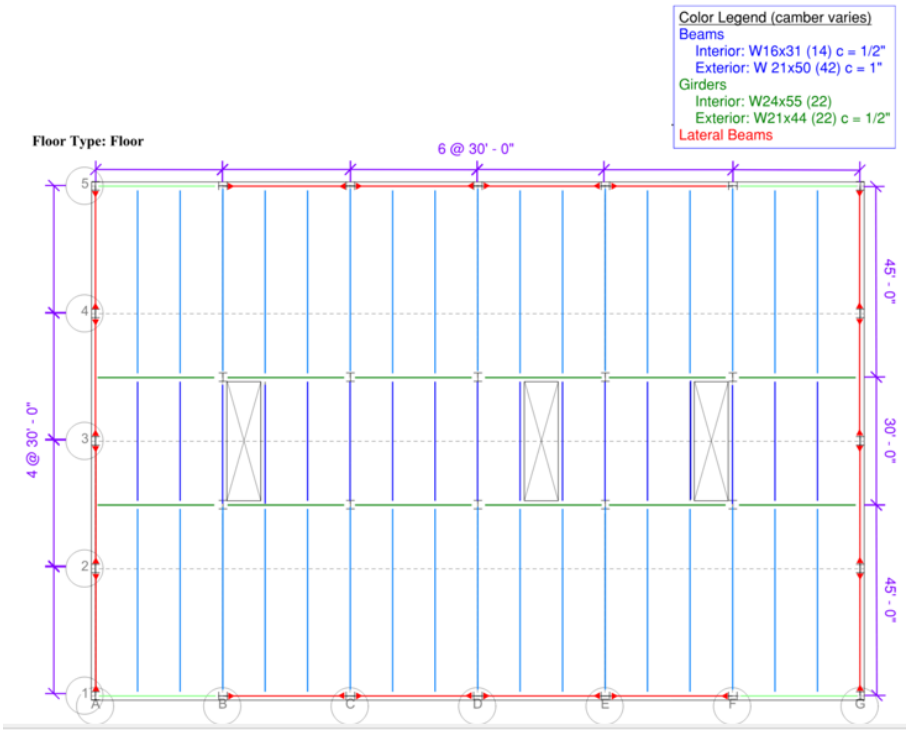

Figure 2-26 Archetype 2: Office occupancy archetype floor framing plan developed for this study.

The following approach/assumptions were used to determine the gravity framing system overstrength contribution:

- Portal frame analysis,
- Flexural capacity of the connections from gravity beams to columns taken as 35% of the bare steel cross section,

- 14 ft story height,
- 50 ksi steel yield strength,
- Flexural capacity of column exceeds flexural capacity of beam connection,
- Story shear in each direction computed as sum of moments divided by story height, and
- Overstrength computed as the average of the two directions, normalized by the floor area.

The resulting average gravity framing system contribution to overstrength for Archetypes 1 and 2 is 32 psf and 16 psf, respectively, resulting in the gravity framing system overstrength range shown in Table 2-18 for high seismic regions.

Table 2-18 Gravity Framing System Overstrength Range Based on Archetypes 1 and 2 in High Seismic Regions

Lower	Upper	Central
16 psf	40 psf	25 psf

The gravity columns also provide additional overstrength as do the partitions that form the 2-hour shaft walls around the stairs and elevators and the partitions that surround the restrooms. The remainder of the floor partitions generally provide negligible benefit due to the lack of connection to the floor framing above. The estimated partition overstrength contribution for Archetype 2 is 5psf. Combining the estimated contribution of the gravity columns and the partitions to the gravity framing systems values above results in the following gravity system overstrength range for high seismic regions. These overstrength values are also appropriate for very high seismic regions since the gravity framing system design does not change as a result of a change in seismicity.

Table 2-19 Recommended Gravity System Overstrength in Both High Seismic and Very High Seismic Regions

Lower	Upper	Central
20 psf	50 psf	30 psf

As noted previously, FEMA P-2012 is used as the basis for determining the collapses surfaces shown in Chapter 5. The 3-story and 9-story floor plans are shown in Fig. 2-27 below.

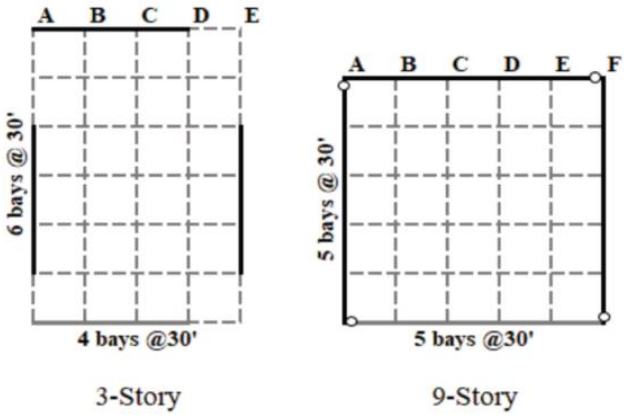

Figure 2-27 3- and 9-story floor plans from FEMA P-2012.

The design base shears were 679 k (31 psf) and 1341 k (60 psf) for the 3-story and 9-story archetypes, respectively. Multiplying these base shear values by the FEMA P-2012 SFRS overstrength values from Table 2-5 results in the following SFRS overstrength values in terms of psf.

Table 2-20 3- and 9-story Archetype SFRS Overstrength Values in Terms of PSF

No. of Stories	ELF-Based Ω	RSA-Based Ω
3	148 psf	79 psf
9	250 psf	107 psf

Combining these SFRS overstrength values with the recommended central gravity system overstrength value (30 psf) shown in Table 2-19 results in the following percentage increase in total overstrength compared to the SFRS overstrength based on analysis method. Both the ATC-63-2/3 and Flores et al. (2014) studies were based on RSA procedures and the increase in total overstrength increase compared to SFRS overstrength results are consistent (30-40%) with the RSA-based increases shown in Table 2-21.

Table 2-21 Total Overstrength Percentage Increase for Gravity System Compared to the SFRS Overstrength for 3-Story and 9-Story Archetypes Based on Analysis Method at the High D Level

No. of Stories	ELF-Based Increase	RSA-Based Increase
3	20%	38%
9	12%	28%

Combining the results of the final recommended SFRS overstrength values for steel SMF (Table 2-11) with the recommended gravity system overstrength values (Table 2-19, the ratio is obtained by converting the seismic demand to psf and dividing into the gravity overstrength) results in Figures 2-28 and 2-29 that show the total steel SMF overstrength values as a function of both S_{MT}

and S_{M1}. (Recall that S_{MT} is the spectral acceleration at the period T used for design of the building. Thus, for a given value of S_{M1}, S_{MT} is much smaller for the 9-story building than for the 3-story building, which appears to truncate the curves for the 9-story building on the S_{MT} chart.). The results from the 9-story archetype, described earlier in this section, influence the results shown in these two figures.

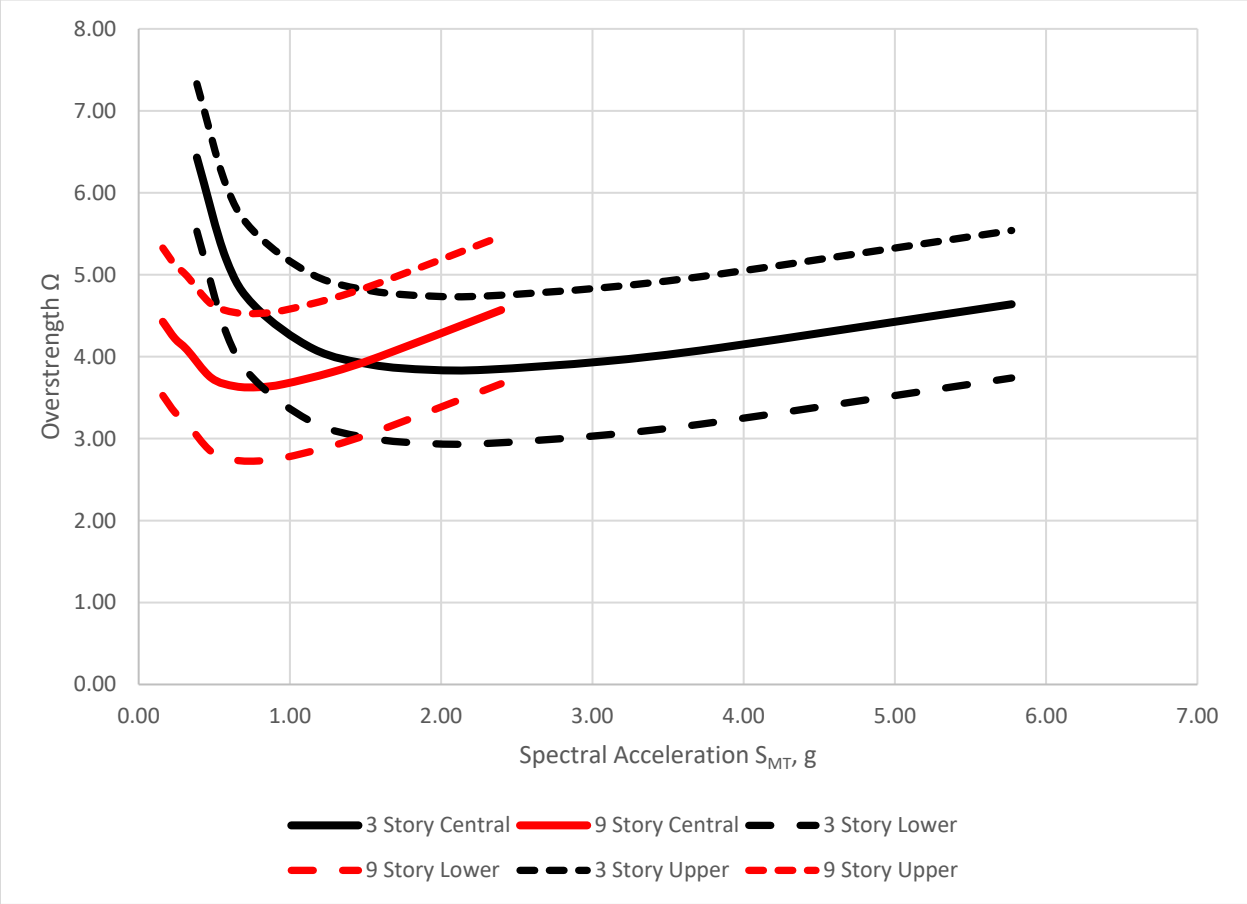

Figure 2-28 Total overstrength for 3-story and 9-story steel SMF as a function of S_{MT}.

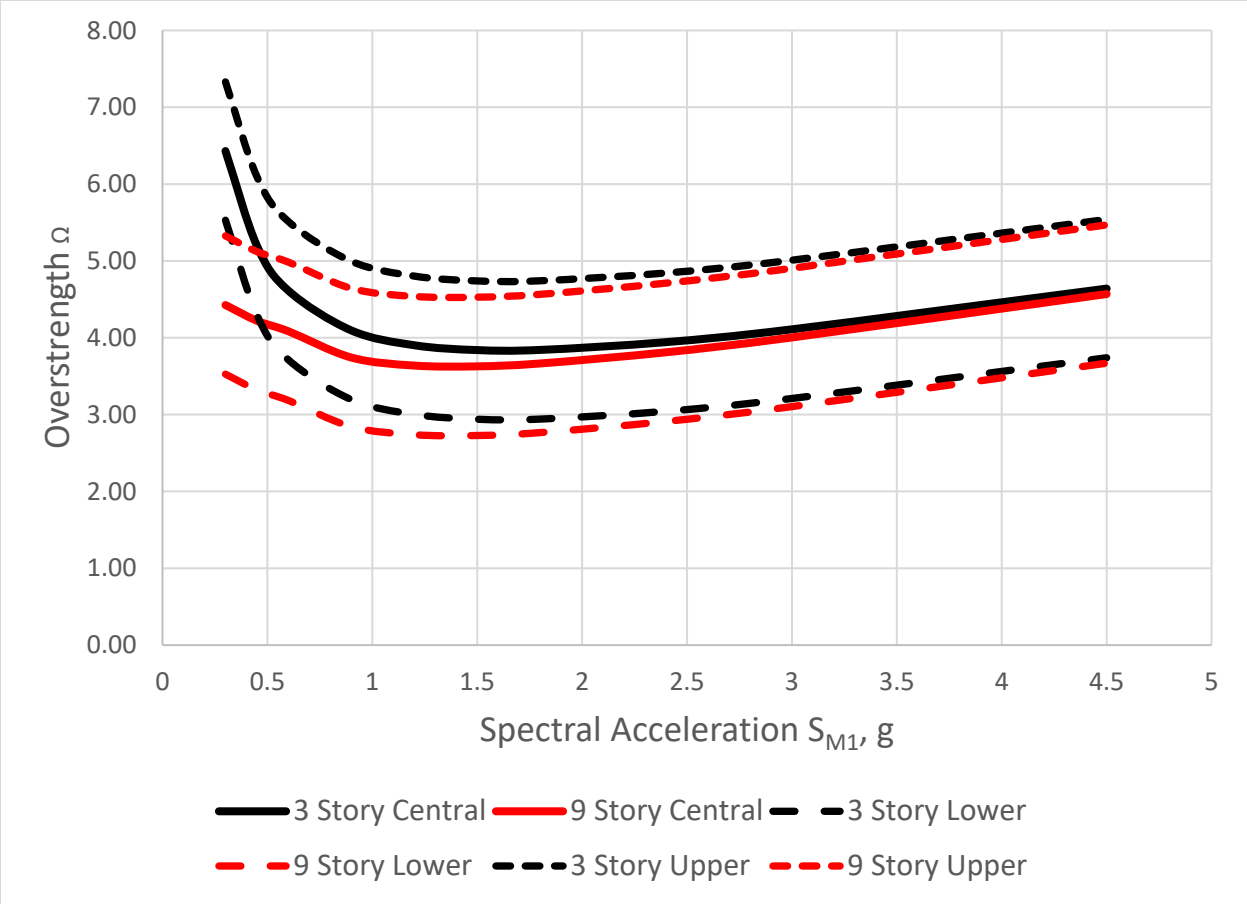

Figure 2-29 Total overstrength for 3-story and 9-story steel SMF as a function of S_{M1}.

2.5 Steel Buckling-Restrained Braced Frame Overstrength

For BRBF buildings, overstrength comes from the SFRS and the gravity system. The SRFS overstrength, as defined previously, is given below:

$$\text{SFRS Overstrength} = \text{Bias in design} \times (1/\varphi) \times (\text{expected/nominal})$$

Given the ability to size the buckling-restrained brace (BRB) to the cross-sectional area predicted by the analysis, the bias in design is typically close to 1.0 since the resulting columns are sized to the strain-hardened capacities of the BRB. Still, some smoothing of the BRB sizes do occur and is more significant in taller buildings. However, this bias is minimally affected by whether the site is in a high seismic or very high seismic location. Based on engineering judgement, it is recommended that the bias in design ranges shown in Table 2-22 be used:

Table 2-22 Bias in Design Ranges for BRBF in Both High Seismic and Very High Seismic Regions

No. of Stories	Lower	Upper	Central
4	1.0	1.1	1.05
9	1.0	1.2	1.1
15	1.0	1.2	1.1

Per AISC 341, the φ factor used in the design of BRB is 0.9. This value is used in the determination of the SFRS overstrength range.

The expected/nominal values for BRB have been developed by CoreBrace, LLC, a U.S.-based BRB supplier. Based on their study of over 19,000 BRB, which consisted of both physical testing and analytical modeling, the resulting BRB strains at 2% story drift are shown in Table 2-23. The 2% story drift value is set by AISC 341 Seismic Provision for Structural Steel Buildings to qualify BRB for use in design.

Table 2-23 BRB Strain Ranges at 2% Story Drift

Mean -1σ	Mean	Mean $+1\sigma$
1.45%	1.69%	2.12%

The resulting strain hardening adjustment factor (ω) and compression strength adjustment factor (β) equations based on these tests at a 70% confidence level are given as:

$$\omega = 20.63\varepsilon + 1.15$$

$$\beta = 4.97\varepsilon + 1.10$$

$$\beta\omega = \beta \times \omega$$

where ε represents the BRB strain at 2% story drift.

The resulting adjustment factors (i.e., overstrength values) are shown in Table 2-24 for strains at 2% story drift.

Table 2-24 Overstrength Values at 2% Story Drift

	ω	β	$\beta\omega$
Mean -1σ	1.45	1.17	1.70
Mean	1.50	1.18	1.77
Mean $+1\sigma$	1.59	1.21	1.91

These values need to be increased based on the material overstrength of the provided material. Typically, the range of specified $F_{y,min}$ to $F_{y,max}$ is 38 ksi-46 ksi, resulting in a maximum material overstrength of 1.21. The resulting range of material overstrength values are used to determine the total post-yield overstrength of the BRBs are shown in Table 2-25.

Table 2-25 Material Overstrength Ranges

Mean -1σ	1.0
Mean	1.15
Mean $+1\sigma$	1.21

Using these factors, the total post-yield (expected/nominal) values for BRB overstrength at 2% story drift are shown in Table 2-26.

Table 2-26 Total Post-Yield Overstrength Values at 2% Story Drift

	ω	β	$\beta\omega$
Mean -1σ	1.45	1.17	1.70
Mean	1.73	1.18	2.04
Mean $+1\sigma$	1.92	1.21	2.31

The core strain statistics were only provided for the 2% story drift case. However, the mean expected/nominal values for BRB at other core strain levels can be determined using the above equations. Increasing the resulting $\beta\omega$ values by the mean material overstrength value of 1.15 results in the post-yield overstrength values shown in Table 2-27.

Table 2-27 Total Post-Yield Overstrength Values are Varying Core Strains

Mean Core Strain	ω	β	$\beta\omega$	Total Post-Yield $\beta\omega$
1.0%	1.36	1.15	1.56	1.79
1.5%	1.46	1.17	1.71	1.97
1.69%	1.50	1.18	1.77	2.04
2.0%	1.56	1.20	1.87	2.16
2.5%	1.67	1.22	2.04	2.35
3.0%	1.77	1.25	2.21	2.54
3.5%	1.87	1.27	2.38	2.74

These total post-yield values can be used when interrogating BRB core strains associated with building collapse performance.

Combining the results from Table 2-22, the $1/\varphi$ value of 1.11, and $\beta\omega$ from Table 2-26, results in the SFRS overstrength values at 2% story drift shown in Table 2-28.

Table 2-28 SFRS Overstrength for BRBF at 2% Story Drift in Both High Seismic and Very High Seismic Regions

No. of Stories	Lower	Upper	Central
4	1.9	2.8	2.4
9	1.9	3.1	2.5
15	1.9	3.1	2.5

The resulting overstrength values do not vary appreciably based on number of stories as indicated in Table 2-28. Given this, the values shown in Table 2-29 are recommended for BRBF SFRS overstrength regardless of height.

Table 2-29 Recommended SFRS Overstrength for BRBF in Both High Seismic and Very High Seismic Regions

Lower	Upper	Central
1.9	3.0	2.5

This information is plotted in Figure 2-30.

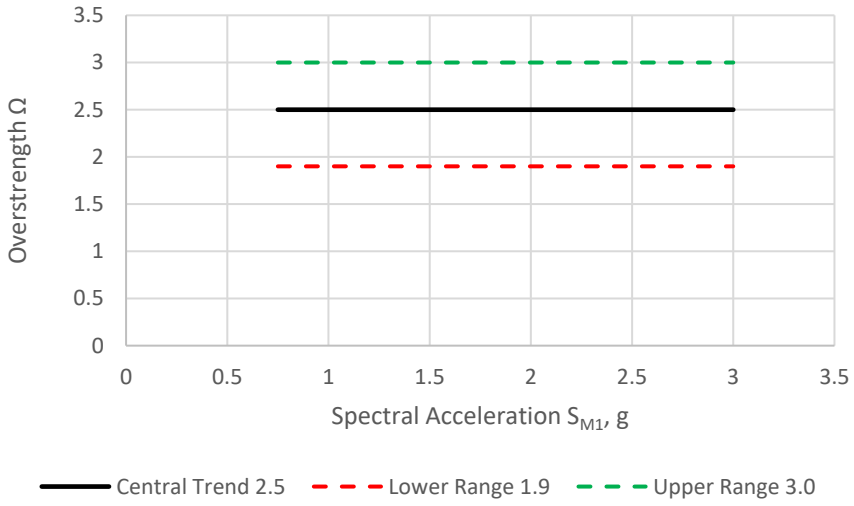

Figure 2-30 SFRS overstrength for BRBF as a function of S_{M1}.

The thesis from Ochoa (2017) evaluated the contributions of the BRB, the BRBF columns, and the gravity columns to the pushover curve for 4-, 9- and 15-story archetype buildings. The results of this study are used to determine the gravity system contribution to BRBF overstrength and displacement capacity.

The floor plan and frame elevations are shown in Figure 2-31 and Figure 2-32, respectively.

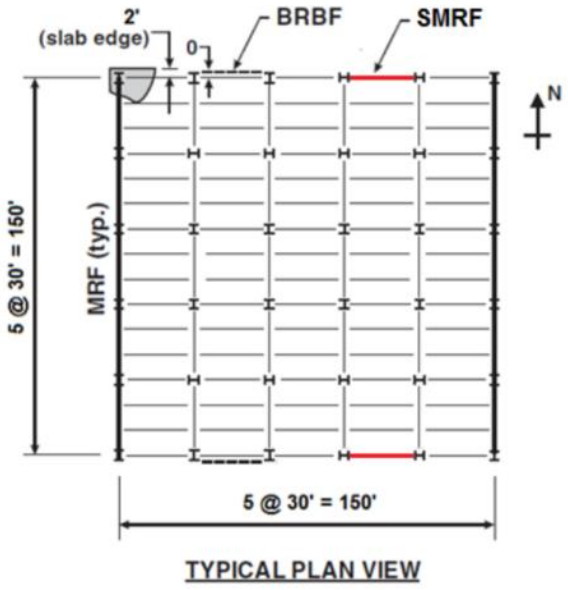

Figure 2-31 Archetype floor plan from Ochoa (2017).

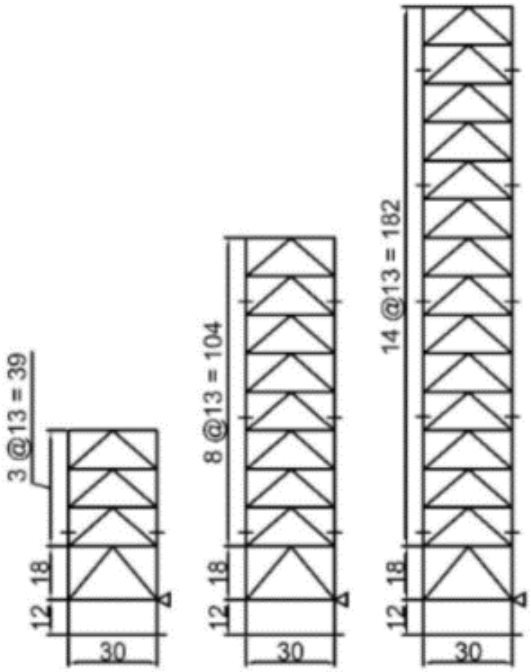

Figure 2-32 Archetype elevations from Ochoa (2017).

This study indicates the BRBF column and gravity column overstrength contributions have a limited effect on V_{max} value for the system pushover but results in increased displacement capacity as indicated in the Figures 2-33 to 2-35 for the three archetypes.

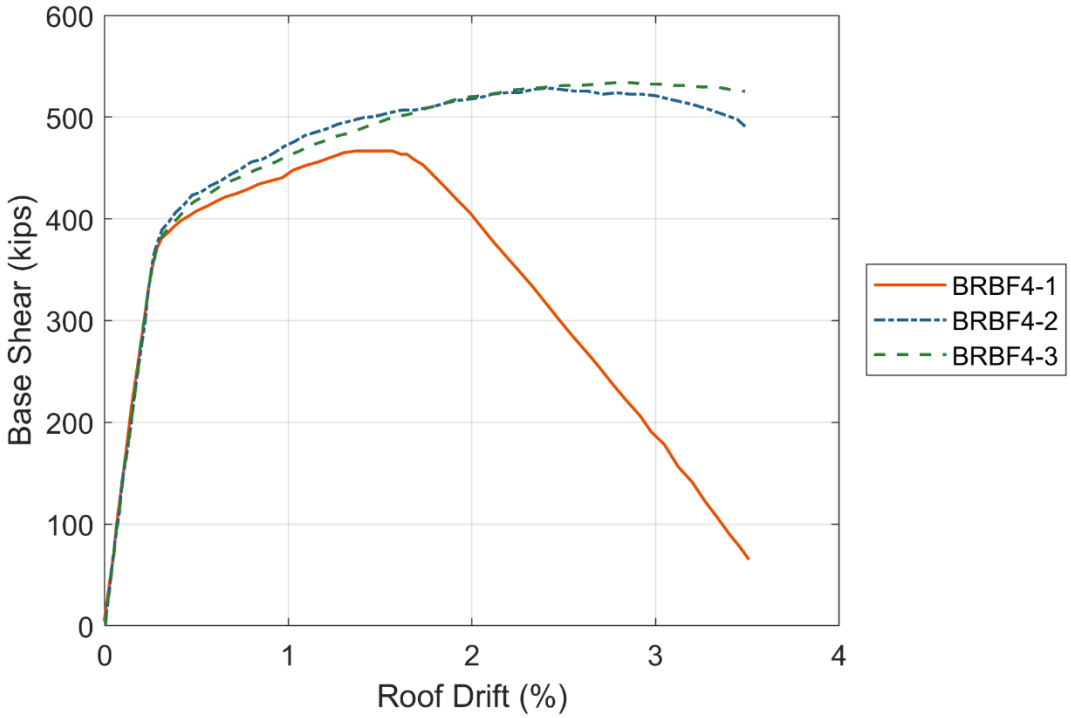

Figure 2-33 4-Story BRBF (BRBF4) pushover curves derived from data by Ochoa (2017).

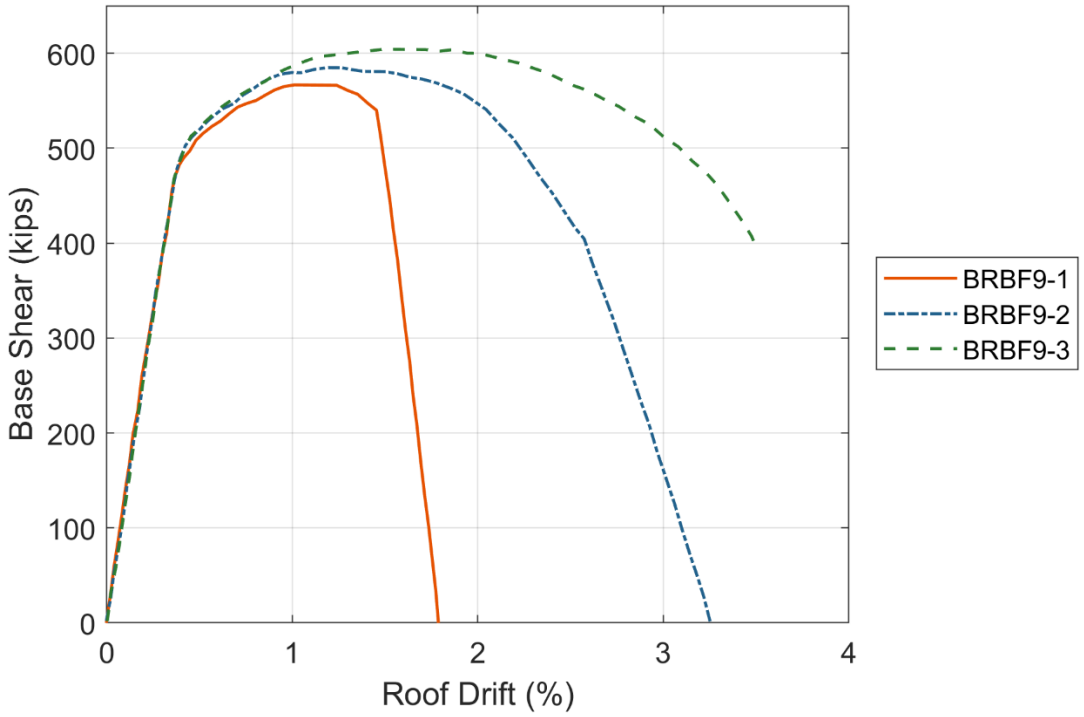

Figure 2-34 9-Story BRBF (BRBF9) pushover curves derived from data by Ochoa (2017).

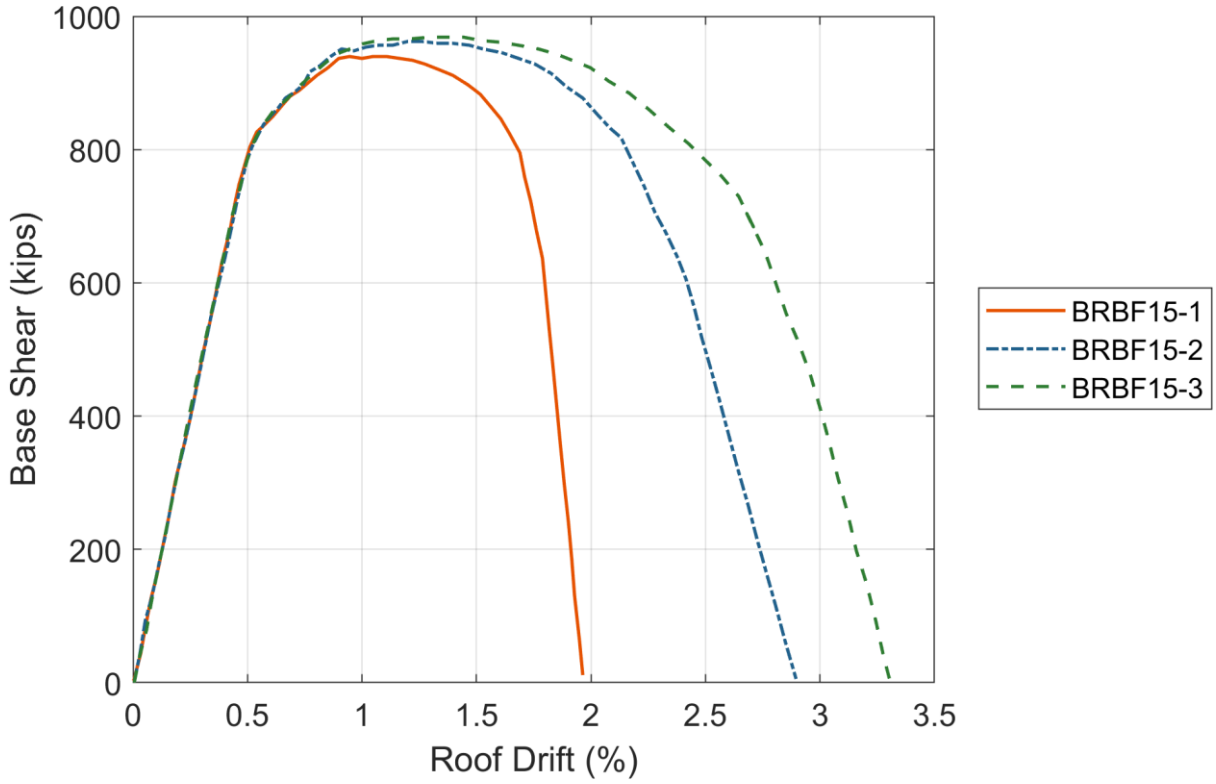

Figure 2-35 15-Story BRBF (BFBF15) pushover curves derived from by Ochoa (2017).

The BRBF -1, BRBF -2 and BRBF -3 pushover curves represent the following SFRS and gravity system details.

- BRBF -1—BRBF columns are oriented in the weak axis. Gravity columns are excluded.
- BRBF -2—BRBF columns are oriented in the strong axis. Gravity columns are excluded.
- BRBF -3—BRBF columns are oriented in the weak axis. Gravity columns are included.

Using the nomenclature shown in Figure 2-36 developed in Chapter 5, the combined pushover curve plateau, as measured by Δ_{pc}, is broadened and the resulting collapse displacement, Δ_u, is increased, which is due to the BRBF columns and gravity columns distributing the yielding to more floors.

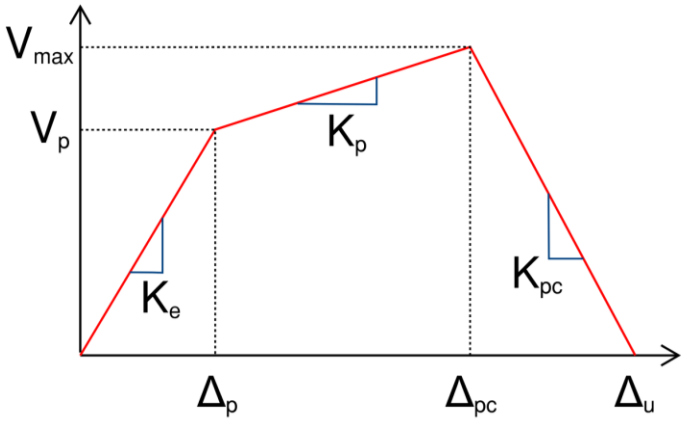

Figure 2-36 Pushover curve nomenclature from Chapter 5.

The effect of distributing the yielding on story drift is shown in Figure 2-37 for the 9-story archetype.

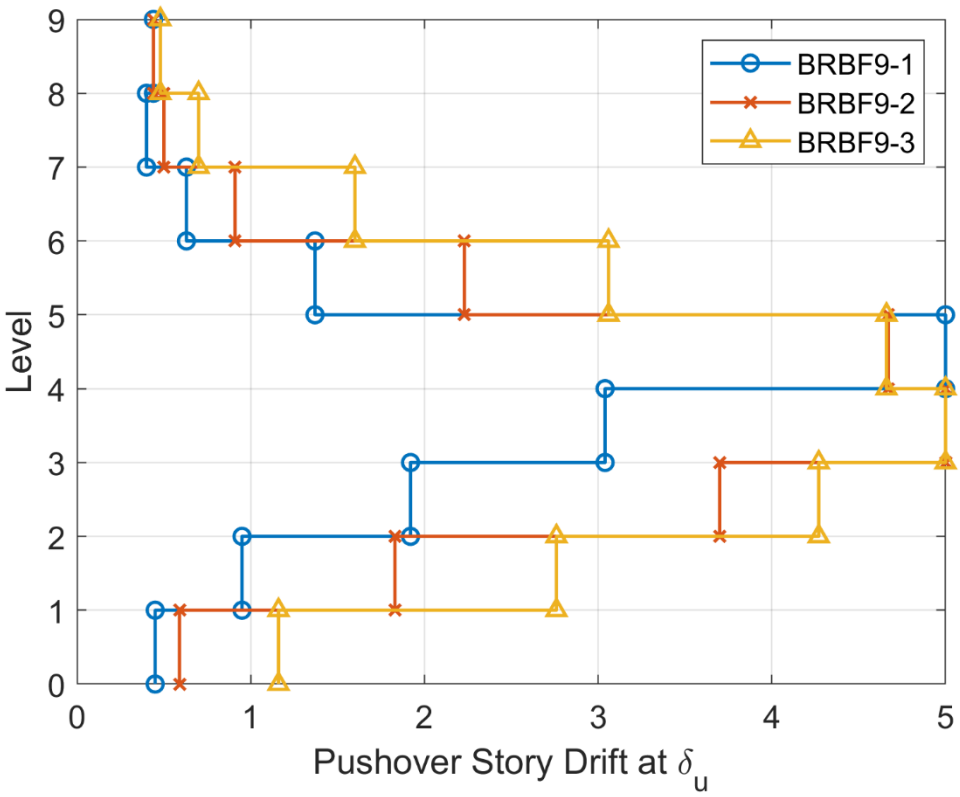

Figure 2-37 9-Story BRBF (BRBF9) pushover story drifts from Chapter 5.

This figure shows the relative contributions of the BRBF columns (BRBF 9-2) and gravity columns (BRBF 9-3). The results indicate the gravity columns spreads the yielding to more floors. The gravity column relative contribution is due, in large part, to the selected archetype where there are four BRBF columns and thirty-two gravity columns. Assuming half of the columns are oriented in the strong axis and half are oriented in the weak axis results in the following relative stiffnesses (based on moment of inertia) and strengths (based on $2M_p$) for the 9-story archetype as shown in Table 2-30 and Table 2-31. The stiffness and strength contribution of the gravity columns exceeds those of the BRBF columns, which is consistent with the pushover story drift plot above. Results are similar for the 4- and 15-story archetypes.

Table 2-30 Summation of Moment Inertia in 9-story Archetype

Level	Summation of I_{xx} BRBF Cols	Summation of I_{yy} BRBF Cols	Summation of I all Gravity Cols
9	584	196	8560
8	584	196	8560
7	4280	1380	13784
6	4280	1380	13784

Table 2-30 Summation of Moment Inertia in 9-story Archetype (continued)

Level	Summation of *Ixx* BRBF Cols	Summation of *Iyy* BRBF Cols	Summation of I all Gravity Cols
5	4280	1380	13784
5	4280	1380	13784
4	9600	3724	24660
3	9600	3724	24660
2	9600	3724	24660
G	15360	5760	30226

Table 2-31 Summation of $2M_p$ in 9-story Archetype

Level	Summation of $2M_p$ (Z_{xx}) BRBF Cols	Summation of $2M_p$ (Z_{yy}) BRBF Cols	Summation of 2_{Mp} (Z) all Grav Cols
9	16000	7600	156800
8	16000	7600	156800
7	74400	34000	247800
6	74400	34000	247800
5	74400	34000	247800
4	142000	72000	418000
3	142000	72000	418000
2	142000	72000	418000
G	216800	109600	505400

The resulting effects on displacement capacity, and the range of contribution from the BRBF and gravity columns, are included in the pushover envelope curves being evaluated in Chapter 5.

2.6 Reinforced Concrete Ductile Coupled Walls Overstrength

For Reinforced Concrete Ductile Coupled Walls overstrength comes from the SFRS and the gravity system. The SRFS overstrength, as defined previously, is given below:

$$\text{SFRS Overstrength} = \text{Bias in design} \times (1/\varphi) \times (\text{expected/nominal})$$

The bias in the design portion of the SFRS overstrength comes from several sources as discussed below.

The selected length and thickness of the Concrete Ductile Coupled Walls represents most of the design bias. The final wall configuration, however, is influenced by the architectural configuration and building program requirements. Wall placement is usually organized around the fixed building core elements such as elevators, stairs, and restrooms. The coupling beam aspect ratios are generally a function of building occupancy. For residential occupancies, due to the typical limited floor-to-floor heights, the coupling beam length-to-depth aspect ratios are generally more than 3. For office occupancies, the floor-to-floor heights range from 13 ft to 15 ft, resulting in coupling beam aspect ratios generally less than 3.

Once the wall and coupling beam configuration is set, the wall thickness is selected to provide sufficient shear and flexural capacity to resist the lateral design loads. For most wall configurations, it is the shear capacity requirement that is the major influence on the selected wall thickness, especially with the new shear requirements specified in ACI 318-19, which amplify the design shear for both the expected flexural capacity and higher mode effects.

In addition to wall length and thickness, the selection of the specified concrete strength, *f'c*, and the volume of shear reinforcement affect the resulting strength of the concrete ductile coupled walls in both shear and flexure. Also affecting the resulting strength over the height of the building are the transitions in wall thickness, specified concrete strength, and rebar.

Only one study is available that evaluated reinforced concrete ductile coupled walls: Tauberg et al. (2019). This FEMA P-695 study was performed to establish the seismic performance factors for this new system that is now included in ASCE/SEI 7-22, with the material-specific details being specified in ACI 318-19. The study included 6-, 8-, 12-, 18-, 24-, and 30-story archetypes. The 6-story archetype studies were limited and were undertaken to help establish the minimum height for the system. The 8-story, 12-story, and 18-story archetypes are used as the basis for determining the collapse surfaces shown in Chapter 5. The overstrength results in this chapter are provided for these same archetypes.

The study evaluated the influence of conventionally reinforced (CR) and diagonally reinforced (DR) coupling beams with aspect ratios ranging from 3.3 to 5.0 for CR and 2.0 to 3.3 for DR coupling beams. The SFRS overstrength results were influenced by the type of coupling beam but were

relatively insensitive to the coupling beam aspect ratio. The resulting SFRS overstrength values based on coupling beam type are summarized in Table 2-32.

Table 2-32 SFRS Overstrength Results Based on Coupling Beam Type

No. of Stories	CR-Based Ω	DR-Based Ω	Average Ω
8	1.6	2.2	1.9
12	1.3	1.5	1.4
18	1.6	2.0	1.8

Based on these results, the SFRS overstrength ranges for the 8-story, 12-story, 18-story archetypes are summarized in Table 2-33.

Table 2-33 SFRS Overstrength Values for 8-story and 12-story, and 18-story Archetypes

No. of Stories	High Seismic		
	Lower	Upper	Central
8	1.6	2.2	1.9
12	1.3	1.5	1.4
18	1.6	2.0	1.8

Although some other studies have shown lower overstrengths in the 10-to-12 story range than for shorter or taller archetypes, a defensible rationale for varying the SFRS overstrength on the basis of height could not be developed for this study. Given this, the values shown in Table 2-33 were averaged over the archetype heights, and the resulting values shown in Table 2-34 are recommended for SFRS overstrength regardless of height.

Table 2-34 Recommended SFRS Overstrength for Concrete Ductile Coupled Walls in Both High Seismic and Very High Seismic Regions

High Seismic		
Lower	Upper	Central
1.3	2.2	1.7

The above results do not incorporate the contribution of the gravity framing system, which needs to be added to obtain the overall building overstrength. Gravity frame system overstrength results for coupled shear walls are not available in the literature. Frame-wall interaction received significant attention in the 1960s, but the focus was on linear behavior; gravity framing system overstrength studies for concrete shear wall systems performing in the post-yield range are very limited.

The US-Japan Cooperative Research Program included shake table testing of a one-fifth scale model of a seven-story reinforced concrete shear wall building that demonstrated the significance of the gravity system on the performance of the shear wall (Charney, 1991). Figure 2-38 shows the plan and elevation of the test structure. Figure 2-39 shows a plot of base shear versus displacement for five different ground motions, and Figure 2-40 shows similar information for overturning moment. Both figures show that the total resistance is substantially higher than the force and moment resisted by just the shear wall. Figure 2-41 graphically represents the outrigger effect that is so significant; in part this is due the migration of the neutral axis in the shear wall after cracking of the concrete at the base of the wall.

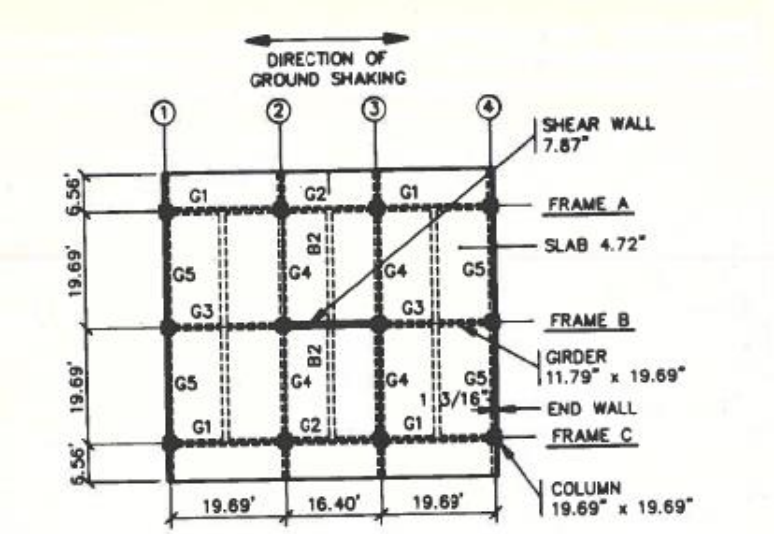

Fig. 1--Typical floor plan of 1/5-scale model

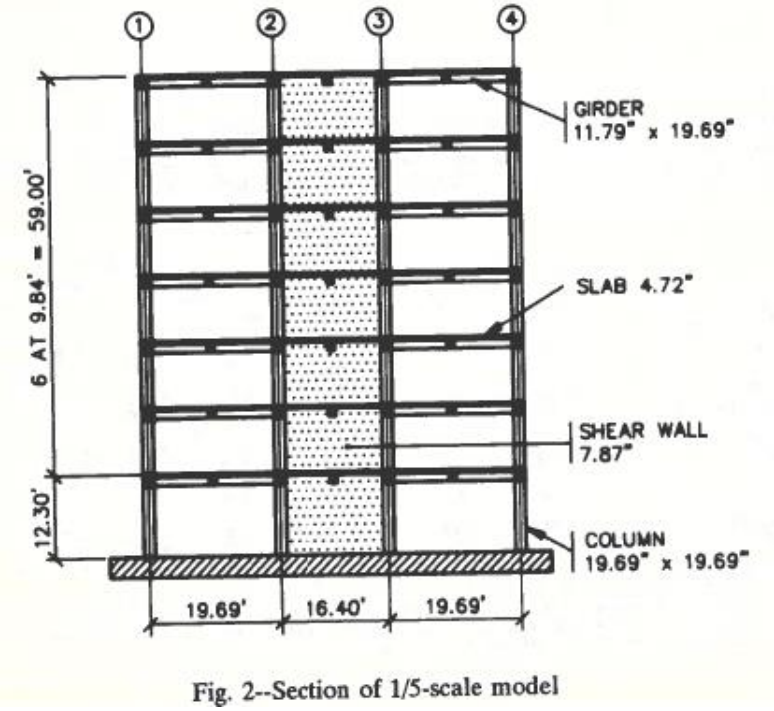

Fig. 2--Section of 1/5-scale model

Figure 2-38 Scale model subject to shake table testing from Charney (1991).

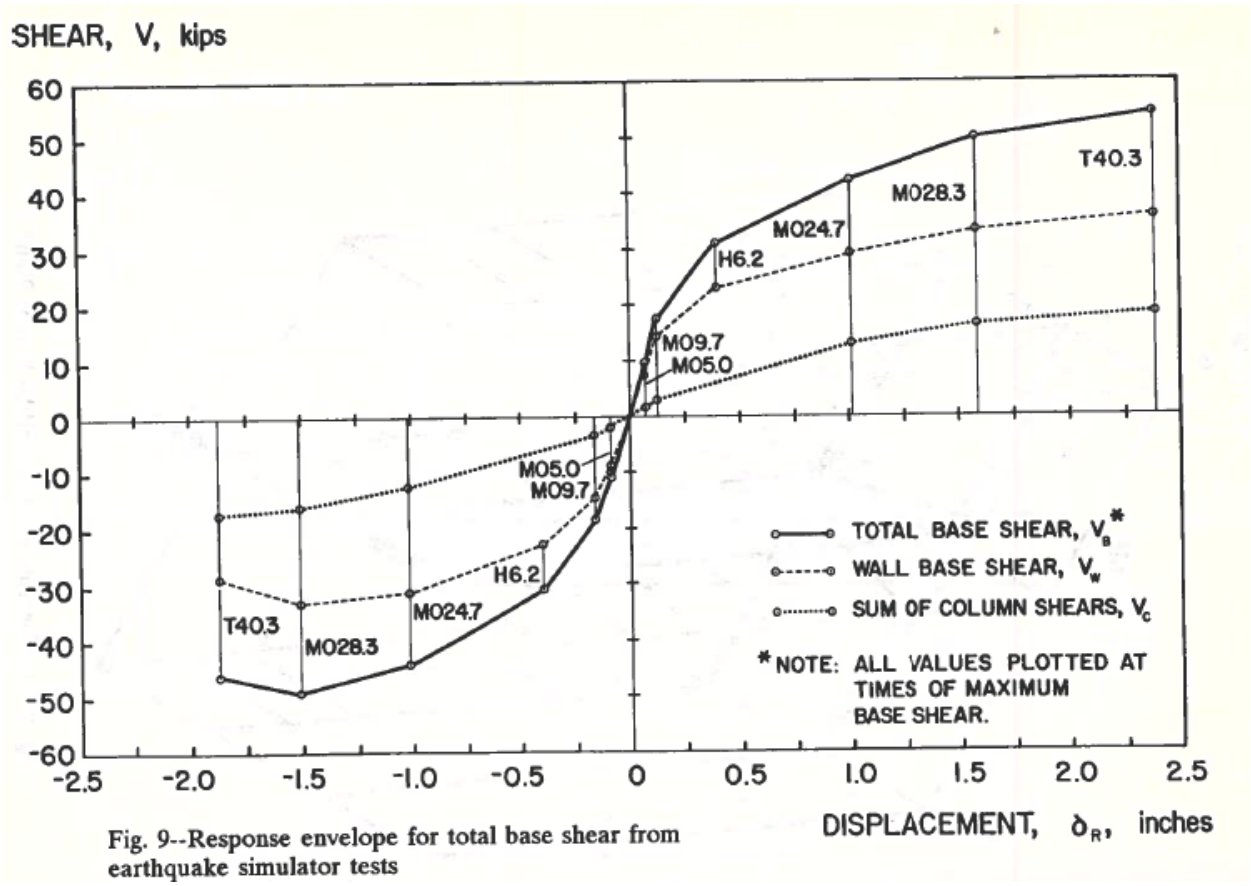

Figure 2-39 Measured base shear showing total shear and portions resisted by the shear wall and the frame from Charney (1991).

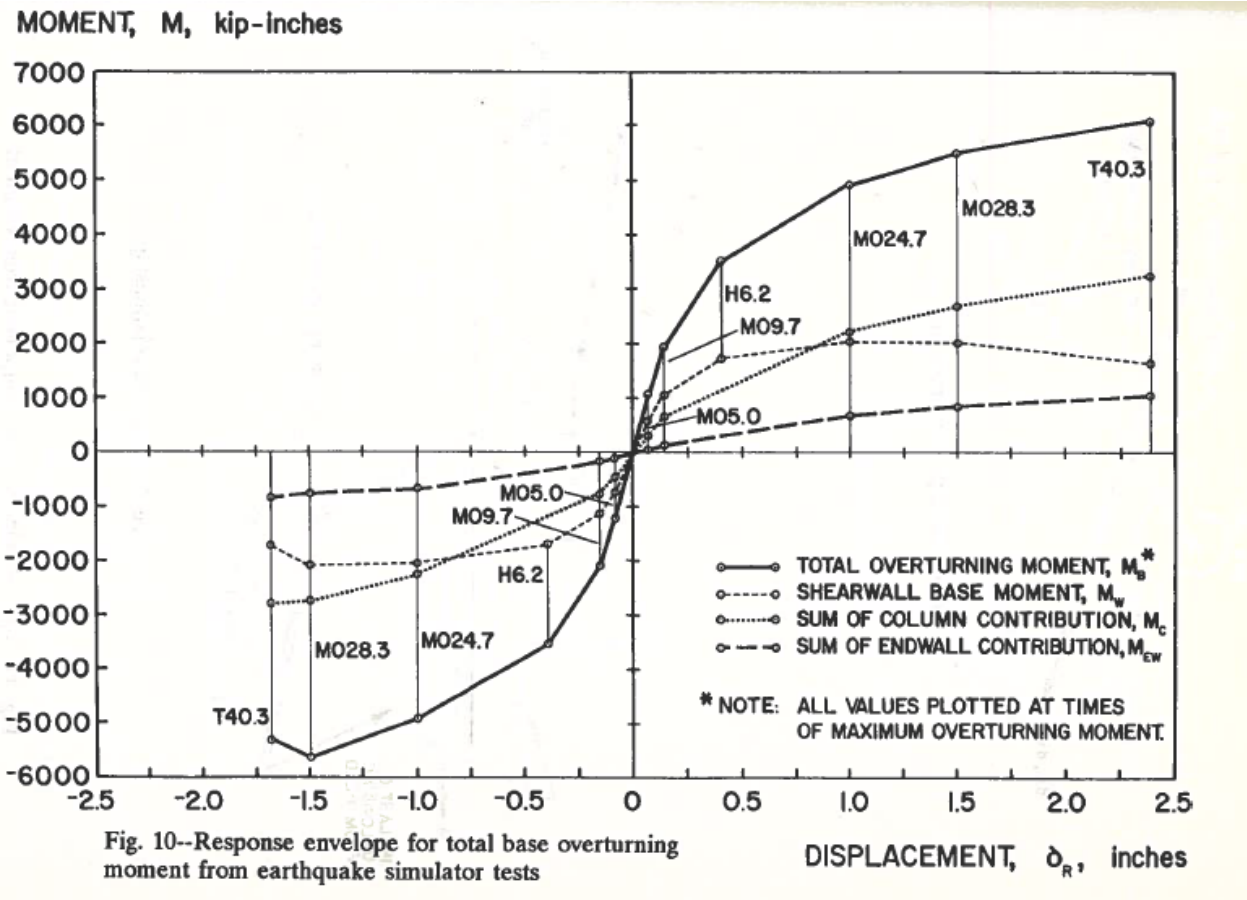

Fig. 10--Response envelope for total base overturning moment from earthquake simulator tests

Figure 2-40 Measured overturning moment showing total moment and portions resisted by the shear wall and the frame from Charney (1991).

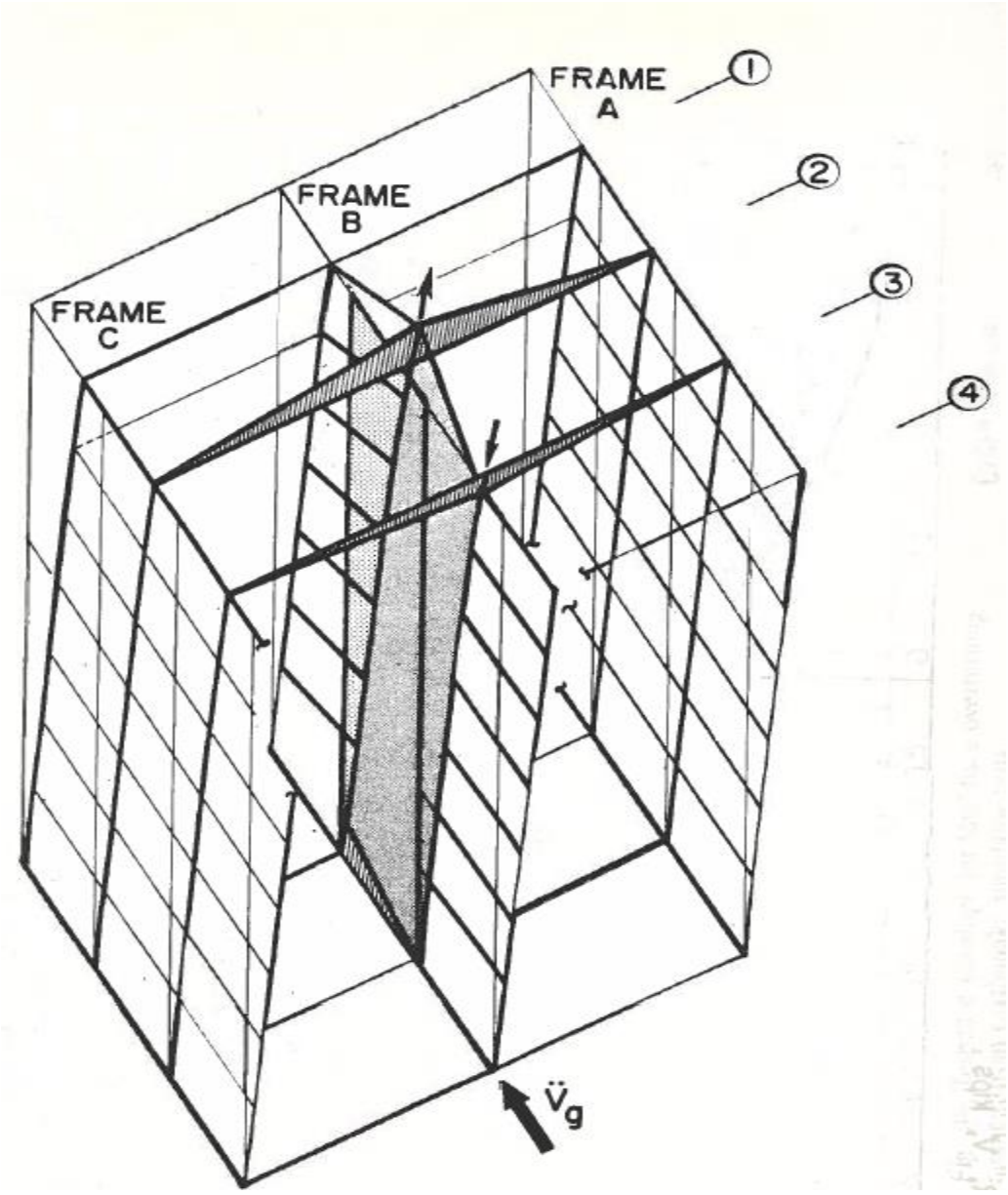

Figure 2-41 Graphic representation of outrigger effect from Charney (1991).

More recently, the ATC-63-2/3 project analytically evaluated the seismic performance of 12-story and 20-story concrete shear wall archetypes (not coupled in-plane) and included the effects of the gravity framing system. The influence of gravity framing system type (slab-column and beam-column) was also evaluated for the 12-story archetype. The typical floor plans are shown in Figure 2-42 to Figure 2-44.

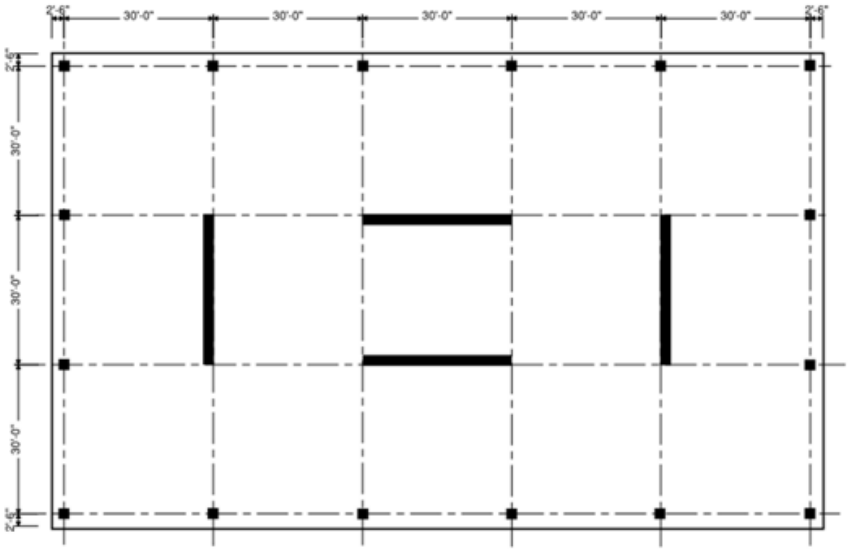

Figure 2-42 12-Story archetype with slab-column floor framing (12SC) from ATC-63-2/3.

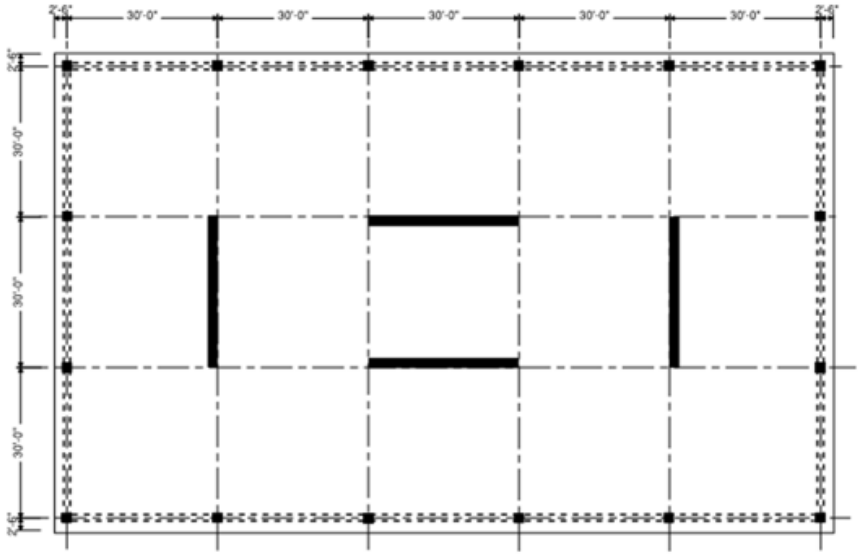

Figure 2-43 12-Story archetype with beam-column floor framing (12BC) from ATC-63-2/3.

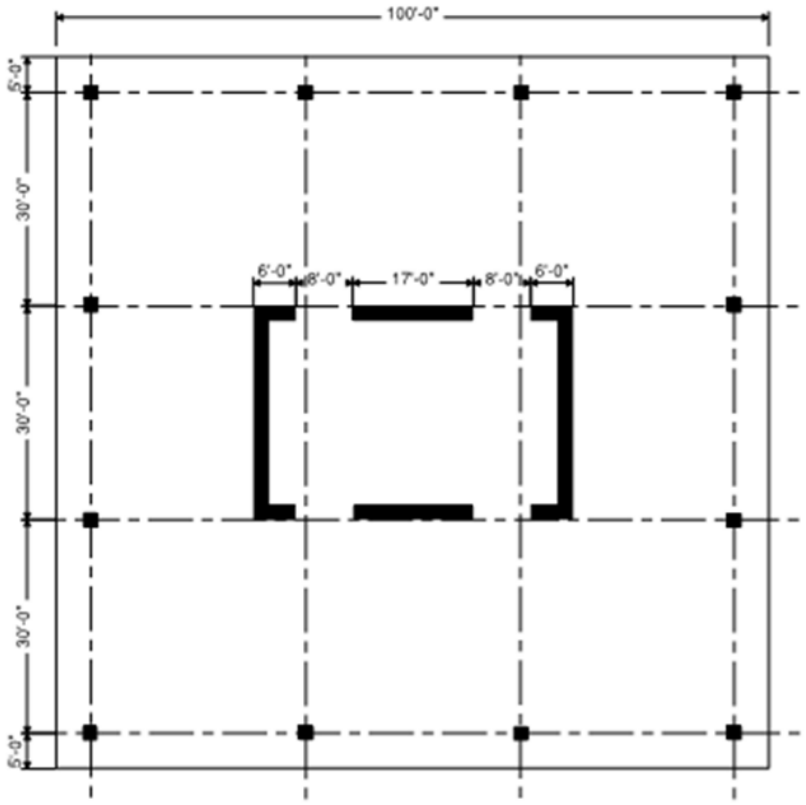

Figure 2-44 20-Story archetype with slab-column floor framing (20SC) From ATC-63-2/3.

The analytical models included both the gravity frame and gravity outriggering effect as depicted in Figure 2-45 for the 20-story archetype. The modeling approach for the 12-story archetype was similar.

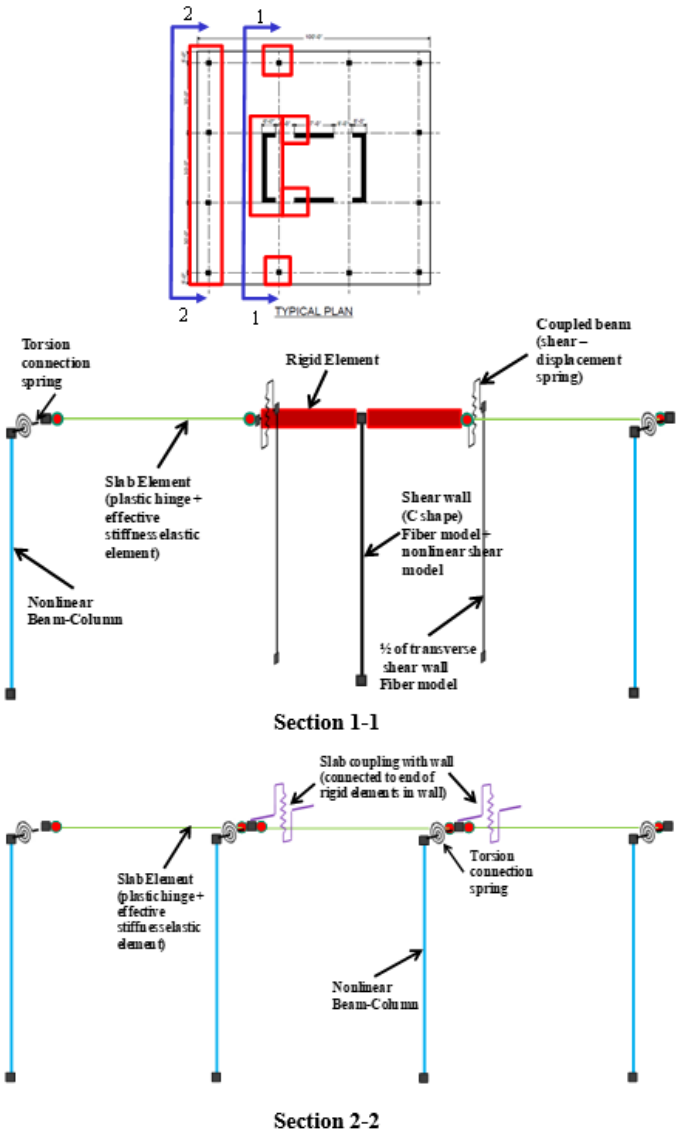

Figure 2-45 Schematic for one story of the 20BC model from ATC-63-2/3.

The resulting pushover results for the three archetypes are shown in Figure 2-46 to Figure 2-48.

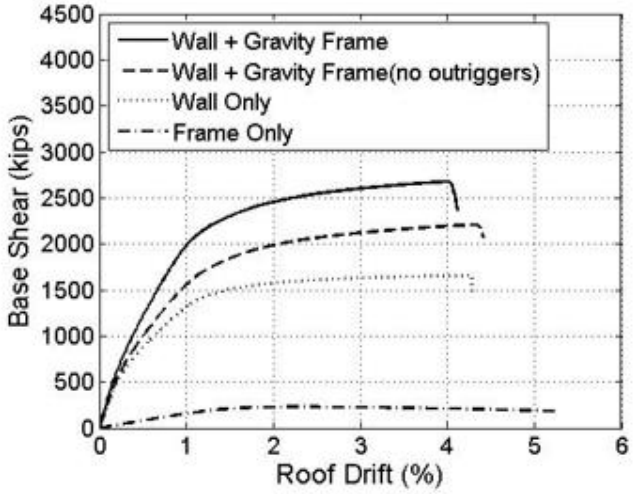

Figure 2-46 Pushover results for 12SC archetype from ATC-63-2/3.

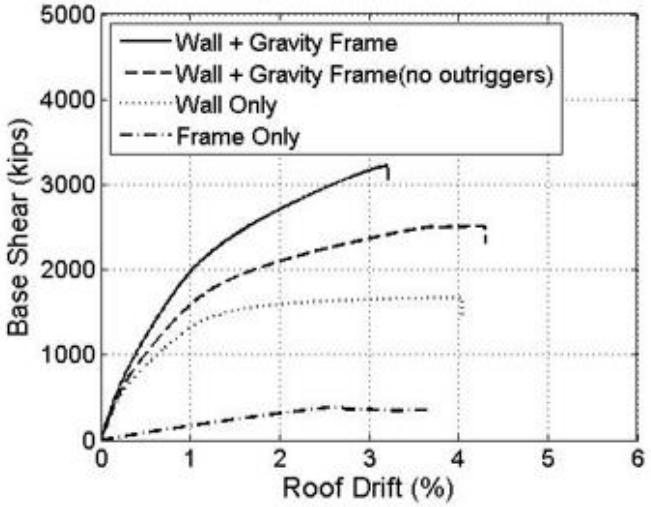

Figure 2-47 Pushover results for 12BC archetype from ATC-63-2/3.

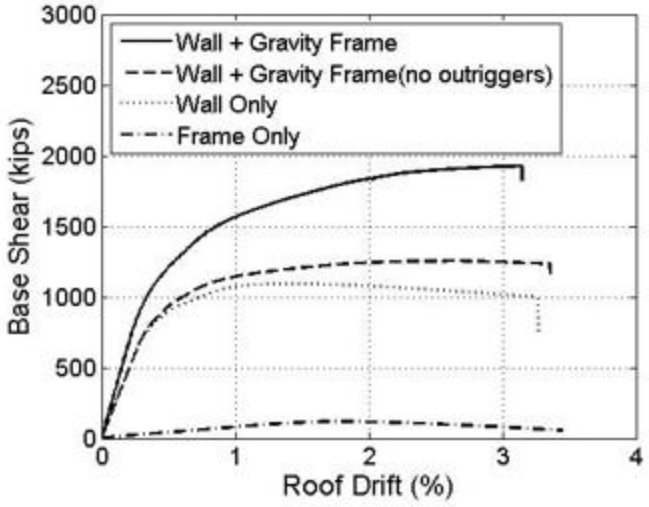

Figure 2-48 Pushover results for 20SC archetype from ATC-63-2/3.

The pushover results for the slab-column archetypes (12SC and 20SC) show that the gravity system outrigger contribution to overstrength exceeds the contribution from the gravity frame alone. The contribution is roughly equal for the beam-column frame archetype (12BC). The resulting quantification of the gravity framing system to the overall strength is summarized in Table 2-35.

Table 2-35 Gravity System Contribution to Overstrength for the 12-Story and 20-Story Archetypes from ATC-63-2/3

Archetype Design ID Number	Gravity System	Overstrength
12BC	None	1.06
12BC	GS	2.06
12SC	None	1.15
12SC	GS	1.82
20SC	None	1.07
20SC	GS	1.88

The listed SFRS overstrength values, associated with "None" on the table, are only slightly larger than one. An earlier FEMA P-695 concrete shear wall study also noted smaller than anticipated overstrength values. Specifically, NIST GCR 12-917-20 found overstrength values for 16- to 30-story archetypes less than 0.5. The report noted the following:

> "Higher modes dominate the seismic load distribution for walls designed using RSA, and the effective height for the RSA load distribution is much less than that associated with the first mode. Thus, when a first mode load pattern is applied to the building model in a pushover

analysis, the nominal flexural strength of the wall is reached at the base of the wall at a base shear that is significantly lower than the design base shear. Thus, the overstrength factor, which is designed to be based on the base shear according to the FEMA P-695 Methodology, is less than one. If the overstrength factor is based on base moment instead, values in excess of 1.0 are computed."

For this study, the gravity system overstrength that is sought should be minimally affected by the discussion above from NIST GCR 12-917-20.

Only the gravity system overstrength from the slab-column archetypes (12SC and 20SC) is being considered. The 12-story beam column archetype (12BC) represents a system that is much less common and would skew the results if included.

As can be derived from Figures 2-42 and 2-44, the gravity frame overstrength is approximately 500 kips and 250 kips for archetypes 12SC and 20SC, respectively. The remaining gravity system overstrength is due to the gravity system outrigger effect. From these figures, the gravity system outrigger effect results in an additional strength of approximately 500 kips and 700 kips for archetypes 12SC and 20SC, respectively, indicating that this effect varies with height as expected. Based on the values from Table 2-35, the increase in overstrength due to the gravity system is as shown in Table 2-36.

Table 2-36 Gravity System Overstrength from ATC-63-2/3

Archetype No.	Overstrength Increase
12SC	60%
20SC	75%

The existing work leaves unanswered the question as to whether there is a difference between frame-wall interaction and outriggering effects between single and coupled shear walls. Simple linear plane-frame models based on the archetype plan for the 20-story building included in the ATC 63-2/3 project were studied to develop an understanding of any difference. 8-, 12-, and 18-story buildings were studied. In these models, the effective stiffnesses of the walls and wall piers were taken as 20 percent of the gross properties, and the effective stiffnesses of the coupling beams were taken as 5 percent of the gross properties; these adjustments were made to account for the fact that the contribution from the slab-column frame interaction and the outriggering effect both reach their maximum after substantial yielding of the reinforcement in the shear wall, or wall piers and coupling beams. Frame wall interaction was studied by comparing the base shear and base overturning moment in the shear wall (and the coupled wall) with and without a plane frame linked to the wall with pinned links. Table 2-37 shows the results; the coupled wall derives more benefit from wall-frame interaction than the solid wall (both sets of archetypes were designed for very high seismic ground motions). This is not unexpected because the coupled wall system is more flexible than the solid wall system.

Table 2-37 Increase in Base Moment Capacity from Frame-Wall Interaction

No. of Stories	Solid Wall	Coupled Wall
8	7%	15%
12	11%	17%
18	23%	30%

Outrigger action was estimated in a more elementary manner. The combined resistance was estimated to be maximum when the tensile strain in the shear wall rebar reached 5 percent. Even considering that the rebar strain decreases rapidly with height, this is sufficient to reach the flexural capacity of the archetypical 8-inch post-tensioned slab spanning 30 feet. The outriggering effect shifts some dead weight of the slab from the adjacent columns to the uplifting end of the shear wall, which directly increases the flexural resistance. For this effect, it is estimated that the benefit to the coupled shear wall is substantially less than for a solid wall. The tension end of the compression pier does not lift very much, and the coupling beams are not expected to benefit from this action, so the moment arm upon which the additional weight acts is substantially less. Table 2-38 shows the increase, combined with that from frame-wall interaction.

Table 2-38 Combined Increase in Base Moment Capacity for Coupled Wall

No. of Stories	Frame-Wall Interaction	Outrigger Effect	Sum
8	15%	19%	33%
12	17%	17%	34%
18	30%	15%	45%

The values in Table 2-38 are substantially less than those in Table 2-36. A part, but not all, of the difference is explained by the expected reduction in the outriggering effect for the coupled walls. Given the very approximate nature of this study and the paucity of data, the values in Table 2-39 were adopted for gravity overstrength for very high seismic regions.

Table 2-39 Overstrength from Gravity System for Coupled Wall System for Very High Seismic Regions

No. of Stories	Lower	Upper	Central
8	30%	50%	40%
12	30%	50%	40%
18	40%	80%	60%

While it is possible that the frame-wall portion of the overstrength might decrease with the stiffer walls that would result from design for higher ground motions, that is expected to be a second order effect. Therefore, it is assumed that the gravity system overstrength will be constant for the ground motions included in this study. This assumption allows the gravity system overstrength to be expressed as a force in terms of pounds per square foot of floor area, as has been done for some of the other systems included in this study. Table 2-40 shows the results of that conversion.

Table 2-41 Overstrength from Gravity System for Coupled Wall System, in Pounds per Square Foot

No. of Stories	Lower	Upper	Central
8	54	90	72
12	60	99	79
18	88	176	132

The values in psf are substantially larger than found for the wood light-frame and steel special moment frame systems but given the higher design demands created by the heavier weight and lower *R* factor, the total overstrength is not actually larger. The total system overstrength for 8-story, 12-story, and 18-story concrete ductile coupled walls values as a function of both S_{MT} and S_{M1} are shown in Figure 2-49 and Figure 2-50. Notice that the curves for the 8- and 12-story buildings are identical when plotted versus S_{M1}, but they are not when plotted versus S_{MT}.

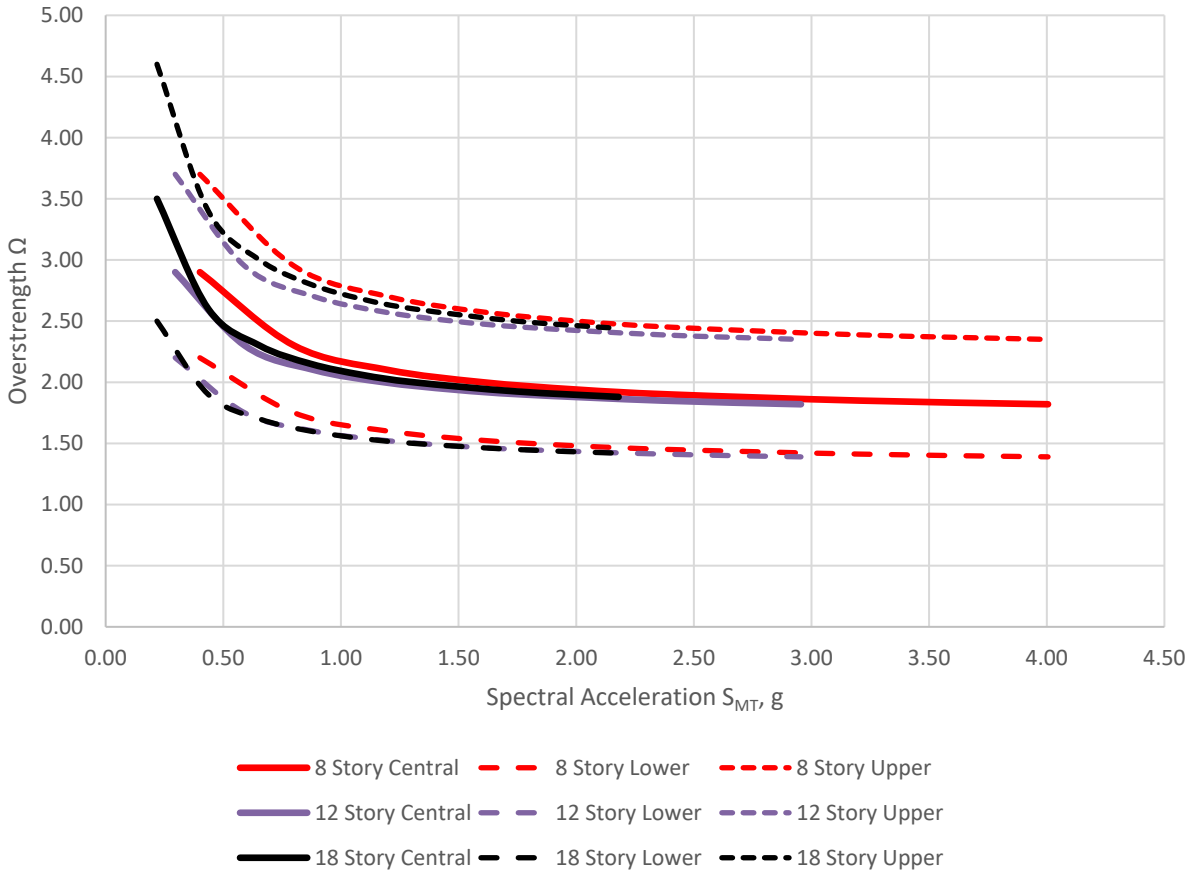

Figure 2-49 Total overstrength for 8-story, 12-story, and 18-story concrete ductile coupled walls as a function of S_{MT}.

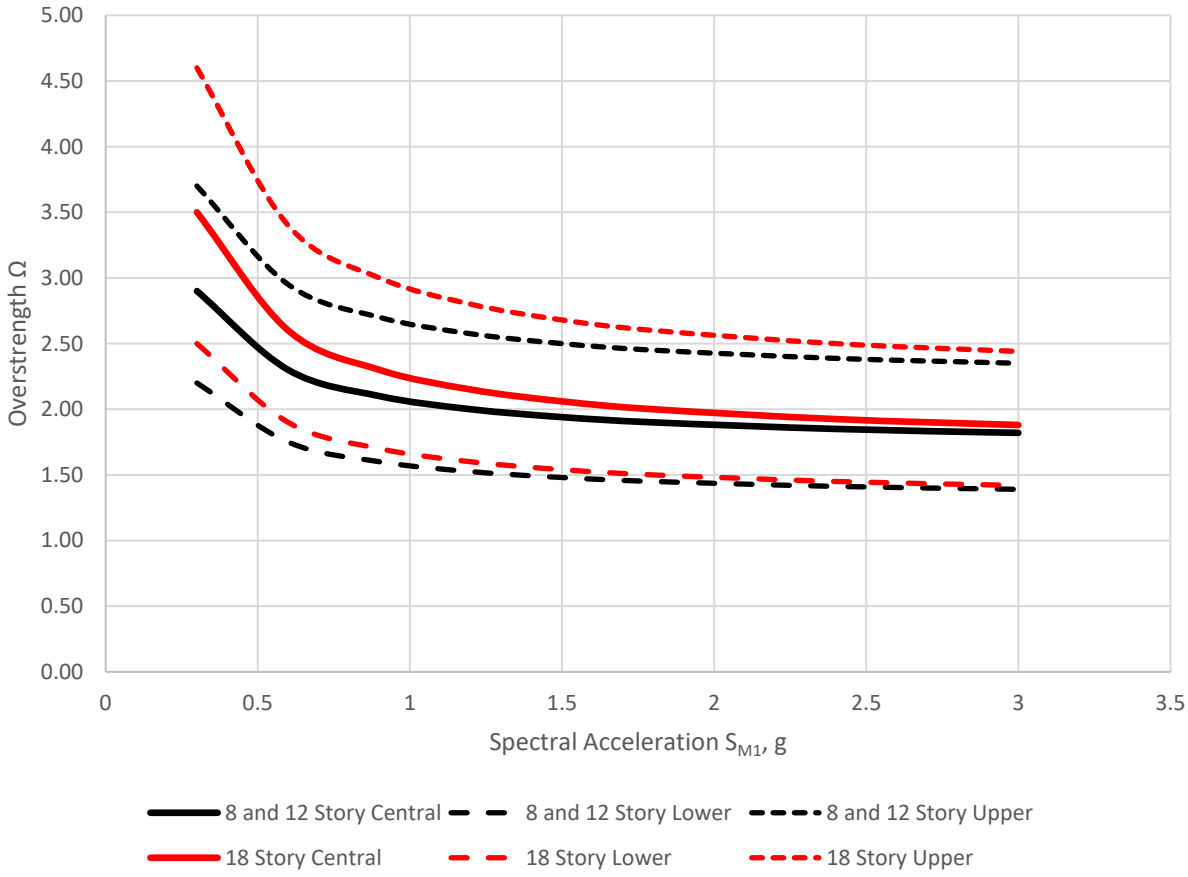

Figure 2-50 Total overstrength for 8-story, 12-story, and 18-story concrete ductile coupled walls as a function of S_{M1}.

2.7 Overstrength Values for Risk Category IV Archetypes

With one exception, archetypes are not available to establish the overstrength increase associated with Risk Category (RC) IV designs. Given this, ranges for the overstrength increase are based on:

- Ratios of required increase in forces and reduced allowable story drift limits associated with RC IV designs,
- Typical ranges of building drifts associated with RC II designs, and
- Simplified analyses and engineering judgement.

The RC IV overstrength increase is estimated relative to the overstrength values determined for RC II archetypes using the following relationship:

$$\Omega = V_{max}/V_{RCII}$$

This clarifies that the computation of probability of collapse is with regard to the MCE_R ground motion, which does not vary with Risk Category, although the target for collapse probability does vary with Risk Category. Therefore, for this project, the overstrength for RC IV is based on RC II demand even though the required strength does vary with Risk Category.

The change in Risk Category adjusts both the strength and stiffness (drift) design requirements as shown in Table 2-42.

Table 2-42 Risk Category Strength and Stiffness Design Requirements

Risk Category	I_e	Allowable Story Drift
II	1.0	0.02
IV	1.5	0.01

A first-order approximation for overstrength increase associated with RC IV systems controlled by strength is a factor of 1.5 times that for RC II. For those controlled by drift the factor is 2.0. The resulting overstrength increase for RC IV systems will, therefore, range between 1.5 and 2.0. RC IV overstrength values are provided for Steel Special Moment Resisting Frames, Steel Buckling-Restrained Braced Frames, and Reinforced Concrete Ductile Coupled Walls in the following sections.

2.7.1 Steel Special Moment Frame RC IV Overstrength Values

As described in Section 2.4, a 9-story, three-dimensional steel SMF archetype was developed using the office floor framing plan presented in Figure 2-26. For the purpose of comparing overstrength for RC II and RC IV structures, the floor framing plan for the RC IV archetype was modified to account for gravity loading and floor vibration criteria consistent with a healthcare occupancy. The superimposed dead load was increased from 15 psf to 30 psf. Detailed information regarding the archetypes is presented in Appendix F. Both archetypes were designed for High D ($S_{DS} = 1.0$ and $S_{D1} = 0.6$) seismic design levels. The RC IV archetype was designed to the 0.01 allowable story drift limit, which controlled the design.

As indicated in Table 2-43, the resulting overstrength values for RC II and RV IV are 3.74 and 6.61, respectively, resulting in an overstrength increase factor of 1.77. The RC II overstrength of 3.74 comes from the data used to create Figure 2-29 in Section 2.4. It should be noted this ratio includes the contribution of the gravity systems and composite action in the SFRS connections, which varied by risk category as noted previously. If the gravity system remained unchanged between the designs, the resulting increase factor would have been less than 1.74.

Table 2-43 Overstrength for RC II and RC IV SMF Archetypes

Risk Category	Overstrength	Overstrength Ratio Relative to RC II
II	3.74	1.0
IV	6.61	1.77

2.7.2 Steel Buckling-Restrained Braced Frame RC IV Overstrength Values

Steel BRBF are not typically drift-controlled. Design story drifts are generally in the 0.0125-0.015 range. The increase in strength for the RC IV structure usually results in a structure that satisfies the RC IV drift limit. Therefore, this results in an overstrength increase factor of 1.5 for RC IV relative to RC II values.

2.7.3 Reinforced Concrete Ductile Coupled Wall RC IV Overstrength Values

Ductile coupled walls are not typically drift-controlled. Design story drifts are generally around 0.015 for buildings without torsion. The 1.5 increase in forces does increase the building stiffness, resulting in thicker, longer, or more walls. This results in a lower bound overstrength increase of 1.5 for RC IV relative to RC II values.

Chapter 3: Procedures for Developing and Utilizing Collapse Surfaces

3.1 Introduction

This chapter provides background and describes methods for the development of collapse surfaces and for the utilization of these surfaces to evaluate the additional collapse "risk" associated with seismic force resisting systems (SFRSs) located in regions of very high seismicity. Collapse surfaces are developed and used in Chapter 4 to evaluate the collapse performance of various archetypes of light-frame wood buildings and in Chapter 5 to evaluate the collapse performance of buildings with (1) steel buckling-restrained braced frames, (2) coupled reinforced-concrete shear walls, and (3) steel special moment resisting frames.

3.2 Collapse Surface Concept

Section 5.4 of FEMA P-2139-1 introduced the concept of a "collapse surface" to describe the interaction of the two primary building response properties (1) strength and (2) displacement capacity governing earthquake collapse performance of a class of structures. In that report, data from a generic collapse performance investigation of simple bilinear SDOF models were used to develop examples of notional collapse surfaces of a generic nonlinear system.

Plots of notional collapse surfaces are shown in Figure 3-1 (copy of Figure 5-13 of FEMA P-2139-1). In this figure, collapse surfaces quantify collapse performance in terms of the Adjusted Collapse Margin Ratio (*ACMR*) plotted as a function of SDOF model pushover strength (V_{max}/W) and drift ratio at the point of incipient collapse for each of four model periods (i.e., T = 0.15 s, 0.25 s, 0.35 s and 0.45 s). Values of *ACMR* were calculated in accordance with the FEMA P-695 methodology (see Section 3.4). The collapse surfaces of this report are based on the conceptual surfaces of FEMA P-2139-1 with two important modifications, (1) collapse performance is evaluated in terms of median collapse acceleration, $\hat{S}_{CT}$, in lieu of *ACMR*, and (2) collapse performance is calculated using sophisticated and realistic two-dimensional nonlinear models of SFRS archetypes of interest, rather than simple bilinear SDOF models of a generic nonlinear system.

In a broader sense, the surface concept developed in this study for evaluating collapse could be used equally well to evaluate other modes of failure and generalized as "failure surfaces," rather than collapse surfaces. However, the collapse surface terminology of FEMA P-2139-1 is retained for this study, which is focused on collapse performance.

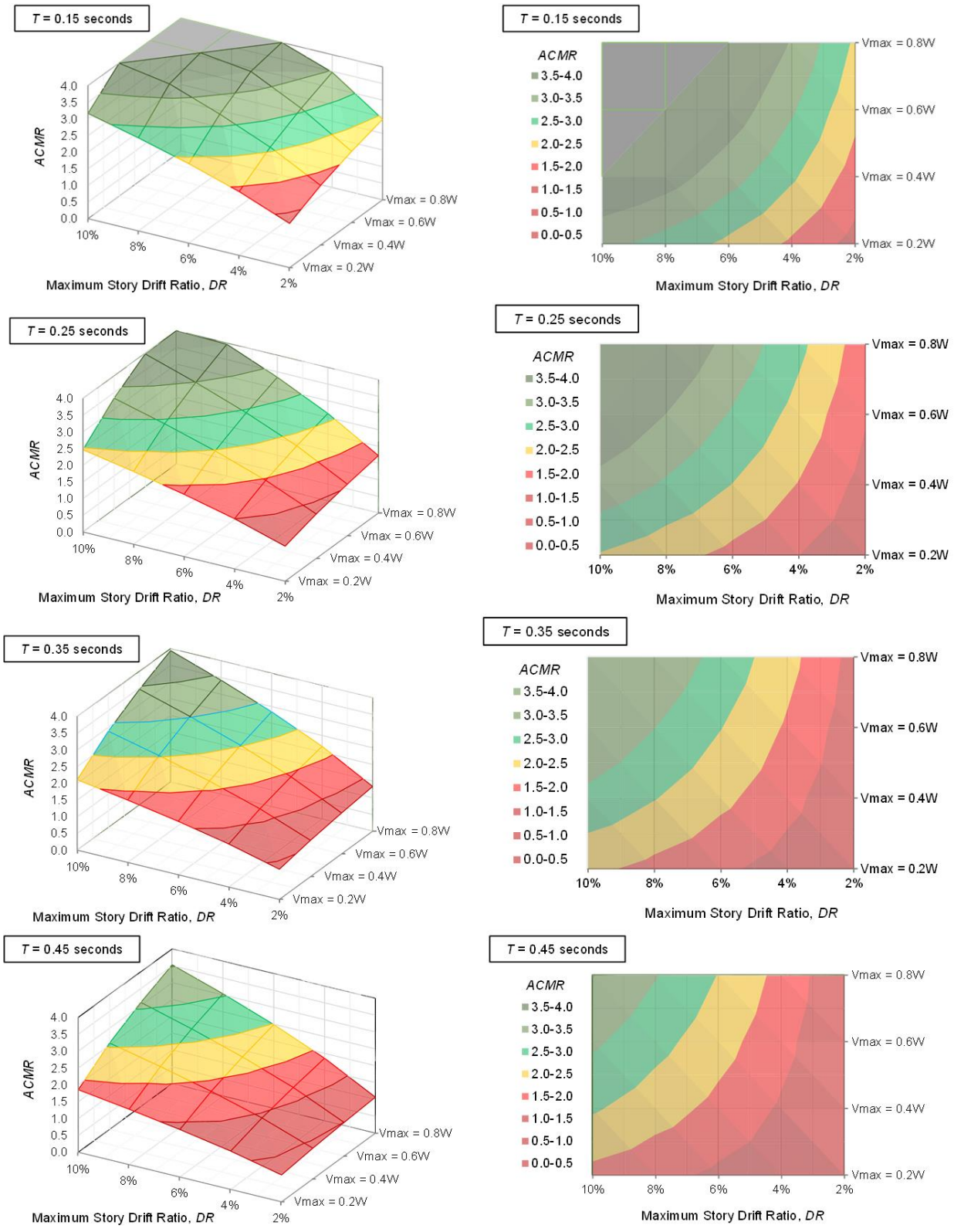

Figure 3-1 **Plots of notional collapse surfaces for SDOF models with periods, *T* = 0.15 seconds, *T* = 0.25 seconds, *T* = 0.35 seconds and *T* = 0.45 seconds, assuming first-story failure (Figure 5-13 of FEMA P-2139-1).**

3.3 Collapse Surface Development Scope and Approach

Collapse surfaces describe median collapse acceleration, $\hat{S}_{CT}$, of the SFRS archetype of interest as a function of maximum (pushover) strength (V_{max}/W) and drift ratio at incipient collapse. Collapse surfaces are defined by a mathematical equation, whose coefficients are determined by regression analysis of a large set of collapse data of the SFRS archetype of interest.

Conceptually, there is a different and unique collapse surface for each configuration and height (i.e., number of stories) of the SFRS archetype of interest. For the light-frame wood SFRS, there are fifteen different collapse surfaces corresponding to the fifteen combinations of three configurations of commercial (COM), multi-family dwelling (MFD) and structure-only (STR) archetypes and five story heights (i.e., 1-story through 5-stories) of light-frame wood buildings.

In Chapter 4 and Chapter 5, collapse data are generated by FEMA P-695 collapse analysis of two-dimensional (2D) nonlinear models of the SFRS archetype of interest that:

1. Accurately characterize the dynamic response and collapse performance of the SFRS archetype configuration of interest (e.g., as validated by comparison with the collapse results of prior studies of the same SFRS archetype configuration),
2. Comprehensively represent typical archetype configurations of various heights of the SFRS archetype configuration of interest (excluding high-rise buildings), and
3. Comprehensively represent the strengths of SFRS archetypes (of both Risk Category II and IV structures) designed for a broad range of MCE_R response spectral accelerations ranging from those of moderate seismicity design (e.g., S_{MS} = 0.75g) to those representing the strongest level of ground motions in regions of very high seismicity (e.g., S_{MS} = 3.0g), where S_{MS} is the value of MCE_R response spectral acceleration, S_{MT}, at short periods.

The first criterion necessitates sophisticated nonlinear modeling of hysteretic behavior while the second and third criteria are best accomplished using nonlinear models with a limited number of degrees of freedom (i.e., models that are computationally efficient for incremental dynamic analysis of large numbers of 2D nonlinear models of different strengths, configurations and heights). 2D nonlinear models with limited degrees of freedom are used in this study to develop collapse surfaces of SFRS archetypes of interest, as described in Chapter 4 and Chapter 5. Values of median collapse acceleration, $\hat{S}_{CT}$, of these models are compared with those of prior studies of the same archetype configuration to verify that the collapse surfaces of this study can reliably predict median collapse performance of the SFRS of interest. For example, collapse performance of the two-degree-of-freedom 2D nonlinear models of light-frame wood archetypes of Chapter 4 is validated by comparison with the collapse performance of the corresponding multi-degree of freedom, three-dimensional (3D) nonlinear models of light-frame wood archetypes of FEMA P-2139-2 for models of the same or similar configuration, height and strength.

Values of median collapse acceleration, $\hat{S}_{CT}$, are calculated in accordance with the methods of FEMA P-695 using both Far-Field and Near-Field record sets. FEMA P-695 requires the use of the Far-Field record set for collapse evaluation of a proposed new SFRS. This record set is used for collapse evaluation of all SFRS archetypes of Chapter 4 and Chapter 5. Appendix A of FEMA P-695 also includes a Near-Field record set of ground motions recorded within 15 km of fault rupture typical of many very high seismic sites. The Near-Field record set is also used for collapse evaluation of selected SFRS archetypes of Chapter 4 to investigate differences in collapse performance (i.e., differences in collapse surfaces) for the same SFRS at sites closer to fault rupture.

The FEMA P-695 methodology (with certain adaptations) is relied on for developing collapse surface data from nonlinear analyses of archetype models. Section 3.4 of this chapter provides a summary of the concepts, methods and terminology of FEMA P-695 as adapted for development of collapse surfaces of SFRS archetypes in Chapter 4 and Chapter 5 and the example collapse surfaces of this chapter.

3.4 Summary of the FEMA P-695 Methodology

This section provides a summary of the concepts, methods and terminology of FEMA P-695 (FEMA 2009) as adapted for development of collapse surfaces of SFRS archetypes in Chapters 4 and 5 and the examples of this chapter. This section is included primarily for those readers not familiar with the FEMA P-695 methodology.

3.4.1 Overview of FEMA P-695 Analysis Methods

The FEMA P-695 methodology relies on collapse simulation through nonlinear response history analysis of archetype models of the SFRS of interest. The methodology accounts for potential uncertainties in ground motions, component design parameters, structural configuration, and behavioral characteristics of structural elements based on available laboratory test data. Analysis methods are rigorously and unambiguously defined by the FEMA P-695 methodology, including the specification (selection and scaling) of ground motion records to be used in response history analysis of nonlinear models.

The FEMA P-695 methodology is intentionally, conservatively biased for collapse evaluation of archetype models of a new SFRS seeking adoption by seismic codes. For example, non-structural components and structural elements (of the gravity system) not part of the SFRS (e.g., gravity system) are excluded from models of the SFRS, although the analysis methods are generally applicable to all building elements subject only to availability of test data required to establish model properties. Intentional conservatisms of the FEMA P-695 methodology are ignored by this study, which seeks to evaluate collapse performance without bias, similar to prior studies of short-period building collapse performance (FEMA, 2020).

FEMA P-695 analysis methods include (1) nonlinear static (pushover) analysis to determine post-yield displacement capacity expressed in terms of the period-based ductility parameter (μ_T) and

(2) incremental dynamic analysis (IDA) to calculate median collapse capacity expressed in terms of corresponding value of response spectral acceleration ($\hat{S}_{CT}$) at the fundamental period, T, (i.e., $T = C_u T_a$ of ASCE/SEI 7-22) of the archetype model of the SFRS of interest. To the extent possible, nonlinear models directly simulate collapse failure modes (i.e., simulated "side-sway" collapse) and necessarily incorporate P-delta effects, which influence collapse of archetype models with large collapse displacement capacity. Where simulating collapse is not possible or practical, "non-simulated" collapse is defined by alternative limit states on structural response (e.g., maximum story drift ratio, as described in Section 3.4.5).

The collapse margin ratio (*CMR*) is defined as the value of median collapse response spectral acceleration divided by the value of MCE_R response spectral acceleration (S_{MT}) at the fundamental period (T) used as the basis for design of the archetype model (i.e., $CMR = \hat{S}_{CT} / S_{MT}$). The larger the value of the *CMR*, the lower the probability of collapse. The adjusted collapse margin ratio (*ACMR*) is the value of the *CMR* adjusted by the spectrum shape factor (*SSF*) to account for the inherent "rareness" of MCE_R ground motions (i.e., $ACMR = SSF \times CMR$). The *SSF* accounts for the post-yield elongation of the elastic fundamental-mode period of the archetype model based on the period-based ductility of the archetype model of the SFRS. The larger the amount of period-based ductility of the model, the larger the adjustment (increase) in the value of the *CMR* and the lower the probability of collapse.

3.4.2 Far-Field and Near-Field Record Sets

The FEMA P-695 methodology provides two sets of ground motion records for collapse assessment using nonlinear dynamic analysis, the Far-Field record set and the Near-Field record set. The Far-Field record set includes 22 component pairs of horizontal ground motions from sites located greater than or equal to 10 km from fault rupture. The Near-Field record set includes 28 component pairs of horizontal ground motions recorded at sites less than 10 km from fault rupture. The record sets do not include the vertical component of ground motion since this direction of earthquake shaking is not considered of primary importance for collapse evaluation and is not required for nonlinear dynamic analysis. The Far-Field record set is the primary record set used by this study for nonlinear response calculations and collapse evaluations.

The Far-Field ground motion record sets include 22 strong-motion records (i.e., records with PGA > 0.2g and PGV > 15 cm/sec.) from all large-magnitude (M > 6.5) events in the PEER NGA West1 database (PEER, 2006). Large-magnitude events dominate collapse risk and generally have longer durations of shaking (which is important for collapse evaluation of nonlinear degrading models). The Far-Field ground motion record set includes records from soft rock and stiff soil sites (e.g., average shear wave velocity of 344 m/s in the upper 30 m), and from shallow crustal sources (predominantly strike-slip and thrust mechanisms). To avoid event bias, no more than two of the strongest records are taken from each earthquake. Response spectra of the 44 individual record components (i.e., 22 records, 2 components each), the median response spectrum, and spectra representing response at plus one- and plus two-standard deviations of the Far-Field record set are shown in Figure 3-2.

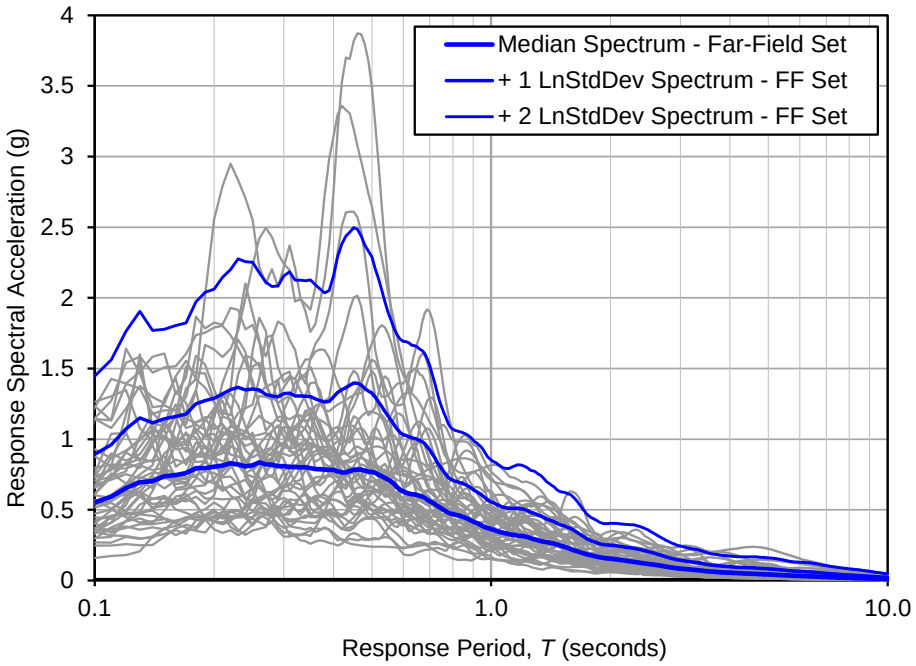

Figure 3-2 Far-Field record set response spectra plots (Figure 6-3 of FEMA P-695).

The Far-Field record set provides a fully defined set of records for use in a consistent manner to evaluate collapse of all possible types of SFRSs located in any seismic region. The FEMA P-695 methodology opted to use actual earthquake records (in contrast to artificial or synthetic records) recognizing that regional variation of ground motions would not be addressed. Large magnitude events are rare, and few existing earthquake ground motion records are strong enough to collapse large fractions of modern, code-compliant buildings. In the United States, strong-motion records date back to the 1933 Long Beach earthquake, with only a few records obtained from each event until the 1971 San Fernando earthquake.

Ground motion records are scaled to represent a specific intensity (e.g., the collapse intensity of the index archetypes of interest). Record scaling involves two steps. First, individual records in each set are "normalized" by their respective peak ground velocities, as described in Appendix A of FEMA P-695. This step is intended to remove unwarranted variability between records due to inherent differences in event magnitude, distance to source, source type and site conditions, without eliminating record-to-record variability. Second, normalized ground motions are collectively scaled to a specific ground motion intensity such that the median spectral acceleration of the record set matches the desired spectral acceleration at the design period, *T*, of the archetype model being analyzed.

The first scaling step was performed as part of the ground motion development process of FEMA P-695 and the record sets of Appendix A of FEMA P-695 already reflect this normalization (e.g., response spectra shown in Figure 3-2 are already "normalized"). The second step is performed as part of incremental dynamic analysis (IDA) procedure.

The IDA procedure requires individual record components (e.g., 44 record components of the "normalized" Far-Field record set) to each be scaled by the same factor such that the median spectral response of the set of scaled record components equals the target response spectral acceleration at the design period, *T*, of the archetype model. Target response is defined at increments of MCE_R response spectral acceleration, S_{MT}, at the design period. Example scaling of median spectral response of the Far-Field record set (and the Near-Field record set) to target response at T = 0.30 s is illustrated in Figure 3-3, where target response (i.e., 2.64g) represents 1.0 times the multi-period response spectrum (MPRS) of MCE_R ground motions of ASCE/SEI 7-22 of a site in Los Angeles, California, assuming Site Class CD site conditions. De-aggregation of site hazard shows 0.30-second MCE_R ground motions to be governed approximately equally by a magnitude M7.3 event at 14 km on the Compton Fault and a magnitude M7.1 event at 7 km on the Puente Hills Fault.

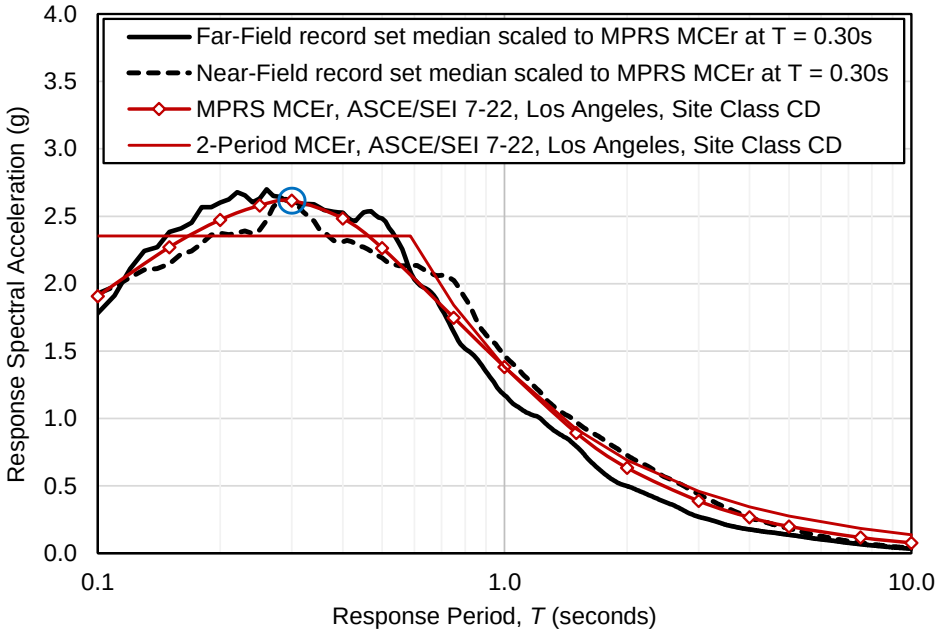

Figure 3-3 Illustration of the scaling of the median spectra of the Far-Field and Near-Field record sets to 1.0 times the multi-period response spectrum (MPRS) of ASCE/SEI 7-22 MCE_R ground motions of ASCES/SEI 7-22 of a site in Los Angeles, California, assuming Site Class CD site conditions, at T = 0.30 s.

FEMA P-695 methods used to scale records for incremental dynamic analysis are the same for Far-Field and Near-Field record sets. For this study, the new multi-period response spectra (MPRS) of ASCE/SEI 7-22 are used in lieu of two-period response spectra of prior editions of ASCE/SEI 7. For reference, Figure 3-3 also includes the two-period MCE_R spectrum of the Los Angeles site, noting that the MPRS of ASCE/SEI 7-22 are the preferred characterization of earthquake ground motions for seismic design. MPRS provide a more reliable value of MCE_R ground motions at the design period, *T*, of the SFRS archetype model of interest. In this sense, Figure 3-3 supersedes Figure 6-4 of

FEMA P-695, which illustrates scaling of the Far-Field record set median to two-period design spectrum of ASCE/SEI 7-05.

3.4.3 Pushover Analysis

FEMA P-695 methods require pushover analysis to determine the over-strength factor, Ω, and the period-based ductility parameter, μ_T, from values of archetype model maximum strength, V_{max}, roof displacement at effective yield, $\delta_{y,eff}$, and ultimate roof displacement, δ_u, where δ_u is assumed to be reached at a post-peak strength of $0.8V_{max}$, as illustrated in Figure 3-4.

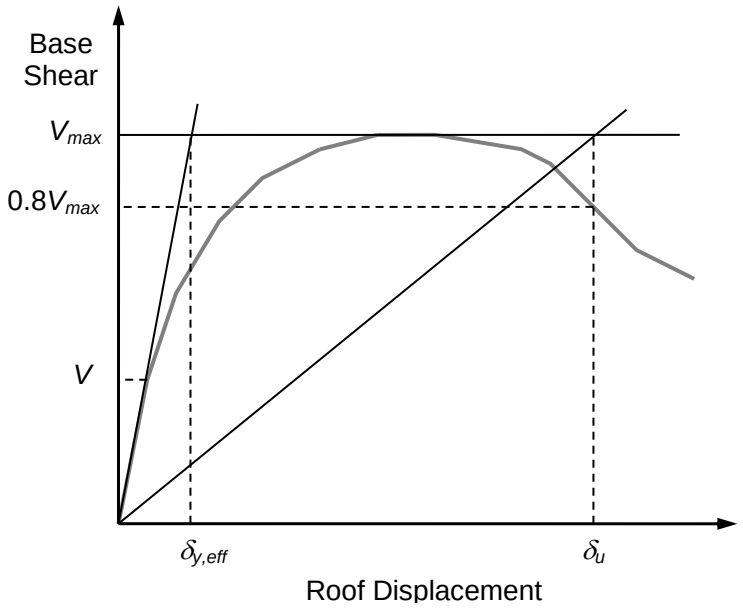

Figure 3-4 Idealized nonlinear pushover curve (Figure 6-5 of FEMA P-695).

The overstrength factor for a given archetype model, Ω, is defined by FEMA P-695 as the ratio of the maximum base shear resistance, V_{max}, to the design base shear, V:

$$\Omega = \frac{V_{max}}{V} \tag{3-1}$$

For development of collapse surfaces, a range of hypothetical values of V_{max} (normalized by archetype model weight, W) are assumed (i.e., rather than calculated from pushover analysis of an archetype model). Values of the design base shear parameter, V, are defined by the ELF design requirements of ASCE/SEI 7-22 for the SFRS of interest and the MCE_R response spectral acceleration, S_{MT}, at the design period of the archetype model:

$$V = \left(\frac{S_{MT}}{1.5\left(R / I_e \right)} \right) W \tag{3-2}$$

Where R is the response modification coefficient of the SFRS and I_e is the earthquake Importance Factor, which depends on Risk Category. The period-based ductility, μ_T, for a given archetype model is defined as the ratio of ultimate roof drift displacement, δ_u, (defined as shown in Figure 3-4) to the effective yield roof drift displacement $\delta_{y,eff}$:

$$\mu_T = \frac{\delta_u}{\delta_{y,eff}} \tag{3-3a}$$

The definition of ultimate roof drift displacement, δ_u, assumes collapse occurs at a post-peak pushover strength of $0.8V_{max}$. A more reliable estimate of roof displacement at collapse may be obtained from the results of incremental dynamic analysis (IDA), which incorporate hysteretic behavior of the archetype model, as well as the collapse capacity beyond a post-peak pushover strength of $0.8V_{max}$ (e.g., residual strength of wood light-frame archetype models). For this study, period-based ductility, μ_T, is calculated using a value of ultimate roof drift displacement, δ_u, corresponding to the median drift ratio at incipient collapse, DR_{IC} (or median DR_{IC}), determined from the IDA results of the archetype model of interest. Calculation of DR_{IC} from IDA results is described in the next section. Substituting δ_u for DR_{IC} provides the following:

$$\mu_T = \frac{DR_{IC}}{\delta_{y,eff}} \tag{3-3b}$$

3.4.4 Incremental Dynamic Analysis

FEMA P-695 methods utilize incremental dynamic analysis (IDA) to determine median collapse capacity of the archetype model of interest. Median collapse capacity is the value of response spectral acceleration, $\hat{S}_{CT}$, at the fundamental period, T, at which the archetype model has a 50 percent probability of collapse. Using the Far-Field record set, median collapse capacity is determined by applying the 44 record components of the record set (i.e., 22 records, 2 components each) to the model incrementally scaled from relatively low to relatively high values of response spectral acceleration. Median collapse capacity is the median value of response spectral acceleration of the record set at which 22 of the 44 record components affects collapse of the archetype model.

The methods of FEMA P-695 focus on quantifying collapse performance from IDA results strictly in terms of response spectral acceleration (i.e., for evaluation of a proposed new SFRS). This study, like prior studies that have utilized FEMA P-695 methods to more broadly investigate collapse

performance (e.g., FEMA P-2139-1), expands the use of IDA results to quantify the collapse displacement capacity of archetype models in terms of the median value of the story drift ratio at incipient collapse, DR_{IC}, of the story governing collapse. Figure 3-5 illustrates IDA results for the 4-story COM wood archetype model, 4C-073-060-030, of Chapter 4. In this example, the archetype model has a design period, T = 0.45 s, a median value of 0.45-second response spectral acceleration at collapse, $\hat{S}_{CT}$ = 3.54g, and a median drift ratio at incipient collapse, DR_{IC} = 7.9% at the first story (i.e., the story governing collapse).

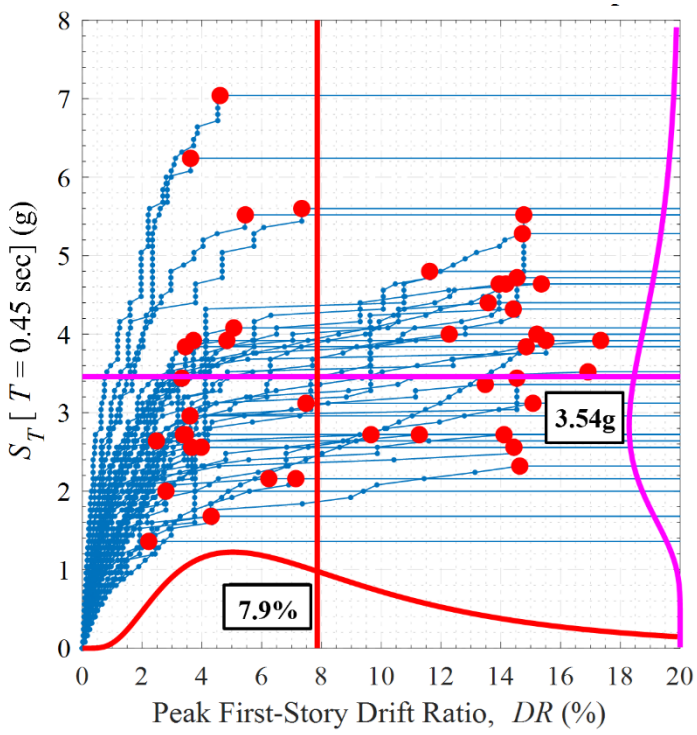

Figure 3-5 **Example plot of the IDA curves of the 4-story COM wood archetype model, 4C-073-060-030, of Chapter 4 and notional probability density functions (PDFs) of 0.45-second response spectral acceleration at collapse, S_T (vertical axis) and peak first-story drift ratio, DR (horizontal axis); red markers represent the incipient collapse points, DR_{IC}, of individual ground motions; horizontal and vertical lines show the median values of collapse acceleration (=3.54g) and collapse displacement (=7.9%).**

The value of median response spectral acceleration at collapse, $\hat{S}_{CT}$, calculated as the geometric mean (geomean) of the 44 data of 0.45-second response spectral acceleration at incipient collapse (i.e., accelerations shown by the horizontal blue lines in Figure 3-5), where these acceleration data are assumed to be lognormally distributed. Similarly, the value of median first-story drift ratio at incipient collapse, DR_{IC} , is calculated as the geomean of the 44 data of first-story drift ratio at

incipient collapse (i.e., DR_{IC} or drift ratio at incipient collapse of individual ground motions shown by the red dots in Figure 3-5), where these drift ratio data are also assumed to be lognormally distributed.

3.4.5 Non-Simulated Collapse

Ideally, models of the SFRS archetype of interest directly simulate all failure modes contributing to collapse (i.e., side-sway collapse due to P-delta effects). FEMA P-695 recognizes that this is not possible (or practical) in all cases and utilizes the concept of "non-simulated" collapse to indirectly evaluate alternative limits on structural response. This study exploits the FEMA P-695 concept of non-simulated collapse to develop collapse surfaces from the results of incremental dynamic analysis at story drift ratios less than those associated with simulated failure (e.g., less than the story drift ratio at incipient collapse, DR_{IC}). This is the same approach as that used to develop the collapse surfaces of FEMA P-2139-1 shown in Figure 3-1.

When considered in the context of incremental dynamic analyses, non-simulated component limit state checks are essentially stipulating a collapse limit prior to the point where an analysis would otherwise simulate collapse. Figure 3-6 shows a plot of the results of an incremental dynamic analysis of an index archetype model, which is subjected to a single ground motion that is scaled to increasing intensities. The point denoted "SC" corresponds to the collapse limit as simulated in the model. The point denoted "NSC" represents the collapse limit as determined by applying a limit state check on a potential collapse mode that is not directly simulated in the model.

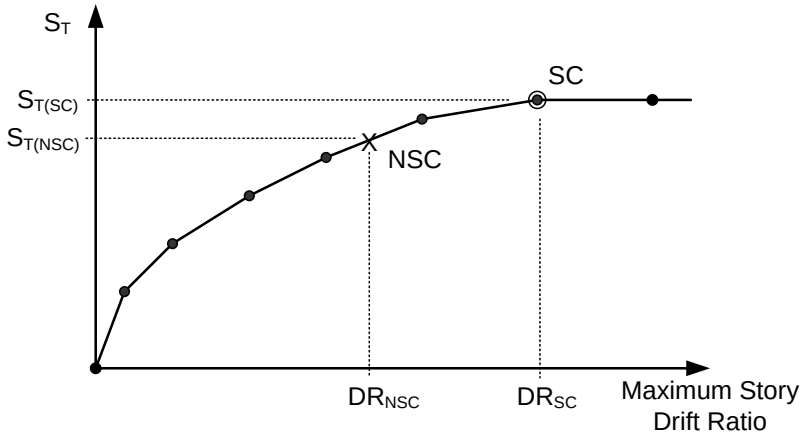

Figure 3-6 Assessment of collapse with simulated and non-simulated modes using incremental dynamic analysis (Figure 5-8 of FEMA P-695).

3.4.6 Evaluation of MCE_R Collapse Performance

Evaluation of MCE_R collapse performance is illustrated in Figure 3-7 using IDA results of the 4-story COM wood archetype model, 4C-073-060-030, shown in Figure 3-5. This archetype model has a design period, T = 0.45 s, and was evaluated for 40 increments of ground motions scaled from 0.1g to 4.0g of 0.45-second response spectral acceleration. In Figure 3-7, collapse fractions at IDA

increments (shown by red dots) and the FEMA P-695 lognormal collapse fragility curve including adjustment for spectrum shape effects are plotted as a function of 0.45-second response spectral acceleration.

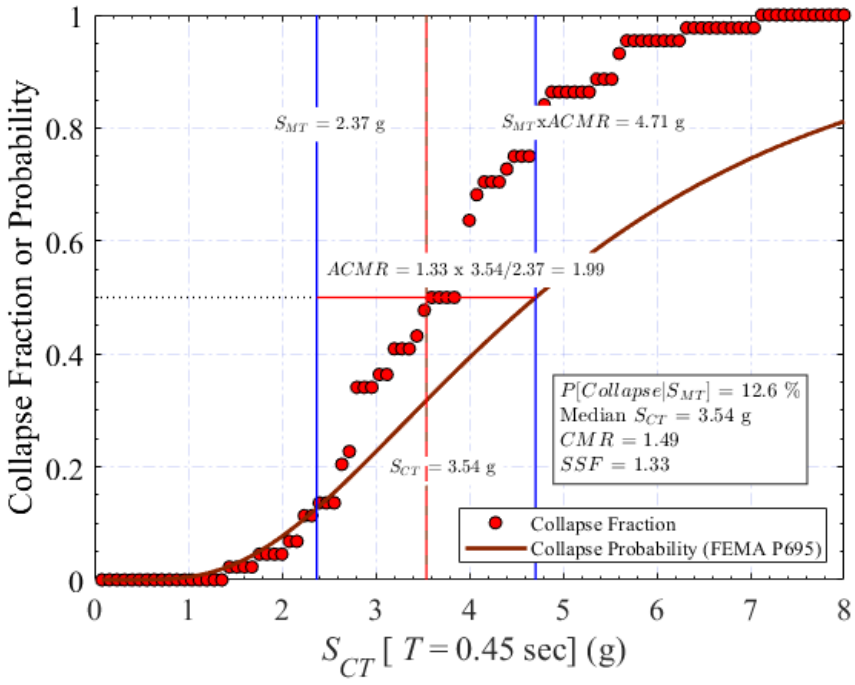

Figure 3-7 Illustration IDA results (collapse fractions) and FEMA P-695 lognormal collapse fragility curve based on median collapse, $\widehat{S}_{CT}$ = 3.54 g, derived from the IDA results, and an assumed lognormal standard deviation of β_{TOT} = 0.60.

The archetype model of this example, 4C-073-060-030, has a peak pushover strength of V_{max}/W = 0.73g, one of the ten hypothetical increments of strength used to model 4-story COM wood archetypes in Chapter 4. As such, the archetype model is not designed per se, and the value of MCE_R ground motion intensity, S_{MT}, is derived from the ASCE/SEI 7-22 wood light-frame design parameters, R/I_e = 6.5/1.0 (assuming Risk Category II design) and the overstrength, Ω, of the model.

By re-arranging and combining terms of Equation 3-1 and Equation 3-2, MCE_R ground motions intensity, S_{MT}, is defined in terms of normalized strength, V_{max}/W, and overstrength, Ω, as follows:

$$S_{MT} = 1.5\ (R/I_e)\ (V_{max}/W)\ /\ \Omega \qquad (3\text{-}4)$$

Assuming Ω = 3.0, a reasonable assumption for the 4-story COM wood archetype model of Chapter 4, which includes nonstructural walls, the value of S_{MT} is calculated,

$$S_{MT} = 1.5\ (6.5/1.0)\ (0.73)\ /\ 3.0 = 2.37g$$

which is approximately the value of S_{MT} at the period, T = 0.45 s, of the multi-period response spectrum of ASCE/SEI 7-22 MCE_R ground motions shown in Figure 3-3 for a site in Los Angeles, California.

The FEMA P-695 methodology defines the collapse margin ratio (*CMR*) as follows:

$$CMR = \hat{S}_{CT} / S_{MT} \tag{3-5}$$

And the value of the adjusted collapse margin ratio (*ACMR*) as follows:

$$ACMR = SSF \times CMR \tag{3-6}$$

Where the value of the *CMR* is adjusted by the spectrum shape factor, *SSF*. For the example 4-story wood COM model of Figure 3-7, *CMR* = 1.49 (i.e., 3.54g / 2.37g) and the value of the *ACMR* = 1.99 (i.e., 1.33 × 1.49), where *SSF* = 1.33 is obtained from Table 7.1b of FEMA P-695. Section 3.4.7 provides background and values of the *SSF*.

The probability of collapse as a function of ground motion intensity (at the period, *T*, of archetype model) is assumed to be lognormally distributed with an adjusted collapse median, $SSF \times \hat{S}_{CT} = ACMR \times S_{MT}$, and a logarithmic standard deviation, β_{TOT}. The adjusted collapse median of the example 4-story COM wood archetype model is, $ACMR \times S_{MT}$ = 1.99 × 2.37g = 4.71g.

The logarithmic standard deviation parameter, β_{TOT}, accounts for total uncertainty of median response due to: (1) record-to-record variability, and uncertainty associated with (2) design requirements (of the SFRS of interest), (3) test data (used to establish nonlinear properties) and (4) modeling methods, as described in Section 7.3 of FEMA P-695. Tables 7-2a – 7-2d of FEMA P-695 specify values of β_{TOT} based on subjective evaluation of the "quality" of the design requirements, test data and modeling methods, respectively.

Reasonably well-defined archetype models have values of total collapse uncertainty, β_{TOT} = 0.45 – 0.70. For reference, Section 21.2.1.2 (Method 2) of ASCE/SEI 7-22 specifies a logarithmic standard deviation value of 0.60 for development of site-specific probabilistic MCE_R ground motions (i.e., the value of the logarithmic standard deviation used by the USGS to develop the MCE_R ground motion maps of Chapter 22 of ASCE/SEI 7-22).

As shown in Figure 3-7, the MCE_R collapse probability is 12.6% for the example COM wood archetype model based on a value of β_{TOT} = 0.60 (and an adjusted median collapse acceleration of 4.71 g.).

The *ACMR* may be recognized as the median of a lognormal distribution of normalized MCE_R response spectral acceleration (i.e., MCE_R response spectral acceleration normalized by S_{MT}) and total collapse uncertainty, β_{TOT}.

$$P\left[\text{Collapse} \mid S_{MT}\right] = \Phi\left(\frac{Ln\left(\frac{1}{ACMR}\right)}{\beta_{TOT}}\right) \tag{3-7}$$

where, $\Phi(.)$ is the cumulative distribution function of standard normal distribution. Equation 3-7 may be solved using tabulated values of cumulative probability (i.e., normal tables) or, as practical matter, readily calculated using statistical software.

3.4.7 Acceptable Values of the *ACMR*

The FEMA P-695 methodology evaluates collapse of a proposed new SFRS in terms of an acceptable value of the *ACMR*, where acceptable values of the *ACMR* are specified in Table 7-3 of FEMA P-695 in terms of a target MCE_R collapse probability (i.e., *ACMR10%* is the acceptable value of the *ACMR* to meet a target MCE_R collapse probability of 10 percent). Acceptable values of *ACMR* are necessarily a function of the value of total collapse uncertainty, β_{TOT}, used to calculate the probability of collapse, as well as the target MCE_R probability of collapse.

Target probabilities of collapse given MCE_R ground motions are defined by Table 1.3-2 of ASCE/SEI 7-22 in terms of risk category, i.e., 10 percent for Risk Category I and II, 5 percent for Risk Category III, and 2.5 percent for Risk Category IV structures.

Acceptable values of the collapse margin ratio are summarized in Table 3-1 as a function of the total collapse uncertainty, β_{TOT}, at target probabilities of collapse given MCE_R ground motions of 2.5%, 5.0%, 10%, 20% and 50%. For example, assuming, β_{TOT} = 0.60, *ACMR2.5%* = 3.25, the acceptable value of the *ACMR* of Risk Category IV structures, and *ACMR10%* = 2.16, the acceptable value of the *ACMR* for Risk Category II structures. In all cases, *ACMR50%* = 1.0, reflecting that no margin on MCE_R ground motions would be required if it was acceptable to have a 50% probability of collapse given MCE_R ground motions.

Table 3-1 Acceptable Values of *ACMR* for Target MCE_R Collapse Probabilities of 2.5%, 5.0%, 10%, 20% and 50% Given Values of Total Collapse Uncertainty from β_{TOT} = 0.45 to β_{TOT} = 0.70 (Similar to Table 7-3 of FEMA P-695)

	ACMR2.5%	*ACMR5.0%*	*ACMR10%*	*ACMR20%*	*ACMR50%*
β_{TOT}	2.5%	5.0%	10%	20%	50%
0.45	2.43	2.10	1.79	1.46	1.00
0.46	2.48	2.14	1.81	1.47	1.00
0.47	2.51	2.17	1.83	1.49	1.00
0.48	2.56	2.20	1.85	1.50	1.00
0.49	2.62	2.24	1.88	1.51	1.00
0.50	2.67	2.28	1.90	1.52	1.00
0.51	2.72	2.31	1.92	1.54	1.00
0.52	2.78	2.36	1.95	1.55	1.00
0.53	2.84	2.39	1.98	1.56	1.00
0.54	2.89	2.44	2.00	1.58	1.00
0.55	2.94	2.48	2.02	1.59	1.00
0.56	3.01	2.51	2.06	1.60	1.00
0.57	3.07	2.56	2.08	1.62	1.00
0.58	3.13	2.60	2.11	1.63	1.00
0.59	3.18	2.65	2.14	1.64	1.00
0.60	3.25	2.69	2.16	1.66	1.00
0.61	3.31	2.73	2.19	1.67	1.00
0.62	3.38	2.78	2.22	1.69	1.00
0.63	3.45	2.82	2.24	1.70	1.00
0.64	3.52	2.87	2.27	1.72	1.00
0.65	3.60	2.92	2.30	1.73	1.00
0.66	3.65	2.98	2.34	1.75	1.00
0.67	3.73	3.01	2.37	1.76	1.00
0.68	3.82	3.07	2.39	1.77	1.00
0.69	3.88	3.13	2.43	1.79	1.00
0.70	3.97	3.16	2.46	1.81	1.00

3.4.8 Spectrum Shape Factor

The spectrum shape factor (*SSF*) accounts for the inherent "rareness" of MCE_R ground motions that have a distinctive spectral shape that differs from the shape of the median spectrum of the set of earthquake ground motion records used for collapse evaluation. In essence, the shape of the spectrum of rare ground motions is peaked at the period of interest (i.e., the fundamental period, *T*,

of the archetype model), and drops off more rapidly (and has less energy) at periods that are longer or shorter than the period of interest. Where ground motion intensities are defined based on the spectral acceleration at the fundamental period, *T*, of the archetype model, and where archetype model has sufficient ductility to respond inelastically at longer periods of vibration without failure, this peaked spectral shape, and more rapid drop at other periods, causes these rare records to be less likely to cause collapse than the median spectrum of the record set.

The most direct approach to account for spectral shape would be to select a unique set of ground motions that have the appropriate shape for each site, hazard level, and structural period of interest. This is not feasible, however, for the generalized procedure of FEMA P-695 for assessing the collapse performance of a class of structures, with a range of possible configurations, located on a number of different sites. To remove this conservative bias, simplified spectral shape factors, *SSF*, which depend on fundamental period, *T*, and period-based ductility, μ_T, are used to adjust collapse margin ratios. Variation of site seismic hazard is accounted for crudely in terms of typical differences in seismic hazard of regions defined by Seismic Design Category (SDC) of ASCE/SEI 7-05. Background and development of spectral shape factors are described in Appendix B of FEMA P-695.

Values of the *SSF* are necessarily different for the different regions of seismic hazard, as defined by SDC, and different for the Far-Field and Near-Field record sets. Values of *SSF* of FEMA P-695 are summarized in Table 3-2 for collapse evaluation using the Far-Field record set and in Table 3-3 for collapse evaluation using the Near-Field record set. In these tables, SDC D refers to the region of high seismicity where site hazard is assumed to be governed by probabilistic MCE_R ground motions and SDC E refers to the region of high seismicity where site hazard is assumed to be governed by deterministic MCE_R ground motions, noting that these assumptions of FEMA P-695 are not valid at all high seismic sites. Typically, seismic hazard at SDC D sites is governed by earthquakes on faults located at least 10 km from the site and seismic hazard at SDC E sites is governed by faults located within 10 km of the site, although this is not always the case. The *SSF*s of Table 3-2 probabilistic MCE_R ground motions (SDC D) are used by this study for collapse evaluation of archetype models using the Far-Field record set. These are same values of the *SSF* required by FEMA P-695 (Table 7.1b) for collapse evaluation of a proposed new SFRS, where near-fault effects are intentionally ignored. The *SSF*s of Table 3-3 deterministic MCE_R ground motions (SDC E) are used by this study for collapse evaluation of archetype models using the Near-Field record set.

Table 3-2 Values of the Spectrum Shape Factor (*SSF*) Required by FEMA P-695 for Calculation of the *ACMR* of Archetype Models Evaluated Using the Far-Field Record Set (Copies of Tables 7.1b and Table B-9, FEMA P-695)

T	Period-Based Ductility, μ_T							
(sec.)	1	1.1	1.5	2	3	4	6	8
Probabilistic MCE_R Ground Motions (SDC D, Table 7.1b, FEMA P-695)								
≤ 0.5	1.00	1.05	1.10	1.13	1.18	1.22	1.28	1.33
0.6	1.00	1.05	1.11	1.14	1.20	1.24	1.30	1.36
0.7	1.00	1.06	1.11	1.15	1.21	1.25	1.32	1.38
0.8	1.00	1.06	1.12	1.16	1.22	1.27	1.35	1.41
0.9	1.00	1.06	1.13	1.17	1.24	1.29	1.37	1.44
1	1.00	1.07	1.13	1.18	1.25	1.31	1.39	1.46
1.1	1.00	1.07	1.14	1.19	1.27	1.32	1.41	1.49
1.2	1.00	1.07	1.15	1.20	1.28	1.34	1.44	1.52
1.3	1.00	1.08	1.16	1.21	1.29	1.36	1.46	1.55
1.4	1.00	1.08	1.16	1.22	1.31	1.38	1.49	1.58
≥ 1.5	1.00	1.08	1.17	1.23	1.32	1.40	1.51	1.61
Deterministic MCE_R Ground Motions (SDC E, Table B-9, FEMA P-695)								
≤ 0.5	1.00	1.03	1.06	1.09	1.12	1.14	1.18	1.21
0.6	1.00	1.04	1.07	1.10	1.13	1.16	1.20	1.23
0.7	1.00	1.04	1.08	1.11	1.14	1.17	1.22	1.26
0.8	1.00	1.04	1.09	1.12	1.16	1.19	1.24	1.28
0.9	1.00	1.05	1.09	1.12	1.17	1.21	1.26	1.31
1	1.00	1.05	1.10	1.13	1.18	1.22	1.28	1.33
1.1	1.00	1.05	1.11	1.14	1.20	1.24	1.30	1.36
1.2	1.00	1.06	1.11	1.15	1.21	1.25	1.32	1.38
1.3	1.00	1.06	1.12	1.16	1.22	1.27	1.35	1.41
1.4	1.00	1.06	1.13	1.17	1.24	1.29	1.37	1.44
≥ 1.5	1.00	1.07	1.13	1.18	1.25	1.31	1.39	1.46

Table 3-3 Values of the Spectrum Shape Factor (*SSF*) Required by FEMA P-695 for Calculation of the *ACMR* of Archetype Models Evaluated Using the Near-Field Record Set (Based on Section B.5, FEMA P-695)

T	Period-Based Ductility, μ_T							
(sec.)	1	1.1	1.5	2	3	4	6	8
Probabilistic MCE_R Ground Motions (SDC D, Section B.5, FEMA P-695)								
≤ 1.5	1.00	1.08	1.17	1.23	1.32	1.40	1.51	1.61
1.6	1.00	1.08	1.17	1.23	1.32	1.39	1.50	1.60
1.7	1.00	1.08	1.17	1.23	1.31	1.38	1.49	1.59
1.8	1.00	1.08	1.16	1.22	1.31	1.38	1.49	1.58
1.9	1.00	1.08	1.16	1.22	1.30	1.37	1.48	1.57
2	1.00	1.08	1.16	1.22	1.30	1.36	1.47	1.56
2.1	1.00	1.08	1.16	1.21	1.29	1.36	1.46	1.55
2.2	1.00	1.08	1.15	1.21	1.29	1.35	1.45	1.54
2.3	1.00	1.07	1.15	1.21	1.29	1.35	1.45	1.53
2.4	1.00	1.07	1.15	1.20	1.28	1.34	1.44	1.52
≥ 2.5	1.00	1.07	1.15	1.20	1.28	1.33	1.43	1.51
Deterministic MCE_R Ground Motions (SDC E, Section B.5, FEMA P-695)								
≤ 1.5	1.00	1.07	1.13	1.18	1.25	1.31	1.39	1.46
1.6	1.00	1.06	1.13	1.18	1.25	1.30	1.38	1.45
1.7	1.00	1.06	1.13	1.18	1.24	1.29	1.38	1.44
1.8	1.00	1.06	1.13	1.17	1.24	1.29	1.37	1.44
1.9	1.00	1.06	1.12	1.17	1.23	1.28	1.36	1.43
2	1.00	1.06	1.12	1.17	1.23	1.28	1.35	1.42
2.1	1.00	1.06	1.12	1.16	1.22	1.27	1.35	1.41
2.2	1.00	1.06	1.12	1.16	1.22	1.27	1.34	1.40
2.3	1.00	1.06	1.11	1.16	1.22	1.26	1.33	1.39
2.4	1.00	1.06	1.11	1.15	1.21	1.25	1.32	1.38
≥ 2.5	1.00	1.05	1.11	1.15	1.21	1.25	1.32	1.37

3.5 Collapse Surface Metrics and Data Sets

This section defines collapse surface metrics, which are the median collapse acceleration ($\hat{S}_{CT}$), the strength parameter (V_{max}/W), the collapse displacement drift ratio parameter (DR), and, implicitly, the number of stories (N). These parameters define the number of 2D nonlinear models and collapse data sets required for development of collapse surfaces.

3.5.1 Median Collapse Acceleration ($\widehat{S}_{CT}$)

The median collapse acceleration, $\hat{S}_{CT}$, is the collapse metric that defines collapse surface failure as a function of period (approximated by the number of stories), strength and displacement capacity of the SFRS archetype of interest.

3.5.2 Strength Parameter (V_{max}/W)

The normalized (pushover) strength, V_{max}/W, is the parameter that defines the strength of the SFRS archetype of interest. The strength parameter can be expressed as:

$$V_{max}/W = \Omega \times (I_e/R) \times (2/3)\, S_{MT} \tag{3-8}$$

Where:

Ω = Overstrength, Equation 6-5 of FEMA P-695

R = Response modification coefficient, Table 12.2-1 of ASCE/SEI 7-22 (e.g., R = 6.5 for light-frame wood structures)

I_e = Importance factor, Table 1.5-2 of ASCE/SEI 7-22 (e.g., I_e = 1.0 for Risk Category II and I_e = 1.5 for Risk Category IV structures)

S_{MT} = MCE_R ground motions intensity at period, T, of the multi-period response spectra of ASCE/SEI 7-22, assuming default site conditions

T = Design period, Equation (5-5) of FEMA P-695 without the limit, $T \geq 0.25$s,

$$T = C_u\ T_a = \ C_u\ C_t\ h_n^x \tag{3-9}$$

where h_n is the archetype height (in feet), the coefficient, C_u, is given in Table 12.8-1 of ASCE/SEI 7-22 and parameters C_t and x are given in Table 12.8.2 of ASCE/SEI 7-22.

Equation 3-8 is not required for development of collapse surfaces, but is necessary for expressing collapse results as a function of MCE_R ground motions intensity, S_{MT}.

The FEMA P-695 methods for evaluating the collapse performance of a proposed (new) SFRS require developing detailed designs of archetypes of that SFRS for a comprehensive, but necessarily limited, number of representative configurations, heights, and MCE_R ground motion intensities (e.g., SDC D_{max}). Such was the approach used to investigate the short-period paradox, as reported in FEMA P-2139-2 for light-frame wood buildings, where the normalized strength, V_{max}/W, and corresponding value of median collapse acceleration, $\hat{S}_{CT}$, were calculated from the 3D nonlinear model of the detailed design of each archetype. The effort required to develop a detailed design and corresponding 3D nonlinear model of each archetype, yielding a single collapse datum, is not practical for populating collapse surfaces that must characterize collapse performance over a broad range of normalized strengths of the SFRS archetype of interest. For this study, 2D nonlinear models assume hypothetical values of V_{max}/W, where a sufficiently large number (e.g., ten increments) of hypothetical values of V_{max}/W are chosen to broadly characterize the range of possible strengths of the SFRS archetype of interest.

As stated in Equation 3-8, the normalized strength, V_{max}/W, of the SFRS archetype of interest is a function of MCE_R ground motions intensity, S_{MT}, which for short-period buildings could be as low as S_{MS} = 0.75g for sites of moderate seismicity or as high as S_{MS} = 3.0g for sites of very high seismicity. Accordingly, values of V_{max}/W must likewise vary over a broad range, made even broader considering the two possible values of the earthquake importance factor, I_e, (i.e., I_e = 1.0 for Risk Category II structures and I_e = 1.5 for Risk Category IV structures). In Chapter 4, for example, ten increments of normalized strengths of the structure of light-frame wood archetypes are assumed to be V_{max}/W = 0.05, 0.10, 0.15, 0.20, 0.30, 0.45, 0.60, 0.80, 1.0 and 1.2, where the first increment, V_{max}/W = 0.05g ≈ 5.0 × (1.0/6.5) × (2/3) × 0.075g, assuming Ω = 5.0, and the last increment V_{max}/W = 1.2g ≈ 2.5 × (1.5/6.5) × (2/3) × 3.0g, assuming Ω = 2.5.

3.5.3 Collapse Displacement Drift Ratio Parameter (DR)

The collapse displacement drift ratio, *DR*, is the peak inelastic displacement at collapse of the story governing collapse divided by the height of that story of SFRS archetype model of interest. The value of *DR* is based on either simulated, side-sway, collapse (i.e., median drift ratio at incipient collapse, DR_{IC}) or an assumed value of *DR* corresponding to non-simulated collapse failure (see Figure 3-6). Non-simulated collapse represents failure modes not explicitly modeled, including potential collapse of the gravity load resisting system, or simply a pragmatic limit on the acceptable drift of the SFRS of interest. It should be noted that *DR* is, in general, not a design parameter that is easily affected by design decisions. Displacement capacity at collapse is more a feature for a given system that is a result of material design standards and common structural engineering practice in high-seismic regions.

For an assumed value of *DR*, the corresponding value of median collapse acceleration, $\hat{S}_{CT}$, is determined as the geometric mean of S_T values of the IDA results at that *DR*. Conceptually, this may be thought of as calculating the median of a vertical slice through the IDA results at the assumed

value of *DR*. This is the same approach as that used to develop the collapse surfaces of FEMA P-2139-1 shown in Figure 3-1.

Values of median collapse acceleration, $\hat{S}_{CT}$, are determined over a broad range of hypothetical values of *DR* from about full yield of SFRS archetype model of interest to a displacement where the model has reached incipient collapse for all but a few of the records. A broad range of hypothetical values of *DR* ensures that collapse surfaces can be interrogated at any possible non-simulated collapse displacement, recognizing that at small values of *DR* the collapse surface will likely not be necessary for collapse evaluation of most archetype models. Vertical slices of IDA results of the 4-story COM light-frame wood archetype, 4C-073-060-030, of Chapter 4 are illustrated by the blue dots in Figure 3-8, which show 27 sets of S_T data at displacements from *DR* = 2.0% to *DR* = 15%, in increments of 0.5%.

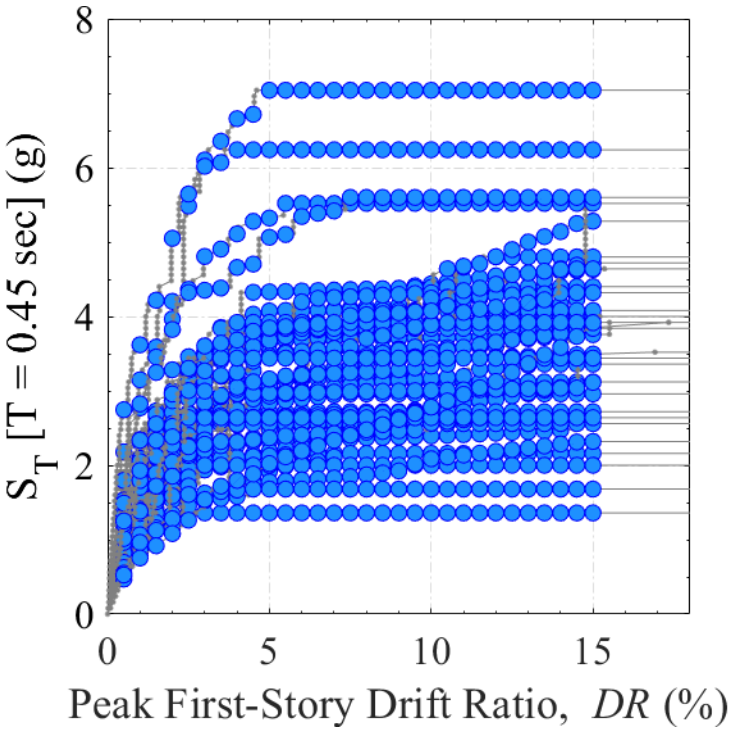

Figure 3-8 Monotonically increasing IDA curves showing 27 sets of S_{CT} data (i.e., 27 sets of vertically aligned blue dots) at increments of *DR* from 2.0% to 15%.

3.5.4 Number of Stories (*N*)

The number of stories, *N*, of archetypes of the SFRS of interest is used in this study as a surrogate for the elastic, fundamental-mode, period of the SFRS archetype model of interest. That is, collapse surfaces are defined in terms of the number of stories of the nonlinear model of the SFRS archetype, rather than the elastic period of the model. This approach permits development of a unique collapse surface for each set of 2D nonlinear models of archetypes that have a common number of stories.

Conceptually, the elastic, fundamental-mode, period of the model, T_1, is the preferred definition of period, which effectively defines the initial stiffness/pre-peak strength of 2D nonlinear models. In general, values of the elastic period are different for each archetype model, complicating the usefulness of the surface (e.g., impossible to plot a single surface that is a function of three parameters). As an alternative, the number of stories of the model (N) provides a more practical scheme for developing a suite of collapse surfaces, i.e., one surface for each building height, defined by the number of stories, at the expense of less precise values of $\hat{S}_{CT}$, since the elastic period need not be the same for all archetypes with the same number of stories. Slight loss of precision in the value of $\hat{S}_{CT}$, associated with story height is not considered significant in terms of the overall accuracy of collapse surfaces, since $\hat{S}_{CT}$, is primarily a function of model strength and post-peak strength displacement capacity, rather than the elastic period of the model.

Typical story heights, in feet, of buildings incorporating the SFRS of interest are used to define 2D nonlinear model properties. Values of the elastic, fundamental-mode, period, T_1, are determined by dynamic analysis of the model of interest, although not used directly to define collapse surfaces. In accordance with the FEMA P-695 methods, the fundamental "design" period, T (i.e., $T = C_u T_a$), based on the total height (h_n) of the archetype configuration (number of stories) of interest, is used to define the scaling period of both MCE_R ground motions intensity, S_{MT}, and median collapse acceleration, $\hat{S}_{CT}$.

3.5.5 Number of 2D Nonlinear Models and Collapse Data Sets

For each archetype configuration (number of stories) of the SFRS of interest, collapse surfaces are derived (by regression analysis) from large sets of collapse data that collectively include (1) the values of median collapse acceleration, $\hat{S}_{CT}$, as determined by IDA of the 2D nonlinear models, and the corresponding values of (2) the normalized strength, V_{max}/W, and (3) the collapse displacement drift ratio, DR, of the respective 2D nonlinear models.

For each SFRS archetype configuration (number of stories), the total number of 2D nonlinear models is the product of the number of different normalized strength levels (i.e., V_{max}/W) times the number of different characterizations of the hysteretic behavior (e.g., backbone curves) at each level of normalized strength. In Chapter 4, for example, light-frame wood models include two, three or four different assumptions of hysteretic behavior for each normalized strength level based on different assumptions of the amount of post-peak residual strength, resulting in roughly 25 to 30 unique 2D nonlinear models of each light-frame wood archetype configuration.

For each archetype configuration (number of stories) of the SFRS of interest, the total number of collapse data is the product of the total number of 2D nonlinear models times the number of different increments of DR (e.g., drift ratio increments corresponding to non-simulated collapse) used to interrogate values of $\hat{S}_{CT}$ from the results of IDA. For 10 increments of V_{max}/W strength and 27 increments of DR (i.e., from DR = 2.0% to DR = 15% at increments of 0.5%), there are a total

number of 270 triplets of collapse data of the SFRS of interest, if there was only a single characterization of hysteretic behavior, or in the case of the light-frame wood models of Chapter 4, approximately 675 triplets of collapse data for each of the 15 different archetype configurations (i.e., 3 archetypes × 5 heights) of the light-frame wood SFRS.

3.6 Development of Collapse Surfaces from Collapse Data

3.6.1 Mathematical Characterization of Median Collapse

There are advantages to characterizing collapse data by a mathematical formula that predicts the value of $\hat{S}_{CT}$ given values of V_{max}/W and DR. Accordingly, regression analysis is used to derive the parameters of a collapse surface equation (of an assumed functional form) to each set of collapse data. In general, collapse data are well behaved, i.e., values of $\hat{S}_{CT}$ change systematically with V_{max}/W and DR, and the collapse surface may be thought of as a practical smoothing of median values of collapse acceleration, $\hat{S}_{CT}$, that have slightly irregular trends due to inherent differences in median ground motions or biases in assumptions used to model hysteretic behavior. In a more complete (theoretical) construct, collapse surfaces could be generalized to be the median of a more comprehensive set of collapse data that retain inherent variability associated with ground motions (i.e., record-to-record variability) and modeling uncertainties, such that a collapse distribution, as well as median collapse, could be explicitly evaluated at any point on the collapse surface (i.e., any combination of V_{max}/W and DR). This is not practical for this study and, in accordance with FEMA P-695 methods, the collapse distribution is assumed to be lognormal with median, $\hat{S}_{CT}$, as defined by the collapse surface, and logarithmic standard deviation, β_{TOT}, where values of, β_{TOT}, are given in Table 3-6.

Regression analysis requires an assumption of an equation (functional form) of the collapse surface that can be fit to the data. The quality of the fit depends on the functional form of the equation. Initially, collapse surfaces were assumed to be described by the simple formula, $\hat{S}_{CT} = C \times (V_{max}/W)^A \times DR^B$, where values of the coefficients, A, B, and C are determined by linear regression of collapse data. However, using collapse data for light-frame wood COM archetypes of Chapter 4, the fit of collapse surfaces to the data was found to have unacceptable biases (i.e., greater than 10%) in predicted values of $\hat{S}_{CT}$, and a more complex polynomial equation was determined to be more suitable for matching collapse data, particularly at values of DR of interest (e.g., DR = 2.5% to DR = 10%). The preferred polynomial functional form of the collapse surface equation is:

$$\hat{S}_{CT} = A \times (V_{max}/W) + B \times (V_{max}/W)^2 + C \times DR + D \times DR^2 + E \times (V_{max}/W) \times DR + F \times (V_{max}/W)^2 \times DR + G \times (V_{max}/W) \times DR^2 + H \times (V_{max}/W)^2 \times DR^2 + I \quad (3\text{-}10)$$

Where values of coefficients, *A*, *B*, *C*, *D*, *E*, *F*, *G*, *H* and *I* are determined by multiple linear regression (Benjamin and Cornell, 1970) of the collapse data set of interest. Some of the terms of Equation 3-10 are likely unnecessary. However, all terms are retained since there is no computational benefit to removing them from the equation and consequences of potential overfitting of data is minimal for the collapse data sets of this project. As a practical matter, values of regression coefficients are readily calculated using statistical software.

Example values of the coefficients of Equation 3-10 are calculated by regression of the set of collapse data of the 25 4-story COM light-frame wood archetype models of Chapter 4. Selected values of collapse data at non-simulated collapse increments of *DR* equal to 2.5%, 5.0%, 7.5%, 10% and 15% are summarized in Table 3-4 for each of the 25 models of the 4-story COM wood archetype. These values of collapse data are selected from the full set of 675 collapse data of this model that incudes collapse data at 27 increments of *DR* from *DR* = 2.0% to *DR* =15%.

As explained in Chapter 4, model names indicate three strength parameters of each model. For example, the 4-story COM wood archetype model 4C-073-060-030 has a total normalized strength V_{max}/W = 0.73g of which V_{STR}/W = 0.60g is the normalized strength of structural walls and normalized residual strength, V_{RS}/W, that is 20% of V_{max}/W (i.e., V_{RS}/W = 0.20 × 0.73g = 0.146g). Two or three different assumptions of residual strength characterize feasible variations of hysteretic properties of the 4-story COM wood archetype. Chapter 4 should be referred to for a more in-depth explanation of light-frame wood archetype models.

Table 3-4 **Example (partial) Set of Collapse Data at Assumed Collapse Increments of *DR* = 2.5%, 5.0%, 7.5%, 10% and 15% Determined by IDA of the 25 4-Story COM Light-Frame Wood Archetype Models of Chapter 4, the Value of the Median Drift Ratio at Incipient Collapse of Each Archetype Model and a Summary of the Fraction of Simulated Side-Sway Collapses at each *DR* Increment**

4-Story COM Wood			Median S_{CT} (g) at *DR*				
Model Name	V_{max}/W	DR_{IC}	2.5%	5.0%	7.5%	10%	15%
4C-018-005-075	0.18	9.3%	1.04	1.21	1.24	1.33	1.33
4C-018-005-060	0.18	6.4%	1.04	1.13	1.21	1.21	1.21
4C-023-010-075	0.23	12.6%	1.24	1.48	1.52	1.57	1.72
4C-023-010-060	0.23	9.2%	1.23	1.39	1.43	1.51	1.51
4C-023-010-045	0.23	5.5%	1.24	1.39	1.42	1.42	1.42
4C-028-015-075	0.28	16.7%	1.40	1.73	1.81	1.85	1.97
4C-028-015-060	0.28	11.3%	1.39	1.64	1.67	1.69	1.82
4C-028-015-045	0.28	7.0%	1.40	1.64	1.69	1.69	1.69
4C-033-020-075	0.33	18.1%	1.52	1.95	2.09	2.19	2.36
4C-033-020-060	0.33	11.9%	1.53	1.86	1.96	2.02	2.25
4C-033-020-045	0.33	8.4%	1.51	1.84	1.91	1.99	1.99
4C-043-030-060	0.43	15.8%	1.84	2.25	2.47	2.66	3.24
4C-043-030-045	0.43	11.6%	1.84	2.24	2.45	2.62	2.94
4C-043-030-030	0.43	8.0%	1.79	2.22	2.43	2.56	2.56
4C-058-045-045	0.58	15.3%	2.16	2.71	2.94	3.18	3.61
4C-058-045-030	0.58	9.0%	2.16	2.71	2.91	3.26	3.26
4C-058-045-020	0.58	6.5%	2.17	2.70	2.97	2.97	2.97
4C-073-060-030	0.73	7.9%	2.52	3.11	3.23	3.54	3.54
4C-073-060-020	0.73	6.3%	2.50	3.10	3.39	3.39	3.39
4C-093-080-030	0.93	8.0%	2.92	3.59	3.74	4.12	4.12
4C-093-080-020	0.93	6.5%	2.81	3.47	3.87	3.87	3.87
4C-113-100-020	1.13	6.7%	3.21	3.88	4.37	4.37	4.37
4C-113-100-010	1.13	4.7%	3.14	4.04	4.04	4.04	4.04
4C-133-120-020	1.33	6.2%	3.57	4.30	4.73	4.73	4.73
4C-133-120-010	1.33	4.9%	3.54	4.60	4.60	4.60	4.60
Fraction of Collapsed Models			0/25	2/25	10/25	17/25	21/25

In Table 3-1, yellow shaded cells indicate that simulated side-sway collapse governs the value of $\hat{S}_{CT}$ (i.e., model has already collapsed due to P-delta). The bottom row of the table shows the fraction of models that have failed due to simulated, P-delta, collapse of the model. These collapse fractions show no collapses at *DR* = 2.5%, indicating that this relatively small drift ratio is not of collapse interest for this model. Simulated collapse fractions increase from 2/25 at *DR*= 5.0% to 21/25 at *DR* = 15%, indicating that collapse performance (and the value of $\hat{S}_{CT}$) are governed primarily by simulated side-sway collapse at large values of *DR*. All collapse data at simulated and non-simulated *DR*s are included in the regression analysis.

Example values of the coefficients of Equation 3-10 determined by linear regression analysis of the full set of 675 collapse data of the 4-story COM wood archetype are summarized in Table 3-5 and the corresponding collapse surface of this archetype is shown in Figure 3-9. Table 3-5 also shows maximum surface (plateau) value of $\hat{S}_{CT}$ = 4.65g. As explained later in this section, the surface plateau effectively limits the applicability of Equation 3-10 to values of normalized strength, V_{max}/W, less than or equal to that of the strongest archetype model (i.e., $V_{max}/W \leq 1.33$g for the 4-story COM wood archetype).

Table 3-5 Example Values of the Coefficients of Equation 3-10 that Define Median Collapse of the 4-story COM Wood Archetype of Chapter 4

Coefficient	Value	Surface Variable
A	1.814	V_{max}/W
B	-0.149	$(V_{max}/W)^2$
C	-6.075	*DR*
D	23.1	DR^2
E	63.9	$(V_{max}/W) * DR$
F	-24.993	$(V_{max}/W)^2 * DR$
G	-227.7	$(V_{max}/W) * DR^2$
H	63.4	$(V_{max}/W)^2 * DR^2$
I	0.700	Intercept
Plateau	4.65	Maximum $\hat{S}_{CT}$

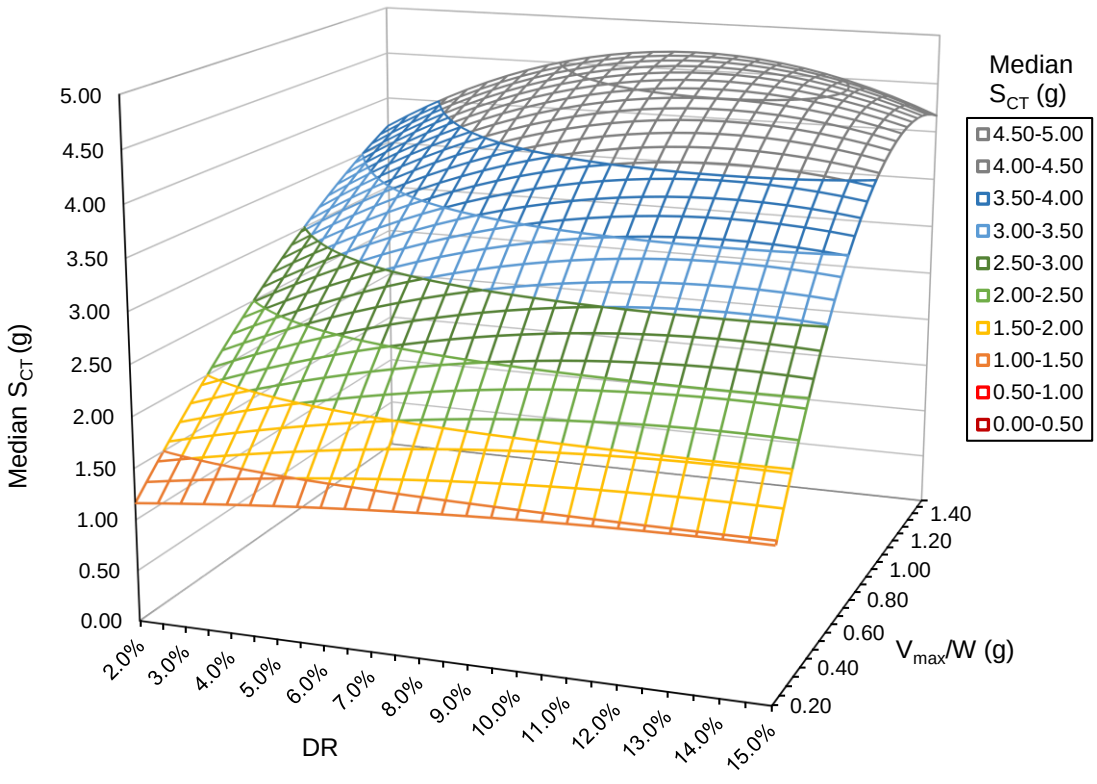

Figure 3-9 Example collapse surface of 4-Story COM Wood archetype, based directly on Equation 3-10 without modification.

Two modifications to the collapse surface of Figure 3-9 are made, noting that they are not necessary to obtain reliable values of $\hat{S}_{CT}$ of primary interest for evaluation of collapse performance (e.g., values of $\hat{S}_{CT}$ corresponding to $DR \leq 10\%$). First, the maximum value of $\hat{S}_{CT}$ of the collapse surface is limited to that calculated for the strongest archetype model (i.e., model with the largest V_{max}/W). This limit constrains the applicability of Equation 3-10 to the range of archetype model strengths by creating a "plateau" at the top of the collapse surface (e.g., at $\hat{S}_{CT}$ = 4.65g for the 4-story COM wood archetype, as shown in Figure 3-10). It should be noted that the plateau only applies as a limit on the portion of collapse surfaces extrapolated to values of V_{max}/W greater than those of the archetype models used to develop collapse surface data (i.e., this limit serves as a practical constraint on the applicability of the portion of the collapse surfaces not constrained by collapse data).

The second modification is a "theoretical" constraint that values of $\hat{S}_{CT}$ should increase monotonically (or remain constant) with increasing *DR* at a given level of normalized strength. At large values of *DR* (e.g., typically greater than 10%), Equation 3-10 can suggest otherwise when collapse data are governed primarily by simulated collapse. The value of the drift ratio, DR_{Smax}, at which the value of $\hat{S}_{CT}$ of the collapse surface is a maximum, $\hat{S}_{CT,max}$, for a given amount of normalized strength, V_{max}/W, is defined in terms of the coefficients of the collapse surface as follows:

$$DR_{Smax} = (C + E \times (V_{max}/W) + F \times (V_{max}/W)^2) / \\ 2 \times (D + G \times (V_{max}/W) + H \times V_{max}/W)^2) \quad (3\text{-}11)$$

where the values of coefficients *C*, *D*, *E*, *F*, *G* and *H* are the same as those of subject collapse surface. The value of $\hat{S}_{CT,max}$ at a given amount of normalized strength, V_{max}/W, is calculated by substituting the value of DR_{Smax} from Equation 3-11 into Equation 3-10. It may be noted that the value of $\hat{S}_{CT,max}$, evaluated at V_{max}/W of the strongest archetype model, defines the collapse surface "plateau" of the first criterion.

The collapse surface of the 4-story COM wood archetype with these two modifications is shown in Figure 3-10. Comparing Figure 3-10 with Figure 3-9 shows that the two "theoretical" modifications have no effect on the collapse surface at values *DR* on primary interest (e.g., *DR* ≤ 10%).

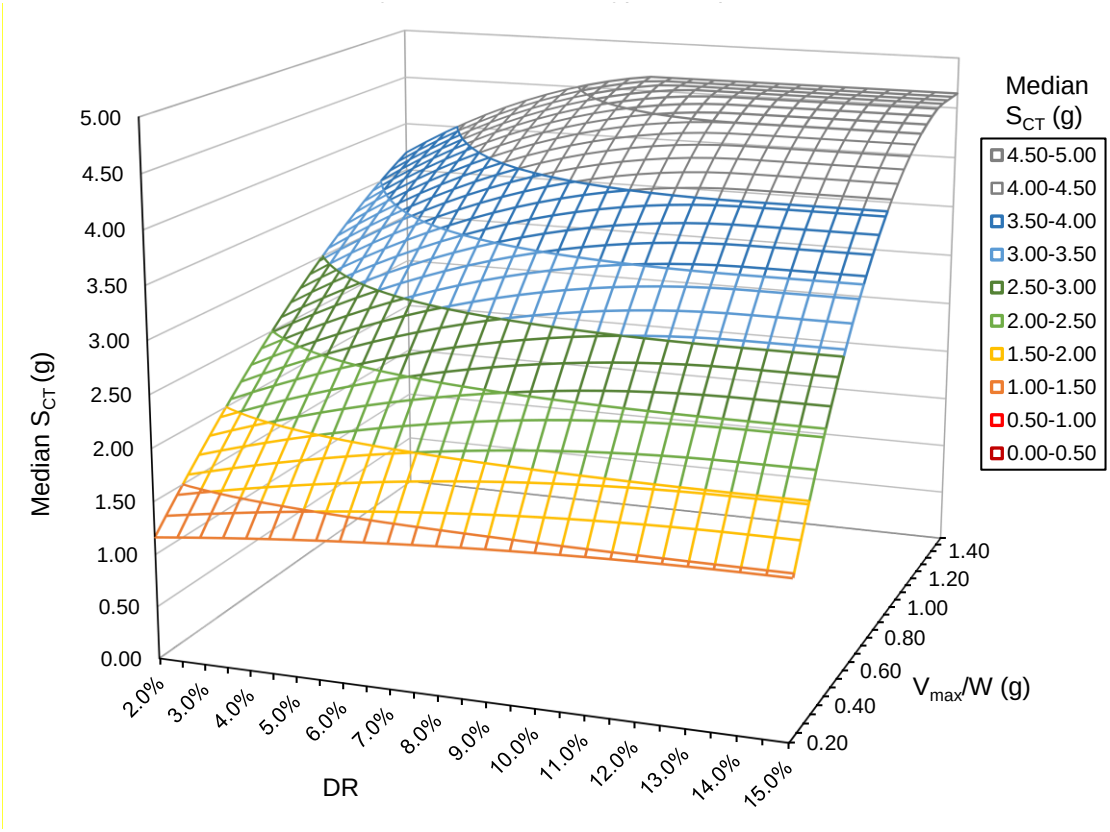

Figure 3-10 Example collapse surface of 4-Story COM Wood archetype, Equation (3-10), including (1) limit on the maximum value of $\hat{S}_{CT}$ (plateau) and (2) theoretical constraint of $\hat{S}_{CT}$ to monotonically increase (or remain the same) with increasing *DR* at a given value of normalized strength.

The collapse data set used for the regression of this example included collapse data for values of *DR* from *DR* = 2.0%, corresponding approximately to the displacement at full yield of models, to *DR* = 15% where all but a few of the models have reached simulated side-sway collapse. The

corresponding correlation of predicted values of $\hat{S}_{CT}$ with the underlying collapse data is 99.0%, indicating a relatively good fit of the collapse surface to this set of collapse data. Repeating the regression analysis using a more constrained set of collapse data for values of *DR* from *DR* = 2.5% to *DR* = 10% was found to improve correlation to 99.6%, although the collapse surface was essentially unchanged, indicating that constraining the collapse data set to the smaller range of *DR* values would not be warranted for this archetype.

3.6.2 Example Validation of Median Collapse Surface

Validation of the "fit" of collapse surface, defined by Equation 3-10, to the collapse data set of the 4-story COM wood is made (1) by plotting the residuals of the regression analysis (i.e., difference in collapse data and collapse surface values of $\hat{S}_{CT}$) as a function of $\hat{S}_{CT}$, and (2) by comparing collapse data and collapse surface values of $\hat{S}_{CT}$, plotted as a function of V_{max}/W. A plot of residuals (normalized by $\hat{S}_{CT}$) as a function of $\hat{S}_{CT}$ is shown in Figure 3-11 for residuals of drift ratios of primary interest (i.e., *DR* = 2.5% to *DR* = 10%).

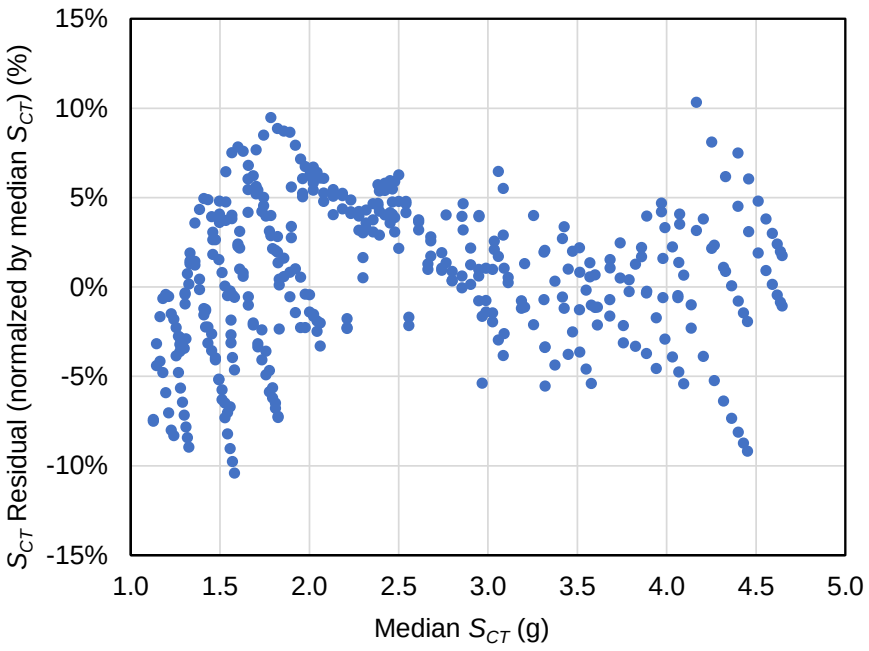

Figure 3-11 Plot of S_{CT} residuals normalized by median S_{CT} of the 4-story COM wood archetype for values of *DR* = 2.5% to *DR* = 10%.

Residual plots are useful in identifying systematic biases or spurious data over the range of values of $\hat{S}_{CT}$ of interest. As shown in Figure 3-11, the plot of S_{CT} residuals, normalized by $\hat{S}_{CT}$, collapse data to be reasonably well distributed around the median of the collapse surface over the range of drift ratios of primary interest (i.e., *DR* = 2.5% to *DR* = 10%) and typically within +/- 5% of the median for

most values of $\hat{S}_{CT}$. This relatively small amount of dispersion around the median is one of the contributing factors to collapse variability that is accounted for by the total collapse uncertainty parameter, β_{TOT}, of the collapse fragility curve (e.g., illustrated in Figure 3-7).

There are systematic (non-random) trends in values of normalized residuals due to the discrete increments of normalized strength, V_{max}/W, and residual strength (V_{RS}/W) used to model the 4-story COM wood archetype and likewise the discrete increments of *DR* used to evaluate non-simulated collapse, reflecting the strong correlation of collapse performance with archetype strength and displacement capacity.

Plots comparing collapse data and collapse surface values of $\hat{S}_{CT}$, are useful for visual verification of the fit of collapse surface to collapse data. Plots comparing collapse data and curves of $\hat{S}_{CT}$ values of collapse surface at *DR* = 2.5%, 5.0%, 7.5% and 10% are shown in Figure 3-12 through Figure 3-15, respectively. These plots generally show curves of median collapse passing through the center of the collapse data at each increment of *DR*.

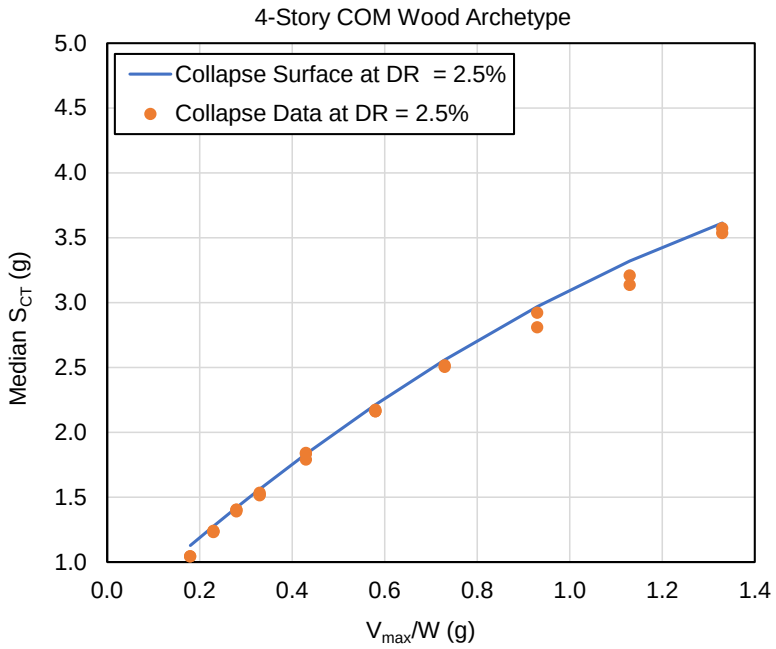

Figure 3-12 Plots of collapse data at *DR* = 2.5% and a curve of the $\hat{S}_{CT}$ values of the collapse surface at *DR* = 2.5% of the 4-story COM wood archetype.

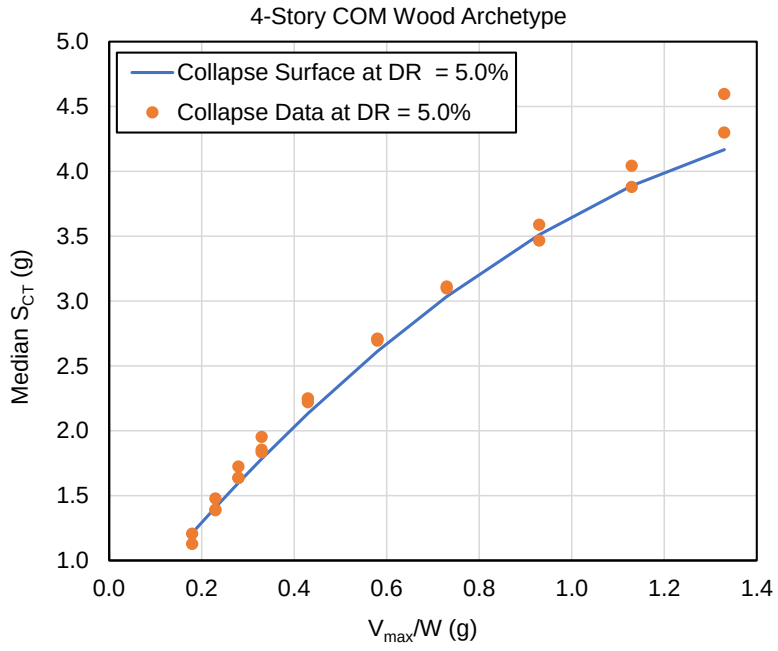

Figure 3-13 **Plots of collapse data at *DR* = 5.0% and a curve of the $\widehat{S}_{CT}$ values of the collapse surface at *DR* = 5.0% of the 4-story COM wood archetype.**

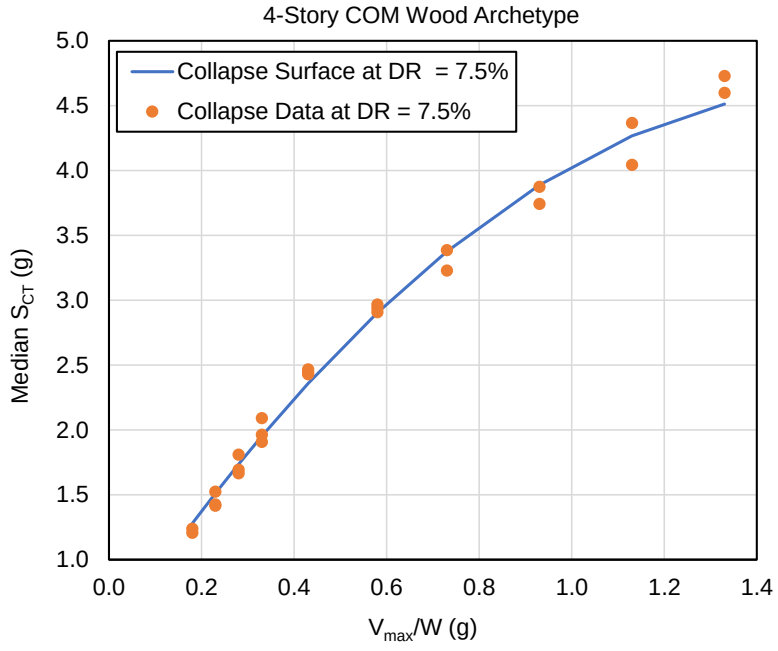

Figure 3-14 **Plots of collapse data at *DR* = 7.5% and a curve of the $\widehat{S}_{CT}$ values of the collapse surface at *DR* = 7.5% of the 4-story COM wood archetype.**

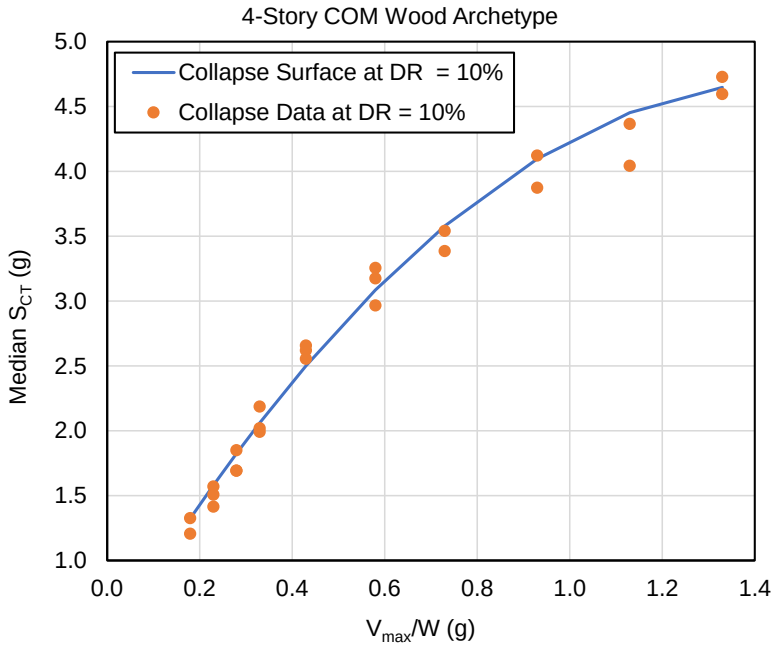

Figure 3-15 Plots of collapse data at *DR* = 10% and a curve of the $\hat{S}_{CT}$ values of the collapse surface at *DR* = 10% of the 4-story COM wood archetype.

3.7 Collapse Performance Metrics

There are two essential collapse performance metrics both of which are derived from values of $\hat{S}_{CT}$ of the collapse surface, (1) the adjusted collapse margin ratio, *ACMR*, and (2) the probability of collapse given MCE_R ground motions, P[Collapse|S_{MT}]. For this study, both collapse performance metrics, *ACMR* and P[Collapse|S_{MT}] are calculated in terms of the level of MCE_R ground motions (i.e., value of S_{MT}), such that increased collapse risk in regions of very high seismicity is investigated by broadly quantifying collapse performance from regions of moderate seismicity to regions of very high seismicity.

3.7.1 Adjusted Collapse Margin Ratio

The adjusted collapse margin ratio, *ACMR*, is derived from values of $\hat{S}_{CT}$ of the collapse surface of the SFRS archetype of interest, as a function of S_{MT}, by combining Equation 3-5 and Equation 3-6, as follows:

$$ACMR = SSF \times \hat{S}_{CT} / S_{MT} \quad (3\text{-}12)$$

where,

ACMR = Adjusted collapse margin ratio, Equation 7-1 of FEMA P-695,

SSF = Spectrum shape factor, Table 7-1a and Table 7-1b of FEMA P-695 for values of period-based ductility, μ_T, defined by Equation 3-3b,

$\hat{S}_{CT}$ = Median collapse response spectral acceleration of the collapse surface at normalized strength, V_{max}/W, and collapse displacement capacity, DR, and

S_{MT} = MCE_R ground motions intensity at the design period, T, of the multi-period response spectra of ASCE/SEI 7-22, assuming default site conditions, as defined by Equation 3-4 of this Chapter using the values of V_{max}/W and DR corresponding to $\hat{S}_{CT}$, and the value of overstrength (Ω) of the archetype of interest designed for S_{MT} (e.g. as specified for different archetypes in Chapter 2).

The *ACMR* parameter is proportional to seismic design criteria (e.g., proportional to design base shear) and hence of importance to quantifying the amount of adjustment of seismic design criteria required to meet collapse performance objectives. Hypothetically, if the value of *ACMR* was deemed low by a factor of two in terms of acceptable collapse performance, an appropriate remedy to achieve target collapse performance, in terms of strength, would be to double the design base shear.

3.7.2 Probability of Collapse given MCE_R Ground Motions

The probability of collapse, P[Collapse|S_{MT}], is calculated as a function S_{MT} assuming a lognormal distribution with a median value defined by the product, $ACMR \times S_{MT}$, of the collapse surface of the SFRS archetype of interest and logarithmic standard deviation defined by the total collapse uncertainty parameter, β_{TOT}.

The probability of collapse, P[Collapse|S_{MT}] is the metric used by ASCE/SEI 7-22 to define collapse performance objectives (i.e., values of target reliability for structural stability of Risk Category I&II, III and IV structures of Table 1.3-2 of ASCE/SEI 7-22). The probability of collapse is not proportional to *ACMR*. That is, hypothetically, if the probability of collapse was deemed high by a factor of two in terms of acceptable collapse performance, and appropriate remedy to achieve target collapse performance, in terms strength, would be to increase design base shear, although not necessarily by factor of two (e.g., typically by a smaller factor).

3.7.3 Total Collapse Uncertainty

The total collapse uncertainty parameter, β_{TOT}, accounts for the many sources uncertainty that contribute to the overall variability of collapse. Larger values of β_{TOT} necessitate larger collapse margins (i.e., larger values of *ACMR*) to achieve collapse performance objectives, in particular, for Risk Category IV structures which have a relatively small target conditional probability of collapse of 2.5% given MCE_R ground motions.

Values of β_{TOT} of this study are consistent with those of Section 7.3 of FEMA P-695, although contributions to total collapse uncertainty from (1) earthquake ground motions (i.e., record-to-record

variability) and the other three sources of uncertainty related to the reliability of the SFRS archetype models, (2) design requirements, (3) test data and (4) modeling are estimated collectively, rather than for each of the four contributing factors. This approach is the same as that used by prior studies of short-period buildings (FEMA, 2020), which assumed a consistent value of β_{TOT} = 0.50 for collapse evaluation of detailed nonlinear models of light-frame wood archetypes, special reinforced masonry archetypes, and steel special concentrically braced fame archetypes.

For comparison, Section 21.2.1 of ASCE/SEI 7-22 specifies a somewhat larger value (0.60) of the logarithmic standard deviation of "generic" collapse fragility required for calculation of risk-targeted MCE_R ground motions. Conversely, Equation (7-5) of FEMA P-695 converges to a value of β_{TOT} = 0.40 for "ductile" SFRSs, where the contribution to total collapse uncertainty is dominated by the record-to-record variability of the earthquake ground motions (i.e., estimated by FEMA P-695 as β_{RTR} = 0.40).

FEMA P-695 methods are intended for collapse evaluation of a specific SFRS using the same modeling assumptions for each archetype design, including the same non-simulated collapse displacement when archetypes are evaluated using non-simulated collapse failure. For example, these methods incorporate uncertainty in failure-mode displacement in modeling uncertainty (β_{MDL}), although the value of β_{MDL} (and hence β_{TOT}) is typically assumed to be the same for all collapse evaluations of the same SFRS.

For this study, which incorporates a range of hypothetical values of non-simulated collapse displacement, *DR*, the value of β_{TOT} is assumed to increase with the value of *DR*, all else equal. The increase in the value of β_{TOT} reflects (1) a modest, systematic increase in the inherent uncertainty in failure-mode displacement with increasing values of *DR* (i.e., median failure at *DR* = 7.5% is fundamentally less certain than at *DR* = 5.0%, all else equal) and (2) a significant decrease in displacement variability at very small values of *DR*, where the effects of earthquake ground motion record-to-record variability are significantly reduced (i.e., corresponding to values of period-based ductility, $\mu_T \leq 3.0$), the latter of which is not of practical significance to the collapse performance of the "ductile" SFRS archetypes investigated by this study.

For Risk Category II archetypes, values of β_{TOT} are assumed to vary uniformly in increments of 0.01 from β_{TOT} = 0.45 at *DR* = 2.5% to β_{TOT} = 0.60 at *DR* = 10% for collapse evaluation of light-frame wood archetypes of Chapter 4, noting that the value of β_{TOT} = 0.50 at *DR* = 5.0% is the same as the value of β_{TOT} used to evaluate light-frame wood models in FEMA P-2139-2 (FEMA, 2020). For collapse evaluation of other (non-wood) archetypes in Chapter 5, values of β_{TOT} are assumed to vary uniformly in increments of 0.01 from β_{TOT} = 0.55 at *DR* = 2.5% to β_{TOT} = 0.70 at *DR* = 10%, noting that the value of β_{TOT} = 0.60 at *DR* = 5.0% is the same as the value of logarithmic standard deviation of "generic" collapse fragility required by Section 21.2.1 of ASCE/SEI 7-22 for calculation of risk-targeted MCE_R ground motions. The larger values of β_{TOT} of non-wood archetypes reflect the inherent larger uncertainty of nonlinear modeling and failure modes of those archetypes. For Risk Category IV archetypes, values of β_{TOT} are decreased uniformly by 0.05, to reflect reduced

uncertainty in design and construction associated with enhanced regulatory review. Values of β_{TOT} used in Chapter 4 to evaluate the collapse probability of wood archetypes and in Chapter 5 to evaluate collapse of non-wood archetypes are summarized in Table 3-6.

Table 3-6 Summary of the Values of Total Collapse Uncertainty, β_{TOT}, Used to Evaluate the MCE_R Collapse Probability, P[Collapse|S_{MT}], of Wood Archetypes in Chapter 4 and Non-Wood Archetypes of Chapter 5

SFRS Archetype	Risk Category	Total Collapse Uncertainty (β_{TOT}) at *DR*[1]				
		2.5%	5.0%	7.5%	10%	15%
Wood	II	0.45	0.50	0.55	0.60	0.60
Wood	IV	0.40	0.45	0.50	0.55	0.55
Non-Wood	II	0.55	0.60	0.65	0.70	0.70
Non-Wood	IV	0.50	0.55	0.60	0.65	0.65

(1) Values of β_{TOT} vary linearly between discrete values shown in the table.

In general, the relatively small, systematic increase in the values of β_{TOT} with increase in *DR* only modestly affects the values of P[Collapse|S_{MT}] at the 10% collapse objective of Risk Category II archetypes, but has a more significant effect on values of P[Collapse|S_{MT}] at the 2.5% collapse objective of Risk Category IV archetypes.

3.8 Example Comparison of Collapse Performance in Regions of Moderate, High, and Very High Seismicity

An example comparison of collapse performance in regions of moderate, high, and very high seismicity is made in this section using the example collapse surface of the 4-story COM light-frame wood archetype shown in Figure 3-10. Collapse performance is evaluated for both Risk Category II design and Risk Category IV design of the 4-story COM light-frame wood archetype. Example results are taken from *Excel* spreadsheet calculations of the collapse performance metrics, *ACMR* and P[Collapse|S_{MT}], and summarized in the tables and shown in the figures of this section. The format of the tables and figures of this section serve as prototypes for presentation of collapse performance results in Chapters 4 and 5.

This example illustrates conceptually the three sequential steps for developing collapse performance metrics of a given SFRS archetype (1) extract values $\hat{S}_{CT}$ from the collapse surface of the SFRS archetype of interest, (2) calculate values of *ACMR* as a function of S_{MT} from the extracted values $\hat{S}_{CT}$ and (3) calculate values of P[Collapse|S_{MT}] as a function of S_{MT} for values of *ACMR* (i.e., *SSF* × $\hat{S}_{CT}$).

1. **Values of $\hat{S}_{CT}$.** Values of $\hat{S}_{CT}$ extracted from the collapse surface shown in Figure 3-10 are summarized in Table 3-7 for Risk Category II archetypes and in Table 3-8 for Risk Category IV archetypes of the 4-story COM light-frame wood SFRS, Values of $\hat{S}_{CT}$ are extracted at discrete increments of V_{max}/W and selected values of *DR* (i.e., 2.5%. 5.0%, 7.5%, 10% and DR_{IC}).

   The discrete increments of V_{max}/W correspond to values of S_{MT} ranging from moderate (e.g., S_{MT} = 0.70g) to very high seismic (e.g., S_{MT} = 3.0g) regions of interest and are calculated using Equation 3-8 using values of overstrength, Ω, summarized in either Table 3-9 for Risk Category II structures or Table 3-10 for Risk category IV structures.

   Table 3-7 and Table 3-8 include values of $\hat{S}_{CT}$ at DR_{IC}, the median value of *DR* at incipient collapse, and the corresponding value of the DR_{IC}. Values of DR_{IC} are based on the trend in the values of DR_{IC} summarized in Table 3-4 for the 25 archetype models of the 4-story of COM wood archetype, where this trend is determined as a curve fit to the 25 DR_{IC} data of that table. Values of DR_{IC} are influenced by hysteretic modeling assumptions and in the case of the 4-Story COM wood archetype, vary from about 10.5% at V_{max}/W = 0.32g to 5.3% at V_{max}/W = 1.24g, due to differences in residual strength modeling assumptions.

2. **Values of *ACMR*.** Values of the *ACMR*, calculated using Equation 3-12, are summarized in Table 3-9 for Risk Category II archetypes and in Table 3-10 for Risk Category IV archetypes of the 4-story COM light-frame wood building, and plotted in Figure 3-16 and Figure 3-17, respectively, as a function of S_{MT} for drift ratios of primary interest, i.e., *DR* = 5%, *DR* = 7.5%, *DR* = 10% and *DR* = DR_{IC}.

   Table 3-9 and Table 3-10 include the S_{MT}-dependent values of overstrength, Ω, and typical values of the *DR*-dependent *SSF* factor used with Equation 3-12 to calculate *ACMR*. The S_{MT}-dependent values of Ω are based on the recommendations of Chapter 2 regarding the median overstrength of commercial light-frame wood buildings. The *DR*-dependent values of *SSF* are based on Table 3-2 (assuming probabilistic MCE_R ground motions) for values of period-based ductility, μ_T, corresponding to the *DR* of interest.

   Figure 3-16 and Figure 3-17 include horizontal lines showing acceptable values the *ACMR* of Table 3-1 (e.g., *ACMR10%* for Risk Category II archetypes and *ACMR2.5%* for Risk Category IV archetypes) based on the *DR*-dependent values of β_{TOT} given in Table 3-6. Acceptable values of *ACMR* are shown for drift ratios of primary interest, i.e., *DR* = 5%, *DR* = 7.5%, *DR* = 10% and *DR* = DR_{IC}.

3. **Values of P[Collapse|S_{MT}].** Values of the conditional MCE_R collapse probability, P[Collapse|S_{MT}], based on the *ACMR* values of (2) and the *DR*-dependent values of β_{TOT} of Table 3-6, are summarized in Table 3-11 for Risk Category II archetypes and in Table 3-12 for Risk Category IV archetypes of the 4-story COM wood building, and plotted in Figure 3-17 and Figure 3-18,

respectively, as a function of S_{MT} for drift ratios of primary interest, i.e., DR = 5%, DR = 7.5%, DR = 10% and $DR = DR_{IC}$. Table 3-11 and Table 3-12 include the DR-dependent values of β_{TOT} used to calculate P[Collapse|S_{MT}].

Figure 3-18 and Figure 3-19 each include a horizontal line showing acceptable values the P[Collapse|S_{MT}] (e.g., 10 percent for Risk Category II archetypes in Figure 3-18 and 2.5% for Risk Category IV archetypes in Figure 3-18). Collapse probabilities of Risk Category II structures are similar at DR = 7.5%, DR = 10% and $DR = DR_{IC}$ (Figure 3-18) due to the effect of increased collapse uncertainty at larger drift displacements offsetting the benefit of increased displacement capacity, and likewise for Risk Category IV archetypes (Figure 3-19), except at very large values of S_{MT} where collapse probabilities at $DR = DR_{IC}$ increase as values of DR_{IC} tend toward DR_{IC} = 5.0%.

Table 3-7 **Selected Values of $\widehat{S}_{CT}$ Extracted From the Example Collapse Surface of the 4-Story COM Wood Archetype Shown in Figure 3-10 at Discrete Values of V_{max}/W and Corresponding to Increments of MCE_R S_{MT} from 0.70g to 3.0g. Values of $\widehat{S}_{CT}$ are Selected at Collapse Drift Ratios, DR = 2.5%, 5.0%, 7.5%, 10% and 15%, and at the Median Drift Ratio of Incipient Collapse. Discrete Values of V_{max}/W are based on Equation 3-8 Assuming R/I_e = 6.5/1.0 (i.e., Risk Category II Seismic Design) and Values of Overstrength, Ω, of Table 3-9**

MCE_R S_{MT} (g)	V_{max}/W	Median Collapse Acceleration, $\widehat{S}_{CT}$ (g) at DR						DR_{IC}
		2.5%	5.0%	7.5%	10%	15%	DR_{IC}	
0.70	0.32	1.55	1.77	1.93	2.04	2.10	2.05	10.5%
0.80	0.35	1.61	1.85	2.03	2.15	2.21	2.16	10.3%
0.90	0.37	1.68	1.94	2.13	2.26	2.32	2.26	10.2%
1.00	0.40	1.75	2.02	2.23	2.36	2.43	2.36	10.1%
1.10	0.42	1.81	2.11	2.32	2.47	2.53	2.46	9.9%
1.20	0.45	1.87	2.19	2.42	2.57	2.64	2.56	9.8%
1.30	0.47	1.94	2.27	2.51	2.66	2.74	2.65	9.7%
1.40	0.49	2.00	2.34	2.60	2.76	2.83	2.74	9.6%
1.50	0.52	2.06	2.42	2.69	2.85	2.93	2.83	9.4%
1.60	0.54	2.12	2.50	2.77	2.95	3.02	2.91	9.3%
1.70	0.57	2.18	2.57	2.86	3.04	3.11	2.99	9.2%
1.80	0.59	2.24	2.64	2.94	3.12	3.20	3.07	9.1%
1.90	0.61	2.29	2.71	3.02	3.21	3.28	3.14	9.0%
2.00	0.64	2.35	2.78	3.10	3.29	3.36	3.22	8.9%
2.10	0.66	2.41	2.85	3.17	3.37	3.44	3.29	8.7%
2.20	0.69	2.46	2.92	3.25	3.45	3.52	3.35	8.6%
2.30	0.71	2.52	2.98	3.32	3.52	3.59	3.42	8.5%
2.40	0.73	2.57	3.05	3.39	3.59	3.66	3.48	8.4%
2.50	0.76	2.62	3.11	3.46	3.66	3.73	3.54	8.3%
2.60	0.78	2.67	3.17	3.52	3.73	3.79	3.60	8.2%
2.70	0.81	2.72	3.23	3.59	3.80	3.86	3.65	8.1%
2.80	0.83	2.77	3.29	3.65	3.86	3.92	3.70	8.0%
2.90	0.86	2.82	3.35	3.71	3.92	3.98	3.75	7.9%
3.00	0.88	2.87	3.40	3.77	3.98	4.03	3.80	7.8%

Table 3-8 **Selected Values of $\widehat{S}_{CT}$ Extracted from the Example Collapse Surface of the 4-Story COM Wood Archetype Shown in Figure 3-10 at Discrete Values of V_{max}/W and Corresponding to Increments of MCE_R S_{MT} from 0.70g to 3.0g. Values of $\widehat{S}_{CT}$ are Selected at Non-Simulated Collapse Drift Ratios, DR = 2.5%, 5.0%, 7.5%, 10% and 15%, and at the Median Drift Ratio of Incipient Collapse, due to P-Delta Failure. Discrete Values of V_{max}/W are Based on Equation 3-8 Assuming R/I_e = 6.5/1.5 (i.e., Risk Category IV Seismic Design) and Values of Overstrength, Ω, of Table 3-10**

MCE_R S_{MT} (g)	V_{max}/W	Median Collapse Acceleration, $\widehat{S}_{CT}$ (g) at DR						DR_{IC}
		2.5%	5.0%	7.5%	10%	15%	DR_{IC}	
0.70	0.41	1.78	2.06	2.28	2.41	2.48	2.41	10.0%
0.80	0.45	1.87	2.19	2.42	2.57	2.64	2.56	9.8%
0.90	0.48	1.97	2.31	2.55	2.71	2.79	2.70	9.6%
1.00	0.52	2.06	2.42	2.69	2.85	2.93	2.83	9.4%
1.10	0.55	2.15	2.53	2.81	2.99	3.06	2.95	9.3%
1.20	0.59	2.24	2.64	2.94	3.12	3.20	3.07	9.1%
1.30	0.63	2.32	2.75	3.06	3.25	3.32	3.18	8.9%
1.40	0.66	2.41	2.85	3.17	3.37	3.44	3.29	8.7%
1.50	0.70	2.49	2.95	3.28	3.48	3.55	3.38	8.6%
1.60	0.73	2.57	3.05	3.39	3.59	3.66	3.48	8.4%
1.70	0.77	2.65	3.14	3.49	3.70	3.76	3.57	8.2%
1.80	0.81	2.72	3.23	3.59	3.80	3.86	3.65	8.1%
1.90	0.84	2.80	3.32	3.68	3.89	3.95	3.73	7.9%
2.00	0.88	2.87	3.40	3.77	3.98	4.03	3.80	7.8%
2.10	0.92	2.94	3.48	3.86	4.06	4.11	3.87	7.6%
2.20	0.95	3.01	3.56	3.94	4.14	4.19	3.93	7.5%
2.30	0.99	3.08	3.63	4.01	4.22	4.26	3.99	7.3%
2.40	1.02	3.14	3.70	4.08	4.28	4.32	4.05	7.2%
2.50	1.06	3.20	3.77	4.15	4.35	4.38	4.10	7.1%
2.60	1.10	3.27	3.83	4.21	4.40	4.43	4.14	6.9%
2.70	1.13	3.32	3.89	4.27	4.46	4.48	4.18	6.8%
2.80	1.17	3.38	3.95	4.32	4.50	4.52	4.22	6.7%
2.90	1.20	3.44	4.01	4.37	4.54	4.56	4.25	6.5%
3.00	1.24	3.49	4.06	4.42	4.58	4.59	4.28	6.4%

Table 3-9 Example Values of the Adjusted Collapse Margin Ratio (*ACMR*) Calculated from the Values of $\widehat{S}_{CT}$ Summarized in Table 3-7 for the 4-Story COM Wood Archetype, Assuming Risk Category II Seismic Design (i.e., R/I_e = 6.5/1.0)

			Typical Spectrum Shape Factor (*SSF*) at *DR*					
			1.16	1.25	1.33	1.33	1.33	varies
MCE_R S_{MT} (g)	Strength Property		*ACMR* at *DR*					
	Ω	V_{max}/W	2.5%	5.0%	7.5%	10%	15%	DR_{IC}
0.70	4.53	0.32	2.57	3.16	3.67	3.87	3.99	3.90
0.80	4.25	0.35	2.34	2.90	3.38	3.57	3.68	3.59
0.90	4.04	0.37	2.17	2.70	3.15	3.33	3.43	3.35
1.00	3.87	0.40	2.03	2.53	2.96	3.14	3.23	3.15
1.10	3.73	0.42	1.91	2.40	2.81	2.98	3.06	2.98
1.20	3.62	0.45	1.81	2.28	2.68	2.84	2.92	2.83
1.30	3.52	0.47	1.73	2.18	2.57	2.73	2.80	2.71
1.40	3.44	0.49	1.66	2.10	2.47	2.62	2.69	2.60
1.50	3.37	0.52	1.59	2.02	2.38	2.53	2.60	2.50
1.60	3.30	0.54	1.54	1.96	2.30	2.45	2.51	2.41
1.70	3.25	0.57	1.49	1.89	2.23	2.37	2.43	2.33
1.80	3.20	0.59	1.44	1.84	2.17	2.31	2.36	2.26
1.90	3.15	0.61	1.40	1.79	2.11	2.24	2.30	2.19
2.00	3.11	0.64	1.36	1.74	2.06	2.19	2.23	2.13
2.10	3.08	0.66	1.33	1.70	2.01	2.13	2.18	2.07
2.20	3.04	0.69	1.30	1.66	1.96	2.08	2.13	2.02
2.30	3.01	0.71	1.27	1.63	1.92	2.04	2.08	1.97
2.40	2.98	0.73	1.24	1.59	1.88	1.99	2.03	1.92
2.50	2.96	0.76	1.22	1.56	1.84	1.95	1.98	1.87
2.60	2.94	0.78	1.19	1.53	1.80	1.91	1.94	1.83
2.70	2.91	0.81	1.17	1.50	1.77	1.87	1.90	1.79
2.80	2.89	0.83	1.15	1.47	1.73	1.83	1.86	1.75
2.90	2.88	0.86	1.13	1.45	1.70	1.80	1.82	1.71
3.00	2.86	0.88	1.11	1.42	1.67	1.76	1.79	1.67

Table 3-10 Example Values of the Adjusted Collapse Margin Ratio (*ACMR*) Calculated from the Values of $\widehat{S}_{CT}$ Summarized in Table 3-8 for the 4-Story COM Wood Archetype, Assuming Risk Category IV Seismic Design (i.e., R/I_e = 6.5/1.5)

			Typical Spectrum Shape Factor (*SSF*) at *DR*					
			1.16	1.25	1.33	1.33	1.33	varies
MCE_R S_{MT} (g)	Strength Property		*ACMR* at *DR*					
	Ω	V_{max}/W	2.5%	5.0%	7.5%	10%	15%	DR_{IC}
0.70	3.80	0.41	2.95	3.70	4.33	4.59	4.72	4.59
0.80	3.62	0.45	2.72	3.43	4.02	4.27	4.38	4.25
0.90	3.48	0.48	2.54	3.21	3.77	4.01	4.12	3.98
1.00	3.37	0.52	2.39	3.03	3.57	3.80	3.89	3.75
1.10	3.27	0.55	2.27	2.89	3.40	3.62	3.71	3.56
1.20	3.20	0.59	2.16	2.76	3.26	3.46	3.54	3.39
1.30	3.13	0.63	2.07	2.65	3.13	3.32	3.40	3.24
1.40	3.08	0.66	2.00	2.55	3.01	3.20	3.27	3.11
1.50	3.03	0.70	1.93	2.47	2.91	3.09	3.15	2.99
1.60	2.98	0.73	1.86	2.39	2.82	2.99	3.04	2.88
1.70	2.95	0.77	1.81	2.32	2.73	2.89	2.94	2.78
1.80	2.91	0.81	1.76	2.25	2.65	2.81	2.85	2.68
1.90	2.88	0.84	1.71	2.19	2.58	2.72	2.76	2.59
2.00	2.86	0.88	1.67	2.13	2.51	2.65	2.68	2.51
2.10	2.83	0.92	1.63	2.08	2.44	2.57	2.61	2.43
2.20	2.81	0.95	1.59	2.03	2.38	2.50	2.53	2.36
2.30	2.79	0.99	1.55	1.98	2.32	2.44	2.46	2.28
2.40	2.77	1.02	1.52	1.93	2.26	2.37	2.39	2.21
2.50	2.76	1.06	1.49	1.89	2.21	2.31	2.33	2.14
2.60	2.74	1.10	1.46	1.85	2.15	2.25	2.27	2.08
2.70	2.73	1.13	1.43	1.81	2.10	2.20	2.21	2.01
2.80	2.71	1.17	1.40	1.77	2.05	2.14	2.15	1.95
2.90	2.70	1.20	1.38	1.73	2.01	2.08	2.09	1.90
3.00	2.69	1.24	1.35	1.69	1.96	2.03	2.03	1.84

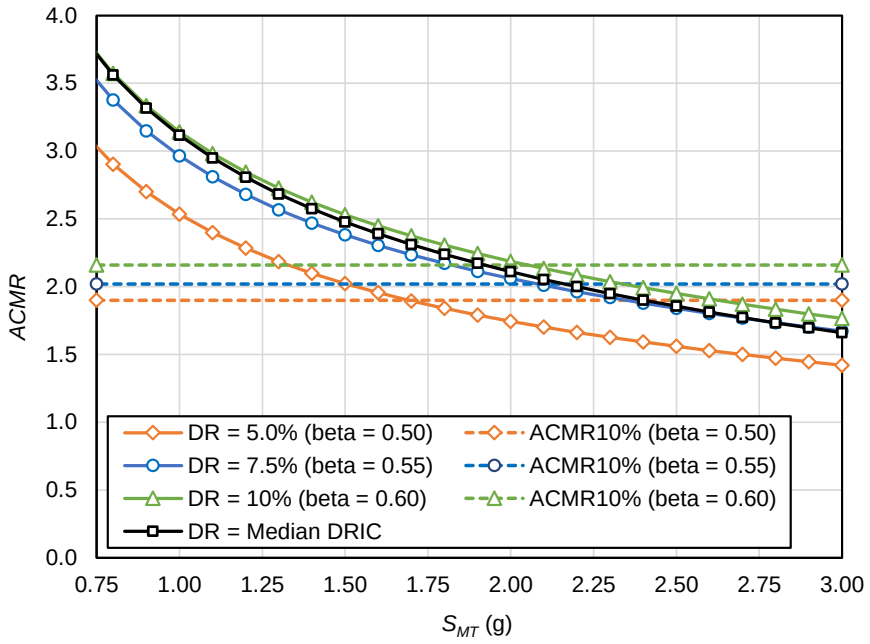

Figure 3-16 **Plots of the example values of *ACMR* of Table 3-9 as a function of S_{MT} for the 4-Story COM wood archetype, assuming Risk Category II seismic design (i.e., R/I_e = 6.5/1.0), and acceptable values of *ACMR* for Risk Category II structures (*ACMR10%*) at non-simulated collapse drift ratios, *DR* = 5.0%, 7.5% and 10%.**

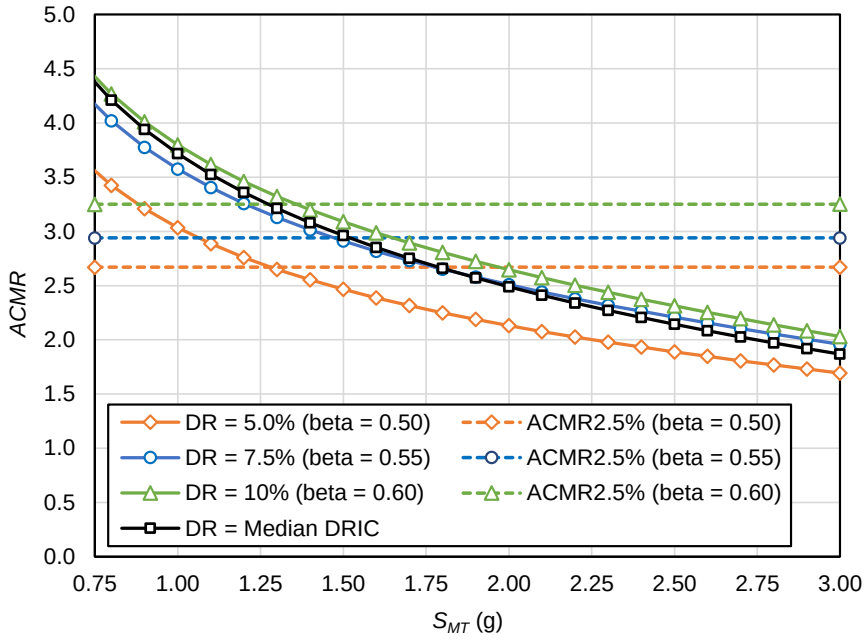

Figure 3-17 **Plots of the example values of *ACMR* of Table 3-10 as a function of S_{MT} for the 4-Story COM wood archetype, assuming Risk Category IV seismic design (i.e., R/I_e = 6.5/1.5), and acceptable values of *ACMR* for Risk Category IV structures (*ACMR2.5%*) at non-simulated collapse drift ratios, *DR* = 5.0%, 7.5% and 10%.**

Table 3-11 Example Values of the MCE_R Collapse Probability, P[Collapse|S_{MT}], Calculated from the Values of *ACMR* Summarized in Table 3-9 for the 4-Story COM Wood Archetype, Assuming Risk Category II Seismic Design (i.e., R/I_e = 6.5/1.0)

			Total Collapse Variability (β_{TOT}) at *DR*					
			0.45	0.50	0.55	0.60	0.60	varies
MCE_R S_{MT} (g)	Strength Property		P[Collapse|S_{MT}] at *DR*					
	Ω	V_{max}/W	2.5%	5.0%	7.5%	10%	15%	DR_{IC}
0.70	4.53	0.32	1.8%	1.1%	0.9%	1.2%	1.1%	1.2%
0.80	4.25	0.35	2.9%	1.7%	1.3%	1.7%	1.5%	1.7%
0.90	4.04	0.37	4.3%	2.4%	1.9%	2.2%	2.0%	2.2%
1.00	3.87	0.40	5.8%	3.1%	2.4%	2.8%	2.5%	2.8%
1.10	3.73	0.42	7.5%	4.0%	3.0%	3.4%	3.1%	3.4%
1.20	3.62	0.45	9.3%	4.9%	3.7%	4.1%	3.7%	4.0%
1.30	3.52	0.47	11.2%	5.9%	4.3%	4.7%	4.3%	4.7%
1.40	3.44	0.49	13.1%	6.9%	5.0%	5.4%	4.9%	5.3%
1.50	3.37	0.52	15.0%	7.9%	5.7%	6.1%	5.6%	6.0%
1.60	3.30	0.54	16.9%	9.0%	6.4%	6.8%	6.3%	6.7%
1.70	3.25	0.57	18.9%	10.1%	7.2%	7.5%	6.9%	7.3%
1.80	3.20	0.59	21%	11.1%	7.9%	8.2%	7.6%	8.0%
1.90	3.15	0.61	23%	12.2%	8.7%	8.9%	8.3%	8.8%
2.00	3.11	0.64	24%	13.3%	9.5%	9.6%	9.0%	9.5%
2.10	3.08	0.66	26%	14.4%	10.2%	10.3%	9.7%	10.2%
2.20	3.04	0.69	28%	15.5%	11.0%	11.1%	10.4%	11.0%
2.30	3.01	0.71	30%	16.6%	11.8%	11.8%	11.2%	11.8%
2.40	2.98	0.73	31%	17.6%	12.6%	12.5%	11.9%	12.6%
2.50	2.96	0.76	33%	18.7%	13.4%	13.3%	12.7%	13.4%
2.60	2.94	0.78	35%	19.8%	14.2%	14.1%	13.4%	14.2%
2.70	2.91	0.81	36%	21%	15.0%	14.8%	14.2%	15.0%
2.80	2.89	0.83	38%	22%	15.8%	15.6%	15.0%	15.9%
2.90	2.88	0.86	39%	23%	16.7%	16.4%	15.8%	16.8%
3.00	2.86	0.88	41%	24%	17.5%	17.2%	16.6%	17.7%

Table 3-12 Example Values of the MCE_R Collapse Probability, P[Collapse|S_{MT}], Calculated from the Values of *ACMR* Summarized in Table 3-10 for the 4-Story COM Wood Archetype, Assuming Risk Category IV Seismic Design (i.e., R/I_e = 6.5/1.5)

			Total Collapse Variability (β_{TOT}) at *DR*					
			0.40	0.45	0.50	0.55	0.55	varies
MCE_R S_{MT} (g)	Strength Property		P[Collapse|S_{MT}] at *DR*					
	Ω	V_{max}/W	2.5%	5.0%	7.5%	10%	15%	DR_{IC}
0.70	3.80	0.41	0.3%	0.2%	0.2%	0.3%	0.2%	0.3%
0.80	3.62	0.45	0.6%	0.3%	0.3%	0.4%	0.4%	0.4%
0.90	3.48	0.48	1.0%	0.5%	0.4%	0.6%	0.5%	0.5%
1.00	3.37	0.52	1.5%	0.7%	0.6%	0.8%	0.7%	0.7%
1.10	3.27	0.55	2.0%	0.9%	0.7%	1.0%	0.9%	0.9%
1.20	3.20	0.59	2.7%	1.2%	0.9%	1.2%	1.1%	1.1%
1.30	3.13	0.63	3.4%	1.5%	1.2%	1.5%	1.3%	1.3%
1.40	3.08	0.66	4.2%	1.9%	1.4%	1.7%	1.6%	1.5%
1.50	3.03	0.70	5.1%	2.3%	1.7%	2.0%	1.8%	1.8%
1.60	2.98	0.73	6.0%	2.7%	2.0%	2.3%	2.2%	2.1%
1.70	2.95	0.77	7.0%	3.1%	2.3%	2.7%	2.5%	2.4%
1.80	2.91	0.81	8.0%	3.6%	2.6%	3.0%	2.8%	2.7%
1.90	2.88	0.84	9.0%	4.1%	3.0%	3.4%	3.2%	3.0%
2.00	2.86	0.88	10.1%	4.7%	3.4%	3.8%	3.6%	3.4%
2.10	2.83	0.92	11.3%	5.3%	3.8%	4.3%	4.1%	3.8%
2.20	2.81	0.95	12.4%	5.9%	4.3%	4.8%	4.6%	4.3%
2.30	2.79	0.99	13.6%	6.5%	4.8%	5.3%	5.1%	4.8%
2.40	2.77	1.02	14.8%	7.2%	5.3%	5.8%	5.6%	5.4%
2.50	2.76	1.06	16.1%	8.0%	5.8%	6.4%	6.2%	6.0%
2.60	2.74	1.10	17.3%	8.7%	6.4%	7.0%	6.8%	6.7%
2.70	2.73	1.13	18.6%	9.5%	7.0%	7.6%	7.5%	7.5%
2.80	2.71	1.17	20.0%	10.4%	7.7%	8.3%	8.2%	8.3%
2.90	2.70	1.20	21.3%	11.2%	8.4%	9.1%	9.0%	9.1%
3.00	2.69	1.24	22.7%	12.2%	9.2%	9.9%	9.8%	10.1%

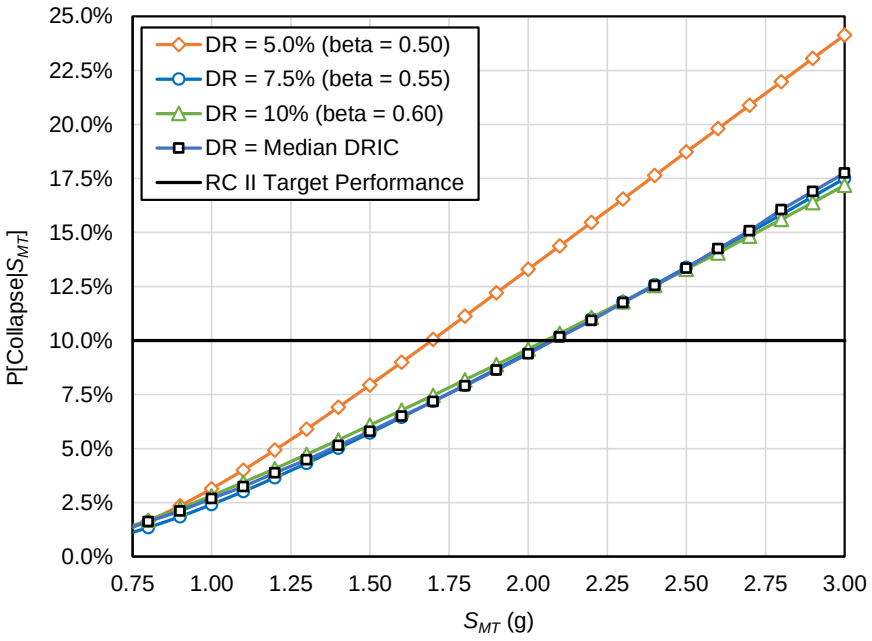

Figure 3-18 **Plots of the example values of P[Collapse|S_{MT}] of Table 3-6 as a function of S_{MT} for the 4-Story COM Wood Archetype, assuming Risk Category II seismic design (i.e., R/I_e = 6.5/1.0), and target collapse performance of Risk Category II structures (i.e., 10%).**

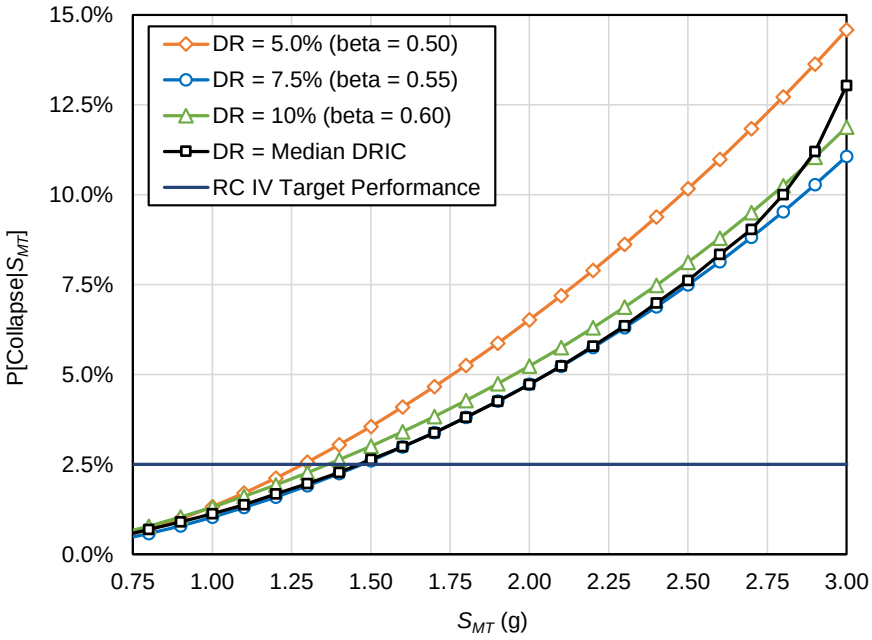

Figure 3-19 **Plots of the example values of P[Collapse|S_{MT}] of Table 3-8 as a function of S_{MT} for the 4-Story COM Wood Archetype, assuming Risk Category IV seismic design (i.e., R/I_e = 6.5/1.5), and target collapse performance of Risk Category IV structures (i.e., 2.5%).**

Chapter 4: Numerical Study of Wood Light-frame Buildings

4.1 Introduction

This chapter describes the procedures used to develop nonlinear numerical models of wood light-frame buildings and the analysis methods used to determine the seismic response behavior and collapse performance.

4.2 Overview and Approach

Chapter 3 describes the process for developing collapse surfaces. Figure 4-1 graphically illustrates the framework. First, a class of buildings is defined based on: (1) seismic-force-resisting system (SFRS), (2) occupancy type, and (3) number of stories. Next, a numerical model is created to assess the primary building response properties and seismic performance.

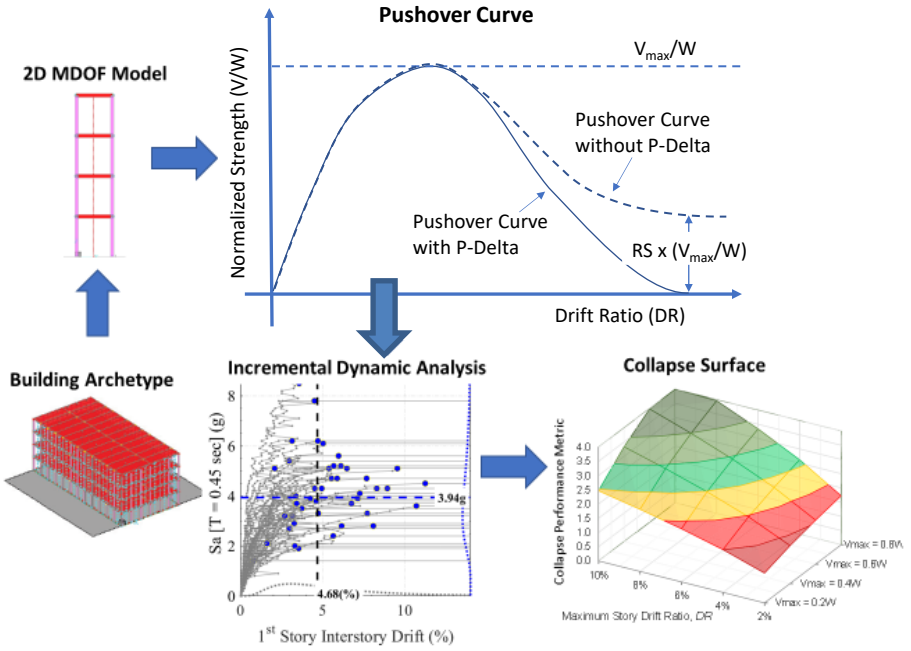

Figure 4-1 Framework for developing a collapse surface for a class of buildings.

The primary building response properties are strength and displacement capacity. Strength is quantified using the normalized pushover strength (V_{max}/W), where V_{max} is the peak strength on the pushover curve of the structure of interest and W is the effective seismic weight. FEMA P-2139-2 showed that for wood systems displacement capacity is tied to the post-peak residual strength (RS) ratio of the structure's pushover curve. The residual strength ratio is used as a proxy to incorporate

non-simulated sources of strength in wood buildings (e.g., stairwells, moment restraint from out-of-plane walls, sheathing panels below and above the window openings).

Incremental dynamic analysis (IDA) using an ensemble of ground motions is carried out to quantify the seismic performance in terms of the median spectral acceleration ($\hat{S}_{CT}$) that causes the building to collapse. The displacement capacity is defined using (1) the median of the inter-story drift ratios at incipient collapse or (2) a user-prescribed non-simulated drift ratio (drift limit) on IDA curves.

The development of 2D multi-degree-of-freedom (MDOF) wood building models and the validation of the 2D MDOF models used to generate the collapse surfaces for various classes of wood buildings used in this study can be found in Appendix B. The next sections discuss the development of wood building models (study matrices) used to generate the collapse surfaces for various classes of buildings.

4.3 Collapse Surface Model and Study Matrix

4.3.1 Wood Light-Frame Archetypes

A total of 15 classes of wood light-frame buildings, organized by occupancy (or configuration) and number of stories, are considered:

1. **Occupancy**: structure only (STR), commercial buildings (COM), and multi-family dwellings (MFD)
2. **Number of stories**: 1, 2, 3, 4, and 5 stories

The structure-only archetype represents wood light-frame buildings with the lateral strength coming only from the SFRS and without contribution from nonstructural components (e.g., finish materials and partition walls). The STR archetype is used to evaluate the minimum seismic performance specified in the building code. The COM archetype is used to study the seismic performance of buildings with a relatively open floor plan and some partition walls. The MFD archetype is used to characterize wood buildings with large number of partition walls, as is typically seen in multi-family apartments and hotels. Both the COM and MFD archetypes are assumed to have the same SFRS strength (V_{STR}/W) with the COM and MFD archetypes representing lower- and upper-bound estimates of nonstructural strength (V_{NS}/W) in wood buildings, respectively.

4.3.2 Nonstructural Strength Model

The detailed COM and MFD archetypes developed in FEMA P-2139-2 (see Table 4-1 and Table 4-2) were analyzed to develop the nonstructural strength model of this study. Six baseline archetypes were developed each for COM and MFD occupancies in FEMA P-2139-2 consisting of one-, two- and four-story buildings for high seismic (HS) regions (S_{MS} = 1.5g) and very high seismic (VHS) regions (S_{MS} = 2.25g).

Six variant archetypes were created each for COM and MFD by removing the nonstructural elements from the baseline models (identified by model IDs with "-NS" in Table 4-1 and Table 4-2). These variant models represent buildings with SFRS and no nonstructural components (i.e., structure only). Pushover analyses were performed for both the baseline and variant models to determine the peak strength (V_{max}). The second-to-last column in Table 4-1 and Table 4-2 show the normalized nonstructural strength (V_{NS}/W). The last column shows the nonstructural strength model used in this study:

$$\frac{V_{NS}}{W} = \begin{cases} \dfrac{0.5}{N} & for \quad COM \\ \dfrac{0.9}{N} & for \quad MFD \end{cases} \tag{4-1}$$

where N is the number of stories. As can be seen, except for the 1-story models, the normalized nonstructural strength values computed using the above equation match those from the FEMA P-2139-2 reasonably well. Note that in Table 4-1, the structure-only strength of the as-designed buildings (Model IDs with "-NS") in VHS are consistently higher than those in HS, which reflects that the strength of SFRS increases with increasing seismicity. However, the contribution of nonstructural partition walls remains constant for HS and VHS (see column marked V_{NS}/W)

Table 4-1 Nonstructural Contributions of FEMA P-2139-2 COM Models

Seismicity	# Stories	Model ID	W (kips)	V_{max} (kips)	V_{max}/W	V_{NS} (kips)	V_{NS}/W	$0.5/N$
HS	1	COM1B	180.0	100.6	0.56	43.6	0.24	0.50
		COM1B-NS	180.0	57.0	0.32			
VHS	1	COM4B	180.0	120.5	0.67	43.7	0.24	0.50
		COM4B-NS	180.0	76.7	0.43			
HS	2	COM2B	493.3	236.0	0.48	117.7	0.24	0.25
		COM2B-NS	493.3	118.4	0.24			
VHS	2	COM5B	493.3	276.2	0.56	125.8	0.26	0.25
		COM5B-NS	493.3	150.4	0.30			
HS	4	COM3B	1119.9	347.2	0.31	128.5	0.11	0.13
		COM3B-NS	1119.9	218.7	0.20			
VHS	4	COM6B	1119.9	492.7	0.44	131.5	0.12	0.13
		COM6B-NS	1119.9	361.3	0.32			

Table 4-2 Nonstructural Contributions of FEMA P-2139-2 MFD Models

Seismicity	# Stories	Model ID	W (kips)	V_{max} (kips)	V_{max}/W	V_{NS} (kips)	V_{NS}/W	$0.9/N$
HS	1	MFD1B	140.5	183.16	1.30	144.2	1.03	0.90
		MFD1B-NS	140.5	38.99	0.28			
VHS	1	MFD4B	140.5	198.11	1.41	139.9	1.00	0.90
		MFD4B-NS	140.5	58.26	0.41			
HS	2	MFD2B	363	246.82	0.68	160.0	0.44	0.45
		MFD2B-NS	363	86.8	0.24			
VHS	2	MFD5B	362.9	264.31	0.73	142.7	0.39	0.45
		MFD5B-NS	362.9	121.57	0.33			
HS	4	MFD3B	971.2	359.34	0.37	145.4	0.15	0.23
		MFD3B-NS	971.2	213.92	0.22			
VHS	4	MFD6B	971.2	424.49	0.44	124.8	0.13	0.23
		MFD6B-NS	971.2	299.72	0.31			

4.3.3 Strength Parameter

The design base shear coefficient (C_S) in ASEC/SEI 7-22 is given by the following expression:

$$C_S = \frac{V}{W} = \frac{2/3 \times S_{MT}}{R/I_e} \tag{4-2}$$

where, V is the design base shear. R is the response modification factor which is 6.5 for wood light-frame buildings, and I is the important factor (1.0 for Risk Category II structures and 1.5 for Risk Category IV structures). The maximum considered earthquake (MCE_R) response spectral acceleration at the design period (S_{MT}) was varied to cover regions of moderate seismicity (S_{MT} = 0.75g) to very high seismicity (S_{MT} = 3.0g). Note that S_{MT} is the ASEC/SEI 7 acceleration value at MCE_R hazard level at the upper limit of code period (C_uT_a). The ASEC/SEI 7 design acceleration, S_{DT}, is equal to $2/3 \times S_{MT}$.

The peak strength of SFRS, V_{STR}/W, is:

$$\frac{V_{STR}}{W} = \Omega_{STR} \frac{2/3 \times S_{MT}}{R/I_e} \tag{4-3}$$

Where Ω_{STR} is the ratio of the actual peak strength of SFRS to the design strength V (i.e., structural overstrength of SFRS). The design strength (V) is equal to the code specified design base shear coefficient (C_s) times the seismic weight (W). For wood light-frame buildings, the structural overstrength, Ω_{STR}, was estimated to range from approximately 1.9 to 2.8, with an average of 2.35 (Section 2.3.1). Substituting the ranges of values considered for the variables in the above equation

allows one to estimate the lower and upper bounds of normalized pushover strength of the SFRS without nonstructural wall finishes. To encompass the full range of all design variables (S_{MT} and I_e), 10 increments of V_{STR}/W were considered (i.e., 0.05g, 0.10g, 0.15g, 0.20g, 0.30g, 0.45g, 0.60g, 0.80g, 1.0g, and 1.2g).

4.3.4 Residual Strength Parameter

Six hypothetical levels of residual strength (*RS*) ratios of 10%, 20%, 30%, 45%, 60%, and 75% of the peak strength were considered. The amounts of residual strength from non-simulated sources typically do not vary with the level of structural strength. To maintain similar magnitudes of residual strength over the full range of V_{STR}/W, 2 or 3 out of 6 residual strength ratios were considered for each level of V_{STR}/W with the low *RS* values associated with high V_{STR}/W and high RS values associated with low V_{STR}/W.

To illustrate the assignment of RS based on V_{STR}/W, consider two nominally identical 4-story MFD buildings with one located in a low seismic zone and the other in a high seismic zone (see Table 4-3). The values to S_{MT} were selected to achieve two of the V_{STR}/W values considered in this study. The SFRS strengths (V_{STR}/W) for Risk Category II computed using Equation 4-3 were 0.16 and 0.45 for low and high seismic zones, respectively (R = 6.5, I = 1.0, and Ω_{STR} = 2.35). The nonstructural strength, which comes from nonstructural components such as partition walls, remains constant regardless of the minimum required strength of the SFRS, V_{STR}/W. The nonstructural strength was estimated to be V_{NS}/W = 0.9/4 = 0.23 (see Equation 4-1). To maintain similar amounts of residual strength for these two buildings, the low V_{STR}/W was assigned a high RS of 0.60 and the high V_{STR}/W was assigned a low RS of 0.30, resulting in approximately the same residual strengths (see last column of Table 4-3, $V_{RS}/W = V_{max}/W \times RS$).

Table 4-3 Example Assignments of RS Based on V_{STR}/W to Achieve Consistent Level of Residual Strength for Two 4-story MFD Buildings (I_e = 1.0, R = 6.5, Ω_{STR} = 2.35)

Seismicity	S_{MT} (g)	V_{STR}/W	V_{NS}/W	V_{max}/W	*RS*	V_{RS}/W
Low	0.65	0.16	0.23	0.38	0.60	0.23
High	1.85	0.45	0.23	0.67	0.30	0.20

4.3.5 Ground Motions

The FEMA P-695 Far-Field and Near-Field ground motion sets were used to evaluate the collapse performance of wood light-frame buildings. The Far-Field record set was used as the primary set to evaluate all three archetypes (STR, COM and MFD). To investigate the influence of ground motions near fault rupture sites on the collapse performance of wood light-frame buildings, the MFD models were also analyzed using the Near-Field record set.

4.3.6 Study Matrices

Table 4-4 summarizes the variables considered and modeling assumptions for the matrices of wood light-frame archetype models. A total of 20 collapse surfaces were developed with approximately 25 models for each collapse surface using both the Far-Field and Near-Field record sets. Note that only the MFD models were analyzed using the Near-Field record set.

20 Collapse Surfaces:

a) 3 occupancies (STR, COM and MFD) x

b) 5 heights (1-story, 2-story, 3-story 4-story and 5-story) for each archetype x

c) 2 ground motion sets (Far-Field for all 3 archetypes and Near-Field for MFD only) x

Approximately 25 Models:

a) 10 strengths (e.g., V_{max}/W = 0.05, 0.1, 0.15, 0.2, 0.3, 0.45, 0.6, 0.8, 1,0 and 1.2 for STR models) x

b) 2 to 3 residual strengths for each V_{max}/W.

To generate the 20 collapse surfaces, 465 2D MDOF models were created and analyzed (approximately 25 models for each surface × 20 surfaces) in this study. The numbers of models analyzed for each collapse surface grouped by archetype and number of stories are summarized in Table 4-5.

Table 4-4 Variables and Modeling Assumptions of the 2D MDOF Models

Parameter	Details
Number of Stories	1, 2, 3, 4, and 5 (5 variables)
Story Weights	100 kips for typical story and 60 kips for roof
Story Height	10 feet (floor-to-floor), 9-foot clear height
Wood (OSB) Backbone Model	Continuous tie-down rod system
Number of Nonlinear Hysteresis Elements	Two nonlinear hysteresis elements: one structural and one nonstructural
Vertical Distribution of SFRS Shear Strength	Equivalent Lateral Force (ELF) Procedure
Normalized Strength (V_{max}/W)	Normalized pushover strength (0.05g–1.25g) (10 variables)
Residual Strength Ratio	10%, 20%, 30%, 45%, 60%, and 75% (3 out of 6 variables)
Archetype configuration	COM, MFD, and STR (3 variables)
Damping	1% of critical damping
IDA analysis	44 FEMA P-695 Far Field ground motions (uniaxial motions)
	5% Damped Spectral Acceleration at the upper bound of the code approximate period (C_uT_a)
	Simulated and non-simulated collapse
	S_a increment of IDA is a function of pushover strength

Table 4-5 Number of Models for Each Occupancy and Number of Stories

# Stories	Far-Field Record Set			Near-Field Record Set		
	COM	MFD	STR	COM	MFD	STR
1	22	18	19	-	18	-
2	27	24	19	-	24	-
3	26	28	19	-	28	-
4	25	26	19	-	26	-
5	24	27	19	-	27	-
Total	124	123	95	-	123	-

An example study matrix for the COM models is shown in Table 4-6. The empty cells in Table 4-6 indicate values of seismic response parameters (median spectral acceleration, $\hat{S}_{CT}$, and drift ratio, *DR*, at incipient collapse) to be determined from the FEMA P-695 collapse evaluations of the wood models using IDA. Cells with black shading represent combinations of target strength (V_{max}/W) and residual strength (i.e., fraction of V_{max}/W) that are deemed unrealistically low or unrealistically high values of residual strength, V_{RS} (i.e., values of V_{RS} that would be less than 10 percent or greater than 30 percent of model weight, *W*). Wood light-frame models are not provided and were not analyzed for these combinations of peak strength and residual strength. The study matrices for the MFD and STR models are provided in Table 4-7 and Table 4-8, respectively. There are 124, 123, and 95 models for COM, MFD and STR archetypes, respectively (i.e., empty cells in Table 4-6 to Table 4-8).

Table 4-6 Study Matrix of Wood Models with COM Nonstructural Wall Finishes (NS)

N	V_{STR}/W	V_{NS}/W	V_{max}/W	Residual Strength (RS) Ratio					
				0.75	0.60	0.45	0.30	0.20	0.10
1	0.05	0.50	0.55						
1	0.10	0.50	0.60						
1	0.15	0.50	0.65						
1	0.20	0.50	0.70						
1	0.30	0.50	0.80						
1	0.45	0.50	0.95						
1	0.60	0.50	1.10						
1	0.80	0.50	1.30						
1	1.00	0.50	1.50						
1	1.20	0.50	1.70						
2	0.05	0.25	0.30						
2	0.10	0.25	0.35						
2	0.15	0.25	0.40						
2	0.20	0.25	0.45						
2	0.30	0.25	0.55						
2	0.45	0.25	0.70						
2	0.60	0.25	0.85						
2	0.80	0.25	1.05						
2	1.00	0.25	1.25						
2	1.20	0.25	1.45						
3	0.05	0.17	0.22						
3	0.10	0.17	0.27						
3	0.15	0.17	0.32						
3	0.20	0.17	0.37						
3	0.30	0.17	0.47						
3	0.45	0.17	0.62						
3	0.60	0.17	0.77						
3	0.80	0.17	0.97						
3	1.00	0.17	1.17						
3	1.20	0.17	1.37						
4	0.05	0.13	0.18						
4	0.10	0.13	0.23						
4	0.15	0.13	0.28						
4	0.20	0.13	0.33						
4	0.30	0.13	0.43				x		
4	0.45	0.13	0.58						
4	0.60	0.13	0.73						
4	0.80	0.13	0.93						
4	1.00	0.13	1.13						
4	1.20	0.13	1.33						
5	0.05	0.10	0.15						
5	0.10	0.10	0.20						
5	0.15	0.10	0.25						
5	0.20	0.10	0.30						
5	0.30	0.10	0.40						
5	0.45	0.10	0.55						
5	0.60	0.10	0.70						
5	0.80	0.10	0.90						
5	1.00	0.10	1.10						
5	1.20	0.10	1.30						

Table 4-7 Study Matrix of Wood Models with MFD Nonstructural Wall Finishes (NS)

N	V_{STR}/W	V_{NS}/W	V_{max}/W	Residual Strength (RS) Ratio					
				0.75	0.60	0.45	0.30	0.20	0.10
1	0.05	0.90	0.95						
1	0.10	0.90	1.00						
1	0.15	0.90	1.05						
1	0.20	0.90	1.10						
1	0.30	0.90	1.20						
1	0.45	0.90	1.35						
1	0.60	0.90	1.50						
1	0.80	0.90	1.70						
1	1.00	0.90	1.90						
1	1.20	0.90	2.10						
2	0.05	0.45	0.50						
2	0.10	0.45	0.55						
2	0.15	0.45	0.60						
2	0.20	0.45	0.65						
2	0.30	0.45	0.75						
2	0.45	0.45	0.90						
2	0.60	0.45	1.05						
2	0.80	0.45	1.25						
2	1.00	0.45	1.45						
2	1.20	0.45	1.65						
3	0.05	0.30	0.35						
3	0.10	0.30	0.40						
3	0.15	0.30	0.45						
3	0.20	0.30	0.50						
3	0.30	0.30	0.60						
3	0.45	0.30	0.75						
3	0.60	0.30	0.90						
3	0.80	0.30	1.10						
3	1.00	0.30	1.30						
3	1.20	0.30	1.50						
4	0.05	0.23	0.28						
4	0.10	0.23	0.33						
4	0.15	0.23	0.38						
4	0.20	0.23	0.43						
4	0.30	0.23	0.53						
4	0.45	0.23	0.68						
4	0.60	0.23	0.83						
4	0.80	0.23	1.03						
4	1.00	0.23	1.23						
4	1.20	0.23	1.43						
5	0.05	0.18	0.23						
5	0.10	0.18	0.28						
5	0.15	0.18	0.33						
5	0.20	0.18	0.38						
5	0.30	0.18	0.48						
5	0.45	0.18	0.63						
5	0.60	0.18	0.78						
5	0.80	0.18	0.98						
5	1.00	0.18	1.18						
5	1.20	0.18	1.38						

Table 4-8 Study Matrix of Wood Models with Structural Walls Only (STR)

N	V_{STR}/W	V_{NS}/W	V_{max}/W	Residual Strength (RS) Ratio					
				0.75	0.60	0.45	0.30	0.20	0.10
1	0.05	0.00	0.05	■	■	■	■	■	■
1	0.10	0.00	0.10	■	■	■	■	■	■
1	0.15	0.00	0.15		■	■	■	■	■
1	0.20	0.00	0.20			■	■	■	■
1	0.30	0.00	0.30				■	■	■
1	0.45	0.00	0.45	■				■	■
1	0.60	0.00	0.60	■	■				■
1	0.80	0.00	0.80	■	■	■			■
1	1.00	0.00	1.00	■	■	■			
1	1.20	0.00	1.20	■	■	■	■		
2	0.05	0.00	0.05	■	■	■	■	■	
2	0.10	0.00	0.10	■	■	■	■	■	■
2	0.15	0.00	0.15		■	■	■	■	■
2	0.20	0.00	0.20			■	■	■	■
2	0.30	0.00	0.30				■	■	■
2	0.45	0.00	0.45	■				■	■
2	0.60	0.00	0.60	■	■				■
2	0.80	0.00	0.80	■	■	■			■
2	1.00	0.00	1.00	■	■	■			
2	1.20	0.00	1.20	■	■	■	■		
3	0.05	0.00	0.05	■	■	■	■	■	■
3	0.10	0.00	0.10	■	■	■	■	■	■
3	0.15	0.00	0.15		■	■	■	■	■
3	0.20	0.00	0.20			■	■	■	■
3	0.30	0.00	0.30				■	■	■
3	0.45	0.00	0.45	■				■	■
3	0.60	0.00	0.60	■	■				■
3	0.80	0.00	0.80	■	■	■			■
3	1.00	0.00	1.00	■	■	■			
3	1.20	0.00	1.20	■	■	■	■		
4	0.05	0.00	0.05	■	■	■	■	■	■
4	0.10	0.00	0.10	■	■	■	■	■	■
4	0.15	0.00	0.15		■	■	■	■	■
4	0.20	0.00	0.20			■	■	■	■
4	0.30	0.00	0.30				■	■	■
4	0.45	0.00	0.45	■				■	■
4	0.60	0.00	0.60	■	■				■
4	0.80	0.00	0.80	■	■	■			■
4	1.00	0.00	1.00	■	■	■			
4	1.20	0.00	1.20	■	■	■	■		
5	0.05	0.00	0.05	■	■	■	■	■	■
5	0.10	0.00	0.10	■	■	■	■	■	■
5	0.15	0.00	0.15		■	■	■	■	■
5	0.20	0.00	0.20			■	■	■	■
5	0.30	0.00	0.30				■	■	■
5	0.45	0.00	0.45	■				■	■
5	0.60	0.00	0.60	■	■				■
5	0.80	0.00	0.80	■	■	■			■
5	1.00	0.00	1.00	■	■	■			
5	1.20	0.00	1.20	■	■	■	■		

4.3.7 Model ID and Nomenclature

Figure 4-2 shows the nomenclature of collapse surface model ID in the form of AA-BBB-CCC-DDD. The first two entries (AA) denote the number of stories and occupancy types (e.g., 1C = 1-story commercial building and 4M = 4-story multi-family dwelling). The next 3 digits (BBB) denote the total normalized peak strength without P-delta (e.g., 043 represents $V_{max}/W = 0.43$). The second set of three digits (CCC) denotes the contribution of normalized strength from structural elements (e.g., 020 represents $V_{STR}/W = 0.20$). The last three digits (DDD) denote the combined residual strength of the building (e.g. 030 represents 30% residual strength). The nomenclature of the model names is as follows:

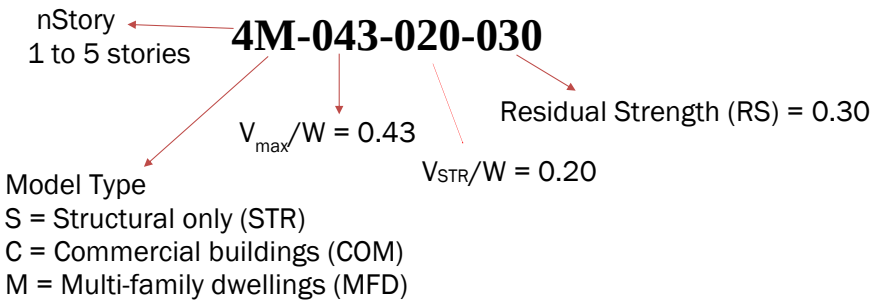

Figure 4-2 Nomenclature and model IDs of collapse surface models.

4.4 Wood Building Model Development

To illustrate the development of a typical model for collapse surface evaluation, an example model is chosen from Table 4-6 (the cell with an "X" mark), a 4-story model with normalized pushover strength of 0.43, structural strength ratio V_{STR}/W of 0.30, and residual strength ratio of 0.30. The name of the model is 4C-043-030-030**.** The total seismic weight is 360 kips and the inter-story height is 10 ft. An illustrative schematic view of this model is shown in Figure 4-3.

The properties of the model are computed as follows and summarized in Table 4-9:

- Total height of the model, h_n = 40 ft [4 stories × 10 ft per story]
- Total normalized strength (structural + nonstructural), $V_{max}/W = 0.43$
- Normalized structural strength, $V_{STR}/W = 0.30$
- $S_{MT} = 1.5 \times (R/I_e)(V_{max}/W)/\Omega$ [assume Risk Category II, $I_e = 1.0$, see Chapter 3, Equation 3-4]

  $= 1.5 \times (R/I_e)(V_{STR}/W)/\Omega_{STR} = 1.5 \times (6.5/1.0)(0.30)/2.35$ [$\Omega_{STR} = 2.35$, see Chapter 2]

  = 1.25g
- Nominal nonstructural strength $V_{NS}/W = V_{max}/W - V_{STR}/W = 0.13$

- Residual strength ratio, *RS* = 0.30.

$$V_{max} = 0.43 \times 360 = 154.8 \text{ kips}$$

$$V_{STR} = 0.30 \times 360 = 108 \text{ kips}$$

$$V_{RS} = 0.30 \times 154.8 = 46.44 \text{ kips}$$

The approximate code period for the model is calculated as follows (ASEC/SEI 7-22): $T_{code} = C_u T_a = 1.4(0.02)(h_n)^{0.75} = 0.45$ s

where h_n is the building height (i.e., 40 feet).

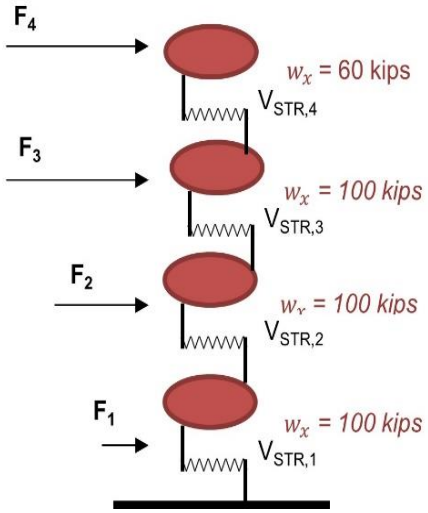

Figure 4-3 An example 4-story COM model (4C-043-030-030). F_x is the equivalent lateral force, w_x is the story weight, and $V_{STR,x}$ is the story structural strength.

Table 4-9 Example Model Properties

Property	Value
Name (ID)	4C-043-030-030
Archetype Configuration	COM
Floor Weight (kips)	100
Roof Weight (kips)	60
Story Height (ft)	10
Number of Stories	4
Total Weight (kips)	360
Total height (ft)	40
NS/STR Strength	0.43
V_{max}/W - Total (Pushover with P-delta)	To be determined from pushover analysis
V_{max}/W Target - Total	0.43
V_{STR}/W Target - SFRS	0.30
V_{NS}/W Target - NS only (nominal value)	0.13
V_{NS}/W Actual - NS only	To be determined (see Section 4.4.1)
Residual Strength (% of V_{max})	0.30

4.4.1 Vertical Distribution of Structural Strengths

The Equivalent Lateral Force (ELF) procedure is used to compute the vertical distribution of seismic forces following section 12.8.3 in ASEC/SEI 7-22. The ELF calculations are presented in Table 4-10. Equations 12.8-12, 12.8-13 and 12.8-14 from ASEC/SEI 7-22 are used for ELF calculations. The equivalent lateral seismic force, F_x (kips), at each level x is equal to $C_v V_{STR}$ and,

$$C_{vx} = \frac{w_x h_x^k}{\sum_{i=1}^{n} w_i h_i^k} \tag{4-4}$$

Where C_{vx} is the vertical distribution factor for assigned to level (or floor) x, w_x (or w_i) is the story weight (100 kips per floor and 60 kips at the roof), and h_x (or h_i) is the story height measured from ground. The required story shear strength, $V_{STR,\,x}$, is the cumulative sum of F_x from level x to the roof level (n).

Table 4-10 ELF Calculations for Example Model 4C-043-030-030

Level x	Height (ft)	w_x (kips)	$w_x h_x$ (ft×kips)	C_{vx}, Vertical Distribution Factor	F_x (kips)	$V_{STR,x}$ (kips)
4	40	60	2400	0.286	30.86	30.86
3	30	100	3000	0.357	38.57	69.43
2	20	100	2000	0.238	25.71	95.14
1	10	100	1000	0.119	12.86	108.00
SUM		360	8400	1.000	108.00	

$V_{STR,x}$ is the peak strength of SFRS in the x-th story. The normalized structural backbone curve for OSB with continuous tie-down rod system (Figure 4-4) is used and scaled to match the peak strength $V_{STR,x}$ in each story (Figure 4-5). In this example, the normalized structural OSB parameters used are the fitted Residual Strength (RESST) hysteresis values shown in Table B-9 of Appendix B with RS = 30%.

Since the peak strengths of the structural and nonstructural walls do not occur at the same displacement (see Figure 4-6), direct numeric summation of the peak structural strength (V_{STR}) and nominal nonstructural strength (V_{NS}) does not yield the total peak strength (V_{max}). The actual values of peak nonstructural strength (V_{NS}) and residual strength (RS) ratio of V_{NS} are varied iteratively until the combined structural and nonstructural backbone curve matches the target total strength V_{max} and the total residual strength ratio RS (Figure 4-6). For Model 4C-043-030-030, the actual nonstructural strength V_{NS} is 59 kips and actual nonstructural RS is 0.22. Since the peak strength of the nonstructural wall occurs at a displacement that is smaller than that of the structural wall, the actual V_{NS}/W (59 kips/360 kips = 0.16) is expected to be slightly higher than the nominal V_{NS}/W (0.13) shown in Table 4-10. The RESST hysteresis parameters for structural walls and nonstructural walls are shown in Tables 4-11a and 4-11b, respectively (see Appendix D Table D-1 for variable definitions). Note that the same nonstructural contribution is assumed for each story.

Figure 4-4 to Figure 4-6 show the backbone curves without P-delta effects. When the appropriate gravity loads are applied to each level and P-delta effects are included in the nonlinear pushover analysis, the post-peak residual plateau force will drop to zero (see Section 4.5.2).

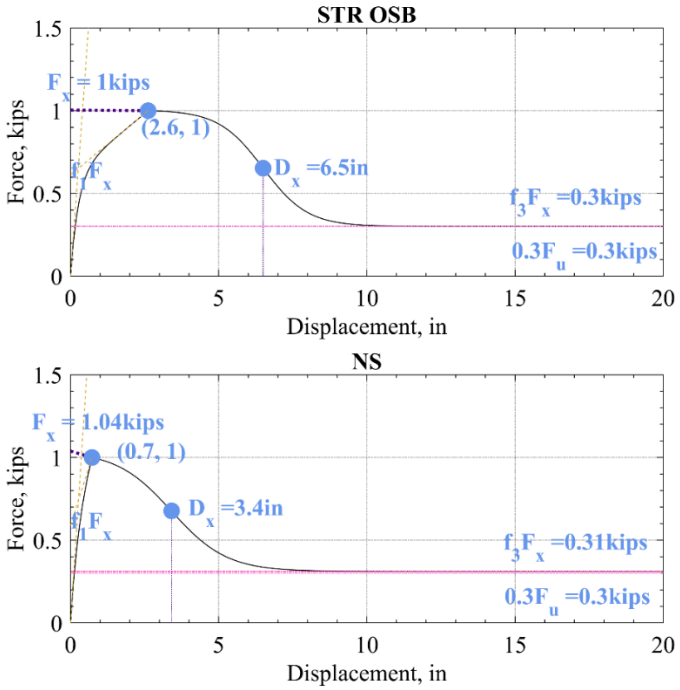

Figure 4-4 Normalized structural and nonstructural backbone curves.

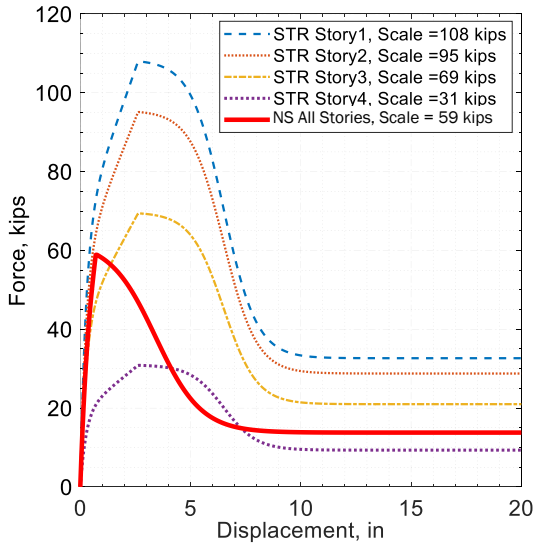

Figure 4-5 Scaled structural and nonstructural backbone curves for Model 4C-043-030-030.

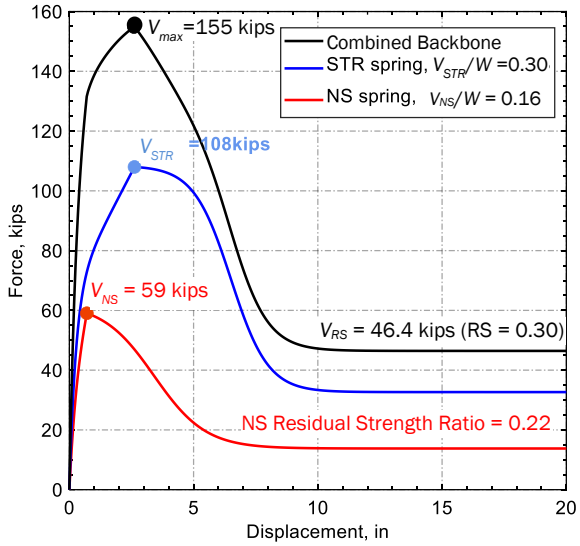

Figure 4-6 **Structural, nonstructural, and combined building backbone curves for Model 4C-043-030-030.**

Table 4-11a **Structural RESST Hysteresis Parameters for Model 4C-043-030-030**

Story No.	K_o (kip/in.)	r_1	r_2	r_3	r_4	F_x (kips)	f_1	f_2	f_3	D_x (in.)	α	β	F_u (kips)	D_u (in.)
1	266.19	0.06	-0.10	1.01	0.01	108.43	0.61	0.16	0.30	6.50	0.60	1.15	108.00	2.62
2	234.50	0.06	-0.10	1.01	0.01	95.52	0.61	0.16	0.30	6.50	0.60	1.15	95.14	2.62
3	171.12	0.06	-0.10	1.01	0.01	69.70	0.61	0.16	0.30	6.50	0.60	1.15	69.43	2.62
4	76.06	0.06	-0.10	1.01	0.01	30.98	0.61	0.16	0.30	6.50	0.60	1.15	30.86	2.62

Table 4-11b **Nonstructural RESST Hysteresis Parameters for Model 4C-043-030-030**

Story No.	K_o (kip/in.)	r_1	r_2	r_3	r_4	F_x (kips)	f_1	f_2	f_3	D_x (in.)	α	β	F_u (kips)	D_u (in.)
All Stories	163.66	0.23	-0.07	1.45	0.01	62.27	0.57	0.10	0.22	3.41	0.38	1.09	58.99	0.70

4.5 Numerical Analyses

For each building model, the following three analyses were performed:

- Modal analyses to evaluate elastic natural periods and mode shapes,
- Nonlinear static pushover analyses, and
- Nonlinear IDAs in accordance with the FEMA P-695 methodology for a defined set of MCE_R ground motion intensities.

4.5.1 Modal Analysis

Modal analyses were performed by solving the eigenvectors for the mode shapes and eigenvalues for the periods of the 2D MDOF models. Figure 4-7 shows the first mode shape of Model 4C-043-030-030. The corresponding fundamental period of the model (T_1) was 0.44 seconds. Among models or buildings of the same height and peak strength, the numerically determined first mode periods may be different depending on the amount of structural (V_{STR}/W) and nonstructural (V_{NS}/W) elements. The model first-mode periods of all the 4-story COM models can be found in Table H-10 in Appendix H. When evaluating the collapse performance of each model, the code period for each class of the buildings of the same height computed using Equation 3-9 (e.g., $C_u T_a$ = 0.45 seconds for this 4-story wood light-frame building) was used to scale the ground motions in incremental dynamics analysis. The procedure for IDA is discussed in Section 4.5.3.

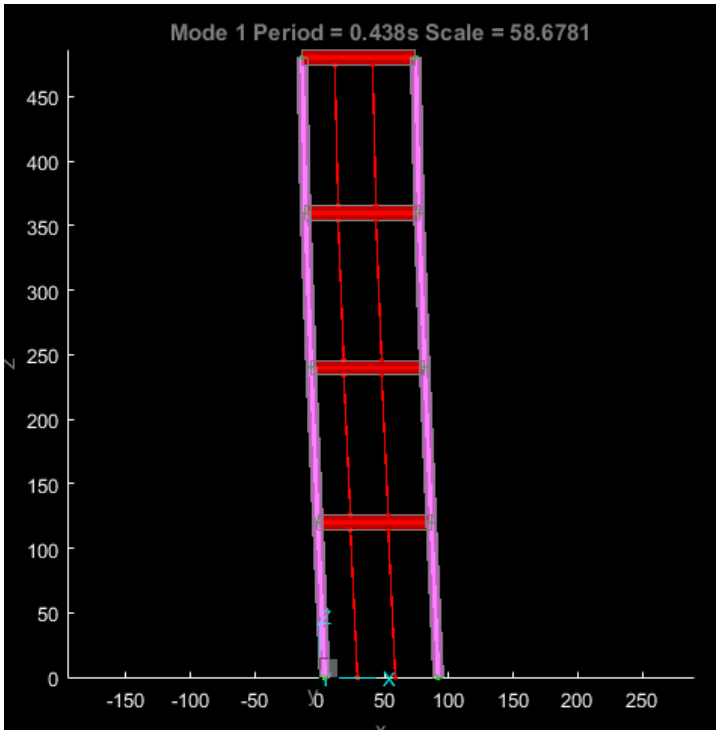

Figure 4-7 Fundamental period and mode shape of Model 4C-043-030-030.

4.5.2 Nonlinear Static Pushover Analysis

Figure 4-8 shows the pushover curve in terms of base shear versus roof displacement for Model 4C-043-030-030. P-delta effects were taken into consideration resulting in the post-peak residual plateau force dropping to zero at roof displacement of about 16 inches. Note that the peak strength obtained via pushover analysis with P-delta effects (V_{max}/W = 0.41) was slightly lower than the as-designed peak strength (V_{max}/W = 0.43). To create the collapse surface, the as-designed peak strength (i.e., without P-delta effects) was used.

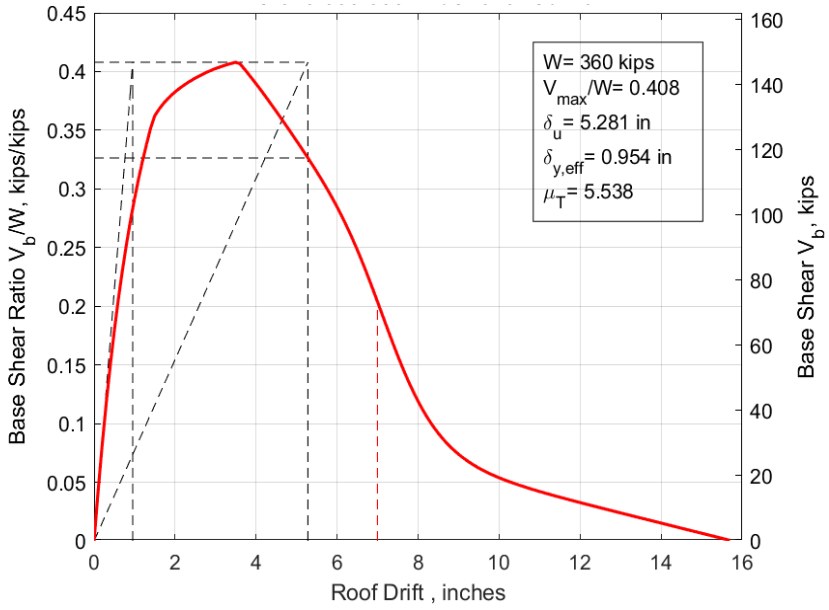

Figure 4-8 Pushover curve for Model 4C-043-030-030.

4.5.3 Nonlinear Incremental Dynamic Analysis

The *Timber3D* program was used to perform the IDAs in accordance with the FEMA P-695 methodology. The intensity levels were increased with a 0.05g increment up to an intensity level for which all ground motions caused collapse of the model.

P-delta effects were included by performing gravity load analysis prior to each nonlinear time history analysis. The Rayleigh damping model was used with 1% damping (percentage of critical damping) assigned to the first two modes.

Collapse was explicitly simulated using *Timber3D* by tracking the vertical drop of a control node on the roof of the building model. The model was deemed to have collapsed when the vertical drop of the roof control node exceeded a prescribed value. In this validation study, a simulated collapse flag was triggered, and the time history analysis was terminated when the vertical drop of the control node exceeded 25% of the inter-story height (30 inches).

Figure 4-9 shows the IDA curves obtained for the example model (4C-043-030-030). Solid blue markers on the IDA curves indicate points of incipient collapse (IC) (i.e., the last survival intensity levels of each of the 44 ground motions). Also shown in the figure are the fitted lognormal probability density functions (PDFs) of inter-story drift ratios (*DR*s) and spectral acceleration (S_a) values at incipient collapse. The median inter-story drift and spectral acceleration at incipient collapse (*simulated collapse*) were 8.0% and 2.51g, respectively, for this 4C-043-030-030 model. The median S_a resulting in collapse ($\hat{S}_{CT}$) was taken as the median S_a at incipient collapse plus the S_a increment of the IDA ($\hat{S}_{CT}$ = 2.51g + 0.05g = 2.56g).

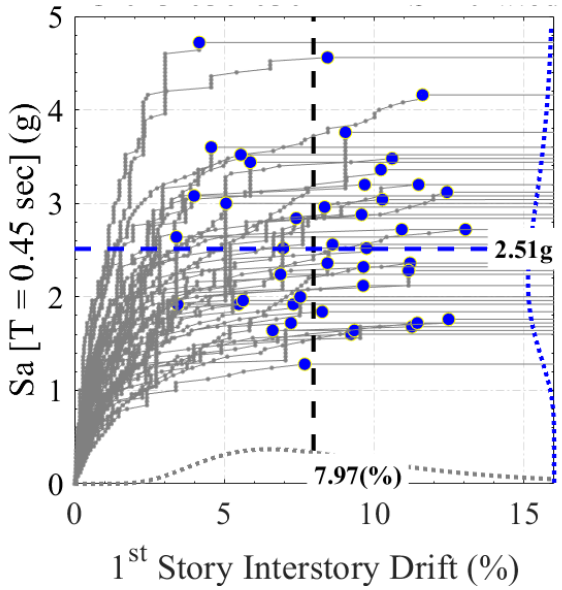

Figure 4-9 IDA curves and probability density functions of inter-story drifts and spectral accelerations at incipient collapse for Model 4C-043-030-030 (Far-Field Motion).

In addition to simulated collapse, a *non-simulated collapse* criterion based on *DR* limit was defined. A non-simulated collapse occurred when the peak inter-story *DR* exceeded a prescribed *DR* limit. Prior to recording the non-simulated collapse data, the raw IDA curves shown in Figure 4-9 were converted into monotonically increasing IDA cures (Figure 4-10). In general, the peak inter-story *DR* is expected to increase as the shaking intensity or S_a increases. However, it is not uncommon to observe peak *DR* to temporarily reduce when a particular ground motion is scaled up to a higher intensity in IDA (i.e., resurrection phenomenon). To alleviate this issue, a monotonically increasing IDA curve was derived for each ground motion by recording the maximum *DR* at and lower than the intensity being considered.

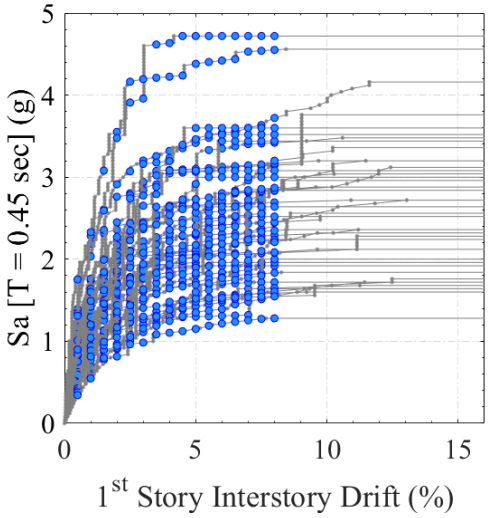

Figure 4-10 Monotonically increasing IDA curves and probability density functions of inter-story drifts and spectral accelerations at incipient collapse for Model 4C-043-030-030 (Far-Field Ground Motions).

In Figure 4-10, each group of circular blue markers aligned vertically represent the non-simulated collapse spectral accelerations of the 44 ground motions for a given *DR* limit. A series of non-simulated collapse *DR* limits, beginning with *DR* of 0.5% and increasing with an increment of 0.5% up to the median incipient collapse *DR* determined using the simulated collapse criterion, was used to record the non-simulated collapse S_a values. A median collapse spectral acceleration ($\hat{S}_{CT}$) was then computed for each of the non-simulated collapse *DR* limits.

4.6 Collapse Surface Development

Example summaries of wood model data required for subsequent development of collapse surfaces are shown in Table 4-12 for the 4-story wood models with COM nonstructural wall finishes. Example model properties and input parameters (*N*, V_{max}/W, V_{STR}/W, and RS) are shown in Table 4-6. Values of V_{max}/W shown in these tables are based on "target" amounts of structural (STR) and nonstructural (NS) strength. Actual values of V_{max}/W were determined from the pushover analysis of each model, as described above. Example format of median response spectral acceleration resulting in collapse ($\hat{S}_{CT}$) and the corresponding median 1st story drift ratio at incipient collapse (DR_{IC}) is shown in Table 4-12. For Model 4C-043-030-030 (see Figure 4-9), the simulated collapse $\hat{S}_{CT}$ and DR_{IC} recorded in Table 4-12 are 2.56g and 8.0%, respectively. As explained above, six values of residual strength ratio are assumed for each model; however, some of the V_{max}/W and *RS* combinations were deemed unrealistic, and these combinations were excluded (black cells in Table 4-6). Table 4-12 summarizes the 1st-story drift ratio (*DR*) and median collapse capacity ($\hat{S}_{CT}$) results from IDAs for both simulated collapse and non-simulated collapse using a prescribed *DR* limit (*DR* = 7.5% for this example). The notation DR_{IC} represents the median 1st story drift ratio at incipient collapse obtained from IDAs based on simulated collapse for a given model. The grey-colored cells in the non-simulated collapse

columns refer to the models that collapsed at a *DR* lower than 7.5%. In that case, the non-simulated collapse $\hat{S}_{CT}$ is equal to the simulated collapse $\hat{S}_{CT}$. Note that Table 4-12 shows the results for one non-simulated *DR* limit (i.e., one vertical slice of data from Figure 4-10). The non-simulated collapse $\hat{S}_{CT}$ values at *DR* = 2.5%, 5%, 7.5%, 10% and 15% for the 4-story COM models may be found in Table H-10 in Appendix H.

Table 4-12 Example Summary of 1st-Story Drift Ratio (*DR*) and Median Collapse Spectral Acceleration ($\hat{S}_{CT}$) of the 4-story COM Models

Model ID	Pushover Properties				Simulated Collapse		Non-simulated Collapse at *DR* = 7.5%
	V_{NS}/W actual	V/W w/o P-Δ	V/W with P-Δ	RS	$\hat{S}_{CT}$ (g)	DR_{IC}	$\hat{S}_{CT}$ (g)
4C-018-005-075	0.13	0.18	0.16	0.75	1.33	9.3%	1.24
4C-018-005-060	0.14	0.18	0.17	0.60	1.21	6.4%	1.21
4C-023-010-075	0.13	0.23	0.21	0.75	1.72	12.6%	1.52
4C-023-010-060	0.14	0.23	0.21	0.60	1.51	9.2%	1.43
4C-023-010-045	0.15	0.23	0.22	0.45	1.42	5.5%	1.42
4C-028-015-075	0.13	0.28	0.26	0.75	2.10	16.7%	1.81
4C-028-015-060	0.14	0.28	0.26	0.60	1.82	11.3%	1.67
4C-028-015-045	0.15	0.28	0.26	0.45	1.69	7.0%	1.69
4C-033-020-075	0.13	0.33	0.31	0.75	2.61	18.1%	2.09
4C-033-020-060	0.14	0.33	0.31	0.60	2.25	11.9%	1.96
4C-033-020-045	0.15	0.33	0.31	0.45	1.99	8.4%	1.91
4C-043-030-060	0.14	0.43	0.41	0.60	3.79	15.8%	2.47
4C-043-030-045	0.16	0.43	0.41	0.45	2.94	11.6%	2.45
4C-043-030-030	0.16	0.43	0.41	0.30	2.56	8.0%	2.43
4C-058-045-045	0.16	0.58	0.56	0.45	4.25	15.3%	2.94
4C-058-045-030	0.16	0.58	0.56	0.30	3.26	9.0%	2.91
4C-058-045-020	0.17	0.58	0.56	0.20	2.97	6.5%	2.97
4C-073-060-030	0.16	0.73	0.71	0.30	3.54	7.9%	3.23
4C-073-060-020	0.17	0.73	0.71	0.20	3.39	6.3%	3.39
4C-093-080-030	0.16	0.93	0.91	0.30	4.12	8.0%	3.74
4C-093-080-020	0.17	0.93	0.91	0.20	3.87	6.5%	3.87
4C-113-100-020	0.17	1.13	1.11	0.20	4.37	6.7%	4.37
4C-113-100-010	0.18	1.13	1.11	0.10	4.04	4.7%	4.04
4C-133-120-020	0.17	1.33	1.31	0.20	4.73	6.2%	4.73
4C-133-120-010	0.18	1.33	1.31	0.10	4.60	4.9%	4.60

Using the values of *DR* of interest (i.e., *DR* = 2% to *DR* = 15%, see Chapter 3), the collapse $\hat{S}_{CT}$ values for each class of building (e.g. 4-story commercial buildings) were fit to the collapse surface equation discussed in Chapter 3 (Equation 3-10), where *A, B, C, D, E, F, G, H* and *I* are the coefficients of the collapse surface equation determined by linear regression using the collapse data set of interest. The best-fit coefficients obtained from least-square regression of Equation 3-10 for the 15 classes of buildings (3 archetypes × 5 different heights) subjected Far-Field record set are presented in Tables 4-13, 4-14, and 4-15 for COM, MFD, and STR models, respectively. The adequacy of the fit is quantified using the goodness-of-fit (multiple *R*) shown in the last row in these tables. A value close to unity indicates the surface equation with the coefficients is a good fit.

Table 4-13 Collapse surface $\widehat{S}_{CT}$ Equation Coefficients for COM Models Subjected to Far-Field Motions

Coefficient	Independent Variable	1-Story	2-Story	3-Story	4-Story	5-Story
A	V_{max}/W	1.52	1.24	1.53	1.81	2.42
B	$(V_{max}/W)^2$	-0.133	0.065	0.032	-0.149	-0.510
C	*DR*	-2.94	0.56	-3.34	-6.08	-2.71
D	DR^2	7.80	17.05	9.87	23.12	7.77
E	$(V_{max}/W)\times DR$	37.07	44.72	55.27	63.93	50.10
F	$(V_{max}/W)^2\times DR$	-10.28	-16.05	-18.25	-24.99	-18.13
G	$(V_{max}/W)\times DR^2$	-97.65	-172.74	-147.88	-227.68	-161.84
H	$(V_{max}/W)^2\times DR^2$	9.55	47.18	8.03	63.36	25.77
I	Intercept	0.217	0.387	0.611	0.701	0.603
	Goodness-of-fit	0.98	0.97	0.99	0.99	0.99

Table 4-14 Collapse Surface $\widehat{S}_{CT}$ Equation Coefficients for MFD Models Subjected to Far-Field Motions

Coefficient	Independent Variable	1-Story	2-Story	3-Story	4-Story	5-Story
A	V_{max}/W	2.06	2.05	1.15	1.60	1.71
B	$(V_{max}/W)^2$	-0.251	-0.265	0.290	-0.053	-0.065
C	*DR*	-2.23	3.72	-9.01	-8.15	-7.93
D	DR^2	33.59	-2.76	49.44	32.83	27.19
E	$(V_{max}/W)\times DR$	19.64	27.12	67.29	63.78	60.51
F	$(V_{max}/W)^2\times DR$	-1.56	-6.14	-25.81	-22.85	-23.42
G	$(V_{max}/W)\times DR^2$	-67.35	-69.29	-252.31	-230.13	-194.97
H	$(V_{max}/W)^2\times DR^2$	-8.36	-7.90	79.00	60.31	46.79
I	Intercept	-0.169	0.059	0.676	0.715	0.739
	Goodness-of-fit	0.98	0.97	0.98	0.99	0.99

Table 4-15 Collapse Surface $\widehat{S}_{CT}$ Equation Coefficients for STR Models Subjected to Far-Field Motions

Coefficient	Independent Variable	1-Story	2-Story	3-Story	4-Story	5-Story
A	V_{max}/W	0.37	1.65	2.35	1.95	2.42
B	$(V_{max}/W)^2$	0.348	-0.297	-0.545	-0.150	-0.558
C	*DR*	-0.71	6.74	5.13	0.94	4.84
D	DR^2	-13.25	-32.20	-21.73	-15.30	-35.58
E	$(V_{max}/W)\times DR$	53.27	33.80	37.59	58.68	44.03
F	$(V_{max}/W)^2\times DR$	-21.09	-8.45	-7.34	-26.34	-13.28
G	$(V_{max}/W)\times DR^2$	-126.73	-40.01	-78.59	-175.39	-121.02
H	$(V_{max}/W)^2\times DR^2$	12.58	-54.31	-49.21	41.13	-16.04
I	Intercept	0.542	0.383	0.540	0.732	0.622
	Goodness-of-fit	0.98	0.98	0.99	0.99	0.99

A 3D plot of the 4-story COM collapse surface fit is shown in Figure 4-11. The x-axis is the normalized strength of the model (V_{max}/W), the y-axis is the 1st story *DR* (simulated or non-simulated), and the z-

axis is the collapse performance in terms of median collapse acceleration ($\hat{S}_{CT}$). The IC data points are taken from columns 6 and 7 of Table 4-12. Note that the non-simulated collapse $\hat{S}_{CT}$ presented in the last column of Table 4-12 for a *DR* limit of 7.5% represent only a "slice" of data presented in the collapse surface plot in Figure 4-11.

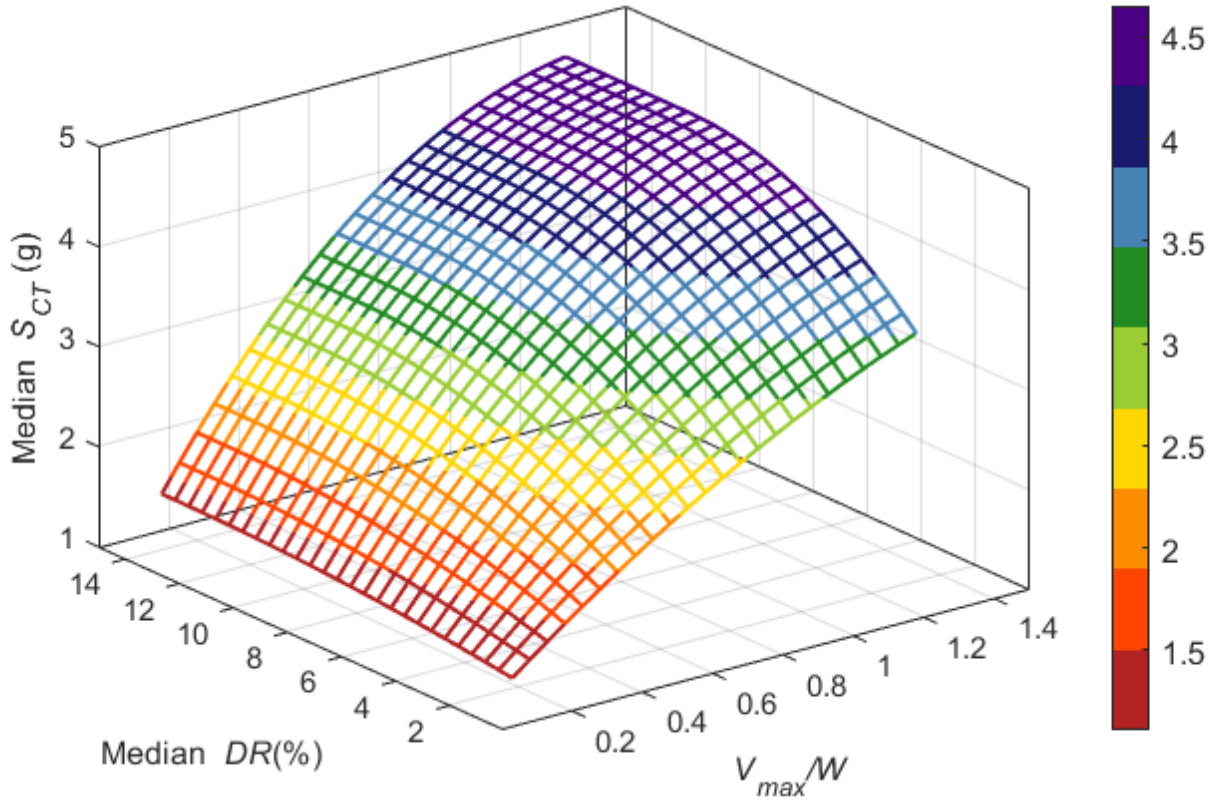

Figure 4-11 Collapse surface of 4-story COM models (Far-Field Motions).

Figure 4-12 shows the residuals of the regression analysis for 4-story COM models. The residuals of $\hat{S}_{CT}$ scatter round zero, which shows the collapse surface fit is unbiased. For *DR* ratios in the range of interest (typically below 10%), the residual errors are within +/- 10%. Figure 4-13 shows the collapse surface predicted $\hat{S}_{CT}$ and the actual data obtained from IDAs for four *DR* ratios of interest (2.5%, 5%, 7.5% and 10%). Note that the $\hat{S}_{CT}$ values (blue dots) for *DR* = 7.5% are reported in the last column of Table 4-12. As can be seen, the collapse prediction curves pass through the center of the scatter data points (i.e., unbiased). The goodness-of-fit (multiple *R*) values for all classes of buildings are over 0.97 (last row of Tables 4-13, 4-14, and 4-15) which confirm the functional form of Equation 4-5 is suited for predicting the $\hat{S}_{CT}$ values obtained from IDAs.

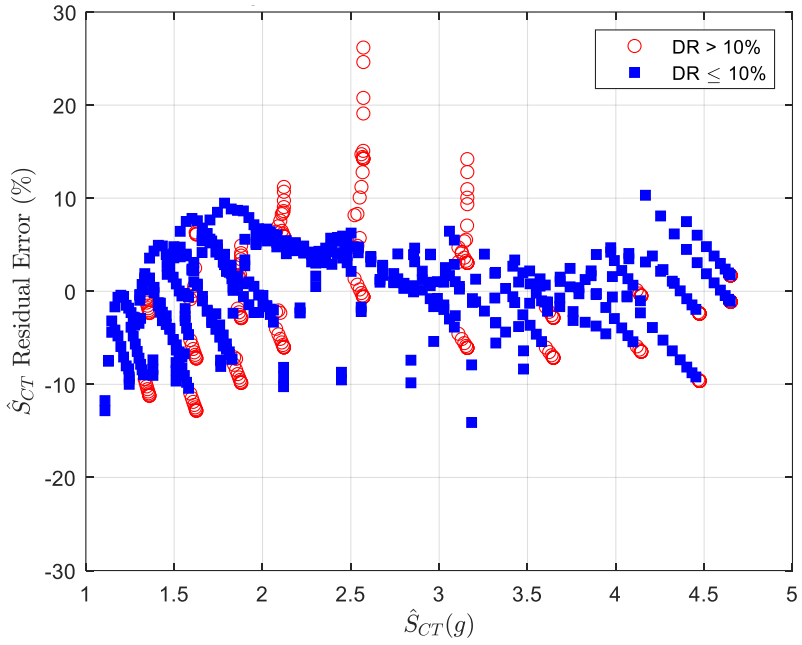

Figure 4-12 **Residual errors of the collapse surface of the 4-story COM wood light-frame archetype (Far-Field Motions).**

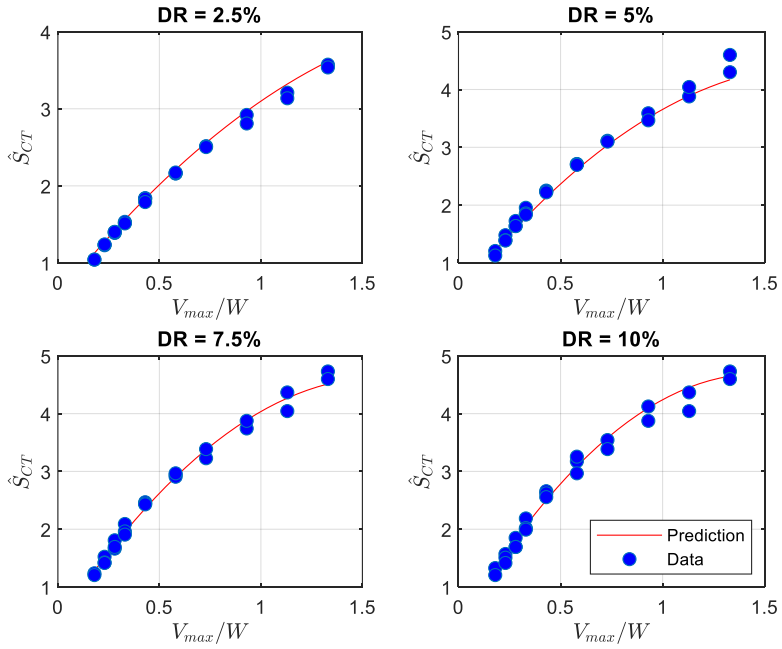

Figure 4-13 **Plots of collapse data from IDAs and prediction curves of the $\hat{S}_{CT}$ values of the collapse surface at *DR* = 2.5%, 5%, 7.5% and 10% of the 4-story COM wood light-frame archetype (Far-Field Motions).**

4.6.1 Median Drift Ratio at Incipient Collapse

The median 1st-story drift ratio at incipient collapse (DR_{IC}) versus peak strength (V_{max}/W) results obtained from IDAs for the 4-story COM wood light-frame archetype subjected to Far-Field ground motions are plotted in Figure 4-14. From the results of IDAs, it was observed that the peak drift ratio at incipient collapse tends to decrease with increasing peak strength V_{max}/W. Further investigation is needed to provide a definitive explanation for this observed decrease. Nonetheless, to capture the observed trend, the DR_{IC} values of all models for each class of building (e.g., 4-story COM, see column 7 of Table 4-12) were fit to the following exponential decay equation.

$$DR_{IC} = C_0 \exp[C_1 (V_{max}/W)] \quad (4\text{-}5)$$

Where C_0 is the DR_{IC} at the y-intercept and C_1 is the decay rate. The fitted DR_{IC} coefficients for COM, MFD, and STR models subjected to Far-Field ground motions are summarized in Table 4-16.

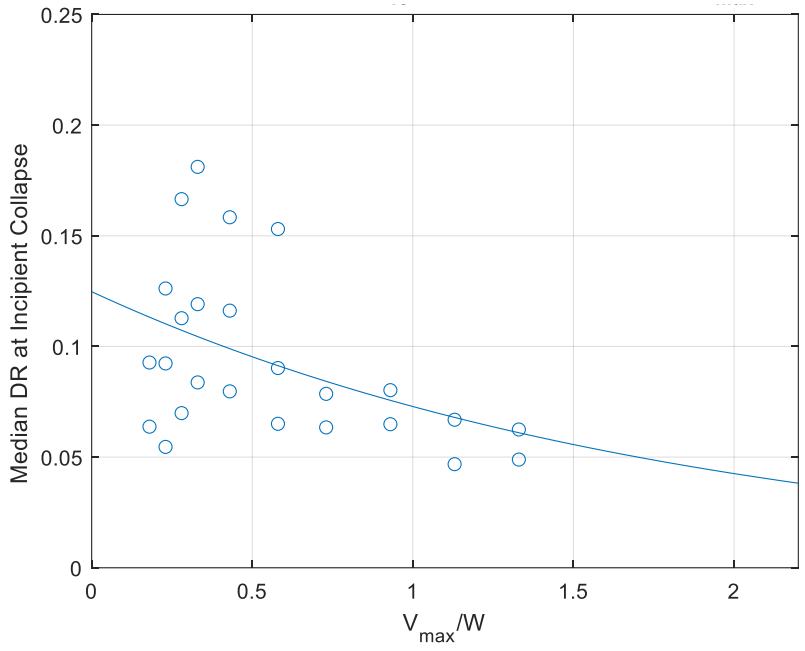

Figure 4-14 **Plot of median 1st-story drift ratio at incipient collapse data from IDAs and prediction curve of the DR_{IC} of the 4-story COM Wood light-frame archetype (Far-Field Motions).**

Table 4-16 Median 1-Story Incipient Collapse Drift Ratio (DR_{IC}) Equation Coefficients for COM, MFD, and STR Models Subjected to Far-Field Motions

Archetype	Coefficient	1-Story	2-Story	3-Story	4-Story	5-Story
COM	C_0	0.159	0.200	0.170	0.125	0.109
	C_1	-0.376	-0.705	-0.559	-0.538	-0.524
MFD	C_0	0.189	0.209	0.199	0.175	0.142
	C_1	-0.477	-0.600	-0.701	-0.847	-0.615
STR	C_0	0.102	0.143	0.135	0.097	0.088
	C_1	-0.154	-0.381	-0.516	-0.398	-0.394

4.7 Collapse Performance Evaluation

The collapse surface of each building class fitted from the results of incremental dynamic analyses are utilized to evaluate the collapse performance in terms of adjusted collapse margin ratio (*ACMR*) and MCE_R collapse probability. The next sections discuss the process of computing the collapse performance metrics.

4.7.1 Median Collapse Intensity for Models

The median collapse intensity $\hat{S}_{CT}$ for a given peak strength (V_{max}/W) and drift ratio (*DR*) can be computed using Equation 3-10 and the coefficients presented in Table 4-13 to Table 4-15 for COM, MFD, and STR archetypes, respectively. Figure 4-15 shows the $\hat{S}_{CT}$ contours computed using Equation 3-10 and coefficients for 4-story COM models (Table 4-13). For example, substituting V_{max}/W = 0.33, *DR* = 0.075 (7.5%), and the coefficients of 4-Story COM models into Equation 3-10 yields $\hat{S}_{CT}$ = 1.95g. Table 4-12 shows the $\hat{S}_{CT}$ obtained from IDA for Model 4C-033-020-060 was 1.96g.

The blue dotted line in Figure 4-15 represents the median incipient collapse drift ratio DR_{IC} computed using Equation 4-5. The red dashed line in Figure 4-15 marks the beginning of the "plateau" of the collapse surface. For a given peak strength of V_{max}/W, the $\hat{S}_{CT}$ is assumed to increase monotonically with increasing *DR* until it reaches a "plateau," beyond which the $\hat{S}_{CT}$ remains constant. The beginning of the plateau, DR_{Smax}, can be computed using Equation (3-11) (see Section 3.6), where coefficients *C*, *D*, *E*, *F*, *G*, and *H* are the same surface coefficients as defined for Equation 3-10. Equation 3-11 was obtained by taking the partial differentiation of Equation 3-10 with respect to *DR*, setting the partial differential equation equal to zero (i.e., location of zero slope or "plateau") and solving for the DR. For example, substituting V_{max}/W = 0.33 into Equation 3-11 yields DR_{Smax} = 0.136 (13.6%). To determine the $\hat{S}_{CT}$ for a 4-story COM building with a V_{max}/W = 0.33 and

DR = 0.15 (15%), since the *DR* is greater than DR_{Smax} = 0.136, the maximum drift ratio *DR* = 0.136 must be used when evaluating Equation 3-10.

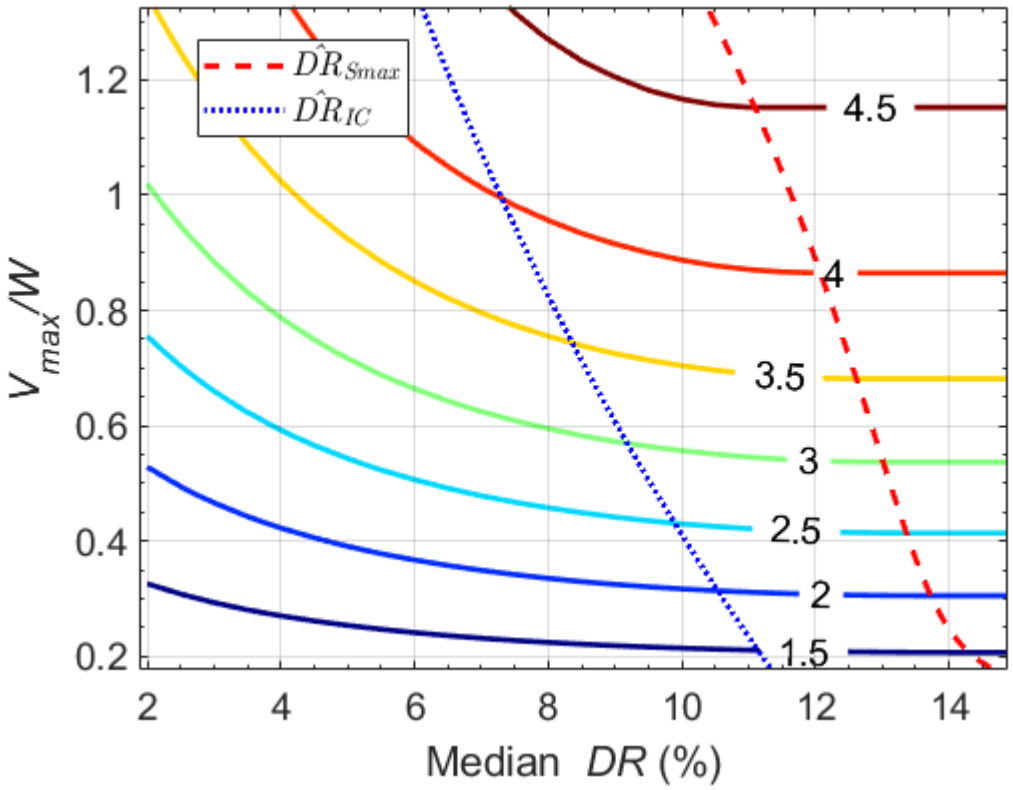

Figure 4-15 Collapse $\hat{S}_{CT}$ contours of the 4-story COM Wood light-frame archetype. Dotted blue line represents median DR_{IC}.

4.7.2 Overstrength

Figure 4-16 depicts the relationships between design strength (*V*), actual peak strength of SFRS (V_{STR}), total peak strength (V_{max}) and structural overstrength (Ω_{STR}) and total building overstrength (Ω). Based on design code (ASEC/SEI 7-22), the normalized design strength (V/W) or design base shear coefficient (C_s) is given in Equation 4-2.

The structural overstrength, Ω_{STR} is:

$$\Omega_{STR} = \frac{V_{STR}/W}{V/W} \tag{4-6}$$

and the total building overstrength including structural and nonstructural contributions, Ω, is:

$$\Omega = \Omega_{STR} \frac{V_{max}/W}{V_{STR}/W} \tag{4-7}$$

For wood light-frame buildings, the average structural overstrength was determined to be 2.35 (See Chapter 2).

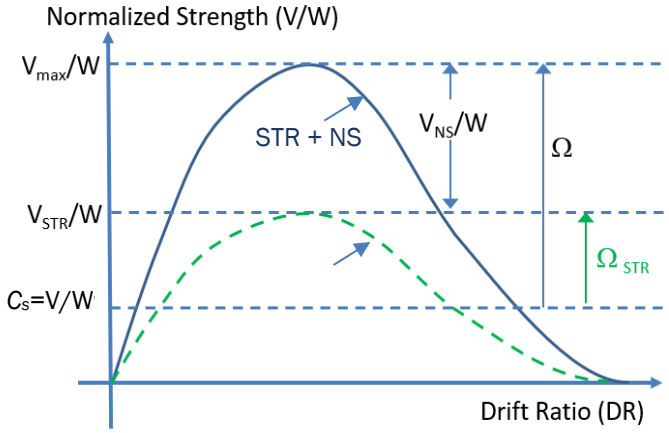

Figure 4-16 Illustration of structural overstrength (Ω_{STR}) and total building overstrength (Ω).

The amount of nonstructural contribution, typically a function of the occupancy type and the amount of partition walls, is based on the nonstructural strength model discussed in Section 2.3. As the seismicity or design S_{MT} increases, the amount of nonstructural strength (absolute value) likely will remain constant (i.e., the amount of partition walls do not increase with increasing S_{MT}), the resulting total overstrength from nonstructural elements will reduce with increasing S_{MT}.

Using a structural overstrength Ω_{STR} of 2.35, the underlying total overstrength, Ω, for the commercial buildings of different heights are computed and shown in Figure 4-17. These total overstrengths include both the contributions of SFRS (structural) and nonstructural elements.

The total overstrength, Ω, is given by the following expression:

$$\Omega = \Omega_{STR} + \Omega_{NS} = \Omega_{STR} + \frac{P_{NS}}{\frac{2}{3} \times \frac{S_{MT}}{R/I_e} \times \left[25 + (N-1) \times 45\right]} \tag{4-8}$$

Where, Ω_{NS} is the overstrength from nonstructural elements, N is the number of stories of the building, and P_{NS} is the unit area shear strength contribution from nonstructural elements (in psf or lb/ft^2). The P_{NS} is taken as (see Chapter 2):

P_{NS} = 40 psf (MFD 1 to 5 stories)

= 25 psf (COM 2 to 5 stories)

= 10 psf (COM 1-story)

Using the same approach, the total overstrength of MFD buildings for different heights and for Risk Category II (I_e = 1) are presented in Figure 4-18. Since MFD buildings typically contain more partition walls (i.e., larger V_{NS}/W values), the total overstrengths are higher than that of the COM counterparts. More information on the development of the overstrengths for COM and MFD archetypes may be found in Section 2.3 of Chapter 2.

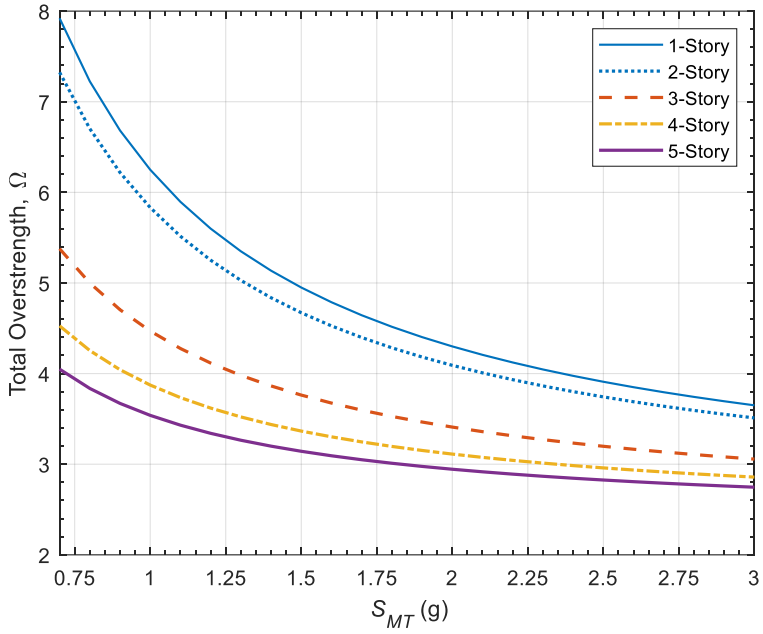

Figure 4-17 Total overstrength versus S_{MT} for 1- to 5-story COM buildings (Ω_{STR} = 2.35) for Risk Category II (I_e = 1).

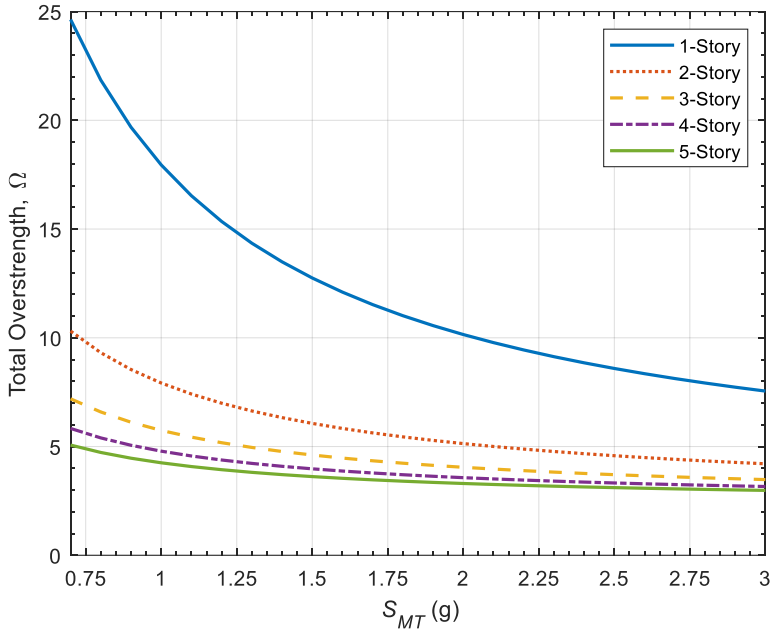

Figure 4-18 Total overstrength versus S_{MT} for 1- to 5-story MFD buildings (Ω_{STR} = 2.35) for Risk Category II (I_e = 1).

4.7.3 Adjusted Collapse Margin Ration vs S_{MT}

Once the structural overstrength is known, the peak strength (V_{max}/W) can be computed by providing a range of MCE_R spectral acceleration (S_{MT}) of interest into the following expression:

$$\frac{V_{max}}{W} = \frac{2}{3}\left(\frac{S_{MT} \times \Omega(S_{MT})}{R / I_e}\right) \tag{4-9}$$

Equation 4-9 is derived from Equation 3-4. In this study, S_{MT} ranging from 0.70g to 3.0g was used to evaluate the collapse performance of wood buildings from moderate to very high seismic regions. Note that the overstrength for wood light-frame building (Ω) is a function of design spectral acceleration, S_{MT} (See Chapter 2 for more discussion).

The seismic performance of an archetype building defined in terms of the median collapse spectral acceleration, $\hat{S}_{CT}$, was obtained from Equation 3-10 and Equation 3-11. The *ACMR* per FEMA P-695 is computed using Equation 3-5 and Equation 3-6, where *SSF* is the ductility based spectral shape factor given in Table 7-1b in FEMA P-695. For low-rise wood light-frame buildings with significant ductility (μ_T > 8), *SSF* is typically equal to 1.33 for Far-Field record set. To evaluate the collapse performance at a lower non-simulated drift ratio limit (e.g., *DR* = 2.5%), the *SSF* may be lower than 1.33. The *SSF* for *DR* = 2.5%, 5%, 7.5%, 10%, and 15% are 1.16, 1.25, 1.32, 1.33, and 1.33, respectively (See Chapter 3, Table 3-2). For Near-Fault record set, the *SSF* for *DR* = 2.5%, 5%, 7.5%, 10%, and 15% are 1.22, 1.35, 1.44, 1.46, and 1.46, respectively (See Chapter 3, Table 3-3).

Using the median collapse spectral accelerations ($\hat{S}_{CT}$) obtained from the collapse surfaces for STR, COM, and MFD archetypes and the equations presented for V_{max}/W and *ACMR*, the relationships of *ACMR* versus design acceleration (S_{MT}) are plotted in Figures 4-18, 4-19, and 4-20 for 4-story STR, COM, and MFD archetypes, respectively, Risk Category II (I_e = 1).

A higher *ACMR* value means the building is safer against collapse under a MCE_R ground motion. The horizontal dashed lines in Figure 4-19 to Figure 4-21 represents the minimum *ACMR* required to achieve the target probability of collapse of 10% for Risk Category II design. Note that the actual *ACMR* to achieve the target 10% collapse probability depends on the total uncertainty of the collapse fragility curve (β_{TOT}).

Figure 4-18 shows that the *ACMR*s for STR-only models (i.e., SFRS without nonstructural elements) are lower than that of COM and MFD models. This indicates the nonstructural walls and finish materials contribute significantly to the overall seismic performance of wood light-frame buildings.

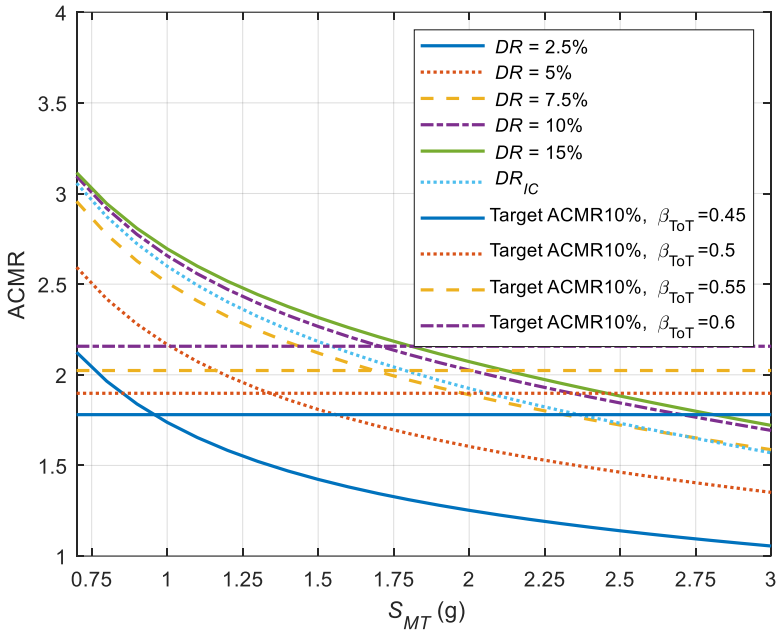

Figure 4-19 Adjusted collapse margin ratio (*ACMR*) versus MCE_R spectral acceleration (S_{MT}) for 4-Story STR-only models for Risk Category II (I_e = 1.0). Dotted blue line represents median DR_{IC}.

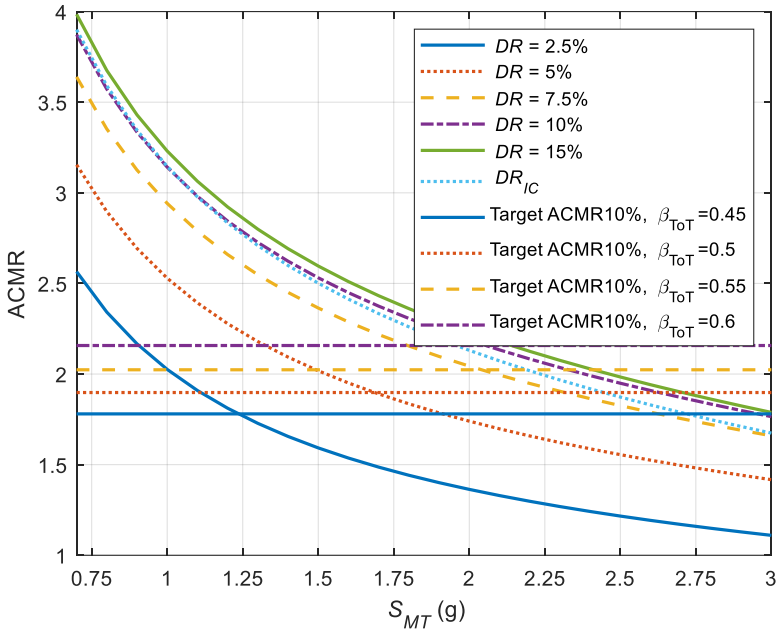

Figure 4-20 Adjusted collapse margin ratio (*ACMR*) versus MCE_R spectral acceleration (S_{MT}) for 4-Story COM models for Risk Category II (I_e = 1.0). Dotted blue line represents median DR_{IC}.

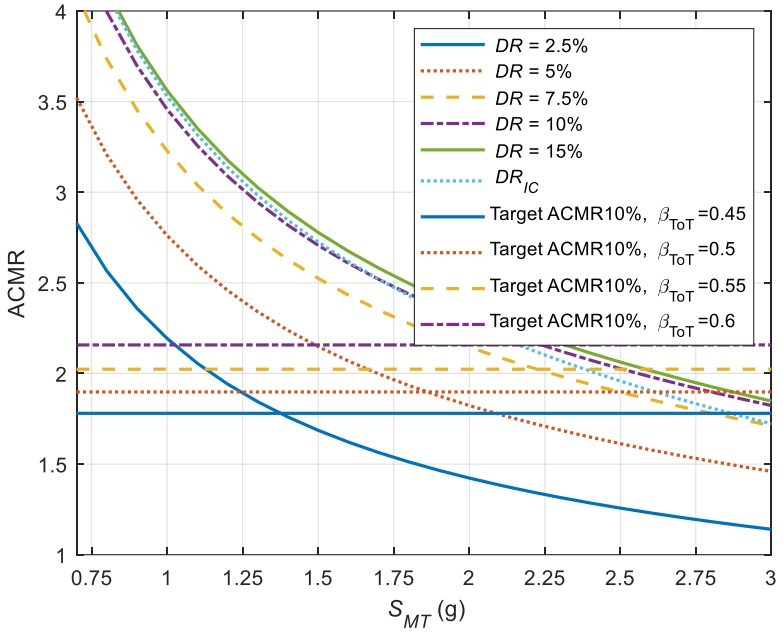

Figure 4-21 Adjusted collapse margin ratio (*ACMR*) versus MCE_R spectral acceleration (S_{MT}) for 4-Story MFD models for Risk Category II (I_e = 1.0). Dotted blue line represents median DR_{IC}.

Selected values of $\hat{S}_{CT}$ used to compute the *ACMR* presented in Figure 4-20 for the 4-story COM wood light-frame archetype are shown in Table 4-17. The discrete values of V_{max}/W are based on

Equation 4-9 assuming R/I_e = 6.5/1.0 for Risk Category II seismic design. The values of overstrength, used in Equation 4-9, are computed using Equation 4-8 and shown in Table 4-18 for the example 4-story COM wood light-frame archetype. The $\hat{S}_{CT}$ values are computed using the surface Equation 3-10 with the fitted coefficients presented in Table 4-13. The DR_{IC} shown in the last column in Table 4-17 are computed using Equation 4-5 and the coefficients presented in Table 4-16. The values of *ACMR* shown in Figure 4-20 for 4-story COM models are computed using Equation 3-6 and listed in Table 4-18. The values of $\hat{S}_{CT}$, *ACMR* and Ω for all classes of buildings considered in this study may be found in Appendix H. For the 4-story STR and MFD archetypes, the corresponding tabulated $\hat{S}_{CT}$ values may be found in Table H-164 and Table H-97, respectively, and for the *ACMR* values may be found in Table H-166 and Table H-99, respectively.

Table 4-17 **Selected Values of $\hat{S}_{CT}$ Extracted from the Collapse Surface of the 4-Story COM wood Light-Frame Archetype Shown in Figure 4-11 at Discrete Values of V_{max}/W and Corresponding to Increments of MCE_R S_{MT} from 0.70g to 3.0g. Values of $\hat{S}_{CT}$ are selected at collapse drift ratios, DR = 2.5%, 5.0%, 7.5%, 10% and 15%, and at the median drift ratio of incipient collapse, DR_{IC}**

MCE_R S_{MT} (g)	V_{max}/W	Median Collapse Acceleration, $\hat{S}_{CT}$ (g) at DR						DR_{IC}
		2.5%	5.0%	7.5%	10%	15%	DR_{IC}	
0.7	0.32	1.55	1.77	1.93	2.04	2.10	2.05	10.47%
0.8	0.35	1.61	1.85	2.03	2.15	2.21	2.16	10.34%
0.9	0.37	1.68	1.94	2.13	2.26	2.32	2.26	10.21%
1.0	0.40	1.75	2.02	2.23	2.36	2.43	2.36	10.07%
1.1	0.42	1.81	2.11	2.32	2.47	2.53	2.46	9.94%
1.2	0.45	1.87	2.19	2.42	2.57	2.64	2.56	9.82%
1.3	0.47	1.94	2.27	2.51	2.66	2.74	2.65	9.69%
1.4	0.49	2.00	2.34	2.60	2.76	2.83	2.74	9.57%
1.5	0.52	2.06	2.42	2.69	2.85	2.93	2.83	9.44%
1.6	0.54	2.12	2.50	2.77	2.95	3.02	2.91	9.32%
1.7	0.57	2.18	2.57	2.86	3.04	3.11	2.99	9.20%
1.8	0.59	2.24	2.64	2.94	3.12	3.20	3.07	9.08%
1.9	0.61	2.29	2.71	3.02	3.21	3.28	3.14	8.97%
2.0	0.64	2.35	2.78	3.10	3.29	3.36	3.22	8.85%
2.1	0.66	2.41	2.85	3.17	3.37	3.44	3.29	8.74%
2.2	0.69	2.46	2.92	3.25	3.45	3.52	3.35	8.62%
2.3	0.71	2.52	2.98	3.32	3.52	3.59	3.42	8.51%
2.4	0.73	2.57	3.05	3.39	3.59	3.66	3.48	8.40%
2.5	0.76	2.62	3.11	3.46	3.66	3.73	3.54	8.29%
2.6	0.78	2.67	3.17	3.52	3.73	3.79	3.60	8.19%
2.7	0.81	2.72	3.23	3.59	3.80	3.86	3.65	8.08%
2.8	0.83	2.77	3.29	3.65	3.86	3.92	3.70	7.98%
2.9	0.86	2.82	3.35	3.71	3.92	3.98	3.75	7.88%
3.0	0.88	2.87	3.40	3.77	3.98	4.03	3.80	7.77%

Table 4-18 Example Values of the Adjusted Collapse Margin Ratio (*ACMR*) Calculated from the Values of $\widehat{S}_{CT}$ Summarized in Table 4-17 for the 4-Story COM Wood Light-Frame Archetype, Assuming Risk Category II Seismic Design (i.e., R/I_e = 6.5/1.0)

MCE_R S_{MT} (g)	Strength Property		Typical Spectrum Shape Factor (*SSF*) at *DR*					
			1.16	1.25	1.32	1.33	1.33	varies
			ACMR at *DR*					
	Ω	V_{max}/W	2.5%	5.0%	7.5%	10%	15%	DR_{IC}
0.7	4.53	0.32	2.57	3.15	3.67	3.87	3.99	3.90
0.8	4.25	0.35	2.34	2.90	3.38	3.57	3.68	3.59
0.9	4.04	0.37	2.17	2.69	3.15	3.33	3.43	3.35
1.0	3.87	0.40	2.03	2.53	2.96	3.14	3.23	3.15
1.1	3.73	0.42	1.91	2.39	2.81	2.98	3.06	2.98
1.2	3.62	0.45	1.81	2.28	2.68	2.84	2.92	2.83
1.3	3.52	0.47	1.73	2.18	2.57	2.73	2.80	2.71
1.4	3.44	0.49	1.66	2.09	2.47	2.62	2.69	2.60
1.5	3.37	0.52	1.59	2.02	2.38	2.53	2.60	2.50
1.6	3.30	0.54	1.54	1.95	2.30	2.45	2.51	2.41
1.7	3.25	0.57	1.49	1.89	2.23	2.37	2.43	2.33
1.8	3.20	0.59	1.44	1.84	2.17	2.31	2.36	2.26
1.9	3.15	0.61	1.40	1.79	2.11	2.24	2.30	2.19
2.0	3.11	0.64	1.36	1.74	2.06	2.19	2.23	2.13
2.1	3.08	0.66	1.33	1.70	2.01	2.13	2.18	2.07
2.2	3.04	0.69	1.30	1.66	1.96	2.08	2.13	2.02
2.3	3.01	0.71	1.27	1.62	1.92	2.04	2.08	1.97
2.4	2.98	0.73	1.24	1.59	1.88	1.99	2.03	1.92
2.5	2.96	0.76	1.22	1.56	1.84	1.95	1.98	1.87
2.6	2.94	0.78	1.19	1.52	1.80	1.91	1.94	1.83
2.7	2.91	0.81	1.17	1.50	1.77	1.87	1.90	1.79
2.8	2.89	0.83	1.15	1.47	1.73	1.83	1.86	1.75
2.9	2.88	0.86	1.13	1.44	1.70	1.80	1.82	1.71
3.0	2.86	0.88	1.11	1.42	1.67	1.76	1.79	1.67

4.7.4 Probability of Collapse at MCE_R Ground Motion S_{MT}

Figure 4-22 shows the relationship between *ACMR* and collapse probability at MCE_R ground motion (S_{MT}) estimated using the FEMA P-695 methodology. A higher *ACMR* means a lower MCE_R collapse probability, P[collapse|S_{MT}]. Assuming the collapse fragility curve follows a lognormal distribution,

the MCE_R collapse probability can be computed using Equation 3-7, where $\Phi(.)$ is the cumulative distribution function of standard normal distribution and β_{TOT} is the total uncertainty (or dispersion) of the lognormal fragility curve.

For wood light-frame buildings with modern construction and analyzed using good quality test data and numerical models, the total uncertainty term, β_{TOT}, was estimated to be around 0.5 (FEMA P-2931-2). It was observed in laboratory testing of wood light-frame shear walls, the variability of restoring forces for nominally identical wood shear walls typically increases with increasing wall drift (see Figure D-15 in Appendix D. Therefore, in this study, the total uncertainty β_{TOT} is assumed to increase with increasing drift ratio following the trend shown in Figure 4-23 (also see Chapter 3). Figure 4-12 shows the residuals of the collapse surface predicted $\hat{S}_{CT}$ for *DR* > 10% are higher than that of *DR* < 10%. This further supports the assumption that β_{TOT} increases with increasing *DR*. For Risk Category IV structures, the reduced uncertainty values shown in Figure 4-23 reflect the enhancement in design and construction.

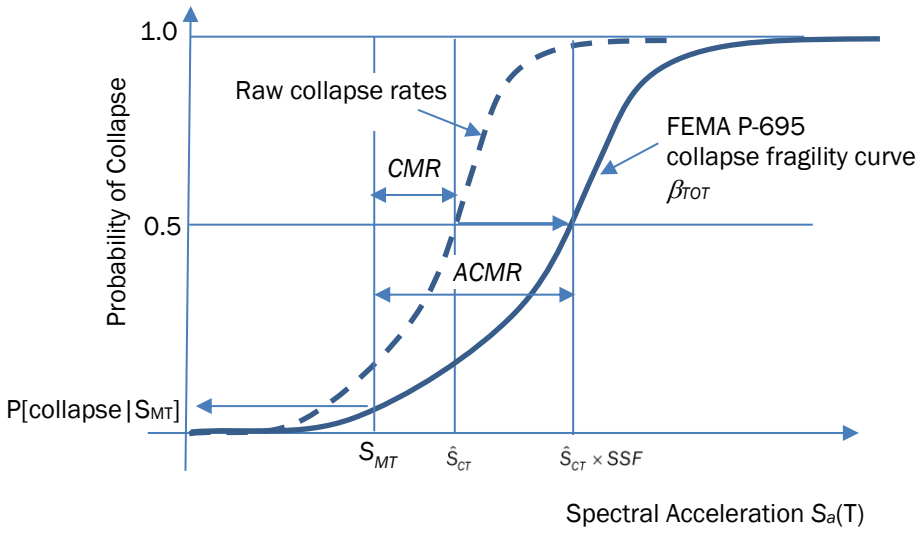

Figure 4-22 Adjusted collapse margin ratio (*ACMR*) and FEMA P-695 collapse fragility curve.

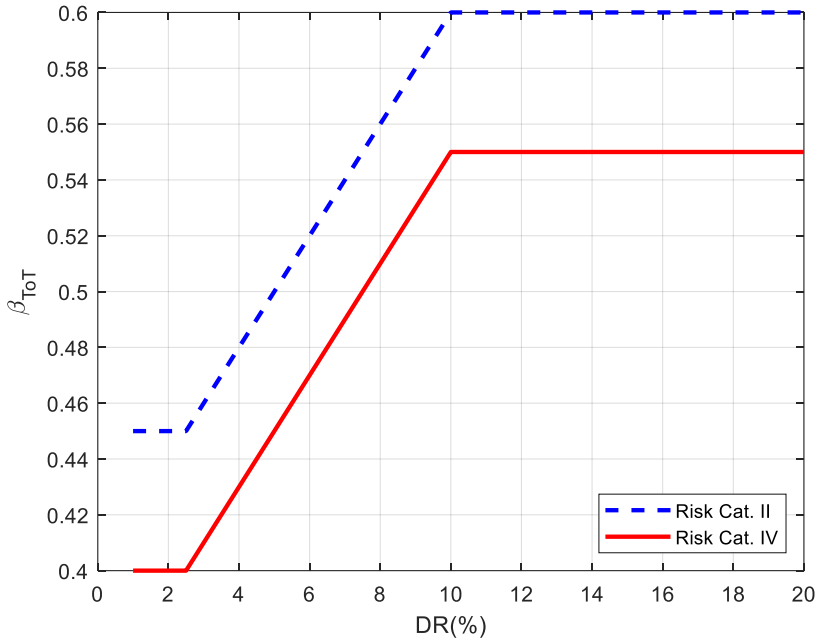

Figure 4-23 Plot of total uncertainty versus drift ratio of wood light-frame archetypes.

Figure 4-24 shows the collapse probabilities of the 4-story COM wood light-frame archetype given S_{MT} for Risk Category II. As observed in FEMA P-2931-2, the collapse probability increases with increasing S_{MT} signaling the collapse risk of buildings located in very high seismic region is higher than that in moderate seismic region. Full-scale shake table tests and observations following earthquakes have shown that global collapse of wood buildings typically occur at *DR* greater than 7.5% (FEMA P-2139-2).

Table 4-19 Example Values of the MCE_R Collapse Probability Calculated from the Values of $\widehat{S}_{CT}$ Summarized in Table 4-17 for the 4-Story COM Wood Light-Frame Archetype, Assuming Risk Category II Seismic Design (i.e., R/I_e = 6.5/1.0)

			Total Collapse Variability (β_{TOT}) at *DR*					
			0.45	0.50	0.55	0.60	0.60	varies
MCE_R S_{MT} (g)	Strength Property		P[Collapse|S_{MT}] at *DR*					
	Ω	V_{max}/W	2.5%	5.0%	7.5%	10%	15%	DR_{IC}
0.7	4.53	0.32	1.8%	1.1%	0.9%	1.2%	1.1%	1.2%
0.8	4.25	0.35	2.9%	1.7%	1.3%	1.7%	1.5%	1.7%
0.9	4.04	0.37	4.3%	2.4%	1.9%	2.2%	2.0%	2.2%
1.0	3.87	0.40	5.8%	3.2%	2.4%	2.8%	2.5%	2.8%
1.1	3.73	0.42	7.5%	4.0%	3.0%	3.4%	3.1%	3.4%
1.2	3.62	0.45	9.3%	5.0%	3.7%	4.1%	3.7%	4.0%
1.3	3.52	0.47	11.2%	6.0%	4.3%	4.7%	4.3%	4.7%
1.4	3.44	0.49	13.1%	7.0%	5.0%	5.4%	4.9%	5.3%
1.5	3.37	0.52	15.1%	8.0%	5.7%	6.1%	5.6%	5.9%
1.6	3.30	0.54	17.0%	9.1%	6.4%	6.8%	6.3%	6.6%
1.7	3.25	0.57	18.9%	10.1%	7.2%	7.5%	6.9%	7.3%
1.8	3.20	0.59	20.8%	11.2%	7.9%	8.2%	7.6%	8.0%
1.9	3.15	0.61	22.7%	12.3%	8.7%	8.9%	8.3%	8.7%
2.0	3.11	0.64	24.5%	13.4%	9.5%	9.6%	9.0%	9.4%
2.1	3.08	0.66	26.3%	14.5%	10.2%	10.3%	9.7%	10.1%
2.2	3.04	0.69	28.1%	15.6%	11.0%	11.1%	10.4%	10.9%
2.3	3.01	0.71	29.8%	16.7%	11.8%	11.8%	11.2%	11.6%
2.4	2.98	0.73	31.5%	17.8%	12.6%	12.5%	11.9%	12.4%
2.5	2.96	0.76	33.2%	18.9%	13.4%	13.3%	12.7%	13.2%
2.6	2.94	0.78	34.8%	19.9%	14.2%	14.1%	13.4%	14.0%
2.7	2.91	0.81	36.3%	21.0%	15.0%	14.8%	14.2%	14.8%
2.8	2.89	0.83	37.9%	22.1%	15.8%	15.6%	15.0%	15.6%
2.9	2.88	0.86	39.4%	23.2%	16.7%	16.4%	15.8%	16.5%
3.0	2.86	0.88	40.8%	24.3%	17.5%	17.2%	16.6%	17.4%

Figure 4-24 shows the MCE_R probability of collapse versus design S_{MT} curves plotted using the data presented in Table 4-19 for selected non-simulated drift limits of *DR* = 2.5%, 5.0%, 7.5%, 10% and 15%, and at the median drift ratio of incipient collapse, DR_{IC}. As can be seen, the curves associated with $DR \geq 7.5\%$ yield similar collapse probabilities as the curve based on DR_{IC} (i.e., median

simulated collapse drift ratio). The curve derived from DR_{IC} represents the best estimate of the collapse probability for the 4-story COM wood light-frame archetype. Figure 4-24 (or Table 4-19) shows that 4-story COM buildings in regions with S_{MT} greater than approximately 2.1g may not meet the target collapse risk specified in the current building code for Risk Category II (i.e., 10%). If a more stringent *DR* limit of 2.5% is specified, 4-story COM buildings in regions with S_{MT} greater than approximately 1.25g may not meet the code objective.

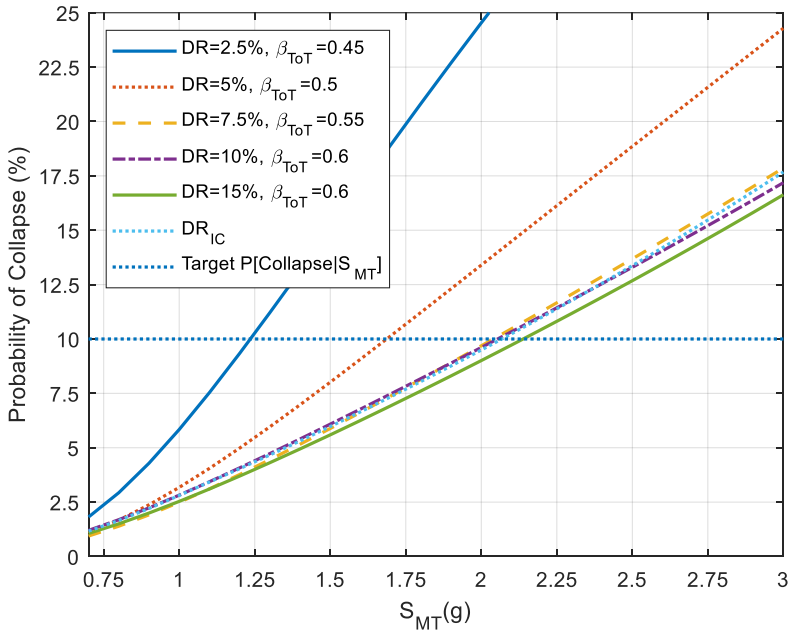

Figure 4-24 MCE$_R$ collapse probabilities of 4-story COM wood light-frame archetype models, Risk Category II (I_e = 1). Dotted blue line represents median DR_{IC}.

Figure 4-25 to Figure 4-27 show the collapse probability versus design S_{MT} for 1-story COM, MFD, and STR archetypes for Risk Category II design (R/I_e = 6.5/1.0). The tabulated values of P[Collapse|S_{MT}] for 1-story COM, MFD, and STR models may be found in Appendix H, Tables H-16, H-83, and H-150, respectively. Similar to the results observed for 4-story COM archetype, the P[Collapse|S_{MT}] curves based on non-simulated drift limits of $DR \geq 7.5\%$ are reasonably close to that based on DR_{IC}. Using the curve based on the median simulated collapse drift ratio (DR_{IC}), Figure 4-24 estimates that 1-story COM buildings in region with S_{MT} greater than approximately 1.8g may not meet the target performance specified in the current building code (i.e., P[Collapse|S_{MT}] =10%). If a very stringent *DR* limit of 2.5% is assumed, the threshold value for S_{MT} for non-performance 1-story COM buildings designed using the current code procedure drops to approximately 1.0g (see Figure 4-22). In other words, 1-story COM buildings in regions with S_{MT} greater than approximately 1.0g have a 10% chance of experiencing peak 1st-story drift of greater than 2.5%.

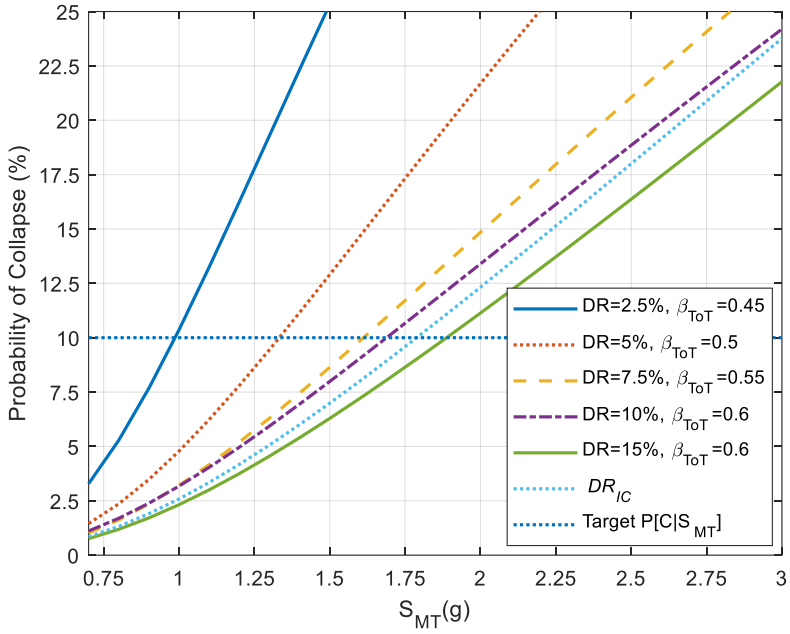

Figure 4-25 MCE_R collapse probabilities of 1-story COM wood light-frame archetype models, Risk Category II (I_e = 1). Dotted blue line represents median DR_{IC}.

Compared to COM buildings, Figure 4-26 shows the 1-story MFD buildings have lower MCE_R collapse probabilities than COM buildings. This is because the 1-story MFD buildings with multi-units have more partition walls (i.e., higher total building overstrength from nonstructural partition walls). As expected, under the same S_{MT}, the STR-only model has the highest collapse probabilities when compared to COM and MFD buildings (See Figure 4-27). This is because the STR model does not consider any contribution from the nonstructural elements. Note that in Figure 4-27, the P[collapse|S_{MT}] curve for the 1-story STR archetype considering a non-simulated collapse drift limit of *DR* = 2.5% is not in the view of the figure. This is because the collapse probabilities for the range of S_{MT} values considered (0.7g to 3g) are higher than 25% (see Table H-150 in Appendix H).

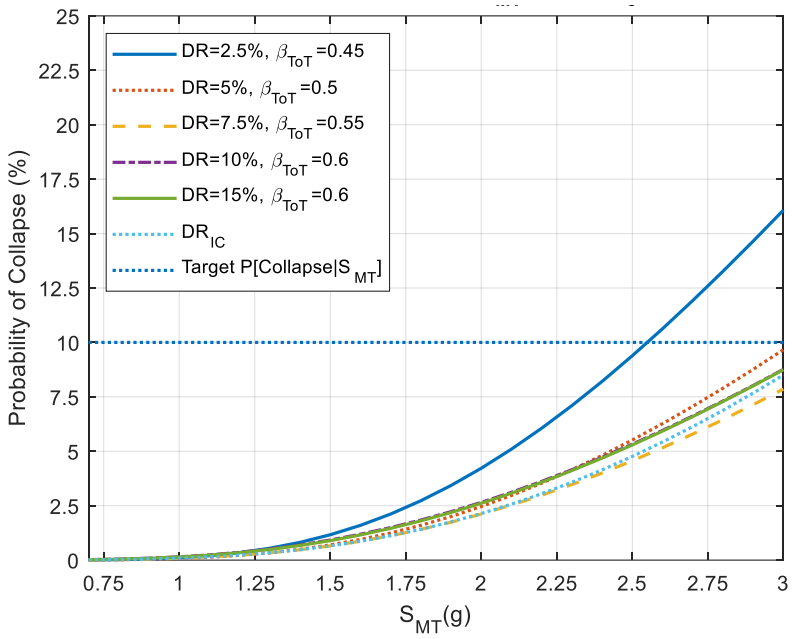

Figure 4-26 MCE_R collapse probabilities of 1-story MFD wood light-frame archetype models, Risk Category II (I_e = 1). Dotted blue line represents median DR_{IC}.

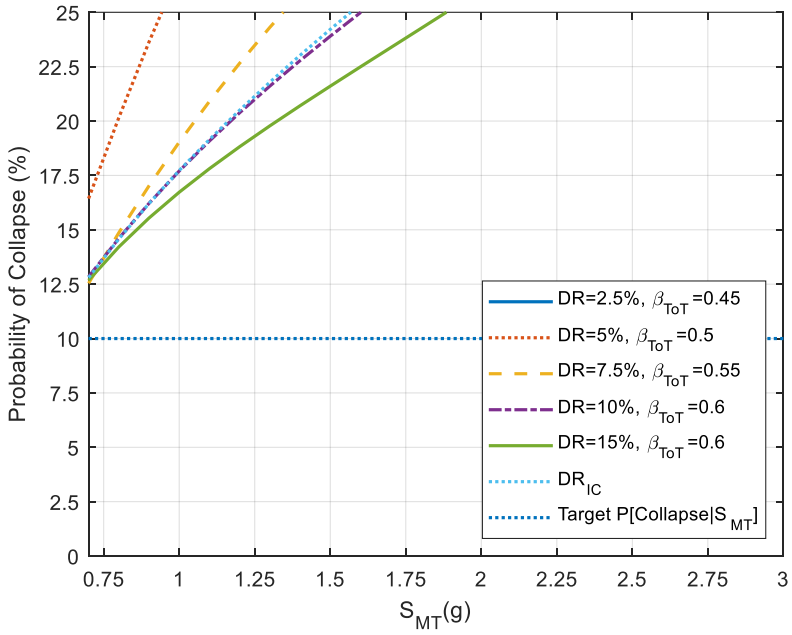

Figure 4-27 MCE_R collapse probabilities of 1-story STR wood light-frame archetype models, Risk Category II (I_e = 1). Dotted blue line represents median DR_{IC}.

Similar plots of MCE_R collapse probabilities for 2-story COM, MFD and STR-only wood buildings are presented in Figures 4-28, 4-29, and 4-30, respectively (see Tables H-22, H-89, and H-156 for tabulated values). Based on the simulated collapse drift limit curve (DR_{IC}), Figure 4-28 shows that 2-story COM buildings in regions with S_{MT} greater than approximately 2.1g may not meet the code

specified performance for Risk Category II. For 2-story MFD buildings and using the same DR_{IC} as the limit (note that DR_{IC} and DR=7.5% curves are similar), the S_{MT} value in which the collapse probability may exceed the code target for Risk Category II (P[collapse|S_{MT}] = 10%) increases to approximately 2.4g (Figure 4-29). For 2-story buildings without any nonstructural elements (2-story STR models), Figure 4-30 indicates that buildings in regions with S_{MT} of greater than approximately 1.1g would have more than 10% probability of experiencing peak inter-story drift of greater than 7.5%.

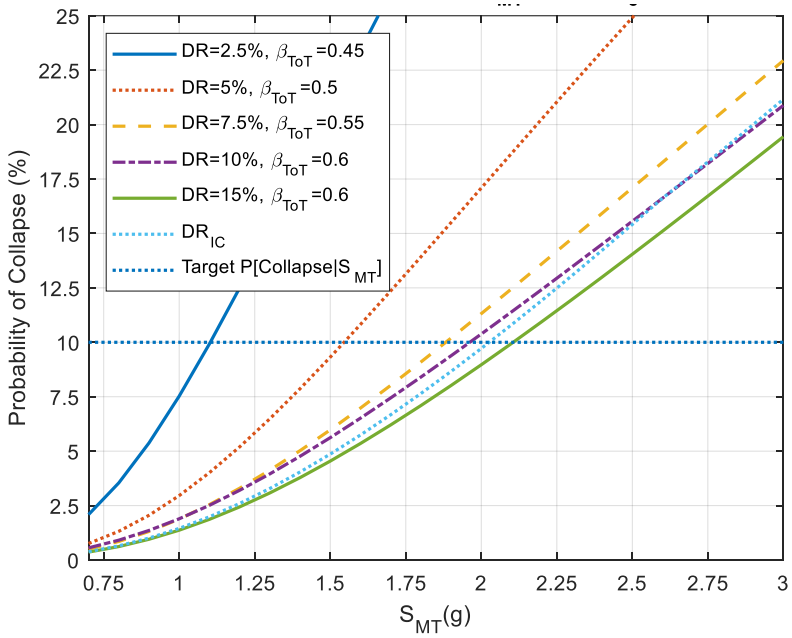

Figure 4-28 MCE_R collapse probabilities of 2-story COM wood light-frame archetype models, Risk Category II (I_e = 1). Dotted blue line represents median DR_{IC}.

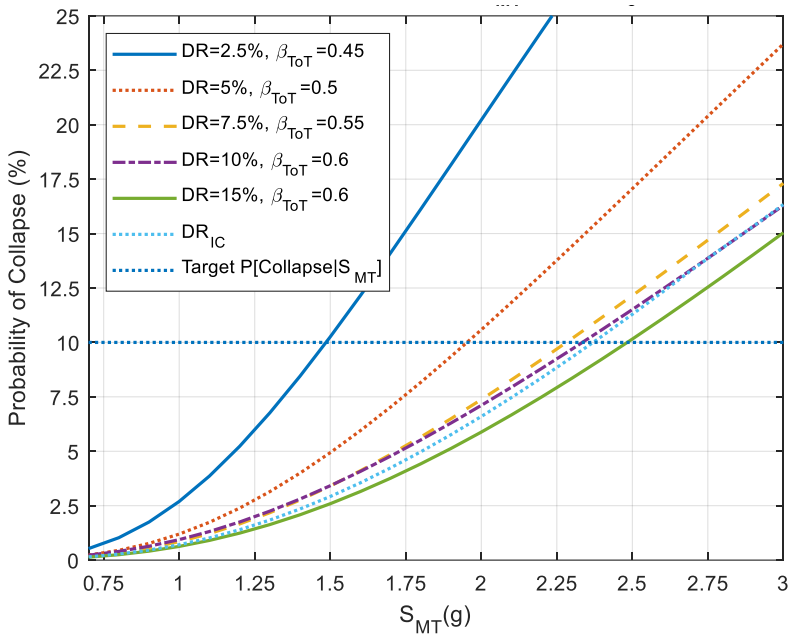

Figure 4-29 **MCE$_R$ collapse probabilities of 2-story MFD wood light-frame archetype models, Risk Category II (I_e = 1). Dotted blue line represents median DR_{IC}.**

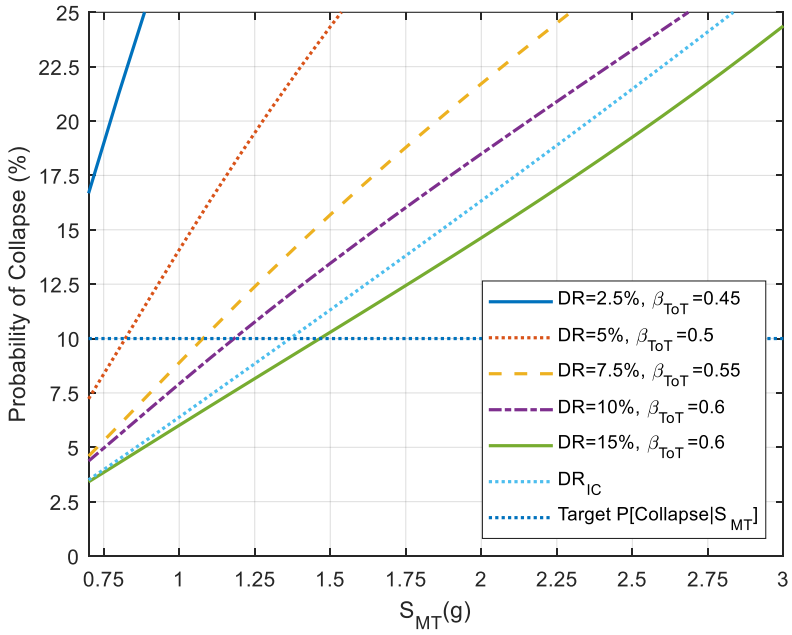

Figure 4-30 **MCE$_R$ collapse probabilities of 2-story STR wood light-frame archetype models, Risk Category II (I_e = 1). Dotted blue line represents median DR_{IC}.**

4.7.5 Collapse Performance by Height and Archetype

Figure 4-31 to Figure 4-35 compare the MCE_R collapse performance of the three archetypes grouped by height (or number of stories) for Risk Category II design. As expected, for a given height and design S_{MT}, the MFD archetype has the best performance (lowest collapse probability), followed by COM archetype and then STR. All COM buildings in region with $S_{MT} \leq 1.8g$ (controlled by 1-story COM, see Figure 4-31) are expected to meet target seismic performance specified in the design code (i.e. $P[collapse|S_{MT}] < 10\%$). Note that the floor plan of 1-story COM archetype is different from 2-story to 5-story COM archetypes. The 1-story COM archetype has an open floor plan with less nonstructural elements (less partition walls) than the taller COM archetypes (see Chapter 2). For the MFD archetypes, the 1-story MFD archetype exhibits the best performance (lowest collapse probability for a given S_{MT}) and the 5-story MFD has the lowest performance. From the MFD curves shown in Figure 4-31 to Figure 4-34, MFD buildings designed for Risk Category II and located in regions with S_{MT} equal or less than approximately 2.0g (controlled by 5-story MFD) are expected to meet the code target performance ($P[collapse|S_{MT}] < 10\%$). In regions with relatively high seismicity (i.e., $S_{MT} >$ 2.0g), an increase in the strength of SFRS may be needed to maintain or achieve the code target performance level.

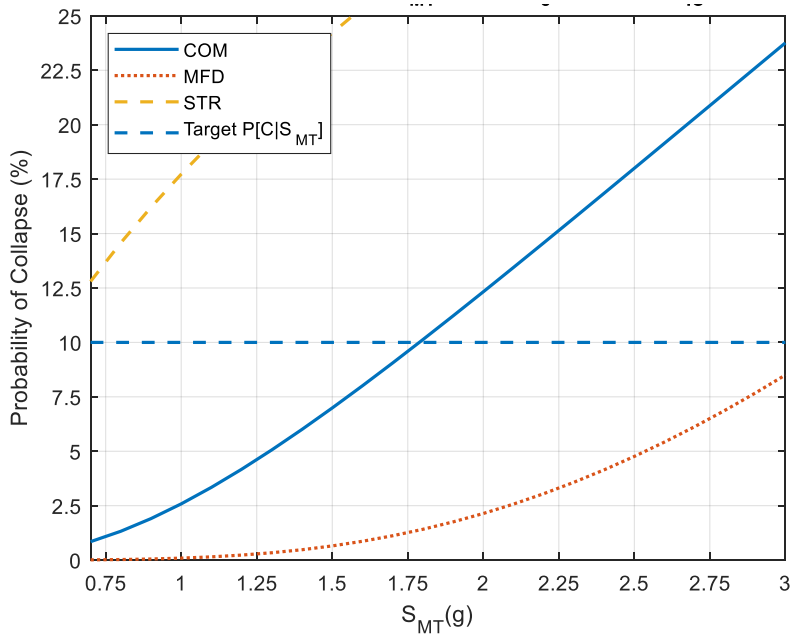

Figure 4-31 MCE_R collapse probabilities of 1-story COM, MFD, and STR wood light-frame archetype models, Risk Category II (I_e = 1).

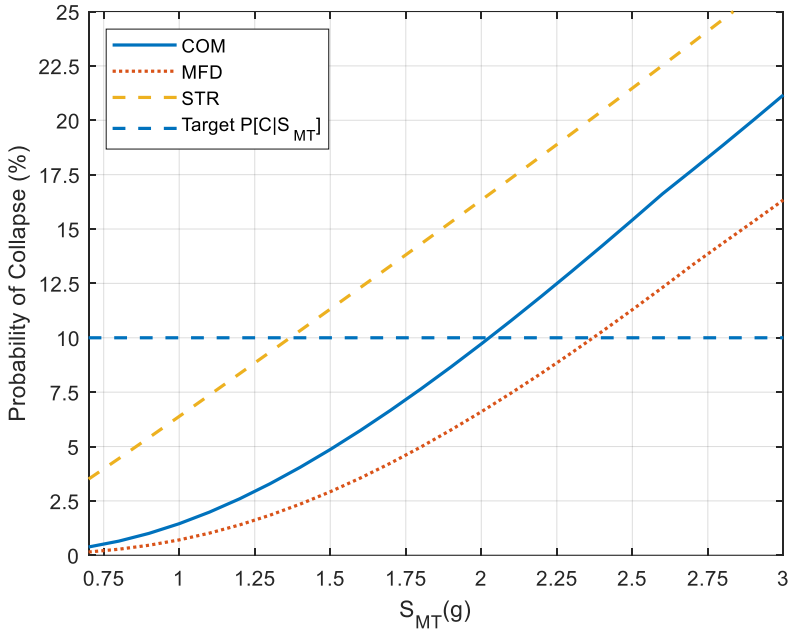

Figure 4-32 **MCE_R collapse probabilities of 2-story COM, MFD, and STR wood light-frame archetype models, Risk Category II (I_e = 1).**

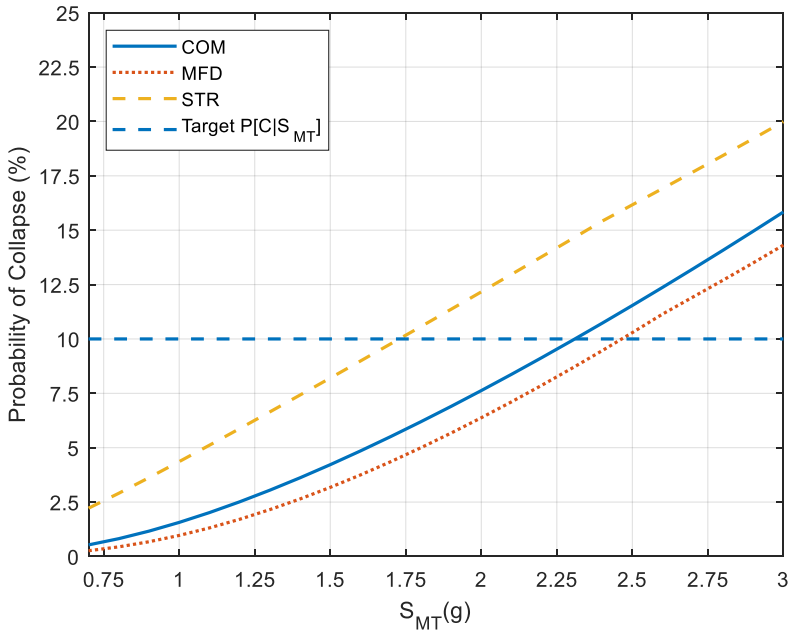

Figure 4-33 **MCE_R collapse probabilities of 3-story COM, MFD, and STR wood light-frame archetype models, Risk Category II (I_e = 1).**

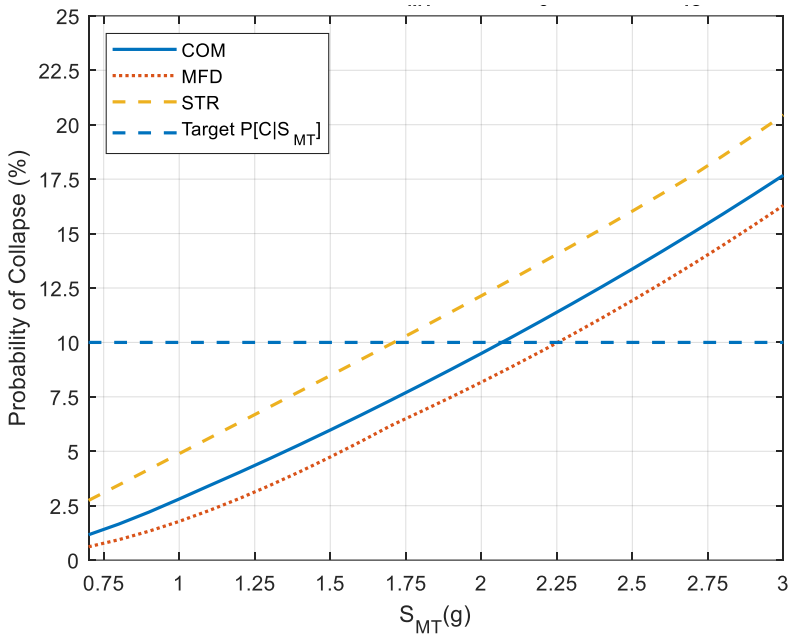

Figure 4-34 MCE_R collapse probabilities of 4-story COM, MFD, and STR wood light-frame archetype models, Risk Category II (I_e = 1).

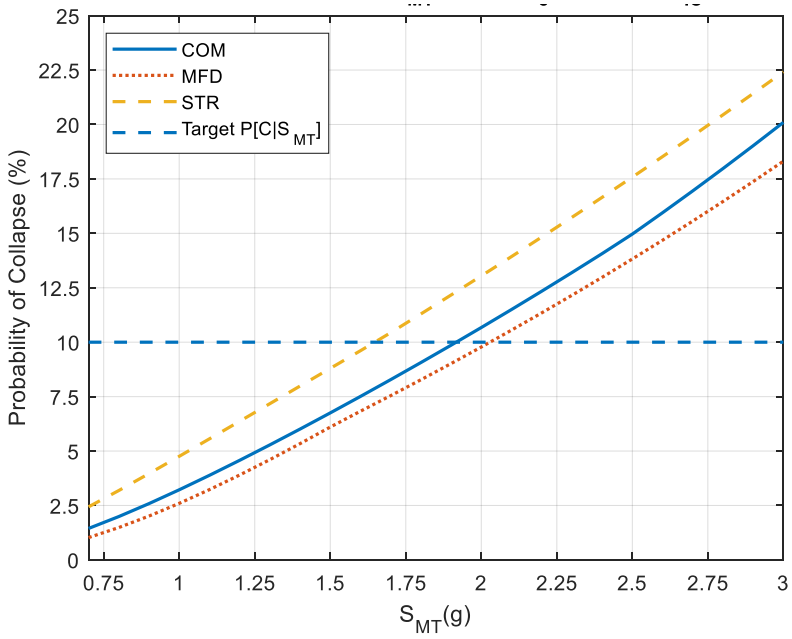

Figure 4-35 MCE_R collapse probabilities of 5-story COM, MFD, and STR wood light-frame archetype models, Risk Category II (I_e = 1).

4.7.6 Influence of Risk Category Design

Figure 4-36 and Figure 4-37 compare the MCE_R probabilities of collapse versus S_{MT} for selected building heights (1-story and 5-story) designed to Risk Categories II (I_e = 1) and IV (I_e = 1.5) for COM and MFD archetypes, respectively. As discussed in the previous section, DR_{IC} represents the best estimate for the displacement capacity at incipient collapse. Hence, the collapse performance curves presented in Figure 4-36 and Figure 4-37 are based on DR_{IC}. The collapse probability limits specified in ASEC/SEI 7 are 10% and 2.5% for Risk Categories II and IV, respectively. The intersection point of the code specified collapse probability limit (horizontal line) and a given MCE_R collapse probability curve marks the non-performance S_{MT} limit, beyond which the collapse probability of the as-designed archetype is expected to exceed the code specified target collapse probability. For 1-story COM buildings, the non-performance S_{MT} limits for Risk Category II and IV are approximately 1.8g and 1.4g, respectively. A similar trend is observed for the taller archetype (5-story COM), where the non-performance S_{MT} limit reduces from approximately 1.9g for Risk Category II to 1.7g for Risk Category IV.

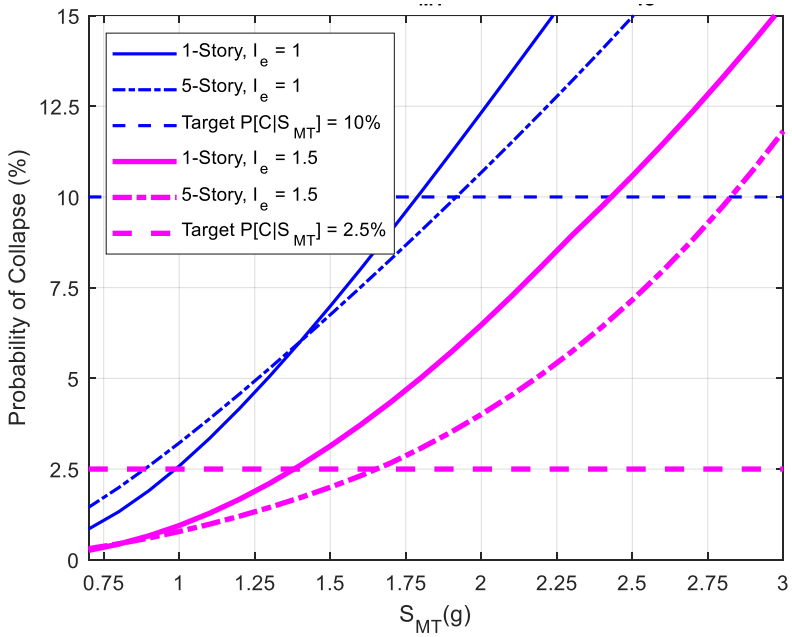

Figure 4-36 MCE_R collapse probabilities of 1-story and 5-story COM wood light-frame archetype models designed for Risk Categories II (I_e = 1.0) and IV (I_e = 1.5).

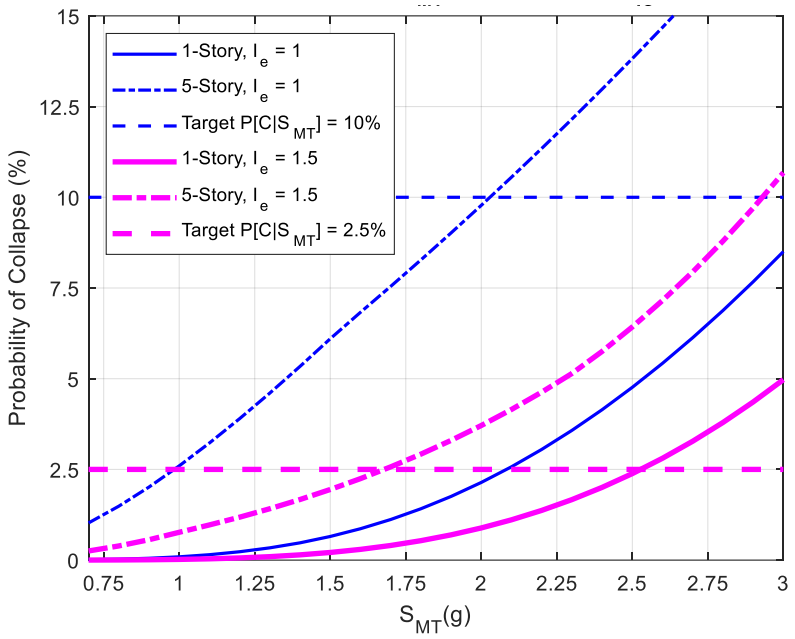

Figure 4-37 MCE_R collapse probabilities of 1-story and 5-story MFD wood light-frame archetype models designed for Risk Categories II (I_e = 1.0) and IV (I_e = 1.5).

For MFD wood light-frame archetypes, the non-performance S_{MT} limits for 1-story MFD wood light-frame buildings are greater than 3g for Risk Category II and about 2.5g for Risk Category IV. For the taller 5-story MFD archetype, the non-performance S_{MT} limits are approximately 2.0g for Risk Category II and 1.7g for Risk Category IV.

Table 4-20 compares the non-performance S_{MT} limits between Risk Categories II and IV. The information listed in Table 4-20 is also presented as a bar chart in Figure 4-38. As can be seen, all three archetypes (COM, MFD, and STR) exhibit a consistent trend with the non-performance S_{MT} limit reducing from Risk Categories II to Risk Category IV. The differences between the non-performance S_{MT} limits range from about 10% to 25%, with the non-performance S_{MT} limits of the Risk Category IV designs being consistently lower than their Risk Category II counterpart designs.

Table 4-20 Non-Performance S_{MT} Limits for Design Risk Categories II and IV for Far-Field Record Set

No. Stories	Non-Performance S_{MT} Limit (g)								
	COM			MFD			STR		
	RC II	RC IV	% Diff. (IV-II)/II	RC II	RC IV	% Diff. (IV-II)/II	RC II	RC IV	% Diff. (IV-II)/II
	P_{col}= 10%	P_{col}= 2.5%		P_{col}= 10%	P_{col}= 2.5%		P_{col}= 10%	P_{col}= 2.5%	
1	1.79	1.38	-23%	>3	2.53	n/a	<0.7	<0.7	n/a
2	2.03	1.54	-24%	2.37	1.78	-25%	1.37	1.12	-18%
3	2.31	1.79	-22%	2.47	1.92	-22%	1.73	1.41	-18%
4	2.07	1.74	-16%	2.25	1.86	-17%	1.71	1.55	-10%
5	1.92	1.65	-14%	2.03	1.68	-17%	1.65	1.49	-10%

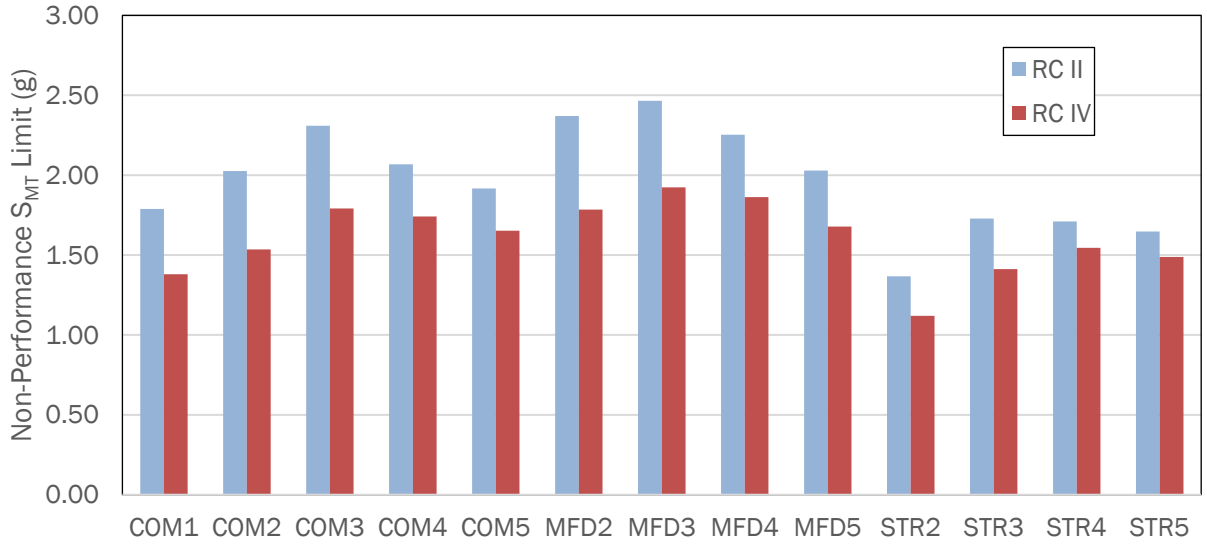

Figure 4-38 Comparison of Non-Performance S_{MT} Limits for Design Risk Categories II and IV for Far-Field Record Set.

4.7.7 Influence of Ground Motion Record Sets

All three sets of archetypes (COM, MFD, and STR) were analyzed using the FEMA P-695 Far-Field record set. The MFD archetypes also were analyzed using the Near-Field record set to investigate the influence of the ground motions on the seismic collapse performance of wood buildings. The collapse surface $\hat{S}_{CT}$ equation coefficients and median peak first-story collapse drift ratio (DR_{IC})

coefficients for 1-story to 5-story MFD models subjected to Near-Field ground motions are listed in Table 4-21 and Table 4-22, respectively.

Table 4-21 Collapse Surface $\widehat{S}_{CT}$ Equation Coefficients for MFD Models Subjected to Near-Field Motions

Coefficient	Independent Variable	1-Story	2-Story	3-Story	4-Story	5-Story
A	V_{max}/W	1.63	1.49	1.53	0.81	1.32
B	$(V_{max}/W)^2$	-0.095	0.086	-0.044	0.345	0.041
C	*DR*	-10.86	-3.83	-3.40	-1.88	-6.25
D	DR^2	73.79	32.49	21.72	8.88	17.52
E	$(V_{max}/W) \times DR$	24.59	35.11	33.22	29.23	43.75
F	$(V_{max}/W)^2 \times DR$	-3.62	-13.49	-10.05	-7.79	-16.49
G	$(V_{max}/W) \times DR^2$	-103.89	-142.40	-119.21	-101.75	-127.46
H	$(V_{max}/W)^2 \times DR^2$	6.97	45.20	21.71	11.81	27.26
I	Intercept	0.070	0.224	0.309	0.578	0.470
Goodness-of-fit		0.98	0.99	0.99	0.96	0.99

Table 4-22 Median Peak First-Story Incipient Collapse Drift Ratio (DR_{IC}) Equation Coefficients for MFD Models Subjected to Near-Field Motions

Archetype	Coefficient	1-Story	2-Story	3-Story	4-Story	5-Story
MFD	C0	0.209	0.193	0.188	0.174	0.148
	C1	-0.612	-0.552	-0.662	-0.826	-0.516

Figure 4-39 compares the MCE_R collapse probabilities of 1-story, 3-story, and 5-story MFD models designed for Risk Category II and subjected to Far-Field and Near-Field ground motions sets. Except for the 1-story archetype, Figure 4-39 shows 3-story and 5-story MFD buildings are more prone to collapse when subjected to Near-Field ground motions, with higher MCE_R collapse probabilities for a given S_{MT} when compared to the results based on Far-Field ground motions. The same trend is observed for MFD buildings designed to Risk Category IV (see Figure 4-40). Except for the 1-story archetype, the MCE_R collapse probability curves for 3-story and 5-story MFD buildings subjected to Near-Field ground motions are shifted to the left of the corresponding curves for Far-Field ground motions. Table 4-23 provides the S_{MT} non-performance limit values for the 3-story and 5-story MFD buildings.

Table 4-23 summarizes the non-performance S_{MT} limits of MFD models subjected to Far-Field and Near-Field ground motions designed for Risk Categories II and IV. Similarly, Figure 4-41 presents the same information in bar chart. For ease of reference, the results presented in Table 4-20 for MFD models subjected to Far-Field ground motions are repeated here in Table 4-23. The relative differences of the non-performance S_{MT} limits between design Risk Categories II and IV for both the Far-Field and Near-Field record sets are similar (between 17 to 25%, see columns 4 and 7 of Table 4-23). In general, the non-performance S_{MT} limits of the MFD models subjected to Near-Field ground motions are noticeably lower than those subjected to Far-Field ground motions (see Figure 4-41), which confirms that the Near-Field ground motions pose more risk of collapse than Far-Field ground motions. The differences are particularly significant (>30%) for taller MFD models (3-story and taller, see last two columns of Table 4-23). This suggests enhanced design beyond the current code procedure may be needed for MFD wood light-frame buildings in Near-Fault regions.

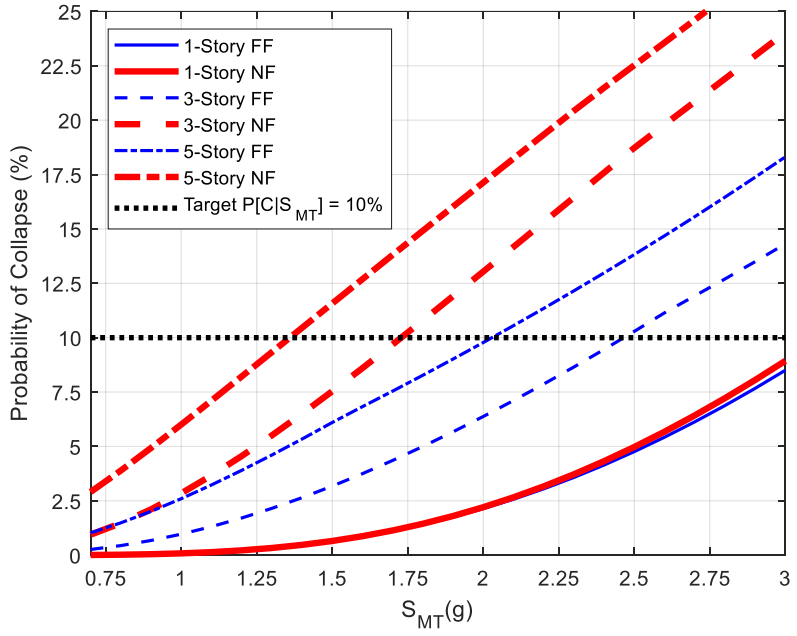

Figure 4-39 Comparison between MCE_R collapse probabilities of 1-story, 3-story, and 5-story MFD wood light-frame archetype models designed for Risk Category II (I_e = 1.0) subjected to Far-Field and Near-Field record sets.

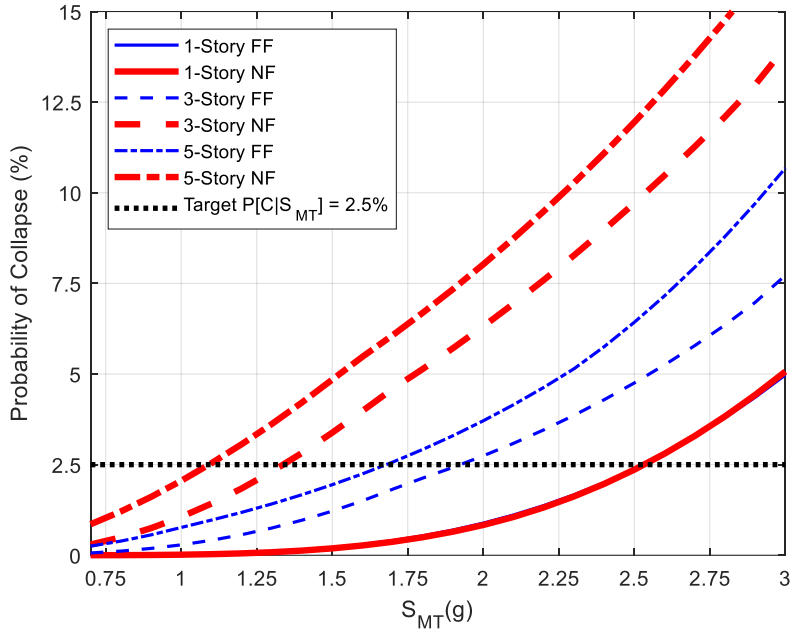

Figure 4-40 **Comparison between MCE_R collapse probabilities of 1-story, 3-story, and 5-story MFD wood light-frame archetype models designed for Risk Category IV (I_e = 1.5) subjected to Far-Field and Near-Field record sets.**

Table 4-23 **Non-Performance S_{MT} Limits for Far-Field and Near-Field Record Sets for MFD Archetypes**

No. Stories	Non-Performance S_{MT} (g)							
	MFD Near-Field (NF)			MFD Far-Field (FF)			% Diff. (NF-FF)/FF	
	RC II	RC IV	% Diff. (IV - II)/II	RC II	RC IV	% Diff. (IV - II)/II	RC II	RC IV
	P_{col}=10%	P_{col}=2.5%		P_{col}=10%	P_{col}=2.5%		P_{col}=10%	P_{col}=2.5%
1	>3	2.53	n/a	>3	2.53	n/a	n/a	0%
2	2.10	1.60	-24%	2.37	1.78	-25%	-11%	-10%
3	1.73	1.34	-23%	2.47	1.92	-22%	-30%	-31%
4	1.31	1.02	-22%	2.25	1.86	-17%	-42%	-45%
5	1.36	1.09	-20%	2.03	1.68	-17%	-33%	-35%

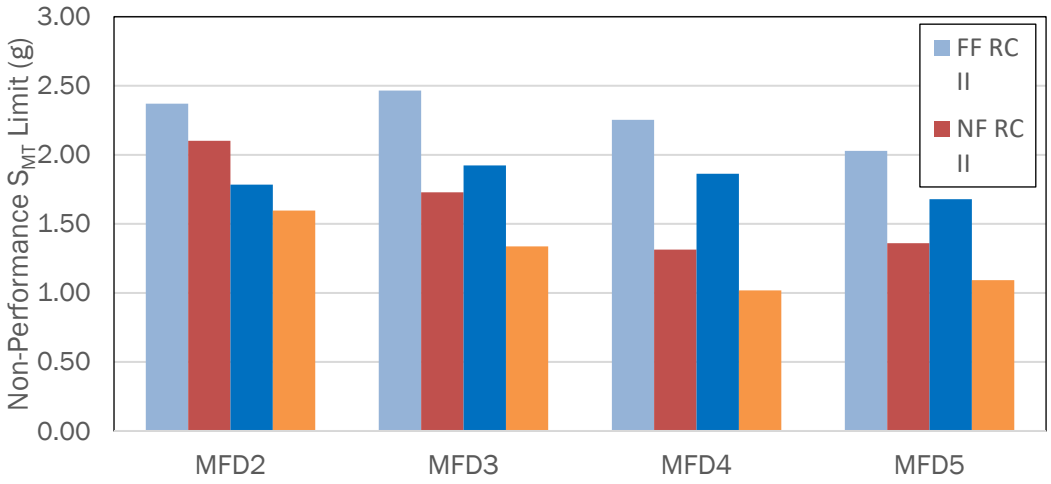

Figure 4-41 Comparison of non-performance S_{MT} limits for design Risk Categories II and IV for Far-Field (FF) and Near-Field Record Sets for MFD models.

4.8 Summary and Concluding Remarks

The seismic response behavior and collapse performance of three types of wood light-frame occupancies (commercial buildings, multi-family dwellings, and structure only) were analyzed and evaluated via nonlinear numerical models. The collapse performance was quantified using *ACMR* and probability of collapse at MCE_R design spectral acceleration at the code period (P[collapse|S_{MT}]).

- The analysis results confirm that the probabilities of collapse of as-designed wood light-frame buildings per current design procedures are systematically higher in regions of very high seismicity (i.e., S_{MS} > 1.5g). This phenomenon can be partially explained by the contribution of nonstructural partition walls in wood light-frame buildings to seismic performance. While the strength of the SFRS increases with increasing seismicity or MCE_R design spectral acceleration, S_{MT}, for a code conforming design of wood light-frame building, the total strength of nonstructural partition walls remains the same for a given occupancy type. As observed in prior studies (e.g., FEMA P-2139-2), the nonstructural elements play a significant role in the seismic performance of wood light-frame buildings.

- While the absolute performance of a wood light-frame building designed for Risk Category IV with a target P[collapse|S_{MT}] of 2.5% is better than that designed for Risk Category II with a target P[collapse|S_{MT}] of 10%, the findings in this study reveal that the as-designed Risk Category IV building is more likely to not meet the intended performance. The non-performance S_{MT} limits for Risk Category IV designs are consistently lower than that of the corresponding Risk Category II designs.

- Limited study of the influence of Near-Field ground motions on the seismic performance of wood light-frame buildings was carried out. The analysis results showed that wood light-frame buildings analyzed using the Near-Field ground motions exhibited significantly higher collapse risk than those subjected to Far-Field ground motions.

Chapter 5: Numerical Studies of Non-Wood Buildings

5.1 Introduction

This chapter presents the development of equivalent single-degree-of-freedom (eSDOF) models that are used to generate collapse data for steel buckling restrained braced frame (BRBF), steel special moment resisting frame (SMF), and reinforced concrete ductile coupled wall (DCW) systems. For each system, a validation of the eSDOF approach is provided by comparison of median spectral acceleration at collapse with that from detailed models available in the literature. After validation, the eSDOF models are modified, such as by the inclusion of gravity frame response, to include relevant behaviors that were neglected in the referenced detailed studies. Then, their strength is systematically varied to develop families of eSDOF systems for analysis. Collapse data are generated for each family of eSDOF model, and collapse surfaces are fit to the results. Following the process in Chapter 4 for wood light-frame structures, which is described in a step-by-step manner in Appendix C, the collapse surfaces are then combined with the overstrength recommendations from Chapter 2 to study the variation of *ACMR* and probability of collapse with design spectral acceleration at the ASCE/SEI 7 period, S_{MT}.

It is important to note the limitations of the models, analyses, and results presented Section 5.2 through Section 5.7. The eSDOF models are intended to represent systems with different deterioration and hysteretic characteristics that are similar to those systems used in regions of very high seismicity. The eSDOF models are used to investigate trends in collapse "risk" in regions of very high seismicity, and the results are not sufficient enough as the basis for judging the adequacy of the seismic force modification factor, *R*, of ASCE/SEI 7 for individual systems. Instead, the strength and other characteristics were systematically scaled using an understanding of each system's behavior and as such are an approximation of the response of the system with different strengths. Other simplifications used to develop the eSDOF models may also impact the actual collapse data and are highlighted throughout this section to ensure that the collapse data are not misinterpreted. It should be recognized that collapse surfaces should be developed using as detailed a modeling approach as possible. However, the eSDOF models represent the key differences in behavior between the systems considered and are used determine whether the characteristics of these systems change the outcome found in Chapter 4; namely, that the probability of collapse increases with increasing S_{MT}.

In addition to the eSDOF models, four detailed archetypes and models were developed for steel SMF systems, providing data to compare against the eSDOF results. Section 5.8 provides an overview of these designs, models, analyses, and findings, which are presented in more detail in Appendix F. The models use state-of-the-art methods for frame analysis of SMFs through collapse. Complete IDAs were performed on three of the designs that represent SMFs designed for three different levels of MCE_R seismic hazard.

5.2 Background and Approach

Background. In this study, eSDOFs with nonlinear behavior are used to expediently generate collapse surfaces for three structural systems commonly used in regions with very high seismicity. Nonlinear SDOFs have been used in previous studies to examine the behavior of complex structural systems subjected to earthquake loading, dating back to the beginning of modern earthquake engineering. More recently, Ibarra and Krawinkler (2005) used nonlinear SDOFs to simulate the response of steel moment resisting frames through collapse. As part of that work, they developed nonlinear material models that included between and in-cycle deterioration of strength and stiffness that were used in both the SDOF models and as lumped plasticity models in more detailed multiple-degree-of-freedom (MDOF) models of steel moment frames. Ibarra and Krawinkler (2005) then used the models to study the impact of different deterioration modes on collapse. They made several important observations that inform the current work.

- Equivalent SDOFs can be used for computing the collapse capacity of MDOF structures with large P-delta effects but the impact of P-delta in the inelastic range must be considered.
- Equivalent SDOF systems can produce relatively accurate, but conservative, estimates of MDOF collapse capacity.
- Prior to collapse, non-deteriorating models estimate engineering demand parameters (EDPs) with reasonable accuracy as long as the onset of strength deterioration in the backbone curve (indicated by the capping displacement, δ_c) is not surpassed.
- Ductility capacity and post-capping stiffness are the two parameters that most influence collapse capacity of a system.
- Cyclic deterioration is an important factor in estimating collapse, but it is not the dominant factor.
- Pinching in hysteretic behavior was found to have only a small impact on collapse capacity.
- The effect of small residual strengths (i.e., less 20% of peak strength) were found to be practically negligible.
- Tangent stiffness damping produces significantly lower (sometimes by 20%) estimates of collapse capacity than mass proportional damping.
- P-delta effects should be included in the backbone response.

Similarly, FEMA P-440 (FEMA, 2009) used SDOF systems to study the effects of strength and stiffness degradation in seismic response, and in particular, on the collapse capacity of structural systems. The study used eight nonlinear springs representing different types of nonlinear behavior and used those to develop over 700 spring systems that consisted of one or a combination of the basic behaviors. Collapse analysis was then performed to determine the impact of the various spring properties on collapse capacity. Some key findings relevant to the current work include:

- Definition of the force-displacement capacity boundary (commonly known as the backbone behavior) critically affects collapse capacity.

- When a cyclic envelope curve derived from a single cyclic load history is used as the capacity boundary, the numerical behavior is likely to be conservative.
- In most cases, in-cycle strength degradation dominates the response relative to cyclic degradation (i.e., between cycle degradation), suggesting that in many cases cyclic degradation can be neglected.
- Pinching and other forms of stiffness degradation were found to not have a significant impact on the collapse capacity relative to the capacity boundary and in-cycle degradation.

FEMA P-2012 (FEMA, 2018) studied the seismic performance of buildings with configurations irregularities. While many complex models were used in that study, SDOF models were also used to support a parametric study of torsionally irregular buildings. The calibration of the SDOF models was similar to the calibrations performed in Appendix E as part of the current work. A mode shape representative of the deformed shape of the building near collapse was used to transform the backbone behavior of systems from an MDOF to an SDOF space. The median collapse spectral acceleration of the SDOF models compared well with their MDOF baselines. Then the SDOF models were used to expand the range of parameters studied. As described below, this is the approach adopted here to generate collapse surface data for BRBFs, SMFs, and DCWs.

Approach. The approach for developing and utilizing eSDOF models to generate collapse surfaces for interrogation with regards to collapse risk in regions of very high seismicity is outlined here.

- Select common systems used in very high seismic regions.
- Gather data from detailed numerical models used in previous studies.
- Develop eSDOF models that can simulate, to a reasonable extent, the collapse behavior of selected systems.
- Generalize the behaviors and eSDOF model inputs to broaden the scope of the numerical studies. Of primary importance is to vary the strength of the systems and consider how other behaviors may vary with strength.
- Identify the limitations of the modeling approach for each system and discuss the impact of modeling simplifications on collapse behavior.
- Use incremental dynamic analysis and the FEMA P-695 ground motions to quantify collapse.
- Develop collapse surfaces for systems with different characteristics.
- Use the generated collapse surfaces and the overstrength recommendations from Chapter 2 to generate *ACMR* and probability of collapse in terms of S_{MT}. Note that overstrength is not a property of the backbone curves for the eSDOF systems and that it is applied after the surface is generated. Section 5.6 describes the application of overstrength in computing the *ACMR* and probability of collapse in terms of S_{MT} for each system.

It should be emphasized that eSDOF models differ from traditional SDOF models. An eSDOF model is created based on the results of a nonlinear MDOF model. An eSDOF model translates the detailed model's collapse failure mode, system pushover curve, period, and force and displacement relation into a nonlinear SDOF model that, as will be shown, accurately represents the MDOF model collapse

performance trends. This approach is appropriate for MDOF models with collapse controlled by a single dominate collapse mode, which is the case for the systems investigated here.

Appendix E contains details on the development and validation of eSDOF models for all baseline models considered.

System Selection for Model Development and Validation. This study was focused on new buildings that are designed and built in areas of very high seismicity. Therefore, the selection of baseline systems for the development and validation of eSDOF models was limited to those systems most common in such areas. Chapter 4 presents collapse surfaces for wood light-frame buildings, which are by far the most common structural system. The other systems of interest are BRBFs, SMFs, and DCWs. Three primary references were selected for obtaining model characteristics and collapse performance data for validation of developed eSDOF models. For BRBFs, a thesis from the University of Illinois (Ochoa, 2017) is used because it describes a detailed investigation exploring several BRBF archetypes using a well-vetted detailed computational model (Zaruma and Fahnestock, 2018, provides a succinct summary of that work). For SMFs, the work described in FEMA P-2012 (FEMA 2018) is referenced, in particular the detailed computational models and collapse results for the baseline SMFs in that study. Finally, for DCWs, the work by Tauberg, Kolozvari, and Wallace (2019) is referenced, which uses detailed computational models to investigate the collapse performance of a series of archetypes.

5.3 Development of eSDOF Models for Selected Systems

Appendix E describes in detail the process of developing eSDOF models and provides the complete validation of the eSDOF models used for the selected systems. A brief outline of the process and the results for key validation studies are provided here:

1. The equations of ASCE/SEI 7 Chapter 18 are used to move from an MDOF space to an eSDOF space.
2. The displaced shape of the structure under consideration at large deformations is normalized by the roof displacement and used as the mode shape for transformation to eSDOF space.
3. The pushover curve is used to develop “backbone” properties of the eSDOF.
4. If the referenced literature indicates the possibility for reasonable designs to have substantially different backbone response those differences are considered by developing multiple “families” having different backbones for that structural system.
5. Hysteretic behavior, including deterioration, appropriate for each structural system of study is selected.
6. Limitations for each group eSDOF models are identified.
7. Incremental dynamic analysis is performed on the eSDOFs and the results are transformed back into to MDOF space using the equations of ASCE/SEI 7 Chapter 18.

Collapse data from detailed models of the three systems considered were gathered from the literature. For selected archetypes from those studies, eSDOF models were developed. Collapse analyses were performed using incremental dynamic analysis on the eSDOF systems. The resulting median spectral accelerations at collapse compared well with the data from the detailed MDOF models in the literature, as shown in Table 5-1, which summarizes the values from Appendix E. Most eSDOF models produce median collapse spectral accelerations within 10% of the values from the MDOF models in the literature with only one exceeding that threshold but remaining within 15%. Importantly, this comparison of eSDOF results with the results from detailed models suggests that by capturing the key behaviors of the system (i.e., the backbone curve, the average displaced shape at large deformations, the cyclic deterioration, and the hysteretic response) the eSDOF models are capable of approximating the median collapse spectral acceleration of the systems. Notably, the collapse criteria used in the MDOF studies was also used, as closely as possible, in the eSDOF models used to validate the process and generate the results in Table 5-1. Notably, a maximum of 5% story drift was used for the BRBFs, the IDAs for the SMFs were allowed to reach a plateau, and the DCWs were limited to 3% roof drift. In the analyses described in the sections below, those criteria are somewhat modified.

Table 5-1 Median Spectral Acceleration at Collapse from MDOF Models in the Literature and eSDOF Models as Derived in Appendix E

System	Archetype Name in Reference	$\hat{S}_{CT}$ from MDOF (g)	$\hat{S}_{CT}$ from eSDOF (g)
BRBFs, MDOF Results from Ochoa (2017)			
4-Story BRBF	BRBF4-2	1.22	1.19
9-Story BRBF	BRBF9-2	0.65	0.63
15-Story BRBF	BRBF15-2	0.52	0.44
SMFs, MDOF Results from FEMA (2018)			
3-Story SMF	V0300203(1)	2.59	2.39
9-Story SMF	V0900201(1)	0.74	0.73
DCWs, MDOF Results from Tauberg et al. (2019)			
8-Story DCW	8H-*DR*-3.0	1.95	1.77
12-Story DCW	12H-*DR*-3.0	1.39	1.42
18-Story DCW	18H-*DR*-3.0	1.02	1.09

5.4 Generalized eSDOF Model Parameters

After completing validation of the eSDOF concept for the selected structural systems, sets of generalized model parameters were selected for representing each system with the goal of

generating collapse surfaces. In all cases, the systems are represented using nonlinear behaviors available in *OpenSees*. These nonlinear behaviors, known generally as Ibarra-Medina-Krawinkler models, use a trilinear backbone response shown in Figure 5-1 and can also include various forms of deterioration and hysteretic rules. In the figure, the yield force and displacement are denoted V_p and Δ_p, the capping force and displacement are denoted V_{pc}, and Δ_{pc}, the ultimate displacement is denoted Δ_u, the elastic stiffness is denoted K_e, the post-yield stiffness is denoted K_p, and the post-capping stiffness is denoted K_{pc}. This section describes the baseline values of these parameters and their variation for the parametric study of each system considered. It also describes the hysteretic behavior adopted for each system and the limitations of each eSDOF model.

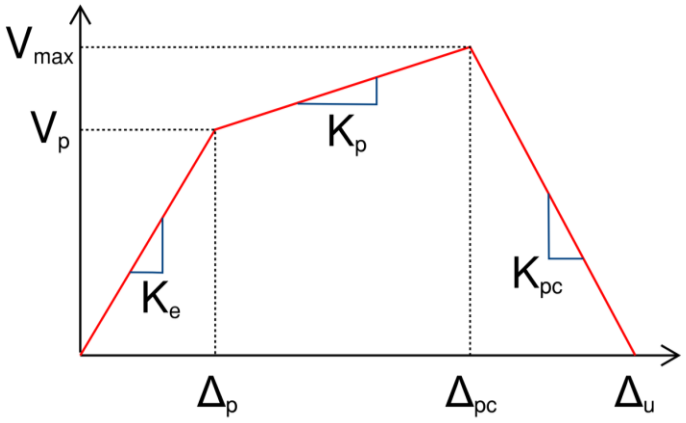

Figure 5-1 Generic backbone response for eSDOF models.

In addition to the backbone response, the development of eSDOF models requires the deformed shape of the structure at large displacements, preferably after peak strength and from a pushover analysis conducted per FEMA P-695. This deformed shape is then normalized by the roof displacement to create what is termed here to be the "pushover mode shape" of the structure. It is assumed in the eSDOF model development and interpretation of results that the building is always in this pushover shape at large displacements until collapse.

5.4.1 BRBF eSDOF Models

SDOF models representing 4-, 9-, and 15-story BRBFs were developed from the models in Ochoa (2017). The best performing BRBF models (denoted with a -3 in the study for each story height) included the nonlinear behavior of the braces, frame action within the BRBFs with weak axis column bending and the stiffness contribution from the gravity frame. It was also deemed important to consider BRBFs with columns oriented for strong axis bending within the BRBF in tandem with the gravity frame columns. This combination was not considered in Ochoa (2017) and instead the properties of this system were constructed using the response of other archetypes in that study as described below.

Table 5-2 below shows a description of the baseline eSDOF models considered in this study. The A and B models represent two "families" of BRBF behavior that are approximated here with eSDOF models: one where columns in the BRBF are oriented for weak axis bending and one where they are

oriented for strong axis bending. In both cases, the contribution of the gravity columns to the nonlinear response is included. As shown, the Family A models are derived directly from the - 3 archetypes in Ochoa (2017) while the Family B models are generated as described below.

Importantly, the archetype structures in Ochoa (2017) were not redesigned in detail and the only difference was the approximation of the impact of column orientation within the BRBF. Thus, the baseline designs should be considered as having been designed for the design base shear and using design methods used by Ochoa (2017) and detailed in Appendix E. Design values for base shear and seismic weight for these designs are given in Table E-2 in Appendix E.

Table 5-2 BRBF Baseline eSDOF Models and Components that are Included in Backbone Response

Baseline Model Name	Archetype and Model from Ochoa (2017)	System Components Included in Approximate Response
BRBF-4-A	BRBF4-3	BRBs, frame action of BRBFs with weak axis columns, gravity columns
BRBF-4-B	N.A.	BRBs, frame action of BRBFs with strong axis columns, gravity columns
BRBF-9-A	BRBF9-3	BRBs, frame action of BRBFs with weak axis columns, gravity columns
BRBF-9-B	N.A.	BRBs, frame action of BRBFs with strong axis columns, gravity columns
BRBF-15-A	BRBF15-3	BRBs, frame action of BRBFs with weak axis columns, gravity columns
BRBF-15-B	N.A.	BRBs, frame action of BRBFs with strong axis columns, gravity columns

The results for the other archetypes presented in Ochoa (2017) were studied to approximate the response of a BRBF building with the same layout and sizes as those in the original study, but that also includes the BRBF columns bending about their strong axis along with the gravity frame columns participating in the response. Table 5-3 presents the complete list of non-dual system BRBF models studied from Ochoa (2017). It was found that both strong axis BRBF columns and gravity columns change the fundamental behavior of the system. The behavior changed by: (i) slightly increasing the maximum strength, and (ii) more evenly distributing drift demand over more stories than had been engaged without those contributions to stiffness. This second point is essentially a consideration of the benefits of the spine effect that stiff columns provide. Point (ii) is critical as it allows for an increase in the total deformation of the system (i.e., the roof drift), and it reduces the magnitude of the negative slope (K_{pc}) due to P-delta effects after BRB fracture because more stories are reaching large deformations.

Figure 5-2 shows the story drift profile of the 9-story BRBFs at δ_u from pushover analysis as defined by FEMA P-695. The BRBF9-1 model, which has weak axis column bending in the BRBF and no modeled gravity frame columns, has a clear single soft story. In contrast, the BRBF9-2 and BRBF9-3 models, which have strong axis BRBF columns and consider the gravity frame columns, respectively, have large drift distributed over more stories. By adapting the criterion from ASCE/SEI 7 where a story is considered soft when its stiffness is less than 60% of the adjacent stories, one can infer that only those stories with a drift of 60% of the maximum story drift will participate in the sidesway collapse mechanism. This maximum corresponds to stories with drift above approximately 3% in the figure below. The BRBF9-1 model has two stories that may participate in the collapse mechanism while the BRBF9-3 model has four. So, to develop Family B of the BRBF eSDOFs, which include both strong axis bending of the BRBF columns and the gravity columns, the more uniform distribution of drift demand along the height of the structure is considered. The process by which the story drift profile is more evenly distributed is detailed next.

Table 5-3 Selected BRBF Archetypes and Models from Ochoa (2017).

Archetype (Ochoa 2017 designation)	No. Stories	Notes for numerical model in Ochoa (2017)
BRBF4-1	4	▪ BRBF columns in weak axis bending; No gravity columns modeled
BRBF4-2	4	▪ BRBF columns in strong axis bending; No gravity columns modeled
BRBF4-3	4	▪ BRBF columns in weak axis bending; Gravity columns modeled
BRBF9-1	9	▪ BRBF columns in weak axis bending; No gravity columns modeled
BRBF9-2	9	▪ BRBF columns in strong axis bending; No gravity columns modeled
BRBF9-3	9	▪ BRBF columns in weak axis bending; Gravity columns modeled
BRBF15-1	15	▪ BRBF columns in weak axis bending; No gravity columns modeled
BRBF15-2	15	▪ BRBF columns in strong axis bending; No gravity columns modeled
BRBF15-3	15	▪ BRBF columns in weak axis bending; Gravity columns modeled

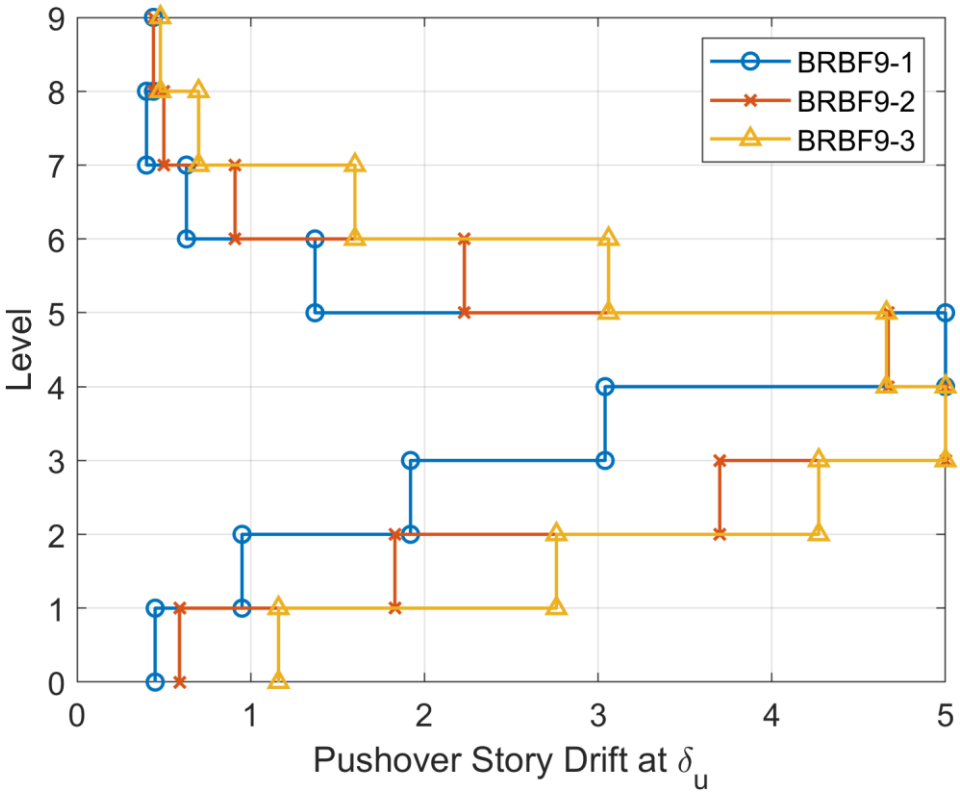

Figure 5-2 Displacement profile for 9-Story BRBFs from Ochoa (2017).

Development of BRBF A and B Baseline Backbone Behaviors

The following steps were taken to develop the pushover mode shape and the backbone curves for the baseline Family B eSDOF models:

1. Pushover curves and displacement profiles at δ_u from Ochoa were digitized for all models in Table 5-3.
2. V_p and Δ_p of Family B baseline models are taken as the same as the other models because the braces are the same and they dominate strength and stiffness before yield.
3. It was observed from Ochoa that most models have a maximum story drift of 5% at δ_u in pushover analysis. Thus, the drift profiles were all normalized (i.e., scaled) so that they all had a maximum story drift of 5%.
4. The approximate drift profile for Family B baselines at the three different building heights was created by adding to the drift profile of the BRBF-1 archetype. Two contributions were added to capture the two desired sets of behavior:
   a) The contribution of strong axis BRBF column bending to drift capacity was considered by adding the difference between the BRBF-2 and BRBF-1 drift profiles.

b) The contribution of the gravity frame to drift capacity was considered by adding the difference between the BRBF-3 and BRBF-1 drift profiles.

c) A limit of 5% story drift was imposed, regardless of how much the differences in (a) and (b) could have supplied.

d) The result for the 15-story BRBF is shown in Figure 5-3 below. These story drift profiles were then converted into displacements and normalized by the roof drift to produce the pushover mode shape for the Family B baselines.

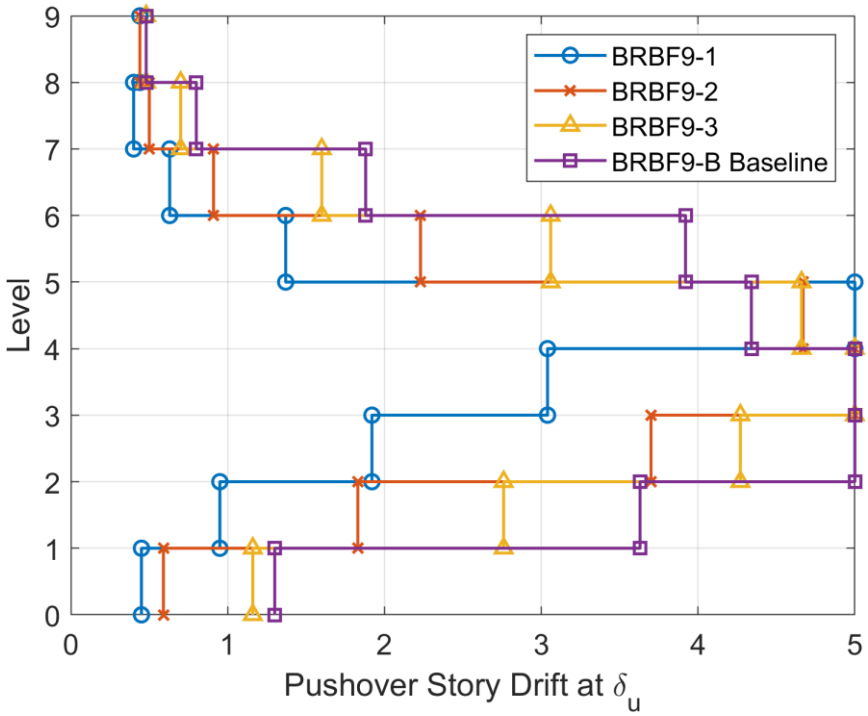

Figure 5-3 Story drift profile for BRBFs from Ochoa (2017) and that approximated for baseline BRBF-15-B.

5. The new drift profile developed in step 4 was used to calculate Δ_{pc} as the roof displacement value when the maximum story drift is 5%.

6. V_{pc} was calculated using the Δ_{pc} from step 5 and K_p from the corresponding Family A baseline. The post-yield slope was found to be largely the same between the BRBF-1, BRBF-2, and BRBF-3 models for a given building height.

7. Finally, K_{pc} was estimated by considering the negative P-delta stiffness provided only by the stories forming the collapse mechanism. A story was considered to participate in the collapse mechanism if it reached 60% of the maximum story drift in the profile at δ_u, per the ASCE/SEI 7 criterion detailed above. To estimate a negative P-delta stiffness it was assumed that all the deformation during collapse was localized only to those stories exceeding the threshold because the stories not involved in the mechanism are likely to unload as the base shear reduces. The ratio of this calculated P-delta stiffness to K_{pc} for the -3 model from Ochoa (2017) was then used to scale the K_{pc} for the -3 and Family B baselines. Note that because the pushover curves in the

Ochoa (2017) were terminated before reaching zero base shear in several cases, it was not possible to use the -3 model to do this scaling in all cases.

The resulting trilinear approximations for the Family B eSDOF baselines are shown in Figure 5-4 along with the pushover data provided in Ochoa (2017) and the trilinear fits of the Ochoa pushover curves. As shown, the Family A backbone responses match the -3 models from Ochoa (2017) reasonably well and are shown with K_{pc} projected to zero strength. Note that in Figure 5-4, the Family A eSDOF backbone is given as the trilinear estimation of BRBF4-3 from Ochoa (2017). The Family B backbone curves reach a larger roof drift at capping and at zero strength and have somewhat reduced post-capping degradation (i.e., a less negative K_{pc}) providing a reasonable approximation of the impact of strong axis column orientation within the BRBF. Table 5-4 shows the final pushover mode shapes for both BRBF eSDOF families that are used as described in Appendix E to translate from MDOF to eSDOF space for approximation of roof drift and drift at the story controlling collapse.

Table 5-4 Final Pushover Mode Shapes for BRBF Models

Story	BRBF 4A Story Drift (%)	BRBF 4B Story Drift (%)	BRBF 9A Story Drift (%)	BRBF 9B Story Drift (%)	BRBF 15A Story Drift (%)	BRBF 15B Story Drift (%)
1	0.24	0.33	0.67	0.67	0.02	0.02
2	0.55	0.57	0.18	0.20	0.05	0.05
3	0.83	0.81	0.36	0.39	0.12	0.12
4	1.0	1.0	0.57	0.58	0.21	0.22
5			0.76	0.74	0.35	0.34
6			0.89	0.88	0.50	0.47
7			0.95	0.95	0.64	0.61
8			0.98	0.98	0.76	0.74
9			1.0	1.0	0.83	0.83
10					0.87	0.88
11					0.90	0.91
12					0.93	0.94
13					0.95	0.96
14					0.98	0.99
15					1.0	1.0

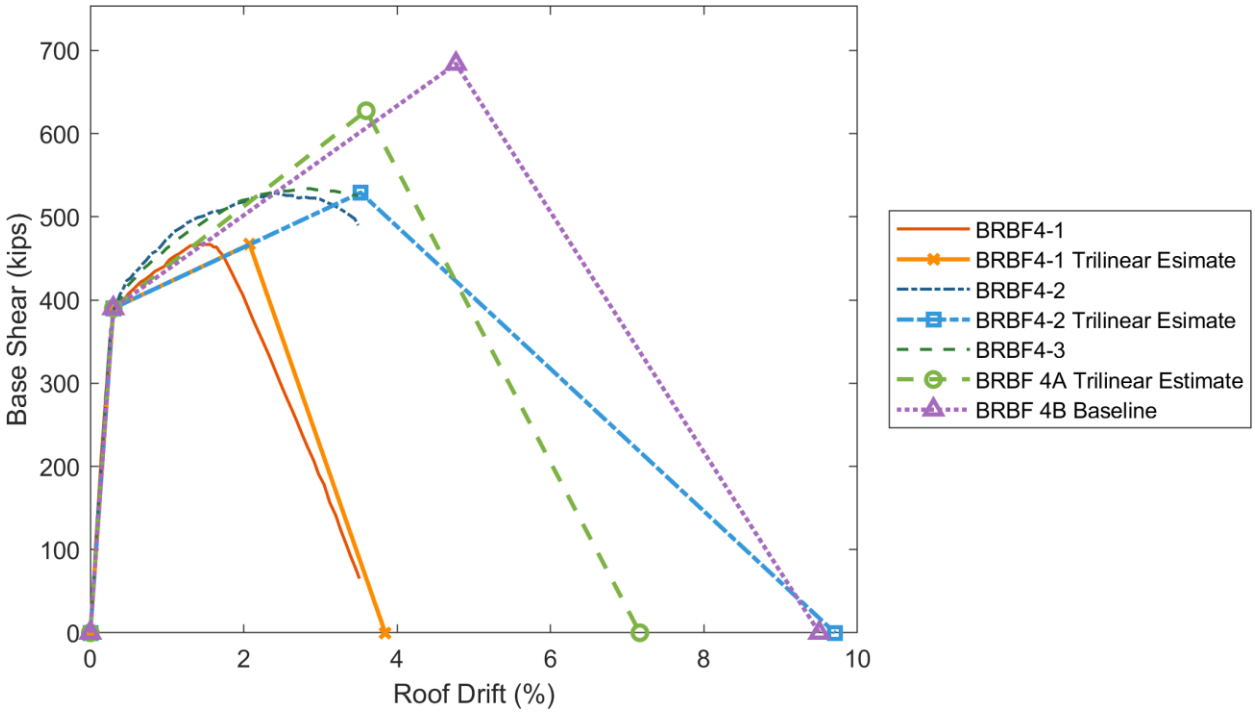

(a) 4-Story BRBFs

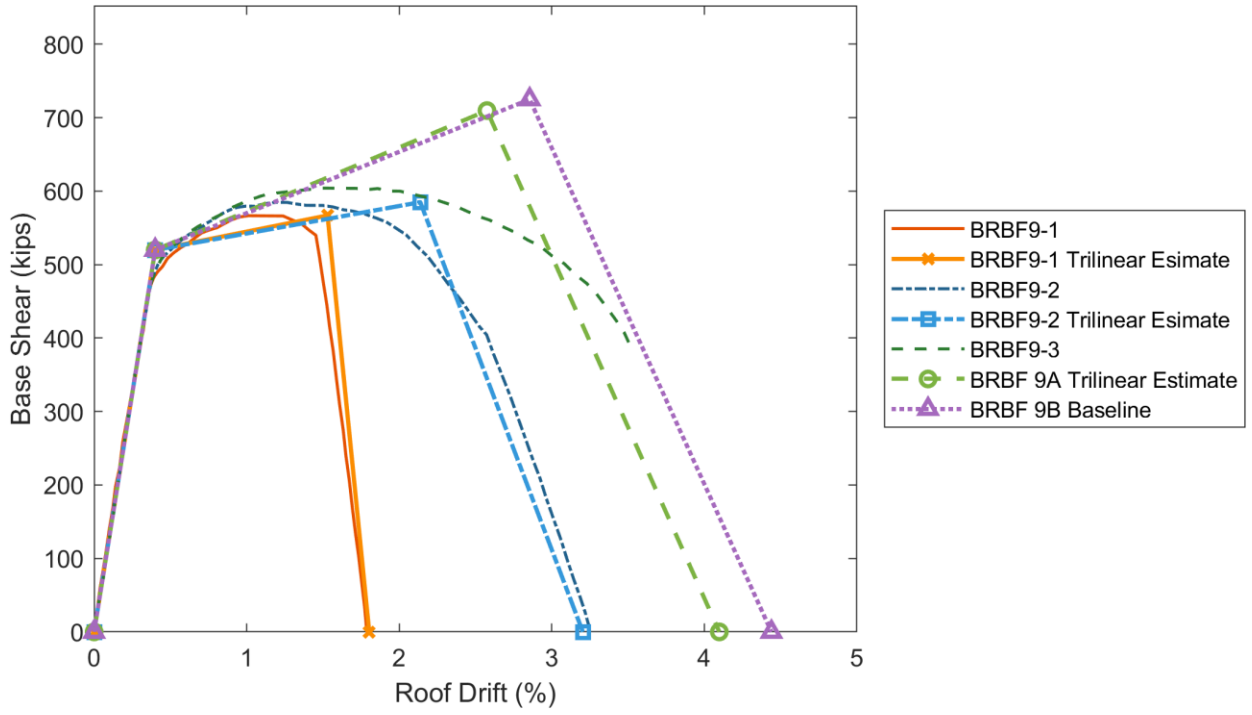

(b) 9-story BRBFs

Figure 5-4 Comparison of pushover curves from Ochoa (2017), trilinear fits, and the baseline Family B backbone curves.

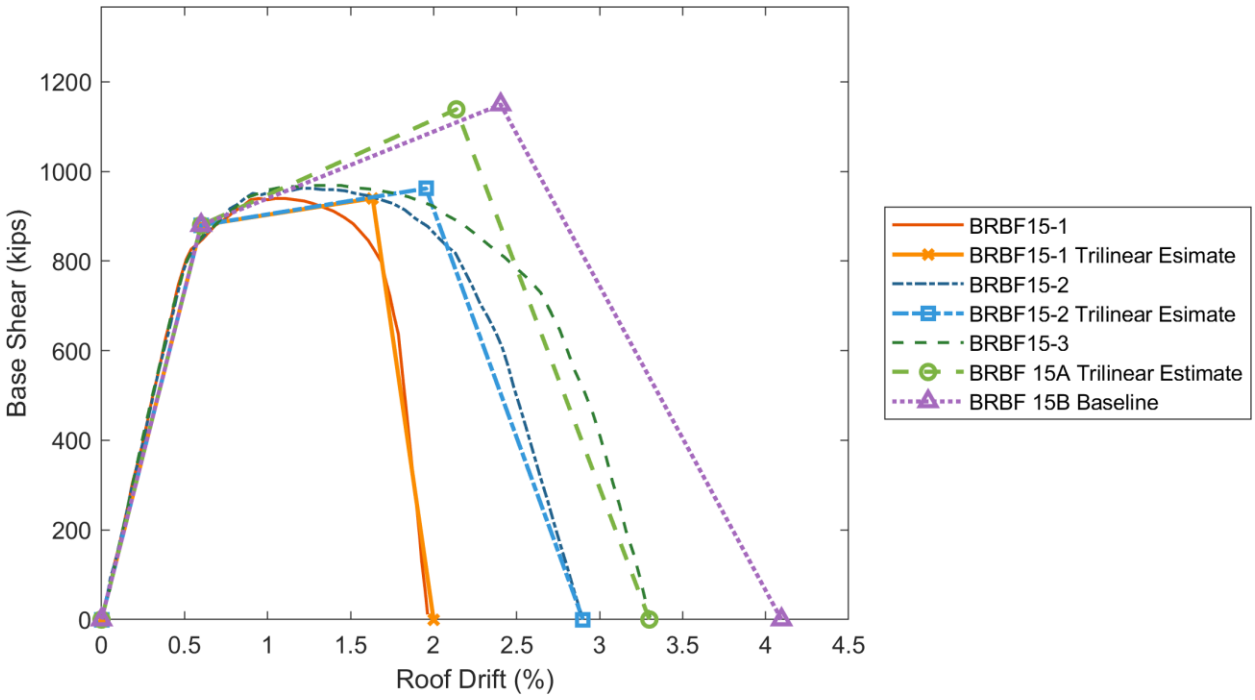

(c) 15-story BRBFs

Figure 5-4 Comparison of pushover curves from Ochoa (2017), trilinear fits, and the baseline Family B backbone curves. (continued)

Development of BRBF A and B Backbone Families

In the referenced study by Ochoa (2017), strain hardening for the BRBs in the MDOF model was simulated using ultimate brace strengths derived from large-scale test data in Fahnestock (2007). Since that work, CoreBrace has compiled strain hardening from thousands of BRB tests as described in Chapter 2. The final modification of the baseline Family A and B models is therefore to update their post-yield stiffness using the BRB strain hardening data presented in Chapter 2. Figure 5-5 shows the comparison between the BRBF strain hardening used in Ochoa (2017) and that based on the CoreBrace data as described in Chapter 2 for both BRBs in tension and compression. As shown, there is a significant difference. In order to include this in the baseline models for Family A and B eSDOF BRBFs the following steps were taken:

1. The strain hardening ratio at 2.5% strain was calculated for the both the BRB model used by Ochoa (2017) and that provided by CoreBrace. The strain hardening ratio is the current stress divided by the yield stress and was computed separately for tension and compression.
2. The strain hardening ratios for tension and compression were then averaged separately for the Ochoa (2017) BRB model and the CoreBrace model.
3. The post-yield stiffness, K_p, for both the Family A and B baseline models was then increased by the strain hardening from the CoreBrace model divided by the strain hardening ratio from the model used by Ochoa (2017).

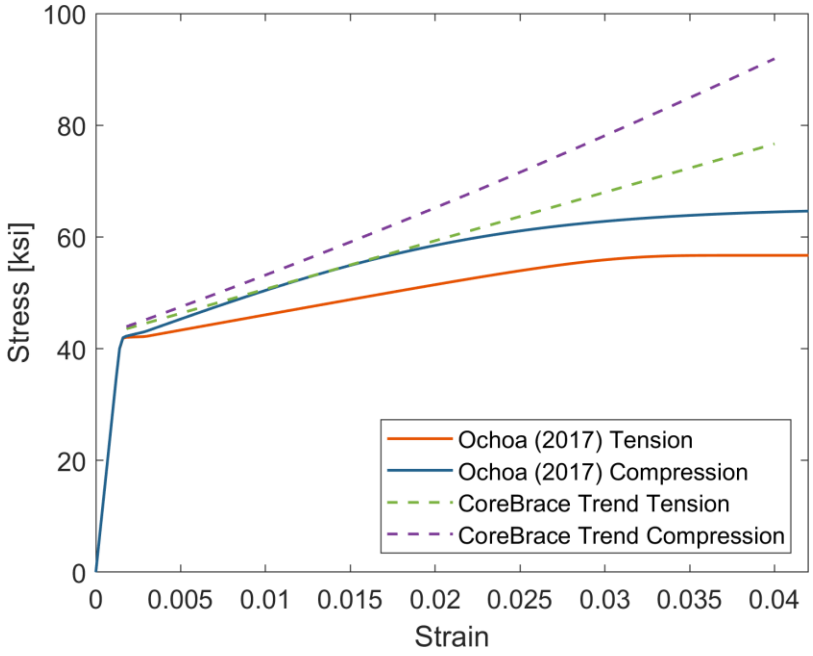

Figure 5-5 BRB stress-strain behavior used in Ochoa (2017) compared with the strain hardening data provided by CoreBrace.

After developing the pushover mode shapes and backbone curves for the Family A and B baselines BRBFs for each story height, the strength of the baseline models is scaled to create a family of backbones from which are used to generate collapse surfaces. Scaling the strength represents using BRBFs with larger and smaller cross-sections. In scaling the strength, it is important to assess what other parameters of the baseline backbone response should change as many of those parameters are directly tied to the strength (or seismic weight) of the system.

The following rules were implemented to modify each backbone point in relation to the changes in strength when generating the complete family of eSDOF models to represent BRBFs at each building height.

1. For each building height, the Family A and B baseline models serve as the anchors for two families of BRBFs. Family A represents weak axis column bending in the BRBF with gravity frame columns included in the response, and Family B represents strong axis column bending in the BRBF with gravity frame columns included in the response. For all baselines, the effect of strain hardening in the BRBs was increased to represent the data provided by CoreBrace as described above.
2. The initial elastic stiffness and yield strength are scaled proportionally because both quantities represent changes in BRB cross sectional area.
3. Δ_{pc} is kept the same for the entire family. This is because each family has a unique pushover mode shape that is assumed to be independent of strength. In all cases, Δ_{pc} is the roof drift when the maximum story drift is 5%. However, K_p does change as it is largely a result of BRB strain hardening and is proportional to BRB cross sectional area, as are strength and initial stiffness.

The ratio of K_p to K_e in the baseline models is used to calculate the K_p in each new backbone from the scaled K_e. This slope, along with the set $\Delta_{pc,}$ gives a capping strength, V_{pc}.

4. K_{pc} scales with changing W because the P-delta effects are expected to scale linearly with changes in the seismic weight. But a limit on roof drift is enforced, even if stronger models could theoretically have more resistance to P-delta effects.

Figure 5-6 shows the resulting backbone curves for each family for the 4-, 9-, and 15-story BRBFs. Values for strength parameters are normalized by the seismic weight, W, stiffness parameters are given as V/W per unit roof drift, and displacements are given as roof drifts. Note that the backbone curve overlaid with a black dashed line indicates the backbone that most closely represents the backbone from the original MDOF study. The backbones overlaid with a black dotted line most closely match the eSDOF model with a strength corresponding to SDC D_{max} for R = 8 and with overstrength as recommended in Chapter 2. The key values for the curves corresponding to SDC D_{max} are given in Table 5-5.

Table 5-5 BRBF Backbone Curve Parameters for Models with a Strength Corresponding to SDC D_{max} for R = 8 and with Overstrength as Recommended in Chapter 2 (Ω = 2.5)

Model	V_p/W	V_{max}/W	Δ_p (Roof Drift %)	Δ_{pc} (Roof Drift %)	Δ_u (Roof Drift %)
BRBF 4A	0.14	0.23	0.3	3.6	7.2
BRBF 4B	0.14	0.23	0.3	4.8	9.5
BRBF 9A	0.09	0.12	0.4	2.6	5.1
BRBF 9B	0.09	0.12	0.4	2.8	5.7
BRBF 15A	0.06	0.08	0.6	2.1	3.8
BRBF 15B	0.06	0.08	0.6	2.4	4.8

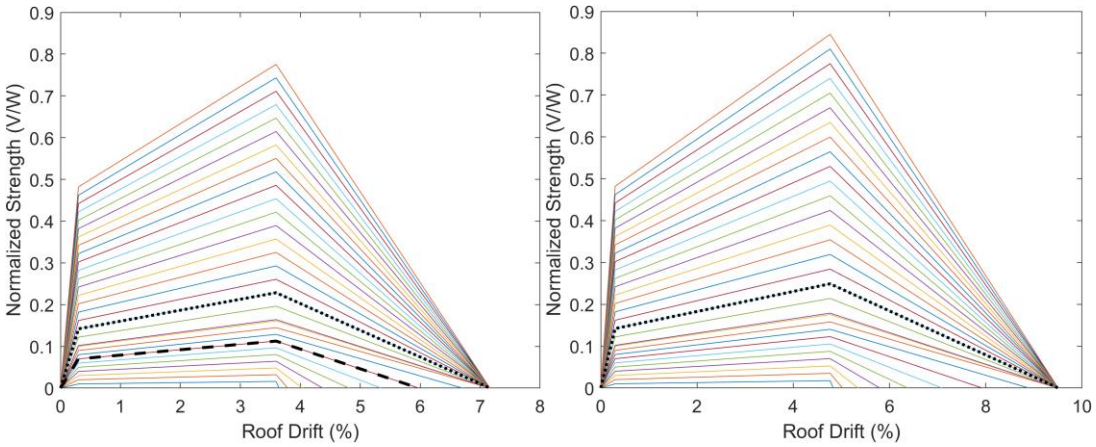

(a) 4-Story Family A backbone curves **(b) 4-Story Family B backbone curves**

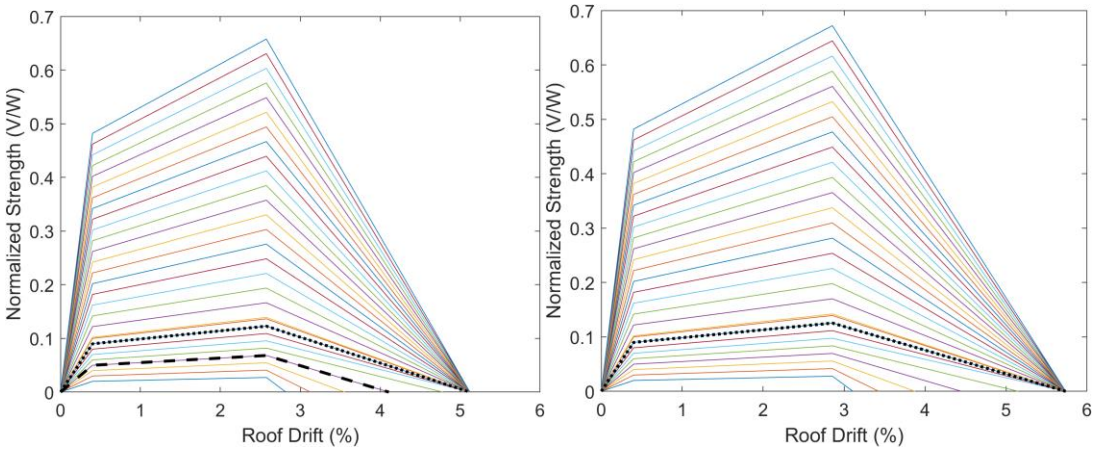

(c) 9-Story Family A backbone curves **(d) 9-Story Family B backbone curves**

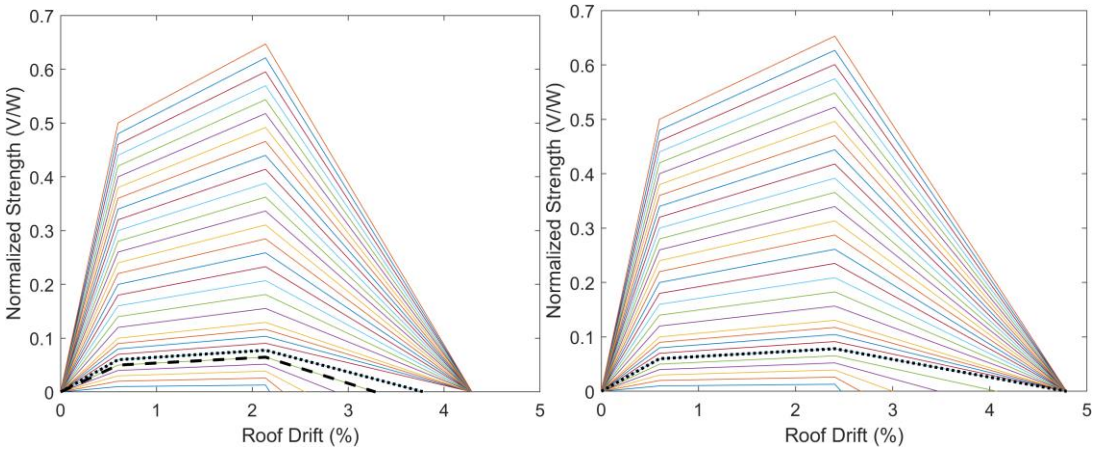

(e) 15-Story Family A backbone curves **(f) 15-Story Family B backbone curves**

Figure 5-6 BRBF backbone curves for the 9-Story BRBFs for Family A (weak axis BRBF columns and gravity columns) and Family B (strong axis BRBF columns and gravity columns).

After developing these families of BRBFs, each backbone was converted to an eSDOF backbone using its pushover mode shape as described in Appendix E. Incremental dynamic analysis was performed on the eSDOFs and the results were converted back into MDOF space again using the pushover mode shape.

Discussion of BRBF eSDOF Modeling Limitations

It is important to note some key limitations for the families of eSDOF models of BRBFs and their potential impact on response:

1. Models of different strengths were not redesigned and instead strength was scaled and other backbone properties were modified as described above. Therefore, the models and results should not be used to interpret the impact of code design parameters such as *R* as they do not reflect models of detailed archetypes.
2. Strain hardening values provided by BRB manufacturers are substantially larger than those used in Ochoa (2017). The values are appropriate for defining the backbone response but may overestimate the post-yield stiffness after inelastic cycling, which would result in unconservative estimates of collapse capacity across all models (i.e., larger collapse capacities than that achieved with a model with less strain hardening). However, this would not prevent the models from revealing trends related to collapse capacity versus S_{MT}.
3. The story and roof drift at capping may decrease with increasing strength as larger capacity BRBs require larger gusset plates and may have shorter brace lengths. This was not included here as the capping drift was constant regardless of strength because detailed designs were not done. Reducing the capping drift with increasing BRBF strength would reduce the collapse spectral acceleration for those models.
4. The pushover mode shapes are derived from models using smaller-than-expected BRB strain hardening. It is expected that increasing the strain hardening would better distribute the drift demand and increase the roof drift at capping. This would increase the estimates of BRBF collapse capacity but was not included here.
5. Only a small amount of cyclic deterioration was considered. Additional deterioration would decrease the collapse capacity of the eSDOF models. Deterioration may result from local buckling of beams and columns within the BRBF and also from local yielding and weld fractures in the BRB connection region.
6. The selected archetypes from Ochoa (2017) that were used to generate the baseline eSDOF properties were designed for Risk Category II. Therefore, the may not be representative of risk Category IV structures, especially because the drift limit for such structures is smaller.

5.4.2 SMF eSDOF Models

The baseline eSDOF models of SMFs are derived from archetype designs and models used in FEMA P-2012 (FEMA, 2018) for 3- and 9-story SMFs. That study was focused on the effects of irregularities, but the authors developed baseline regular SMF models for comparison. These regular

baseline models were designed to replace the 3- and 9-story SMFs originally developed for the SAC Project (FEMA, 2000). The archetype designs, their configurations, design approach, design parameters, detailed modeling considerations, and collapse analysis results selected from FEMA P-2012 to be the baselines for the eSDOF models here are summarized in detail in Appendix E. Notably, the models used in collapse analysis in FEMA P-2012 considered only the moment frames and neglected gravity frame response.

Appendix E also discusses the validation of the approach for modeling SMFs with eSDOF systems and demonstrates good agreement between the median spectral acceleration at collapse, $\hat{S}_{CT}$, for the complex MDOF models used in FEMA P-2012 and the eSDOF models used here. Like the BRBF eSDOF models described above, modifications were made to the eSDOF models for SMFs to account for behaviors not considered in the FEMA P-2012 study. Again, two families of SMF eSDOF models were developed. The first, Family A, considers only the moment resisting frame and neglects the impact of the gravity frame completely and corresponds directly to the selected archetype in FEMA P-2012. Family B considers the impact of the gravity frame on the system response, which results in larger post-yield stiffness, more uniform distribution of drift demands, and larger roof drift at zero lateral strength.

To create the baseline Family B backbone curve, a study by Flores et al. (2014) was reviewed. That study considered the impact of the gravity frame response on 4- and 8- story SMF nonlinear static response. Flores et al. (2014) used the SMF archetypes from NIST 10-917-8 (NIST, 2010) whose analyses considered only the SMF response. For those archetypes, Flores (2014) added gravity frame models that considered gravity frame connections having 35%, 50% and 70% of the gravity framing beam's plastic moment strength and included the actual gravity column stiffness.

The analyses by Flores et al. (2014) showed that considering the gravity framing increases both the initial elastic stiffness and the post-yield stiffness of the system (i.e., K_e and K_p) and that they increase by similar amounts. The increase in stiffness corresponds to an increase in strength at Δ_{pc} of the system that is the strength provided by the gravity frame connections reaching their plastic capacity.

Chapter 2 discussed the expected strength of gravity frames in SMFs. For a typical archetype building it was shown that the additional lateral strength capacity is approximately 16 psf regardless of the number of stories as derived from a simple portal frame analysis with the connections contributing a moment capacity of 35% of the gravity beam plastic flexural strength. This additional base shear capacity was added to the Family A baseline backbone curve to create the baseline Family B baseline backbone curve as illustrated in Figure 5-7. The additional strength at Δ_{pc} for the archetype models was calculated to be $0.1V_{max}/W$ for the 3-story models, and $0.035V_{max}/W$ for the 9-story models.

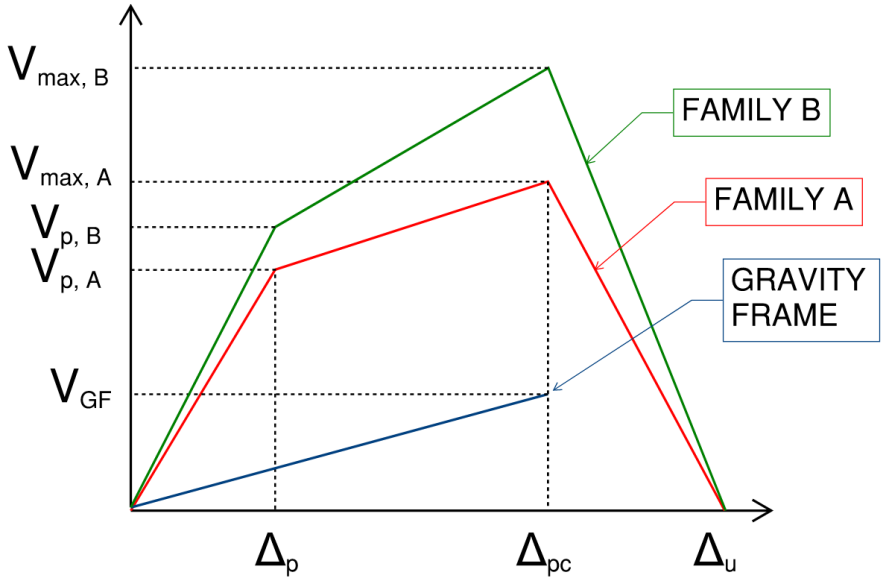

Figure 5-7 Illustration of generating the Family B SMF baseline backbone curves by adding the approximate gravity frame response to the Family A curves.

The final modification that was made to Family A to generate the Family B baseline backbone curves was to consider the impact of the gravity frame on the pushover mode shape, i.e., the distribution of story drift at large drift, near Δ_{pc}. There are no data available in the literature to determine this. Instead engineering judgement and the observations from the BRBF study above were used. Figure 5-8 shows the distribution of story drift near Δ_{pc} for the 3- and 9-story Family A SMF models that are from analysis data in the FEMA P-2012 study. The figure also shows the assumed pushover mode shape for Family B SMF models. As shown, Family B assumes a more uniform distribution of story drift. This pushover shapes, shown in Table 5-6, are used to compute the eSDOF modal properties as described in Appendix E and to compute a limit for Δ_u after scaling it up with increasing SMF strength. That limit Δ_u for both Family A and Family B SMF models corresponds to the roof drift when the maximum story drift reaches 10%.

Table 5-6 Final Pushover Mode Shapes for SMF Models

Story	SMF 3A Story Drift (%)	SMF 3B Story Drift (%)	SMF 9A Story Drift (%)	SMF 9B Story Drift (%)
1	0.26	0.33	0.16	0.15
2	0.62	0.67	0.30	0.26
3	1.0	1.0	0.44	0.38
4			0.56	0.49
5			0.66	0.59
6			0.75	0.70
7			0.84	0.80
8			0.93	0.90
9			1.0	1.0

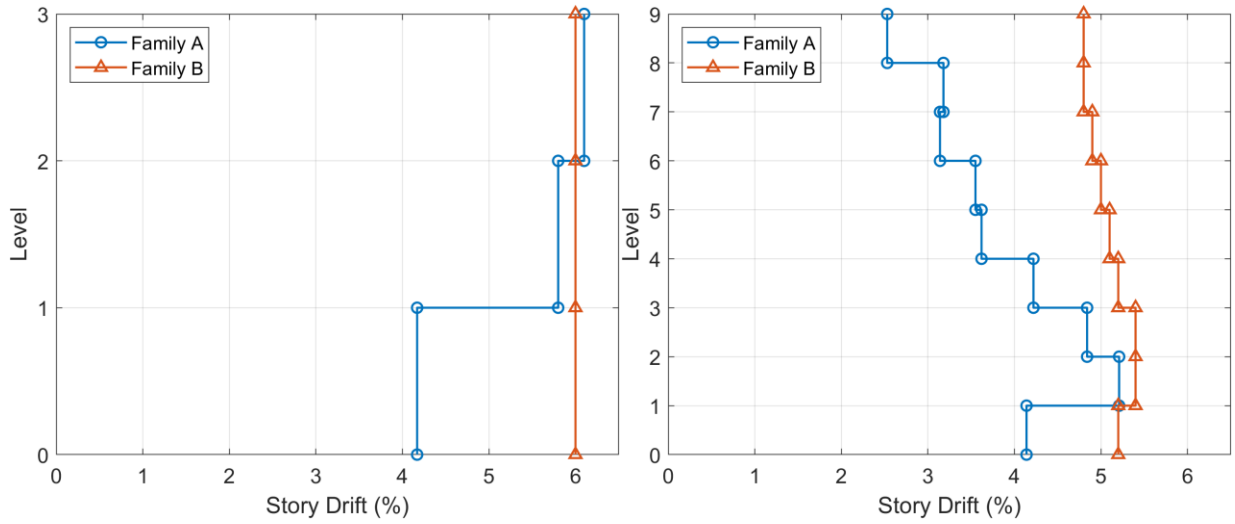

(a) 3-Story **(b) 9-Story**

Figure 5-8 Pushover mode shapes for 3- and 9-Story Family A and B SMF eSDOF models.

As noted in Appendix E, cyclic deterioration is considered in the SMF eSDOF models. The deterioration model is identical to that used for the lumped plasticity models at the beam and columns ends that were used in the detailed models in FEMA P-2012 except that it is applied to the base shear versus roof drift response. The deterioration parameter for cyclic strength deterioration, λ, is computed using the methodology established by Lignos and Krawinkler (2011a) where the deterioration is a function of the local compactness of a steel cross section. Deterioration parameters developed by Lignos and Krawinkler (2011b) and updated at a web-based database

(http://resslabtools.epfl.ch/component/) were used for the girders at the stories with the largest deformations from the analyses in FEMA P-2012 for the selected archetypes. Those deterioration parameters were the same for both Family A and B models and were λ = 68 for the eSDOFs representing the 3-story models and λ = 76 eSDOFs representing the 9-story models.

Development of SMF A and B Families

After developing the baseline eSODF backbone response for the baseline SMF structures, complete families of backbone were developed by scaling the maximum strength of the models, i.e., the value V_{max}/W. As with BRBFs, when scaling strength, it was necessary to consider the corresponding changes in other backbone parameters. The following rules were implemented to modify each backbone point in relation to the changes in strength when generating the complete family of eSDOF models to represent SMF's at each building height. The Family A backbones were generated with a process very similar to the BRBF families.

1. For each building height, the Family A baseline models again serve as the anchors family, where Family A represents only the lateral force resisting system (LFRS) in the response.
2. The initial elastic stiffness and yield strength are scaled proportionally as shown in Flores (2014).
3. Δ_{pc} is kept the same for the entire family as shown in Flores (2014). Like with the BRBFs, K_p does change: the ratio of K_p to K_e in the baseline models is used to calculate the K_p in each new backbone from the scaled K_e. This slope, along with the set Δ_{pc}, gives a capping strength, V_{pc}.
4. K_{pc} scales with changing W because the P-delta effects are expected to scale linearly with changes in the seismic weight. But a limit on roof drift corresponding to a maximum story drift of 10% is enforced, even if stronger models could theoretically have more resistance to P-delta effects.

To generate Family B backbones, the Family A backbones were modified by adding the effect of the gravity frame as described above. Each Family A backbone has a corresponding Family B backbone where the difference is adding $0.1V_{max}/W$ for the 3-story models, and $0.035V_{max}/W$ for the 9-story models. Additionally, Δ_u, for the Family B backbone curves is then modified for the pushover mode shapes shown in Figure 5-8.

Figure 5-9 shows the resulting backbone curves for each family for the 3-, 9-story SMF eSDOF models. Values for strength parameters are normalized by the seismic weight, W, stiffness parameters are given as V/W per unit roof drift, and displacements are given as roof drifts. Again, the backbones that most closely match the original MDOF models are overlaid with a black dashed line. The backbones overlaid with a black dotted line most closely match the eSDOF model with a strength corresponding to SDC D_{max} for R = 8 and with overstrength as recommended in Chapter 2. The corresponding values for the key points are provided in Table 5-7. It is important to note that the structures were not redesigned, in that no sizes for beams and columns were computed and no checks on drift limits were applied. Further, the cyclic deterioration parameter was not changed from the baseline models that were used to validate the eSDOF approach, i.e., λ = 68 for the eSDOFs representing the 3-story models and λ = 76 eSDOFs representing the 9-story models.

Discussion of SMF eSDOF Modeling Limitations

It is important to note some key limitations for the families of eSDOF models of SMFs and their potential impact on response:

1. Models of different strengths were not redesigned and instead strength was scaled as described above. Therefore, the models and results should not be used to interpret the impact of code design parameters such as *R* as they do not reflect models of detailed archetypes.
2. Deterioration was not changed when strength was scaled. It is likely that increasing the strength and corresponding girder and column section sizes would result in a decrease in deterioration with increasing strength. This would have the impact of increasing the collapse capacity of the larger strength SMFs relative to the analysis results presented below.
3. The capping point was not changed with strength. It is likely that increasing the strength and corresponding girder and column section sizes would decrease the story drift and roof drift at capping as many reports have shown a decrease in RBS connection rotation capacity with increasing section depth. This would have the impact of decreasing the collapse capacity of the larger strength SMFs relative to the analysis results presented below.
4. The selected archetypes from FEMA P-2012 that were used to generate the baseline eSDOF properties were designed for Risk Category II. Therefore, the models may not be representative of risk Category IV structures, especially in that the drift limit for such structures is smaller.

Table 5-7 SMF Backbone Curve Parameters for Models with a Strength Corresponding to SDC D_{max} for R = 8 and with Overstrength as Recommended in Chapter 2.

Model	Ω	V_p/W	V_{max}/W	Δ_p (Roof Drift %)	Δ_{pc} (Roof Drift %)	Δ_u (Roof Drift %)
SMF 3A	2.8	0.28	0.30	0.96	4.7	6.8
SMF 3B	4.1	0.32	0.42	0.96	4.7	8
SMF 9A	2.8	0.10	0.11	0.95	2.4	4.8
SMF 9B	3.7	0.12	0.15	0.95	2.4	6.3

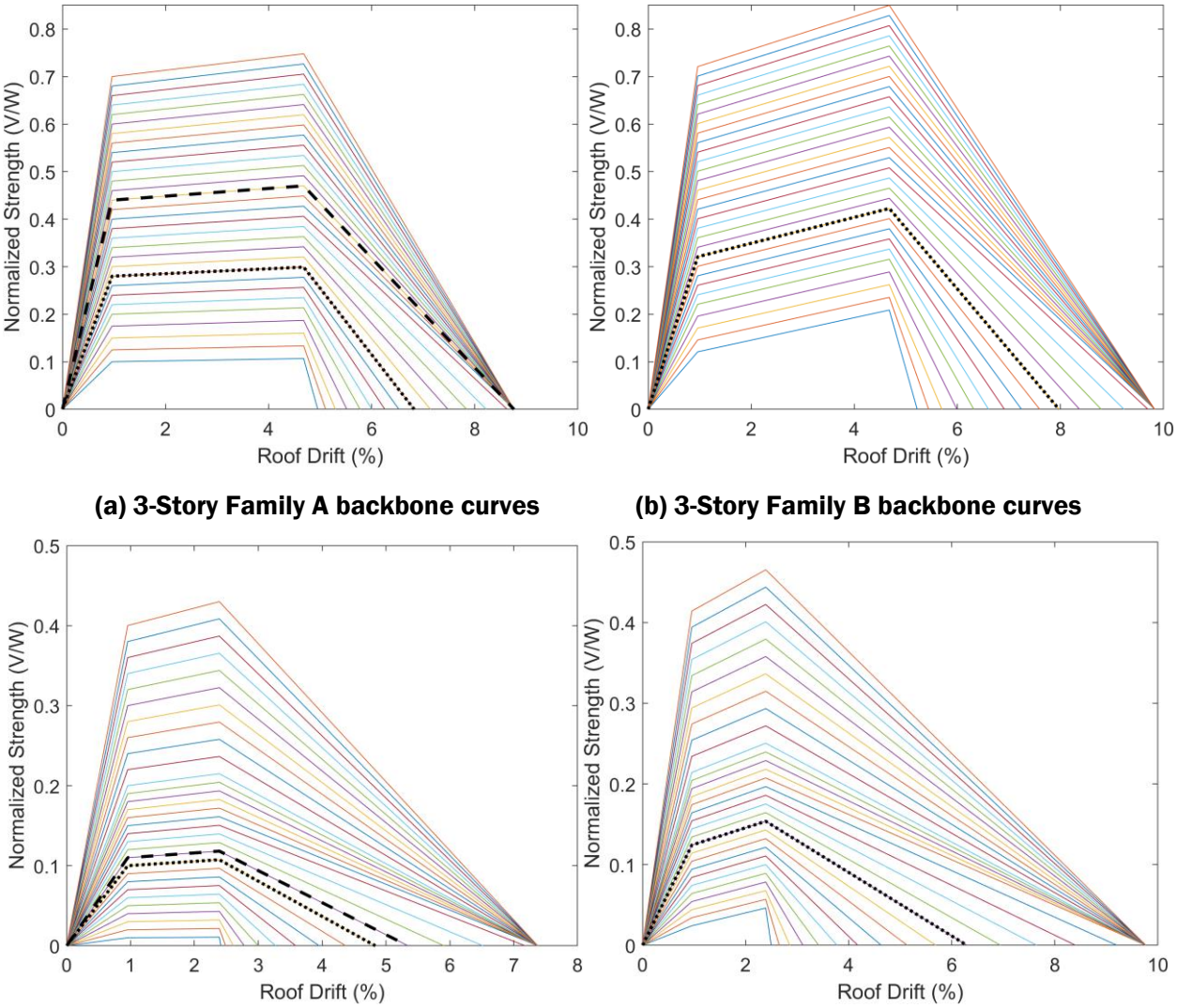

(a) 3-Story Family A backbone curves **(b) 3-Story Family B backbone curves**

(c) 9-Story Family A backbone curves **(d) 9-Story Family B backbone curves**

Figure 5-9 SMF backbone curves for the 3- and 9-Story SMFs for Family A (SMF Only) and B (SMF and Gravity Frame).

5.4.3 DCW eSDOF Models

This section discusses the development of eSDOF models for DCWs (Ductile Coupled Walls). The eSDOF baseline models are based on selected 8-, 12- and 18-story archetypes from Tauberg et al. (2019). Appendix E summarizes the designs, their configurations, design approach, design parameters, detailed modeling considerations, and collapse analysis results for archetypes from Tauberg et al. (2019) that are selected to be the baselines for the eSDOF models here. The validation of the eSDOF approach for DCWs was done for the selected baseline archetypes and is in Appendix E where the collapse analysis results are compared between models for DCWs from Tauberg et al. (2019) to the results of calibrated eSDOF collapse analyses.

The DCW models in Tauberg et al. (2019) did not consider the gravity framing and the potential impact from outriggering effects. For DCW buildings with steel gravity systems, this effect is

negligible as the stiffness of the slab on metal deck and steel gravity connections are small relative to the stiffness of the wall. However, in building with post-tensioned (PT) concrete slabs and gravity columns there can be significant additional strength provided from outriggering effects. Therefore, two families of DCW eSDOF models were developed. Family A considers the wall itself and is typical of DCW building with steel gravity framing and Family B that considers the additional strength and stiffness provided by outriggering in DCW buildings with PT floor systems. In both cases, 8-, 12- and 18- story buildings are considered. Family A is derived directly from the wall-only archetype models from Tauberg at al. (2019) that are described in Appendix E. Family B is developed from those models modified to account for the interaction of the gravity system.

The literature is sparse on the impact of outriggering on shear walls in a generic sense that may be useful for modifying the backbone behavior of the eSDOF models for DCWs in Appendix E. One unpublished study was conducted as part of the ATC-63-2/3 Project (ATC, 2013). A draft of that report was obtained by the project team and studied to help understand the impact of outriggering from the gravity framing on the overall response of reinforced concrete wall buildings. In that study, pushover and incremental dynamic analyses were conducted on 12- and 20-story models of buildings with shear walls and PT slab gravity systems. The models used were two-dimensional and considered only the in-plane contribution of the gravity system. The walls were modeled with nonlinear beam-column elements with fiber discretized cross sections that were aggregated with a nonlinear shear behavior. The PT slabs were modeled with elastic beam-elements with an effective stiffness and nonlinear hinges at their ends. The gravity columns were modeled with nonlinear beam-column elements. The results are used below to develop modifications to the baseline backbone behaviors from Tauberg et al.

Figure 5-10 shows the results of pushover analyses for the 12- and 20- story models where the models considered: (i) wall only, (ii) wall and gravity frame without outriggers, and (iii) wall and gravity frame with outriggers. The key observations from these results that pertain to modifying the backbone behavior derived for the archetypes from Tauberg et al. are:

1. The gravity frame with outriggers increase the strength and stiffness for both the 12- and 20-story models;
2. The increase in post-yield stiffness is considerably larger for the 20-story model;
3. For the 12-story model the increase in effective elastic stiffness and post-yield stiffness are proportional to the increase in strength (this was verified by digitizing the curves and computing the effective elastic stiffness and the post-yield stiffness).

Given these observations, and the fact that strength will again be scaled for the DCWs as it was for the BRBFs and SMFs, Family B baseline backbone curves for the 8-, 12- and 18-story DCW archetypes from Tauberg et al. (2019) were developed by considering a combination of different overstrength values relative to Family A and different post-yield (i.e., K_p) stiffness. For the 8- and 12- story DCWs, Family B will have a different overstrength factor from Family A. Since the strength and stiffness will be scaled to generate the complete family of backbone curves for each family and it was observed that the increase in strength and stiffness for outriggering effects was proportional, the backbones generated for Family A will contain the Family B backbone curves just offset at larger

strengths. Thus, a different overstrength factor will suffice to account for outriggering for the 8- and 12- story DCWs.

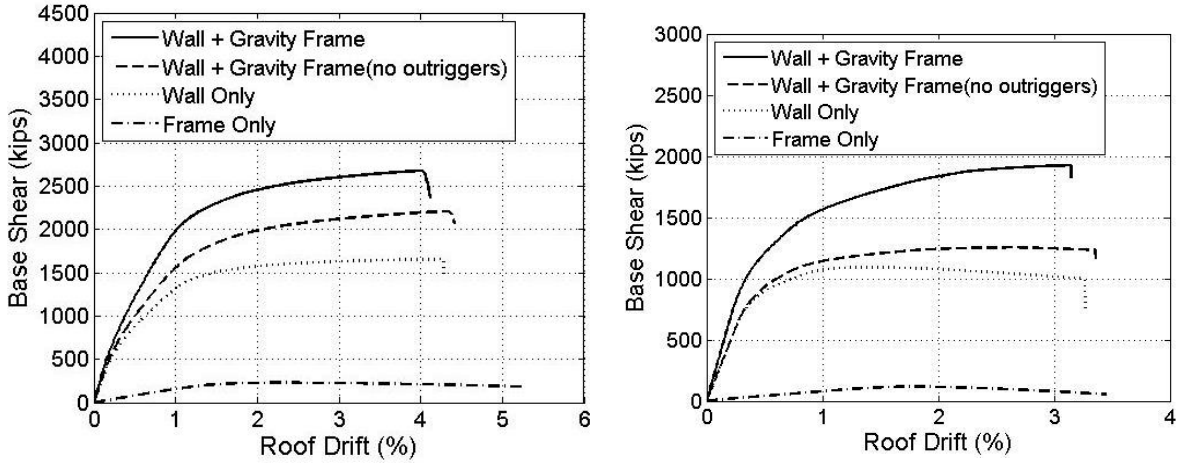

(a) 12-story **(b) 20-story**

Figure 5-10 Nonlinear static analysis results for archetype shear wall buildings from ATC-63-2/3.

For the 18-story DCW, an increase in strength and stiffness will be used along with a considerably larger elastic and post-yield stiffness, K_e and K_p. The increase in stiffness was derived from the 20-story model in ATC-63-2/3 as shown in Figure 5-11. The pushover response of the wall only and wall plus gravity frame models were approximated with bilinear behavior and then a linear "gravity frame and outriggering" stiffness was approximated. This was then normalized by the weight of the archetype building from ATC-63-2/3 to give a stiffness in terms of *V/W* and roof drift. Since the gravity framing is assumed not to change as the strength of the DCW changes, that stiffness was simply added to each 18-story Family A backbone curve to create the Family B DCW backbone curves.

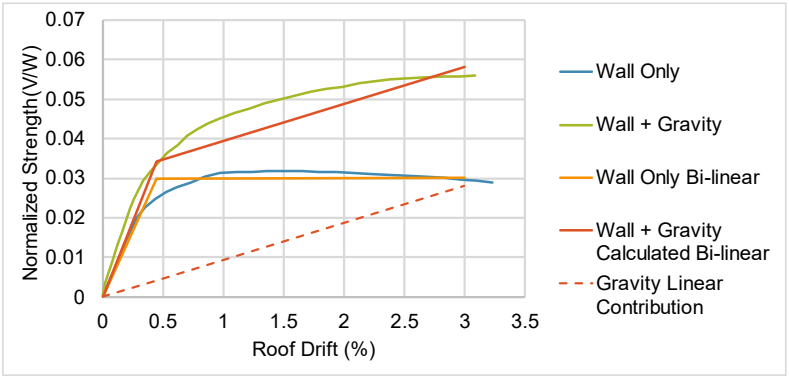

Figure 5-11 Approximating the increase in stiffness due to outriggering from the 20-Story archetype shear wall building response from ATC-63-2/3.

As noted in Appendix E, cyclic deterioration was not considered for the DCW eSDOF models. However, peak-oriented behavior such as that illustrated in Figure C-30 was considered (i.e., where during reloading the initial stiffness is not used, instead a stiffness that connects zero force to the

previous peak reached on the backbone is used). This was accomplished using the peak-oriented IMK material model in *OpenSees*. Finally, there was insufficient data available to adjust the pushover mode shapes to account for outriggering effects. Therefore, the final pushover mode shapes shown in Table 5-8 are those derived directly from Tauberg et al. (2019).

Table 5-8 Final Pushover Mode Shapes for DCW Models

Story	DCW 8A Story Drift (%)	DCW 8B Story Drift (%)	DCW 12A Story Drift (%)	DCW 12B Story Drift (%)	DCW 18A Story Drift (%)	DCW 18B Story Drift (%)
1	0.06	0.06	0.02	0.02	0.01	0.01
2	0.15	0.15	0.05	0.05	0.04	0.04
3	0.27	0.27	0.12	0.12	0.07	0.07
4	0.40	0.40	0.20	0.20	0.11	0.11
5	0.54	0.54	0.30	0.30	0.16	0.16
6	0.69	0.69	0.40	0.40	0.22	0.22
7	0.85	0.85	0.50	0.50	0.27	0.27
8	1.0	1.0	0.60	0.60	0.33	0.33
9			0.70	0.70	0.39	0.39
10			0.80	0.80	0.46	0.46
11			0.90	0.90	0.52	0.52
12			1.0	1.0	0.59	0.59
13					0.66	0.66
14					0.73	0.73
15					0.80	0.80
16					0.87	0.87
17					0.93	0.93
18					1.0	1.0

Development of DCW A and B Families

After developing the baseline eSODF backbone response for the baseline DCW structures, complete families of backbone were developed by scaling the maximum strength of the models, i.e., the value V_{max}/W. As with SMFs and BRBFs, when scaling strength, it was necessary to consider the

corresponding changes in other backbone parameters. The following rules were implemented to modify each backbone point in relation to the changes in strength when generating the complete family of eSDOF models to represent DCW's at each building height. The Family A backbones were generated with a process very similar to the SMF and BRBF Family A backbones.

1. For each building height, the Family A baseline models again serve as the anchors for the family, where Family A represents only the lateral force resisting system (LFRS) in the response.
2. The initial elastic stiffness and yield strength are scaled proportionally.
3. Δ_{pc} is kept the same for the entire family. Similar to BRBFs, K_p does change: the ratio of K_p to K_e in the baseline models is used to calculate the K_p in each new backbone from the scaled K_e. This slope, along with the fixed $\Delta_{pc,}$ gives a capping strength, V_{pc}.
4. K_{pc} is not relevant for the DCW archetypes and is shown only for completeness as the material model used in *OpenSees* requires that it be specified. As discussed below, collapse for the DCW eSDOF is determined using a non-simulated collapse mode applied as a cap on roof drift, similar to what was done in Tauberg et al. (2019).

The Family B backbone curves for 8- and 12-story eSDOF DCW models are the same as the Family A backbones. A different overstrength value is used to account for the impact of gravity frame and outriggering. For the 18-story DCW models, a linear stiffness is added to each Famliy A backbone to create the Family B backbones. That stiffness was derived from the ATC 63-2/3 data as described above. Figure 5-12 shows the Family A backbone curves for the 8- and 12-story DCW eSDOF models and the Family A and B backbone curves for the 18-story models. The backbones overlaid with a black dashed line most closely match the original MDOF models. The backbones overlaid with a black dotted line most closely match the eSDOF model with a strength corresponding to SDC D_{max} for R = 8 and with overstrength as recommended in Chapter 2. The values for key points for the SDC D_{max} are given in Table 5-9.

Table 5-9 DCW Backbone Curve Parameters for Models with a Strength Corresponding to SDC D_{max} for R = 8 and with Overstrength as Recommended in Chapter 2.

Model	Ω	V_p/W	V_{max}/W	Δ_p (Roof Drift %)	Δ_{pc} (Roof Drift %)	Δ_u (Roof Drift %)
DCW 8A	1.7	0.15	0.17	0.83	3.6	61
DCW 8B	2.0	0.19	0.21	0.83	3.6	7.6
DCW 12A	1.7	0.13	0.14	0.9	3.5	6.9
DCW 12B	2.1	0.16	0.17	0.9	3.5	6.9
DCW 18A	1.7	0.085	0.094	0.41	3.5	5.7

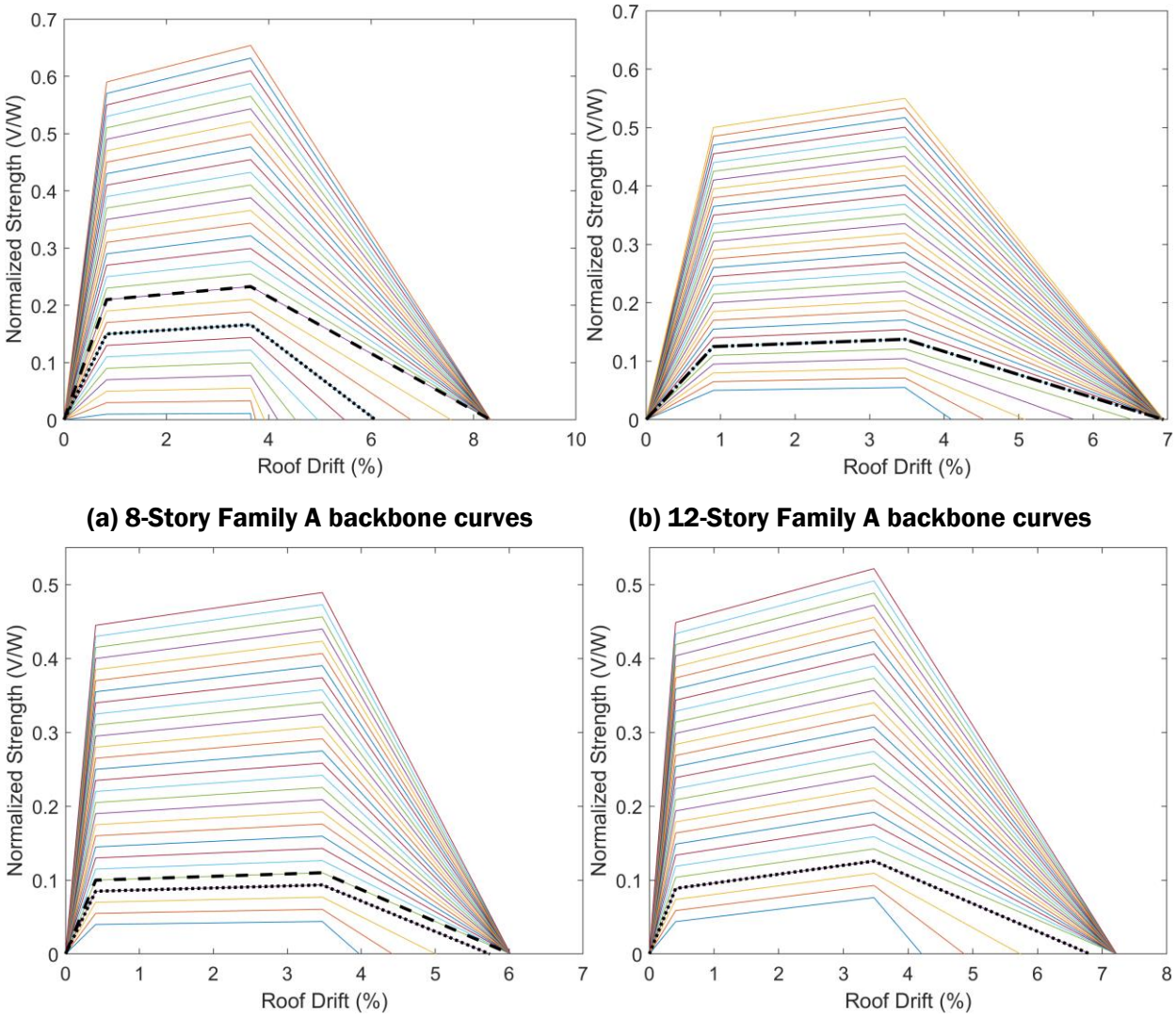

(a) 8-Story Family A backbone curves

(b) 12-Story Family A backbone curves

(c) 18-Story Family A backbone curves

(d) 18-Story Family B backbone curves

Figure 5-12 DCW backbone curves for the 8-, 12- and 18-story DCWs for Family A (DCW only) and B (DCW and gravity frame outriggering). Note Family B is only shown for the 18-Story.

Discussion of DCW eSDOF Modeling Limitations

It is important to note some key limitations for the families of eSDOF models of DCWs and their potential impact on response:

1. The lack of information from detailed models in the literature and even experimental results on the behavior of walls past the capping point results in the application of what is likely to be a conservative roof drift limit as a nonsimulated collapse mode. While this is consistent with the approach taken in Tauberg et al. (2019) and other studies of RC shear wall seismic collapse performance, it is conceivable that DCW buildings have more drift capacity than considered here. Thus, it is important that the results here not be used to judge the adequacy of the R and I_e values but instead to elucidate trends of probability of collapse with increasing S_{MT}.

2. New designs were not performed when the strength was scaled within the DCW families as described above. It is possible that constraints exist that would make designs at larger strengths infeasible due to wall size limitations and reinforcing steel congestion.
3. All eSDOF models assume flexural failure. At some strengths, it may not be practical to achieve this.
4. The roof drift at capping was not modified within a given family. It is possible that some design choices that would be used to increase strength may increase or decrease drift capacity.
5. The selected archetypes from Tauberg et al. (2019) that were used to generate the baseline eSDOF properties were designed for Risk Category II. Therefore, they may not be representative of Risk Category IV structures, especially because the drift limit for such structures is smaller.

5.5 Collapse Surfaces Derived from SDOF Analyses

OpenSees was used to perform incremental dynamic analyses (IDAs) in accordance with the FEMA P-695 methodology using the 44 far-field ground motions. As described in Chapter 3, the ground motions were scaled as a group such that the median acceleration response spectrum of the ground motion ensemble at the prescribed code period ($C_u T_a$) matched the prescribed intensity level (FEMA P-2139-2). The intensity level was incremented at 0.02g up until the SDOF model failed to converge for a 0.5g range of S_a or when the maximum story drift exceeded 18%. The IDA curves were converted to monotonically increasing curves to remove cases where drift capacity occasionally decreases with increasing S_a before then continuing to increase. The IDAs were then interrogated at the drift ratios used for surface development. Incipient collapse for the BRBF and SMF models was chosen as the first of these to occur:

- The increase in drift ratio reached between two successive intensity levels was 5% or more,
- The SDOF model no longer converged, or
- A story drift limit of 18% was reached.

For the DCW models, a non-simulated collapse limit was necessary because such a limit is applied even in complex MDOF models like those used in Tauberg et al (2019). Using the roof drift failure criteria from Wallace and Abdullah (2019) and discussed in Appendix E (see Figure E-27), roof drift limits were approximated for the 8-, 12- and 18-story models as 3.8%, 3.6%, and 3.6%. These values correspond to maximum story drift limits of 4.8%, 4.4%, and 4.5%, respectively. These values correspond to the capping point of the backbone curves shown in Figure 5-12, as those are the last point for which information in the original studies was available. Notably, these roof drift limits are larger than those used in Tauberg et al. (2019) where the limit was recomputed at each time step as a function of the compression zone size in the wall.

Collapse surfaces like those described in Section 4.6 were then fit to the data at incremental values of V_{max}/W and drift ratios from 2% up to the drift ratio at incipient collapse. As in Section 4.6, a plateau is enforced for each family at high values of drift ratio (DR) and V_{max}/W in both directions. This manipulation to the curve surface was determined by computing the partial derivative of the

surface equation and finding the *DR* and V_{max}/W values that correspond to the maximum $\hat{S}_{CT}$. Values of $\hat{S}_{CT}$ are then constant for increasing *DR* and V_{max}/W above those that produce the maximum $\hat{S}_{CT}$. The surfaces for each family as well as a summary table for each building type are shown below. The tables include the surface coefficients along with the R^2 value for the fit of the surface, the percent of the residuals within ±5%, as well as archetype information like the ASCE/SEI 7 code period, S_{MT} for SDC D_{max} based on that period, and the linear fits developed to predict DR_{IC} as a function of V_{max}/W where applicable. Note that DR_{IC} for the SMFs was taken as constant as it did not vary appreciably with V_{max}/W and this was confirmed with the detailed models described in Section 5.8. Finally, the table includes the values of R/I_e needed to achieve a 10% and 2.5% target probability of collapse at the archetype S_{MT}. If no value of $\hat{S}_{CT}$ from the collapse surface exists for a given archetype to achieve the target collapse reliability, a value of R/I_e is not provided.

Generally, all collapse surfaces are able to represent the collapse data very well. All goodness-of-fit values, given as R^2 values in the following tables, for the surfaces are above 0.9. This can be seen using the surface and data cross sections that are shown below each surface in Section 5.5.1 through Section 5.5.3. The tables at the end of each of those sections (Tables 5-10, 5-11, and 5-12) provide the data necessary to generate each collapse surface and provide the goodness of fit (R^2) and residuals for the fit of the surface to the analysis data.

5.5.1 BRBF Collapse Surfaces

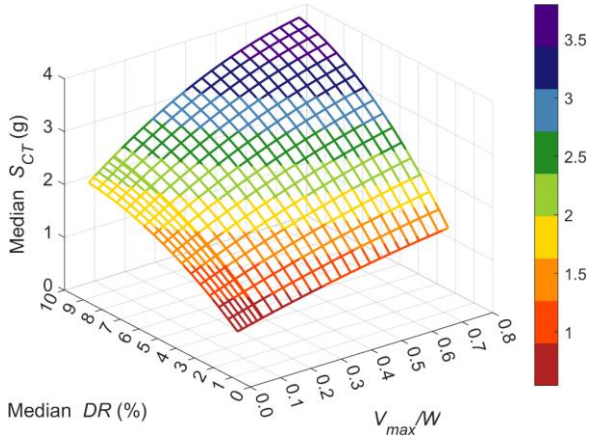

(a) BRBF-4-A Collapse Surface

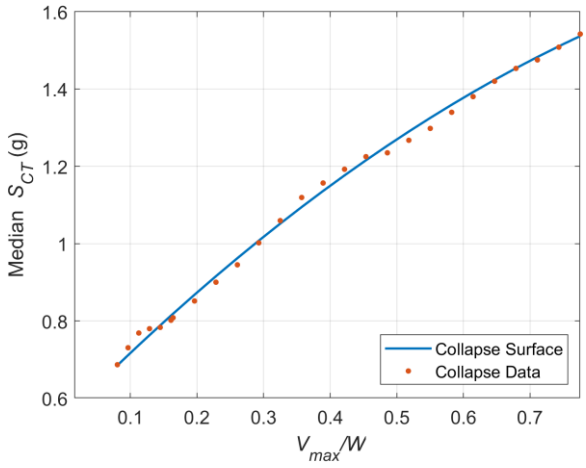

(b) Section cut at 2.5% *DR*

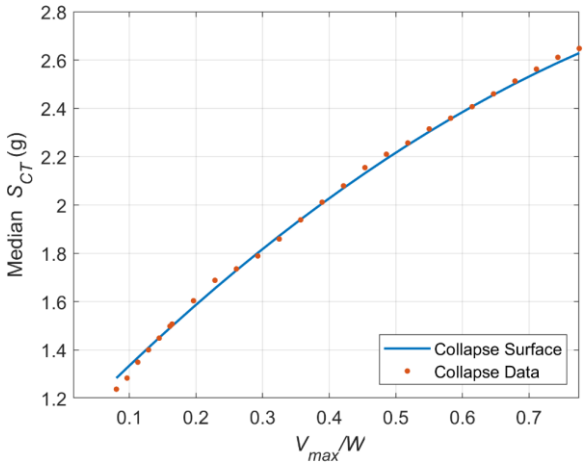

(c) Section cut at 5% *DR*

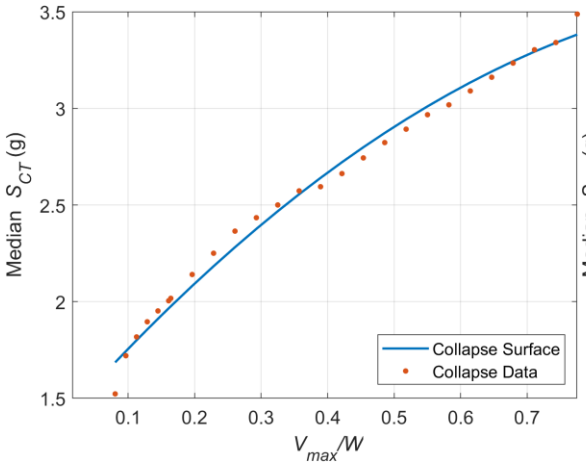

(d) Section cut at 7.5% *DR*

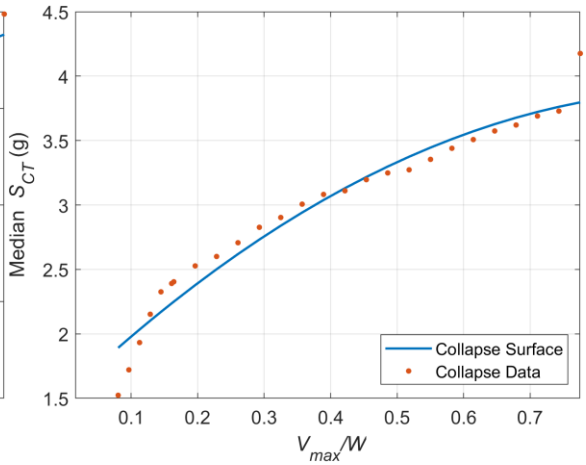

(e) Section cut at 10% *DR*

Figure 5-13 4-Story BRBF Family A surface and surface section cuts with IDA data.

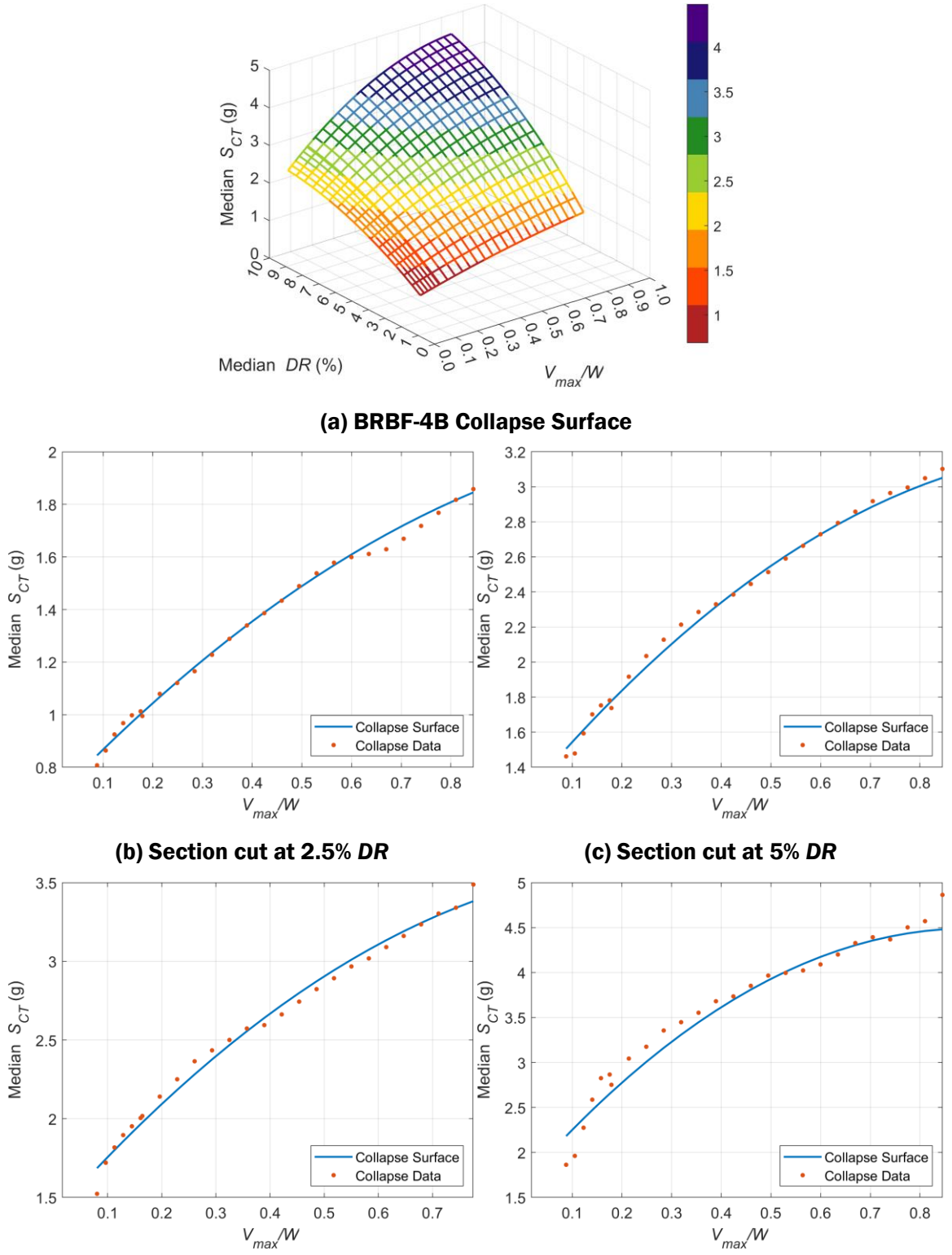

(a) BRBF-4B Collapse Surface

(b) Section cut at 2.5% *DR*

(c) Section cut at 5% *DR*

(d) Section cut at 7.5% *DR*

(e) Section cut at 10% *DR*

Figure 5-14 4-Story BRBF Family B surface and surface section cuts with IDA data.

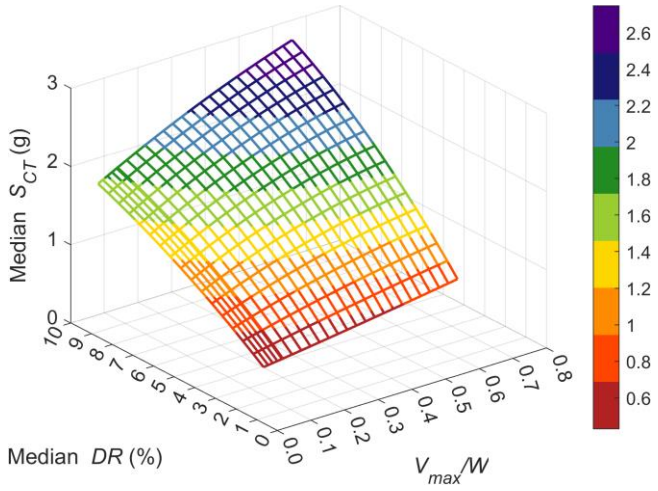

(a) BRBF-9-A Collapse Surface

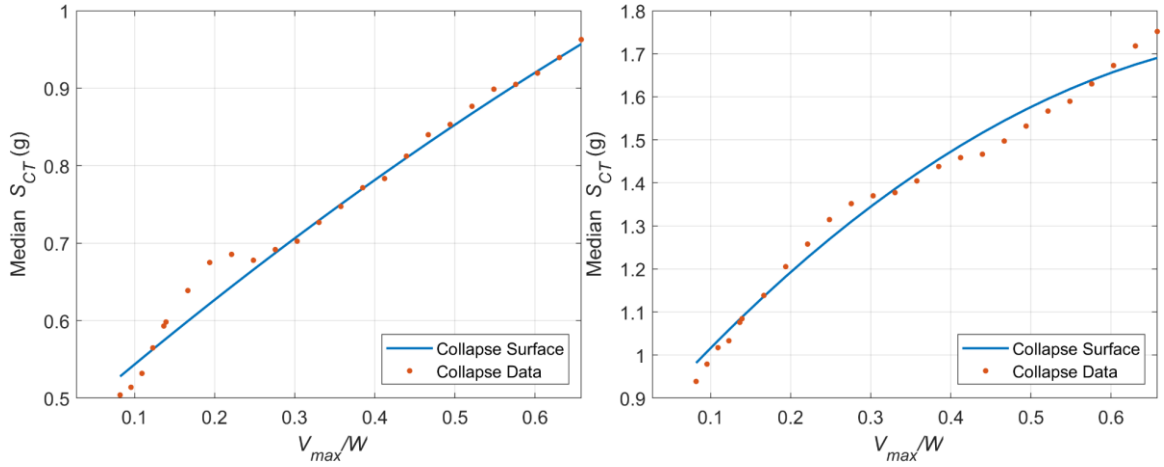

(b) Section cut at 2.5% *DR*

(c) Section cut at 5% *DR*

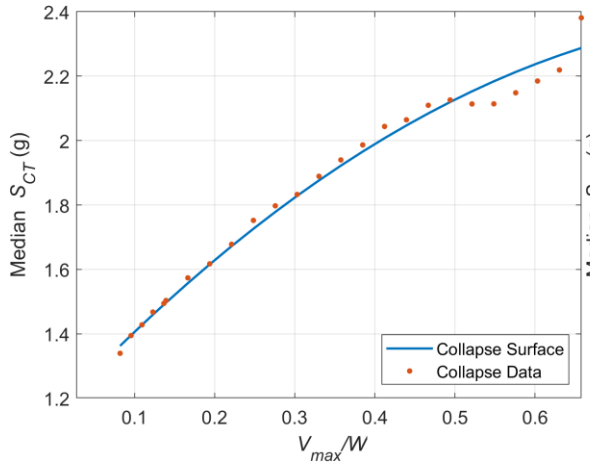

(d) Section cut at 7.5% *DR*

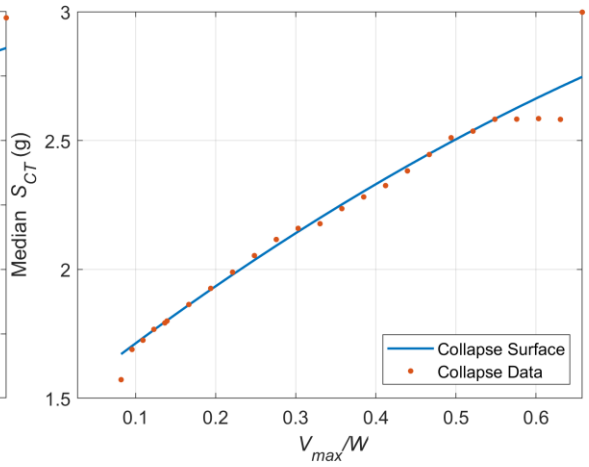

(e) Section cut at 10% *DR*

Figure 5-15 9-Story BRBF Family A surface and surface section cuts with IDA data.

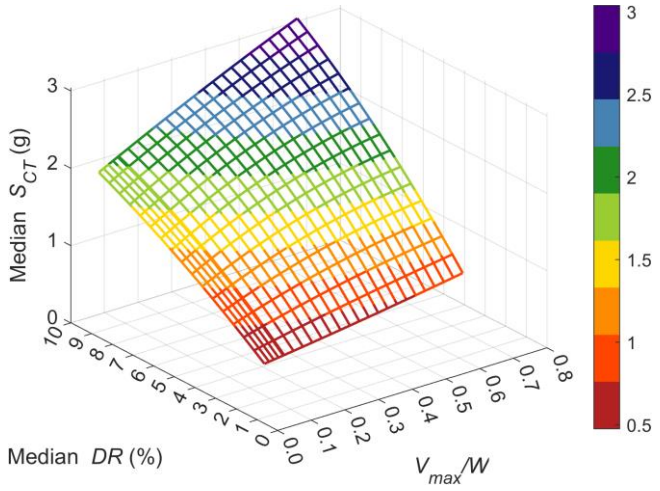

(a) BRBF-9-B Collapse Surface

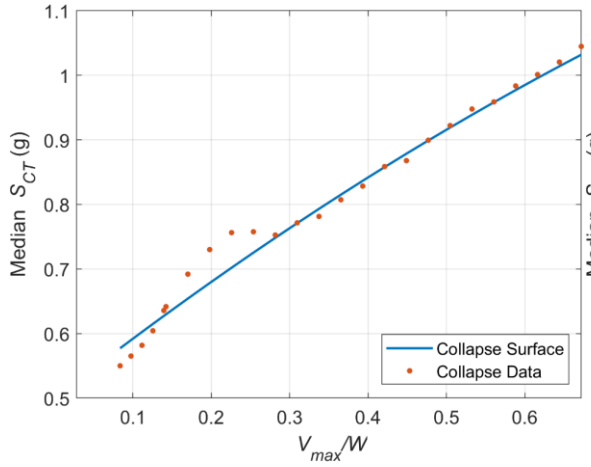

(b) Section cut at 2.5% *DR*

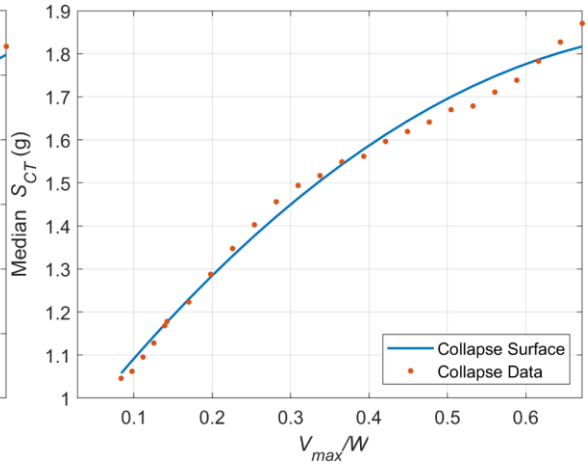

(c) Section cut at 5% *DR*

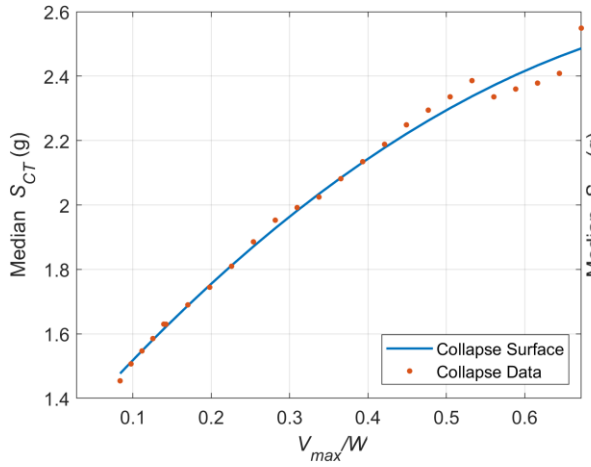

(d) Section cut at 7.5% *DR*

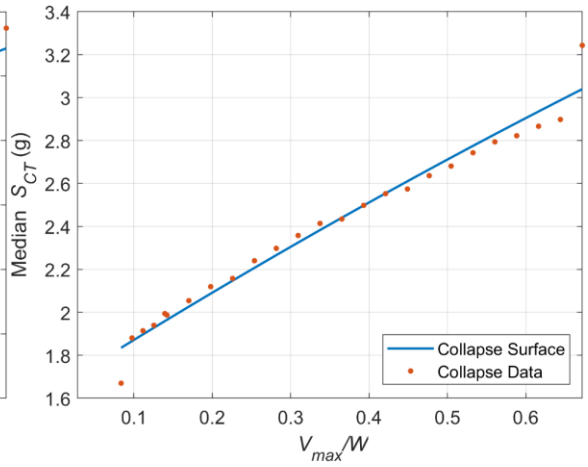

(e) Section cut at 10% *DR*

Figure 5-16 9-Story BRBF Family B surface and surface section cuts with IDA data.

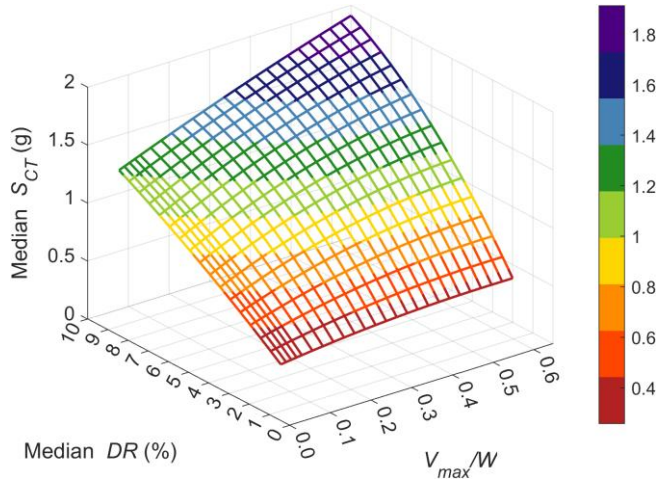

(a) BRBF-15-A Collapse Surface

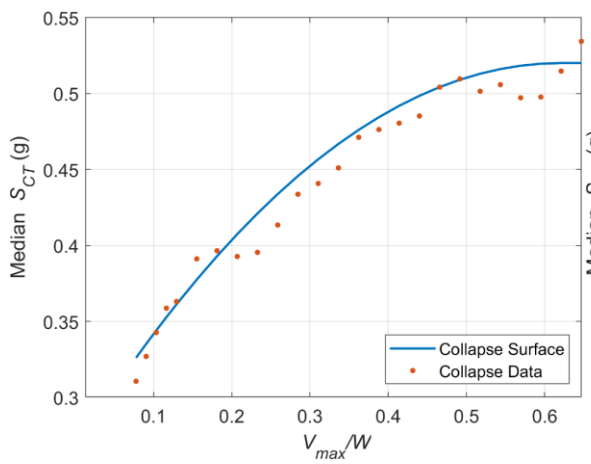

(b) Section cut at 2.5% *DR*

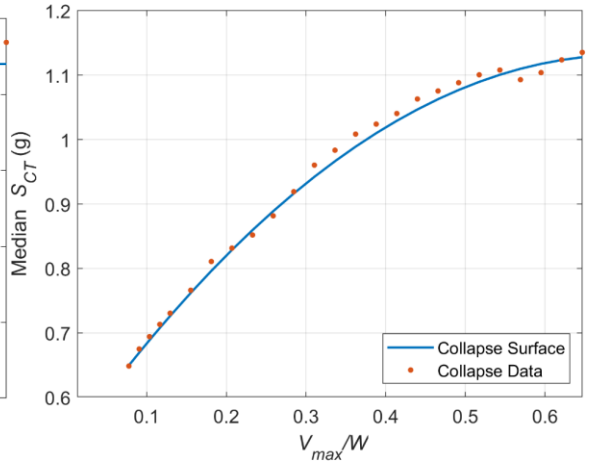

(c) Section cut at 5% *DR*

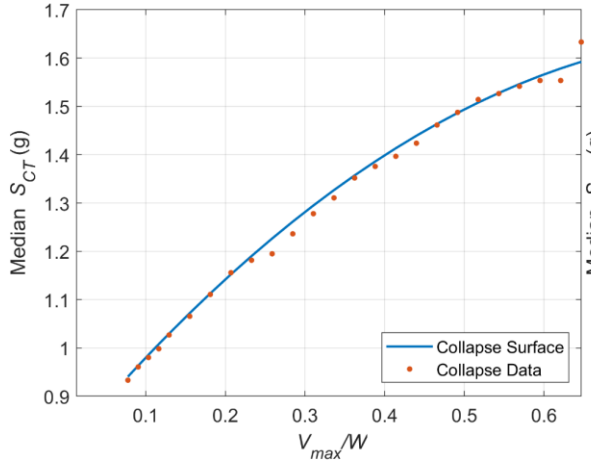

(d) Section cut at 7.5% *DR*

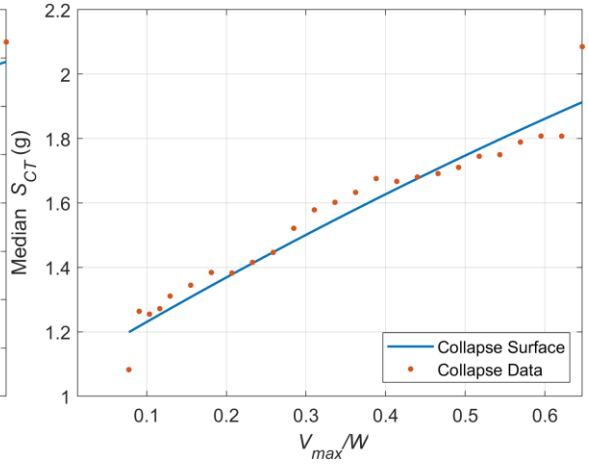

(e) Section cut at 10% *DR*

Figure 5-17 15-Story BRBF Family A surface and surface section cuts with IDA data.

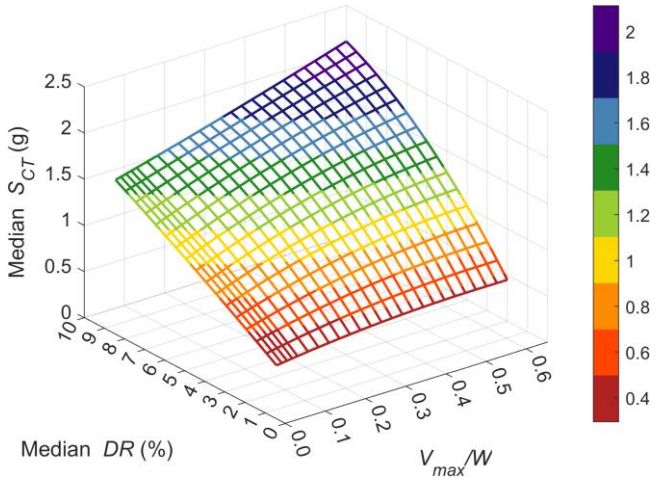

(a) BRBF-15-B Collapse Surface

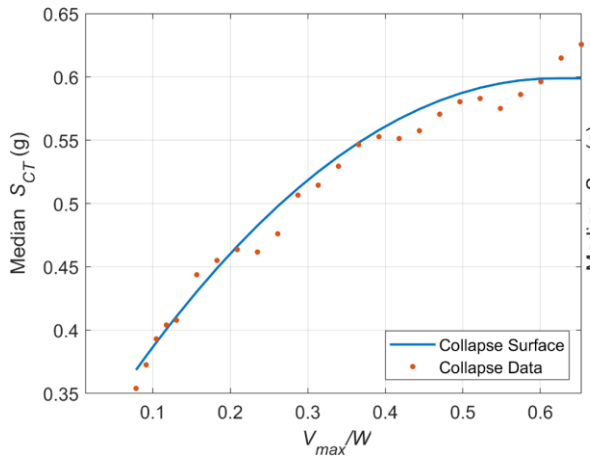

(b) Section cut at 2.5% *DR*

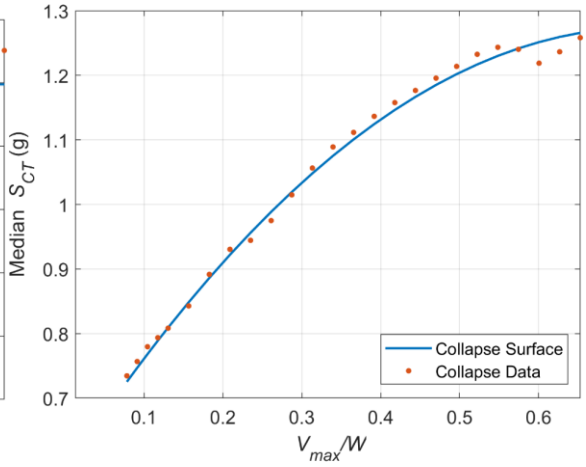

(c) Section cut at 5% *DR*

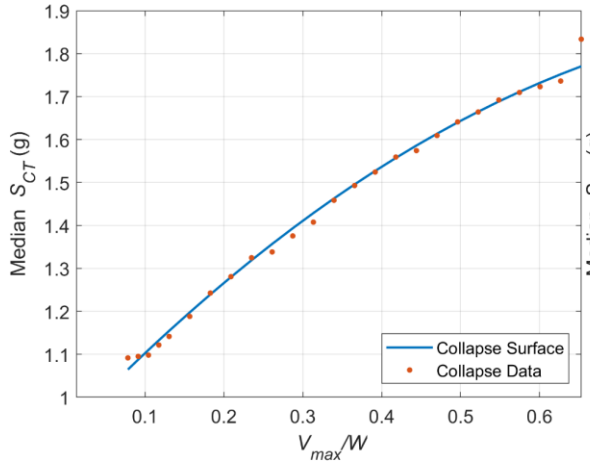

(d) Section cut at 7.5% *DR*

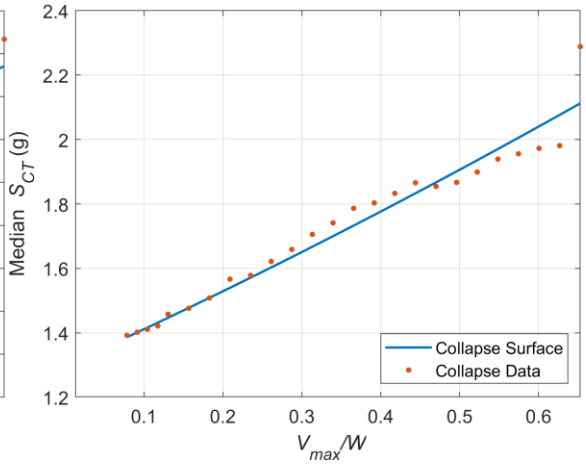

(e) Section cut at 10% *DR*

Figure 5-18 15-Story BRBF Family B surface and surface section cuts with IDA data.

Table 5-10 BRBF Archetype Information, Surface Coefficients, and Goodness of Fit Metrics

Family	BRBF-4A	BRBF-4B	BRBF-9A	BRBF-9B	BRBF-15A	BRBF-15B
A	0.63	0.63	-1.05	-1.41	-0.81	-0.78
B	-0.37	-0.19	1.62	2.08	0.62	0.52
C	32.1	34.8	15.55	14.2	9.1	8.93
D	-153.7	-174.1	-15.62	8.6	14.3	35.3
E	45.4	52.9	92.2	113.4	79.0	87.0
F	-5.5	-16.3	-89.4	-115.2	-65.2	-68.6
G	-27.5	37.2	-571.4	-762.6	-562.0	-680.6
H	-159.4	-167.4	652.2	910.68	559.8	653.9
I	-0.16	-0.08	0.08	0.14	0.03	0.05
R^2	0.99	0.99	0.99	0.99	0.99	0.99
% Resid ±5%	95	95	97	96	95	96
Intercept	9.72	10.0	9.69	9.86	9.76	9.72
Slope	-0.15	-0.05	-0.24	-0.28	-0.43	-0.37
$T = C_u T_a$	0.871	0.871	1.54	1.54	2.23	2.23
S_{MT} SDC D_{max}	1.03	1.03	0.58	0.58	0.40	0.40

5.5.2 SMF Collapse Surfaces

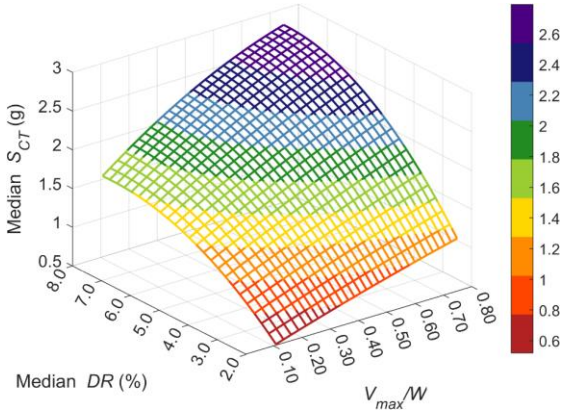

(a) SMF-3-A Collapse Surface

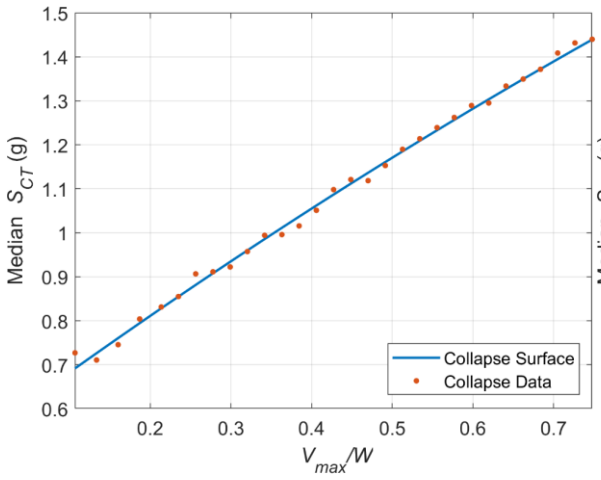

(b) Section cut at 2.5% *DR*

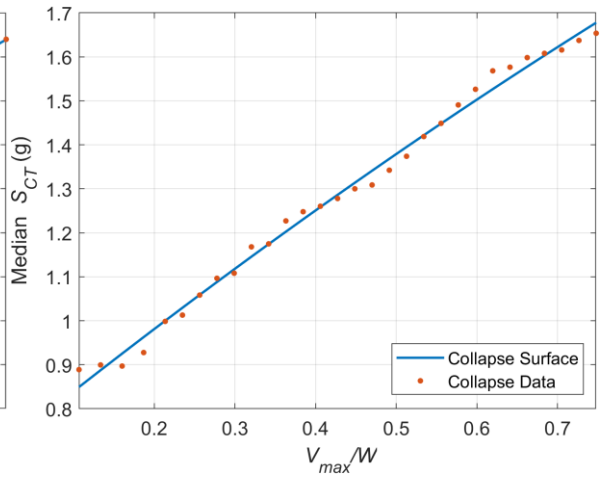

(c) Section cut at 3% *DR*

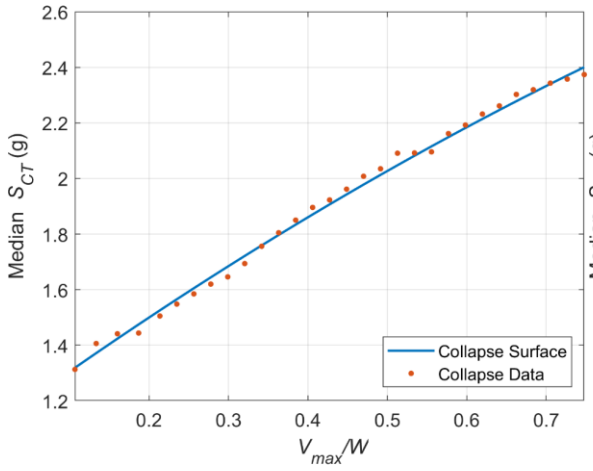

(d) Section cut at 5% *DR*

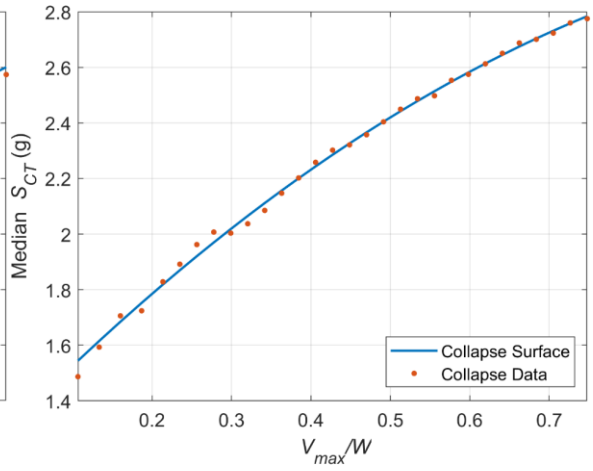

(e) Section cut at 7.5% *DR*

Figure 5-19 3-Story SMF Family A surface and surface section cuts with IDA data.

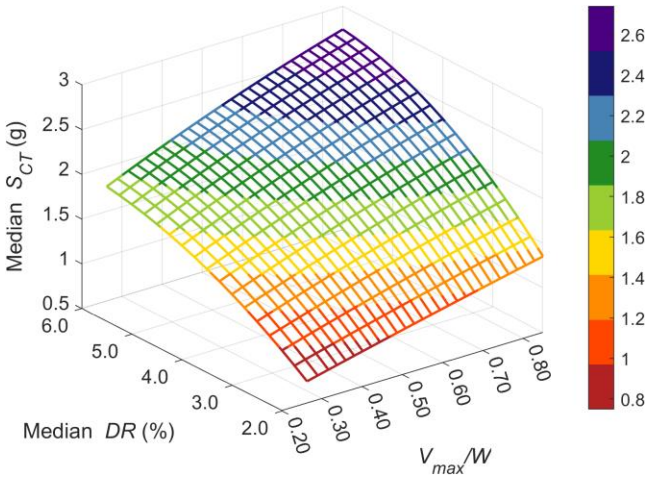

(a) SMF-3B Collapse Surface

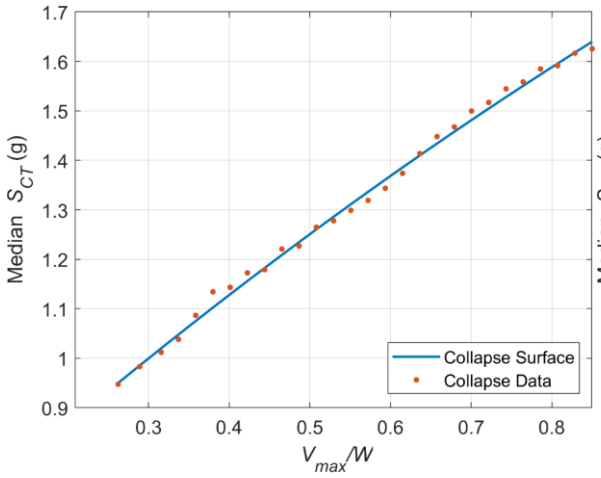

(b) Section cut at 2.5% *DR*

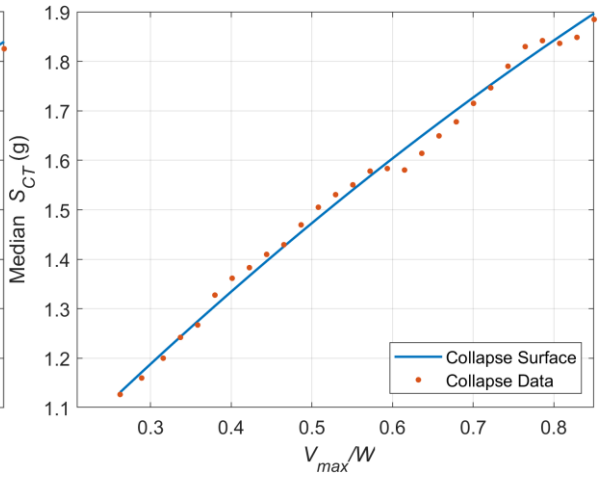

(c) Section cut at 3% *DR*

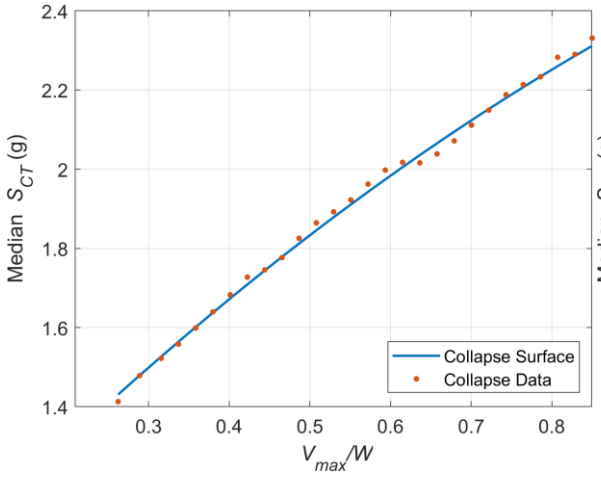

(d) Section cut at 4% *DR*

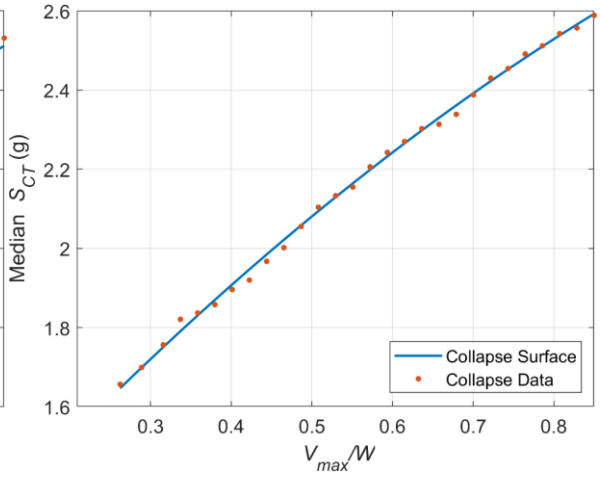

(e) Section cut at 5% *DR*

Figure 5-20 3-Story SMF Family B surface and surface section cuts with IDA data.

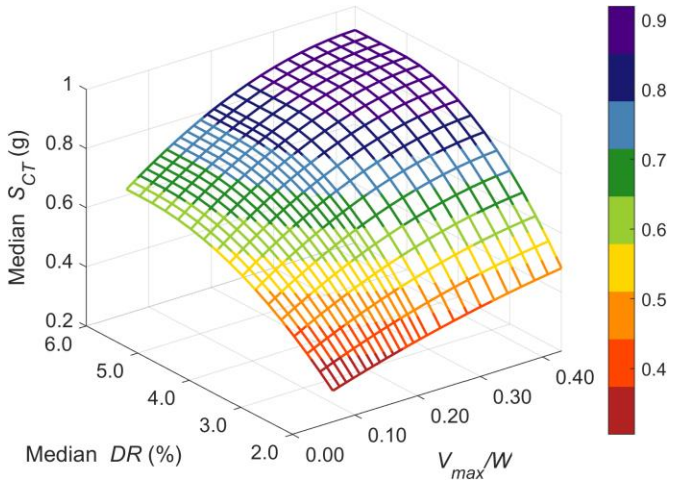

(a) SMF-9A Collapse Surface

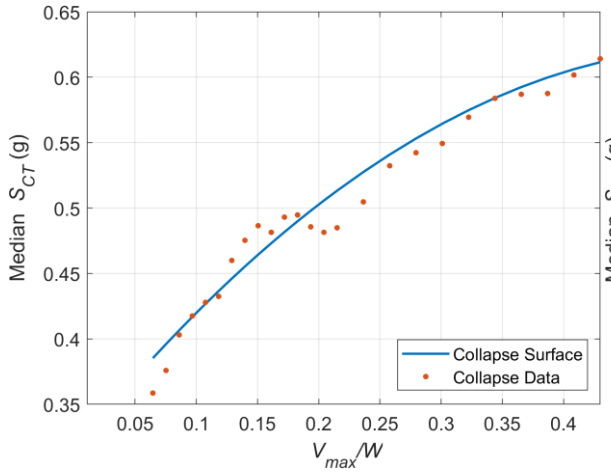

(b) Section cut at 2.5% *DR*

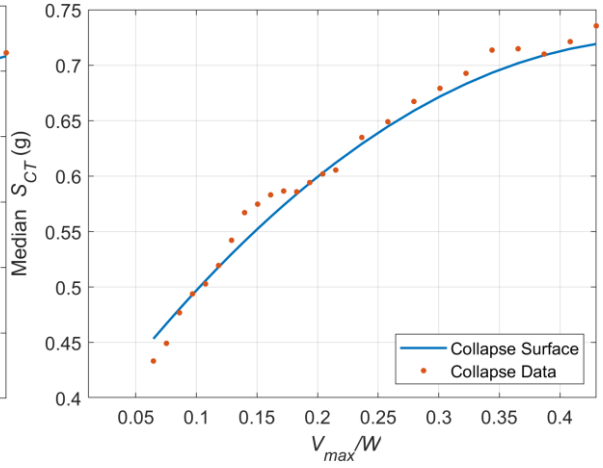

(c) Section cut at 3% *DR*

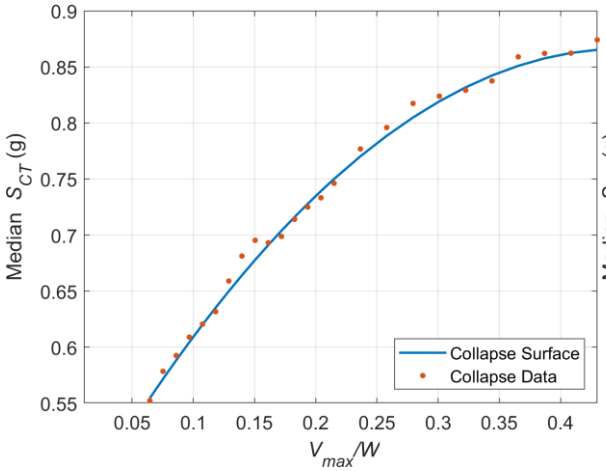

(d) Section cut at 4% *DR*

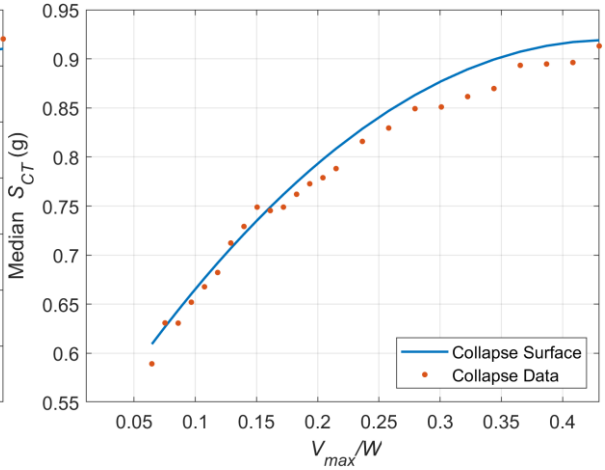

(e) Section cut at 5% *DR*

Figure 5-21 9-Story SMF Family A surface and surface section cuts with IDA data.

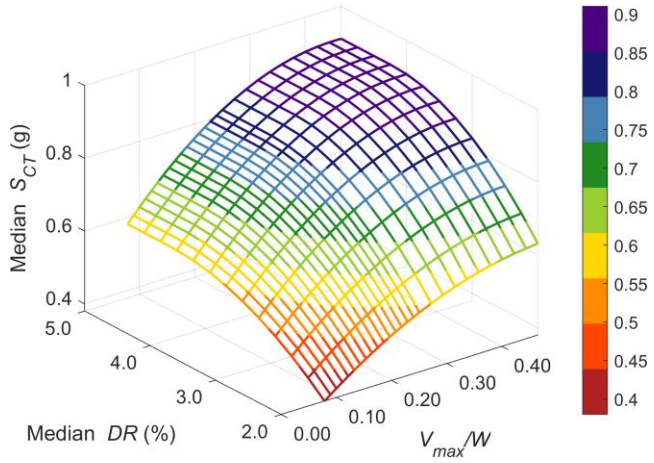

(a) SMF-9B Collapse Surface

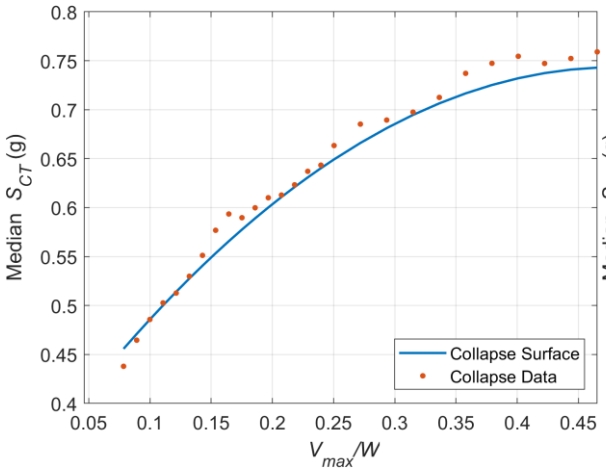

(b) Section cut at 2.5% *DR*

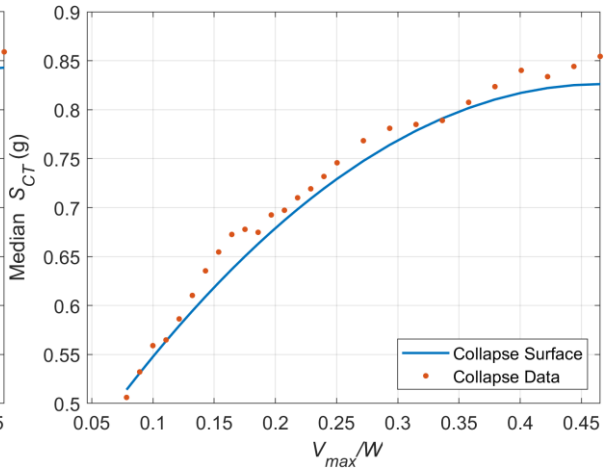

(c) Section cut at 3% *DR*

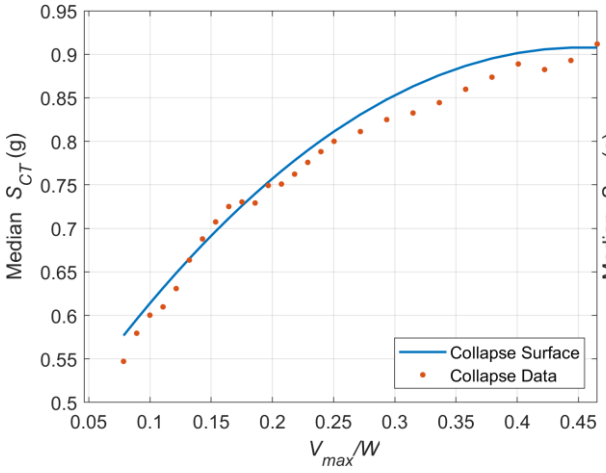

(d) Section cut at 4% *DR*

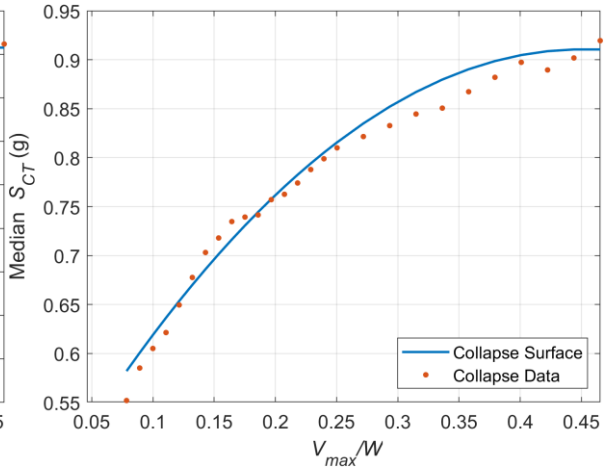

(e) Section cut at 5% *DR*

Figure 5-22 9-Story SMF Family B surface and surface section cuts with IDA data.

Table 5-11 SMF Archetype Information, Surface Coefficients, and Goodness of Fit Metrics

Family	SMF-3A	SMF-3B	SMF-9A	SMF-9B
A	0.75	-0.63	-1.77	-0.60
B	-0.44	0.76	2.79	1.13
C	46.7	34.29	17.02	21.9
D	-328.8	-188.74	-132.17	-243.2
E	21.4	109.21	159.4	132.5
F	18.6	-53.9	-209.0	-164.6
G	105.9	-1013.2	-1702.7	-1594.6
H	-380.1	529.9	2178.3	1928.10
I	-0.41	-0.16	-0.03	-0.06
R^2	0.99	0.99	0.99	0.98
% Resid ±5%	99.6	100	96.9	98.6
Intercept	N/A for SMF's – median DR_{IC} taken as 5%			
Slope				
$T = C_u T_a$	0.73	0.73	1.83	1.83
S_{MT} SDC D_{max}	1.23	1.23	0.49	0.49
R/I_e 10%	7.65	8.3	5.4	6.85
R/I_e 2.5%	N/A	2.8	N/A	N/A

5.5.3 DCW Collapse Surfaces

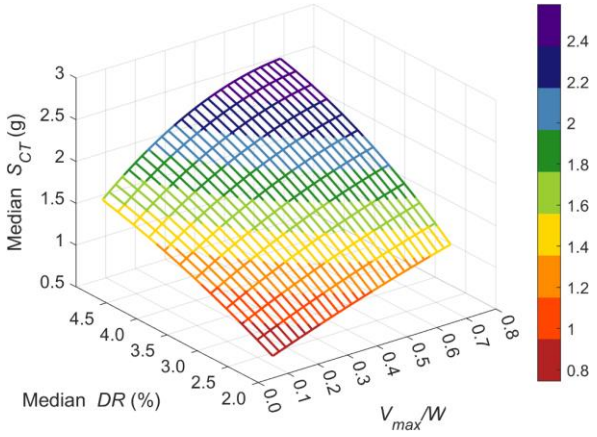

(a) DCW-8A Collapse Surface

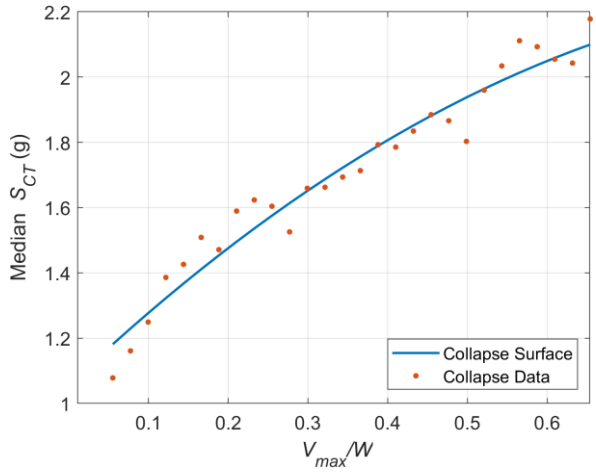

(b) Section cut at 3.2% *DR*

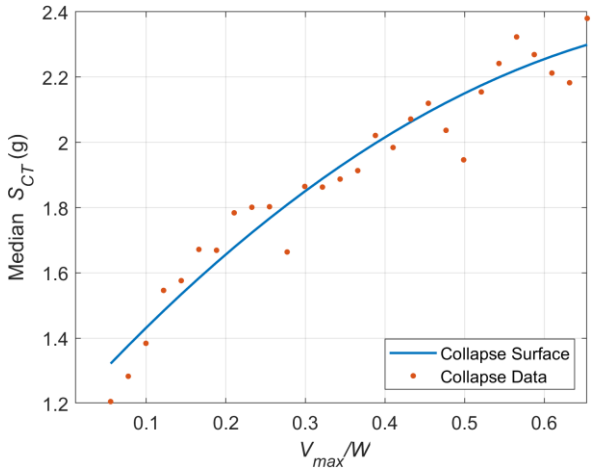

(c) Section cut at 3.8% *DR*

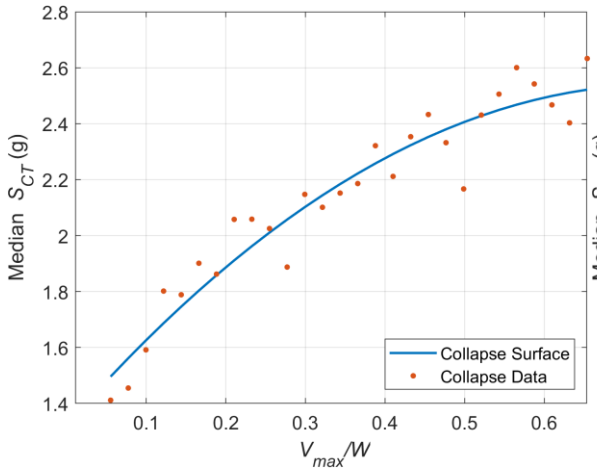

(d) Section cut at 4.6% *DR*

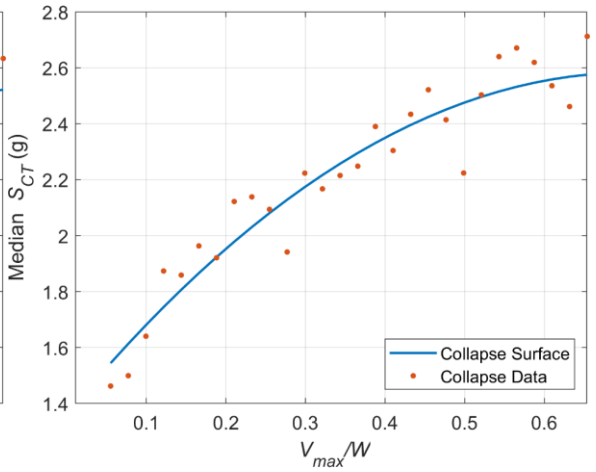

(e) Section cut at 4.8% *DR*

Figure 5-23 8-Story DCW Family A surface and surface section cuts with IDA data.

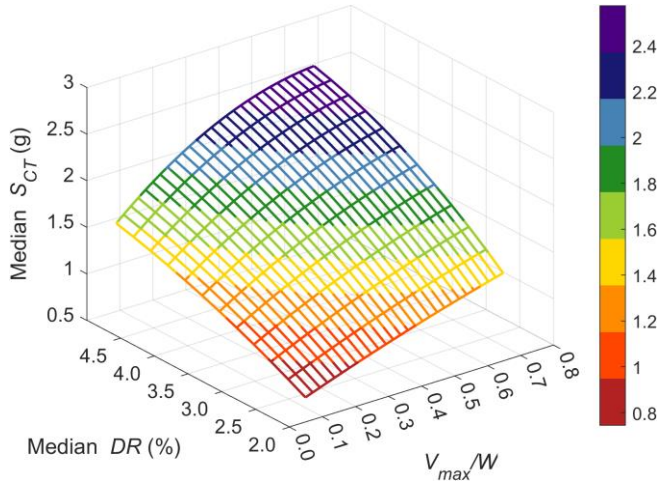

(a) DCW-8B Collapse Surface

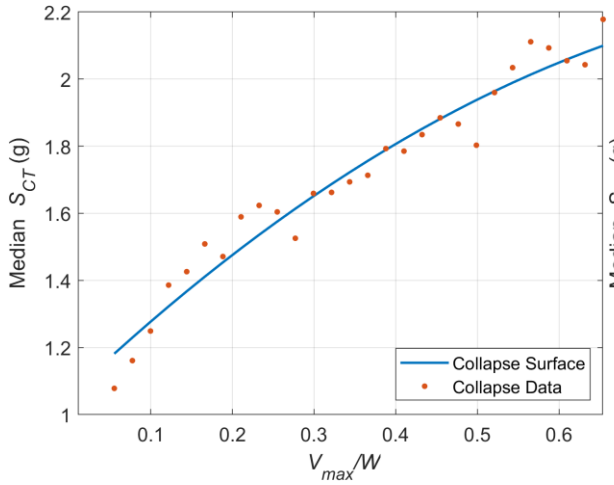

(b) Section cut at 3.2% *DR*

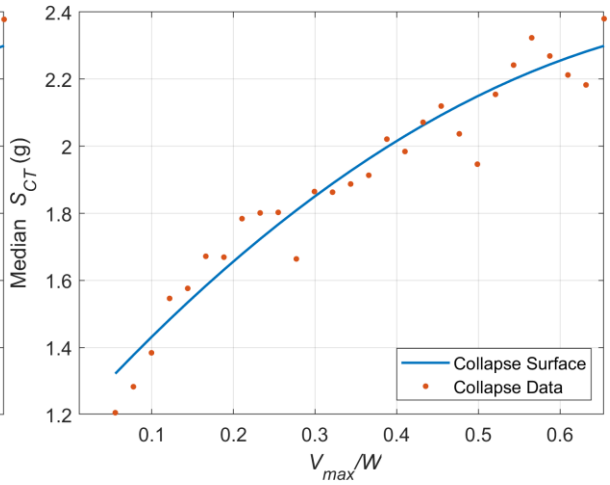

(c) Section cut at 3.8% *DR*

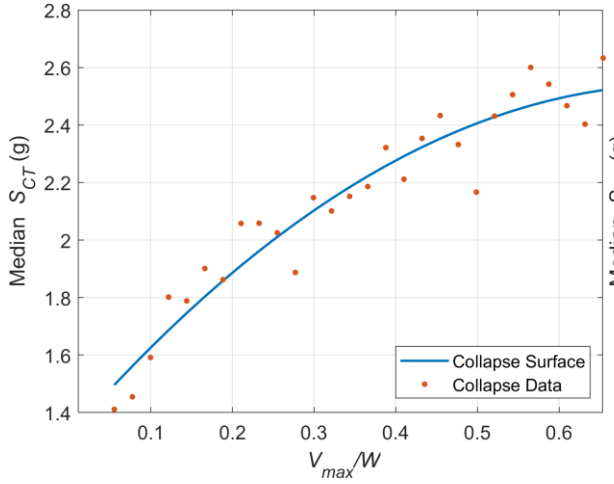

(d) Section cut at 4.6% *DR*

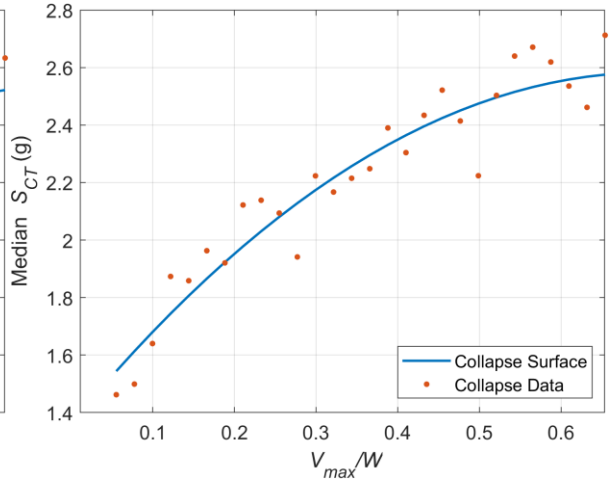

(e) Section cut at 4.8% *DR*

Figure 5-24 8-Story DCW Family B surface and surface section cuts with IDA data.

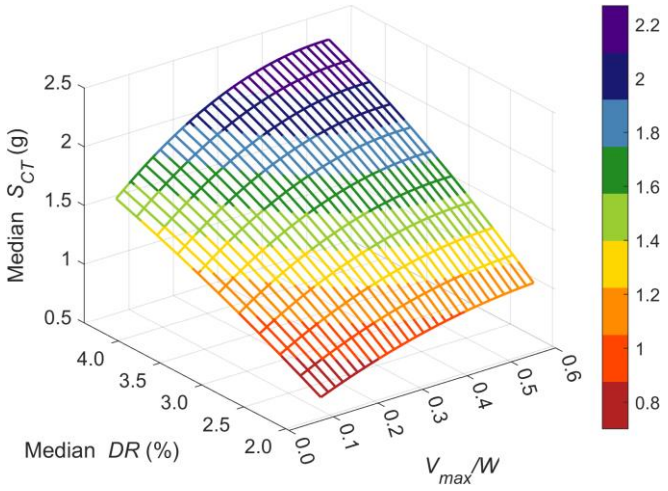

(a) DCW-12A Collapse Surface

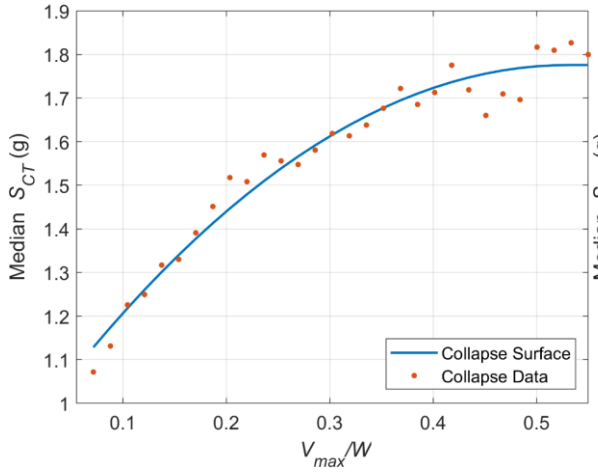

(b) Section cut at 2.4% *DR*

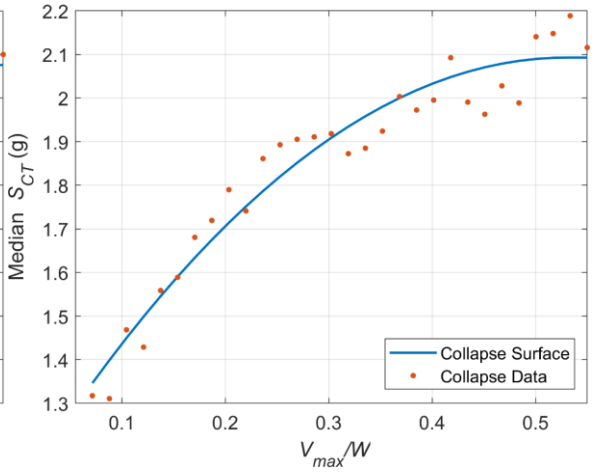

(c) Section cut at 3.2% *DR*

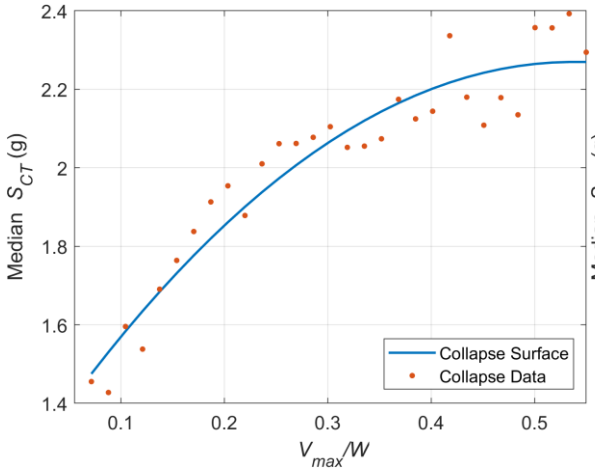

(d) Section cut at 3.8% *DR*

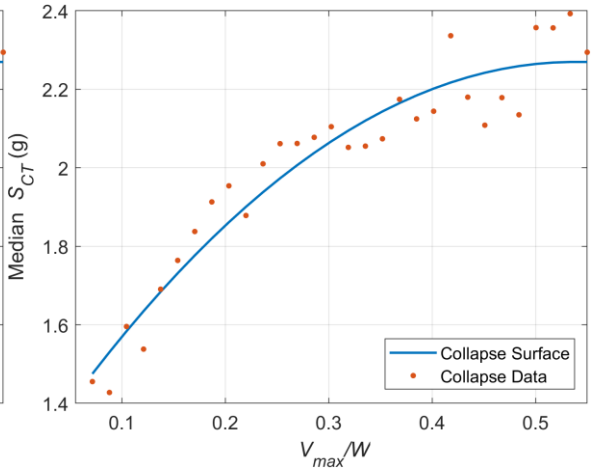

(e) Section cut at 4.2% *DR*

Figure 5-25 12-Story DCW Family A surface and surface section cuts with IDA data.

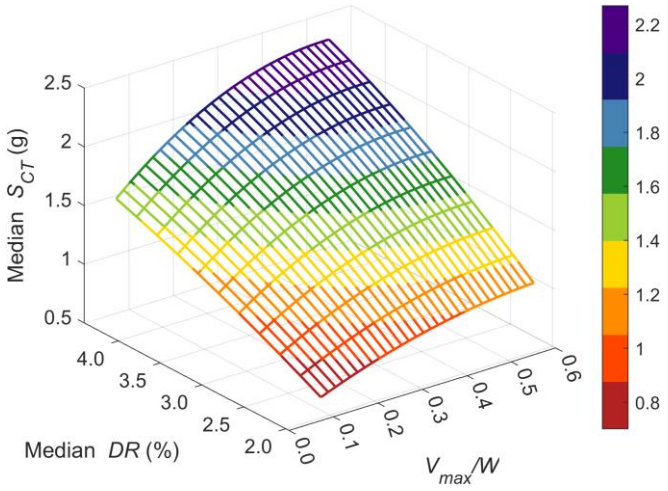

(a) DCW-12B Collapse Surface

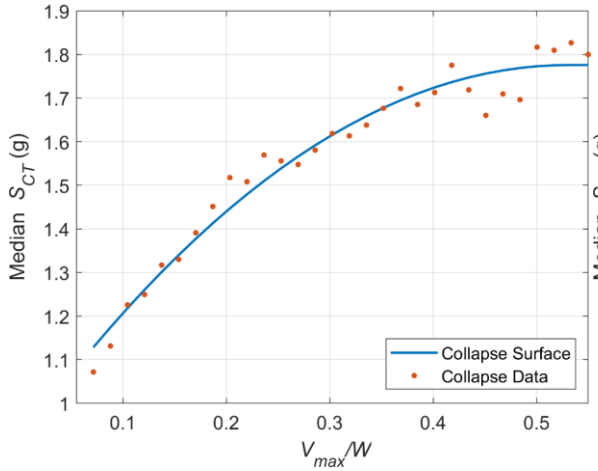

(b) Section cut at 2.4% *DR*

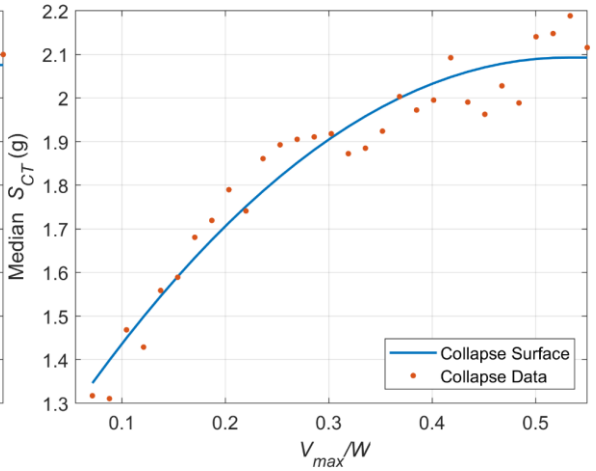

(c) Section cut at 3.2% *DR*

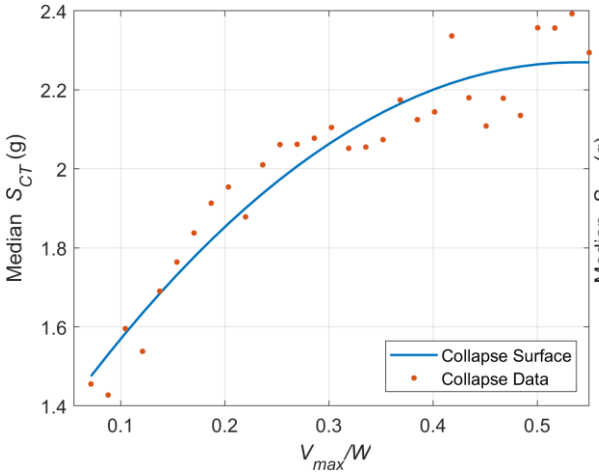

(d) Section cut at 3.8% *DR*

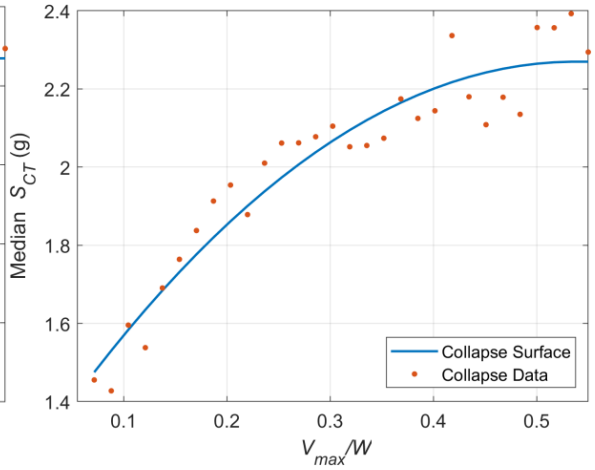

(e) Section cut at 4.2% *DR*

Figure 5-26 12-Story DCW Family B surface and surface section cuts with IDA data.

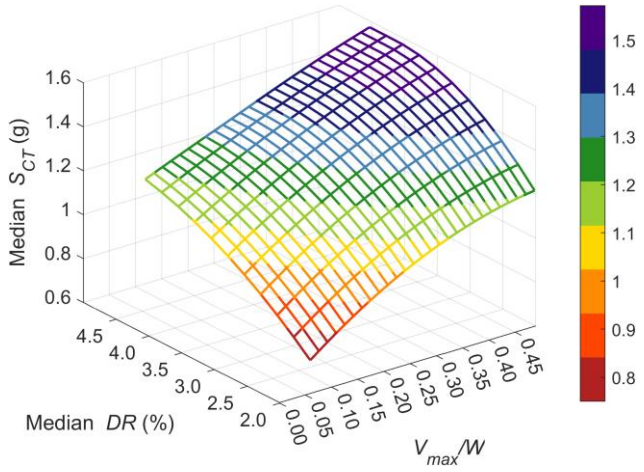

(a) DCW-18A Collapse Surface

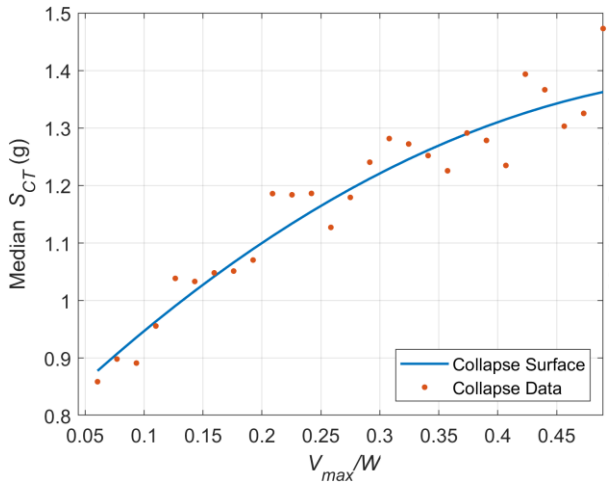

(b) Section cut at 2.5% *DR*

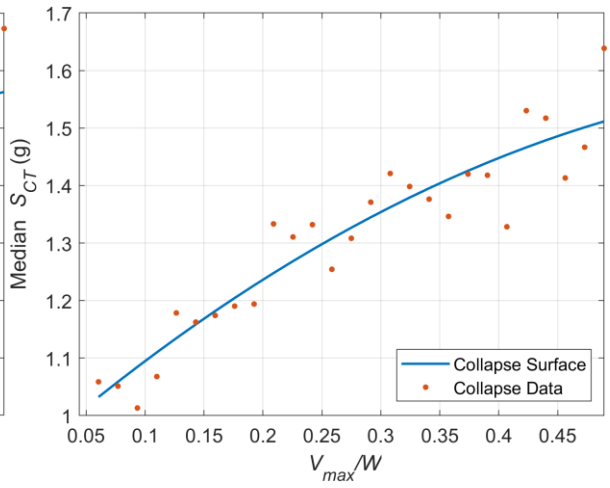

(c) Section cut at 3.2% *DR*

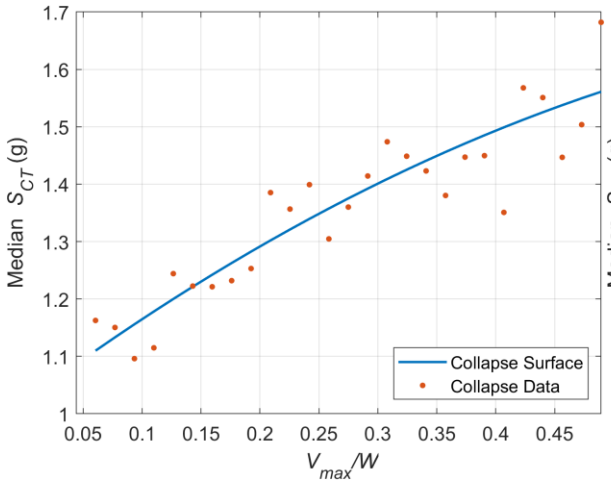

(d) Section cut at 3.8% *DR*

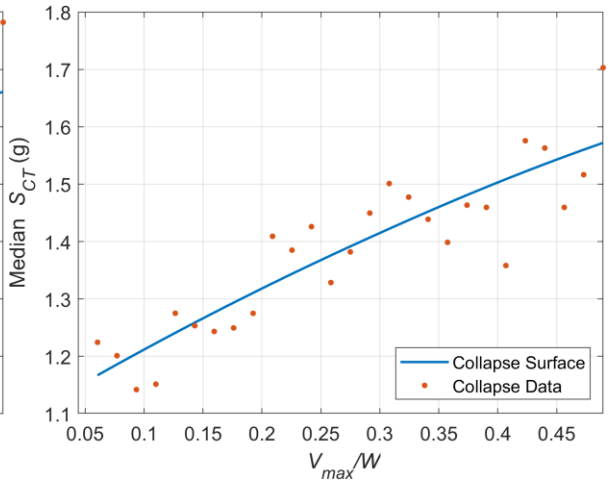

(e) Section cut at 4.4% *DR*

Figure 5-27 18-Story DCW Family A surface and surface section cuts with IDA data.

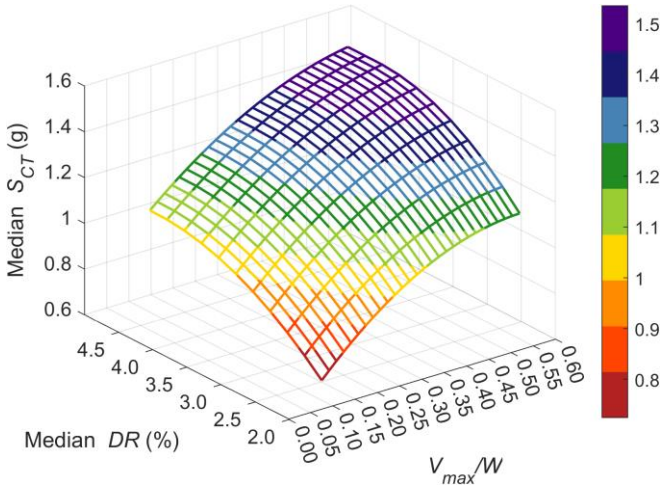

(a) DCW-18B Collapse Surface

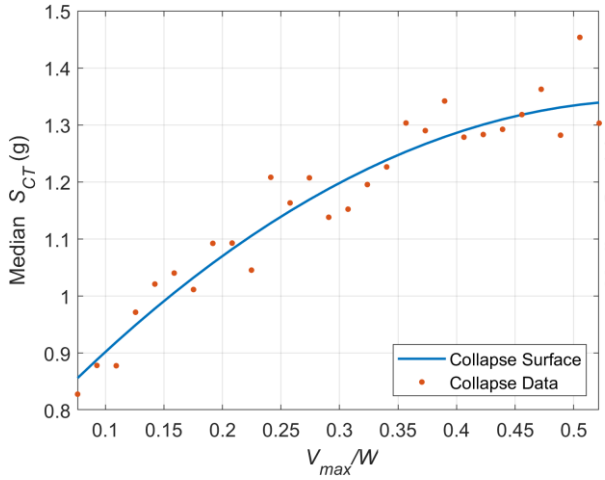

(b) Section cut at 2.5% *DR*

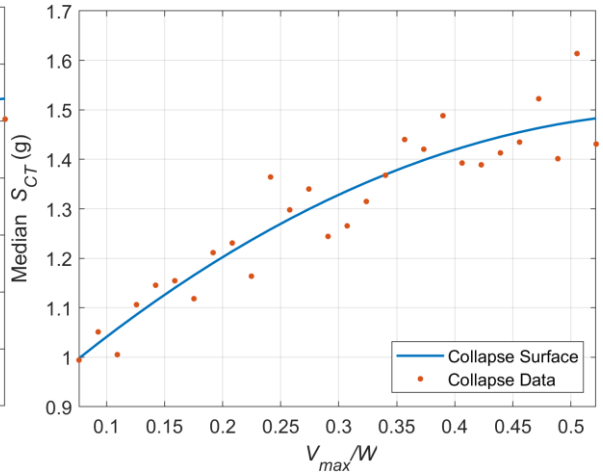

(c) Section cut at 3.2% *DR*

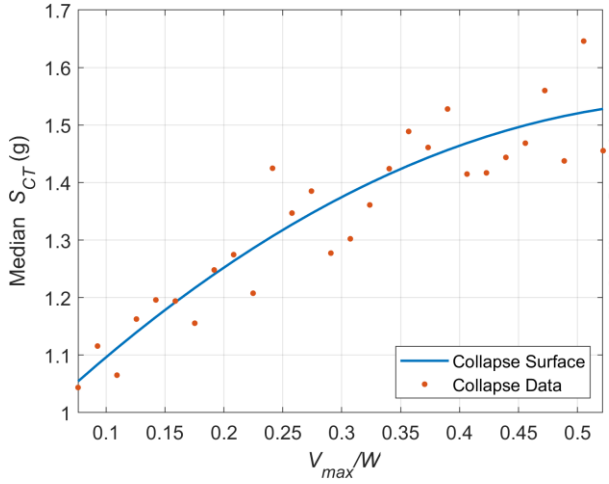

(d) Section cut at 3.8% *DR*

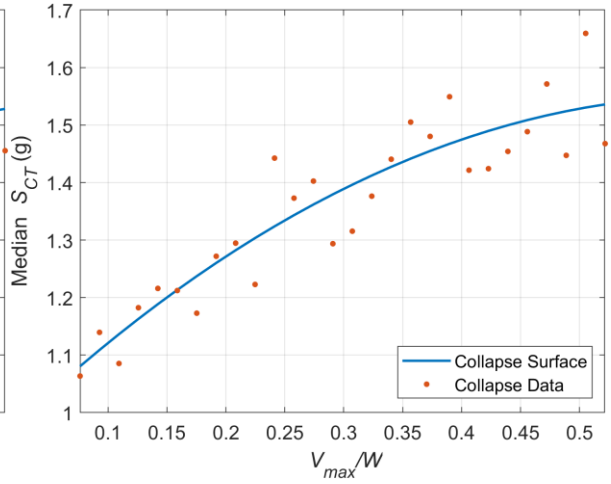

(e) Section cut at 4.4% *DR*

Figure 5-28 18-Story DCW Family B surface and surface section cuts with IDA data.

Table 5-12 DCW Archetype Information, Surface Coefficients, and Goodness of Fit Metrics

Family	DCW-8A	DCW-8B	DCW-12A	DCW-12B	DCW-18A	DCW-18B
A	-0.22	-0.22	-2.48	-2.48	1.7	3.0
B	0.34	0.34	3.53	3.53	-2.2	-3.9
C	50.3	50.32	31.20	31.20	40.7	55.5
D	-373.2	-373.21	-86.63	-86.63	-320.8	-612.0
E	78.9	78.86	270.7	270.73	47.9	-36.6
F	-14.5	-14.52	-322.1	-322.09	3.9	105.2
G	-64.8	-64.79	-2840.5	-2840.48	-1369.2	296.9
H	-881.7	-881.69	3610.0	3610.05	866.0	-1238.7
I	-0.20	-0.20	0.01	0.01	-0.1	-0.3
R^2	0.98	0.98	0.99	0.99	0.92	0.92
% Resid ±5%	80.3	80.30	90.9	90.90	80.5	80.5
Intercept	N/A for shear walls – median DR_{IC} taken as capping displacement.					
Slope						
$T = C_u T_a$	0.75	0.75	1.01	1.01	1.37	1.37
S_{MT} SDC D_{max}	1.20	1.20	0.89	0.89	0.66	0.66
R/I_e 10%	6.05	7.45	15.4	19	N/A	N/A
R/I_e 2.5%	N/A	N/A	3.85	4.7	10.6	6.7

5.6 Evaluation of Performance in VHS Using Collapse Surfaces

As discussed in Chapter 3 and Chapter 4, the surfaces in Section 5.5 were used to predict median collapse intensity, $\hat{S}_{CT}$, for a given peak strength and drift ratio. The peak strength, V_{max}/W, is given by Equation 3-2 and discrete values of *DR* were chosen: 2.5%, 5%, 7.5%, 15%, and the calculated median *DR* value at incipient collapse, median DR_{IC} (DR_{IC}). Here, DR_{IC} is calculated as a linear function of V_{max}/W for the BRBFs and SMFs and is a constant value for the DCWs. The linear functions were developed from the incipient collapse data from each family, and two examples of the fits are shown in Figure 5-29 and Figure 5-30.

The BRBF archetypes consistently had an almost constant DR_{IC} as shown in an example in Figure 5-29. This trend was true regardless of strength and number of stories. This trend is because the

collapse pushover mode typically has most of the drift concentrated in one to three stories. As discussed previously, the story drift is limited to 10% in each of the archetypes, and because the BRBs are assumed to have fractured at that point, no deterioration is allowed for in the model and the system collapses.

The DR_{IC} for the 3-story Family A SMF is shown in Figure 5-30. As shown, DR_{IC} decreases with increasing strength from 8% to just above 7%. This change is also small although not as small as it was for the BRBFs. The change in DR_{IC} with strength is due largely to the impact of deterioration as the larger strength models collapse in ground motions that are scaled to larger spectral accelerations. This results in additional cycling for the higher strength models and increases deterioration. Given this, and the results of the detailed analysis of SMFs in Section 5.8, DR_{IC} was assumed to remain constant for the SMFs.

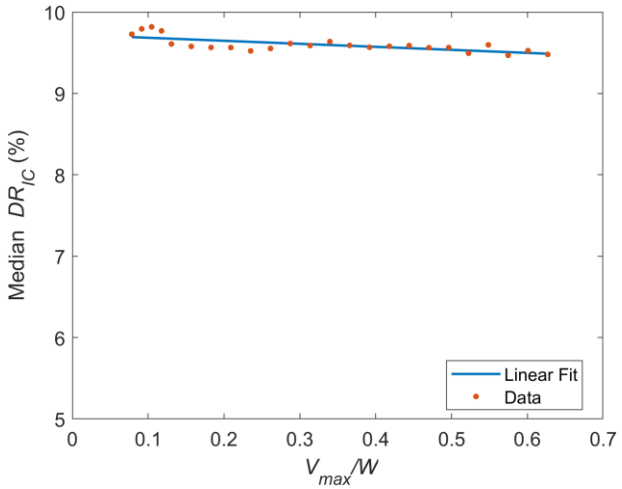

Figure 5-29 Linear fit of median DR_{IC} as a function of V_{max}/W from the 15-story BRBF Family B.

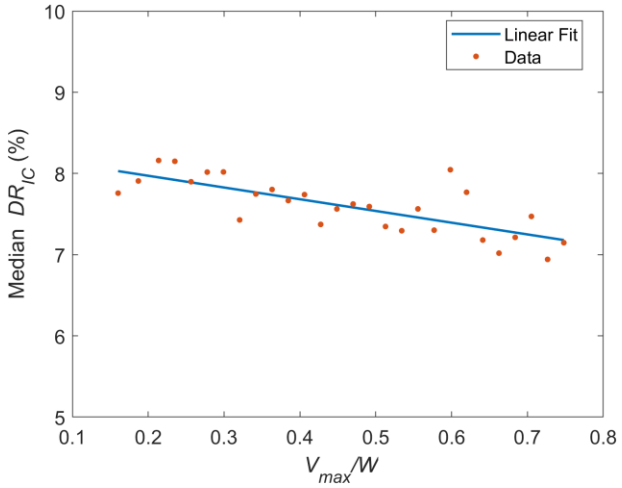

Figure 5-30 Linear fit of median DR_{IC} as a function of V_{max}/W from the 3-story SMF Family A. For subsequent calculation, median DR_{IC} was taken as constant.

The FEMA P-695 procedure summarized in Section 3.4 was implemented to calculate the collapse margin ratio (*CMR*) using the $\hat{S}_{CT}$ values from the surfaces at a range of S_{MT} values per Equation 3-5. The adjusted collapse margin ratio (*ACMR*) was calculated per Equation 3-6 and the spectrum shape factor (SSF) was chosen from Table 3-2 using the prescribed code period for the given family. The period-based ductility, μ_T, used in Table 3-2 was calculated per Equation 3-5 where the δ_u was taken as the calculated median DR_{IC} and the δ_y was taken as the yield story drift ratio of the original backbone families. Plots of *ACMR* versus S_{MT} are shown below for both Risk Category II and IV in Section 5.6.1 through Section 5.6.3. In those plots, the acceptable *ACMR* values come from Table 3-1 using the β values specified in Table 3-6. The β value for calculations using DR_{IC} are interpolated within Table 3-6. Finally, Equation 3-7 was used to calculate the probability of collapse given S_{MT}.

The baseline models that were selected from the referenced studies for each system were used to check that $\hat{S}_{CT}$ values were near expected values. Note that modifications to each model were made to develop the Family A backbones for each system as described above. Therefore, it is no longer expected that the $\hat{S}_{CT}$ matches as closely as it did in Table 5-1. Key changes included increasing the post-yield stiffness of the BRBFs to account for obtained BRB strain hardening data (See Chapter 2) and modifying the roof drift at collapse for the DCWs. Table 5-13 below shows the baseline models, their V_{max}/W, $\hat{S}_{CT}$, the $\hat{S}_{CT}$ resulting from the validation of the eSDOF process as described in Appendix E, and the $\hat{S}_{CT}$ for the Family A model with the nearest V_{max}/W where the Family A models contain all the modifications discussed in Section 5.4. Also shown is the ASCE/SEI 7 period. As shown, the $\hat{S}_{CT}$ values from the analysis of eSDOF systems are reasonably close to those obtained from the detailed analyses for the systems in the references with the exception of the BRBFs. In the case of the BRBFs, modifications were made the baseline that increase the $\hat{S}_{CT}$ for the eSDOFs significantly relative to those from the MDOF study. Those modifications were to increase the post-yield stiffness due to new BRB strain hardening data from a BRB manufacture and to make the drift distribution in the pushover mode shape more uniform to account for the spine effect of the gravity framing. This increase in $\hat{S}_{CT}$ and an overstrength factor used here as recommended in Chapter 2 that exceeds the overstrength used in Ochoa (2017) results in a small probability of collapse at S_{MT} for the BRBFs. For the SMFs, the $\hat{S}_{CT}$ values are close to those from the literature. For the 3-story SMF the overstrength that is used for the eSDOFs as recommended in Chapter 2 is lower than that from the FEMA P-2012 3-story model. However, the FEMA P-2012 study baseline model was designed by ELF. As a result, the *ACMR* for the three-story SMF eSDOF model representing the selected baseline from FEMA P-2012 had a larger *ACMR* and associated probability of collapse at S_{MT}. For the 9-story model SMF, the inverse is true. The overstrength used for the eSDOF is larger than that used for the MDOF in FEMA P-2012 and the *ACMR* for the 9-story eSDOF model is greater than that from FEMA P-2012. Finally, the $\hat{S}_{CT}$ values for the eSDOF DCWs with strength closest to those selected from the Tauberg et al. (2019) study are larger than the $\hat{S}_{CT}$ values from Tauberg because a somewhat larger roof drift at collapse imposed as a non-simulated collapse mode was used for the eSDOF models.

Table 5-13 Comparison of *ACMR* for MDOF Models from the Literature Used as Baselines and the eSDOF Model with the Nearest Strength

Archetype Designation from Literature	V_{max}/W MDOF	eSDOF Model	V_{max}/W SDOF	T (sec)	$\hat{S}_{CT}$ (g) MDOF	$\hat{S}_{CT}$ (g) eSDOF Used for Validation (App. E)	$\hat{S}_{CT}$ (g) eSDOF as Modified in Section 5.4
BRBF4-2 (Ochoa 2017)	0.13	BRBF-4A	0.12	0.87	1.22	1.19	2.02
BRBF9-2 (Ochoa 2017)	0.06	BRBF-9A	0.06	1.54	0.65	0.63	1.59
BRBF15-2 (Ochoa 2017)	0.04	BRBF-15A	0.06	2.23	0.52	0.44	1.13
V0300203(1) (FEMA P-2012)	0.49	SMF-3A	0.46	0.73	2.59	2.39	2.35
V0900201(1) (FEMA P-2012)	0.08	SMF-9A	0.08	1.83	0.74	0.73	0.64
8H-*DR*-3 (Tauberg et al. 2019)	0.23	DCW-8A	0.23	0.75	1.95	1.77	2.02
12H-*DR*-3 (Tauberg et al. 2019)	0.11	DCW-12A	0.13	1.02	1.39	1.42	1.65
18H-*DR*-3 (Tauberg et al. 2019)	0.11	DCW-18A	0.10	1.38	1.02	1.09	1.23

OVERSTRENGTH

Values of overstrength, Ω, are as recommended from Chapter 2. For the BRBFs, a constant overstrength 2.5 was used for both Family A and B. As noted in Chapter 2 that overstrength is larger due to design assumptions, brace expected strength, and brace strain hardening. For the SMFs, Family A was meant to represent SMFs where the gravity frame is neglected (i.e., where the gravity frame columns are oriented for weak-axis bending). As noted in Chapter 2, without the gravity frame, the SMF overstrength is largely due to design assumptions, drift limits, and material expected strength. A function for overstrength that varies with S_{MT} was developed in Chapter 2 for SMF and used here. For SMF Family B where the gravity framing is included, the overstrength was also found to vary as a function of S_{MT} as described in Chapter 2. In this case the central values from Figure 2-28 were used. Similarly, for the DCWs, the overstrength was a constant value of 1.7 for Family A where the effect of gravity framing was not included (i.e., representing a DCW core with steel gravity framing). For DCW Family B it was taken to vary with S_{MT} described in Chapter 2 and

illustrated in Figure 2-50. The summary tables in Appendices I, J, and K show the overstrength values used for each value of S_{MT} for the BRBFs, SMFs, and DCWs, respectively. As discussed above, the values of overstrength applied to eSDOF collapse results differ from those values in the referenced literature for each system.

5.6.1 BRBF Adjusted Collapse Margin Ratios and Probability of Collapse

The BRBF eSODF models have large *ACMR*s and low probabilities of collapse at S_{MT} at the SDC D_{max} boundary as shown in Figure 5-31 through Figure 5-36. BRBFs are expected to perform well given their deformation capacity and lack of strength degradation. However, these analyses may over predict the collapse capacity for the reasons mentioned above. Namely, that cyclic strength degradation due to beams and column local buckling and/or BRB connection deterioration was not considered as they were not important drivers of the response for the MDOF analyses in Ochoa (2017). However, at larger strengths these degradation modes may contribute to the response. Additionally, the eSDOF models may overestimate the post-yield stiffness after repeated cycling since the strain hardening data provided by CoreBrace included both isotropic and kinematic hardening. It is expected that after cycling when isotropic hardening occurs, the cyclic yield strength increases but the post-yield stiffness is relatively flat. The material model used here is more consistent kinematic hardening until the capping point is reached.

Despite the shortcomings and simplifications of the models, Figure 5-31 through Figure 5-36 show clear trends between S_{MT}, *ACMR*, and P[Collapse|S_{MT}]. The results indicate that for systems that behave as a BRBF, i.e., those that have little cyclic deterioration, large deformation capacity, somewhat concentrated drifts as particular stories, and where the capping point doesn't shift significantly with increasing strength (i.e., the drift at which a BRB fractures, which is based largely on brace strain), *ACMR* decreases and P[Collapse|S_{MT}] increases with increasing S_{MT}.

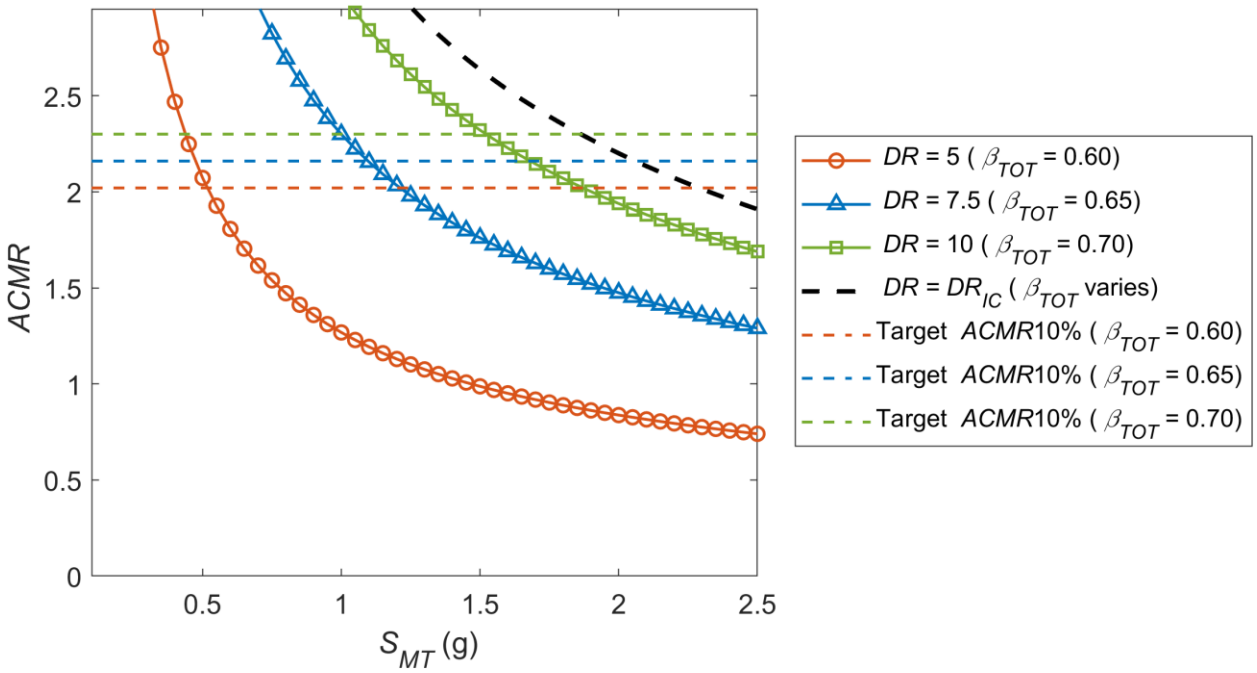

(a) BRBF-4A adjusted collapse margin ratio versus S_{MT} for R = 8, RC II (I_e = 1.0)

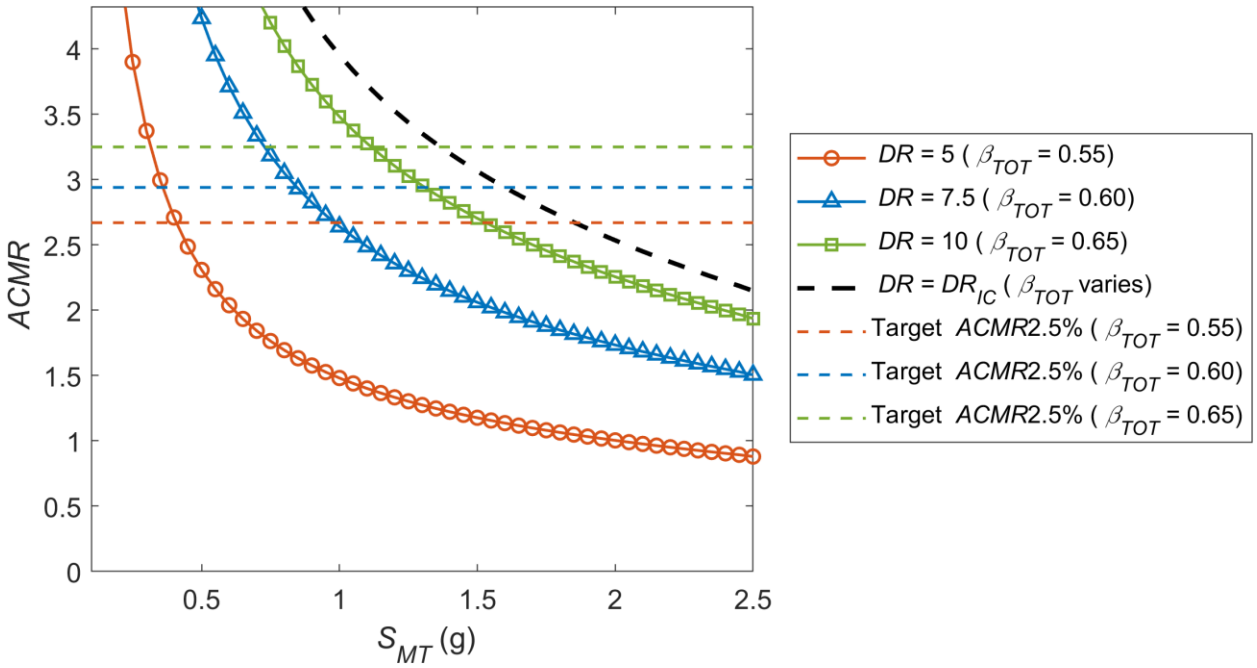

(b) BRBF-4A adjusted collapse margin ratio versus S_{MT} for R = 8, RC IV (I_e = 1.5)

Figure 5-31 4-Story BRBF Family A adjusted collapse margin ratio and probability of collapse versus S_{MT} for Risk Categories II and IV. Dashed black line represents median DR_{IC}.

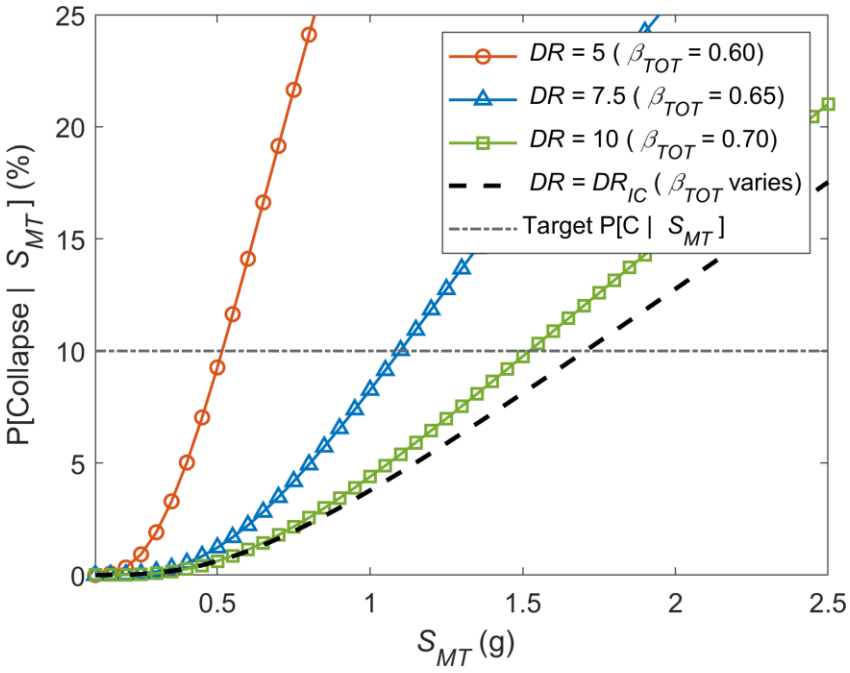

(c) BRBF-4A probability of collapse versus S_{MT} for R = 8, RC II (I_e = 1.0)

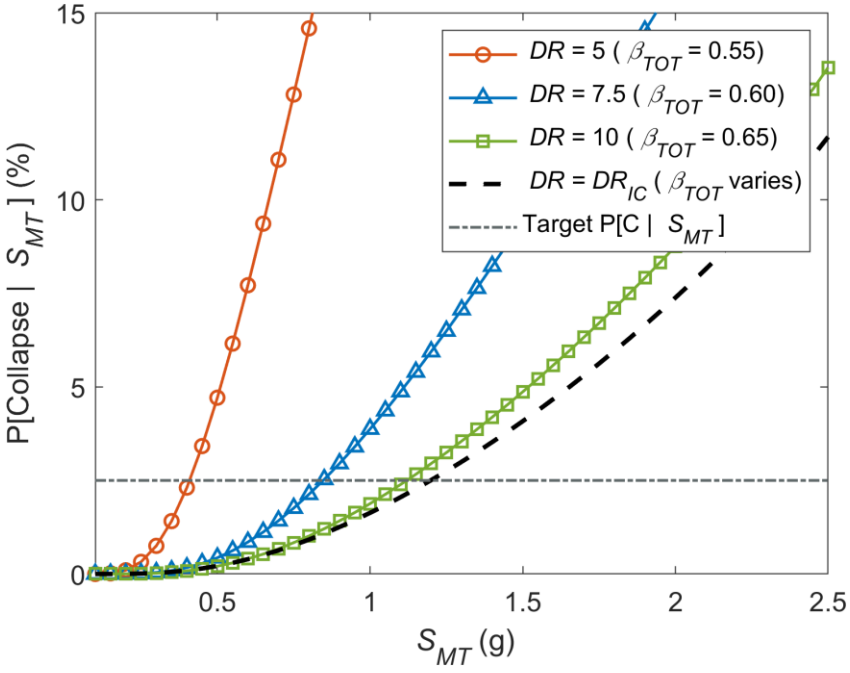

(d) BRBF-4A probability of collapse versus S_{MT} for R = 8, RC IV (I_e = 1.5)

Figure 5-31 4-Story BRBF Family A adjusted collapse margin ratio and probability of collapse versus S_{MT} for Risk Categories II and IV. Dashed black line represents median DR_{IC}. (continued)

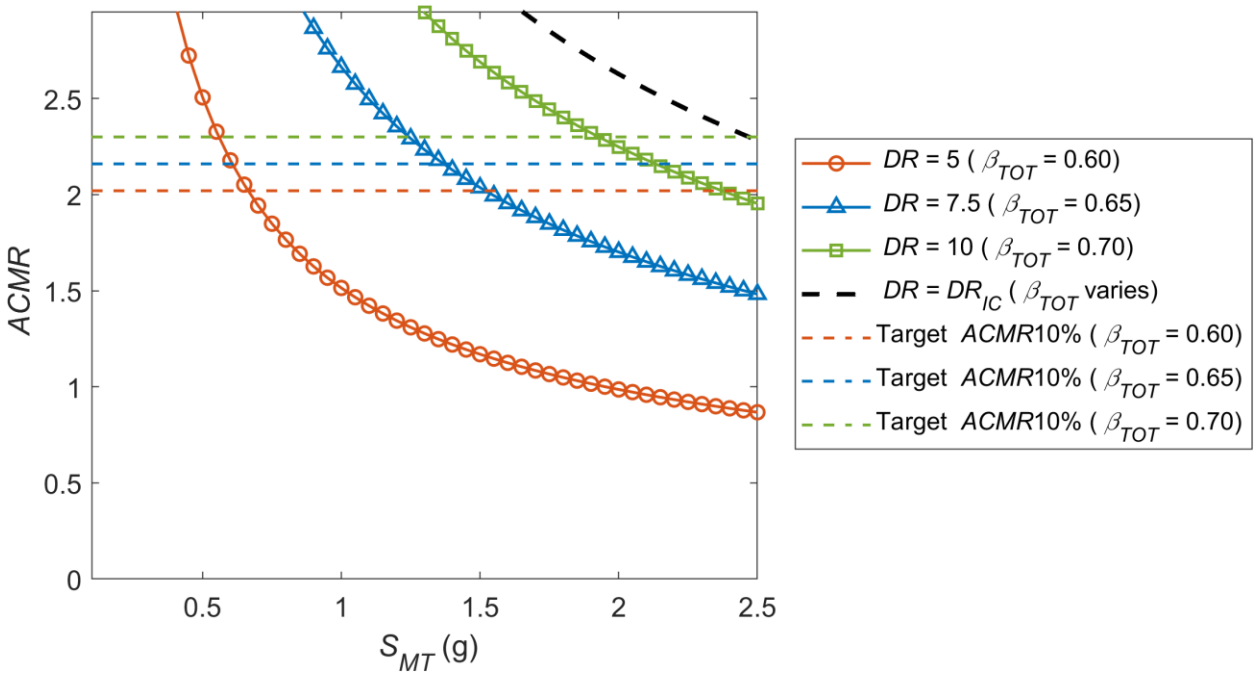

(a) BRBF-4B adjusted collapse margin ratio versus S_{MT} for R = 8, RC II (I_e = 1.0)

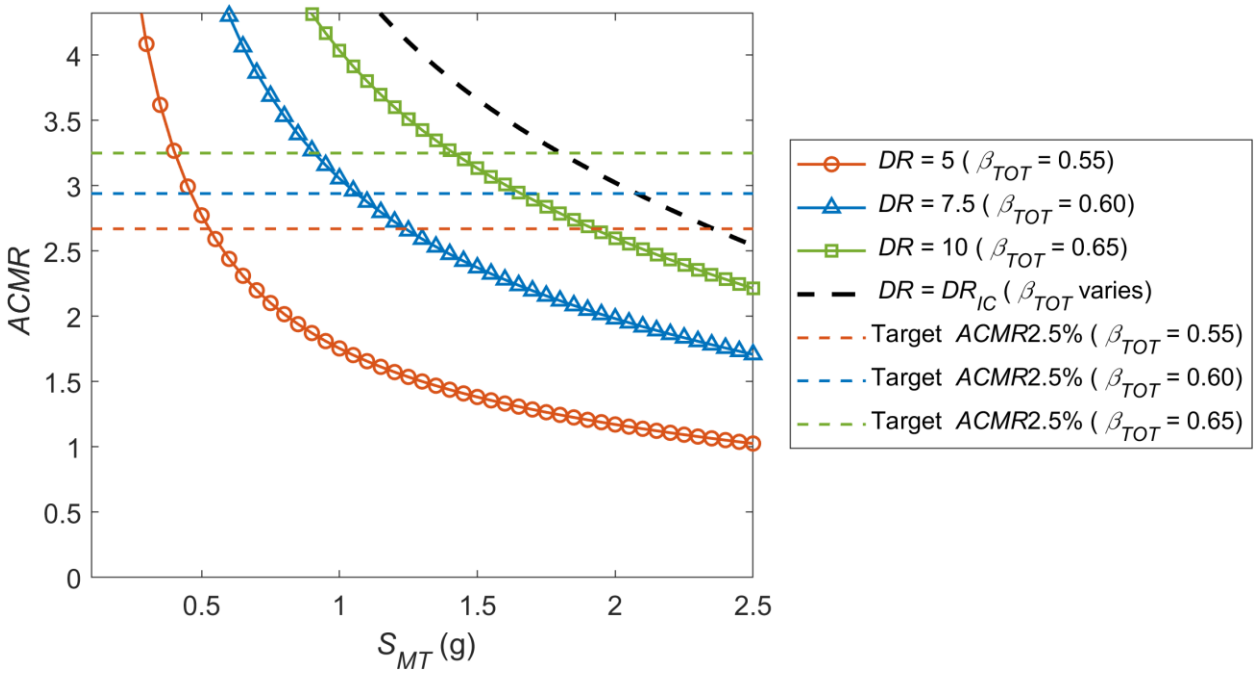

(b) BRBF-4B adjusted collapse margin ratio versus S_{MT} for R = 8, RC IV (I_e = 1.5)

Figure 5-32 4-Story BRBF Family B adjusted collapse margin ratio and probability of collapse versus S_{MT} for Risk Categories II and IV. Dashed black line represents median DR_{IC}.

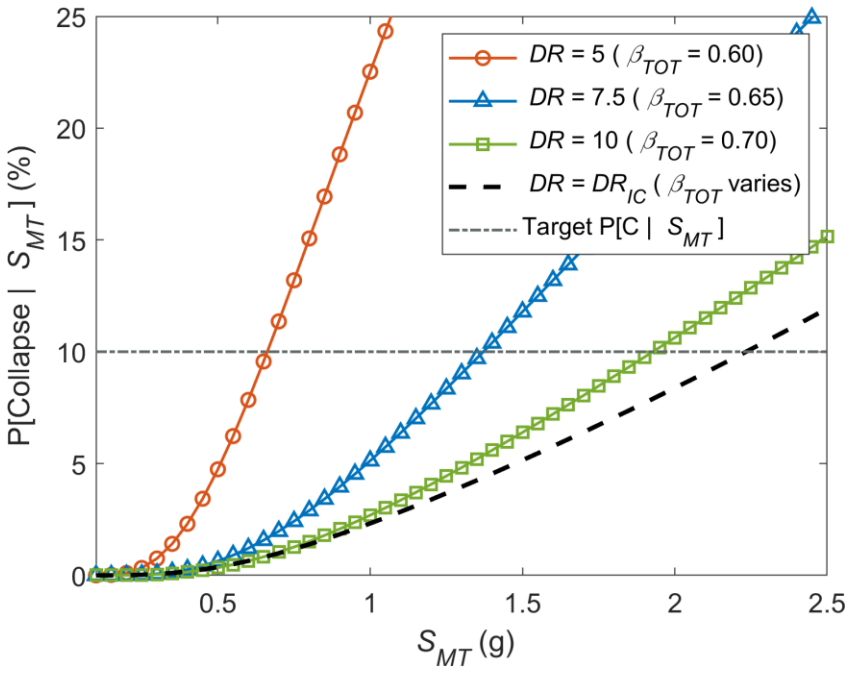

(c) BRBF-4B probability of collapse versus S_{MT} for R = 8, RC II (I_e = 1.0)

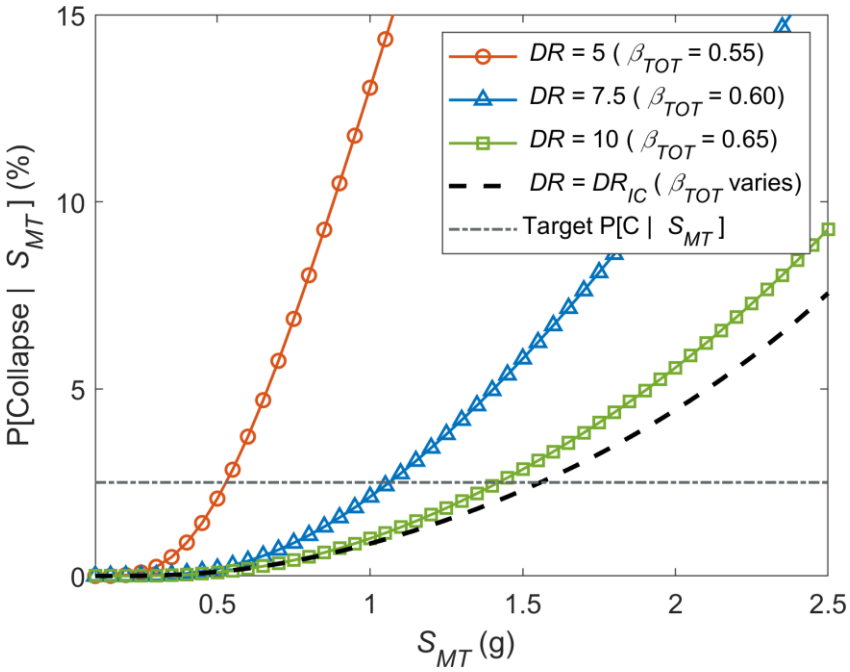

(d) BRBF-4B probability of collapse versus S_{MT} for R = 8, RC IV (I_e = 1.5)

Figure 5-32 4-Story BRBF Family B adjusted collapse margin ratio and probability of collapse versus S_{MT} for Risk Categories II and IV. Dashed black line represents median DR_{IC}. (continued)

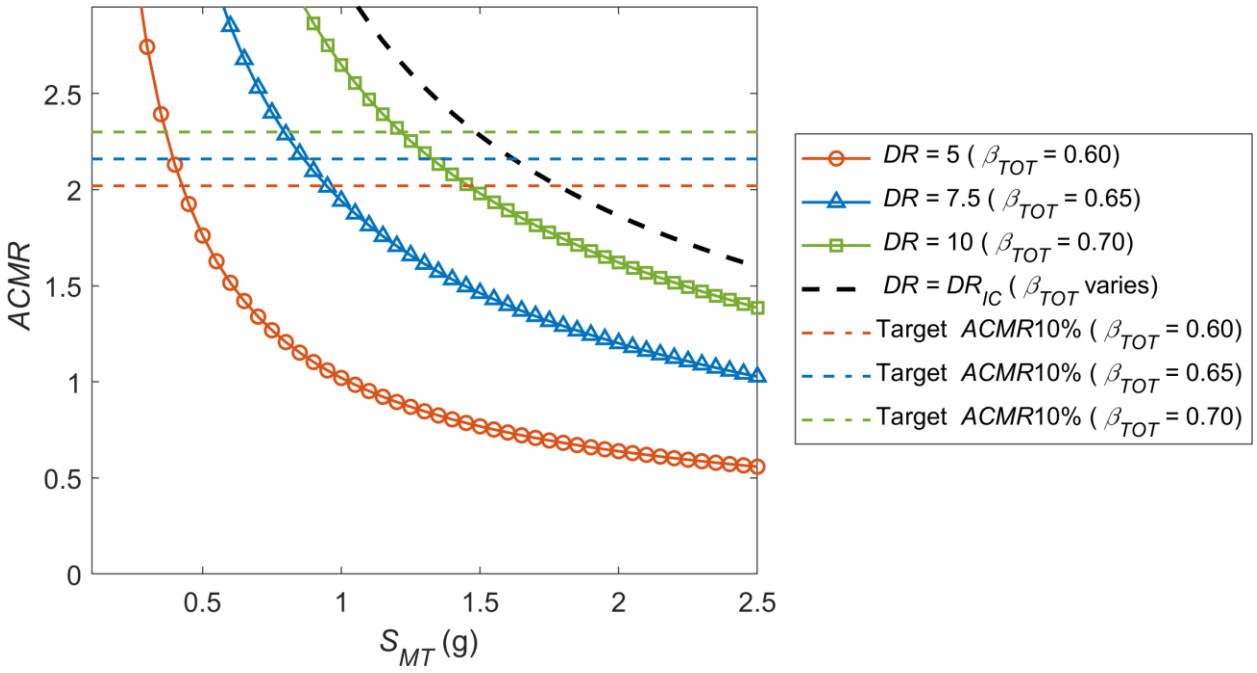

(a) BRBF-9A adjusted collapse margin ratio versus S_{MT} for R = 8, RC II (I_e = 1.0)

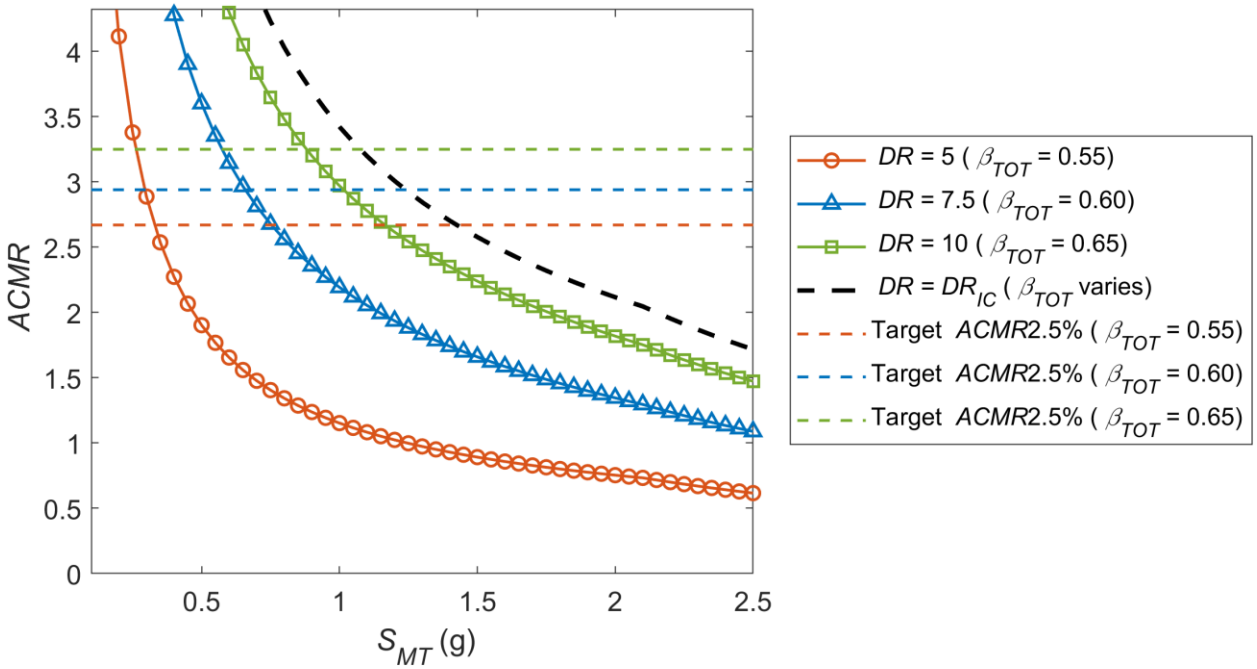

(b) BRBF-9A adjusted collapse margin ratio versus S_{MT} for R = 8, RC IV (I_e = 1.5)

Figure 5-33 9-Story BRBF Family A adjusted collapse margin ratio and probability of collapse versus S_{MT} for Risk Categories II and IV. Dashed black line represents median DR_{IC}.

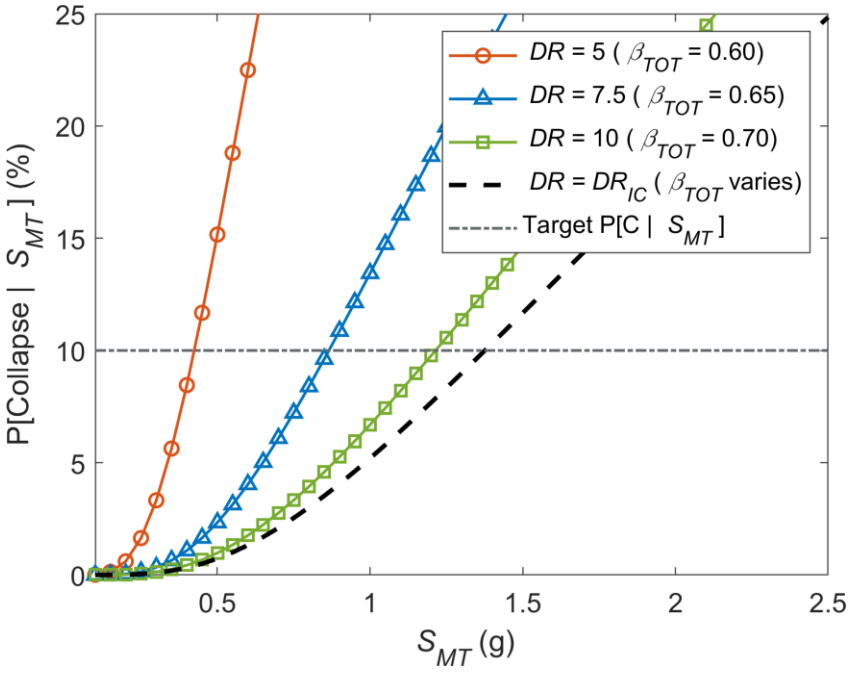

(c) BRBF-9A probability of collapse versus S_{MT} for R = 8, RC II (I_e = 1.0)

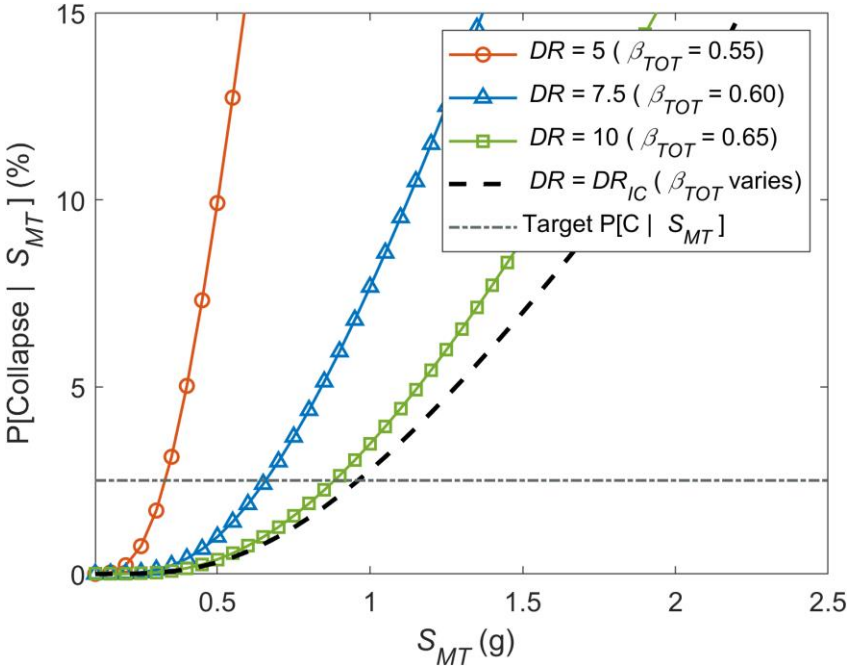

(d) BRBF-9A probability of collapse versus S_{MT} for R = 8, RC IV (I_e = 1.5)

Figure 5-33 9-Story BRBF Family A adjusted collapse margin ratio and probability of collapse versus S_{MT} for Risk Categories II and IV. Dashed black line represents median DR_{IC}. (continued)

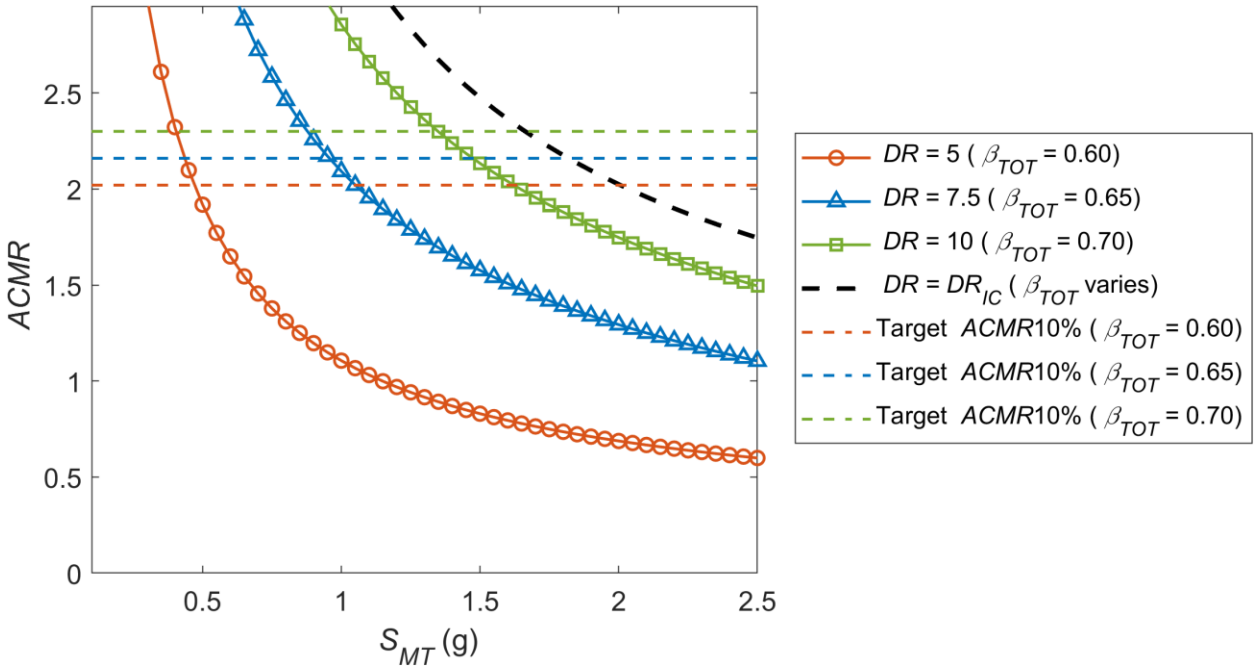

(a) BRBF-9B adjusted collapse margin ratio versus S_{MT} for R = 8, RC II (I_e = 1.0)

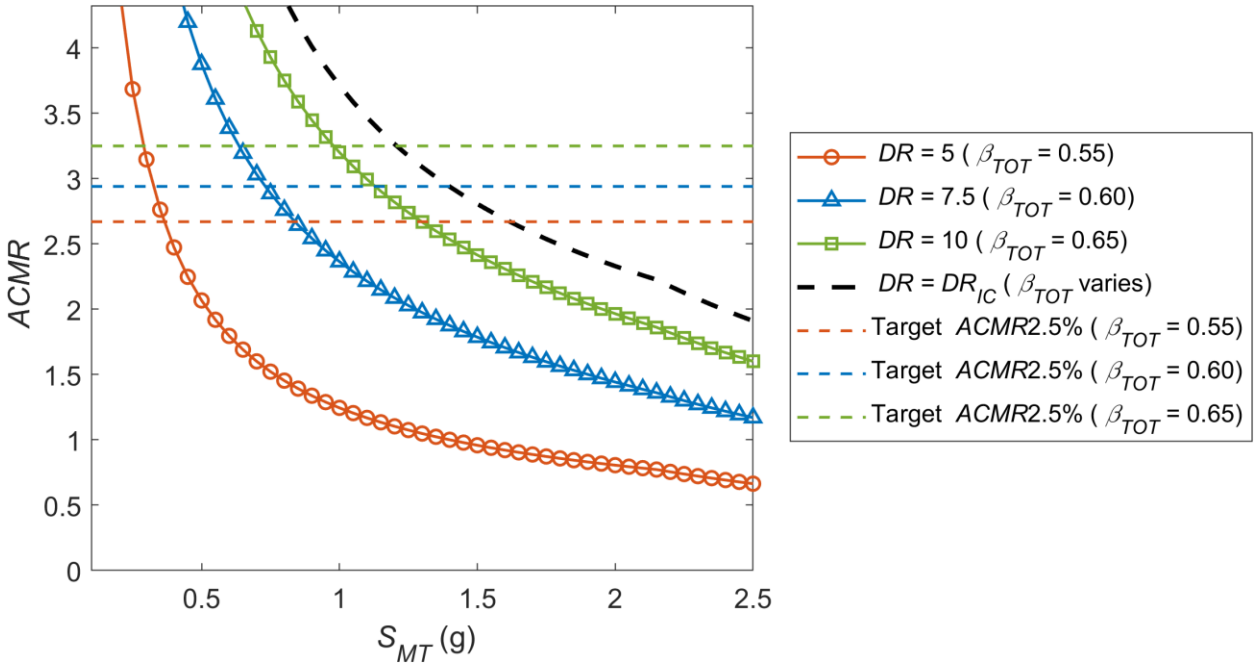

(b) BRBF-9B adjusted collapse margin ratio versus S_{MT} for R = 8, RC IV (I_e = 1.5)

Figure 5-34 9-Story BRBF Family B adjusted collapse margin ratio and probability of collapse versus S_{MT} for Risk Categories II and IV. Dashed black line represents median DR_{IC}.

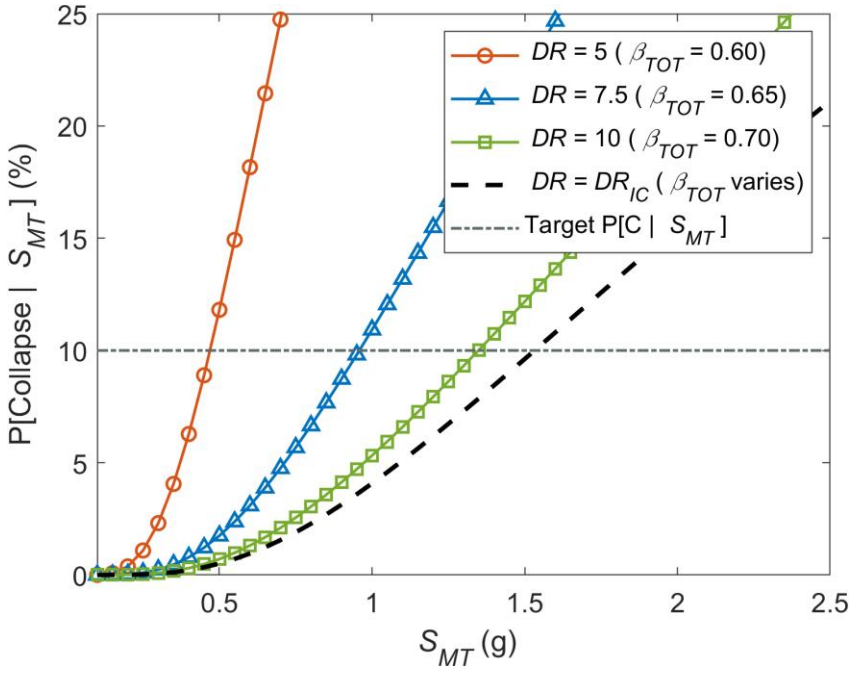

(c) BRBF-9B probability of collapse versus S_{MT} for R = 8, RC II (I_e = 1.0)

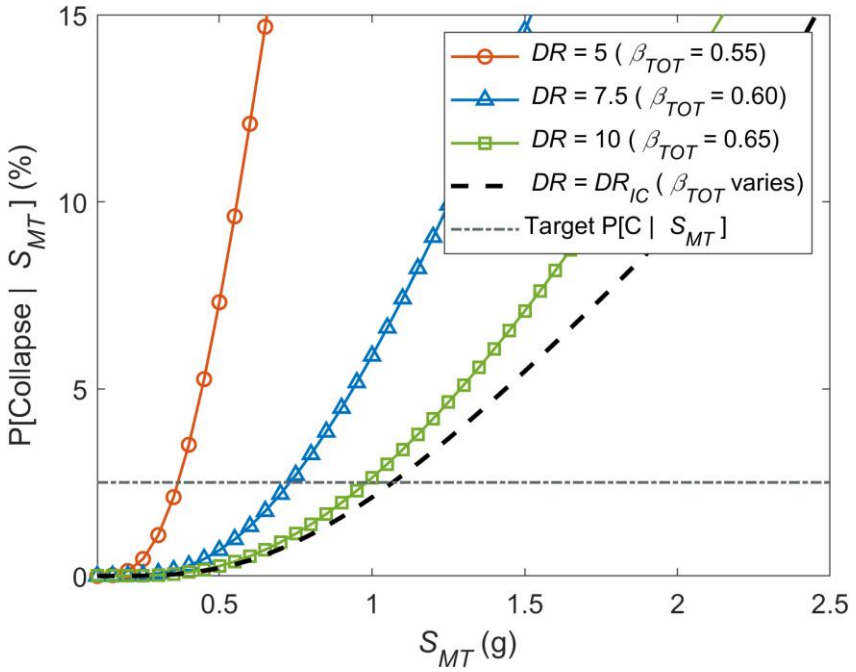

(d) BRBF-9B probability of collapse versus S_{MT} for R = 8, RC IV (I_e = 1.5)

Figure 5-34 9-Story BRBF Family B adjusted collapse margin ratio and probability of collapse versus S_{MT} for Risk Categories II and IV. Dashed black line represents median DR_{IC}. (continued)

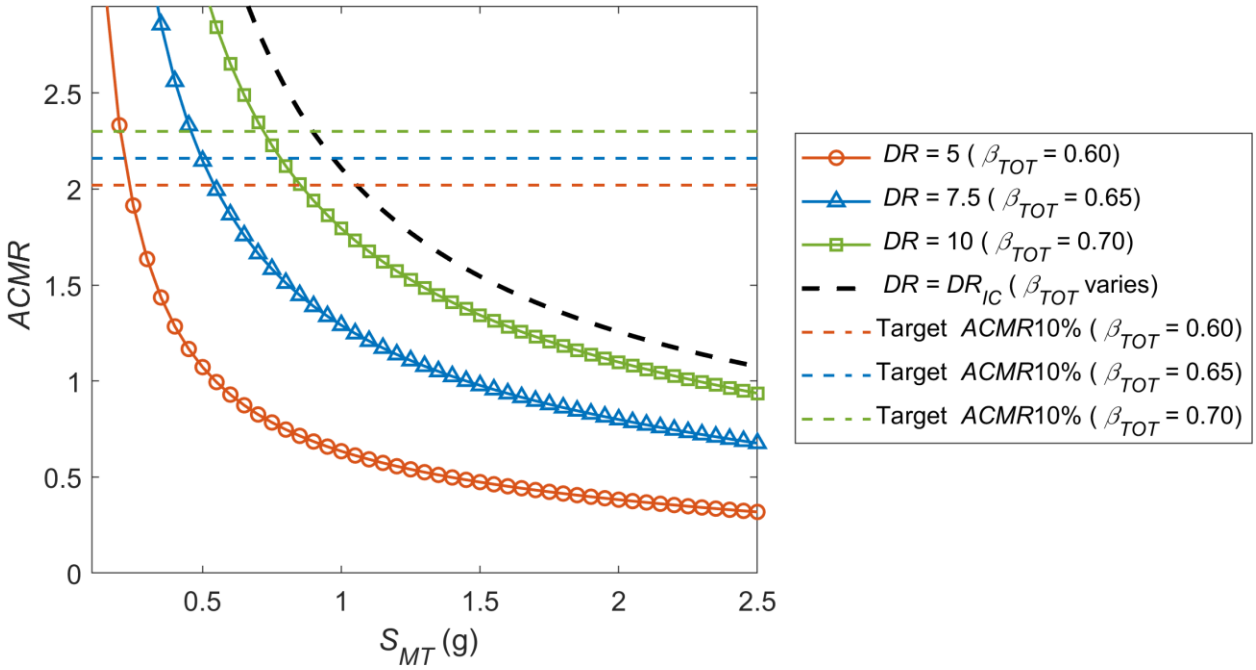

(a) BRBF-15A adjusted collapse margin ratio versus S_{MT} for R = 8, RC II (I_e = 1.0)

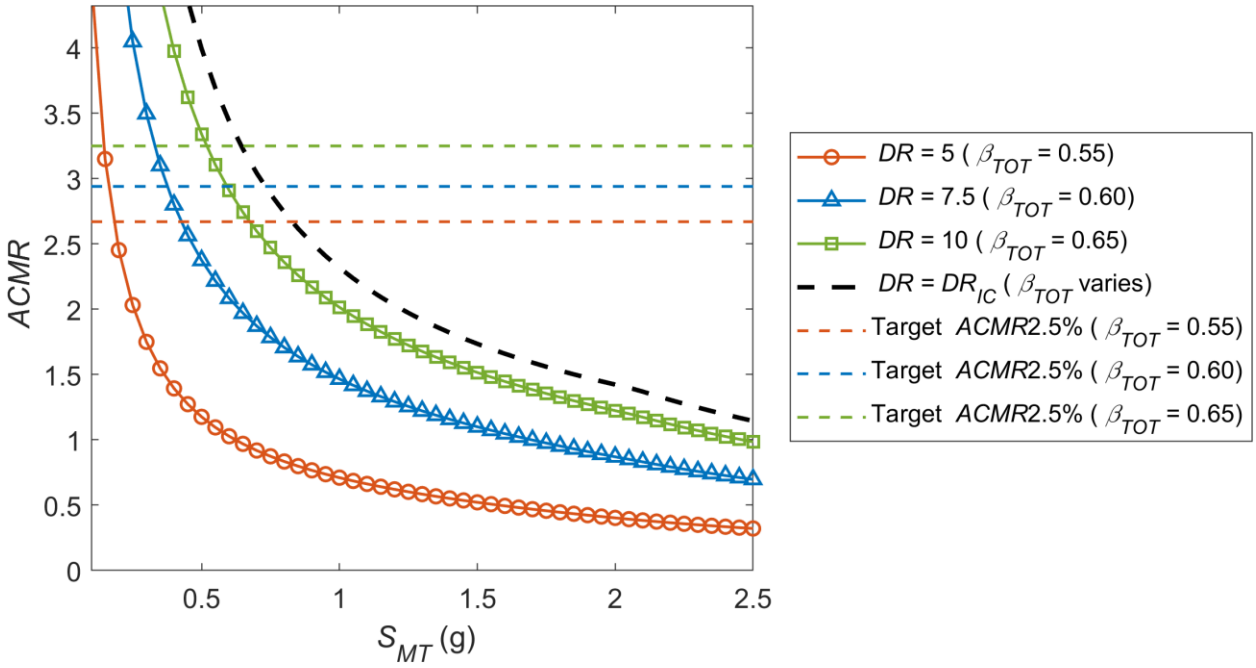

(b) BRBF-15A adjusted collapse margin ratio versus S_{MT} for R = 8, RC IV (I_e = 1.5)

Figure 5-35 15-Story BRBF Family A adjusted collapse margin ratio and probability of collapse versus S_{MT} for Risk Categories II and IV. Dashed black line represents median DR_{IC}.

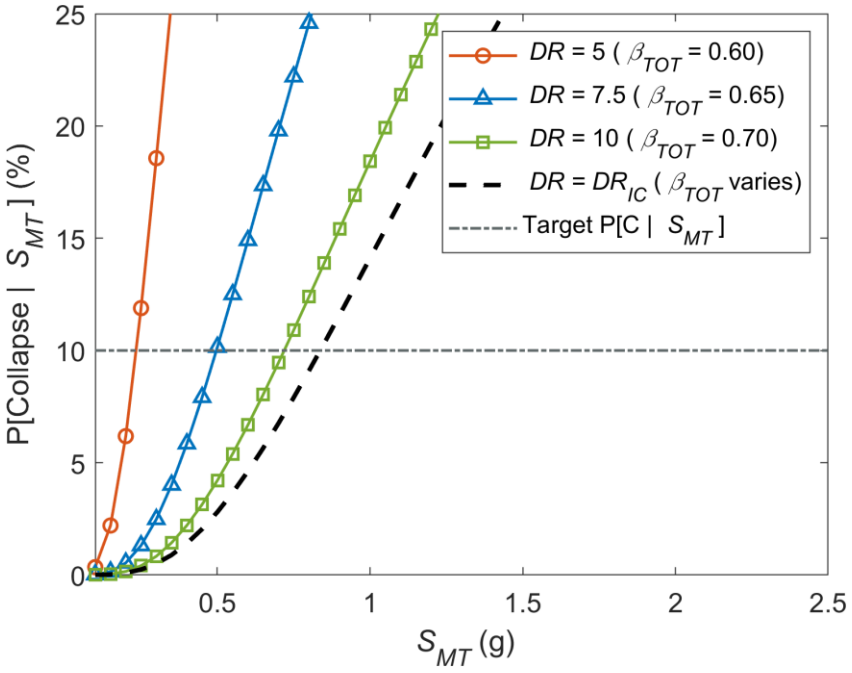

(c) BRBF-15A probability of collapse versus S_{MT} for R = 8, RC II (I_e = 1.0)

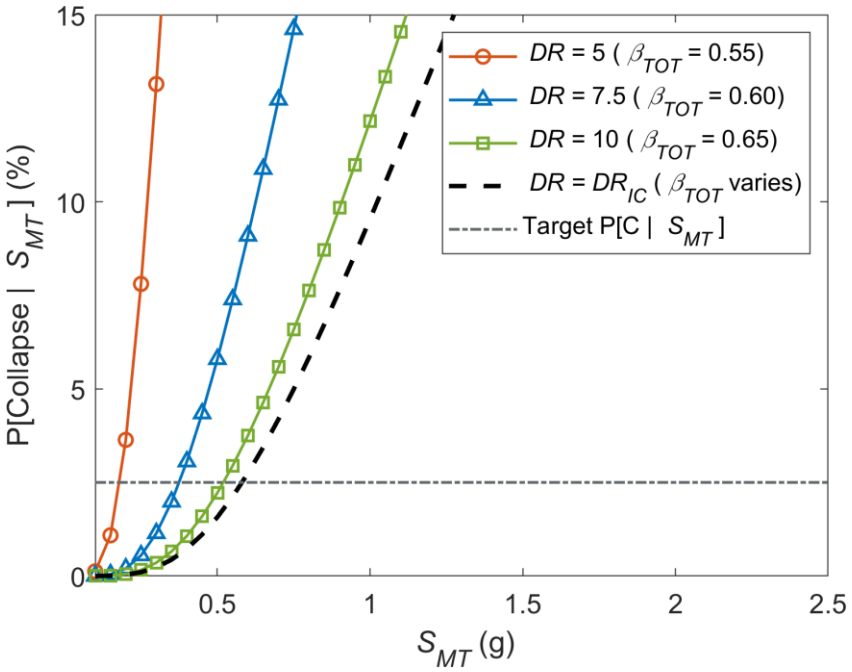

(d) BRBF-15A probability of collapse versus S_{MT} for R = 8, RC IV (I_e = 1.5)

Figure 5-35 15-Story BRBF Family A adjusted collapse margin ratio and probability of collapse versus S_{MT} for Risk Categories II and IV. Dashed black line represents median DR_{IC}. (continued)

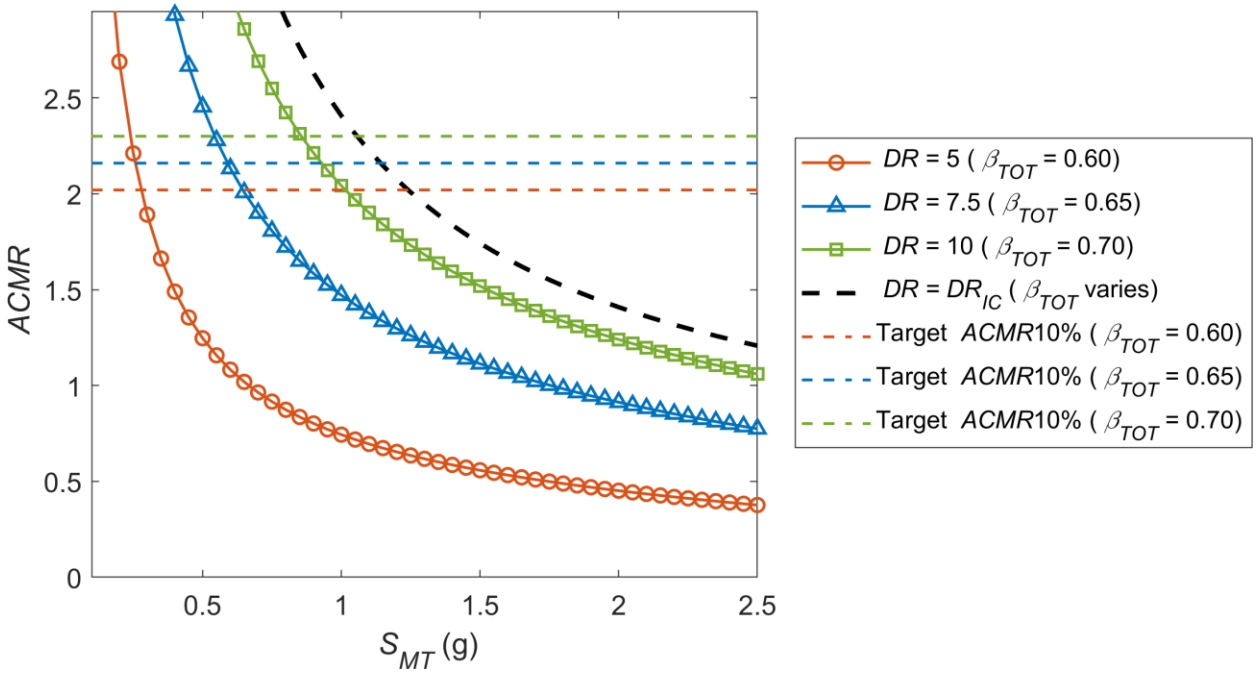

(a) BRBF-15B adjusted collapse margin ratio versus S_{MT} for R = 8, RC II (I_e = 1.0)

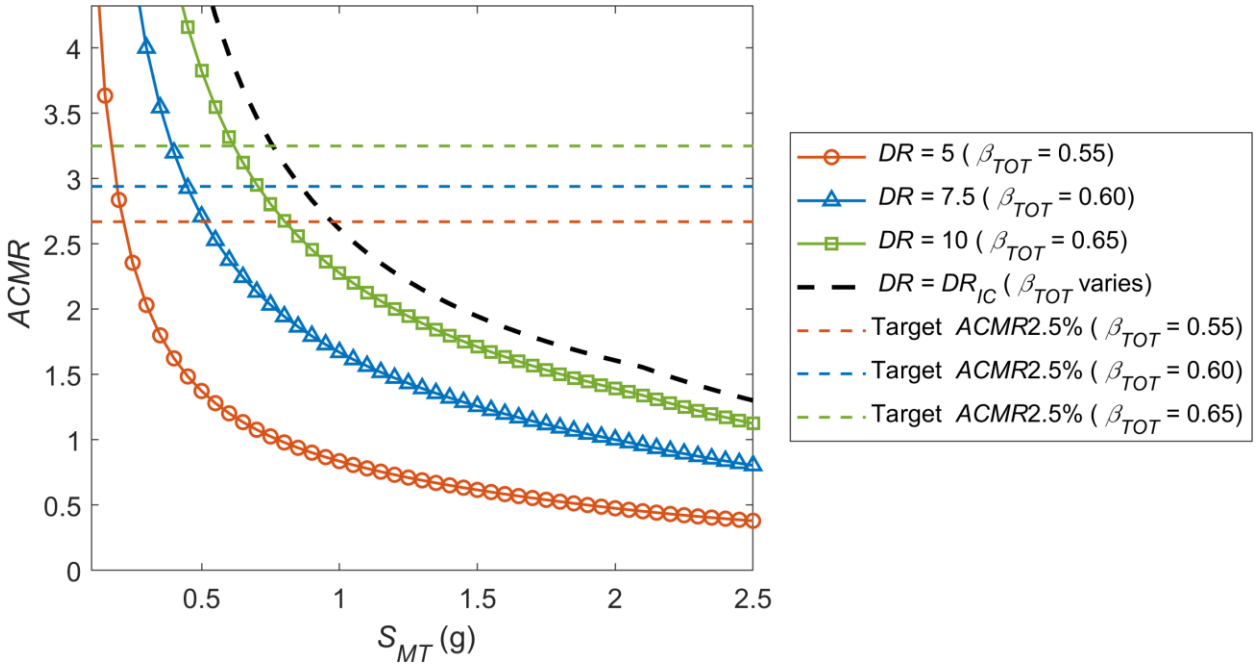

(b) BRBF-15B adjusted collapse margin ratio versus S_{MT} for R = 8, RC IV (I_e = 1.5)

Figure 5-36 15-Story BRBF Family B adjusted collapse margin ratio and probability of collapse versus S_{MT} for Risk Categories II and IV. Dashed black line represents median DR_{IC}.

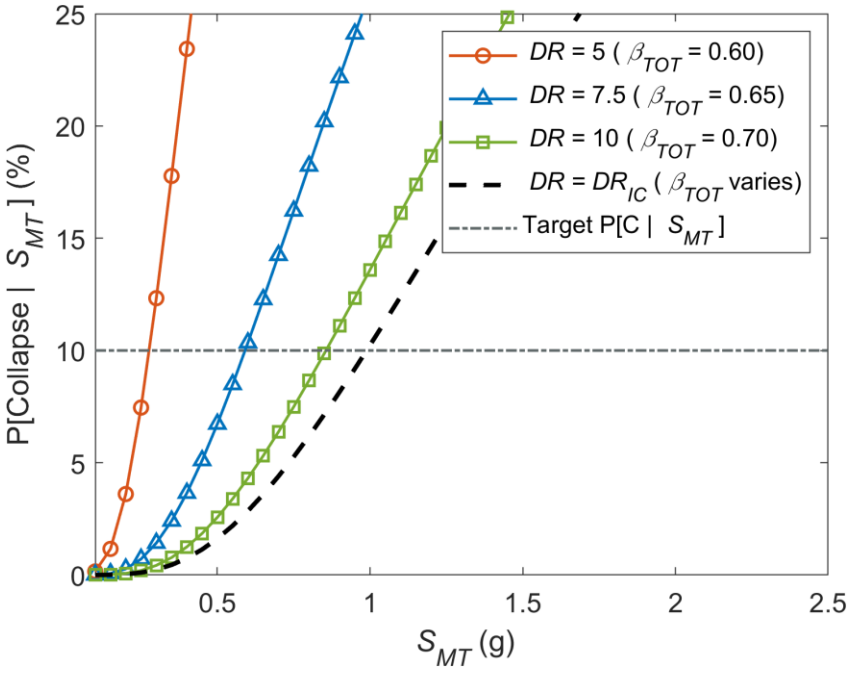

(c) BRBF-15B probability of collapse versus S_{MT} for R = 8, RC II (I_e = 1.0)

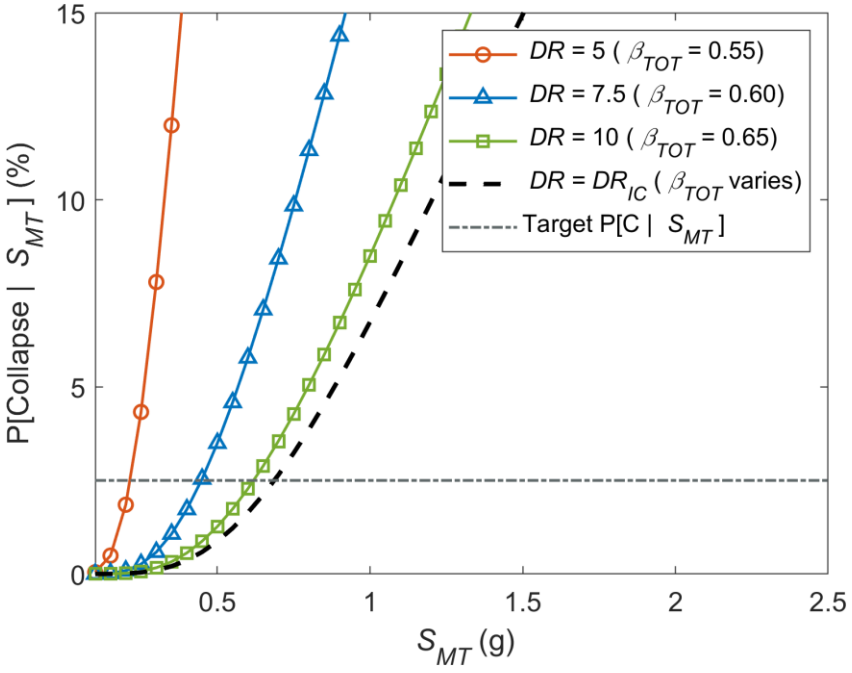

(d) BRBF-15B probability of collapse versus S_{MT} for R = 8, RC IV (I_e = 1.5)

Figure 5-36 15-Story BRBF Family B adjusted collapse margin ratio and probability of collapse versus S_{MT} for Risk Categories II and IV. Dashed black line represents median DR_{IC}. (continued)

5.6.2 SMF Adjusted Collapse Margin Ratios and Probability of Collapse

The SMF eSODF analysis results indicate that SMFs just meet (or slightly exceed) the collapse probability targets for SDC D_{max}. As shown in Table 5-4, this is consistent with previous SMF studies that have simulated SMF with RBS connections including FEMA P-2012, which was used as the baseline for the eSDOF SMF models. The overstrength factors used for the RC IV results are 1.5 times those used for the RC II results (i.e., those shown in Figure 2-29). This 1.5 factor increase for the RC IV structures is less than the 1.77 factor in Table 2-43. An additional source of conservatism for the eSDOF SMF models is the deterioration, which may be too large for the models with larger strength than the baseline models. The girders and columns would likely be stockier than those in the baseline models, and this would lead to slower deterioration. Combined, these factors mean that the RC IV results presented here may overpredict collapse risk.

Despite the simplifications of the models, Figure 5-37 through Figure 5-40 show clear trends between S_{MT}, *ACMR* and P[Collapse|S_{MT}]. The results indicate that for systems that behave as a SMF, i.e., those that have considerable cyclic deterioration, large monotonic deformation capacity, somewhat uniformly distributed drifts, and where the capping point doesn't shift significantly with increasing strength (i.e., the drift at which a SMF connection fractures, which is based largely on connection rotation capacity), *ACMR* decreases and P[Collapse|S_{MT}] increases with increasing S_{MT}.

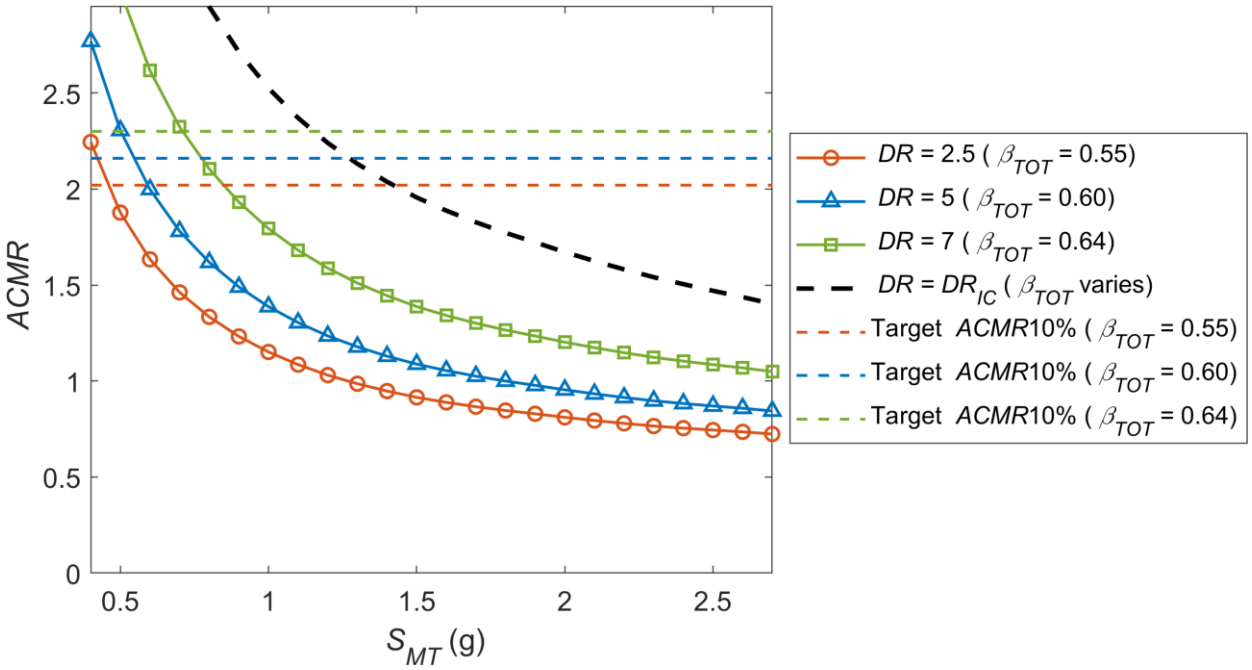

(a) SMF-3A adjusted collapse margin ratio versus S_{MT} for R = 8, RC II (I_e = 1.0)

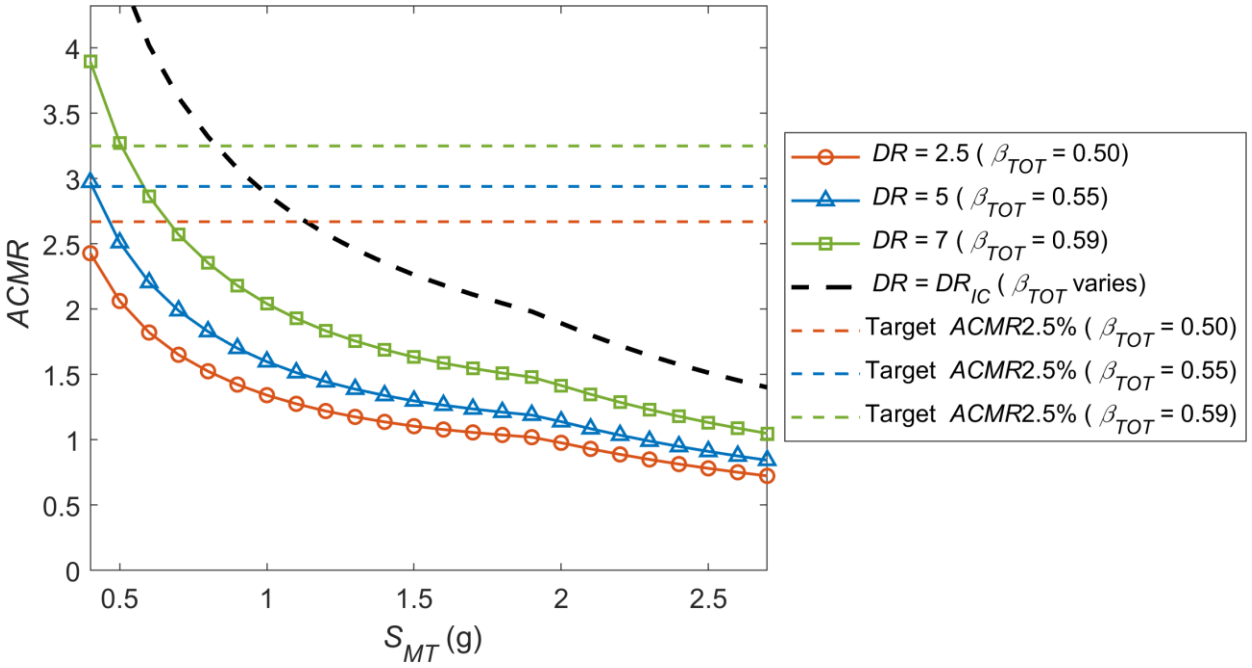

(b) SMF-3A adjusted collapse margin ratio versus S_{MT} for R = 8, RC IV (I_e = 1.5)

Figure 5-37 3-Story SMF Family A adjusted collapse margin ratio and probability of collapse versus S_{MT} for Risk Categories II and IV. Dashed black line represents median DR_{IC}.

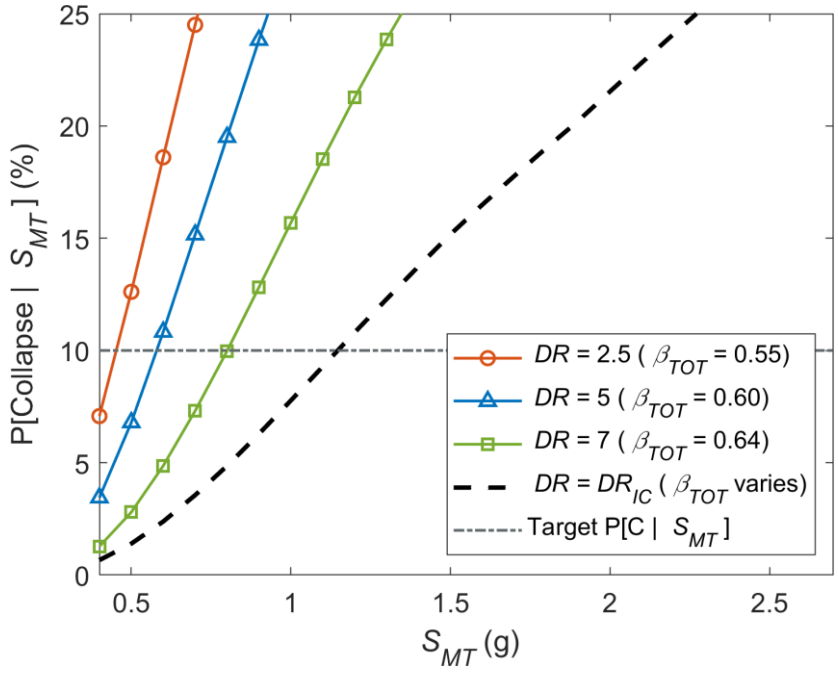

(c) SMF-3A probability of collapse versus S_{MT} for R = 8, RC II (I_e = 1.0)

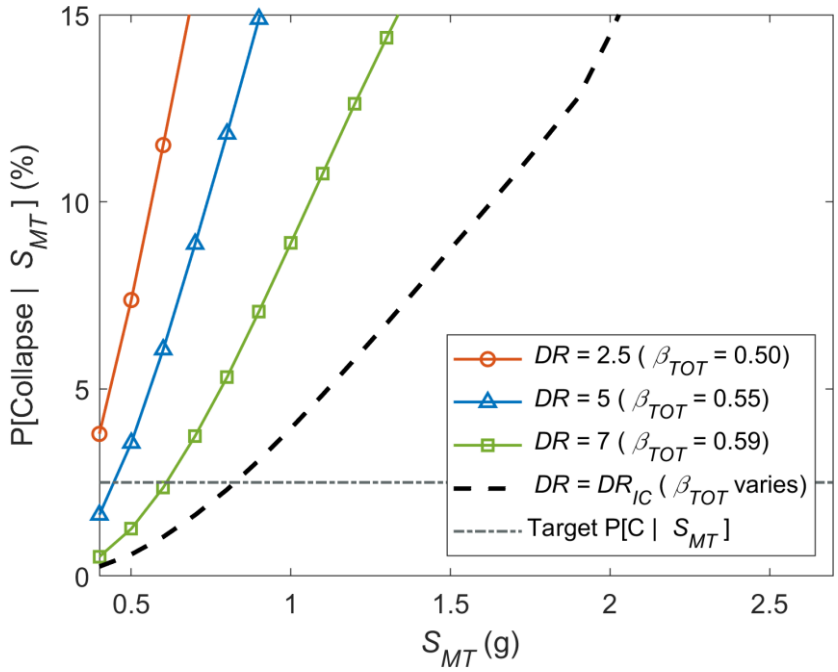

(d) SMF-3A probability of collapse versus S_{MT} for R = 8, RC IV (I_e = 1.5)

Figure 5-37 3-Story SMF Family A adjusted collapse margin ratio and probability of collapse versus S_{MT} for Risk Categories II and IV. Dashed black line represents median DR_{IC}. (continued)

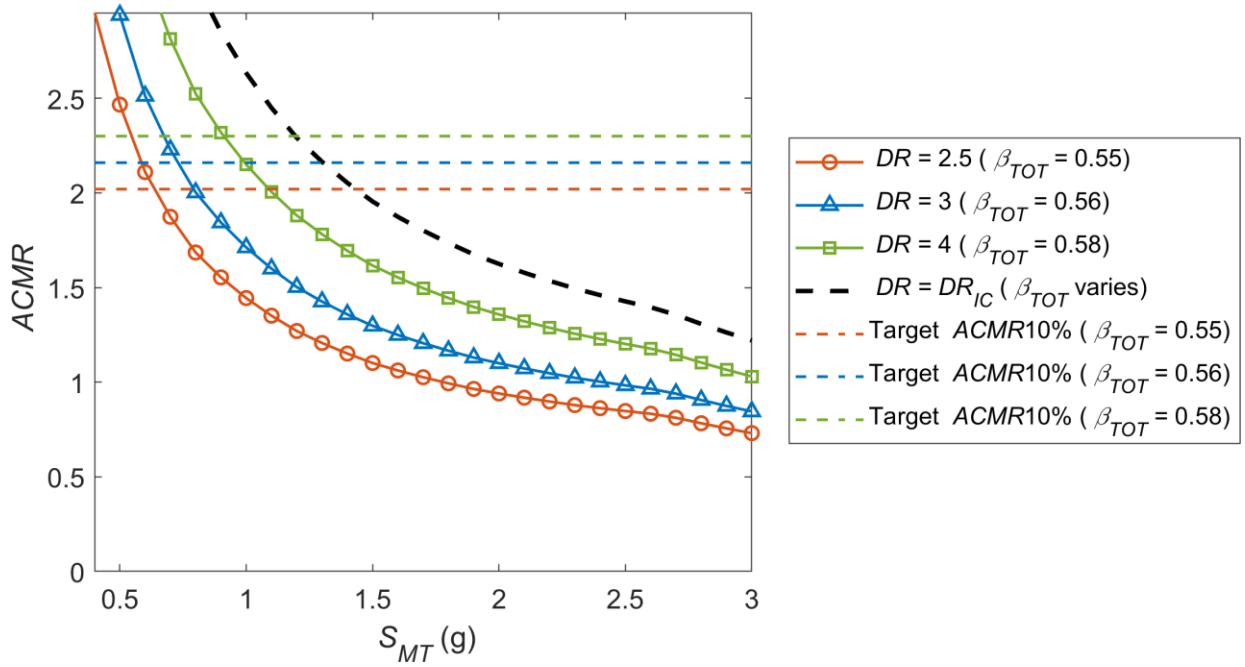

(a) SMF-3B adjusted collapse margin ratio versus S_{MT} for R = 8, RC II (I_e = 1.0)

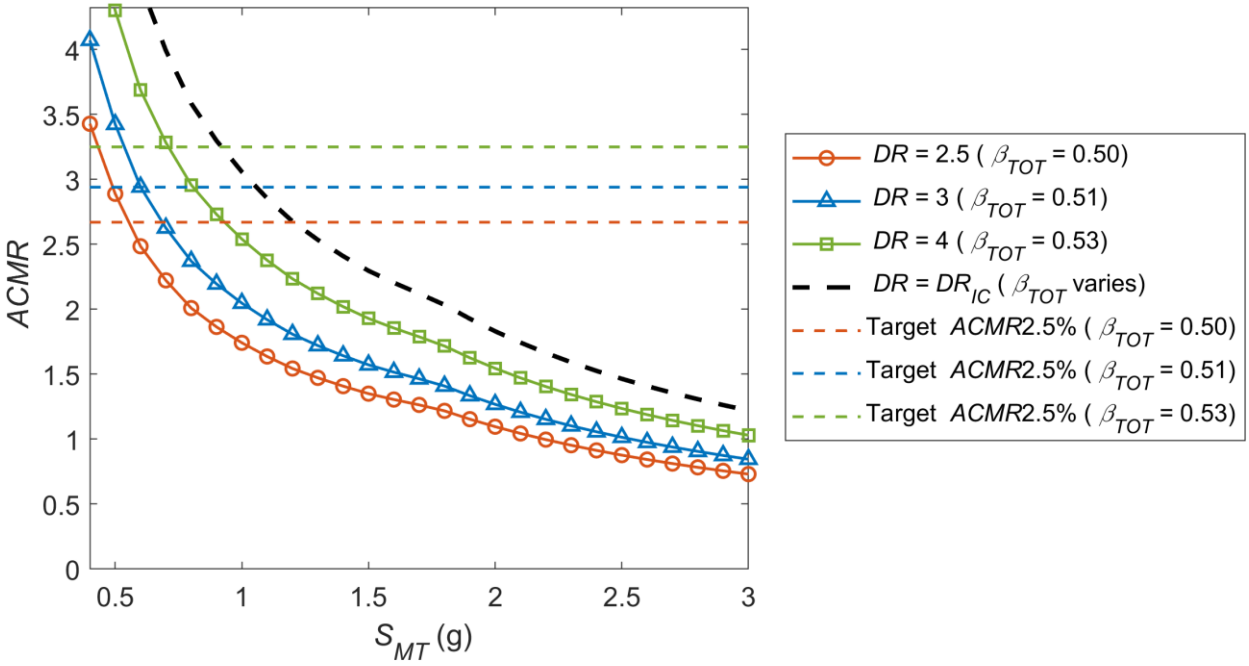

(b) SMF-3B adjusted collapse margin ratio versus S_{MT} for R = 8, RC IV (I_e = 1.5)

Figure 5-38 **3-Story SMF Family B adjusted collapse margin ratio and probability of collapse versus S_{MT} for Risk Categories II and IV. Dashed black line represents median DR_{IC}.**

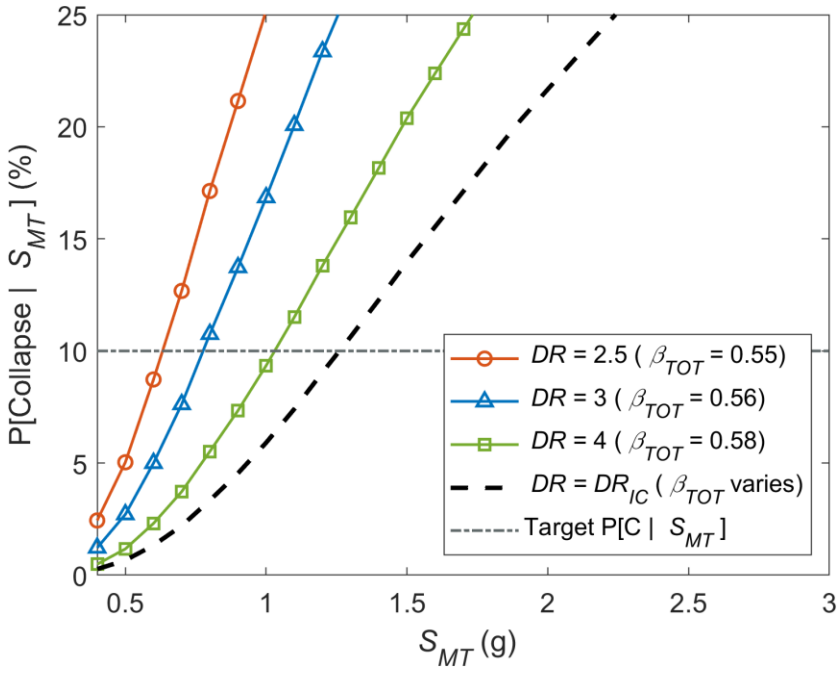

(c) SMF-3B probability of collapse versus S_{MT} for R = 8, RC II (I_e = 1.0)

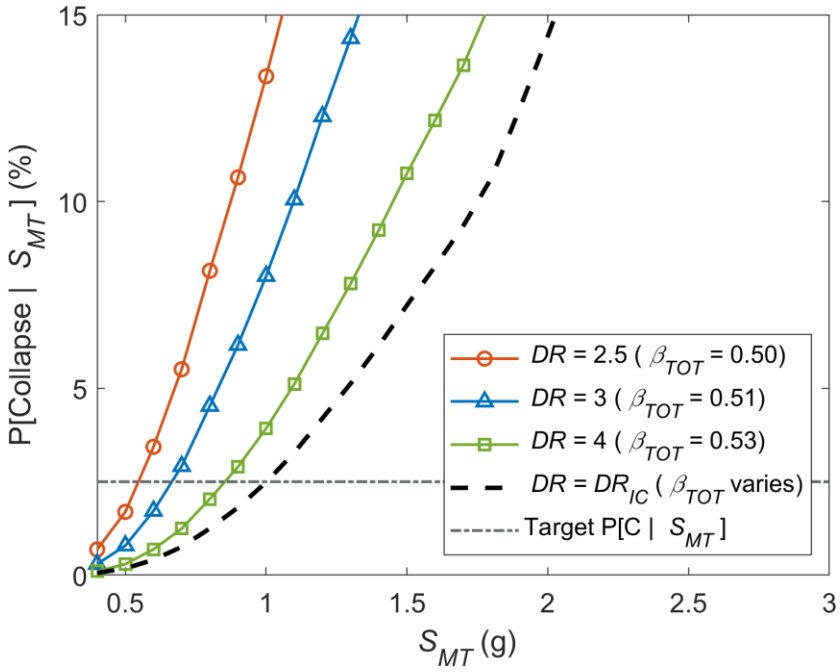

(d) SMF-3B probability of collapse versus S_{MT} for R = 8, RC IV (I_e = 1.5)

Figure 5-38 3-Story SMF Family B adjusted collapse margin ratio and probability of collapse versus S_{MT} for Risk Categories II and IV. Dashed black line represents median DR_{IC}. (continued)

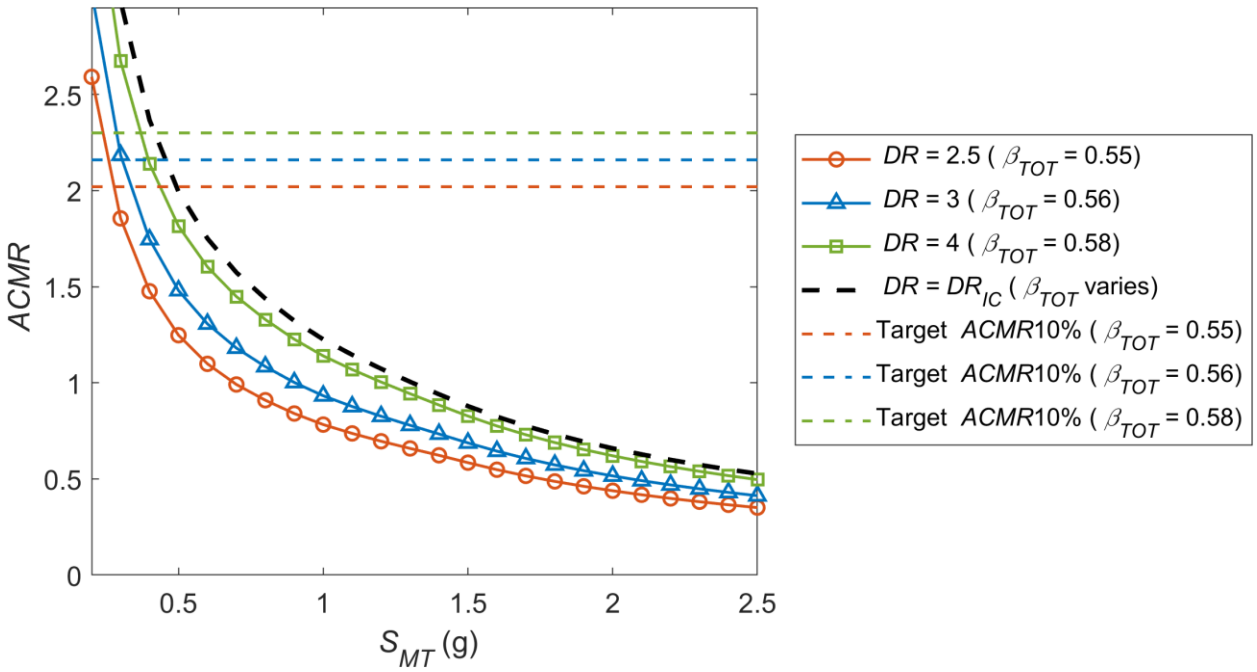

(a) SMF-9A adjusted collapse margin ratio versus S_{MT} for R = 8, RC II (I_e = 1.0)

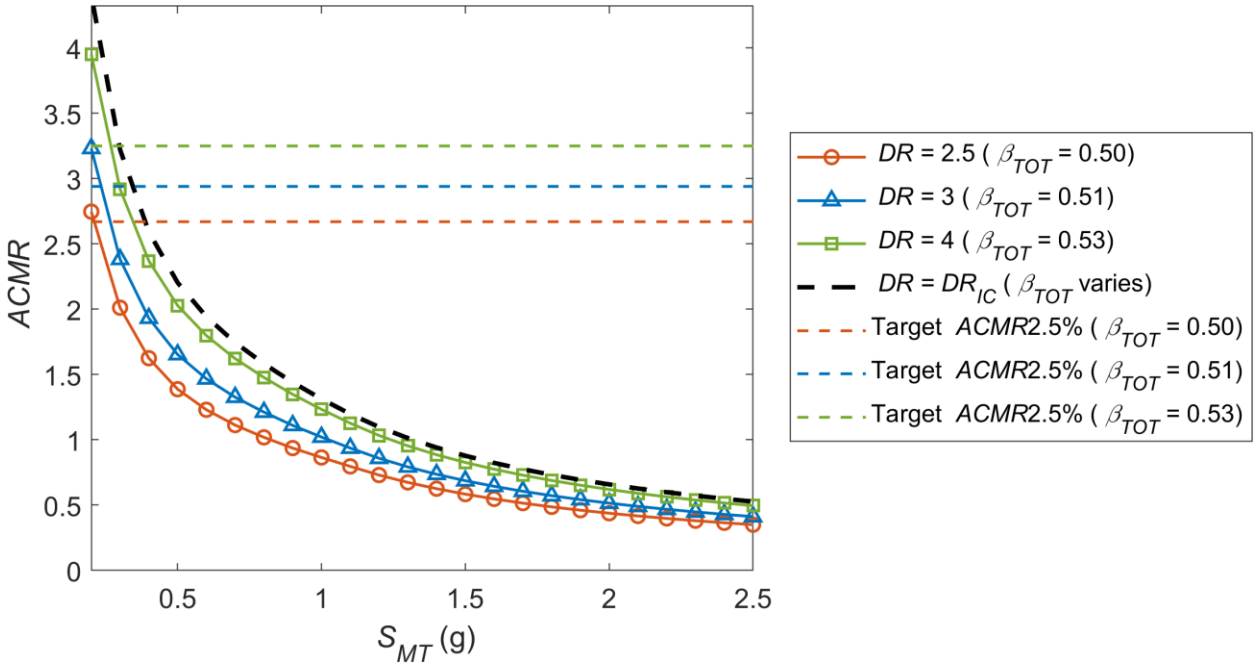

(b) SMF-9A adjusted collapse margin ratio versus S_{MT} for R = 8, RC IV (I_e = 1.5)

Figure 5-39 9-Story SMF Family A adjusted collapse margin ratio and probability of collapse versus S_{MT} for Risk Categories II and IV. Dashed black line represents median DR_{IC}.

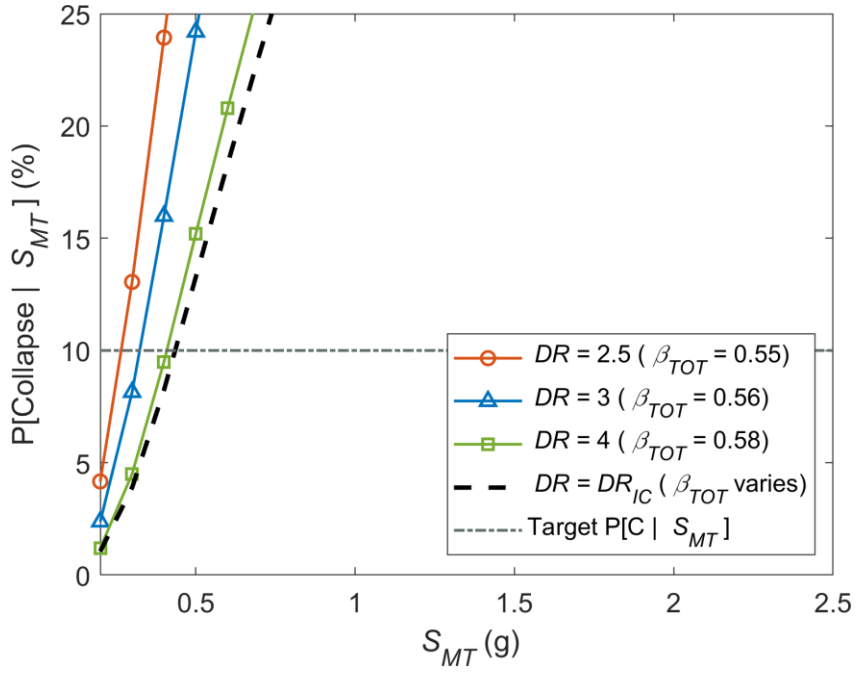

(c) SMF-9A probability of collapse versus S_{MT} for R = 8, RC II (I_e = 1.0)

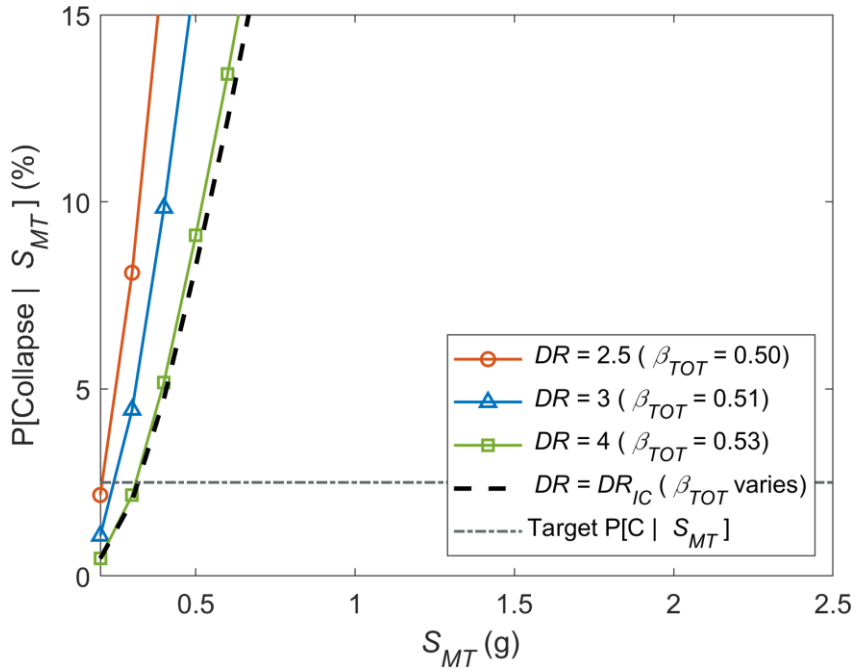

(d) SMF-9A probability of collapse versus S_{MT} for R = 8, RC IV (I_e = 1.5)

Figure 5-39 9-Story SMF Family A adjusted collapse margin ratio and probability of collapse versus S_{MT} for Risk Categories II and IV. Dashed black line represents median DR_{IC}. (continued)

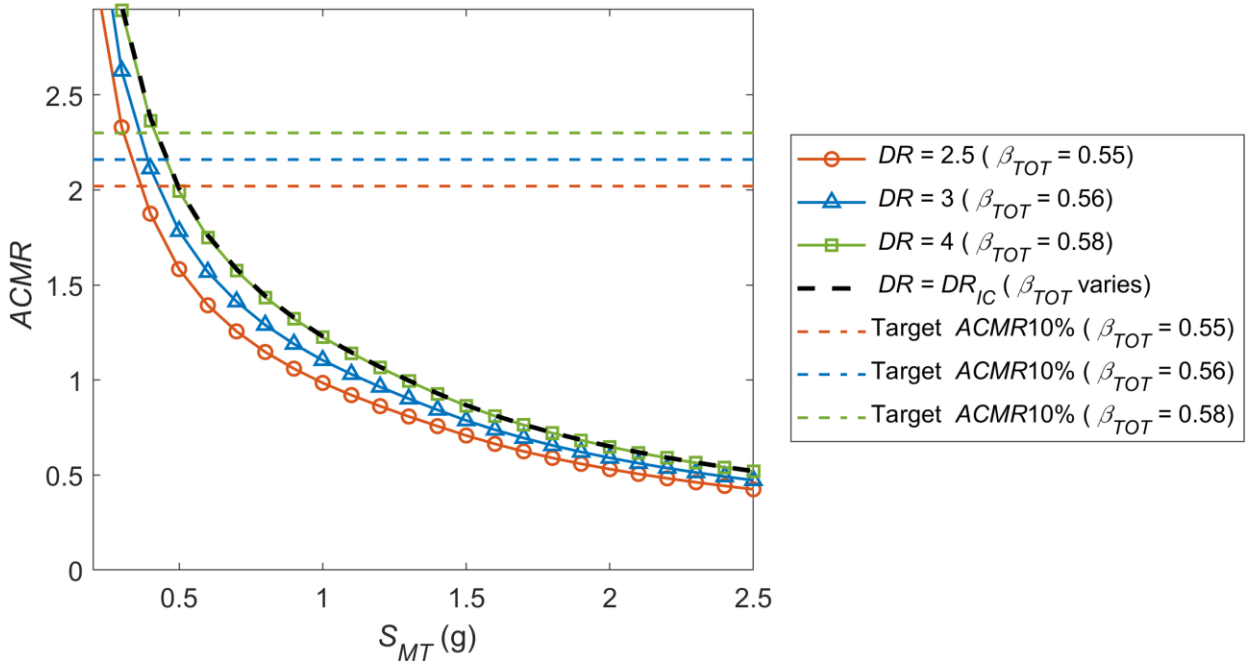

(a) SMF-9B adjusted collapse margin ratio versus S_{MT} for R = 8, RC II (I_e = 1.0)

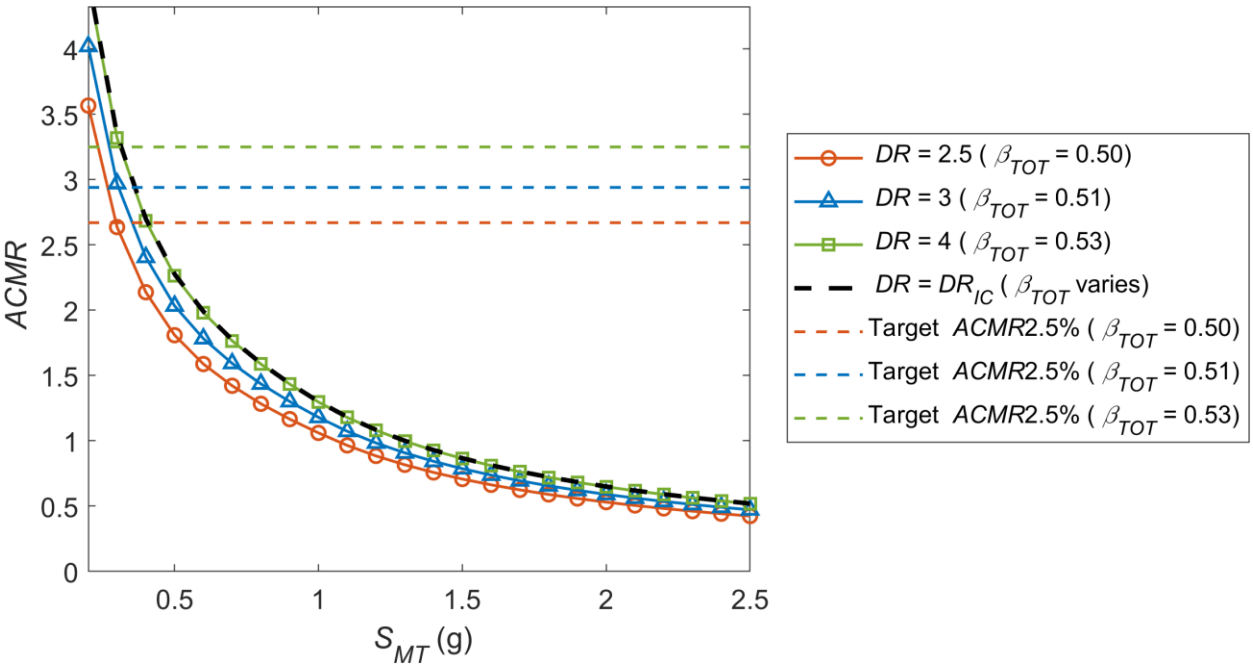

(b) SMF-9B adjusted collapse margin ratio versus S_{MT} for R = 8, RC IV (I_e = 1.5)

Figure 5-40 9-Story SMF Family B adjusted collapse margin ratio and probability of collapse versus S_{MT} for Risk Categories II and IV. Dashed black line represents median DR_{IC}.

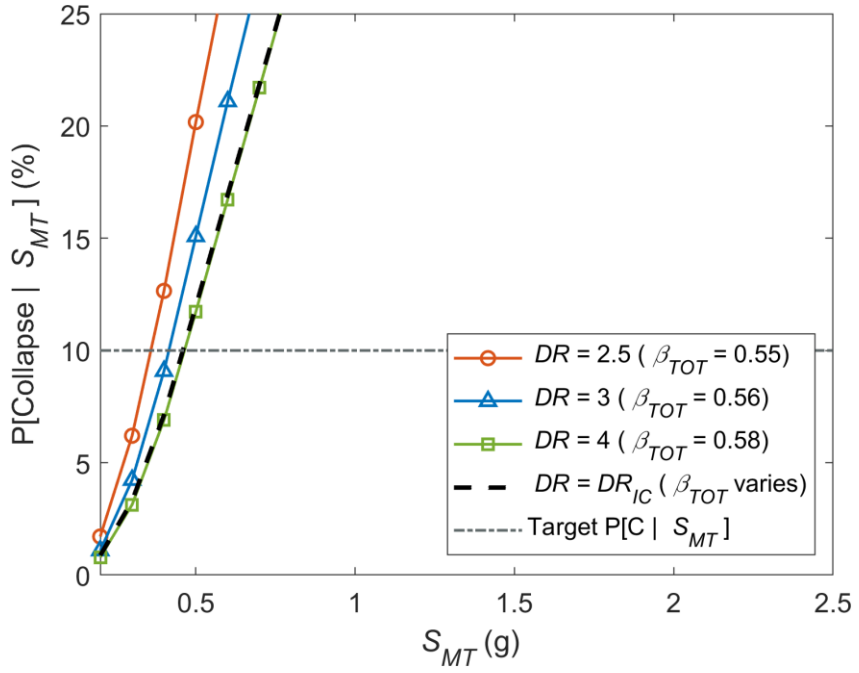

(c) SMF-9B probability of collapse versus S_{MT} for R = 8, RC II (I_e = 1.0)

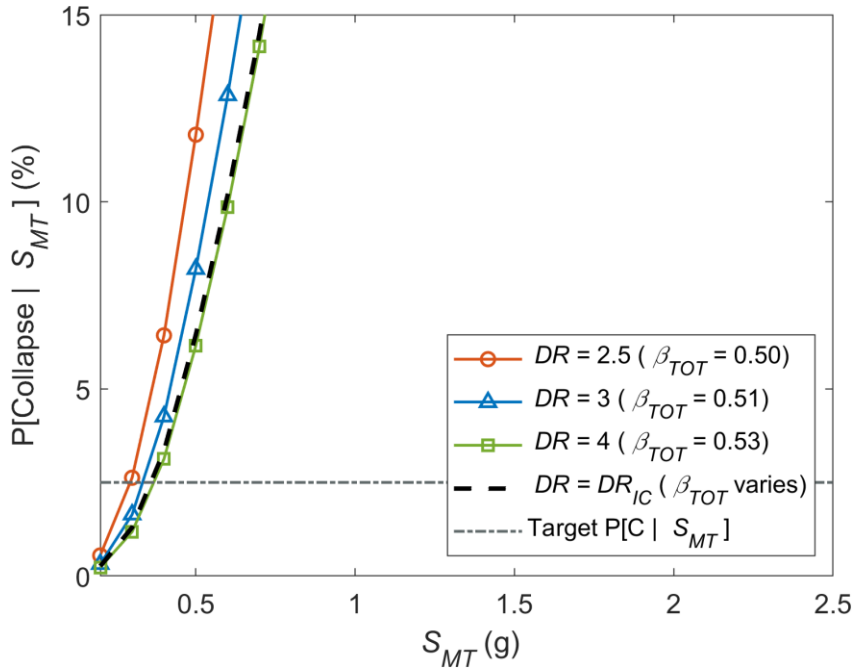

(d) SMF-9B probability of collapse versus S_{MT} for R = 8, RC IV (I_e = 1.5)

Figure 5-40 9-Story SMF Family B adjusted collapse margin ratio and probability of collapse versus S_{MT} for Risk Categories II and IV. Dashed black line represents median DR_{IC}.(continued)

5.6.3 DCW Adjusted Collapse Margin Ratios and Probability of Collapse

The DCW eSODF analysis results indicate that DCWs meet the collapse probability targets for SDC D_{max}. This is consistent with the results in Tuaberg et al. (2019) where many archetypes and performance groups just met the 10% probability of collapse criteria for SDC D_{max}. As noted above, there is little evidence that RC walls lose their lateral load capacity at the imposed non-simulated collapse mode roof drifts used here and therefore these results are likely conservative, i.e., they are likely to over-predict the actual collapse probability. However, the values used here are consistent with what has been done previously in research looking at the collapse performance of RC walls. Further, at larger strengths it is likely that walls would have to be reconfigured and this was not accounted for here.

Again, despite the shortcomings and simplifications of the models, Figure 5-41 through Figure 5-46 show clear trends between S_{MT}, *ACMR* and P[Collapse|S_{MT}]. The results indicate that for systems that behave as a DCW, i.e., those that have little cyclic deterioration, limited roof drift capacity (not exceeding 4%), peak-oriented hysteretic behavior (i.e., slightly pinched), uniformly distributed story drifts, and where the capping point doesn't shift significantly with increasing strength, *ACMR* decreases and P[Collapse|S_{MT}] increases with increasing S_{MT}.

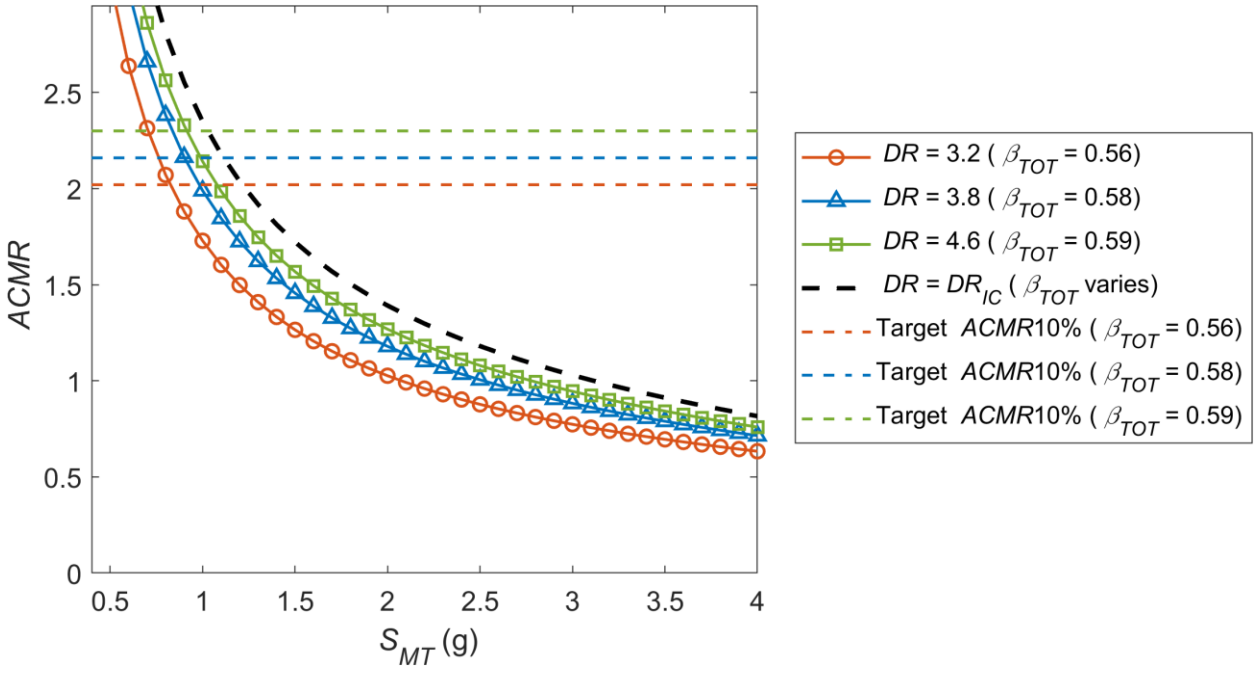

(a) DCW-8A adjusted collapse margin ratio versus S_{MT} for R = 8, RC II (I_e = 1.0)

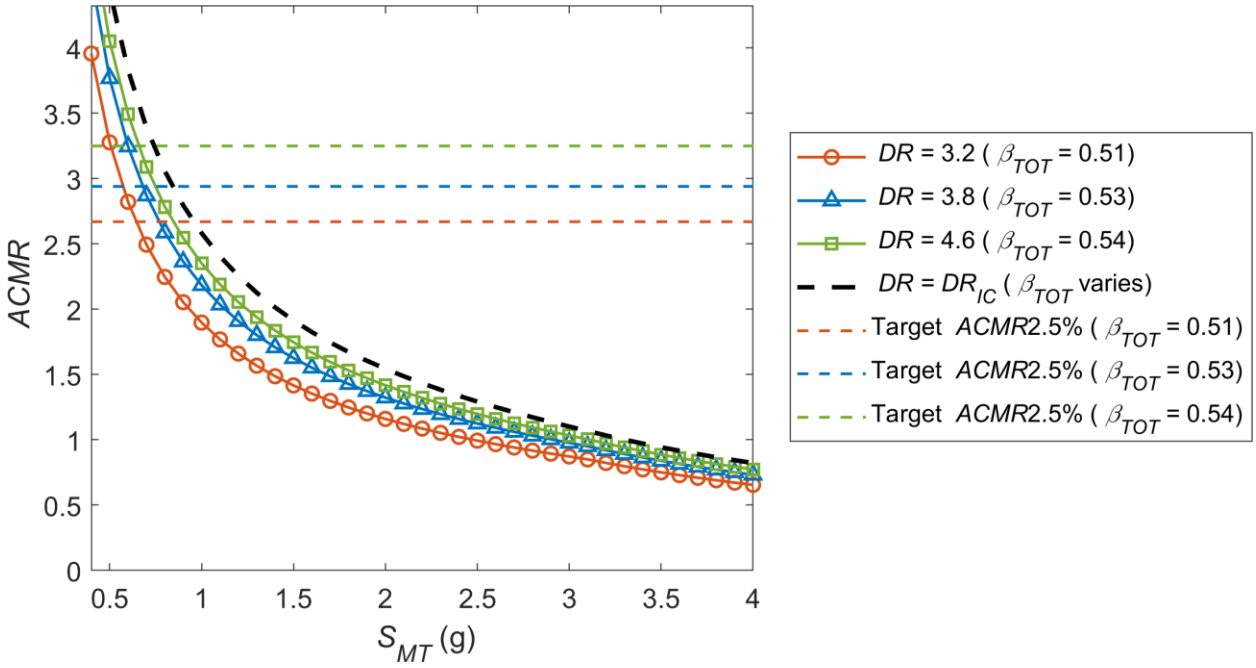

(b) DCW-8A adjusted collapse margin ratio versus S_{MT} for R = 8, RC IV (I_e = 1.5)

Figure 5-41 8-Story DCW Family A adjusted collapse margin ratio and probability of collapse versus S_{MT} for Risk Categories II and IV. Dashed black line represents median DR_{IC}.

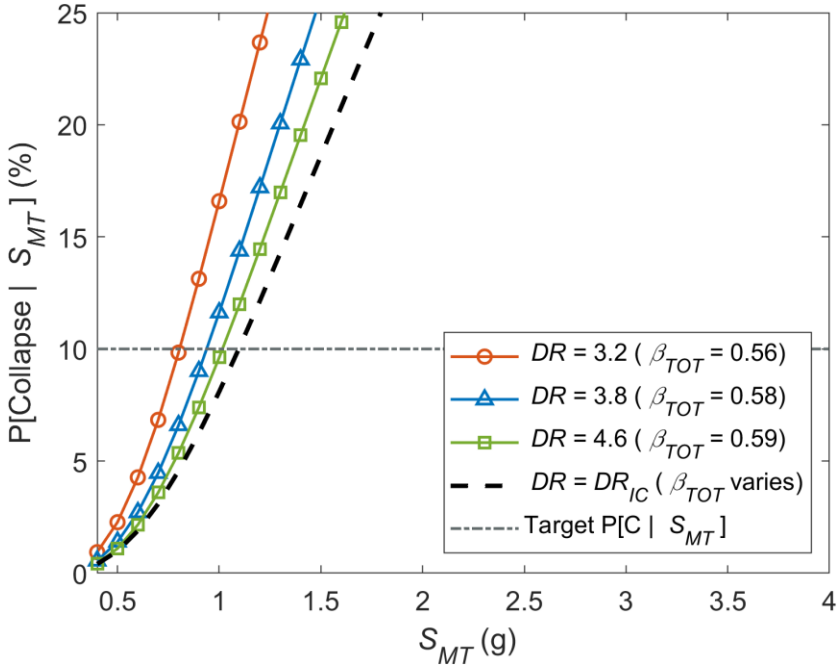

(c) DCW-8A probability of collapse versus S_{MT} for R = 8, RC II (I_e = 1.0)

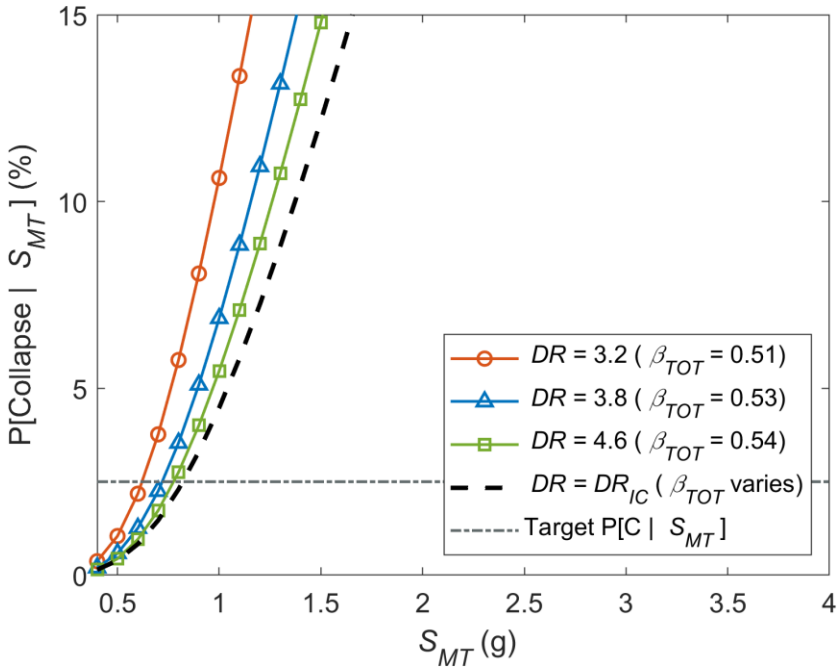

(d) DCW-8A probability of collapse versus S_{MT} for R = 8, RC IV (I_e = 1.5)

Figure 5-41 8-Story DCW Family A adjusted collapse margin ratio and probability of collapse versus S_{MT} for Risk Categories II and IV. Dashed black line represents median DR_{IC}. (continued)

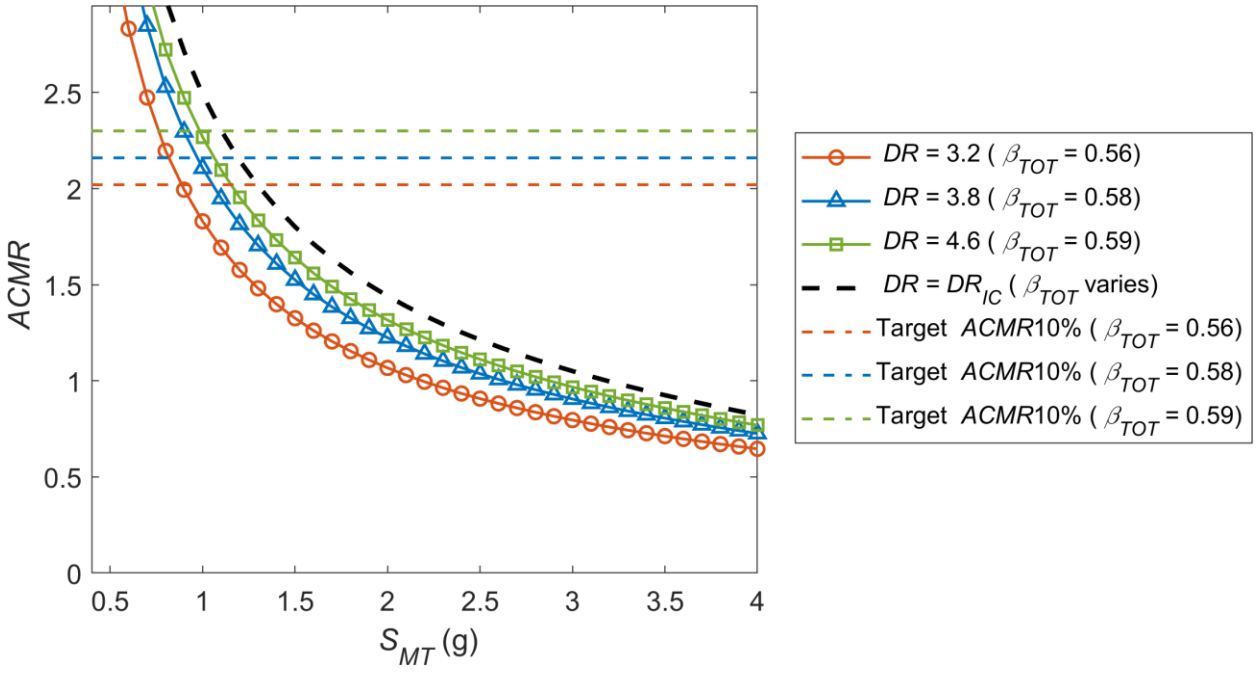

(a) DCW-8B adjusted collapse margin ratio versus S_{MT} for R = 8, RC II (I_e = 1.0)

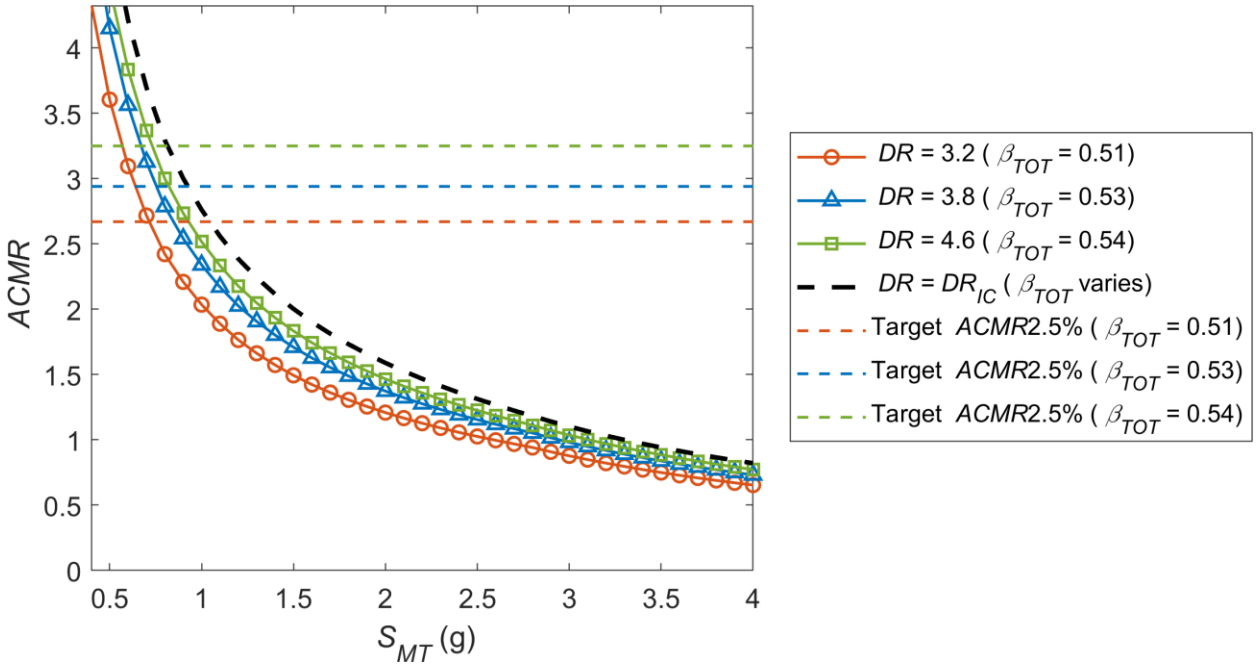

(b) DCW-8B adjusted collapse margin ratio versus S_{MT} for R = 8, RC IV (I_e = 1.5)

Figure 5-42 8-Story DCW Family B adjusted collapse margin ratio and probability of collapse versus S_{MT} for Risk Categories II and IV. Dashed black line represents median DR_{IC}.

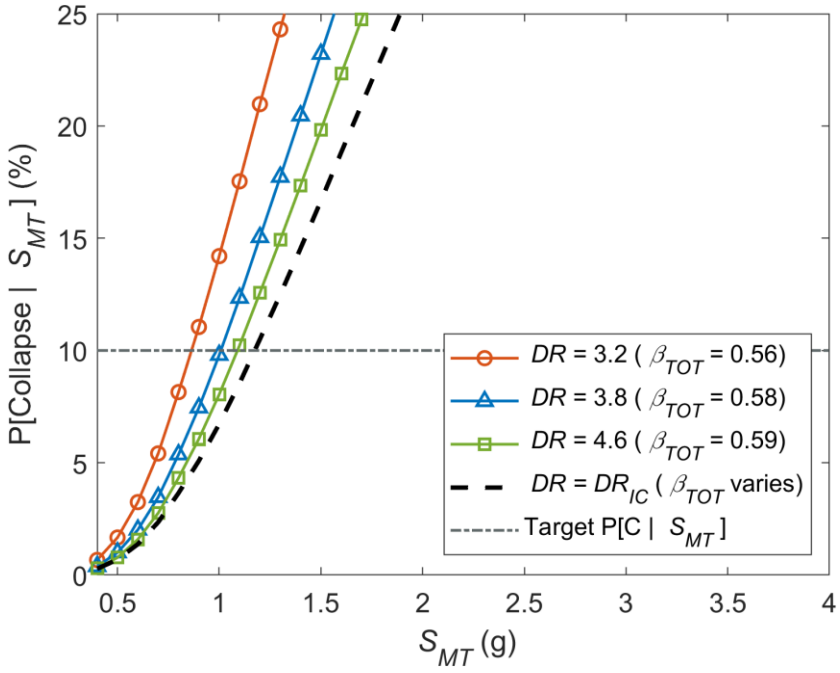

(c) DCW-8B probability of collapse versus S_{MT} for R = 8, RC II (I_e = 1.0)

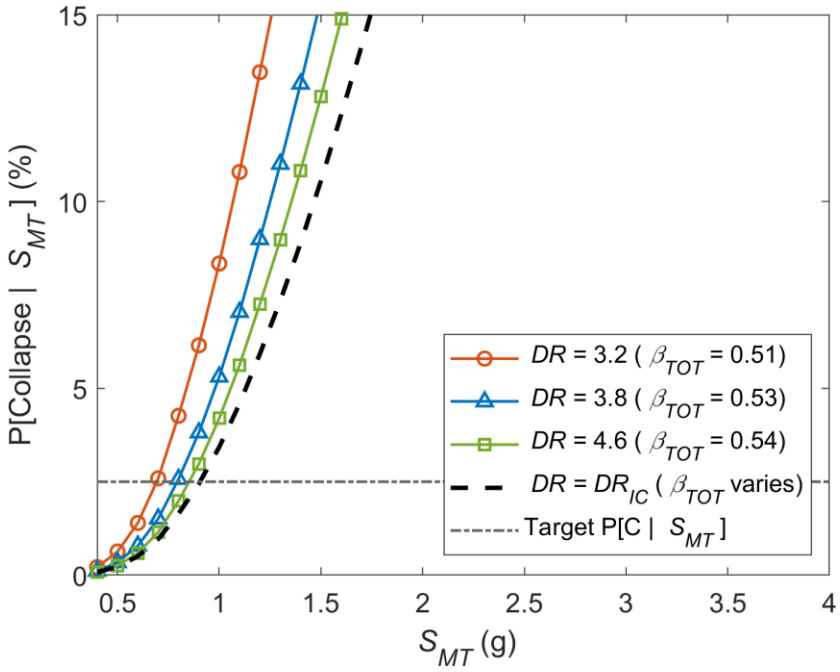

(d) DCW-8B probability of collapse versus S_{MT} for R = 8, RC IV (I_e = 1.5)

Figure 5-42 8-Story DCW Family B adjusted collapse margin ratio and probability of collapse versus S_{MT} for Risk Categories II and IV. Dashed black line represents median DR_{IC}. (continued)

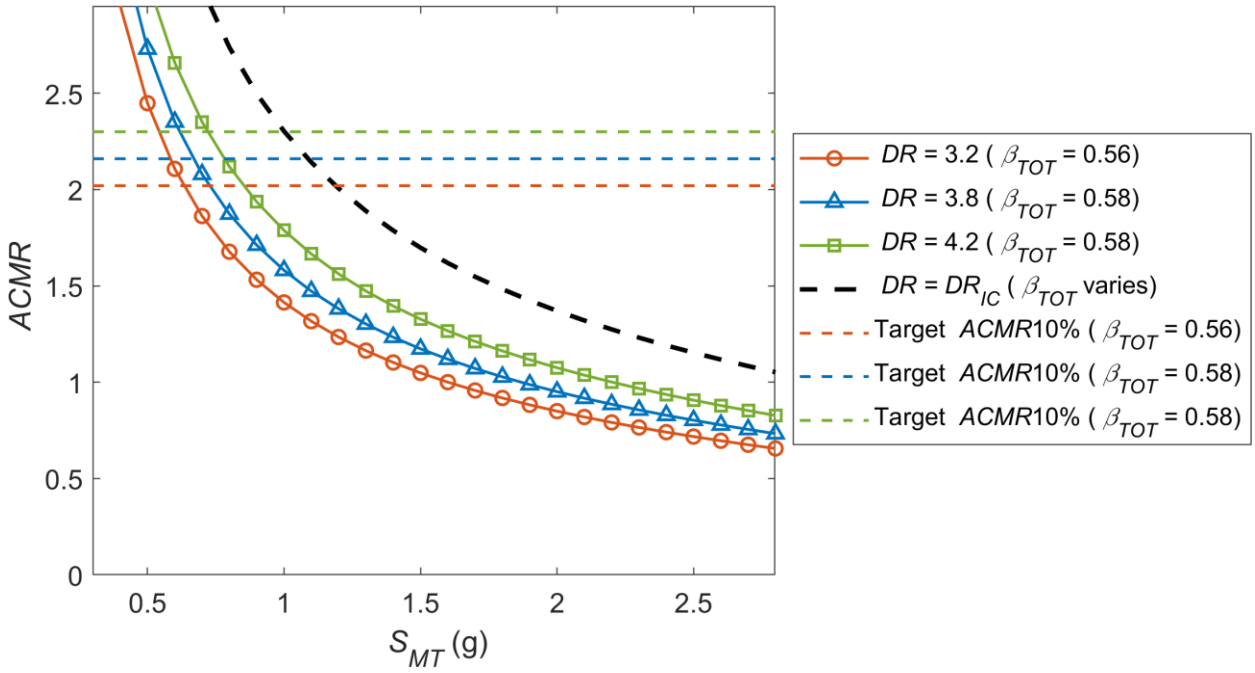

(a) DCW-12A adjusted collapse margin ratio versus S_{MT} for R = 8, RC II (I_e = 1.0)

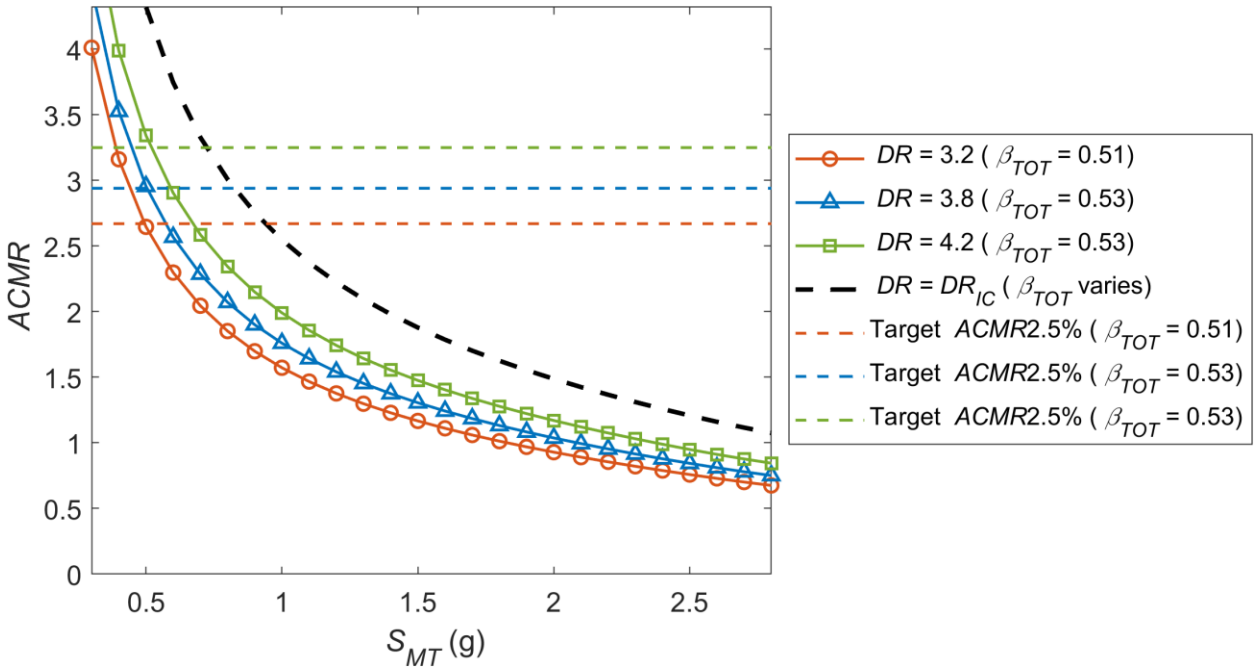

(b) DCW-12A adjusted collapse margin ratio versus S_{MT} for R = 8, RC IV (I_e = 1.5)

Figure 5-43 12-Story DCW Family A adjusted collapse margin ratio and probability of collapse versus S_{MT} for Risk Categories II and IV. Dashed black line represents median DR_{IC}.

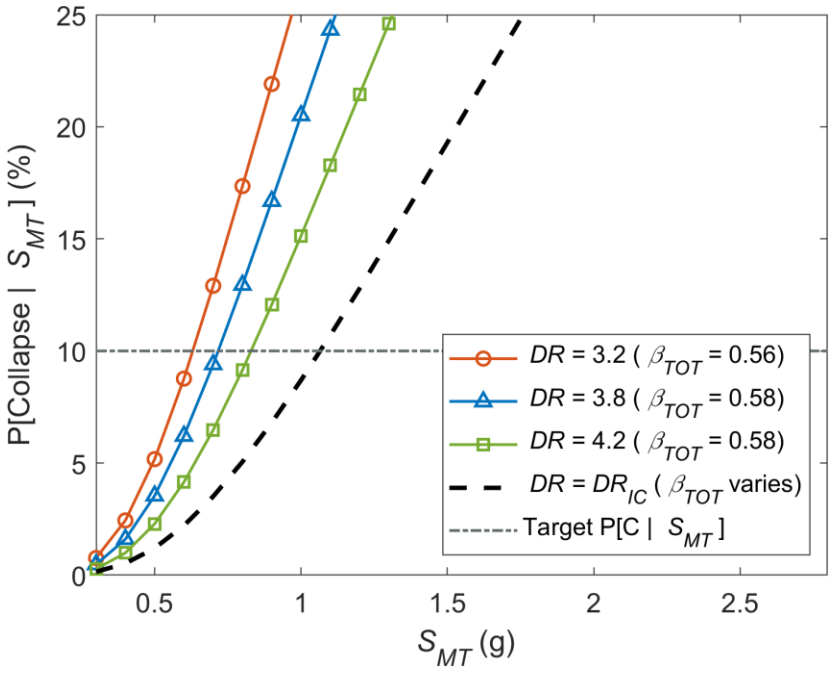

(c) DCW-12A probability of collapse versus S_{MT} for R = 8, RC II (I_e = 1.0)

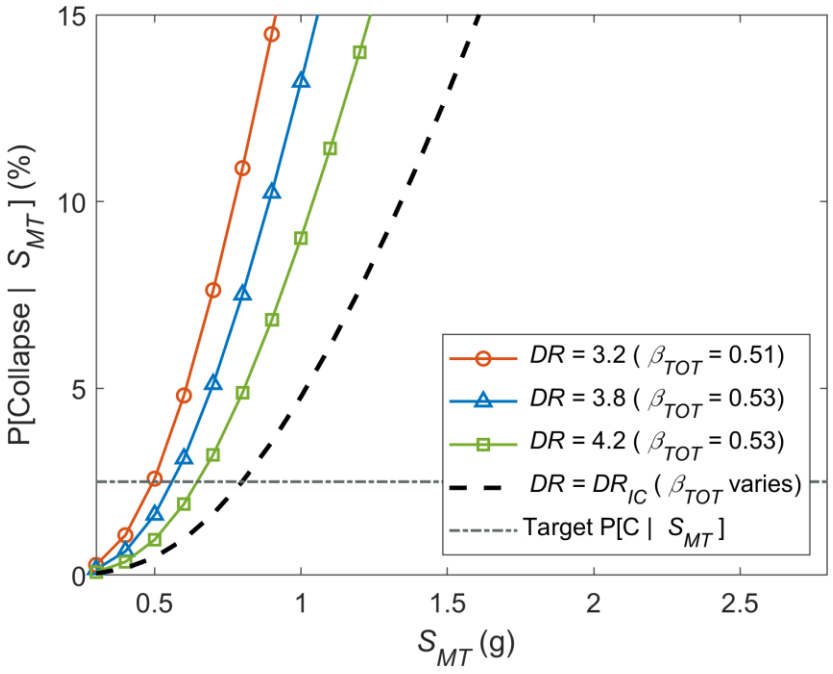

(d) DCW-12A probability of collapse versus S_{MT} for R = 8, RC IV (I_e = 1.5)

Figure 5-43 12-Story DCW Family A adjusted collapse margin ratio and probability of collapse versus S_{MT} for Risk Categories II and IV. Dashed black line represents median DR_{IC}. (continued)

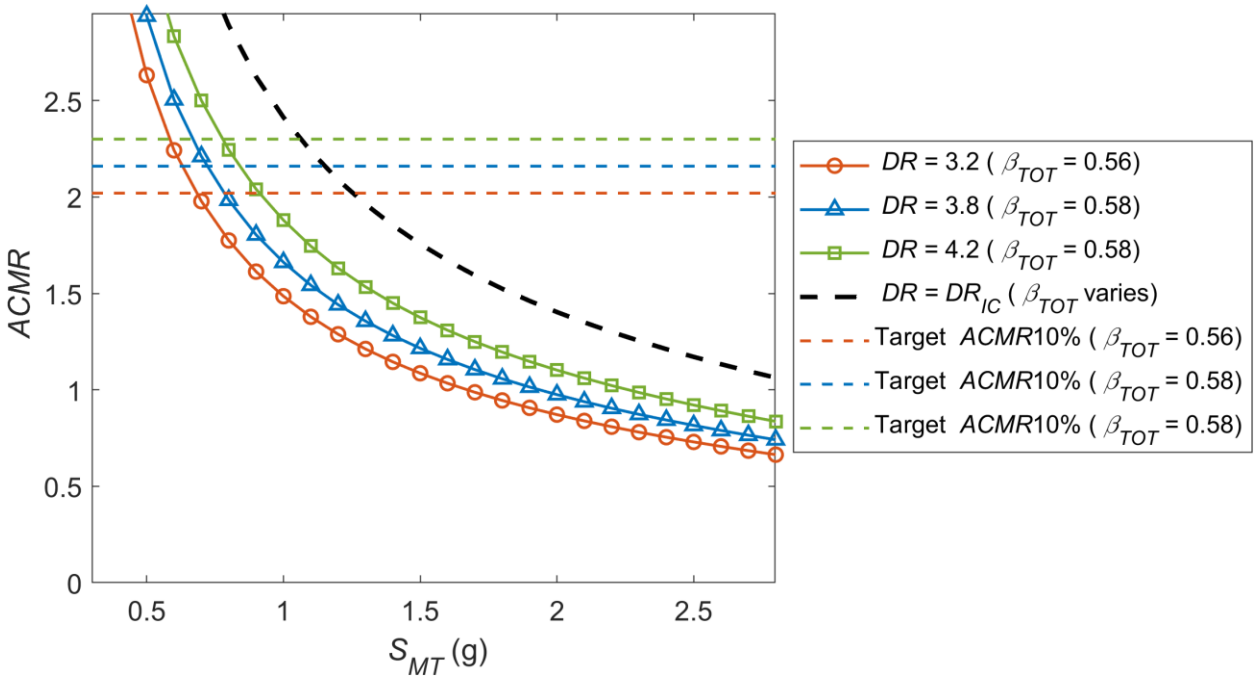

(a) DCW-12B adjusted collapse margin ratio versus S_{MT} for R = 8, RC II (I_e = 1.0)

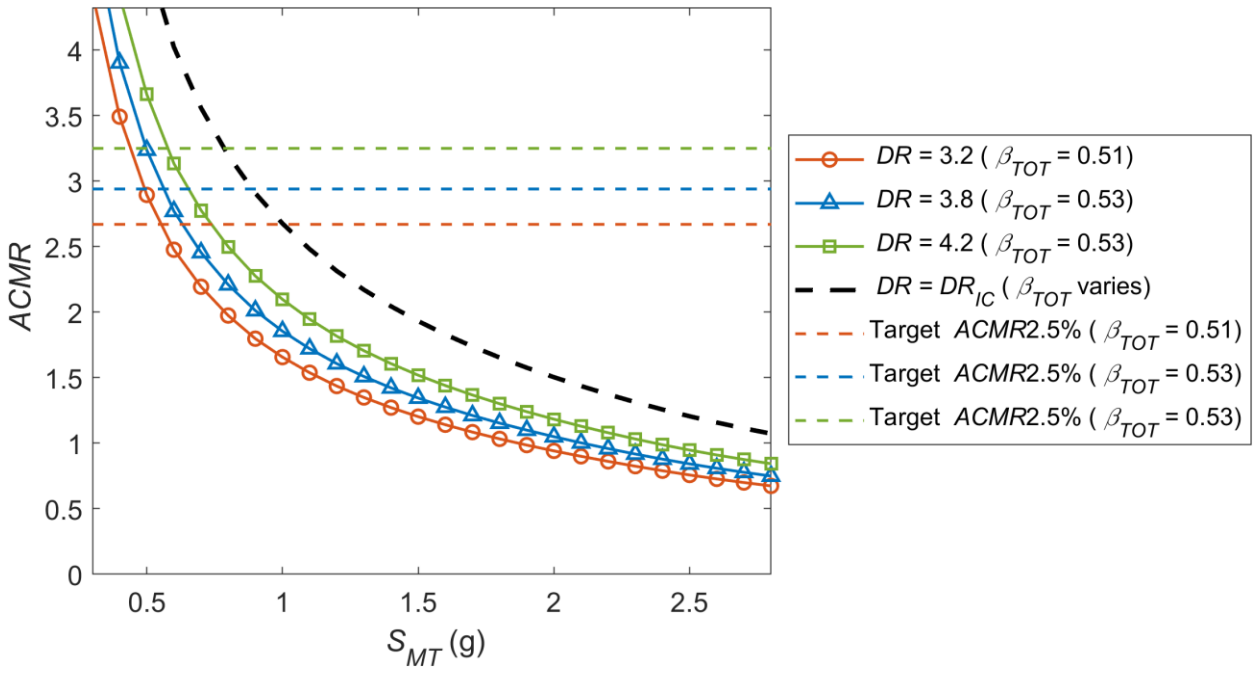

(b) DCW-12B adjusted collapse margin ratio versus S_{MT} for R = 8, RC IV (I_e = 1.5)

Figure 5-44 12-Story DCW Family B adjusted collapse margin ratio and probability of collapse versus S_{MT} for Risk Categories II and IV. Dashed black line represents median DR_{IC}.

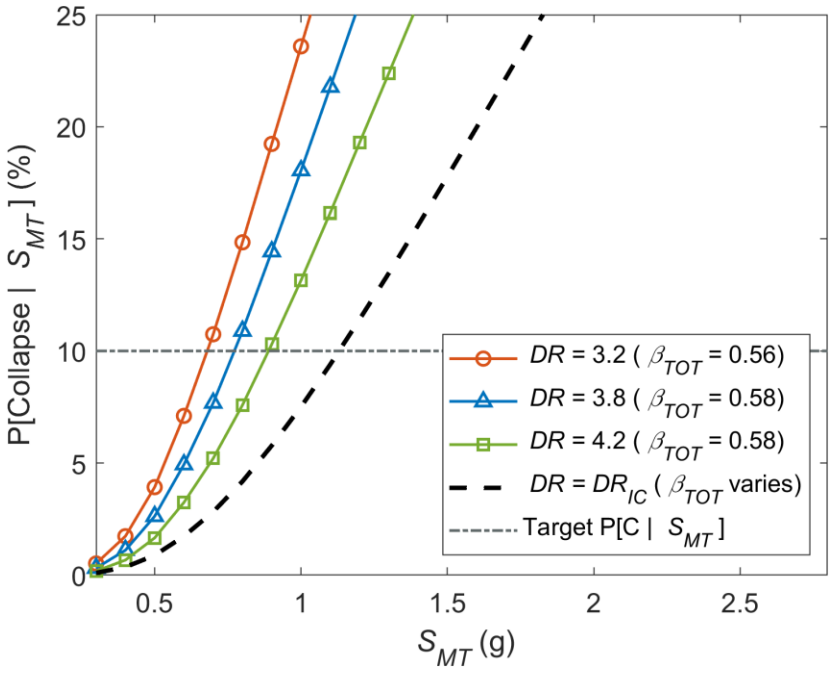

(c) DCW-12B probability of collapse versus S_{MT} for R = 8, RC II (I_e = 1.0)

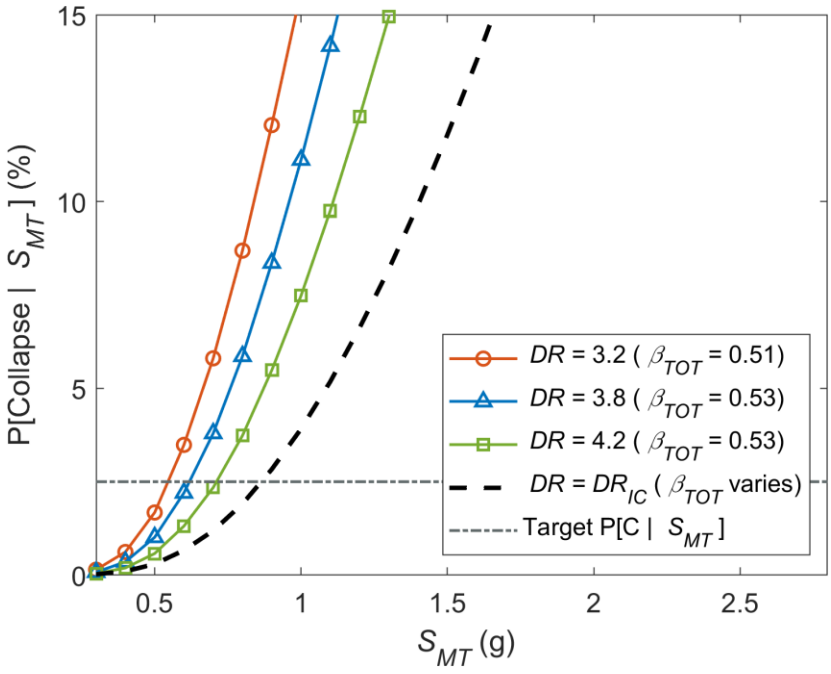

(d) DCW-12B probability of collapse versus S_{MT} for R = 8, RC IV (I_e = 1.5)

Figure 5-44 12-Story DCW Family B adjusted collapse margin ratio and probability of collapse versus S_{MT} for Risk Categories II and IV. Dashed black line represents median DR_{IC}. (continued)

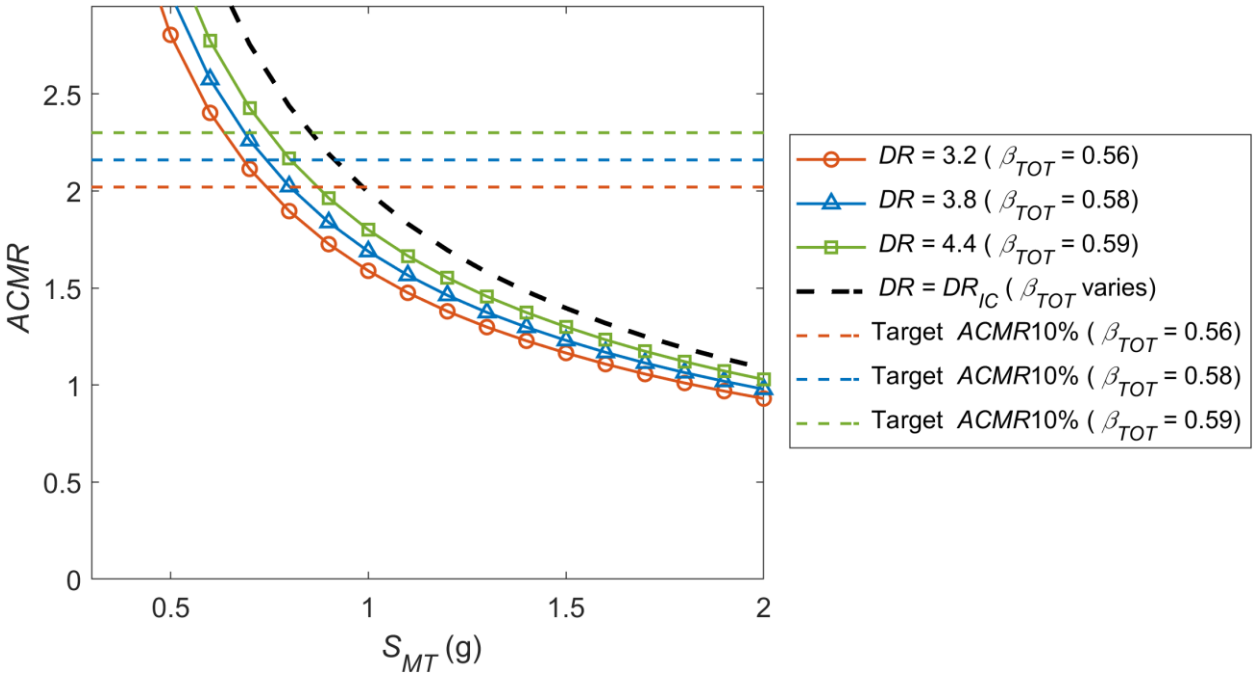

(a) DCW-18A adjusted collapse margin ratio versus S_{MT} for R = 8, RC II (I_e = 1.0)

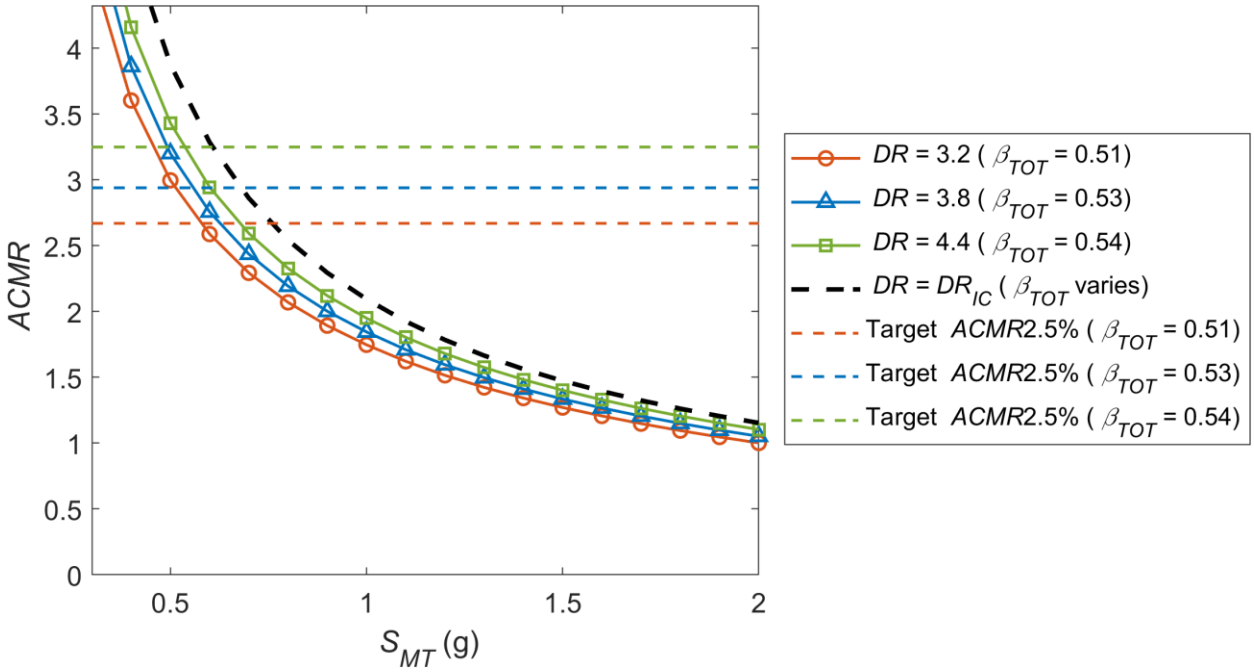

(b) DCW-18A adjusted collapse margin ratio versus S_{MT} for R = 8, RC IV (I_e = 1.5)

Figure 5-45 18-Story DCW Family A adjusted collapse margin ratio and probability of collapse versus S_{MT} for Risk Categories II and IV. Dashed black line represents median DR_{IC}.

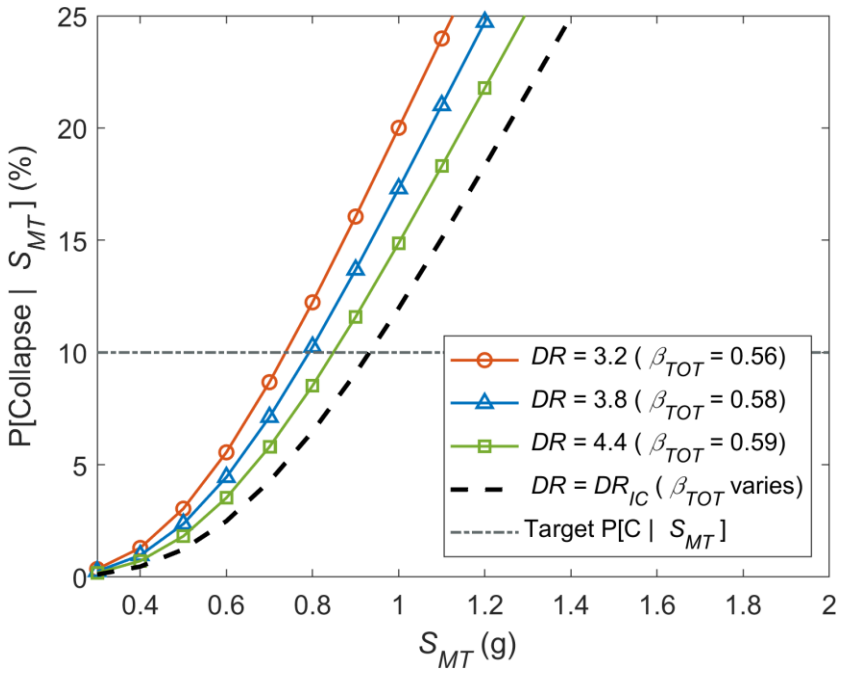

(c) DCW-18A probability of collapse versus S_{MT} for R = 8, RC II (I_e = 1.0)

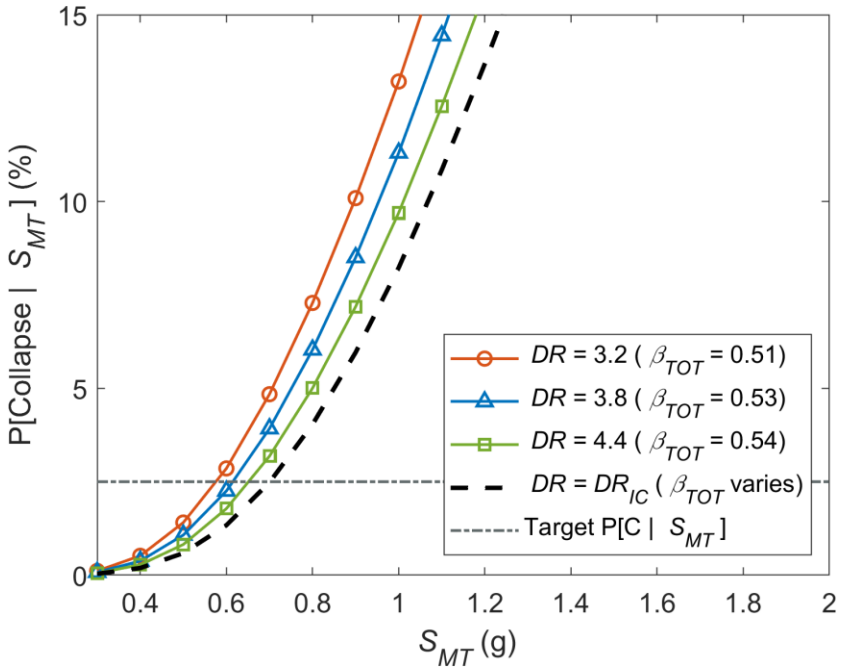

(d) DCW-18A probability of collapse versus S_{MT} for R = 8, RC IV (I_e = 1.5)

Figure 5-45 18-Story DCW Family A adjusted collapse margin ratio and probability of collapse versus S_{MT} for Risk Categories II and IV. Dashed black line represents median DR_{IC}. (continued)

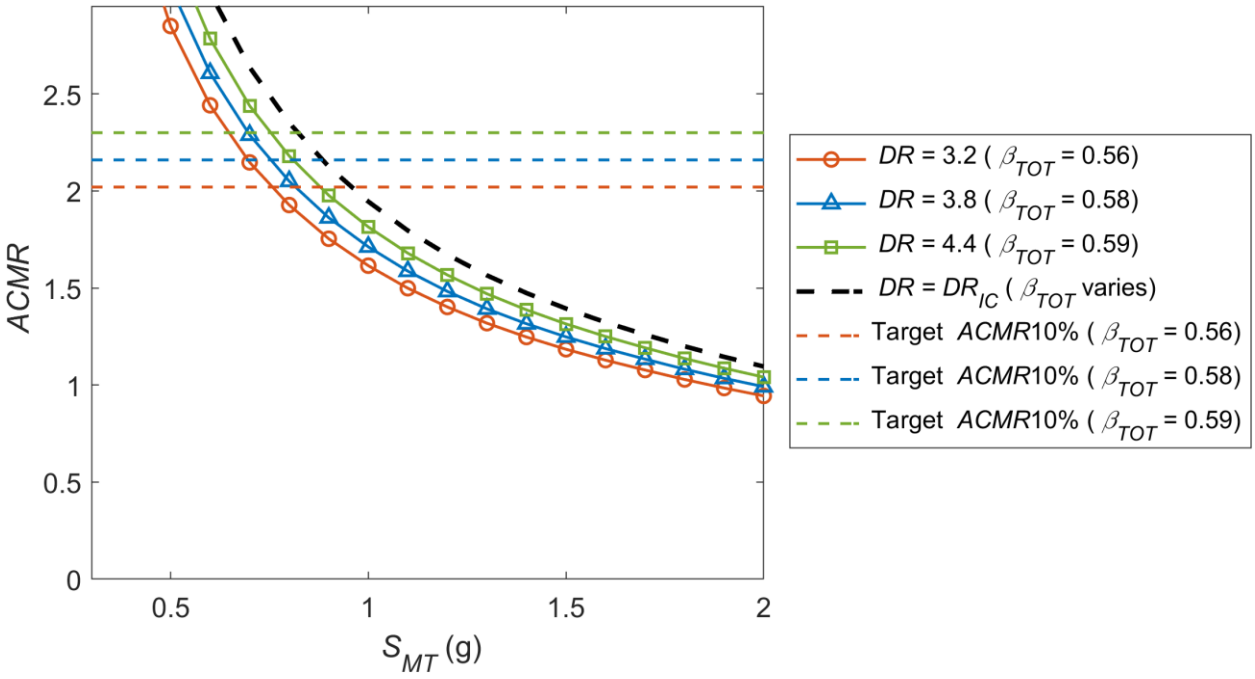

(a) DCW-18B adjusted collapse margin ratio versus S_{MT} for R = 8, RC II (I_e = 1.0)

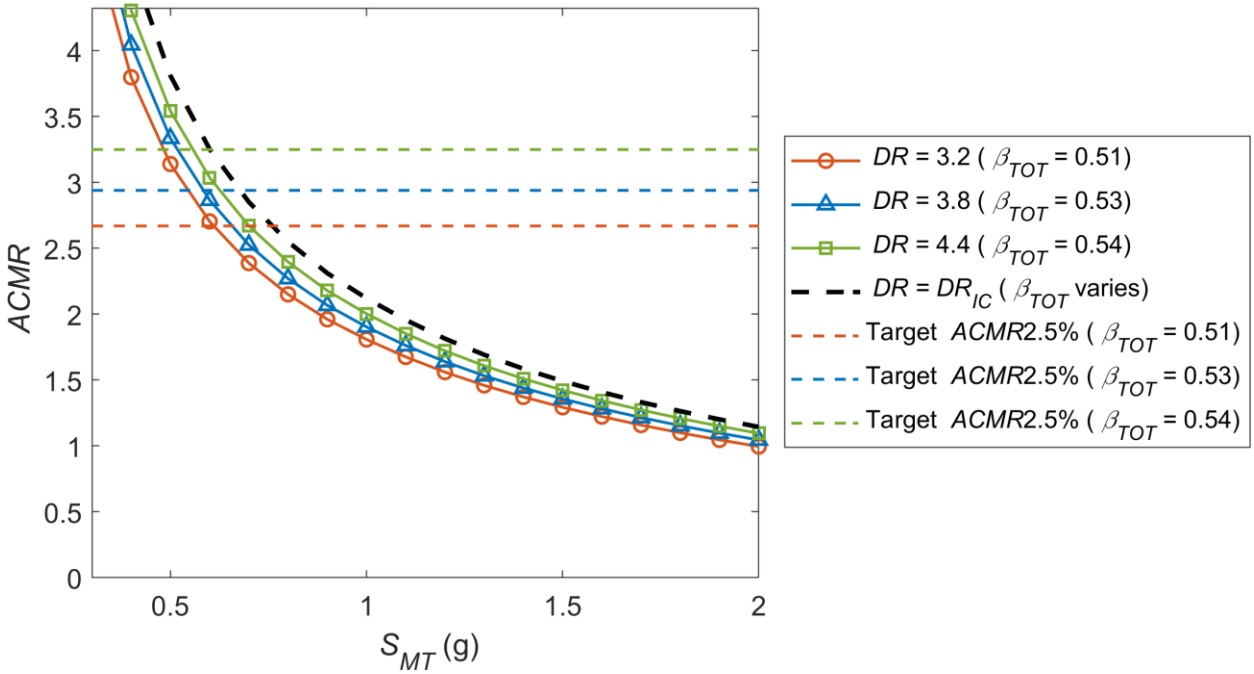

(b) DCW-18B adjusted collapse margin ratio versus S_{MT} for R = 8, RC IV (I_e = 1.5)

Figure 5-46 18-Story DCW Family B adjusted collapse margin ratio and probability of collapse versus S_{MT} for Risk Categories II and IV. Dashed black line represents median DR_{IC}.

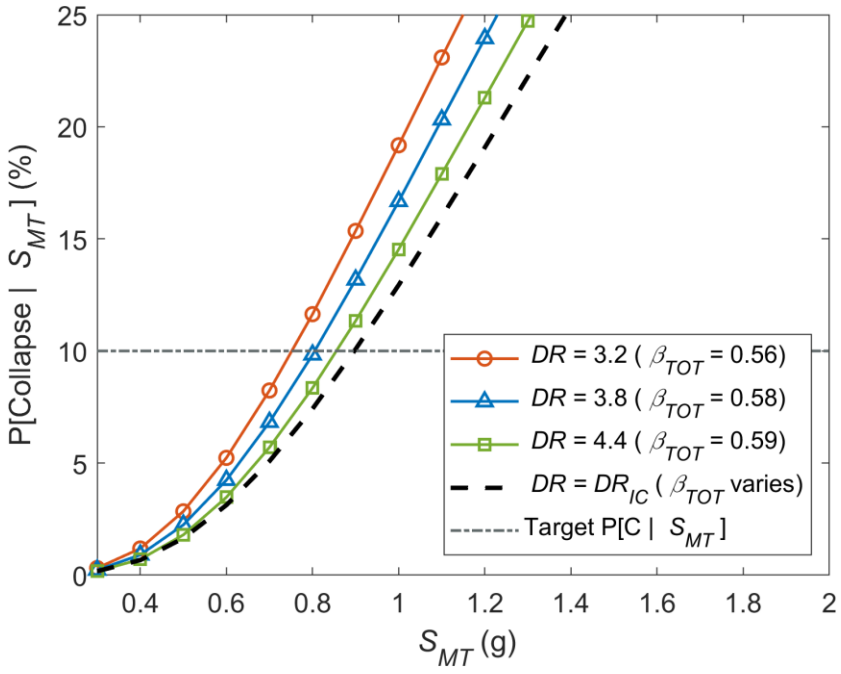

(c) DCW-18B probability of collapse versus S_{MT} for R = 8, RC II (I_e = 1.0)

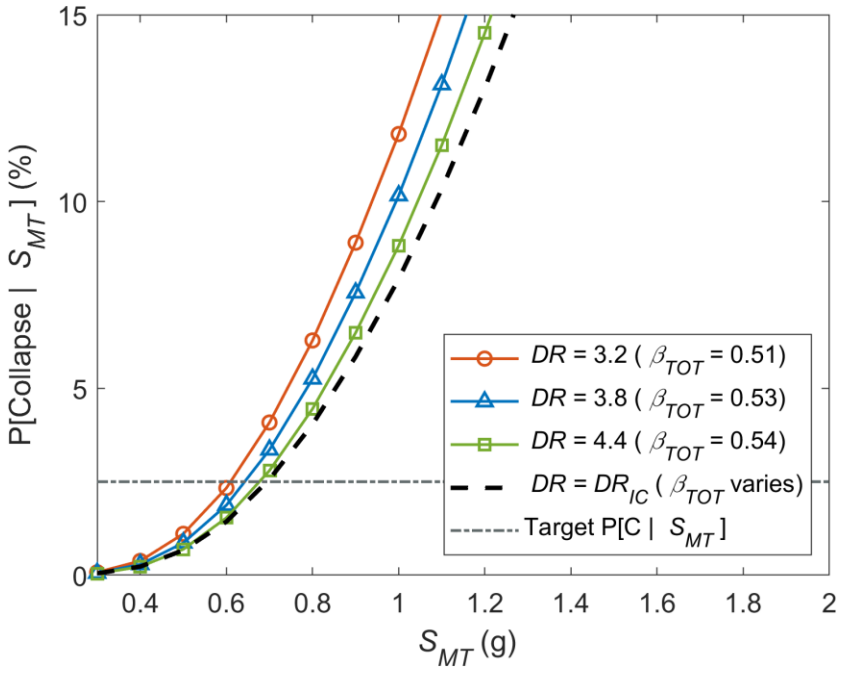

(d) DCW-18B probability of collapse versus S_{MT} for R = 8, RC IV (I_e = 1.5)

Figure 5-46 18-Story DCW Family B adjusted collapse margin ratio and probability of collapse versus S_{MT} for Risk Categories II and IV. Dashed black line represents median DR_{IC}. (continued)

5.7 Comparisons within Structural System Type

Figure 5-47 through Figure 5-49 show the probability of collapse versus S_{MT} at median DR_{IC} for all R = 8 and I_e = 1 for the Family A and B models for BRBFs, SMFs, and DCWs, respectively. As shown, the probability of collapse consistently increases with S_{MT}. The trends are consistent between family, across structural system, and across building heights, with the probability of collapse curves shifting to the left or right but maintaining the same general shape. Notably, the differences between families within a structural system are small, especially for the SMFs and DCWs, indicating that the impact of gravity framing, while important, does not disrupt the general trend of increasing collapse risk with increasing S_{MT}. There is a larger difference between Family A and B for the BRBFs because of the significant change in the pushover mode shape for that system in the presence of the gravity framing and strong axis column orientation within the BRBF. Other systems had either a small change in pushover mode shape or none at all between families.

The modeling assumptions and simplifications used in the eSDOF analyses may shift these curves to the left or to the right with respect to S_{MT}. As noted above the results presented here should not be used to interpret the appropriateness of the seismic force modification factor or the importance factor in ASCE/SEI 7. However, the analyses show that for systems with different types of realistic behavior, including strength, overstrength, drift capacity, hysteretic behavior and deterioration, there is a clear trend of increasing collapse probability with increasing S_{MT} for all the systems considered.

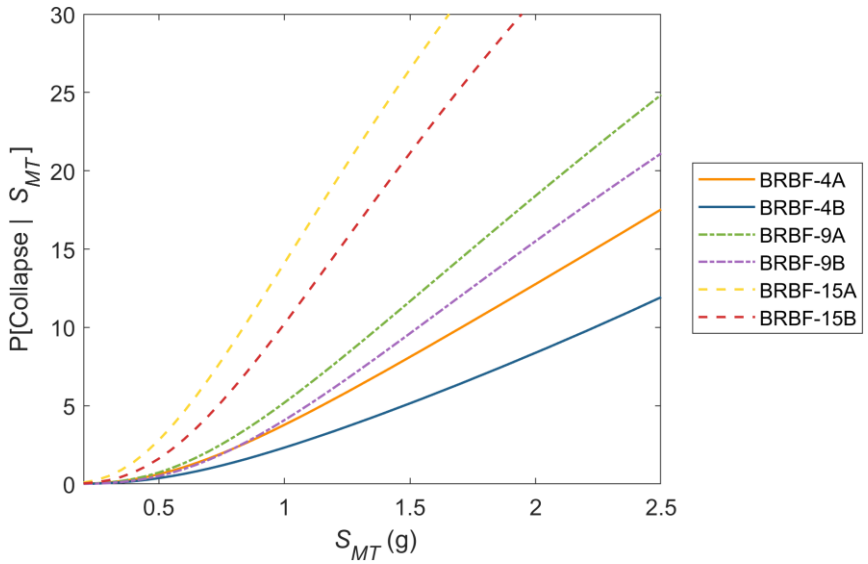

Figure 5-47 BRBF probability of collapse versus S_{MT} at median DR_{IC} for all families.

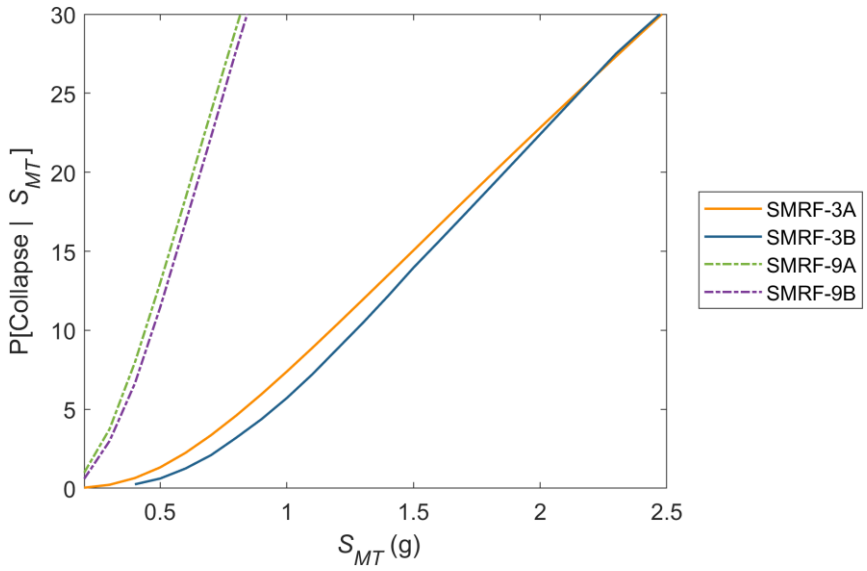

Figure 5-48 SMF probability of collapse versus S_{MT} at median DR_{IC} for all families.

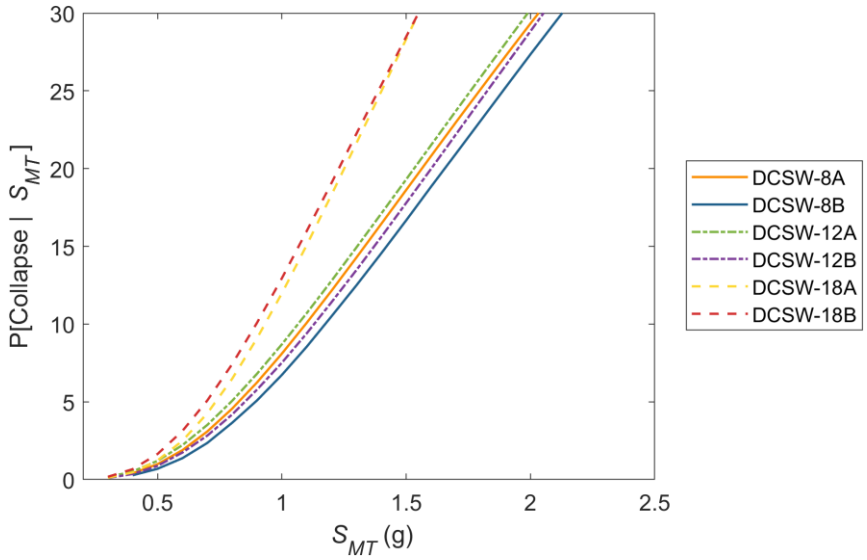

Figure 5-49 DCW probability of collapse versus S_{MT} at median DR_{IC} for all families.

5.8 Detailed Models of SMF

Detailed designs and models of 9-story SMFs were developed to examine and verify the trends found in the eSDOF analyses. The designs, model details, and results are presented in detail in Appendix F and a summary of the important points are presented here.

5.8.1 Archetype SMF Designs

Three archetype designs were prepared for a 9-story Risk Category (RC) II office building for seismic hazard levels corresponding to SDC D_{max} (High D), 1.5 times SDC D_{max} (Very High Seismic), and 2.0 times SDC D_{max} (Ultra High Seismic). The 1.5 and 2.0 factors are related to increases in S_{DS} relative to the High D value. These factors are 2.0 and 3.0, instead of 1.5 and 2.0, when the increases are measured by changes in S_{D1}. The differences in changes between S_{DS} and S_{D1} are a result of differences in the spectral shape at default site conditions in ASCE/SEI 7-22. In addition, a 9-story RC IV healthcare building was designed for the SDC D_{max} (High D) hazard level. Table 5-14 shows the seismic design parameters. For the design of the High D and Very High Seismic archetypes, the ASCE/SEI 7 upper bound period of 1.83 sec was used, whereas for the Ultra High Seismic archetype, the first mode period from eigenvalue analysis was found to be 1.52 sec and was used.

Table 5-14 Seismic Design Parameters Used in the Archetype Designs

Design Level	S_{MS} (g)	S_{DS} (g)	S_{M1} (g)	S_{D1} (g)	S_1 (g)	T (sec)	S_{MT} (g)
High D	1.5	1.0	0.9	0.6	0.47	1.83	0.49
Very High Seismic	2.25	1.5	1.8	1.2	0.72	1.83	0.98
Ultra High Seismic	3.0	2.0	2.7	1.8	1.07	1.52	1.78

Schematics of the plan layout and elevation of the archetypes are shown in Figure 5-50 and Figure 5-51. As shown, the buildings are rectangular with perimeter SMFs and have a taller first story. The gravity frame system was designed by Magnusson Klemencic Associates, and the SMFs were designed by the AISC Steel Solutions Center. The designs used the modal response spectrum analysis procedure in ASCE/SEI 7. Consistent with RC II requirements, the allowable story drift was limited to 0.02*h* per ASCE/SEI 7-22 Table 12.12-1. The RC IV healthcare archetype was designed for the High D seismic design level. Consistent with RC IV requirements, the allowable story drift was limited to 0.01*h* per ASCE/SEI 7-22 Table 12.12-1. The designed member sizes are given in Appendix F, and a detailed calculation package for each archetype is available at https://femap2343.atcouncil.org. Importantly, the column sizes for all archetypes were limited to W14 sections such that the impacts of combined local and lateral-torsional buckling did not have to be simulated. All SMFs were designed with Reduced Beam Section (RBS) beam-to-column connections.

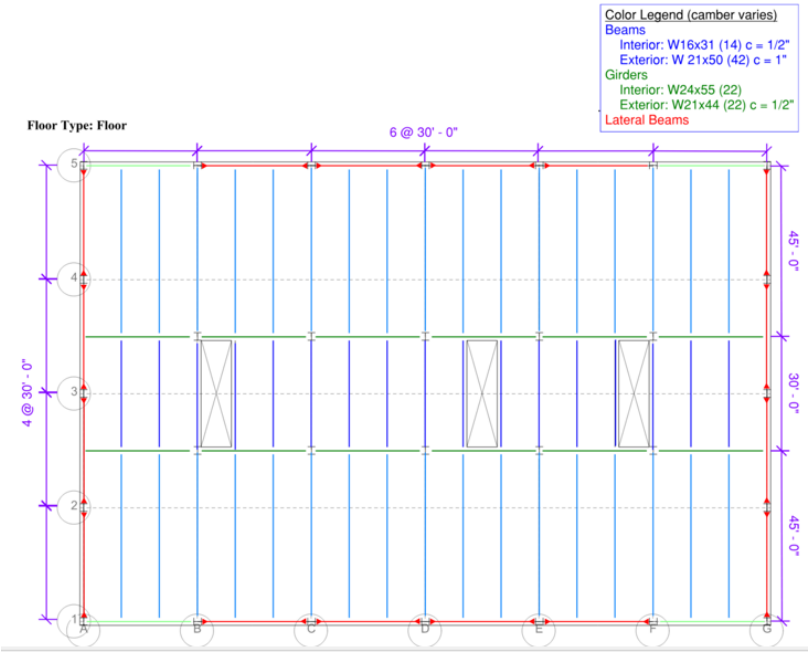

Figure 5-50 9-story office building archetype floor framing plan.

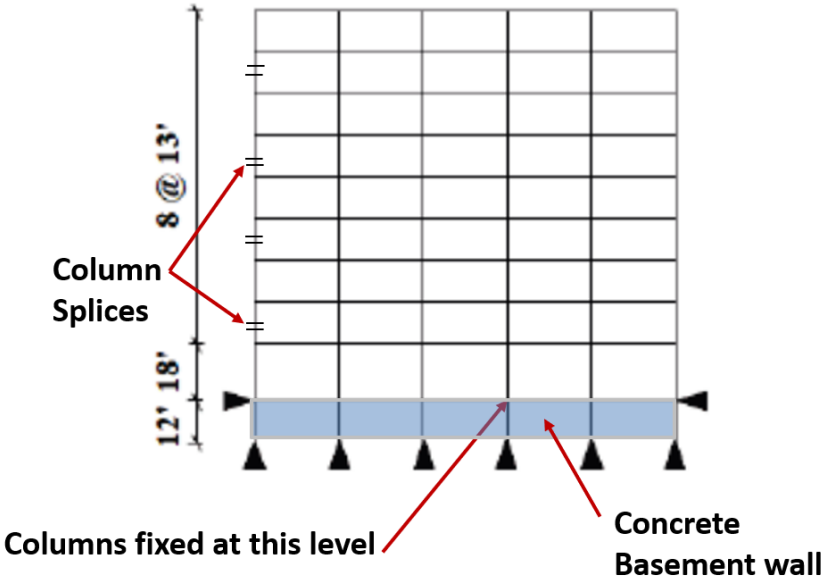

Figure 5-51 Generic 9-story archetype frame elevation.

5.8.2 Detailed SMF Models

Nonlinear models of the SMFs were developed in *OpenSeesPy* (Zhu et al., 2018), the python scripting version of *OpenSees*, and are described in detail in Appendix F. The models were developed in 2D and represent one of the SMFs in the building and the gravity framing that would be tributary to that SMF. Nonlinear behavior of beams, columns and panel zones in the SMF was considered. Figure 5-52 shows a general model schematic with associated labels and column line references

that correspond to the plan layout in Figure 5-50. As shown, the model included one complete moment frame line in the E-W direction, one complete gravity frame line in the E-W direction, and two columns from the moment frame in the N-S direction. Gravity loads tributary to all columns were included in the model. A single additional "dummy" column was included to place additional gravity load and mass that is in the seismic weight tributary to the moment frame considered but not included in the tributary area of the columns included in the model. The mass included in the model corresponded to the calculated seismic weight and the gravity loads included corresponded to 1.05*D*+0.25*L* as recommended by FEMA P-695. SMF columns were assumed to be embedded into basement walls. Gravity frame columns were assumed to extend into a 14-foot-tall basement level and are therefore modeled with a linear rotational spring at their bases that represents the stiffness of the basement level column assuming a pin end condition at the basement floor. Stiffness and mass proportional Raleigh damping was applied targeting 2.5% as described Appendix F. The beams and columns in both the SMF and gravity frames are modeled with P-delta element transformations in *OpenSeesPy* to account for nonlinear geometric effects.

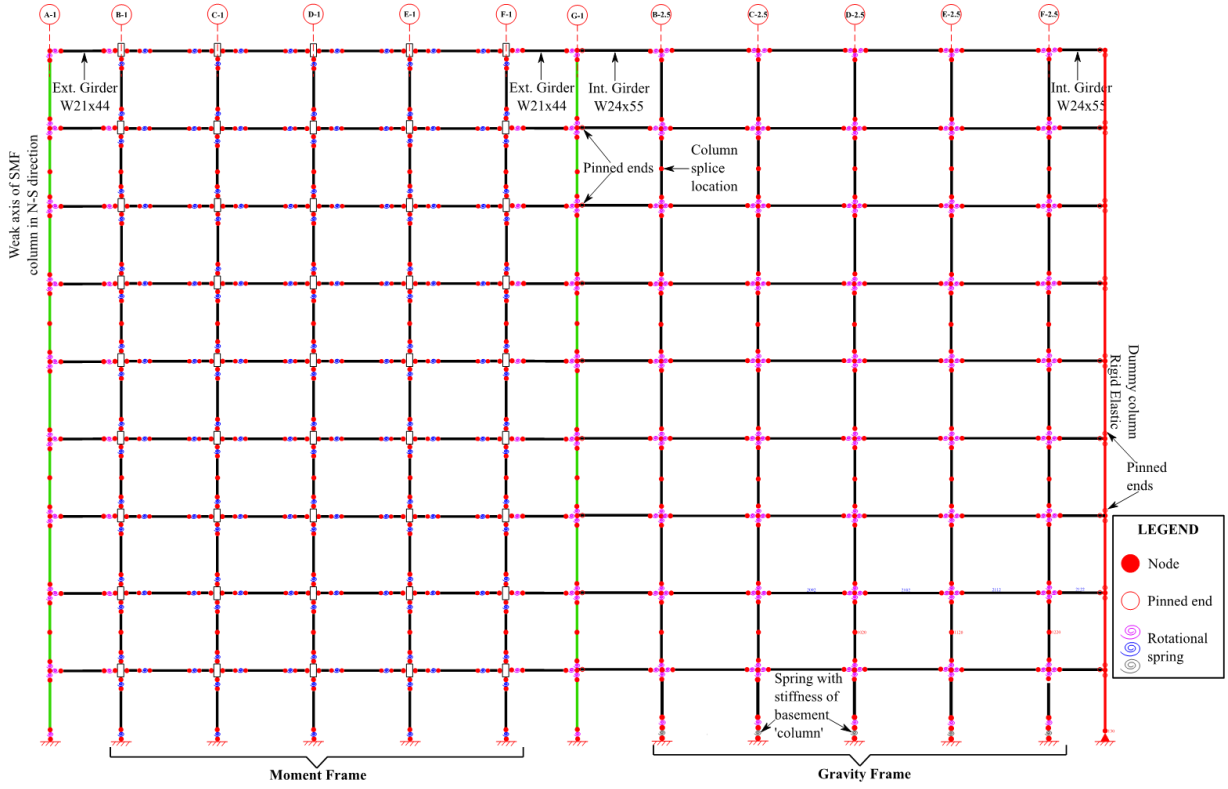

Figure 5-52 Numerical model schematic.

The SMFs were modeled using elastic beam-column elements with lumped plasticity, zero-length nonlinear rotational springs, near their ends to model the inelastic flexural behavior. A nonlinear model for the panel zones is included as well. Composite action was considered in the development of the springs representing the RBS beams. The gravity columns included in the model were modeled similarly. The gravity frame connections were modeled using rotational springs at the beams ends to simulate the shear tab connections. Details of the development of all nonlinear

component models are provided in Appendix F and in general followed the recommendations in NIST (2017b) with deterioration parameters based on the work of Lignos and Krawinkler (2011) with values updated from the online database available at http://resslabtools.epfl.ch/component/.

5.8.3 Collapse Analysis Results from Detailed SMF Models and Comparison with eSDOF Results

Nonlinear static analyses were conducted on the four archetype models and the result pushover curves in terms of *V/W* versus roof drift are shown in Figure 5-53. The pushover analyses were performed according to the recommendations of FEMA P-695, which imposes a largely first-mode lateral force pattern. The pushover curves are shown to the point where the solution becomes unstable. As illustrated in Appendix F, that corresponds to the point where a ground level column hinge reaches its assumed rotation capacity (0.1 rads) and drops to zero strength. The roof displacement capacity is a bit larger for the Very High Seismic model relative to the High and Ultra High Seismic models. It also appears that the roof displacement at peak strength is larger for the Very High Seismic and Ultra High Seismic models than for the High D model. Further, the overall behavior of the RC IV High Seismic model and the Very High Seismic model are similar, so nonlinear dynamic analyses were not performed on the RC IV design, as the expected response would be similar to the Very High Seismic model. Appendix F shows story drift profiles for the models at different levels of roof drift. In all cases, the drift distribution begins as relatively uniform but by 3% roof drift becomes concentrated on the two lowest levels.

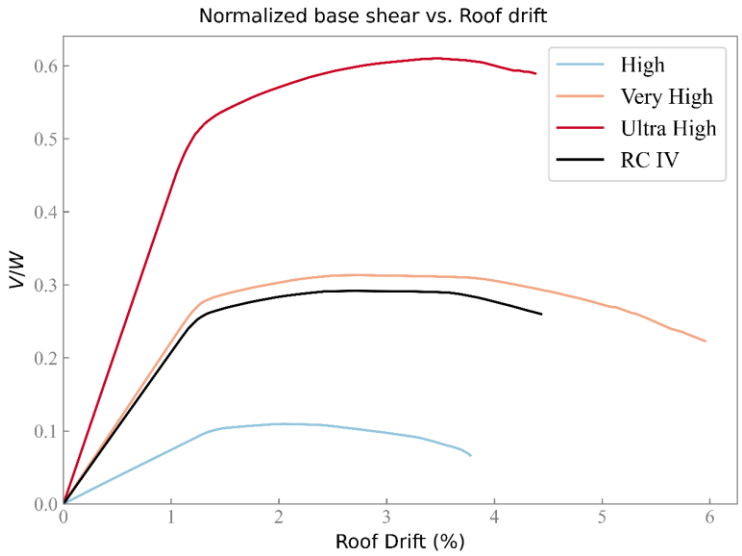

Figure 5-53 Pushover curves for the SMF designs.

Three models (High D, Very High Seismic, and Ultra High Seismic) were also analyzed for two ground motions, one scaled to S_{MT} for the design and then the same motion scaled to $2.0S_{MT}$ for the designs. The purpose of these analyses was to verify the nonlinear dynamic response for a ground motion near MCE_R and one near collapse. The results presented in Appendix F for these analyses show that the models were able to compute the nonlinear dynamic response of the structures through collapse. The results in Appendix F also show that the drift profile near or at collapse

approaches a concentrated floor over the lower two levels, which is where column failures occur. Importantly, the maximum drift at MCE_R is lowest for the High Seismic design (4.5% at the top story) and for the Very High Seismic design (4.25% at the 1st story) and increases significantly for the Ultra High Seismic design (7.25% at the ground floor). The behavior of the Ultra High Seismic design appears closer to collapse at MCE_R for this example ground motion than the Very High Seismic and High Seismic designs, although these observations were for only a single ground motion.

Incremental dynamic analysis was conducted using the FEMA P-695 Far-Field ground motion set (44 individual ground motion components) for the High Seismic, Very High Seismic, and Ultra High Seismic models. Table 5-15 summarizes the results of the IDA analyses and shows the results of computation of probability of collapse at MCE_R for the High D, Very High Seismic and Ultra High Seismic designs. Probability of collapse is shown for values of β equal to 0.5 and 0.6. Note that the eSDOF analysis in Chapter 5 used β equal to 0.6. The calculation of overstrength, spectral shape factor, collapse margin ratio (*CMR*) and adjusted collapse margin ratio (*ACMR*) were carried out in accordance with FEMA P-695 and the MCE_R collapse probabilities were computed as described in Chapter 3. As shown, the probability of collapse at MCE_R increases with increasing MCE_R used for design.

Table 5-15 also shows the median roof drift at collapse, which can be compared to the maximum roof drift from the pushover analyses presented previously. The roof drift at collapse is consistent with the roof drift at the point of non-convergence in the nonlinear static analyses, indicating that the structure losses stability at that roof drift and that the nonlinear static analysis generally predicts the proper collapse mode.

Table 5-15 Summary of IDA Results for the Detailed MDOF Models of SMFs and Probability of Collapse at MCE_R Calculations

Arch.	S_{MT} (g)	Period Used for IDA Scaling (sec)	V_{max}/W	Ω	DR_{IC} (%)	Median Roof Drift at Collapse (%)	$\hat{S}_{CT}$ (g)	*SSF*	*ACMR*	P[coll | S_{MT}] (β = 0.5) (%)	P[coll | S_{MT}] (β = 0.6) (%)
High D	0.49	1.83	0.11	2.49	8.20	4.02	0.94	1.35	2.60	2.8	5.6
Very High	0.98	1.83	0.31	3.82	8.79	4.82	1.55	1.47	2.32	4.6	8.1
Ultra High	1.78	1.52	0.61	4.11	9.11	4.42	1.70	1.26	1.20	35.8	38.1

The detailed SMF MDOF model results indicate that overstrength increases with increasing design spectral acceleration, at least between High D and the Very High Seismic designs. This is an important factor that helps to mitigate the increase in collapse probability with increasing design spectral acceleration. Additionally, there is a small increase in median DR_{IC} with increasing design demand that also helps mitigate the increase in collapse probability with increasing design spectral acceleration. When comparing the High D design's performance with that of the Very High Seismic

design's performance, the *ACMR* and collapse probabilities are similar thanks to the substantial increase in overstrength. However, when comparing the Very High Seismic design to the Ultra High Seismic design, the overstrength is similar and collapse probability for the Ultra High Seismic design is substantially larger and greatly exceeds the target 10% upper bound. See Appendix F for additional discussion.

The IDA and probability of collapse results from the analysis of detailed SMF models were compared with IDA and probability of collapse results from eSDOF analyses as described in Appendix F. In particular, two versions of the eSDOF models were considered. First, eSDOF models were developed for the detailed SMF designs using the detailed model results and following the steps outlined in Appendix E as implemented in Appendix F.

Table 5-16 shows the results of incremental dynamic analysis of the eSDOF models developed from the detailed MDOF nonlinear static analyses and building properties. The table shows that the eSDOF analysis are able to produce similar median collapse spectral accelerations, *ACMR*s, and probabilities of collapse at S_{MT} as the detailed SMF models. An exception is the eSDOF model for the Very High Seismic design, which overestimates the median collapse spectral acceleration relative to the detailed MDOF analysis results. A possible reason for this is related to the MDOF model exhibiting a rapid increase in concentrated drift at the lower level after reaching peak strength. This response is not reflected in the eSDOF model, which uses the deformed shape of the MDOF at peak strength.

Overall, these results are similar to those presented in this chapter for the other systems. Taken together, these results again show that eSDOF models can be used to study trends in collapse performance when calibrated to the pushover curves, cyclic deterioration characteristics, and pushover mode shapes of detailed models.

Table 5-16 Comparison of Collapse Analysis Results for the Detailed SMF Models, eSDOF Models Developed from the Detailed SMF Models, and eSDOF Models Developed from the FEMA P-2012 Models and Used for the eSDOF Analysis in Sections 5.2 through Section 5.7

Arch.	S_{MT} (g)	V_{max}/W	Ω	DR_{IC} (%)	$\hat{S}_{CT}$ (g)	CMR	SSF	ACMR	P[coll|S_{MT}] (β = 0.6) (%)
Section 5.8 Detailed MDOF SMF Results									
High D	0.49	0.11	2.49	8.20	0.94	1.92	1.35	2.60	5.6
Very High	0.98	0.31	3.82	8.79	1.55	1.58	1.47	2.32	8.1
Ultra High	1.78	0.61	4.11	9.11	1.70	0.96	1.26	1.26	38.1
eSDOF SMF Results: Models Calibrated to Section 5.8 Detailed SMF Models									
High D	0.49	0.12	2.49	8.66	1.00	2.04	1.35	2.76	4.5
Very High	0.98	0.31	3.82	8.13	1.60	1.63	1.47	2.39	7.3
Ultra High	1.78	0.61	4.11	8.44	2.06	1.16	1.26	1.45	26.7
eSDOF SMF Results for Models Developed and Analyzed in Sections 5.2-5.7									
High D	0.50	0.12	3.70	4.59	0.70	1.40	1.43	2.01	12.0
Very High	1.00	0.31	3.70	4.59	0.86	0.86	1.43	1.23	36.3
Ultra High	1.80	0.62	4.20	4.59	0.91	0.49	1.43	0.72	70.8

Table 5-16 also compares the collapse results for the 9-story eSDOF SMF models developed and analyzed in Section 5.2 to Section 5.7 with those results from the detailed SMF models described in this section. For this comparison, eSDOF models from Section 5.4.2 have been selected that have S_{MT} values close to those corresponding to the High D, Very High Seismic, and Ultra High Seismic designs. Note that the SMF eSDOF models in previous sections of this chapter were developed using the pushover response and pushover mode shape from the results of FEMA P-2012. As shown, the eSDOF results are pessimistic relative to the results for the detailed models here. The cause of these differences are discussed in detail in Appendix F. In summary they relate to: (1) the median story drift at incipient collapse, median DR_{IC}, is larger in the detailed models, which is because the hinge rotations at failure used in the current study are larger than those used in FEMA P-2012, (2) the

deterioration parameter, λ, for the Bilinear IMK model used to represent the full building response in the eSDOF analyses was more severe than that used for the RBS and column hinges in the detailed MDOF models, and (3) most importantly, the detailed SMF models showed that the displacement at peak system strength was larger for the Very High Seismic and Ultra High Seismic designs relative to the High D design. This suggests that there is, up to a point, an increase in drift capacity with increasing S_{MT}. The eSDOF SMF models presented in Section 5.2 through Section 5.7 all have the same displacement at peak system strength for a given building height.

In summary, the trend of increasing collapse probability with increasing design spectral acceleration appears in both the eSDOF analyses and in the results of analyses of the more detailed SMF models. Some mitigating factors in the detailed SMF models slow the trend but do not eliminate it. The most important factors are an increase in overstrength with increasing design spectral acceleration, an increase in median DR_{IC} with increasing S_{MT}, and an increase in the displacement at peak system strength with increasing S_{MT}. The detailed SMF models show that when design spectral accelerations are large: (1) collapse probabilities well above the ASCE/SEI 7 maximum values can occur, and (2) those values are substantially larger than those for structures designed for the SDC D upper boundary.

Chapter 6: Collapse Results and Trends

6.1 Introduction

This chapter summarizes results of the collapse evaluations of Chapter 4 and Chapter 5 and develops trends of increased collapse "risk" in regions of very high seismicity (VHS). Regions of VHS are defined as those areas where MCE_R ground motions of ASCE/SEI 7-22 exceed those of the strongest level of shaking required by FEMA P-695 for collapse evaluation of a new seismic force resisting system (SFRS) proposed for ASCE/SEI 7 (or for justification of an alternative structural system). The VHS boundary is described by the response spectrum of SDC D_{max} ground motions of FEMA P-695, as shown in Figure 6-1. The VHS boundary has a short-period response spectral acceleration plateau of S_{MS} = 1.5g and 1-second response spectral acceleration of S_{M1} = 0.9g, representing default site conditions of the Deterministic Lower Limit (DLL) response spectrum of ASCE/SEI 7-05, the edition of ASCE/SEI 7 when FEMA P-695 was developed. It should be noted that ASCE/SEI 7-05, and later editions, define Seismic Design Category E in terms of the mapped MCE_R response spectral acceleration parameter at 1-second, $S_1 \geq 0.75$g, which is not the same as the VHS boundary of this study, as defined by the response spectrum of SDC D_{max} ground motions of FEMA P-695. For comparison, Figure 6-1 includes plots of ASCE/SEI 7-16 and ASCE/SEI 7-22 Deterministic Lower Limit (DLL) response spectra that reflect updates of ASCE/SEI 7 ground motions since development of FEMA P-695.

For each ASCE/SEI 7 response spectrum plotted in Figure 6-1, the default site condition stipulated in ASCE/SEI 7 is assumed for converting the reference (i.e., mapped) response spectrum provided by the U.S. Geological Survey to the MCE_R response spectrum considering site effects. In this way, the figure shows how assumed default spectral intensities have changed for recent versions of ASCE/SEI 7 and thus the seismic demands used in the design of structures. ASCE/SEI 7-10 response spectra are the same as ASCE/SEI 7-05 response spectra and similarly use a default site condition of Site Class D. ASCE/SEI 7-16 uses a default site condition that envelops (or takes the maximum of) Site Class C and Site Class D site response. ASCE/SEI 7-22 uses a default site condition that envelops Site Class C, CD, and D site response, where Site Class CD is a new site class. ASCE/SEI 7-22 has two ways to calculate response spectra—the traditional two-period approach that is consistent with prior versions of ASCE/SEI 7 and a new multi-period approach. Both two-period and multi-period response spectra of ASCE/SEI 7-22 are shown in Figure 6-1, where the two-period spectrum is derived from the multi-period DLL response spectrum of ASCE/SEI 7-22 assuming default site conditions. Figure 6-1 also shows the ratio of the default DLL spectrum of ASCE/SEI 7-22 to the FEMA P-695 SDC D_{max} spectrum, illustrating the substantial differences (approximate factor 2) between the ground motions in recent editions of ASCE/SEI 7 and those of the VHS boundary at longer response periods.

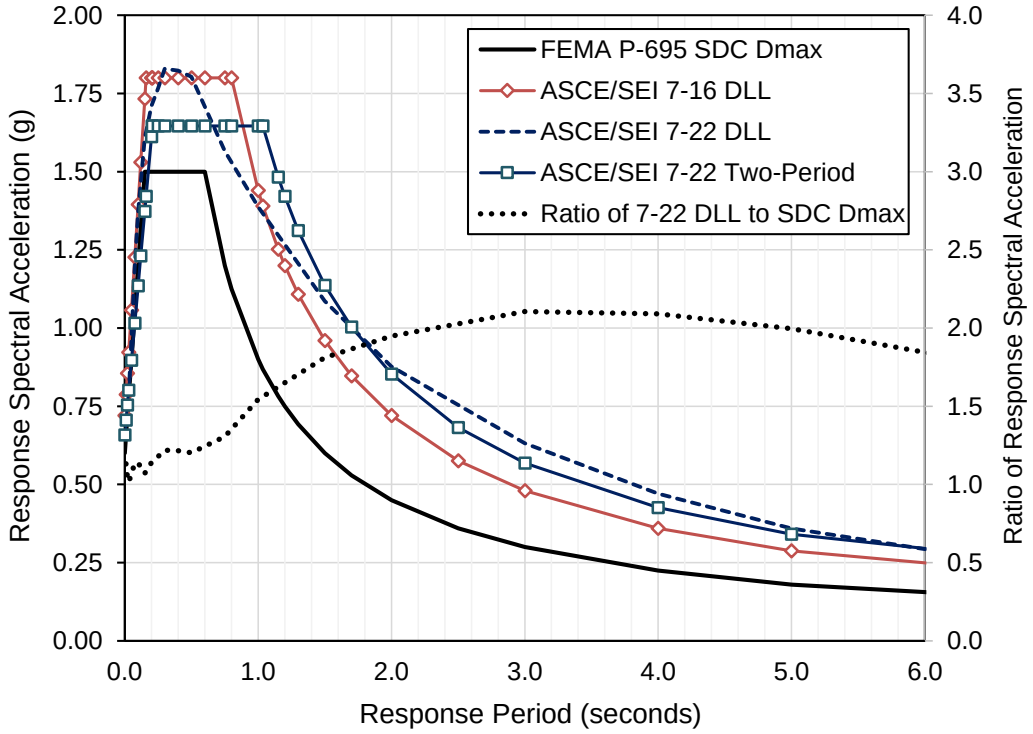

Figure 6-1 **Plot of the VHS boundary (bold curve) based on the SDC D_{max} ground motions of FEMA P-695 (i.e., default Site Class D, ASCE/SEI 7-05/10), and for comparison plots of response spectra of the Deterministic Lower Limit (DLL) of other recent versions of ASCE/SEI 7 assuming default site conditions, and (using the y axis on the right) the ratio of ground motions of the ASCE/SEI 7-22 DLL and FEMA P-695 SDC D_{max}, assuming default site conditions.**

Trends of increased collapse risk (i.e., conditional probability of collapse given MCE_R ground motions) are developed in Section 6.2 to Section 6.4 from the results of the analyses of the wood light-frame archetypes, investigated in Chapter 4, and the analyses of steel buckling restrained brace frame (BRBF), steel special moment resisting frame (SMF), and ductile coupled shear wall (DCW) archetypes, investigated in Chapter 5. Collapse results of those chapters were developed utilizing the collapse surface procedures of Chapter 3 and the related methods of FEMA P-695.

Collapse surfaces describe median collapse response spectral acceleration, $\hat{S}_{CT}$, at the design period (i.e., $T = C_u T_a$) of the archetype model as a function of (1) maximum (pushover) strength of the archetype model (V_{max}/W) and (2) the displacement capacity of the archetype model, as characterized by the median story drift ratio of the governing story at incipient collapse (DR_{IC}, or median DR_{IC}).

"Archetype" Terminology

The term "archetype" is used here to refer generically to the collection of simplified, 2-dimensional multi-degree-of-freedom (2D MDOF) nonlinear models representing different heights and configurations of the wood light-frame SFRS of Chapter 4 and to the collection of simplified, equivalent single-degree-of-freedom (eSDOF) nonlinear models representing different heights and configurations of the three non-wood SFRSs (BRBF, SMF, and DCW) of Chapter 5. Simplified here means that the models have been derived from corresponding detailed nonlinear MDOF models.

Two collapse performance metrics are derived from the collapse surface of each archetype: (1) the adjusted collapse margin ratio (*ACMR*), and (2) probability of collapse given MCE_R ground motions, $P[\text{Collapse}|S_{MT}]$. Both collapse metrics are expressed as a function of MCE_R ground motions at the spectral acceleration at the design period of the archetype, S_{MT}, such that trends in collapse performance can be evaluated as a function of the level of ground shaking.

Collapse performance trends are developed from a total of 31 individual archetypes of the four SFRSs studied by this project, as summarized in Table 6-1. Archetypes represent different heights (number of stories) and configurations of the SFRS of interest. Wood light-frame archetypes represent commercial (COM), multi-family dwelling (MFD), and structure-only (STR) configurations, and non-wood archetypes represent two typical commercial configurations of each of the three non-wood SFRSs (BRBF, SMF and DCW). As required to populate collapse surfaces, a broad range of hypothetical model maximum (pushover) strengths are assumed, rather than being based on detailed designs of specific configurations of the SFRS of interest. Each archetype is also modeled to have representative nonlinear hysteretic (backbone) properties, resulting in approximately 25 to 30 nonlinear models per archetype and a total of about 800 archetype models of the four SFRSs.

Simplified, 2-dimensional multi-degree-of-freedom (2D MDOF) nonlinear models are used for the wood light-frame archetypes, and simplified, equivalent single-degree-of-freedom (eSDOF) nonlinear models were used for the non-wood archetypes. eSDOF models of non-wood SFRSs were used to capture the observed performance trends through a simple analytical method. The eSDOF models are created based on the nonlinear MDOF models and analysis results of prior research studies. Different from traditional SDOF models, an eSDOF model translates the detailed model's collapse failure mode, system pushover curve, period, and force and displacement relation into a nonlinear SDOF model. The eSDOF model is then calibrated to match the corresponding MDOF model performance. This method is shown to accurately represent the MDOF model performance trends (e.g., see Appendix E for validation of eSDOF models derived from non-wood MDOF models).

Additionally, a special study is conducted of four detailed designs (three for RC II and one for RC IV) of different strengths of a 9-story SMF system, where each archetype is represented by a detailed 2D MDOF nonlinear model. This special study provides collapse results for comparison with those based on the eSDOF nonlinear models of 9-story SMF archetypes.

Table 6-1 Summary of the Four Investigated SFRSs, the Archetypes and Models of These SFRSs, and the FEMA P-695 Design Criteria Used to Evaluate Collapse Performance and Trends of These SFRSs in Regions of Very High Seismicity

Table 12.2-1 ASCE/SEI 7-22			Archetype Properties			No. of Models	FEMA P-695 Criteria	
SFRS	ID No.	*R* Factor	Configuration	No. of Stories	ID Name		Period, *T* (sec.)	SDC D_{max} S_{MT} (g)
Light-Frame (Wood) Walls Sheathed with Wood Structural Panels	A.16	6.5	Structural Walls only (STR)	1	STR1	19	0.16	1.50
				2	STR2	19	0.26	1.50
				3	STR3	19	0.36	1.50
				4	STR4	19	0.45	1.50
				5	STR5	19	0.53	1.50
			Commercial Building Occupancy (COM)	1	COM1	22	0.16	1.50
				2	COM2	27	0.26	1.50
				3	COM3	26	0.36	1.50
				4	COM4	25	0.45	1.50
				5	COM5	24	0.53	1.50
			Multi-Family Dwelling Residential Occupancy (MFD)	1	MFD1	18	0.16	1.50
				2	MFD2	24	0.26	1.50
				3	MFD3	28	0.36	1.50
				4	MFD4	26	0.45	1.50
				5	MFD5	27	0.53	1.50
Steel Buckling Restrained Braced Frames	B.26	8	A	4	BRBF4A	30	0.87	1.03
			B	4	BRBF4B	30	0.87	1.03
			A	9	BRBF9A	29	1.54	0.58
			B	9	BRBF9B	29	1.54	0.58
			A	15	BRBF15A	30	2.23	0.40
			B	15	BRBF15B	30	2.23	0.40
Steel Special Moment Frames	C.1	8	A	3	SMF3A	30	0.73	1.23
			B	3	SMF3B	30	0.73	1.23
			A	9	SMF9A	30	1.83	0.49
			B	9	SMF9B	30	1.83	0.49
			C	9	SMF9C[1]	4	1.83/1.52	0.49
Reinforced Concrete Ductile Coupled Walls	B.5	8	A	8	DCW8A	30	0.75	1.20
			B	8	DCW8B	30	0.75	1.20
			A	12	DCW12A	31	1.01	0.89
			B	12	DCW12B	31	1.01	0.89
			A	18	DCW18A	28	1.37	0.66
			B	18	DCW18B	28	1.37	0.66

(1) Special study of three RC II and one RC IV models of a 9-story SMF archetype, see Section 5.8. The Ultra High Seismic design has a design period of 1.52 seconds. The other two designs have a design period of 1.83 seconds.

Collapse performance results and trends are presented in Section 6.2 to Section 6.4, focusing on the following topics:

- **Section 6.2: Collapse Performance and Common Trends of SFRSs.** Collapse performance results are summarized for Risk Category II (RC II) and Risk Category IV (RC IV) designs of each archetype, where collapse performance is evaluated using earthquake ground motions of the Far-Field record set of FEMA P-695. Collapse performance is compared with the target reliability criteria of Table 1.3-2 of ASCE/SEI 7-22 (i.e., 10% probability of failure of RC II structures and 2.5% probability of failure of RC IV structures given MCE_R ground motions) at ground motion levels of 1.0 × SDC D_{max}, 1.5 × SDC D_{max} and 2.0 × SDC D_{max}, where SDC D_{max} of FEMA P-695 represents the VHS boundary and the three levels are typical of the range of VHS ground motions. Trends in collapse performance as a function of the level of MCE_R ground motions are derived from collapse results assuming that SFRSs comply with target reliability criteria of ASCE/SEI 7-22 for MCE_R ground motions defined by the VHS boundary (i.e., 1.0 × SDC D_{max} of FEMA P-695).

- **Section 6.3: Additional Collapse Risk due to Near-Fault Ground Shaking.** Collapse performance results are summarized for RC II and RC IV designs of wood light-frame MFD archetypes, where collapse performance is evaluated using the earthquake ground motions of the Near-Field record set of FEMA P-695. Additional collapse risk due to near-fault ground shaking is evaluated by comparison of Near-Field collapse results with those of wood light-frame MFD archetypes evaluated using Far-Field ground motions.

- **Section 6.4: Adequacy of the Importance Factor (I_e) for Design of Risk Category IV Structures**. The adequacy of the Importance Factor (I_e = 1.5) required by ASCE/SEI 7-22 for design of RC IV structures in VHS regions is evaluated by comparison of collapse performance results of RC IV designs and RC II designs of selected archetypes.

6.2 Collapse Performance and Common Trends of SFRSs

Collapse performance results of wood light-frame (STR, COM and MFD), BRBF, SMF, and DCW archetypes are summarized in Table 6-2 for RC II design criteria (i.e., I_e = 1.0) and in Table 6-3 for RC IV design criteria (i.e., I_e = 1.5). In Table 6-2, green shading indicates compliance with the target reliability of 10% probability of failure given MCE_R ground motions for RC II structures; yellow and red shading indicate collapse probabilities that exceed 10% and 20%, respectively. Similarly, in Table 6-3, green shading indicates compliance with the target reliability of 2.5% probability of failure given MCE_R ground motions for RC IV structures; yellow and red shading indicate collapse probabilities that exceed 2.5% and 5%, respectively. Collapse performance results are shown in these tables for MCE_R ground motions corresponding to three levels of archetype design acceleration, S_{MT} = 1.0 × SDC D_{max} (i.e., the VHS boundary), S_{MT} = 1.5 × SDC D_{max}, and S_{MT} = 2.0 × SDC D_{max} of FEMA P-695. Consistent with FEMA P-695, the same value of S_{MT} is used for design (i.e., archetype strength) and collapse evaluation.

Table 6-2 Summary of the FEMA P-695 Collapse Results of Wood (STR, COM and MFD), BRBF, SMF, and DCW Archetypes, RC II Design (I_e = 1.0), Evaluated Using the Far-Field Record Set

Archetype ID Name	FEMA P-695 Criteria		FEMA P-695 Collapse Results, RC II Design, Far-Field Records					
	Period, T (sec.)	SDC D_{max} S_{MT} (g)	S_{MT} = 1.0 × SDC D_{max}		S_{MT} = 1.5 × SDC D_{max}		S_{MT} = 2.0 × SDC D_{max}	
			ACMR	P[C|S_{MT}]	*ACMR*	P[C|S_{MT}]	*ACMR*	P[C|S_{MT}]
STR1	0.16	1.50	1.51	24.2%	1.31	32.4%	1.16	40.2%
STR2	0.26	1.50	2.07	11.3%	1.70	18.9%	1.45	26.8%
STR3	0.36	1.50	2.30	8.2%	1.90	14.2%	1.64	20.0%
STR4	0.45	1.50	2.18	8.5%	1.82	14.0%	1.57	20.4%
STR5	0.53	1.50	2.11	8.8%	1.74	15.3%	1.50	22.4%
COM1	0.16	1.50	2.43	7.0%	1.86	15.1%	1.53	23.8%
COM2	0.26	1.50	2.70	4.9%	2.00	12.5%	1.60	21.2%
COM3	0.36	1.50	2.82	4.2%	2.19	9.5%	1.82	15.8%
COM4	0.45	1.50	2.50	6.0%	1.99	11.4%	1.67	17.7%
COM5	0.53	1.50	2.34	6.8%	1.88	12.8%	1.57	20.1%
MFD1	0.16	1.50	3.90	0.7%	2.68	3.3%	2.05	8.5%
MFD2	0.26	1.50	3.11	2.9%	2.25	8.8%	1.79	16.3%
MFD3	0.36	1.50	3.04	3.2%	2.30	8.3%	1.87	14.3%
MFD4	0.45	1.50	2.73	4.7%	2.10	10.0%	1.72	16.3%
MFD5	0.53	1.50	2.53	6.1%	1.99	11.8%	1.66	18.3%
BRBF4A	0.87	1.03	3.36	4.0%	2.58	8.6%	2.17	13.2%
BRBF4B	0.87	1.03	3.96	2.5%	3.07	5.5%	2.59	8.7%
BRBF9A	1.54	0.58	4.79	1.2%	3.44	3.7%	2.77	7.0%
BRBF9B	1.54	0.58	5.27	0.9%	3.76	2.9%	3.02	5.6%
BRBF15A	2.23	0.40	4.59	1.4%	3.22	4.6%	2.52	9.1%
BRBF15B	2.23	0.40	5.41	0.8%	3.74	2.9%	2.91	6.2%
SMF3A	0.73	1.23	2.24	10.8%	1.74	19.6%	1.49	27.1%
SMF3B	0.73	1.23	2.29	9.1%	1.71	20.0%	1.45	27.7%
SMF9A	1.83	0.49	1.99	12.8%	1.51	25.5%	1.23	37.1%
SMF9B	1.83	0.49	2.01	12.0%	1.51	24.4%	1.23	36.3%
SMF9C(m)[1]	1.83/1.52	0.49	2.60	5.6%	N/A	N/A	2.32	8.1%
SMF9C(e)[1]	1.83/1.52	0.49	2.76	4.5%	N/A	N/A	2.39	7.3%
DCW8A	0.75	1.20	2.04	12.2%	1.48	25.5%	1.20	37.9%
DCW8B	0.75	1.20	2.15	10.1%	1.54	23.1%	1.24	35.5%
DCW12A	1.01	0.89	2.52	6.7%	1.78	16.4%	1.44	26.8%
DCW12B	1.01	0.89	2.65	5.7%	1.85	14.8%	1.48	25.2%
DCW18A	1.37	0.66	2.92	3.6%	2.99	12.2%	1.56	22.3%
DCW18B	1.37	0.66	2.79	4.3%	1.96	12.7%	1.55	22.9%

(1) Special study of three models of a 9-story SMF archetype, see Section 5.8 (SMF9C(m) refers to results of MDOF models, SMF9C(e) refers to results of eSDOF models of the same archetype).

Table 6-3 Summary of the FEMA P-695 Collapse Results of Wood (STR, COM and MFD), BRBF, SMF, and DCW Archetypes, RC IV Design (I_e = 1.5), Evaluated Using the Far-Field Record Set

Archetype ID Name	FEMA P-695 Criteria		FEMA P-695 Collapse Results, RC IV Design, Far-Field Records					
	Period, T (sec.)	SDC D_{max} S_{MT} (g)	S_{MT} = 1.0 × SDC D_{max}		S_{MT} = 1.5 × SDC D_{max}		S_{MT} = 2.0 × SDC D_{max}	
			ACMR	P[C|S_{MT}]	*ACMR*	P[C|S_{MT}]	*ACMR*	P[C|S_{MT}]
STR1	0.16	1.50	1.96	10.5%	1.64	17.6%	1.38	26.9%
STR2	0.26	1.50	2.55	4.5%	2.03	10.0%	1.66	17.5%
STR3	0.36	1.50	2.85	2.8%	2.30	5.7%	1.91	9.9%
STR4	0.45	1.50	2.73	2.4%	2.19	5.5%	1.79	11.1%
STR5	0.53	1.50	2.61	2.5%	2.10	6.0%	1.73	11.8%
COM1	0.16	1.50	2.78	3.1%	2.13	8.5%	1.72	15.3%
COM2	0.26	1.50	2.99	2.3%	2.18	6.9%	1.71	14.0%
COM3	0.36	1.50	3.29	1.5%	2.52	4.4%	2.03	8.4%
COM4	0.45	1.50	2.99	1.8%	2.32	4.6%	1.84	10.1%
COM5	0.53	1.50	2.82	2.0%	2.18	5.4%	1.74	11.8%
MFD1	0.16	1.50	4.01	0.2%	2.77	1.5%	2.12	5.0%
MFD2	0.26	1.50	3.37	1.4%	2.44	4.7%	1.92	9.8%
MFD3	0.36	1.50	3.45	1.2%	2.57	3.7%	2.03	7.7%
MFD4	0.45	1.50	3.15	1.5%	2.35	4.1%	1.81	10.0%
MFD5	0.53	1.50	2.99	1.9%	2.30	4.9%	1.81	10.7%
BRBF4A	0.87	1.03	3.88	1.8%	3.00	4.4%	2.49	7.8%
BRBF4B	0.87	1.03	4.14	1.4%	3.31	3.3%	2.77	5.9%
BRBF9A	1.54	0.58	5.16	0.5%	3.79	1.9%	3.10	3.9%
BRBF9B	1.54	0.58	5.66	0.4%	4.12	1.4%	3.37	3.0%
BRBF15A	2.23	0.40	4.82	0.7%	3.44	2.8%	2.74	5.8%
BRBF15B	2.23	0.40	5.61	0.4%	3.94	1.6%	3.11	3.9%
SMF3A	0.73	1.23	2.54	6.1%	2.02	12.2%	1.54	23.7%
SMF3B	0.73	1.23	2.64	4.5%	1.99	11.5%	1.49	24.3%
SMF9A	1.83	0.49	2.28	8.3%	1.65	18.7%	1.31	31.6%
SMF9B	1.83	0.49	2.28	6.5%	1.68	17.0%	1.30	31.4%
SMF9C[1]	1.83/1.52	0.49	N/A	N/A	N/A	N/A	2.3	8.0%
DCW8A	0.75	1.20	2.26	7.3%	1.67	17.7%	1.34	30.0%
DCW8B	0.75	1.20	2.39	5.9%	1.73	16.1%	1.36	28.8%
DCW12A	1.01	0.89	2.78	3.5%	2.06	9.8%	1.64	18.6%
DCW12B	1.01	0.89	2.94	2.7%	2.13	8.8%	1.67	17.7%
DCW18A	1.37	0.66	3.03	2.0%	2.11	8.0%	1.64	22.3%
DCW18B	1.37	0.66	3.01	2.1%	2.14	7.7%	1.67	16.6%

(1) Special study of one RC IV model of a 9-story SMF archetype, see Section 5.8.

Plots of the collapse probability of RC II designs (Table 6-2) as a function of S_{MT} normalized by S_{MT} = SDC D_{max} are shown in Figures 6-2, 6-3, and 6-4 for wood STR, COM, and MFD archetypes, respectively; in Figure 6-5 for BRBF archetypes; in Figure 6-6 for SMF archetypes; and in Figure 6-7 for DCW archetypes. Normalization by S_{MT} = SDC D_{max} permits direct comparison of collapse performance of archetypes that have different values of SDC D_{max} (i.e., due to different values of the design period, $T = C_u T_a$). The normalized values of S_{MT} of wood archetypes (Figures 6-2, 6-3, and 6-4) are normalized by the short-period response spectral acceleration parameter, S_{MS} (i.e., SDC D_{max} = 1.5g at short periods, Figure 6-1); whereas the normalized values of S_{MT} of non-wood archetypes (Figures 6-5, 6-6, and 6-7) are normalized by $1/T$ times the 1-second response spectral acceleration parameter, S_{M1} (e.g., SDC D_{max} = 0.9g at 1 second, Figure 6-1).

Also included in these figures are normalized values of S_{MT} of ASCE/SEI 7-22 for selected city sites in regions of VHS. Due to differences in the values of S_{MS} and S_{M1}, the normalized value of S_{MT} of a short-period wood archetype is different from the normalized value of S_{MT} of a non-wood archetype. For example, the normalized value of S_{MT} of San Bernardino is 1.98 (i.e., S_{MS} = 2.97g normalized by 1.5g) for short-period wood archetypes; whereas, the normalized value of S_{MT} of San Bernardino is 3.14 (i.e., S_{M1} = 2.83g normalized by 0.9g) for non-wood archetypes. San Bernardino is a site with extreme ground motions and for perspective, the normalized value of S_{MT} for Charleston is 1.01 (i.e., S_{MS} = 1.52g normalized by 1.5g) for short-period wood archetypes, and the normalized value of S_{MT} of Charleston is 0.86 (S_{M1} = 0.77g normalized by 0.9g) for non-wood archetypes. Values of short-period MCE_R spectral response acceleration, S_{MS}, and 1-second MCE_R spectral response acceleration, S_{M1}, are taken from Table C22-3 and Table C22-4 of ASCE/SEI 7-22 for the selected city sites. Sometimes the "normalized" values of S_{MT} move off the collapse surfaces (i.e., beyond the range of strengths V_{max}/W assumed to develop models), and corresponding values of S_{MT} do not extend the full range of the horizontal axis. This explains why some curves (e.g., BRBF4A of Figure 6-5) appear truncated.

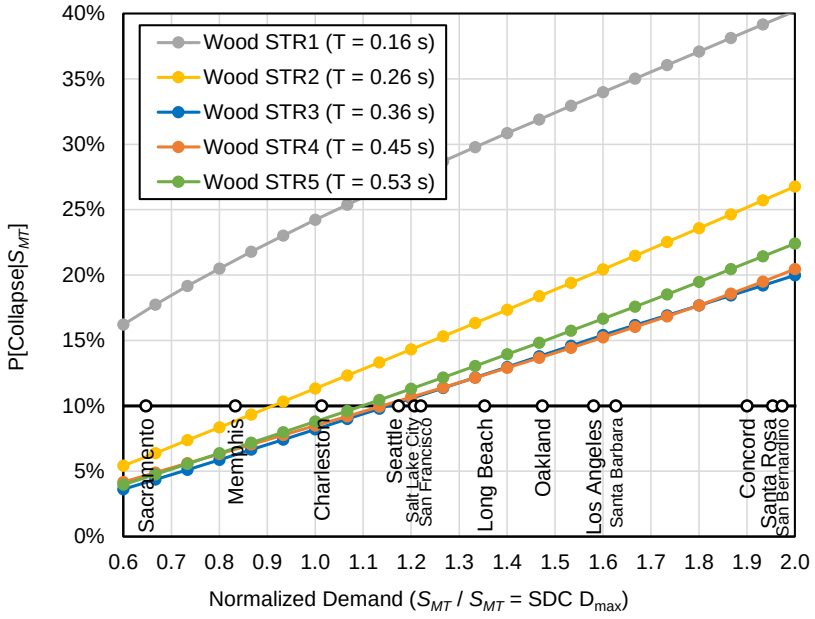

Figure 6-2 **Probability of collapse of wood STR archetypes evaluated using the Far-Field record set and plotted as a function of normalized demand (S_{MT} normalized by S_{MT} = SDC D_{max}). Also shown (1) RC II reliability target of 10% probability of collapse given S_{MT} = SDC D_{max} and (2) normalized values of S_{MT} of ASCE/SEI 7-22 for selected city sites.**

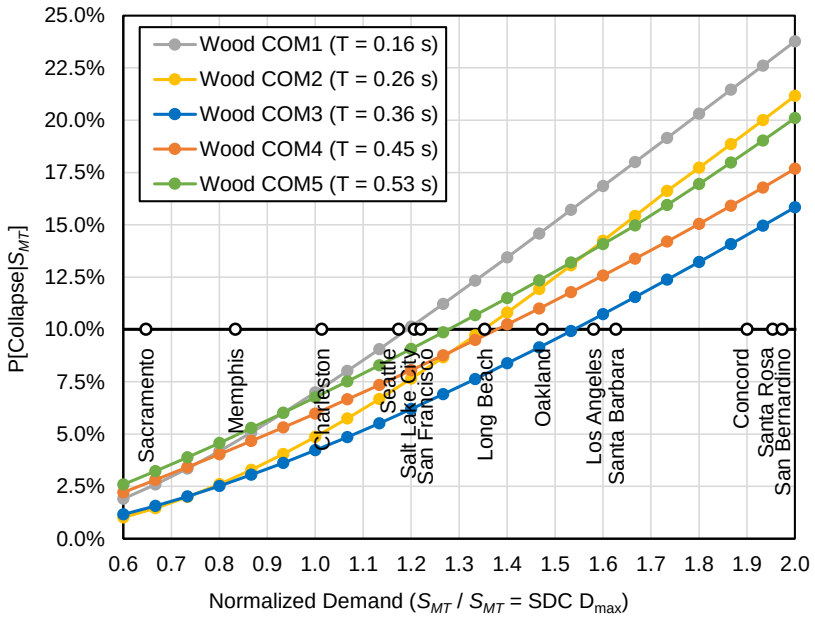

Figure 6-3 **Probability of collapse of wood COM archetypes evaluated using the Far-Field record set and plotted as a function of normalized demand (S_{MT} normalized by S_{MT} = SDC D_{max}). Also shown (1) RC II reliability target of 10% probability of collapse given S_{MT} = SDC D_{max} and (2) normalized values of S_{MT} of ASCE/SEI 7-22 for selected city sites.**

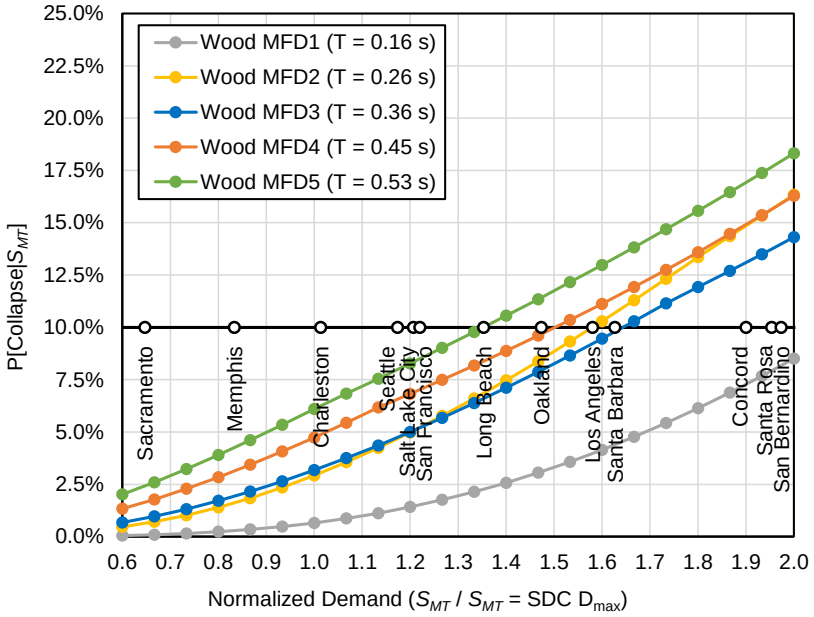

Figure 6-4 **Probability of collapse of wood MFD archetypes evaluated using the Far-Field record set and plotted as a function of normalized demand (S_{MT} normalized by S_{MT} = SDC D_{max}). Also shown (1) RC II reliability target of 10% probability of collapse given S_{MT} = SDC D_{max} and (2) normalized values of S_{MT} of ASCE/SEI 7-22 for selected city sites.**

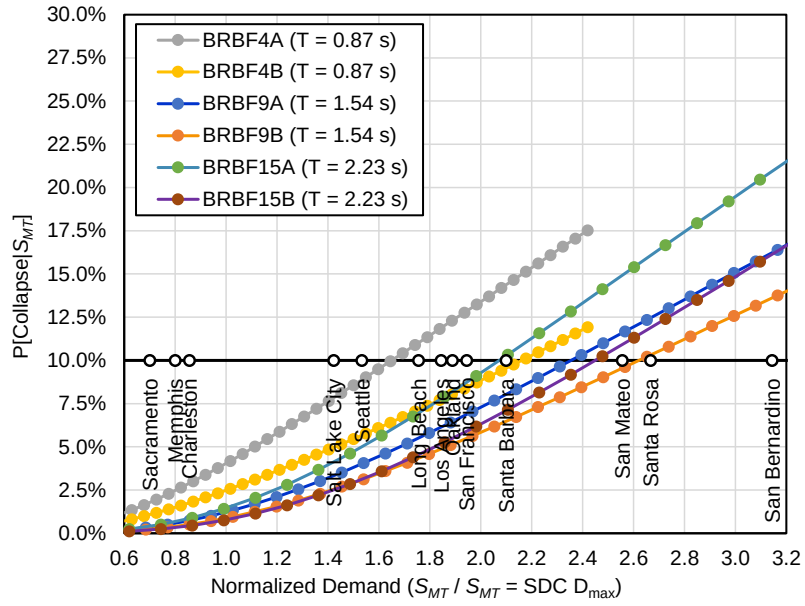

Figure 6-5 **Probability of collapse of BRBF archetypes evaluated using the Far-Field record set and plotted as a function of normalized demand (S_{MT} normalized by S_{MT} = SDC D_{max}). Also shown (1) RC II reliability target of 10% probability of collapse given S_{MT} = SDC D_{max} and (2) normalized values of S_{MT} of ASCE/SEI 7-22 for selected city sites.**

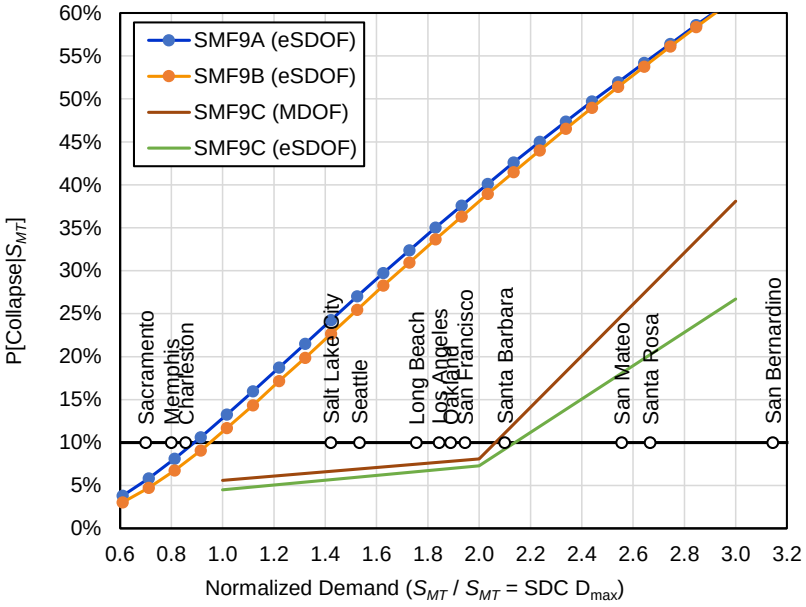

Figure 6-6 **Probability of collapse of SMF archetypes evaluated using the Far-Field record set and plotted as a function of normalized demand (S_{MT} normalized by S_{MT} = SDC D_{max}), including collapse results of the MDOF and eSDOF models of 9–story SMF (SMF9C) archetypes of the special study of Section 5.8. Also shown (1) RC II reliability target of 10% probability of collapse given S_{MT} = SDC D_{max} and (2) normalized values of S_{MT} of ASCE/SEI 7-22 for selected city sites in VHS regions.**

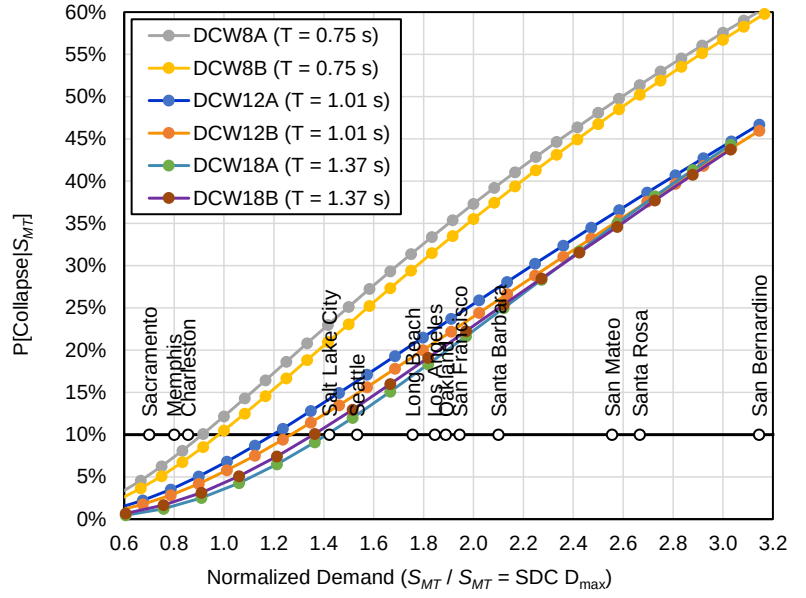

Figure 6-7 **Probability of collapse of DCW archetypes evaluated using the Far-Field record set and plotted as a function of normalized demand (S_{MT} normalized by S_{MT} = SDC D_{max}). Also shown (1) RC II reliability target of 10% probability of collapse given S_{MT} = SDC D_{max} and (2) normalized values of S_{MT} of ASCE/SEI 7-22 for selected city sites.**

As shown by the collapse results of Table 6-2 (RC II design) and Table 6-3 (RC IV design) and as illustrated in Figures 6-2 through Figure 6-7, the probability of collapse in regions of VHS was found to increase monotonically, and significantly, as a function of level of MCE_R ground motions for all archetypes of each of the four SFRS, although the probability of collapse varies substantially for different archetypes of the four SFRSs when evaluated at a common level of MCE_R ground motions (e.g., S_{MT} = SDC D_{max}). That is, some archetypes were found to be more likely to collapse than others, implying that current values of the *R* factor in Table 12.2-1 of ASCE/SEI 7-22 are not achieving uniform collapse performance. However, caution should be exercised in the use of the results of this study as the basis for revision of *R* factors. Rather, revision of *R* factors would necessarily require collapse performance evaluation of more detailed models of each SFRS of interest that, for example, incorporate in-depth design of individual archetypes and refined modeling assumptions (and underlying test data), such as that used by the special study of a 9-story SMF (Section 5.8).

The significant difference in the collapse performance of one-story wood archetypes (STR1, COM1 and MFD1) is directly related to differences in wood archetype model strength and energy dissipation capacity due to the amount of nonstructural wall components that is considered as contributing to lateral strength, where total strength and energy dissipation capacity in COM1 and MFD1 archetypes is significantly increased by nonstructural walls. Wood COM and MFD archetypes, which incorporate realistic amounts of nonstructural wall finishes (e.g., interior wall gyp board, exterior wall stucco) perform better than the wood STR archetypes, which include only structural elements (wood shear walls). However, taller wood archetypes become heavier, thereby increasing the base shear force. Since the collapse mechanism of these models is typically governed by shear failure in the bottom story and the nonstructural walls remain the same independent of the height of the building, the relative contribution of nonstructural strength contribution in the first story will reduce as the building becomes taller (i.e., the structural contribution will increase with a design base shear increase but the nonstructural contribution does not). Therefore, the differences in STR, COM and MFD collapse performance gradually diminish for the taller building archetypes.

The collapse probabilities of the wood COM and MFD archetypes are plausible and consistent with observed performance in past earthquakes. For example, the collapse probabilities of 1-story (0.7%), 2-story (2.9%) and 3-story (3.2%) wood MFD archetypes at S_{MT} = 1.0 × SDC D_{max} (Table 6-2) are consistent with Red Tag data from the 1994 Northridge earthquake (see Section 2.5, FEMA P-2139-2, 2020) and the significantly larger collapse probabilities of these same archetypes at S_{MT} = 1.5 × SDC D_{max} and S_{MT} = 2.0 × SDC D_{max} are consistent with the fraction of newer wood buildings (incorporating wood shear walls) with Heavy damage in the 1995 Kobe earthquake at sites where the shaking was much stronger than that of the 1994 Northridge earthquake (Yamaguchi and Yamazaki, 2000; and Yamazaki and Murao, 2000, Table 2-19; FEMA, 2020).

The significant difference in the collapse performance of the three non-wood archetypes is more challenging to explain, other than noting that the simplified archetype models of this study are derived from more detailed models of prior studies and validated against the collapse results of those prior studies, as described in Chapter 5 (e.g., see comparison of median collapse acceleration, $\hat{S}_{CT}$, of non-wood archetype models in Table 5-1). That is, differences in collapse performance are

largely due to the different modeling assumptions and limitations of the prior studies (e.g., limitations on reinforced-concrete shear wall capacity at large drift ratios due to lack of test data), rather than the use of simplified models. Nonetheless, differences in collapse performance are larger than expected (recognizing that actual experience with these systems in past U.S. earthquakes is limited to about S_{MT} = 1.0 × SDC D_{max}, or less).

For example, BRBF archetypes (Figure 6-5) generally comply with the reliability target of 10% conditional probability of failure of RC II structures for ground motions that are twice as strong as the shaking level of the VHS boundary (i.e., S_{MT} = 2.0 × SDC D_{max}), whereas, SMF archetypes (Figure 6-6) and 8-story DCW archetypes do not comply at the VHS boundary (i.e., S_{MT} = 1.0 × SDC D_{max}), although noncompliance is minimal. It is worth noting that the SMF archetypes and the 8-story DCW archetypes, which slightly exceed the RC II reliability target of 10% probability of failure given MCE_R ground motions, would comply, if a less conservative (more optimistic) value of the total collapse uncertainty parameter, β_{TOT}, had been assumed for the collapse fragility of non-wood archetypes. That is, while the values of median collapse acceleration, $\hat{S}_{CT}$, of non-wood archetypes of this study compare well with those of prior studies (as shown in Chapter 5), the corresponding collapse probabilities of this study are somewhat larger than those of prior studies due to the somewhat larger values of the total collapse uncertainty parameter, β_{TOT}, deemed appropriate for collapse evaluation of the simplified models of non-wood SFRSs of this study. For example, RC II non-wood archetypes of this study were evaluated using a total uncertainty, β_{TOT} = 0.60 at a drift ratio of DR = 5% (Table 3-6); whereas a total uncertainty of β_{TOT} = 0.50 was used in the NIST GCR 10-917-8 study of SMF archetypes. Values of total collapse uncertainty, β_{TOT}, are defined in Table 3-6 as a function of (1) the SFRS (i.e., wood or non-wood), (2) the risk category (RC II or RC IV) and (3) the degree of nonlinear response (i.e., drift ratio, *DR*). The rationale for these values is described in Section 3.7.3. Values of total collapse uncertainty reflect a modest, systematic increase in the inherent uncertainty in failure-mode displacement with increasing values of *DR* (i.e., median failure at *DR* = 7.5% is fundamentally less certain than at *DR* = 5.0%, all else equal). In general, the relatively small, systematic increase in the values of β_{TOT} with increase in *DR* only modestly affects the values of P[Collapse|S_{MT}] and the acceptable value of adjusted collapse performance (i.e., *ACMR10%* for RC II SFRSs, Table 7-3, FEMA P-695). For example, *ACMR10%* = 1.90 when β_{TOT} =0.50 and *ACMR10%* = 2.16 when β_{TOT} =0.60, a difference of roughly 12%.

During the course of the project, concerns were raised over the large differences in collapse performance of non-wood archetype, and, in particular, the relatively poor performance of SMF archetypes, which prompted a special study of SMF archetypes (i.e., Section 5.8). Three detailed designs of a 9-story SMF archetype were prepared, MDOF models developed and collapse performance evaluated for normalized ground motions corresponding to S_{MT} = 1 ×, 2 × and 3 × SDC D_{max} (with respect to S_{D1} values). Collapse results of the three MDOF models are plotted in Figure 6-6 for comparison with the collapse trends of the eSDOF archetypes (SMF3A, SMF3B, SMF9A and SMF9B). While the trend of decreasing collapse performance with increasing shaking intensity is similar to that of the eSDOF archetypes, the values of P[Collapse|S_{MT}] are very different. For example, the probabilities of collapse of the MDOF models do not exceed the target reliability of 10%

probability of failure (RC II structures) until normalized ground motions exceed 2 × SDC D_{max}, whereas, the collapse probabilities of the eSDOF models are about 10% for normalized ground motions of 1 × SDC D_{max}.

The source of differences in collapse performance was investigated and found to be primarily related to differences in the archetype strength (i.e., overstrength) and displacement capacity of the MDOF models compared to that of the eSDOF models, rather than due to the simplifying assumption of the eSDOF models. The three MDOF models of the special study have significantly greater strength and displacement capacity than those of the prior studies (e.g., FEMA P-2012) that were used to develop and validate the eSDOF models of SMF archetypes (i.e., Section 5.3). For example, the pushover strength of the MDOF model designed for 3 × SDC D_{max} is about 40% greater and the displacement capacity is over twice that of the corresponding eSDOF model. The additional strength of the three MDOF models is attributed to designs prepared specifically for VHS ground motions. The additional displacement capacity of the three MDOF models is attributed to the more detailed (and optimistic) modeling of failure mechanisms (e.g., columns are assumed to not fail until reaching 10% story drift ratio). Additional description of the three MDOF models and modeling assumptions is provided in Section 5.8 and Appendix F.

For an “apples-to-apples” comparison of collapse performance of the SMF MDOF and eSDOF models of comparable strength and displacement capacity, a set of eSDOF models was developed from the backbone curves of the MDOF models. Collapse evaluation of these eSDOF models found very similar collapse performance to that of the corresponding MDOF model, as shown by comparison of collapse data in Figure 6-6, demonstrating that eSDOF models can provide reliable estimates of collapse performance when based on the same hysteretic properties as the corresponding MDOF model, underscoring the importance of using detailed models to establish hysteretic properties.

The collapse performance of the BRBF archetypes is arguably somewhat better than that expected for buildings with BRBFs, and conversely, the collapse performance of the SMF and DCW archetypes is arguably somewhat worse than that expected for buildings with these SFRSs (although there is essentially no actual U.S. earthquake experience with these systems where ground motions exceed S_{MT} = 1.0 × SDC D_{max}). Disparity in the “absolute” collapse performance of the different non-wood SFRSs is not the primary focus of this study. Absolute collapse performance refers to values of the *ACMR* and the corresponding probability of collapse given MCE_R ground motions, P[Collapse|S_{MT}], as might be determined from a FEMA P-695 evaluation of the value of the *R* factor proposed for a new SFRS. Investigating absolute collapse performance would necessarily require a more comprehensive set of archetypes and detailed nonlinear models of the specific SFRS (or SFRSs) of interest.

Instead, this study is focused on quantifying trends in collapse performance that are common to all SFRSs. That is, what is the common “relative” increase in probability of collapse with increase in ground shaking in regions of VHS? To this end, collapse performance has been investigated for a variety of SFRSs and archetypes, including, for example, wood STR archetypes, although these archetypes, which are modeled assuming 1% damping and do not include nonstructural wall finishes (e.g., interior wall gypsum board and exterior wall stucco) are inherently pessimistic with respect to collapse performance of actual wood light-frame buildings. Likewise, collapse results of non-wood

SFRSs archetypes are equally useful and essential in quantifying common trends in collapse performance, even if some archetype models of these SFRSs are deemed "pessimistic" or "optimistic" with respect to expected collapse performance.

The intent of studying different SFRSs is to develop a common "generic" trend or trends of collapse performance in regions of VHS, establish an understanding of the root causes of these trends, and, hence, provide a basis for developing recommendations that would be applicable to all SFRSs. The first step in the process was to develop absolute collapse performance trends of the archetypes of the four SFRSs. While the absolute collapse results of archetypes of the four SFRSs (Table 6-2 and Table 6-3) show the same general trends of increasing collapse risk with shaking intensity, the broad range of collapse performance of the different SFRS archetypes complicates quantification of common trends. This shortcoming was circumvented by adjusting collapse results (e.g., values of *ACMR*) of each SFRS archetype to reflect uniform collapse performance in compliance with the target reliability criteria of ASCE/SEI 7-22 (i.e., 10% probability of failure for RC II structures or 2.5% probability of failure for RC IV structures given MCE_R ground motions).

Adjusted values of *ACMR* are determined from collapse surfaces using hypothetical values of the strength ratio, R/I_e, that achieve target reliability for MCE_R ground motions of the VHS boundary (i.e., S_{MT} = 1.0 × SDC D_{max}). The resulting adjusted collapse results have the same probability of collapse, P[Collapse|S_{MT} = SDC D_{max}] = 10% and, by definition, the same ratio of *ACMR10%/ACMR* = 1.0 for all SFRS archetypes adjusted to comply with RC II target reliability, where values of *ACMR10%* (i.e., the acceptable value of *ACMR* for RC II structures of Table 7-3 of FEMA P-695) are given in Table 3-1 as a function of total system collapse uncertainty (β_{TOT}). Similarly, adjusted collapse results have the same probability of collapse, P[Collapse|S_{MT} = SDC D_{max}] = 2.5% and the same ratio of *ACMR2.5%/ACMR* = 1.0 for all SFRS archetypes adjusted to RC IV target reliability, where values of *ACMR2.5%* are given in Table 3-1 as a function of total system collapse uncertainty (β_{TOT}). It may be noted that adjustment to meet target reliability does not require modifying collapse surfaces (i.e., values of median collapse acceleration, $\hat{S}_{CT}$, remain the same). Rather, the adjustment of *ACMR* evaluates collapse performance using a different portion of the same collapse surface of the SFRS archetype of interest.

Hypothetical values of the strength ratio, R/I_e, reflect modest changes to the *R* factor of Table 12.2-1 for archetypes, like those of the RC II designs of the SMF system (Table 6-2), whose collapse performance is close to that of the target reliability criteria. But the hypothetical values of R/I_e are quite different for archetypes, like those of the BRBF system, whose collapse performance is much better than that of target reliability criteria. In some cases, hypothetical values of R/I_e complying with target reliability criteria could not be determined from the collapse surface, implying that the "solution" is not on the collapse surface. Such cases do not mean that collapse performance does not change with the level of shaking. Rather, those archetypes cannot be used to quantify common trends.

Collapse results, adjusted by hypothetical values of R/I_e at S_{MT} = 1.0 × SDC D_{max}, are summarized in Table 6-4 and Table 6-5 for archetypes adjusted to achieve RC II and RC IV target reliabilities,

respectively. Values of the ratio of *ACMR10%/ACMR* (Table 6-4) and *ACMR2.5%/ACMR* (Table 6-5) and the probability of collapse, P[Collapse|S_{MT}], are shown in these tables for values of S_{MT} = 1.5 × SDC D_{max} and S_{MT} = 2.0 × SDC D_{max} of FEMA P-695. Gray shading indicates that the target reliability could not be achieved from the collapse surface of the archetype. Trends in the probability of collapse of archetypes adjusted to RC II target reliability are shown in Figure 6-8 for wood archetypes and in Figure 6-9 for non-wood archetypes. The trends shown in these figures quantify the additional collapse risk (e.g., probability of collapse above the 10% probability of failure at S_{MT} = SDC D_{max}) as a function of normalized demand ground motions (i.e., S_{MT} normalized by SDC D_{max}). Normalization by S_{MT} = SDC D_{max} permits direct comparison of collapse performance of archetypes that have different values of SDC D_{max} (i.e., due to different values of the design period, $T = C_u T_a$).

Trends in the ratios of *ACMR10%/ACMR* of archetypes adjusted to RC II target reliability are shown in Figure 6-10 for wood archetypes, and in Figure 6-11 for non-wood archetypes. Whereas the trends shown in Figure 6-8 and Figure 6-9 quantify the additional collapse risk in regions of VHS, the trends of the ratio of *ACMR10%/ACMR* shown in Figure 6-10 and Figure 6-11 quantify the approximate increase in design acceleration (seismic load) that would be required to mitigate the additional collapse risk (i.e., reduce the probability of collapse to an approximate uniform value of 10% probability of failure in regions of VHS). In this sense, the ratio of *ACMR10%/ACMR* may be thought of (and will be referred to) as the VHS Load Amplifier, which increases monotonically from a value of 1.0 at the VHS boundary as the normalized demand increases from S_{MT} = SDC D_{max} to stronger intensities of MCE_R ground motions. Also shown in Figure 6-8 to Figure 6-11 is the RC II reliability target of 10% probability of collapse given S_{MT} = SDC D_{max} and normalized values of S_{MT} of ASCE/SEI 7-22 for selected sites.

Table 6-4 Summary of Collapse Results of Wood (STR, COM and MFD), BRBF, SMF, and DCW Archetype Evaluated Using the Far-Field Record Set Where Collapse Results are Adjusted for Hypothetical Values of R/I_e that Achieve the RC II Target Reliability of P[Collapse|S_{MT}] = 10% at S_{MT} = SDC D_{max}

Archetype ID Name	FEMA P-695 Criteria		Adjusted Collapse Results for RC II Target Reliability					
			Target Criteria		S_{MT} = 1.5 × SDC D_{max}		S_{MT} = 2.0 × SDC D_{max}	
	Period, T (seconds)	SDC D_{max} S_{MT} (g)	*ACMR*10%	R/I_e	Adjusted P[C|S_{MT}]	VHS Load Amplifier	Adjusted P[C|S_{MT}]	VHS Load Amplifier
STR1	0.16	1.50	2.12	3.8	17.0%	1.22	26.6%	1.48
STR2	0.26	1.50	2.16	6.0	17.2%	1.22	25.0%	1.44
STR3	0.36	1.50	2.16	7.4	16.7%	1.21	23.1%	1.39
STR4	0.45	1.50	2.08	7.1	16.1%	1.19	22.6%	1.37
STR5	0.53	1.50	2.03	7.0	16.9%	1.21	24.3%	1.40
COM1	0.16	1.50	2.16	9.5	20.8%	1.32	31.0%	1.60
COM2	0.26	1.50	2.16	23	24.2%	1.42	38.1%	1.80
COM3	0.36	1.50	2.16	14	20.4%	1.31	30.0%	1.58
COM4	0.45	1.50	2.16	9.1	17.8%	1.26	25.4%	1.48
COM5	0.53	1.50	2.10	8.3	17.9%	1.25	25.7%	1.46

Table 6-4 Summary of Collapse Results of Wood (STR, COM and MFD), BRBF, SMF, and DCW Archetype Evaluated Using the Far-Field Record Set Where Collapse Results are Adjusted for Hypothetical Values of R/I_e that Achieve the RC II Target Reliability of P[Collapse|S_{MT}] = 10% at S_{MT} = SDC D_{max}. (continued)

Archetype ID Name	FEMA P-695 Criteria		Adjusted Collapse Results for RC II Target Reliability					
			Target Criteria		S_{MT} = 1.5 × SDC D_{max}		S_{MT} = 2.0 × SDC D_{max}	
	Period, T (seconds)	SDC D_{max} S_{MT} (g)	$ACMR10$ %	R/I_e	Adjusted P[C|S_{MT}]	VHS Load Amplifier	Adjusted P[C|S_{MT}]	VHS Load Amplifier
MFD1	0.16	1.50						
MFD2	0.26	1.50						
MFD3	0.36	1.50						
MFD4	0.45	1.50	2.16	13	20.2%	1.31	29.8%	1.57
MFD5	0.53	1.50	2.16	9.5	18.8%	1.27	26.8%	1.50
BRBF4A	0.87	1.03	2.44	29	20.6%	1.38	30.6%	1.71
BRBF4B	0.87	1.03	2.46	> 30	21.7%	1.42	33.2%	1.82
BRBF9A	1.54	0.58						
BRBF9B	1.54	0.58						
BRBF15A	2.23	0.40						
BRBF15B	2.23	0.40						
SMF3A	0.73	1.23	2.31	7.3	18.2%	1.28	25.7%	1.52
SMF3B	0.73	1.23	2.22	8.8	21.1%	1.35	30.0%	1.61
SMF9A	1.83	0.49	2.21	5.25	20.6%	1.32	32.9%	1.69
SMF9B	1.83	0.49	2.13	6.6	21.5%	1.38	33.9%	1.66
DCW8A	0.75	1.20	2.18	6.1	21.3%	1.35	33.1%	1.68
DCW8B	0.75	1.20	2.18	7.5	22.1%	1.37	34.4%	1.71
DCW12A	1.01	0.89	2.21	15	21.4%	1.40	35.4%	1.75
DCW12B	1.01	0.89	2.21	19	22.0%	1.41	36.7%	1.79
DCW18A	1.37	0.66						
DCW18B	1.37	0.66						

Table 6-5 Summary of Collapse Results of Wood (STR, COM and MFD), BRBF, SMF, and DCW Archetype Evaluated using the Far-Field Record Set Where Collapse Results are Adjusted for Hypothetical Values of R/I_e that Achieve the RC IV Target Reliability of P[Collapse|S_{MT}] = 2.5% at S_{MT} = SDC D_{max}

Archetype ID Name	FEMA P-695 Criteria		Adjusted Collapse Results for RC IV Target Reliability					
			Target Criteria		S_{MT} = 1.5 × SDC D_{max}		S_{MT} = 2.0 × SDC D_{max}	
	Period, *T* (seconds)	SDC D_{max} S_{MT} (g)	*ACMR*2.5 %	R/I_e	Adjusted P[C|S_{MT}]	*ACMR*2.5 % / *ACMR*	Adjusted P[C|S_{MT}]	*ACMR*2.5 % / *ACMR*
STR1	0.16	1.50	2.78	2.1	9.9%	1.44	23.2%	1.94
STR2	0.26	1.50	2.94	3.1	6.8%	1.32	14.5%	1.71
STR3	0.36	1.50	2.94	4.1	5.1%	1.25	9.2%	1.51
STR4	0.45	1.50	2.70	4.4	5.7%	1.24	11.4%	1.52
STR5	0.53	1.50	2.62	4.3	6.0%	1.25	11.7%	1.51
COM1	0.16	1.50	2.94	3.7	7.0%	1.32	13.4%	1.65
COM2	0.26	1.50	2.94	4.7	7.5%	1.36	14.6%	1.73
COM3	0.36	1.50	2.94	5.8	6.7%	1.29	12.1%	1.56
COM4	0.45	1.50	2.81	5.0	5.8%	1.27	11.4%	1.56
COM5	0.53	1.50	2.71	4.7	6.3%	1.28	12.8%	1.58
MFD1	0.16	1.50						
MFD2	0.26	1.50	2.94	9.1	8.8%	1.40	17.5%	1.76
MFD3	0.36	1.50	2.94	7.3	7.4%	1.32	13.9%	1.62
MFD4	0.45	1.50	2.92	5.4	5.9%	1.31	11.8%	1.64
MFD5	0.53	1.50	2.86	4.8	5.9%	1.29	11.7%	1.60
BRBF4A	0.87	1.03	3.55	6.6	5.6%	1.28	9.5%	1.53
BRBF4B	0.87	1.03	3.59	10.2	5.7%	1.28	9.4%	1.52
BRBF9A	1.54	0.58						
BRBF9B	1.54	0.58						
BRBF15A	2.23	0.40						
BRBF15B	2.23	0.40						
SMF3A	0.73	1.23						
SMF3B	0.73	1.23	2.82	1	11.5%	1.99	24.3%	1.49

Table 6-5 Summary of Collapse Results of Wood (STR, COM and MFD), BRBF, SMF, and DCW Archetype Evaluated using the Far-Field Record Set Where Collapse Results are Adjusted for Hypothetical Values of R/I_e that Achieve the RC IV Target Reliability of P[Collapse|S_{MT}] = 2.5% at S_{MT} = SDC D_{max} (continued)

Archetype ID Name	FEMA P-695 Criteria		Adjusted Collapse Results for RC IV Target Reliability					
			Target Criteria		S_{MT} = 1.5 × SDC D_{max}		S_{MT} = 2.0 × SDC D_{max}	
	Period, *T* (seconds)	SDC D_{max} S_{MT} (g)	*ACMR*2.5 %	R/I_e	Adjusted P[C|S_{MT}]	*ACMR*2.5 % / *ACMR*	Adjusted P[C|S_{MT}]	*ACMR*2.5 % / *ACMR*
SMF9A	1.83	0.49						
SRF9B	1.83	0.49						
DCW8A	0.75	1.20						
DCW8B	0.75	1.20						
DCW12A	1.01	0.89	2.99	3.9	8.0%	1.46	17.3%	1.78
DCW12B	1.01	0.89	3.00	4.7	8.0%	1.48	17.5%	1.79
DCW18A	1.37	0.66						
DCSW18B	1.37	0.66						

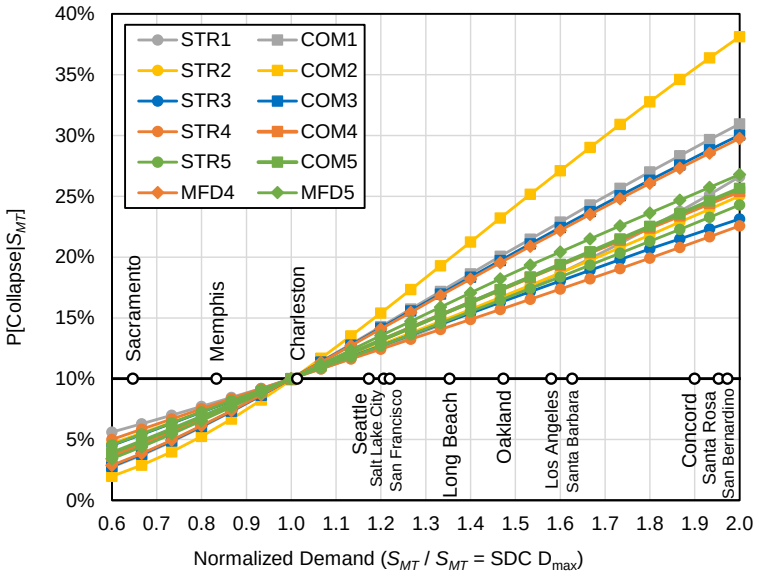

Figure 6-8 Trends in the probability of collapse of wood STR, COM and MFD archetypes as a function of normalized demand (S_{MT} normalized by S_{MT} = SDC D_{max}) for archetypes evaluated using the Far-Field record set and collapse results adjusted for hypothetical values of R/I_e that achieve the RC II target reliability of P[Collapse|S_{MT}] = 10% at S_{MT} = SDC D_{max}.

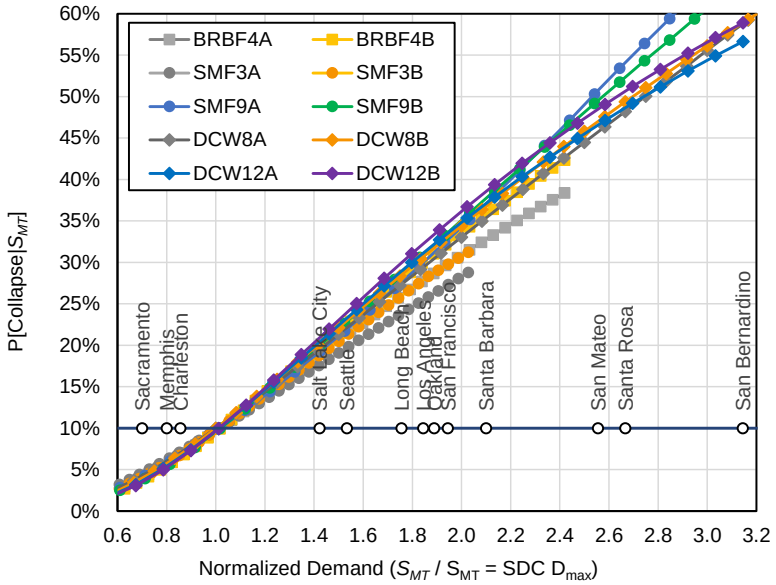

Figure 6-9 **Trends in the probability of collapse of BRBF, SMF and DCW archetypes as a function of normalized demand (S_{MT} normalized by S_{MT} = SDC D_{max}) for archetypes evaluated using the Far-Field record set and collapse results adjusted for hypothetical values of R/I_e that achieve the RC II target reliability of P[Collapse|S_{MT}] = 10% at S_{MT} = SDC D_{max}.**

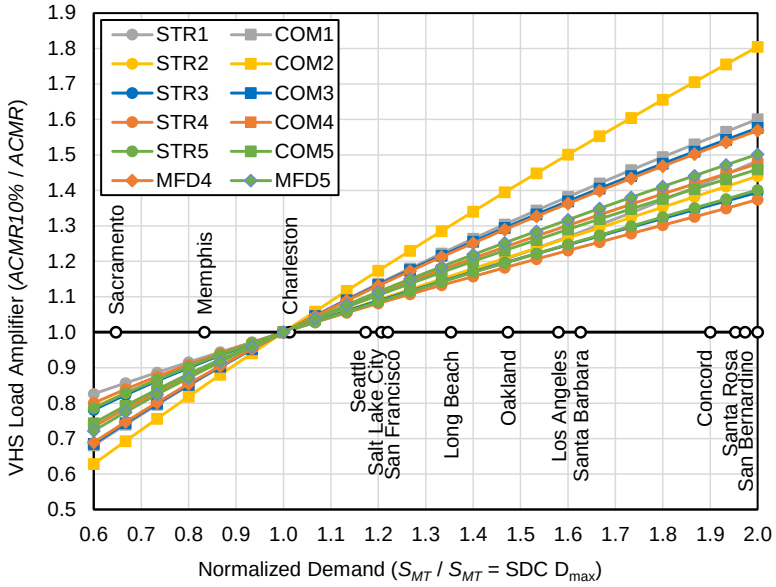

Figure 6-10 **Trends in the VHS Load Amplifier (*ACMR10%/ACMR*) of wood STR, COM and MFD archetypes as a function of normalized demand (S_{MT} normalized by S_{MT} = SDC D_{max}) for archetypes evaluated using the Far-Field record set and collapse results adjusted for hypothetical values of R/I_e that achieve the RC II target reliability of P[Collapse|S_{MT}] = 10% at S_{MT} = SDC D_{max}.**

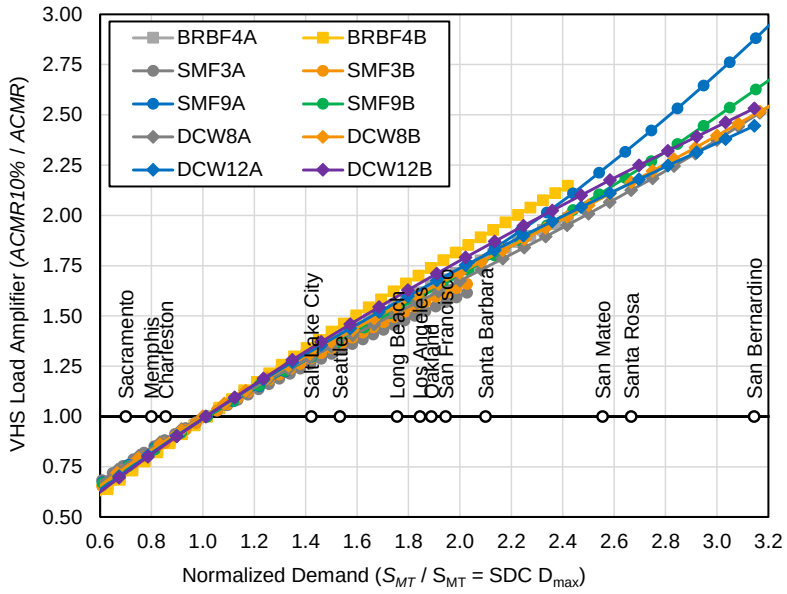

Figure 6-11 Trends in the VHS Load Amplifier (*ACMR10%/ACMR*) of BRBF, SMF and DCW archetypes as a function of normalized demand (S_{MT} normalized by S_{MT} = SDC D_{max}) for archetypes evaluated using the Far-Field record set and collapse results adjusted for hypothetical values of R/I_e that achieve the RC II target reliability of P[Collapse|S_{MT}] = 10% at S_{MT} = SDC D_{max}.

6.2.1 Summary of Observed Trends in Collapse Performance Results

The first overarching observation of collapse performance results is that the values of P[Collapse|S_{MT}] and the VHS Load Amplifier (*ACMR10%/ACMR*) increase as a function of MCE_R ground motions across all SFRS archetypes, as illustrated in Figure 6-8 through Figure 6-11. The second overarching observation of collapse performance results is that the trends in the values of P[Collapse|S_{MT}] and the VHS Load Amplifier (*ACMR10%/ACMR*) as a function of MCE_R ground motions are remarkably similar for the different SFRS archetypes. Similarity of collapse probability trends of different SFRSs is particularly notable considering the often large disparity in the absolute values of probability of collapse, as shown by the comparison of the collapse curves of wood STR archetypes shown in Figure 6-2 with those of wood MFD archetypes shown in Figure 6-4, or by comparison of the collapse curves of BRBF archetypes shown in Figure 6-5 with those of SMF archetypes shown in Figure 6-6.

Although collapse trends are very similar, certain nuances in collapse performance may be discerned from the results of different SFRS archetypes, as discussed below.

1. **Archetype Height (Period).** There is a modest, but discernible, difference between the collapse trends of the short-period wood archetypes, as shown by the plots of the VHS Load Amplifier in Figure 6-10, and that of the non-wood archetypes that have longer periods, as shown by the plots of the VHS Load Amplifier in Figure 6-11.

For example, at normalized MCE_R ground motions that are 1.5 times those of the VHS boundary (i.e., S_{MT} = 1.5 × SDC D_{max}), the average value the VHS Load Amplifier is about 1.27 for wood archetypes and about 1.38 for non-wood archetypes. At normalized demand of 2.0 (i.e., 2 times those of the VHS boundary, S_{MT} = 2.0 × SDC D_{max}), the average VHS Load Amplifier is about 1.50 for wood archetypes and about 1.72 for non-wood archetypes.

Differences in collapse trends of short-period wood archetypes and that of non-wood archetypes that have longer periods may be influenced by other factors than period (e.g., differences in modeling hysteretic behavior, displacement capacity at incipient collapse). It may be noted that there are similar differences in the collapse performance of BRBF and DCW archetypes with period, where the taller configuration of the same archetype has a slightly larger VHS Load Amplifier (i.e., worse collapse performance) than that of the shorter configuration in Table 6-4. However, conversely, collapse performance of wood archetypes of different heights typically shows smaller values of the VHS Load Amplifier (i.e., better collapse performance) for 3-story, 4-story and 5-story configurations than for 1-story and 2-story configuration of the same wood archetype in Table 6-4.

2. **Archetype Strength (Overstrength).** Although the amount of overstrength is very important to collapse performance, the decrease in overstrength with S_{MT} (the initial focus of the study) does not fully explain the strong collapse trends of increasing collapse risk with S_{MT}. Strong trends of increasing collapse risk with S_{MT} are observed for all SFRS archetypes, regardless of archetype overstrength characteristics (i.e., as defined in Chapter 2).

   There is a modest, but discernable, difference between the collapse trends of wood STR, wood COM, and wood MFD archetypes of the same height, where the value of the VHS Load Amplifier is consistently higher for archetypes with greater strength (i.e., archetypes with larger amounts of overstrength due to nonstructural finishes). For example, at normalized demand of 2.0, the average VHS Load Amplifier of 4-story and 5-story configurations of wood archetypes is 1.39 for wood STR archetypes (which have the least strength), 1.47 for wood COM archetypes, and 1.54 for wood MFD archetypes (which have greatest strength). Other than the three models of the special study of a 9-story SMF archetype, there is no discernible difference in the collapse trends of non-wood archetypes due to differences in strength (overstrength), where the overstrength of SMF archetypes increases modestly, the overstrength of DCW archetypes decreases modestly, and the overstrength of BRBF archetypes remains constant with increase in the value of S_{MT} (see Chapter 2).

   With respect to the special study of a 9-story SMF archetype, the "kink" at S_{MT} = 2 × SDC D_{max} of the collapse trend of the SMF9C (MDOF) model, shown in Figure 6-6, is most likely an artifact of the non-uniform variation of the overstrength with S_{MT} of the three MDOF SMF models (Section 5.8). The values of overstrength vary from Ω = 2.5 for the MDOF model designed for S_{MT} = 1 × SDC D_{max}, to Ω = 3.8 for the MDOF model designed for S_{MT} = 2 × SDC D_{max}, and to Ω = 4.1 for the MDOF model designed for S_{MT} = 3 × SDC D_{max} ground motions. The modest increase in the probability of collapse from 5.6% for the MDOF model designed for S_{MT} = 1 × SDC D_{max} ground motions to 8.2% for the MDOF model designed for S_{MT} = 2 × SDC D_{max} ground motions reflects the disproportionate increase in overstrength from Ω = 2.5 to Ω = 3.8 (i.e., > 50% increase),

which largely offsets the effects of two times stronger ground motions. Whereas the very significant increase in the probability of collapse from 8.2% for the MDOF model designed for S_{MT} = 2 × SDC D_{max} ground motions to 38% for the MDOF model designed for S_{MT} = 3 × SDC D_{max} ground motions reflects the modest increase in overstrength from Ω = 3.8 to Ω = 4.1 (i.e., ≈ 8% increase), which is not sufficient to offset the effects of 1.5 times stronger ground motions (with 1.5 times larger displacement demands). Although the three models are based on detailed designs of the 9-story SMF archetype, the "kink" in the collapse trend shown in Figure 6-6 is significantly influenced by the non-uniform variation of overstrength with S_{MT} that is not necessarily representative of the general collapse trends of 9-story SMF archetypes.

3. **Archetype Displacement Capacity between SFRSs.** There are modest, but discernable, differences between the collapse performance of archetypes that have relatively large displacement capacity, i.e., median drift ratio at incipient collapse (DR_{IC}) of the story governing collapse, and archetypes that have relatively modest displacement capacity.

   The impact of displacement capacity is more evident when examining the collapse results prior to adjustment to meet the target reliability (i.e., 10% at normalized demand of 1.0). For example, the relatively small collapse probabilities of BRBF archetypes (Figure 6-5), as compared to the relatively large collapse probabilities of SMF archetypes (Figure 6-6), are significantly influenced by the differences in their respective displacement capacities, where the BRBF archetypes have displacement capacities of about DR_{IC} = 9.5% to 10% for all archetypes (e.g., see Figure 5-26) and the SMF archetypes have displacement capacities of about DR_{IC} = 6.0% to 7.5% for 3-story archetypes (e.g., see Figure 5-27) and DR_{IC} = 4.0% to 5.5% for 9-story archetypes. Additionally, the three special-study SMF archetypes designed and analyzed with detailed models (Appendix F) have a larger displacement capacity than those derived from the FEMA P-2012 model results. As shown, the collapse probability is substantially reduced for the archetypes analyzed in Appendix F that have larger displacement capacity.

4. **Archetype Model Backbone Behavior (non-wood archetypes).** In general, differences in the collapse trends of non-wood archetype models of the same SFRS and height but representing different structural configurations with different backbone behavior and slight differences in deterioration (e.g., SMF3A and SMF3B) are negligible with respect to overall trends in collapse performance.

   However, the lack of discernible differences in collapse trends (e.g., VHS Load Amplifier shown in Figure 6-11) due to differences in backbone behavior within an SFRS does not imply that differences in cyclic load deterioration (and modeling thereof) do not significantly affect collapse performance. For example, the relatively small collapse probabilities of BRBF archetypes (Figure 6-5), as compared to the relatively large collapse probabilities of SMF archetypes (Figure 6-6), are significantly influenced by the differences in the modeling of the cyclic strength deterioration of these archetypes, where the BRBF archetypes are modeled without deterioration during repeated cycles of response (based on test data) and the SMF archetypes are modeled with significant deterioration (in accordance with the modeling assumptions of prior studies).

Ultimately, this difference in deterioration results in the difference in DR_{IC} for the two systems and difference in collapse performance.

In summary, the modest differences in the trends of collapse performance attributed to archetype height (period), strength (overstrength), displacement capacity, and hysteretic behavior cannot be easily distinguished (one from another), nor can such modest differences in trends be reliably quantified from the collapse results. The differences may be best considered collectively as part of the inherent variability of the "generic" trend (or trends) in collapse performance common to all SFRSs. While the detailed SMF models analyzed in Chapter 5 show some increase in overstrength for higher design acceleration and increase in displacement capacity at increasing S_{MT}, collectively they help slow the rising trend of collapse risk.

6.2.2 Discussion of the Root Causes of the Collapse Trends

The following discussion seeks to answer the question, what are the underlying effects that most influence the median values of the collapse acceleration, $\hat{S}_{CT}$, the related values of collapse performance metrics (i.e., VHS Load Amplifier and P[Collapse|S_{MT}]), and hence the trends of these metrics as a function of S_{MT}?

1. **Similarity of Displacement Capacity of Archetype Models of a Given SFRS.** The underlying primary cause of the consistent and strong trends of decreasing collapse performance with S_{MT} is the similarity of the collapse displacement capacity of archetype models for a given SFRS with different strengths.

   In essence, displacement demand increases with S_{MT}, but displacement capacity (i.e., DR_{IC}) for a given SFRS does not. These factors combine to limit the median value of collapse acceleration, $\hat{S}_{CT}$. This similarity in displacement capacity for a given SFRS is caused by inherent limits in the displacement capacity at the peak or capping point in the response curve, P-delta effects, and non-simulated failure assumptions of the same archetype at different strengths. That is, models of the same archetype tend to have approximately the same value of median DR_{IC} for different model strengths. For example, doubling the value of S_{MT} (i.e., doubling both the strength, V_{max}/W, of archetype model, as well as the level of shaking used for collapse evaluation), does not double the value of $\hat{S}_{CT}$.

   Designing an archetype for more force (increasing model strength) does not/cannot significantly increase (and may even somewhat decrease) the displacement capacity of a highly ductile SFRS (i.e., with large R factor). Likewise, designing a structure for less force (i.e., reducing archetype model strength) corresponding to a lower level of design ground motions does not diminish displacement capacity, such that at lower levels of design strength, the corresponding lower level of design ground motions is not strong enough, and hence less likely, to cause peak displacement to exceed the capacity of the structure. This is, in part, the reason that weak and vulnerable buildings have not collapsed in smaller earthquakes or lower levels of earthquake shaking (i.e., the spectral content of the ground motions is relatively weak at longer response

periods that influence peak building displacement). For example, there were no reported collapses of the hundreds of older homes (many of which have weak cripple walls) in the historical districts of Whittier in the 1987 Whittier earthquake, although a short-period acceleration of about 1.8g was recorded nearby (see also discussion of 1987 Whittier earthquake ground motions in Section 3.3.2 of FEMA P-2139-1)

2. **Nonlinearity of Archetype Models**. The collapse trends are related to the degree of nonlinearity of the archetype models. Each of the SFRSs of this study represent highly ductile systems (i.e., with large *R* factors) that have consistently large post-yield nonlinear displacement capacity, typically governed by P-delta collapse. In this sense, differences in collapse performance of these SFRSs due to the degree of archetype model nonlinearity are negligible. Such would not be the case for a small-*R* system with limited post-yield displacement capacity, or, for example, a ductile system designed to remain essentially elastic.

   Conceptually, doubling the strength of an SFRS that remains elastic would, by definition, double the value of $\hat{S}_{CT}$, since the displacement capacity of an elastic system would also double with strength; hence, collapse performance would not decrease with S_{MT}. It is important to note that the observed trends in collapse performance of this study are largely due to the highly nonlinear response of the archetype models where displacement capacity remains similar with increase in S_{MT} and would likely be less pronounced if the archetype models did not have such highly nonlinear response characteristics.

3. **Frequency Content (shape of response spectrum) of Ground Motions.** Theoretically, the collapse trends are related to the frequency content (shape of the response spectrum) of the ground motions at elongated periods of nonlinear response that govern displacement at incipient collapse of highly yielded nonlinear archetype models. But differences in collapse performance due to spectrum shape are difficult to discern from the collapse results of Chapter 4 and Chapter 5, which relied on earthquake records representing a single spectrum shape (e.g., median spectrum of the Far-Field record set).

   Values of $\hat{S}_{CT}$ are evaluated at the design period, *T*, of the archetype ($T = C_u T_a$) in accordance with the IDA methods of FEMA P-695. Conditioning on the elastic design period, *T*, has advantages (e.g., for integration with hazard curves defined in terms of *T*); however, the elastic design period does not represent the period range of the ground motions that govern collapse of a highly yielded nonlinear system, where the “effective” period at incipient collapse is much longer than the elastic period.

   The effective period is a longstanding concept for characterizing the approximate response period of a nonlinear dynamic system based on the secant stiffness at the point of peak response. The effective period (and associated effective damping) play critical roles in the root causes that drive the observed trend. The concepts of the capacity-spectrum method are used in the next section (and in Appendix G) to provide a visual “talking point” for generalization of collapse trends, illustrating the relationship of the value of the VHS Load Amplifier to the

nonlinear response properties of the system of interest and the frequency content (response spectrum shape) of the ground motions used for collapse evaluation.

6.2.3 Generalization of Collapse Trends Using the Capacity-Spectrum Method

This section adapts the capacity-spectrum method (CSM) to illustrate the collapse trends described in the previous section and to provide a basis for generalization of these trends in terms of the nonlinear response properties of the system of interest and the frequency content (response spectrum shape) of the ground motions used for collapse evaluation. The CSM is well suited for illustration of concepts, since it is, in essence, a graphical solution of the peak response of a nonlinear system to earthquake ground motions defined by a response spectrum with equivalent viscous damping consistent with the peak response of the nonlinear system. Background on adaptation of the CSM to collapse evaluation with examples is provided in Appendix G.

The CSM, adapted for collapse evaluation, and the IDA methods of FEMA P-695, serve the same purpose, that is, estimation of median collapse, where in the case of the CSM, ground motions are described by a single response spectrum, rather than by a set of records required for IDA. As shown by the BRBF example of Section G.6, values of the median collapse acceleration, $\hat{S}_{CT}$, estimated using the CSM and the median response spectrum of the Far-Field record set are approximately the same as those calculated by IDA using the records of the Far-Field record.

The CSM relates the capacity of a nonlinear system and earthquake demand, where both capacity curves and demand spectra are characterized by spectral acceleration as a function of spectral displacement (i.e., so-called ADRS format). Capacity curves are derived from nonlinear pushover (or backbone) curves of the archetype model by converting base shear to spectral acceleration and by converting roof drift to spectral displacement using the formulas and assumptions as described in Appendix G (i.e., same methods used to develop the simplified nonlinear models of Chapters 4 and 5). Demand spectra are derived from 5%-damped response spectra (e.g., median spectrum of the Far-Field record set) by adjusting response for effective damping corresponding to hysteretic energy dissipation of the nonlinear system at peak displacement. An additional explanation of the CSM, adapted for collapse evaluation, is provided in Section G.3.

EXAMPLE CALCULATION OF THE VHS LOAD AMPLIFIER USING THE CSM

An example calculation of the VHS Load Amplifier (*ACMR10%/ACMR*) using the CSM is shown in Figure 6-12. In this figure, two notional capacity curves represent a hypothetical archetype modeled with two different strengths, the first with Baseline strength presumed to comply with the 10% target reliability failure rate at the VHS boundary (i.e., S_{MT} = 1.0 × SDC D_{max}) and the second with two times Baseline strength (i.e., S_{MT} = 2.0 × SDC D_{max}). Note the second capacity curve could be any multiple of the Baseline curve, where a multiple of 2.0 is used to illustrate the CSM in Figure 6-12. In this example, the hypothetical archetype represents a high-ductility (R = 8) system with a design period of T = 0.75 s, where the Baseline capacity strength, V_{max}/W = 0.28g, corresponds approximately to a

hypothetical design acceleration of S_{MT} of 1.2g and an overstrength of $\Omega = 2.8$, i.e., V_{max}/W = 0.28g = 1.2g/(1.5 × 8) × 2.8.

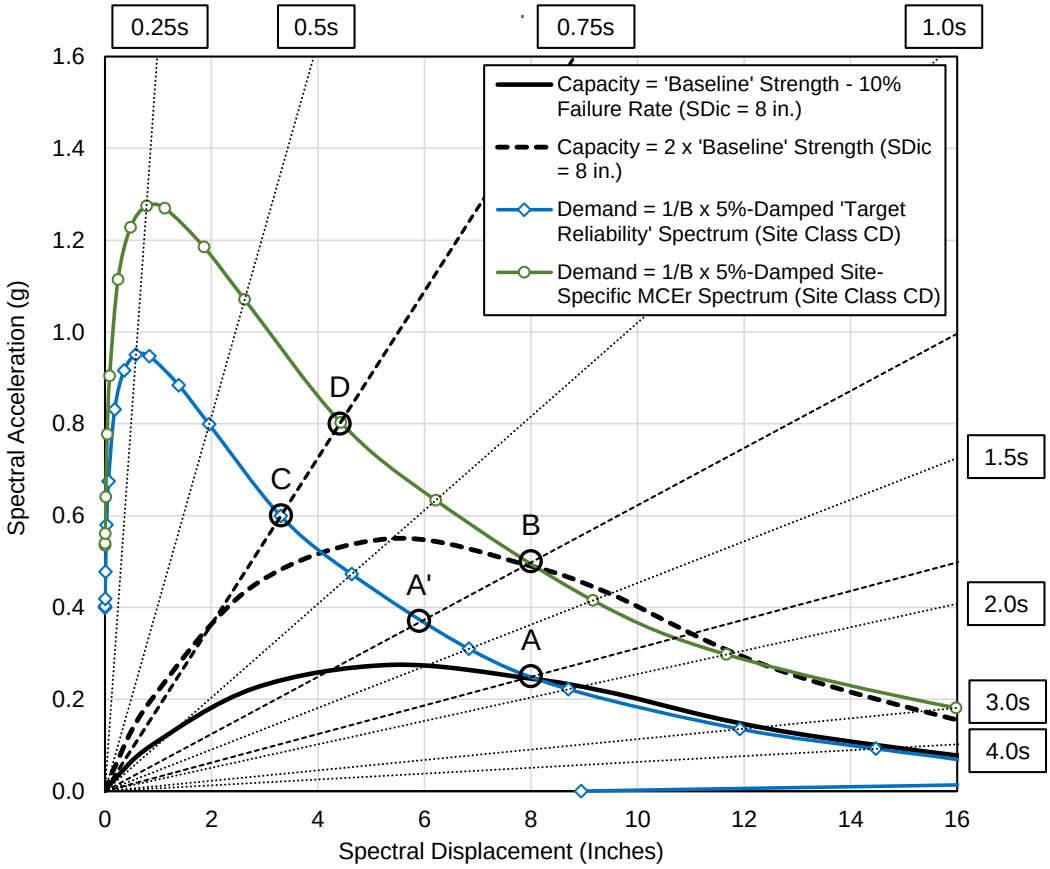

Figure 6-12 Example Illustration of the CSM and control points used for calculation of the VHS Load Amplifier showing two hypothetical capacity (backbone) curves and two Site Class CD demand spectra scaled to match capacity at incipient collapse (Point A and Point B) at spectral displacement, SD_C = 8 in.

In Figure 6-12, demand spectra are scaled to intersect capacity curves at spectral displacements corresponding to median collapse (i.e., identified by points labeled as A and B), where median collapse is assumed to occur at a spectral displacement, SD_C (A) = 8 inches. In this example, the two capacity curves are assumed to have the same failure displacement, although failure displacements need not be the same. Most archetypes of the wood and non-wood SFRSs of this study were found to have the same or similar median collapse displacement of models with different pushover strengths. It may be noted that scaling the demand spectrum to the capacity curve at the collapse displacement is analogous to IDA scaling of records to affect median collapse of a nonlinear archetype model with the same capacity (backbone) curve.

Demand spectra represent 5%-damped response spectra factored by $1/B$, where B is the damping factor corresponding to the effective damping of the capacity curve at incipient collapse.

Conceptually, the *B* factor is the same as that used to modify 5%-damped response spectral acceleration for design of a structure with an isolation or damping system (e.g., *B* coefficients of Table 18.7-1, ASCE/SEI 7-22). In this example, demand spectra characterize the frequency content typical of MCE_R ground motions at a stiff soil (Site Class CD) site. Site class significantly influences the shape (frequency content) of the demand spectrum and the value of the VHS Load Amplifier, as demonstrated by the CSM example of Section G.4. In Figure 6-12, the Target Reliability demand spectrum represents ground motions at the VHS boundary (i.e., S_{MT} = 1.0 × SDC D_{max}); whereas the MCE_R Spectrum represents a stronger level of shaking that, in this example, requires twice as much capacity (i.e., capacity curve strength) to meet target reliability.

Collapse performance is a function of the median collapse acceleration, $\hat{S}_{CT}$, as defined by the spectral accelerations of the demand spectra at the design period *T* (i.e., *T* = 0.75 s in this example) where the demand spectra are scaled to median collapse. In Figure 6-12, these spectral accelerations are identified by points labeled as C and D, where, for example, the median spectral acceleration at Point C corresponds to the demand spectrum scaled to match Baseline capacity at median collapse. The median collapse acceleration, $\hat{S}_{CT}$, is defined in terms of 5%-damped response; whereas the spectral accelerations of the demand spectra of the CSM example of Figure 6-12 are defined in terms of β_{eff}-damped response. Note, ratios of β_{eff}-damped acceleration (e.g., ratio of accelerations at Points C and D) are the same as those of the corresponding 5%-damped accelerations, since the damping adjustment factor, *B*, is the same for both numerator and denominator of the ratio of spectral accelerations.

The value of the VHS Load Amplifier (ACMR10%/*ACMR*) may be estimated from the ratios of the intersection points, A, B, C and D (or A and A') shown in Figure 6-12, by the equation:

$$\text{VHS Load Amplifier} \cong \frac{SA(\text{B})}{SA(\text{A})} \times \frac{SA(\text{C})}{SA(\text{D})} = \frac{SA(\text{A}')}{SA(\text{A})} \tag{6-1}$$

Refer to Section G.3 for the derivation of this equation. Implicit to Equation 6-1 are two simplifying assumptions: (1) the amount of overstrength is the same and (2) the values of effective damping at incipient collapse are the same for the two capacity (backbone) curves, which is approximately the case for wood and non-wood archetypes of this study. A more general formulation of Equation 6-1 is provided in Section G.3 that includes adjustment for overstrength and/or effective damping when not the same for backbone curves of different strengths. In general, such adjustments are of secondary importance to the calculation of the VHS Load Amplifier.

The VHS Load Amplifier is calculated from the control points of the capacity curves and demand spectra of CSM example illustrated in Figure 6-12, as follows:

$$\text{VHS Load Amplifier} \cong \frac{SA(\text{B})}{SA(\text{A})} \times \frac{SA(\text{C})}{SA(\text{D})} = \frac{0.50\,g}{0.25\,g} \times \frac{0.60\,g}{0.80\,g} = 1.5$$

Or

$$\text{VHS Load Amplifier} \cong \frac{SA(A')}{SA(A)} = \frac{0.375\,g}{0.25\,g} = 1.5$$

A value of the VHS Load Amplifier equal to 1.5 is comparable to the range of values of the VHS Load Amplifier of the SFRFs of this study at a normalized demand of 2.0 times the VHS boundary (i.e., S_{MT} = 2.0 × SDC D_{max}).

In general, the collapse of the highly nonlinear systems investigated in this study is governed by response in the velocity domain. That is, even for short-period, wood light-frame archetypes, the effective period at incipient collapse is typically longer than T_S = 0.6 s, the transition period of FEMA P-695 ground motions (e.g., see Figure 3-3). Conversely, the effective period of the taller non-wood archetype is rarely long enough to reach the domain of constant displacement (e.g., T_L = 8 s for sites governed by magnitude M = 7.0 earthquakes, Figure 22-14, ASCE/SEI 7-22). Nonetheless, the idealized domains of constant acceleration and constant displacement provide a useful means of establishing bounds on collapse trends and the value of the VHS Load Amplifier, as described below (and in the CSM example of Section G.4).

Response of a very short-period system in the acceleration domain (i.e., $T_{eff} \le T_S$) would have values of the VHS Load Amplifier = 1.0, regardless of the increase in MCE_R spectral acceleration, S_{MT}, since the value of $\hat{S}_{CT}$ would increase directly in proportion to the increase in S_{MT} assuming overstrength remains the same, i.e., $\Omega(A)/\Omega(B) = 1.0$ in Equation 6-1. That is, the VHS Load Amplifier = 1.0, when $SA(D)/SA(C) = SA(B)/SA(A)$, and $SA(A')/SA(A) = 1.0$ in Equation 6-1. Conversely, response in the displacement domain of a very long-period system (i.e., $T_{eff} \ge T_L$) would have values of the VHS Load Amplifier that increase in proportion to the increase in S_{MT}, since the value of $\hat{S}_{CT}$ would not increase (or decrease) with S_{MT}, (i.e., collapse is only a function of displacement demand). In this case, $SA(A') = SA(B)$ and the VHS Load Amplifier = $SA(B)/SA(A)$ since $SA(C)/SA(D) = 1.0$ in Equation 6-1. Response of systems with effective periods in the velocity domain (i.e., $T_S \ge T_{eff} \ge T_S$), where spectral acceleration is proportional to $1/T$, would have values of the VHS Load Amplifier = $SA(B)/SA(A) \times 1/\sqrt{SA(B)/SA(A)}$, where $SA(C)/SA(D) = 1/\sqrt{SA(B)/SA(A)}$, in Equation 6-1. The value of $SA(C)/SA(D) = 1/\sqrt{SA(B)/SA(A)}$ is a function of the $1/T$ slope of the response spectrum in the velocity domain and the implicit assumption that median collapse displacement (SD_C) is independent of strength, i.e., SD_C (Point B) = SD_C (Point A).

Based on the three idealized domains of the two-period response spectrum, as described above, there would be only one value of the VHS Load Amplifier per domain, that is (1) the VHS Load Amplifier = 1.0 for nonlinear response in the acceleration domain ($T_{eff} < T_S$), (2) the VHS Load Amplifier = $\sqrt{SA(B)/SA(A)}$ for nonlinear response in the velocity domain (i.e., $T_S \ge T_{eff} \ge T_S$) and (3) the VHS Load Amplifier = $SA(B)/SA(A)$ for nonlinear response in the displacement domain (i.e., $T_{eff} \ge T_L$).

While collapse is typically governed by nonlinear response in the velocity domain, the other two domains provide useful bounds on the VHS Load Amplifier.

In contrast to idealized response domains, the multi-period response spectra of ASCE/SEI 7-22 transition gradually from the acceleration domain to the velocity domain, and from the velocity domain to the displacement domain, as illustrated in the plots of Site Class CD multi-period response spectra of Figure 6-12. Hence, values of the VHS Load Amplifier at a given level of MCE_R ground motions would be expected to also change gradually. For example, at normalized demand of 2.0 times Baseline strength, the value of the VHS Load Amplifier would be expected to gradually increase from 1.0 for nonlinear response in the acceleration domain ($T_{eff} < T_S$) to 1.4 in the velocity domain at an effective period where spectral acceleration varies roughly in proportion to $1/T$, and continue to increase gradually from 1.4 to 2.0 for nonlinear response at very long effective periods (i.e., $T_{eff} \geq T_L$). The value of the VHS Load Amplifier of 1.5 of the CSM example illustrated in Figure 6-12 indicates that the effective period, T_{eff}, is essentially in the velocity domain, although the slope of the demand spectrum at T_{eff} is slightly steeper than $1/T$.

Similarly, values of the VHS Load Amplifier calculated using the Far-Field record set would also be expected to vary in a like manner, although the localized irregularity of the frequency content of ground motions, as shown by the median Far-Field spectrum in Figure 3-3, obscures conclusive identification of such trends. It may be noted that the values of the VHS Load Amplifier of wood archetypes shown in Figure 6-10 (approximately 1.4 to 1.6 at a normalized demand of 2.0), which have relatively shorter effective periods, are generally less than those of non-wood archetypes shown in Figure 6-11 (approximately 1.6 to 1.8 at a normalized demand of 2.0), which have relatively longer effective periods, and that the larger values of the VHS Load Amplifier of 1.6 to 1.8 of the non-wood archetypes are consistent with the shape of the median Far-Field spectrum which decays more rapidly than $1/T$ at response periods greater than about 1.5 seconds.

ILLUSTRATION OF NOTIONAL COLLAPSE TRENDS DERIVED FROM CSM EXAMPLES

Figure 6-13 is a plot of notional collapse trends of the VHS Load Amplifier as a function of normalized ground motions. Notional collapse trends are shown for three hypothetical site conditions, Site Class C, Site Class CD, and Site Class D, to illustrate the influence of site class on the VHS Load Amplifier. Notional collapse trends for these three site classes are based on the same nonlinear capacity curve properties (and failure displacement) as those of the prior CSM example. Collapse trends are shown for hypothetical ratios of $SA(B)/SA(A)$ ranging from 1.0 to 3.0, corresponding to normalized ground motions of 1.0 to 3.0 times the VHS boundary, where the VHS boundary is assumed to achieve target reliability. Notional collapse trends include (1) the theoretical upper-bound on collapse performance when peak nonlinear response is in the idealized domain of constant displacement (steep trend shown with red diamonds) and (2) the theoretical lower-bound on collapse performance when peak nonlinear response is in the idealized domain of constant acceleration (flat trend shown with green circles). Collapse trends of actual (high ductility) systems would fall somewhere between these two theoretical bounds. Appendix G provides additional background on the Site Class C, CD and D response spectra and the calculation of notional collapse trends.

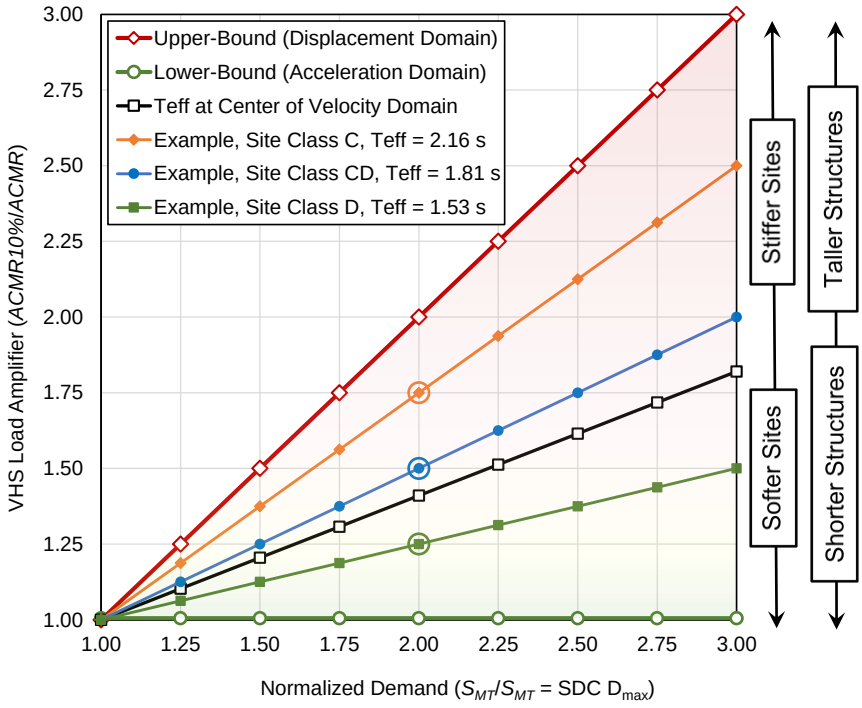

Figure 6-13 **Notional collapse trends of the VHS Load Amplifier derived from CSM examples illustrating the importance of spectrum shape (site class) and period range of interest on collapse performance. Collapse trends include (1) the theoretical upper-bound on collapse performance when peak nonlinear response is in the idealized domain of constant displacement (steep trend line shown with red diamonds) and (2) the theoretical lower-bound on collapse performance when peak nonlinear response is in the idealized domain of constant acceleration (flat trend line shown with green circles).**

For broader context, "generic" site conditions are described qualitatively in Figure 6-13 (on the right side of the figure) as either "stiffer" of "softer," referring implicitly to site class, which complement the three trend lines that illustrate differences in collapse trends for Site Class C, Site Class CD and Site Class D demand spectra. As shown by the three site class curves, collapse trends are steeper for "stiffer" site conditions (and flatter for "softer" site conditions), which would always be the case, although the actual values (slopes) of these three trend lines would be somewhat different, if the period range governing collapse was significantly different.

Likewise, for broader context, the period range of interest is implied qualitatively in Figure 6-13 (on the right side of the figure) by structure height, either "taller" or "shorter," where height is a surrogate for building period, and more specifically the effective period, T_{eff}, at collapse, as might be determined by the CSM, $T_{eff} \approx 0.32 \times \text{SQRT}\,(SD_C/SA_C)$, where SD_C is the collapse spectral displacement in inches, and SA_C is the collapse spectral acceleration in units of gravity.

Figure 6-13 demonstrates notional differences in the VHS Load Amplifier resulting from differences in spectrum shape (site class). For example, the VHS Load Amplifier increases by 40% (0.4 = (1.75-1.25)/1.25) between the Site Class C and Site Class D examples at a normalized demand of 2.0 times the VHS boundary. This notional variability is raised here because, as was described in Section 6.2.2, the effects of the frequency content (shape of response spectrum) of ground motions could not be explored in the analytical studies due to the use of the FEMA P-695 ground motions, which rely on earthquake records representing a single spectrum shape. In general, softer sites produce lower values of the VHS Load Amplifier. It should be noted that the increase in demand associated with the VHS Load Amplifier is on top of the inherent design demand from the corresponding response spectrum, which varies greatly by site class. For example, Site Class D demand would be about two times Site Class C demand for an archetype with a design period in the velocity region. Compare two hypothetical designs (Site Class C and Site Class D) of the same archetype where conceptually both designs achieve the target performance of less than 10% collapse probability given site ground motions. The Site Class D design would be about twice as strong as the Site Class C design but would have a flatter collapse trend (i.e., less increase in the collapse probability with demand). Conversely, the Site Class C design would require less strength to meet the 10% target but would be more susceptible to higher collapse than the Site Class D design at stronger levels of shaking. Furthermore, Figure 6-13 demonstrates notional differences in the VHS Load Amplifier resulting from differences in structure height (as a surrogate for effective period), where shorter structures are expected to have a smaller VHS Load Amplifier than taller structures, all else being equal. Although archetypes of different heights were included in the analytical studies, the range of heights for each SFRS was limited and, similar to spectrum shape, could not be fully explored.

Although, conceptually, representing the same structure height, the collapse trends of the three site classes have somewhat different effective periods, due to differences in capacity (design) strength, ranging from T_{eff} = 1.53 s (Site Class D) to T_{eff} = 2.16 s (Site Class C). If the effective period had been substantially longer (e.g., taller structure), then the three trend lines would all have been steeper and conversely, if the effective period had been shorter (e.g., shorter structure), then the three trend lines would all have been flatter. While significant for large differences in effective period (e.g., structures with very different heights), collapse trends are relatively insensitive to modest changes in the effective period (e.g., due to changes in the strength of the same archetype) and are generally of secondary importance to changes in collapse trends due to different site classes.

The notional collapse trends shown in Figure 6-13 characterize the VHS Load Amplifier in terms of the shape (slope) of the demand spectrum at collapse, by the equation:

$$\text{VHS Load Amplifier} \cong m\left(\frac{SA(\text{B})}{SA(\text{A})}-1\right)+1 \cong m\left(\frac{S_{MT}}{S_{MT}=SDC\ D_{max}}-1\right)+1 \qquad (6\text{-}2)$$

Where SA(A) is the spectral acceleration at collapse of the Baseline capacity curve presumed to achieve target reliability (e.g., 1.0 × SDC D_{max}), SA(B) is the spectral acceleration at collapse of an arbitrary higher increment of the Baseline strength representing site-specific MCE_R ground motions (e.g., S_{MT} = 2.0 × SDC D_{max} in Figure 6-12) and the factor, *m,* is related to the slope of the demand

spectrum at the collapse displacement, i.e., as defined by the ratio of $SA(A')/SA(A)$. Implicit to Equation 6-2 is the assumption that collapse trends increase linearly with normalized demand (consistent, in general, with the collapse trends of Figure 6-10 and Figure 6-11).

Values of m range from $m = 0$, defining the lower-bound on the collapse trend when the slope of the demand spectrum is theoretically flat (i.e., $SA(A') = SA(A)$), where for example the effective period, T_{eff}, is in the acceleration domain, to $m = 1.0$ (i.e., $SA(A') = SA(B)$), defining the upper-bound on the collapse trend when the slope of demand spectrum is theoretically infinite (i.e. the effective period, T_{eff}, is in the displacement domain). A value of $m = 0.41$ represents the slope of the demand spectrum when inversely proportional to the response period, $1/T$ (i.e., the effective period, T_{eff}, is at the nominal center of the velocity domain).

Equation 6-2 is an intentionally simple characterization of collapse trends for illustration of the notional value of the VHS Load Amplifier as a function of normalized demand (i.e., S_{MT}/S_{MT} = SDC D_{max}) in Figure 6-13. Implicit to Equation 6-2 are certain key assumptions:

1. **Collapse Displacement Capacity**. Collapse displacement capacity, SD_C, is assumed to remain the same, $SD_C(B) = SD_C(A)$, for all increments of spectral acceleration, $SA(B)$, in Equation 6-1, which is approximately the case for most archetypes of this study at values of S_{MT} of interest. In general, displacement capacity tends to decrease slightly with S_{MT}, which would affect a somewhat steeper trend line in Figure 6-14 (e.g., for the site class of interest).
2. **Overstrength**. Overstrength is assumed to be constant with increase in the value of S_{MT}, which is valid, or approximately valid, for wood and non-wood archetypes of this study at values of S_{MT} of interest, as described in Chapter 2, with the unique exception of the significant increase in overstrength of one of the models of the special study of a 9-story SMF archetype (Section 5.8).
3. **Effective Damping**. Effective damping is assumed to not change with increase in capacity curve strength and, implicitly, with increase in the value of S_{MT}, which is approximately the case for the wood and non-wood archetypes of this study.
4. **Spectrum Shape Factor (*SSF*).** Implicit to the calculation of the value of the VHS Load Amplifier, Equation 6-1, is the assumption that the value of the spectrum shape factor (*SSF*) does not change with capacity curve strength and, hence with increase in the value of S_{MT}, which is generally the case for the highly nonlinear archetypes of this study.

It may be noted that the portion of the *SSF* required by FEMA P-695 for adjustment of collapse accelerations to account for differences in the shape of the median spectrum of the Far-Field record set and shape of the design spectrum (i.e., Figure 6-1 of FEMA P-695) is eliminated by the CSM when the demand spectrum is based directly on the shape of the multi-period design spectrum of the site class of interest. However, the portion of the *SSF* required to adjust median collapse accelerations to account for the "rareness" of MCE_R ground motions would still be required. Such adjustment would affect the value of *ACMR* (and, implicitly, the value of *ACMR*10%) but not the value of the VHS Load Amplifier.

Equation 6-2 and Equation 6-1 are not influenced by the nonlinear hysteretic properties of the hypothetical capacity curve, other than in the determination of the spectral acceleration and spectral displacement at incipient collapse (e.g., Point A or Point B in Figure 6-12). The implication is that the collapse trends will be the same for all systems with the same spectral acceleration and spectral displacement at incipient collapse, provided the shape (slope) of the demand spectrum at collapse is the same (e.g., same site class). This observation is consistent with the very similar collapse trends of the different wood light-frame archetypes shown in Figure 6-10 and very similar collapse trends of the different non-wood archetypes shown in Figure 6-11, where all archetypes were evaluated using the same set of Far-Field ground motions. That is, although absolute collapse performance is typically different (often very different) for different archetypes (heights) of different systems, collapse trends, as characterized by the VHS Load Amplifier, are conceptually the same for the same site class.

6.3 Additional Collapse "Risk" due to Near-Fault Ground Shaking

The additional collapse risk due to near-fault ground shaking is evaluated by comparison of collapse results of wood light-frame MFD archetypes evaluated using the Near-Field record set of FEMA P-695 with those of same MFD archetypes evaluated using the Far-Field record set of FEMA P-695 ground motions (see Section 4.7.7). The MFD archetypes are selected for study since these are typical configurations of the wood light-frame SFRS, and wood light-frame buildings are the most common SFRS. A shortcoming of the wood light-frame MFD selection is the lack of Near-Field ground shaking results for taller SFRS archetypes, although a prior study that compared collapse margin ratios of 1-story, 2-story and 20-story reinforced-concrete special moment frame archetypes found comparable collapse results for all three heights when evaluated using Near-Field and Far-Field record sets (Appendix Section A.11, FEMA P-695).

The collapse evaluation methods of FEMA P-695 are the same for the two record sets with the notable exception that values of the *SSF* are different, as described in Section 3.4.8. Values of the *SSF* of Far-Field record set analyses of MFD archetypes (and other archetypes) are based on the "probabilistic MCE_R" *SSF* factors of Table 3-2; whereas the values of the *SSF* of Near-Field record set analyses of MFD archetypes are based on the "deterministic MCE_R" *SSF* factors of Table 3-3.

Collapse results of the near-field record analyses of RC II and RC IV designs of the five wood MFD archetypes are summarized in Table 6-6 for three MCE_R ground motions levels corresponding to 1.0 × SDC D_{max} (VHS boundary), 1.5 × SDC D_{max} and 2.0 × SDC D_{max} of FEMA P-695. Green shading indicates compliance with the target reliability. Yellow and red shading indicate collapse probabilities that exceed 10% and 20%, respectively, for RC II structures and that exceed 2.5% and 5.0%, respectively, for RC IV structures.

Table 6-6 Summary of FEMA P-695 Collapse Results of RC II and RC IV Designs of Wood MFD Archetypes Evaluated Using the Near-Field Record Set at Three Ground Motions Levels Corresponding to 1.0 × (VHS Boundary), 1.5 × and 2.0 × SDC D_{max} of FEMA P-695

Archetype ID Name	FEMA P-695 Criteria		FEMA P-695 Collapse Results – Near-Field Records					
			SMT = 1.0 × SDC D_{max}		SMT = 1.5 × SDC D_{max}		SMT = 2.0 × SDC D_{max}	
	Period, *T* (sec.)	SDC D_{max} S_{MT} (g)	*ACMR*	P[C|S_{MT}]	*ACMR*	P[C|S_{MT}]	*ACMR*	P[C|S_{MT}]
Risk Category II design (I_e = 1.0) – target reliability, P[C|S_{MT}] = 10% probability of failure								
MFD1	0.16	1.50	3.69	0.7%	2.54	3.4%	1.96	8.9%
MFD2	0.26	1.50	2.78	4.4%	2.05	11.6%	1.66	19.6%
MFD3	0.36	1.50	2.37	7.5%	1.82	15.9%	1.51	24.0%
MFD4	0.45	1.50	1.98	12.7%	1.55	22.7%	1.30	31.7%
MFD5	0.53	1.50	2.05	11.6%	1.66	19.9%	1.41	27.8%
Risk Category IV design (I_e = 1.5) - target reliability, P[C|S_{MT}] = 2.5% probability of failure								
MFD1	0.16	1.50	3.81	0.2%	2.64	1.5%	2.03	5.1%
MFD2	0.26	1.50	3.08	2.0%	2.27	6.1%	1.82	11.7%
MFD3	0.36	1.50	2.73	3.4%	2.09	7.9%	1.71	14.0%
MFD4	0.45	1.50	2.32	5.7%	1.82	11.4%	1.50	19.2%
MFD5	0.53	1.50	2.49	4.8%	1.97	9.9%	1.62	16.8%

The collapse results of the RC II designs may be compared with those of the far-field record analyses of the same MFD archetypes, as summarized in Table 6-2. Likewise, the collapse results of the RC IV designs may be compared with those of the far-field record analyses of the same MFD archetypes, as summarized in Table 6-3. Near-field and far-field collapse results show similar trends for RC II and RC IV, where in both cases the probability of collapse is greater and the value of the *ACMR* is smaller for near-field collapse results when compared with far-field collapse results at a common level of ground motions.

Ratios of the value of the near-field *ACMR* to the corresponding value of the far-field *ACMR* are summarized in Table 6-7 for each of the three levels of MCE_R ground motions. These *ACMR* ratios indicate the approximate amount of additional design acceleration that would be required to achieve comparable probability of collapse. Ratios of *ACMR* are relatively small for 1-story MFD archetypes, increase with height and are similar for 3-story and taller archetypes. It may be noted that the shorter MFD archetypes are inherently quite strong due to the contribution to their overstrength from nonstructural wall finishes, which contributes to their exceptional collapse performance (i.e., for the

1-story RC II MFD archetype, there is less than a 1% probability of collapse given MCE_R ground motions equal to the VHS boundary, S_{MT} = 1.0 × SDC D_{max}).

Table 6-7 Ratios of *ACMR* of RC II and RC IV designs of MFD archetypes Evaluated Using the Near-Field Record Set (Table 6-6) to Those Evaluated Using the Far-Field Record Set (Tables 6-2 and 6-3) at Ground Motions Levels Corresponding to 1.5 × SDC D_{max} and 2.0 × SDC D_{max} of FEMA P-695

Archetype ID Name	FEMA P-695 Criteria		Ratios of FF *ACMR* / NF *ACMR*		
	Period, *T* (seconds)	SDC D_{max} S_{MT} (g)	S_{MT} = 1.0 × SDC D_{max}	S_{MT} = 1.5 × SDC D_{max}	S_{MT} = 2.0 × SDC D_{max}
Risk Category II Design (I_e = 1.0)					
MFD1	0.16	1.50	1.06	1.05	1.05
MFD2	0.26	1.50	1.12	1.10	1.08
MFD3	0.36	1.50	1.29	1.26	1.24
MFD4	0.45	1.50	1.37	1.36	1.32
MFD5	0.53	1.50	1.23	1.20	1.18
Average (MFD3, MFD4, MFD5)			1.30	1.27	1.25
Risk Category IV Design (I_e = 1.5)					
MFD1	0.16	1.50	1.05	1.05	1.04
MFD2	0.26	1.50	1.10	1.07	1.05
MFD3	0.36	1.50	1.26	1.23	1.19
MFD4	0.45	1.50	1.36	1.29	1.21
MFD5	0.53	1.50	1.20	1.17	1.12
Average (MFD3, MFD4, MFD5)			1.27	1.23	1.17

Ignoring the shorter (1-story and 2-story) MFD archetypes, the average ratio of *ACMR* is about 1.30 for the RC II MFD designs and 1.27 for the RC IV MFD for MCE_R ground motions at the VHS boundary (and somewhat less at 2.0 × SDC D_{max}). That is, an increase in design acceleration of about 1.3 would be required to offset the effects of velocity pulses and other characteristics of the ground motions of the Near-Field record set. An increase in design acceleration of 1.3 would not seem necessary for 1-story and 2-story MFD archetypes, which are already quite strong, but may not be sufficient for other, taller, SFRS archetypes that are more susceptible to the effects of Near-Field ground motions.

Collapse results of wood MFD archetypes evaluated using the Near-Field record set for hypothetical values of R/I_e that achieve the target reliabilities of RC II and RC IV structures at S_{MT} = SDC D_{max} are

summarized in Table 6-8 for MCE_R ground motions levels corresponding to 1.5 × SDC D_{max} and 2.0 × SDC D_{max} of FEMA P-695. Gray shading indicates target reliability could not be achieved. The collapse results of Table 6-8 may be seen to be similar to those of RC II MFD archetypes of Table 6-4 and the RC IV archetypes of Table 6-5 that were evaluated using the Far-Field record set.

Table 6-8 Summary of Collapse Results of Wood MFD Archetypes Evaluated Using the Near-Field Record Set Where Collapse Results are Adjusted for Hypothetical Values of R/I_e That Achieve the Target Reliabilities of RC II and RC IV Structures at S_{MT} = SDC D_{max}.

Archetype ID Name	FEMA P-695 Criteria		Adjusted Collapse Results – Near-Field Records					
			Target Criteria		S_{MT} = 1.5 × SDC D_{max}		S_{MT} = 2.0 × SDC D_{max}	
	Period, *T* (sec.)	SDC D_{max} S_{MT} (g)	*ACMR10%* (*ACMR2.5%*)	R/I_e	Adjusted P[C|S_{MT}]	*ACMR10%* (*ACMR2.5%*) / *ACMR*	Adjusted P[C|S_{MT}]	*ACMR10%* (*ACMR2.5%*) / *ACMR*
Risk Category II target reliability, P[C|S_{MT}] = 10% probability of failure								
MFD1	0.16	1.50						
MFD2	0.26	1.50						
MFD3	0.36	1.50	2.16	8.7	20.5%	1.32	30.3%	1.58
MFD4	0.45	1.50	2.15	5.3	17.8%	1.28	26.3%	1.53
MFD5	0.53	1.50	2.16	5.9	17.6%	1.24	25.2%	1.47
Risk Category IV target reliability, P[C|S_{MT}] = 2.5% probability of failure								
MFD1	0.16	1.50						
MFD2	0.26	1.50	2.94	5.2	7.6%	1.35	14.1%	1.68
MFD3	0.36	1.50	2.91	3.6	5.9%	1.31	11.9%	1.66
MFD4	0.45	1.50	2.67	3.1	6.0%	1.31	11.0%	1.57
MFD5	0.53	1.50	2.84	3.2	6.1%	1.31	13.6%	1.69

Adjusting collapse results using hypothetical values of the ratio, R/I_e, to achieve the same target reliability for MCE_R ground motions of the VHS boundary (i.e., S_{MT} = 1.0 × SDC D_{max}) permits direct comparison of the trends in collapse performance of the same archetype evaluated for different ground motions. For example, trends in collapse probabilities of 4-story and 5-story (and 3-story) MFD archetypes anchored to RC II target reliability and evaluated using the Near-Field record set (i.e., MFD archetypes of Table 6-8) are compared in Figure 6-14 with the collapse probabilities of the same RC II 4-story and 5-story MFD archetypes evaluated using the Far-Field record set (i.e., MFD archetypes of Table 6-4). Trends are not available for the RC II 3-story MFD archetype evaluated using the Far-Field record set (Table 6-4), as explained in Section 6.2.

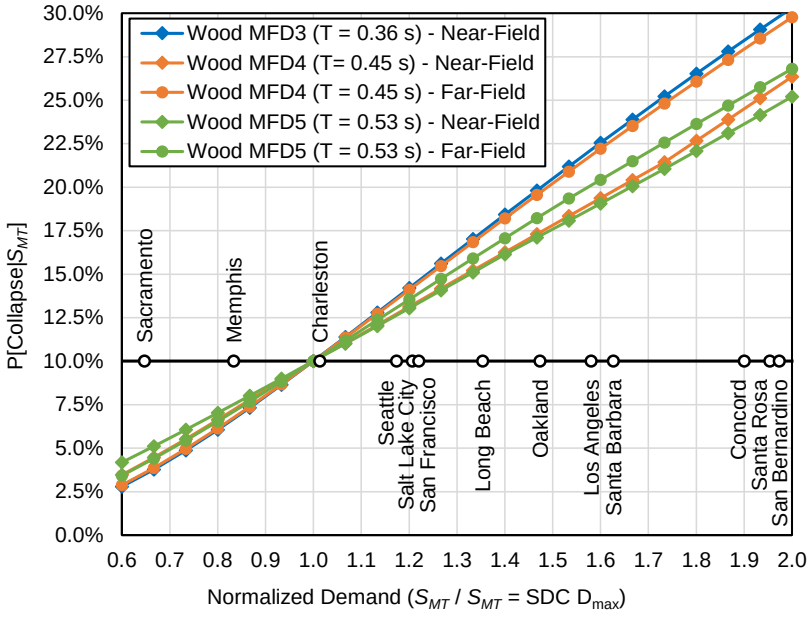

Figure 6-14 Comparison of collapse probability trends of wood MFD archetypes evaluated using the Near-Field record set with those of wood MFD archetypes evaluated using the Far-Field record, where collapse trends are anchored to the Risk Category II target reliability of P[Collapse|S_{MT}] = 10% at S_{MT} = SDC D_{max}, and plotted as a function of MCE_R response spectral acceleration normalized by S_{MT} = SDC D_{max}. Also shown (1) RC II reliability target of 10% probability of collapse given S_{MT} = SDC D_{max} and (2) normalized values of S_{MT} of ASCE/SEI 7-22 for selected city sites.

As shown in Figure 6-14, the collapse trends of archetypes evaluated using the Near-Field record set are similar to those of archetypes evaluated using the Far-Field record set, where slight differences in the trends of the two record sets are attributed to differences in the median shapes of Near-Field and Far-Field response spectra. The similarity of collapse trends indicates that increasing design acceleration (e.g., by a factor of 1.3) to offset the effects of velocity pulses and other characteristics of the ground notions of the Near-Field record set would not significantly lessen the inherent increase in collapse risk with the level of MCE_R ground motions common to these archetypes.

6.4 Importance Factor for Design of Risk Category IV Structures

Comparison of the probabilities of collapse of Table 6-1 for RC II designs of SFRS archetypes and the probabilities of collapse of Table 6-2 for RC IV designs SFRS archetypes with their respective target reliabilities 10% (RC II) and 2.5% (RC IV) of failure given MCE_R ground motions shows a consistent trend that each SFRS archetype better achieves RC II target reliability performance than RC IV target reliability performance. That is, the value of I_e = 1.5 for design of RC IV structures does not appear large enough to achieve the target 2.5% probability of failure for an SFRS archetype that meets the

target 10% probability of failure. This section develops the approximate increase in the I_e factor that would be required to better achieve the target 2.5% probability of failure for design RC IV structures.

Adjustment of the Importance Factor (I_e = 1.5) is based on the values of *ACMR* of Table 6-1 for RC II design of archetypes and the values of *ACMR* of Table 6-2 for RC IV design of archetypes:

$$F_I = 1.5 \times ACMR \text{ (RC II)} \,/\, ACMR \text{ (RC IV)} \tag{6-3}$$

Where the value of the adjustment factor, F_I, is somewhat different for each archetype. The 1.5 factor in Equation 6-3 is the ratio of *ACMR2.5%/ACMR10%* (i.e., 3.25/2.16) for an assumed total collapse uncertainty of β_{TOT} = 0.60 (i.e., logarithmic standard deviation required by Section 21.2.1 of ASCE/SEI 7-22 for calculation of probabilistic MCE_R response spectra). The ratio of *ACMR* values of RC II and RC IV designs effectively adjusts the Importance Factor for RC II target reliability of the archetype (when different from 10% probability of failure) as well as adjusting RC IV target reliability (when different from 2.5% probability of failure).

Values of F_I are summarized in Table 6-9. Values of the adjustment factor are more reliable when based on values of *ACMR* of RC IV archetypes that are close to achieving target reliability without adjustment. Accordingly, the probability of collapse of RC IV archetypes is plotted as a function of the adjustment factors in Figure 6-15 showing trends that are somewhat different for archetypes grouped by (1) 1-story and 2-story wood STR, COM and MFD archetypes, (2) 3-story, 4-story and 5-story wood STR, COM and MFD archetypes and (3) non-wood BRBF, SMF and DCW archetypes of all heights.

Table 6-9 Summary Development of Adjustment Factors, F_I, for Modification of the Importance Factor, I_e, = 1.5, of ASCE/SEI 7-22 to Better Achieve RC IV target Reliability (2.5% probability of failure) of SFRS Archetypes that Achieve RC II Target Reliability (10% probability of failure) for MCE_R Ground Motions Corresponding to S_{MT} = 1.0 × SDC D_{max}

Archetype ID Name	FEMA P-695 Criteria		S_{MT} = 1.0 × SDC D_{max}				F_I Adjustment Factor
	Period, T (seconds)	SDC D_{max} S_{MT} (g)	P[Collapse|S_{MT}]		*ACMR*		
			RC II	RC IV	RC II	RC IV	
STR1	0.16	1.50	24.2%	10.5%	1.51	1.96	1.16
STR2	0.26	1.50	11.3%	4.5%	2.07	2.55	1.22
STR3	0.36	1.50	8.2%	2.8%	2.30	2.85	1.21
STR4	0.45	1.50	8.5%	2.4%	2.18	2.73	1.20
STR5	0.53	1.50	8.8%	2.5%	2.11	2.61	1.21
COM1	0.16	1.50	7.0%	3.1%	2.43	2.78	1.31
COM2	0.26	1.50	4.9%	2.3%	2.70	2.99	1.36
COM3	0.36	1.50	4.2%	1.5%	2.82	3.29	1.28
COM4	0.45	1.50	6.0%	1.8%	2.50	2.99	1.26
COM5	0.53	1.50	6.8%	2.0%	2.34	2.82	1.25
MFD1	0.16	1.50	0.7%	0.2%	3.90	4.01	1.46
MFD2	0.26	1.50	2.9%	1.4%	3.11	3.37	1.38
MFD3	0.36	1.50	3.2%	1.2%	3.04	3.45	1.32
MFD4	0.45	1.50	4.7%	1.5%	2.73	3.15	1.30
MFD5	0.53	1.50	6.1%	1.9%	2.53	2.99	1.27
BRBF4A	0.87	1.03	4.0%	1.8%	3.36	3.88	1.30
BRBF4B	0.87	1.03	2.5%	1.4%	3.96	4.14	1.43
BRBF9A	1.54	0.58	1.2%	0.5%	4.79	5.16	1.39
BRBF9B	1.54	0.58	0.9%	0.4%	5.27	5.66	1.40
BRBF15A	2.23	0.40	1.4%	0.7%	4.59	4.82	1.43
BRBF15B	2.23	0.40	0.8%	0.4%	5.41	5.61	1.45
SMF3A	0.73	1.23	10.8%	6.1%	2.25	2.57	**1.31**
SMF3B	0.73	1.23	9.1%	4.5%	2.24	2.64	**1.27**
SMF9A	1.83	0.49	12.8%	8.3%	2.01	2.21	**1.36**
SMF9B	1.83	0.49	12.0%	6.5%	2.03	2.29	**1.33**
DCW8A	0.75	1.20	12.2%	7.3%	2.04	2.26	1.36
DCW8B	0.75	1.20	10.5%	5.9%	2.15	2.39	1.35
DCW12A	1.01	0.89	6.6%	3.5%	2.52	2.78	1.36
DCW12A	1.01	0.89	5.6%	2.7%	2.65	2.94	1.35
DCW18A	1.37	0.66	3.6%	2.0%	2.92	3.03	1.45
DCW18A	1.37	0.66	4.3%	2.1%	2.79	3.01	1.39

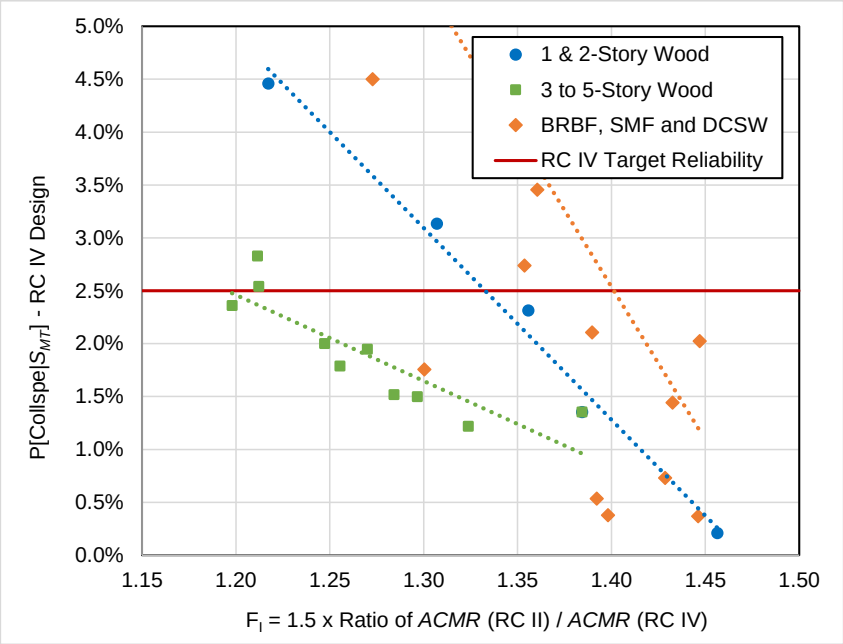

Figure 6-15 Plot of the probability of collapse of RC IV designs of SFRS archetypes as a function of the I_e adjustment factor, F_I, 1.5 times the ratio of the *ACMR* of RC II design to the *ACMR* of RC IV design of archetypes for MCE_R ground motions, S_{MT} = 1.0 × SDC D_{max}.

Trends shown in Figure 6-15 suggest that values of the adjustment factor range roughly from 1.20 for taller wood archetypes to 1.33 for 1-story and 2-story wood archetypes to about 1.40 for non-wood archetypes. Scatter in the values of the adjustment factor also suggest that these values should be considered approximate; however, values of the Importance factor of I_e = 1.8 (i.e., 1.20 × 1.5) to I_e = 2.1 (i.e., 1.4 × 1.5) would better achieve the RC IV target reliability of 2.5% probability of collapse given MCE_R ground motions for SFRS archetype that achieve RC II target reliability of 10% probability of collapse given MCE_R ground motions.

Chapter 7: Recommendations

7.1 Introduction

As shown in Chapter 6, the collapse rates increased for all investigated SFRSs as the amplitude of ground motions used for design strength and analysis increased. The failure rates exceeded the targeted conditional probability of collapse specified in Chapter 1 of ASCE/SEI 7 as the ground motions reached very high levels. In this study, the primary variables found to influence collapse performance are strength and displacement capacity. Increasing the displacement capacity of structural systems qualified for use where ground motions are very high would require extensive system-specific study and perhaps significant changes to engineering practice. However, reducing collapse risk could be achieved through a variety of methods related to increasing required design strength in ASCE/SEI 7. These methods are listed here and described at a conceptual level in Section 7.3.

- Increase design base shear where ground motions for the site are considered to be very high; there are various techniques to explore for achieving this increase.
- Enhance performance of RC IV (and RC III) structures that need improved collapse resistance (increase the I_e factor).
- Allow validation by Chapter 16 for buildings in VHS as an alternative to increasing the seismic base shear demand.
- Allow explicit consideration of non-SFRS resistance.
- Refine the *R* factors, targeting each system specifically.
- Revise the performance acceptance criteria, possibly admitting lower performance for higher ground motions.
- Revise criteria used for developing design ground motions.

Section 7.2 describes key limitations and assumptions related to the analytical studies reported in Chapter 6. These limitations and assumptions should be considered as part of any effort to develop changes to codes or standards because of the work documented in this report. Section 7.4 presents recommendations for future study that emerged from the analytical work documented in this report.

7.2 Limitations and Assumptions

The key limitations and assumptions related to the analytical work described in this report are summarized below.

GENERAL LIMITATIONS AND ASSUMPTIONS

- The scope of this project does not include evaluating and proposing revision of the current values of the *R* factor of existing SFRSs (i.e., Table 12.2-1, ASCE/SEI 7-22), which would necessarily require a more comprehensive set of explicitly designed archetypes and detailed nonlinear models of the specific SFRSs of interest.

- The scope of this project is limited to the collapse method of FEMA P-695, including in particular the use of the Far-Field record set for IDA. That record set effectively characterizes earthquake shaking for only one site class and only for sites governed by shallow crustal events.

- It is assumed that all archetype foundations are capable of resisting the peak ground accelerations and inertial reactions from the ground motions used for IDA. The effects of sliding and soil-structure interaction are not considered.

- The range of archetypes included in this study, with the exception of the detailed steel SMF archetypes (Section 5.8), were those available in the literature and were limited, to the extent possible, to those with designs that were not controlled by the ASCE/SEI 7 minimum base shear equations. Very tall buildings that are governed by wind demands also were excluded.

LIMITATIONS AND ASSUMPTIONS ASSOCIATED WITH CHAPTER 4 (WOOD ARCHETYPES)

- For wood archetypes, the ASCE/SEI 7 drift limits for shear walls were not considered in the design. The drift limits generally do not govern the designs. However, drift limits might impact the designs for certain taller wood archetypes, such as 5-story commercial wood archetypes and Risk Category IV buildings.

- The most recent shear wall test data obtained for OSB were utilized to create the numerical models for wood archetypes. Shear walls sheathed with plywood may exhibit lower stiffness than those sheathed with OSB. The exact extent of how much impact plywood sheathing has on the seismic performance is not clear. Since the current wood code (NDS) does not differentiate the strength between shear walls sheathed with OSB and plywood, the influence on the collapse trends observed in this study is expected to be limited and likely negligible.

- The adjustment factor in the wood design code (NDS) for high aspect ratio (height-to-width ratios greater than two) walls for seismic force resistance was not considered in this study. The use of high aspect ratio shear walls will result in the usable design shear to be reduced.

LIMITATIONS AND ASSUMPTION ASSOCIATED WITH CHAPTER 5 (NON-WOOD ARCHETYPES)

- For each non-wood system, a single archetype at each building height was selected from the literature as the basis for the eSDOF modeled behavior. All eSDOF models within a family were then based on the selected archetype's behavior. This assumes that the overall geometries and configurations of the SFRSs do not change with increasing seismic demand.

- The scaling of the stiffness of the eSDOF models of various systems was based on scaling rules developed from observations of the behavior of detailed models of SDC D_{min} and SDC D_{max} archetypes from the literature. This may not be representative of the stiffness differences between systems designed for seismic hazards larger than SDC D_{max}.

- The displacement at peak strength of each eSDOF model within a family did not vary with strength. This is consistent with observations from the literature when comparing analysis results for detailed models developed to represent SDC D_{min} and SDC D_{max} archetypes.

- For each non-wood archetype of a certain building height and within a given family, the deformed shape of the structure at large deformations, known as the pushover mode shape, was assumed to be constant. This assumes that the distribution of story drifts up the height of a particular building does not change with increasing design seismic demand.

- The MDOF steel SMF models assumed ultimate rotation capacities for the nonlinear springs representing the RBS sections of the beams and the columns that were based on very limited testing for the section sizes used in the model.

Despite the above key limitations and assumptions, and other limitations and assumptions noted in previous chapters, the resulting trends presented in Chapter 6 are still believed to reasonably reflect differences in the expected seismic collapse performance of systems subjected to high and very high-seismic ground motions.

7.3 Recommendations for Changes to ASCE/SEI 7

This section describes a series of conceptual changes to ASCE/SEI 7. A variety of methods are discussed, each related to increasing the required design strength for new structures in order to improve collapse performance in regions of very high seismicity. Each method describes a framework only, recognizing that the final details of any changes would need to be determined by code change committees.

INCREASE DESIGN BASE SHEAR

The design base shear for high seismic hazard regions could be increased to come closer to the target conditional reliabilities for the various risk categories. Four possible approaches are presented that might accomplish this:

Adopt an Amplification Factor – Simplified

Adopt a factor that increases the seismic response coefficient, C_S, when S_{MS} exceeds 1.5g or S_{M1} exceeds 0.9g. This approach would affect all SFRSs equally. Figure 7-1 shows possible design amplification factors as a function of the ratio of design spectral acceleration to a reference spectral acceleration to be adopted as the threshold above which amplification is necessary (elsewhere in this report that reference is taken as the SDC D_{max} demand defined in FEMA P-695). The figure shows two linear amplifiers, one to apply to the short period demand and a second to apply to the 1-second demand, depending on the design period of the structure. The slopes of the lines are approximately equal to the medians shown in Figure 6-10 and Figure 6-11, respectively (at a demand ratio of 2, the value is 1.5 for short period and 1.7 for longer periods). The exponential line included in Figure 7-1 is based on Equation 6-2 with the exponent set to 0.5, representing a region of constant velocity. A slightly higher exponent would better fit the results found in this study. The concept of different amplifiers for short and long periods does capture a portion of the results found in this study. This method does treat all SFRSs equally. However, it does not account for differences in spectral shapes due to site class.

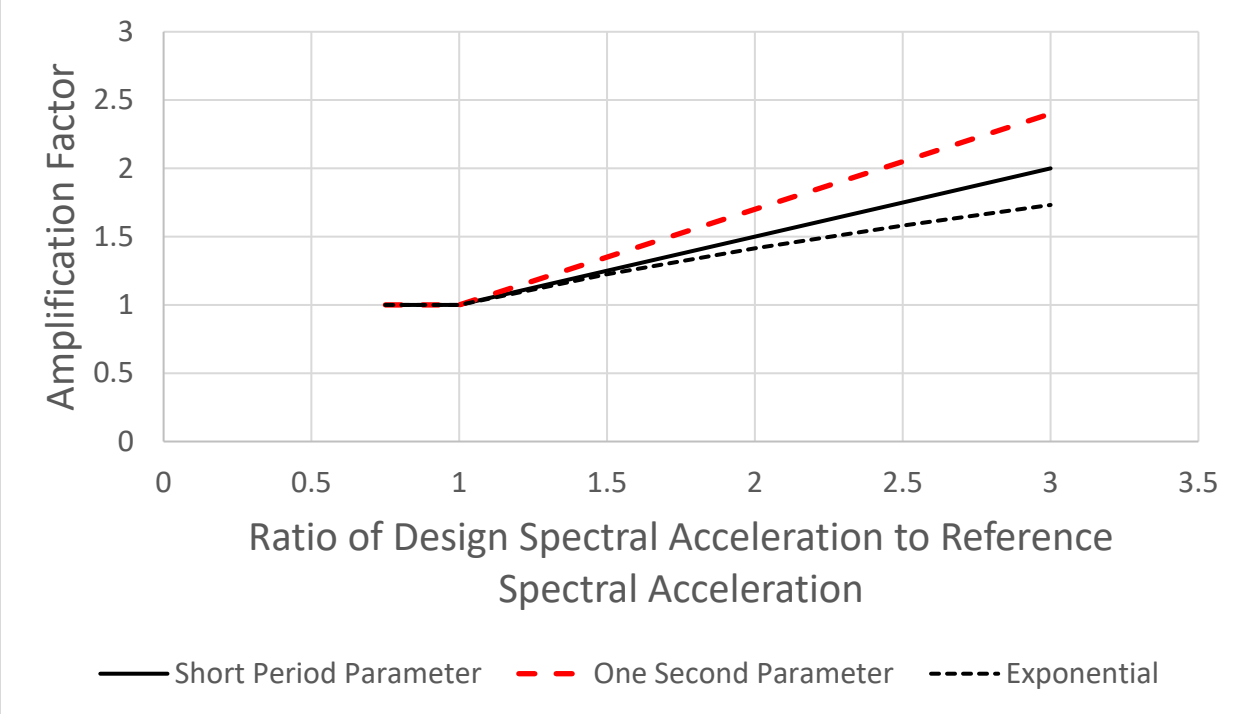

Figure 7-1 Possible design amplifications factors as a function of reference spectral acceleration.

Adopt an Amplification Factor – Site Specific

The amplification factor illustrated in Figure 6-12 can be computed directly from information available to the designer, with a few assumptions. One method to implement this concept would include the following steps:

1. Download the 22-point MCE_R spectral accelerations from the ASCE/SEI 7 Hazard Tool and interpolate to find the acceleration demand at the design period, *T*, for the structure (point D in Figure 6-12).
2. Also compute the acceleration demand at design period, *T*, for the threshold (reference) spectrum. This is Point "C" in Figure 6-12. The threshold could be the FEMA P-695 SDC D_{max} spectrum, the ASCE/SEI 7-22 Deterministic Lower Limit (DLL) for Site Class C (which matches the FEMA P-695 spectrum fairly well), or some other spectrum based upon further study.
3. Scale the MCE_R spectrum to match the reference spectrum at the design period.
4. Compute the corresponding spectral displacements for both the MCE_R and the scaled MCE_R spectra.
5. Compute the effective period of the structure at incipient collapse. The ratio of the effective period to the design period could depend on the *R* and Ω_0 factors but should be bounded. The bounds might also depend on the design period itself, the ratio being smaller for large periods than for short periods.
6. Interpolate the MCE_R spectrum at Teff to find the spectral displacement and acceleration at collapse (point B in Figure 6-12),
7. Using the spectral displacement for point B, interpolate the scaled MCE_R spectrum to find spectral acceleration at point A in Figure 6-12. These displacements at A and B are not true (see Appendix G for discussion of effective damping), but they are useful for this procedure.
8. Using Teff interpolate the scaled MCE_R spectrum to find point A'.
9. Compute the amplifier as described in Equation 6-1.

Figure 7-2 illustrates this method for a three-story wood building on a Site Class CD location in San Bernardino, California (note that the actual displacements on this figure have not been reduced for the effect of yielding on effective damping at collapse). In this instance, the threshold is set as the ASCE/SEI 7-22 DLL for Site Class C. The resulting amplifier is 1.67. The value implied by Figure 7-2 is 1.44. The method would compute a lower amplifier if a higher threshold were selected. For example, it would drop to 1.09 if the threshold were set at 150% of the ASCE/SEI 7 DLL for Site Class C.

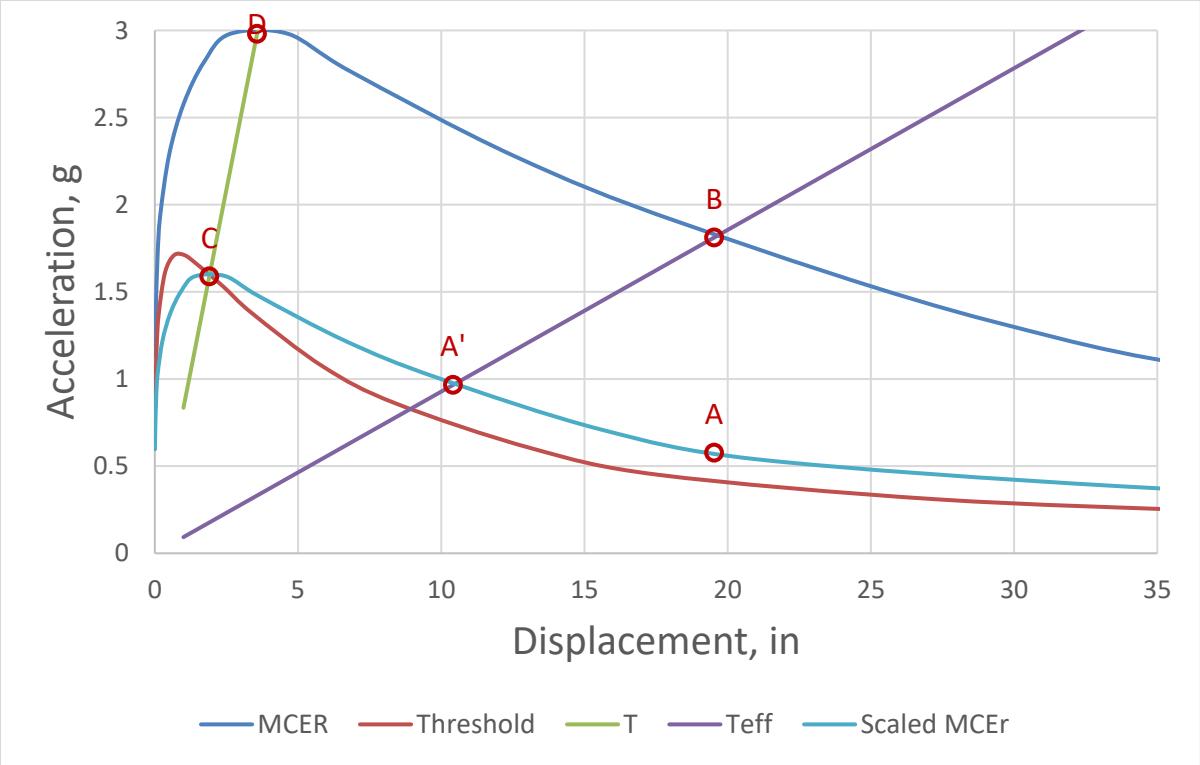

Figure 7-2 Example amplification factor applied to three-story wood frame building in San Bernardino, California.

This method has the advantage of specifically accounting for the site-dependent shape of the MCE_R spectrum, the design period of the structure, and the maximum displacement capacity. However, testing reveals that the method will not produce usable results for longer period structures without additional limitations. More study is needed. It may be feasible to estimate the displacement value by adapting the equation for target displacement in ASCE/SEI 41.

One of the significant issues for any amplification requirement will be the selection of the threshold spectrum. Figure 6-1 shows the ratio of the default DLL spectrum in ASCE/SEI 7-22 to the FEMA P-695 SDC D_{max} spectrum. The figure shows that there are substantial differences between the ground motions in recent editions of ASCE/SEI 7. The selection of a base at which to apply an amplifier to the design ground motion requires many considerations.

Adjust the Coefficient C_u

For many systems, the performance problem may lie in the domain of periods where the response spectrum is nearly a constant velocity. For most such buildings, the strength is controlled by the coefficient for upper limit on calculated period, C_U, placed on the approximate period. A somewhat more indirect, but potentially effective, method is to incorporate a change in the value of C_u, which would result in an increase in design base shear. Implementing this method could be as simple as reducing C_u as a function of S_{D1}. If one assumes stiffness is directly correlated with strength (which is a big assumption), that concept would indicate a function of the square root of the ground motion

parameter. Assuming that the current value of 1.4 is correct for S_{D1} = 0.6, this would reduce C_u to 0.81 at S_{D1} = 1.8. Such an expression would result in unrealistically large values of C_u for small values of S_{D1}. A simple linear expression would be easier to use and could match either approach. For structures that are controlled by the drift criteria, for which the limit on period is currently of no effect, there would be a benefit to including an upper bound period for drift checks. This method would be appropriate for structures with periods in excess of T_s but wouldn't change the design for short-period structures. Figure 7-3 shows a potential scheme for implementing this procedure. Commentary would need to explain the purpose and basis of these approximate approaches.

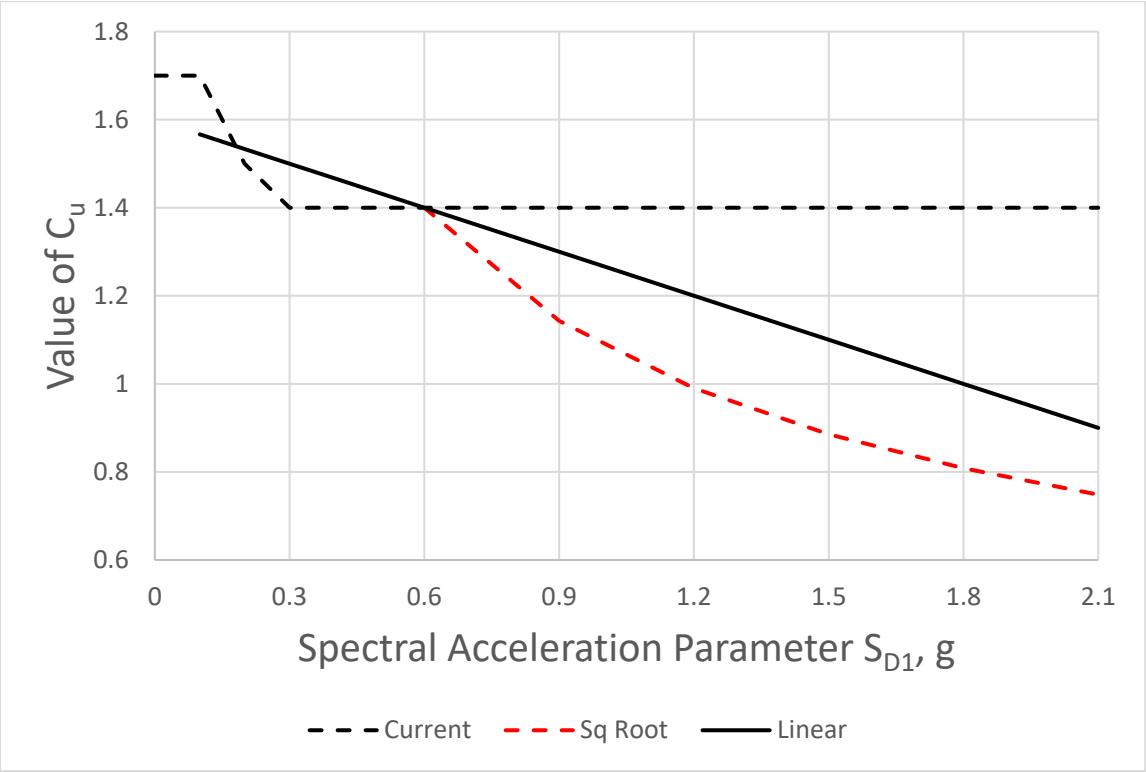

Figure 7-3 Potential revisions to upper limit on calculated period, C_u.

Make the *R* Factor Dependent on Ground Motion Amplitude

Make the *R* factor dependent on the amplitude of the ground motion. The design provisions treat the *R* factor as if it depends only on the detailing of the system, not on the amplitude of the ground motion. There have been concepts discussed to make the *R* factor dependent on the period of vibration (NIST GCR-12-917-20), but they have not been developed to the point of formal proposals. This study shows that the premise of a constant *R* factor is not well founded. Detailing rules for members and connections and restrictions on material properties tend to deliver local deformation capacities. Overall structure deformation capacities depend on those properties, as well as the size of the structure and the structural members and the ability of the system to utilize the deformation capacity throughout the structure. Adjustments for ground motion amplitude would likely be more substantial for large *R* factors than for small *R* factors. The advantage for this approach over the

previous two is that it could be tailored to each system and that it could be combined with the dependence on period of vibration. The disadvantage is that it will require a very substantial effort to achieve a reasonably reliable procedure.

ENHANCE PERFORMANCE OF RC IV (AND RC III) STRUCTURES THAT ACTUALLY NEED IMPROVED COLLAPSE RESISTANCE (INCREASE THE I_E FACTOR)

ASCE/SEI 7 sets target reliabilities in Chapter 1, and the target for RC IV structures is a conditional probability of collapse, given the occurrence of MCE_R ground motion, of 2.5%, as opposed to 10% for RC II structures. This study provides strong evidence that the target for RC IV is not being met, and it is reasonable to expect a similar issue with the target for RC III structures. The solution may be to increase the seismic importance factor, I_e, for a subset of RC IV (and RC III) structures for which the true objective is to reduce the risk of collapse. However, for many RC IV structures, the true objective may well be continuation of function given the MCE_R shaking. This requires reconsideration of the definition of the risk categories, as well as careful coordination with other efforts aimed at standardization of functional recovery. Because solutions for these last issues are not supported by this study, the topic is discussed in the following section on recommended future studies.

ALLOW VALIDATION BY CHAPTER 16 FOR BUILDINGS IN VHS AS AN OPTION TO INCREASING THE SEISMIC BASE SHEAR DEMAND.

The performance-based evaluation procedures of Chapter 16 in ASCE/SEI 7 may offer an alternative to the requirements for increased strength. Further examination of the relation between the acceptance criteria in Chapter 16 and the probability of collapse is warranted before accepting this concept.

EXPLICIT CONSIDERATION OF NON-SFRS RESISTANCE

Allow explicit consideration of non-SFRS resistance as a method to design for higher demand. As noted in Chapter 2, non-SFRS resistance includes nonstructural partitions and gravity systems. For this to be effective, the *R* factor for the system would also have to be reduced while the overstrength of the final structure would be increased by the direct inclusion of the non-SFRS resistance. The following issues should be considered with this approach.

- The level of confidence in the values of resistance to use for design.
- Standardization of details for construction.
- Need for quality assurance during construction.
- Demonstration of the gravity system resistance.

Inclusion of the gravity system resistance for design would require important changes to building code requirements associated with their alteration. For example, alteration requirements for gravity systems would need to be modified to be consistent with those currently required for SFRSs.

REFINE THE *R* FACTORS FOR EACH SFRS

For most SFRSs, updates to *R* factors could probably be accomplished independent of the nature of the occupancy. However, for other systems studied, such as the wood light-frame system, the nature of the occupancy is a strong influence on the total overstrength, and thus the actual collapse risk. Reinforced masonry is another example: the length of walls provided is dependent on the architectural layout, thus schools, warehouses, and big box retail stores generally have substantial overstrength, but commercial buildings, with large amounts of exterior glass and no interior bearing walls, have much less. Implementing an approach to include the nature of a building's occupancy will be difficult and, in the end, is not being recommended.

While not currently implemented, the refinement could include redefining the *R* factor into its constituent parts, as outlined in NIST GCR-10-917-20 and used in the National Building Code of Canada. These constituent parts include an:

- R_d component of *R* related to total system ductility and damping, and
- R_O component of *R* related to system overstrength, which would be more complex than the present Ω_0, potentially involving several parameters.

The factor(s) could be adjusted in very high-seismic locations to achieve acceptable collapse rates. Although this project has demonstrated that the probability of collapse at one level of ground motion is not the same for the systems studied, there are not enough data to implement this type of rigorous change. Refining the *R* factor, whether it's a singular value or broken into constituent parts, would require rigorous FEMA P-695 studies of each of the systems listed in ASCE/SEI 7 Table 12.2-1. Prior to commencing a study of this magnitude, FEMA P-695 should be updated to account for issues associated with VHS locations.

REVISE PERFORMANCE ACCEPTANCE CRITERIA, POSSIBLY ADMITTING LOWER PERFORMANCE

Admit lower performance of buildings in higher ground motion regions by revising the target performance criteria. The effect of the deterministic cap is that probability of collapse over a unit time is higher where the cap applies, but the conditional probability given the occurrence of the MCE_R ground motions is not affected. This study shows that the assumption of a constant conditional probability given those ground motions is not being achieved. If nothing is done to address the issues identified in this study, the option of accepting lower performance is selected by default. It is desirable to make the objectives of the ASCE/SEI 7 seismic provisions clear to users. This could include updating the requirements in ASCE/SEI 7 Chapter 1 and associated commentary.

REVISE CRITERION FOR DEVELOPING GROUND MOTIONS FOR DESIGN

The ASCE/SEI 7 ground motions are based on probabilistic seismic hazard curves developed by the U.S. Geological Survey. However, these design ground motions themselves are based on a conditional probability of collapse, given occurrence of the MCE_R ground motion, that does not vary

with ground motion amplitude. Changing to a targeted collapse probability per unit of time that depends on the amplitude of the ground motion should be explored. Such an approach would provide clarity in the assumed risk of structures located in VHS regions. Collapse probability targets should be recommended by entities such as the Building Seismic Safety Council's Provisions Update Committee in the development of the *NEHRP Recommended Seismic Provisions for New Buildings and Other Structures*, but they would have to be adopted in a consensus standards process, such as is used in the ratification of ASCE/SEI 7, and be further scrutinized for adoption into the *International Building Code*.

7.4 Recommendations for Future Studies

This section describes topics and provides recommendations considered applicable to seismic-code-development committees, including the Provisions Update Committee of the Building Seismic Safety Council, the Seismic Subcommittee of ASCE/SEI 7, the ASCE/SEI 41 Standards Committee on Seismic Evaluation and Retrofit of Existing Buildings, and material-specific standards committees, such as the Wood Design Standards Committee of the American Wood Council and the AISC Committee on Specifications of the American Institute of Steel Construction. Seismic code committees have limited resources and studies would, in most cases, require a funded project to develop the requisite technical basis of any proposals to improve existing codes and standards. Recommendations for future study include:

- Perform collapse analyses using additional very high ground motions.
- Update FEMA P-695.
- Improved models for collapse evaluation in very high and ultra-high seismic regions.
- Study innovative methods to reduce displacement demands and/or increase displacement capacities for systems that depend on significant inelastic response or response modification systems, such as isolation and damping.
- Establish appropriate performance targets for RC IV.
- Review the Use of S_1 to establish the boundary for SDC E.
- Review benchmark buildings in ASCE/SEI 41.

COLLAPSE ANALYSES FOR VERY HIGH GROUND MOTIONS

Collapse analyses are commonly performed using the 22 pairs of horizontal motion records in the FEMA P-695 Far-Field record set. The median spectral shape for those records does not adequately capture the shape of spectra from ground motions created by large magnitude events on soft and moderately soft sites, particularly for periods above one second. Beginning with ASCE/SEI 7-16, the design requirements were modified to capture some of this effect. This study has found that collapse rates for structures with large effective periods (secant stiffness of yielding structure near collapse)

are still quite high. There are some questions about the correlation of those predictions with actual experience in large earthquakes. Therefore, additional collapse analyses should focus on ground motions with large spectral demands at periods well above one second and structures with fundamental and effective periods in the same range. Analyses using long-duration motions should also be included.

UPDATE FEMA P-695

FEMA P-695 has begun to be used extensively, not only in research projects, but in validation of alternative SFRSs. The International Code Council Evaluation Service (ICC-ES) adopted an acceptance criterion (AC494) based upon FEMA P-695 that has now been used for at least three new proprietary SFRSs. Furthermore, other new, non-proprietary (or "generic") systems have been incorporated into ASCE/SEI 7 via review of FEMA P-695 studies by the Building Seismic Safety Council in development of the NEHRP Provisions. Experiences from the research projects and the SFRS validations provide a basis for some modifications.

FEMA P-2139 outlined a series of recommendations regarding updating FEMA P-695, and these needs have been validated by this study. Additional recommendations emerged from this study for consideration in a future update to FEMA P-695, and these include:

- Re-evaluation of the spectral shape factor (*SSF*).
- Evaluation of linear or near-linear behavior.
- Require the Near-Field record set for some situations.
- Review spectral shapes and archetype design criteria.
- Require reporting of the median drift ratio at incipient collapse ($\widehat{DR}_{IC}$) from the IDA.

Re-evaluation of the Spectral Shape Factor

The spectral shape factor, *SSF*, is used in FEMA P-695 to recognize that the spectral shapes associated with MCE_R ground motions are generally unusual. Since the development of FEMA P-695, there has been additional research related to *SSF*. Furthermore, the application in FEMA P-695 depends on a generalized pushover shape that does not apply well to all SFRSs, and an alternative solution was incorporated into ICC-ES AC494, *Qualification of Building Seismic Performance of Alternative Seismic Force-Resisting Systems* (ICC-ES, 2022), that should be considered.

Evaluation of Linear or Near-Linear Behavior

The finding that structures that rely on ductility suffer higher collapse probabilities at very high design ground motions can be interpreted that structures that behave in a linear elastic fashion, such as some masonry wall systems, do not suffer this problem, although that was not studied in detail for this report. As stated in Section 6.2, doubling the strength of an elastic system would, by

definition, double the value of $\hat{S}_{CT}$, since displacement capacity would also increase with strength, and hence trends in collapse performance would not decrease with S_{MT}. FEMA P-695 does have a brief discussion of applying the methodology to structures that remain linear, and it may be reasonable to study this approach in more detail.

Require Near-Field Record Set for Some Situations

FEMA P-695 requires evaluating the collapse performance of buildings using the Far-Field record set. As noted in this and previous studies, use of the Near-Field record set results in higher collapse rates for the archetypes being evaluated, all else equal. From FEMA P-2139, the fundamental question is simply: Does the 10% conditional probability of collapse given the occurrence of the MCE_R ground motion objective of ASCE/SEI 7 really apply to buildings at all possible sites or only to those sites that are not near source? This policy question has not been answered by this study, but it is now in a clearer focus.

Spectral Shapes and Archetype Design Criteria

FEMA P-695 requires testing the performance of archetype designs against a set of ground motions. The archetypes are required to be designed for the default site condition from ASCE/SEI 7-05, which was Site Class D. The median spectrum from the test set of ground motions has the shape most closely related to Site Class C. For some structures this disconnect can be significant, for example where a significant amount of mass participates in the second mode. Furthermore, the default site condition and the spectral shapes in ASCE/SEI 7-22 are quite different from those in ASCE/SEI 7-05.

Require Reporting of the Median Drift Ratio at Incipient Collapse

A key parameter from IDA is the median drift ratio at incipient collapse, $\widehat{DR}_{IC}$. However, $\widehat{DR}_{IC}$ is rarely reported by research projects utilizing FEMA P-695. It is recommended that this parameter be included in the reporting of results of studies using FEMA P-695. Further reporting of this quantity could lead to validation of, or refinement of, the $C_d = R$ concept in FEMA P-695.

IMPROVED MODELS FOR COLLAPSE EVALUATION IN REGIONS OF VERY HIGH AND ULTRA HIGH SEISMIC REGIONS

To further confirm building performance in very high and ultra-high seismic regions, detailed nonlinear models of various seismic-force-resisting systems should be developed and evaluated. As part of this effort, it would be beneficial to have teams independently design archetypes for varying seismicity levels and have teams independently develop and analyze detailed models of those archetypes. Having a suite of realizations of archetype designs, detailed models, and collapse results would help verify the reliability of the findings. In addition to the development of detailed models, the inclusion of sliding and soil-structure interaction should be evaluated to determine its effect on collapse performance in regions of very high seismicity. Another improvement to be considered is the development of component backbones for nonlinear response from actual ground motions rather than cyclic tests with monotonically increasing amplitudes.

STUDY INNOVATIVE METHODS TO REDUCE DISPLACEMENT DEMANDS AND/OR INCREASE DISCPLACEMENT CAPACITIES

Response spectra at very high-seismic sites, especially on softer soils, show extremely large displacement demands for flexible structures. Some types of yielding structures, which fail upon exceeding a given story drift, will find it difficult to reach the overall structural displacement demands in certain height ranges, depending on the particular system. Also, seismic isolation systems, which modify the response in the superstructure but have realistic deformation capacities, could face limitations in very high-seismic regions. These problems can potentially be resolved by innovative configurations of existing systems, or by combinations of existing systems, such as adding damping to reduce displacement demand.

ESTABLISH APPROPRIATE PERFORMANCE TARGETS FOR RC IV

Enhanced collapse prevention, likely to be consistent with what is currently required for RC IV structures, is important for some structures, such as those that have significant risk of off-site consequences should they collapse. Included in this list are facilities that manufacture, process, handle, store, use or dispose of hazardous materials or explosives. These structures should target a low likelihood of collapse given MCE_R ground shaking consistent with the 2.5% value listed in ASCE/SEI 7 Table 1.3-2. To achieve this target, their seismic design forces should be increased, as demonstrated in Chapter 6.

However, for many RC IV structures, the "real" performance objective is functionality at the Design Earthquake, as outlined in Section 1.3.3 of ASCE/SEI 7, which targets this performance for all RC IV buildings. Given this "real" performance objective, a different collapse target given MCE_R ground shaking could be established to be used in addition to the functionality criteria.

REVIEW THE USE OF S_1 TO ESTABLISH THE BOUNDARY FOR SEISMIC DESIGN CATEGORY E

In ASCE/SEI 7, the mapped MCE_R response spectral acceleration parameter at 1-second, S_1, is used to establish the boundary for SDC E and SDC F. Values of S_1 greater than or equal to 0.75 result in the SDC going from D to E (or to F for RC IV structures). Both the use of S_1 and the associated 0.75 trigger should be evaluated. It is recommended that the boundary be established using S_{M1}, in order to account for the effects of site amplification and the resulting change in spectral shape that vary with site class. The trigger should be established based on evaluating the performance of SFRSs on varying site classes.

REVIEW BENCHMARK BUILDINGS IN ASCE/SEI 41

Ground motions for design of moderate- and long-period buildings in regions of high seismicity and on less than hard site conditions were increased in ASCE/SEI 7-16. This study indicates that even larger increases will be needed for buildings in regions of very high seismicity. Appropriate modifications to the criteria for Benchmark Buildings in Section 3.3 of ASCE/SEI 41 should be considered.

Appendix A: Population and Building Exposure in Regions of Very High Seismicity

A.1 Introduction

This appendix presents estimates of population and building exposure (number, occupancy, and value of buildings) in regions of very high seismicity throughout all U.S. states and territories. Consistent with prior chapters, very high-seismic (VHS) regions are defined as those with $S_{MS} > 1.5$ g or $S_{M1} > 0.9$g.

A.2 Scope and Approach

The U.S. Geological Survey provided S_{MS} and S_{M1} at the census tract level based on the values used for ASCE/SEI 7-22 (Luco et al., 2021). The response spectral values assume the default site condition, which for ASCE/SEI 7-22 is defined as the maximum response of Site Classes, C, CD, and D. Population and building exposure are based on the Hazus 6.0 Inventory (FEMA, 2022).

Building replacement values are organized into two groups, residential and non-residential. Non-residential includes commercial, industrial, agricultural, religious, governmental, and educational occupancies. Building replacement values do not include contents. Non-building structures, such as bridges, airports, and roads, are not included.

A.3 Population and Building Exposure as a Function of Ground Motions

Population and building exposure are associated spatially with the MCE_R ground motions of ASCE/SEI 7-22. Spatial associations of population and building exposure with ground motions are made separately for short-period, S_{MS}, and 1-second, S_{M1}, ground motion parameters and binned by the values of these parameters. Binning distinguishes population and building exposure data in VHS regions from population and building exposure data where the shaking is less than or equal to the VHS boundary. Binning by ground motion also shows the distribution of population and building exposure as a function of the level of shaking in the VHS region.

Total U.S. population and building exposure data are summarized in Table A-1 (binned by S_{MS}) and Table A-2 (binned by S_{M1}). These same data are then shown for the West Coast states of California, Oregon, and Washington in Table A-3 and Table A-4. Table A-5 presents the percentage of the population in selected U.S. states and territories that are in regions of very high seismicity, where the VHS boundary is defined by $S_{M1} > 0.9$g.

About 42.9 million people live or work in regions of very high seismicity (defined by $S_{M1} > 0.9$g), and about 11% of U.S. buildings, representing $7.5 trillion in replacement cost, are in regions of very high seismicity (defined by $S_{M1} > 0.9$g). These figures are slightly less when the VHS boundary is defined by $S_{MS} > 1.5$g. The three West Coast states of California, Oregon, and Washington account for 84% of the U.S. population and 80% (by number) of the U.S. building exposure that is in regions of very high seismicity.

California is the major driver, accounting for 30.7 million of the 42.9 million people in VHS regions. However, Utah and Puerto Rico have more exposure, in absolute and relative terms, than Oregon in VHS regions. Utah has about 2.3 million people (or 70%) and Puerto Rico has about 2.2 million people (or 69%), whereas Oregon has about 700,000 people (or 16%) in VHS regions. Other states and territories with significant VHS exposure include Nevada, Alaska, South Carolina, Hawaii, Guam, Missouri, and Tennessee.

Table A-1 Population, Number of Buildings, and Building Replacement Value for all U.S. States and Territories Binned by Values of Short-Period MCE_R Response Spectral Acceleration, S_{MS}, of ASCE/SEI 7-22

ASCE/SEI 7-22 S_{MS} Bins	Population (in millions)	Distribution of Buildings		Replacement Value ($ in billions)		
		Number (in millions)	Percent	Residential Buildings	Non-Res. Buildings	All Buildings
All	335.1	124.5	100%	39,898	22,477	62,375
≤ 1.5g	295.6	112.4	90%	35,309	20,084	55,393
> 1.5g	39.4	12.1	10%	4,590	2,392	6,982
1.5g –1.8g	13.3	4.4	4%	1,636	781	2,416
1.8g – 2.1g	8.4	2.6	2%	968	566	1,534
2.1g – 2.4g	9.6	2.8	2%	1,021	616	1,636
2.4g – 2.7g	5.7	1.6	1%	671	311	982
2.7g – 3.0g	1.9	0.6	0%	241	94	335
≥ 3.0g	0.5	0.2	0%	54	24	78

Table A-2 Population, Number of Buildings, and Building Replacement Value for all U.S. States and Territories Binned by Values of 1-second MCE_R Response Spectral Acceleration, S_{M1}, of ASCE/SEI 7-22

ASCE/SEI 7-22 S_{M1} Bins	Population (in millions)	Distribution of Buildings		Replacement Value ($ in billions)		
		Number (in millions)	Percent	Residential Buildings	Non-Res. Buildings	All Buildings
All	335.1	124.5	100%	39,898	22,477	62,375
≤ 0.9g	292.2	111.2	89%	34,904	19,931	54,835
> 0.9g	42.9	13.3	11%	4,995	2,546	7,540
0.9g –1.2g	12.8	4.5	4%	1,562	688	2,249
1.2g – 1.5g	7.6	2.4	2%	883	479	1,362
1.5g – 1.8g	13.2	3.6	3%	1,371	870	2,241
1.8g – 2.1g	5.5	1.6	1%	703	307	1,010
2.1g – 2.4g	2.0	0.6	0%	254	103	357
≥ 2.4g	1.8	0.6	0%	223	97	320

Table A-3 Population, Number of Buildings, and Building Replacement Value for California, Oregon, and Washington Binned by Values of Short-Period MCE_R Response Spectral Acceleration, S_{MS}, of ASCE/SEI 7-22

ASCE/SEI 7-22 S_{MS} Bins	Population (in millions)	Distribution of Buildings		Replacement Value ($ in billions)		
		Number (in millions)	Percent	Residential Buildings	Non-Res. Buildings	All Buildings
All	51.5	16.2	100%	6,007	3,257	9,264
≤ 1.5g	17.1	6.0	37%	1,983	1,155	3,138
> 1.5g	34.4	10.2	63%	4,024	2,102	6,126
1.5g –1.8g	9.9	3.2	19%	1,257	603	1,860
1.8g – 2.1g	7.6	2.3	14%	884	512	1,395
2.1g – 2.4g	9.1	2.6	16%	957	584	1,541
2.4g – 2.7g	5.6	1.6	10%	659	301	960
2.7g – 3.0g	1.8	0.5	3%	233	88	321
≥ 3.0g	0.3	0.1	1%	34	14	48

Table A-4 Population, Number of Buildings, and Building Replacement Value for California, Oregon, and Washington Binned by Values of 1-second MCE_R Response Spectral Acceleration, S_{M1}, of ASCE/SEI 7-22

ASCE/SEI 7-22 S_{M1} Bins	Population (in millions)	Distribution of Buildings		Replacement Value ($ in billions)		
		Number (in millions)	Percent	Residential Buildings	Non-Res. Buildings	All Buildings
All	51.5	16.2	100%	6,007	3,257	9,264
≤ 0.9g	15.6	5.5	34%	1,811	1,046	2,857
> 0.9g	35.9	10.7	66%	4,196	2,212	6,407
0.9g –1.2g	7.9	2.7	17%	1,017	510	1,527
1.2g – 1.5g	6.6	2.0	13%	786	405	1,191
1.5g – 1.8g	12.7	3.4	21%	1,303	835	2,138
1.8g – 2.1g	5.0	1.5	9%	635	271	906
2.1g – 2.4g	1.9	0.6	4%	240	96	336
≥ 2.4g	1.7	0.5	3%	214	95	309

Table A-5 Percentage of Population in Very High-Seismic Regions for Selected U.S. States and Territories

U.S. State or Territory	Total Population	Population in Very High-Seismic Regions (S_{M1} > 0.9g)	Percentage of Population in Very High-Seismic Regions
California	39,538,223	30,718,589	78%
Washington	7,705,281	4,462,163	58%
Utah	3,271,616	2,304,487	70%
Puerto Rico	3,285,874	2,252,628	69%
Oregon	4,237,256	692,475	16%
Nevada	3,104,614	661,016	21%
Alaska	733,391	523,518	71%
South Carolina	5,118,425	447,451	9%
Hawaii	1,455,271	200,629	14%
Guam	153,898	153,898	100%
Missouri	6,154,913	124,661	2%
Tennessee	6,910,840	105,025	2%

A.4 Maps of Regions of Very High Seismicity

Maps showing regions of very high seismicity defined in terms of $S_{MS} > 1.5g$ and $S_{M1} > 0.9g$ using ASCE/SEI 7-22 ground motions and assuming default site conditions are presented in Figure A-1 and Figure A-2, respectively. Figure A-3 identifies regions of very high seismicity that meet either the short-period ($S_{MS} > 1.5g$) or 1-second ($S_{M1} > 0.9g$) VHS ground motion criterion.

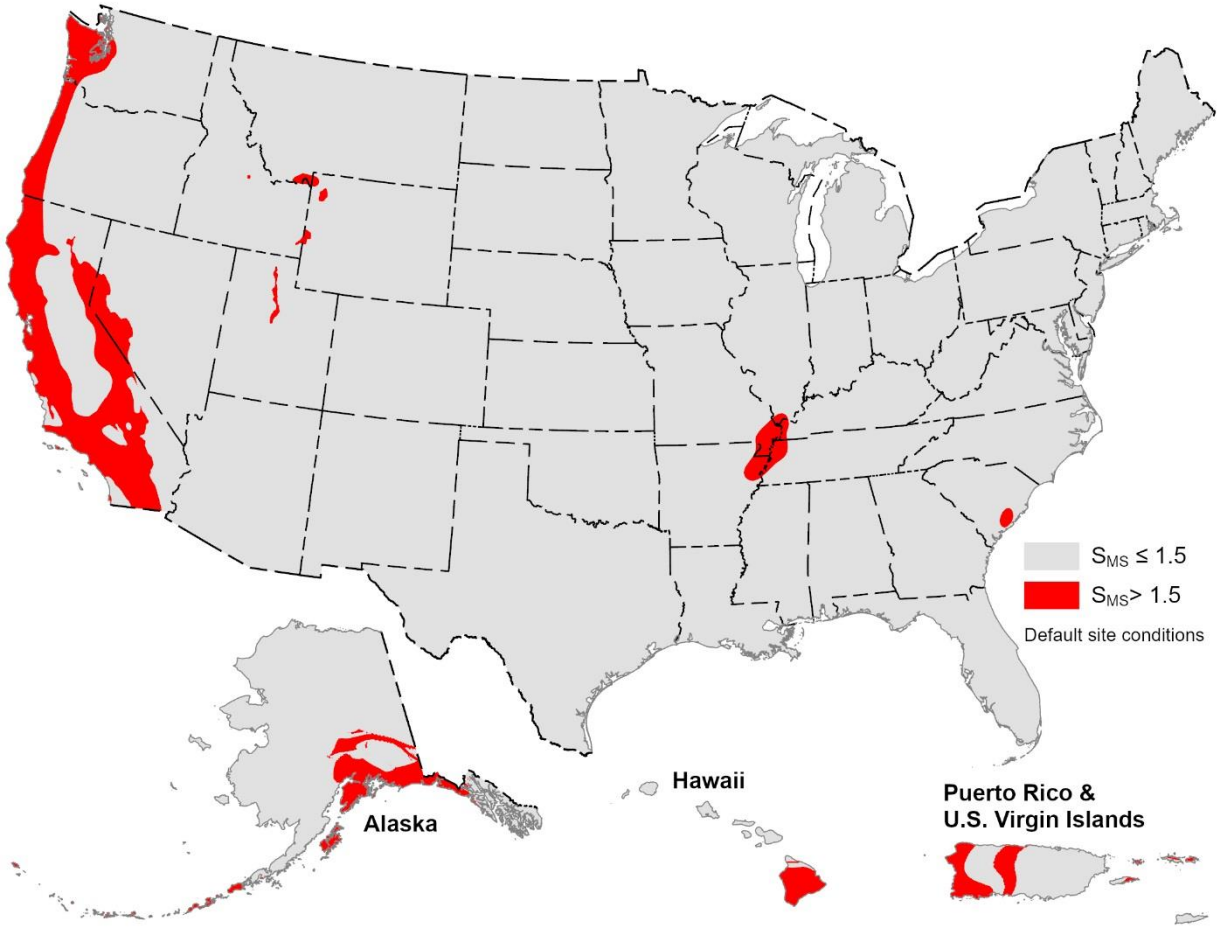

Figure A-1 **Map of U.S. states and territories showing areas of very high seismicity ($S_{MS} > 1.5g$) using ASCE/SEI 7-22 ground motions assuming default site conditions (image credit: USGS).**

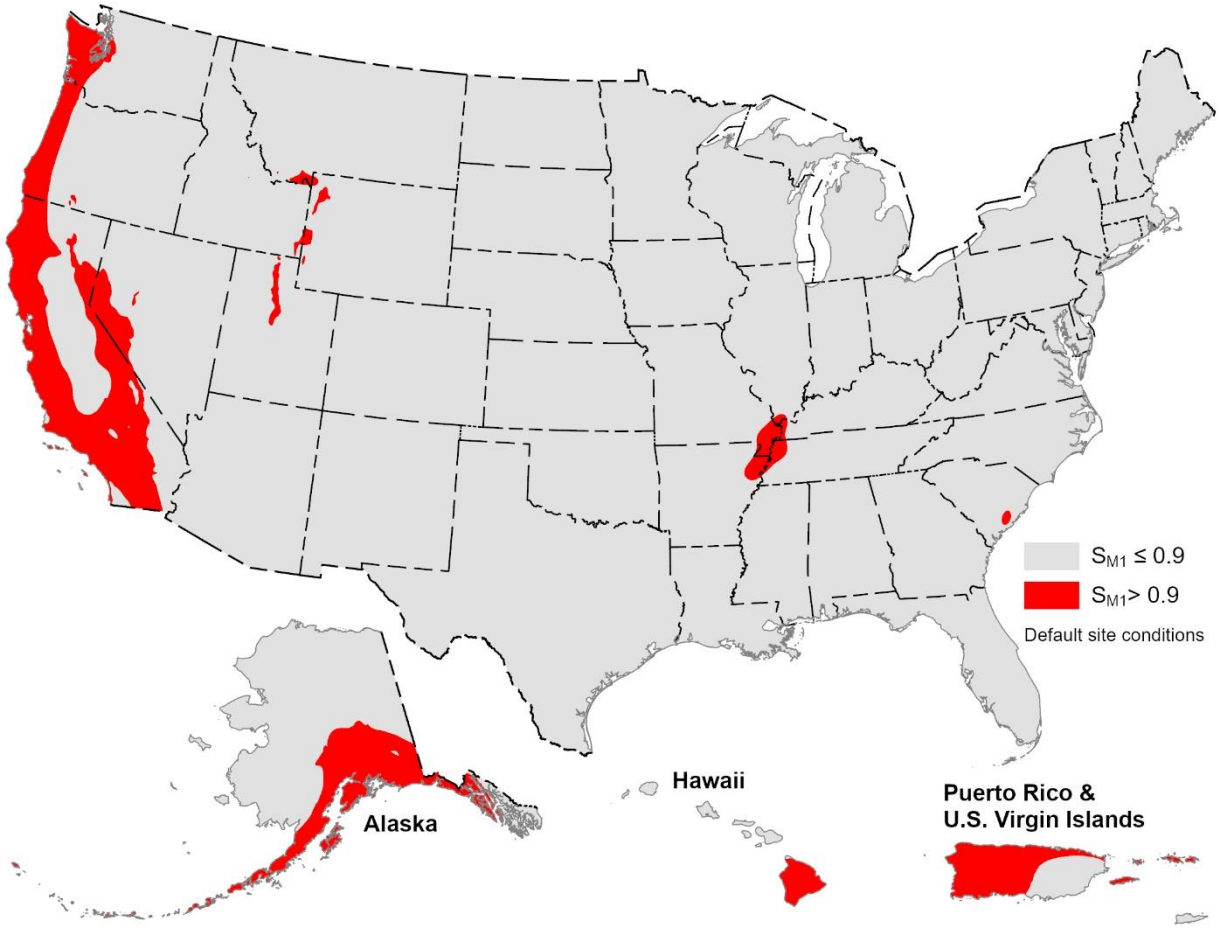

Figure A-2 **Map of U.S. states and territories showing areas of very high seismicity (S_{M1} > 0.9g) using ASCE/SEI 7-22 ground motions assuming default site conditions (image credit: USGS).**

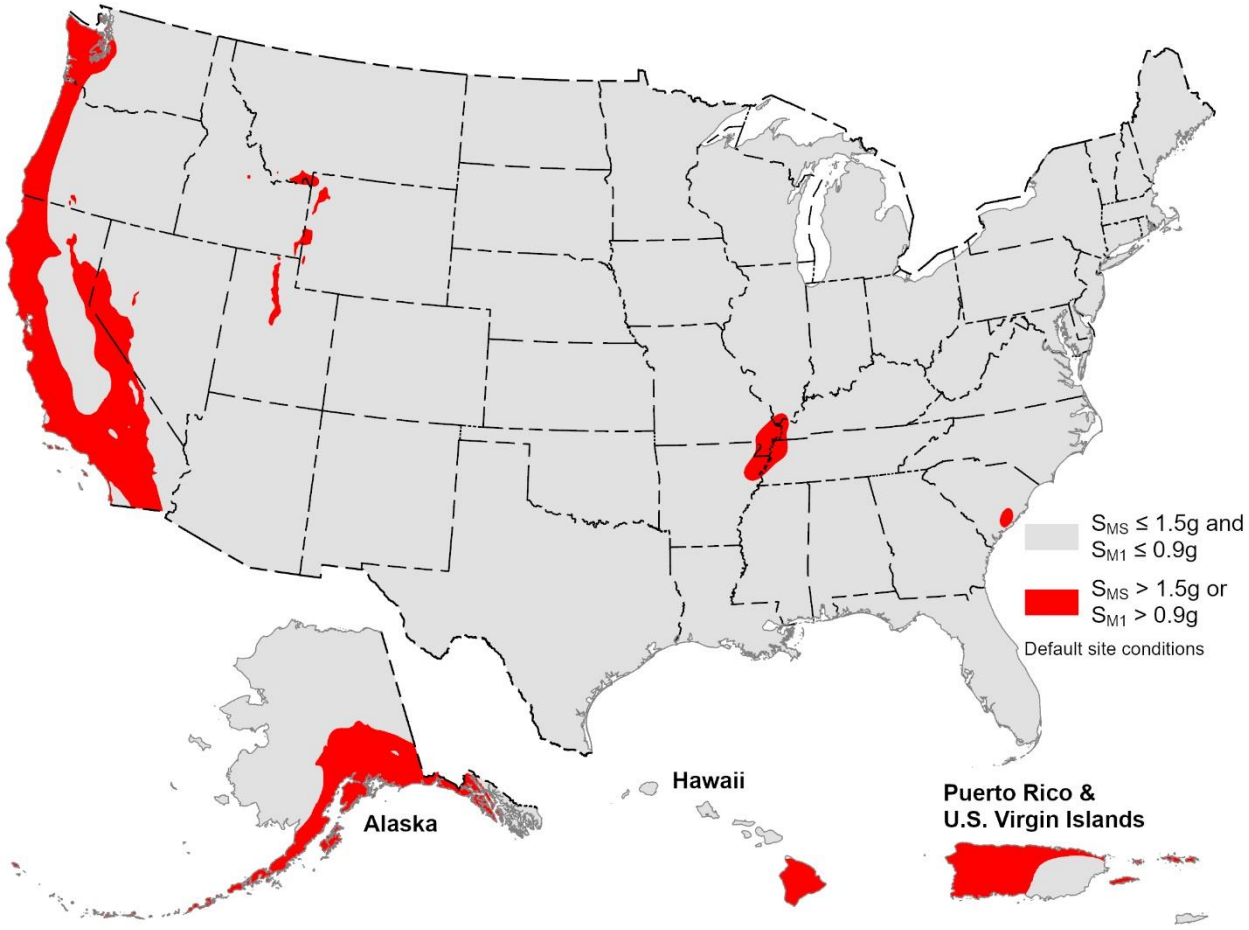

Figure A-3 **Map of U.S. states and territories showing areas of very high seismicity (S_{MS} > 1.5g or S_{M1} > 0.9g) using ASCE/SEI 7-22 ground motions assuming default site conditions (image credit: USGS).**

Appendix B: Sources of Overstrength

B.1 Details on System Overstrength

This appendix provides further detail on the studies of overstrength described in Chapter 2. Specifically, data and analysis behind the computed overstrengths of wood light-frame systems are provided in Section B.2, data and analysis of required strengths for wind loads in areas with very high seismic demands are provided in Section B.3, and an explanation of how the scope of this study was limited by considerations of the minimum base shear equations is provided in Section B.4.

B.2 Wood Light-Frame Buildings

B.2.1 SFRS Overstrength

The ratio of expected strength to nominal strength of wood shear walls of 1.07 cited in Chapter 2 is based upon the nominal strengths provided in the 2021 edition of the *Special Design Provisions for Wind and Seismic* (SDPWS), which is a companion document to the *National Design Specification for Wood Construction*. The previous edition of SDPWS (2015) included two sets of values for nominal strengths of shear walls, one for wind load and the other for seismic loads, and a single resistance factor ($\varphi = 0.8$) for both types of loads. The nominal strengths in the 2021 edition are mostly the same as the values given for wind loads in the 2015 edition, but the resistance factor for seismic loads has been reduced to 0.5, while the resistance factor for wind loads remains 0.8. The result of these changes is that the design strengths of shear walls for wind loads are mostly unchanged, but the design strengths for seismic loads have dropped by about twelve percent. This, in and of itself, does change the overstrength of a building designed under the new provisions from that for a building designed under the prior provisions. This study is focused on designs of the future; therefore, the SFRS overstrength is based upon the bias of 1.07 and resistance factor of 0.5. This could affect direct comparisons with past studies.

B.2.2 Non-SFRS Overstrength from Interior Walls and Partitions

The resistance to racking is provided by the sheathing (and fastening) on the walls; therefore, interior non-SFRS walls are lumped together, whether they are load bearing or not. The resistance to rocking does depend upon dead weight, and that is taken into account by discounting very short partitions. The minimum length adopted is four feet for a free-standing partition and three feet for a segment of a wall connected to other in-line segments by headers over openings, based on the following rational. Overturning resistance at the strength of the gypsum wallboard (GWB) is the limit state. Partitions do not have hold-downs, thus the resistance to uplift is provided by the story above. The weight of the partition itself and the weight of perpendicular partitions at corners are the limiting features.

The peak strength of nonstructural GWB is taken as 200 plf. The typical interior wall has GWB on both faces, thus the resistance is 400 plf. Using 10 psf for the weight of a nonstructural partition and a nine-foot floor-to-ceiling height, the wall would have to be 80 feet long for overturning resistance from the weight of the wall alone to resist overturning. Clearly, the resistance from the floor above is the key element.

Based upon single-story apartments in multistory buildings, in which gypsum concrete is a common floor element for acoustic control, a floor-ceiling weight of 20 psf is reasonable, and 5 psf is a reasonable lower bound for the weight of partitions on the floor above. With a nine-foot ceiling, the resistance required for overturning of a four-foot wall panel amounts to about 140 sf of floor (roughly a 12' × 12' area). Thus, four feet is a reasonable minimum length for a free-standing interior wall.

Wall segments separated by door openings in a continuous line can be shorter than four feet, because the GWB over the head of the opening provides additional overturning resistance. For common seven-foot-high doors and nine-foot ceilings, this allows a reduction from four feet to three feet without changing the required amount of floor area above to resist overturning. The same three-foot length is used for wall segments between a door opening and a right angle corner, where the perpendicular wall segment is at least four feet long.

The length of interior walls within 11 apartments units was surveyed in FEMA P-2139. Twenty-two additional apartments were surveyed, and the data combined for use here. All told, data were taken from nine projects located in California, Utah, Colorado, and Virginia. Some had very large floor plates (Figure B-1), while others were modestly sized (Figure B-2). Most of the projects were market rate rental apartments, as opposed to student housing or condominium, but the data of interest were generally consistent across all types.

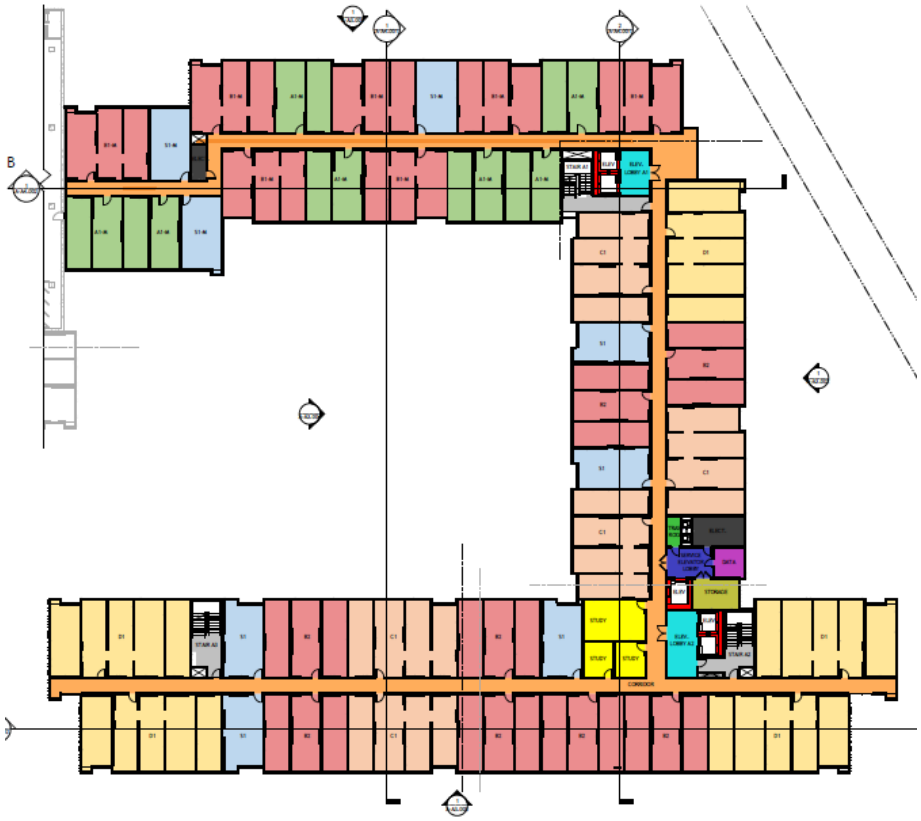

Figure B-1 Student housing plan.

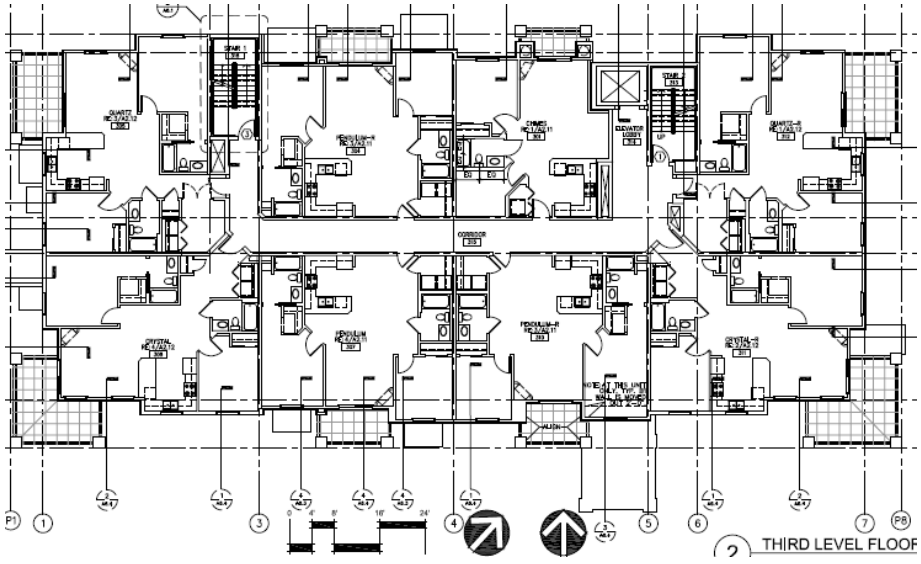

Figure B-2 Condominium plan.

Figure B-3 and Figure B-4 show a small studio unit and a large two-bedroom unit. The majority of the units were one-bedroom apartments.

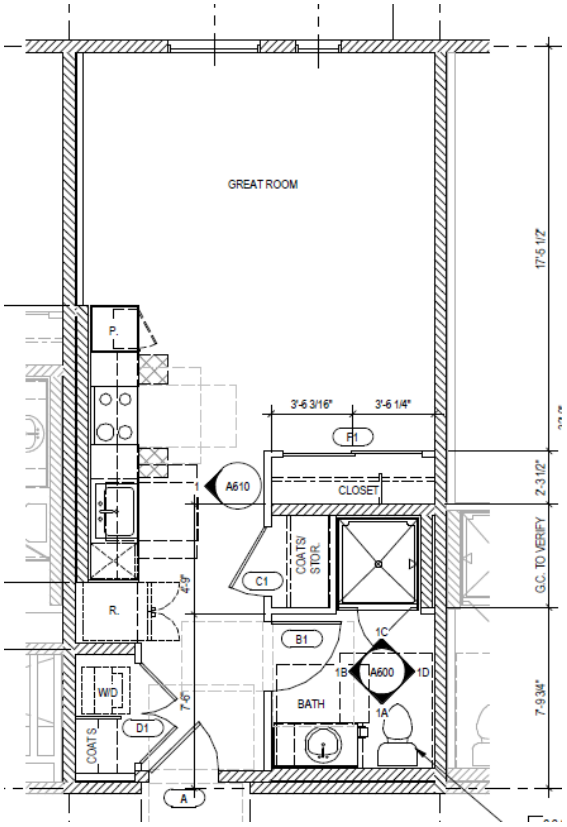

Figure B-3 Studio apartment.

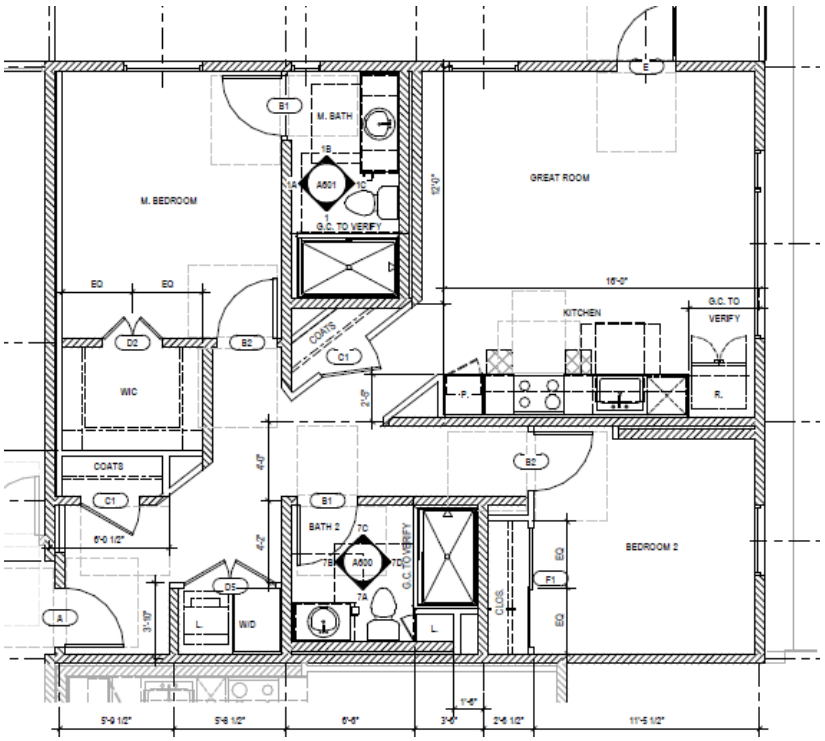

Figure B-4 Large two-bedroom unit.

For each unit, the lengths of interior walls in two orthogonal directions were recorded, as well as the width and depth of the unit. From this, total length of walls, the unit area, and its aspect ratio were computed. The walls at the perimeter of the unit, whether at the corridor, the exterior, or the party wall between units are not included in this data. Table B-1 shows the data for one sample unit.

Table B-1 Survey Data for One Apartment Unit

Unit, Project	Unit Area (ft^2); dimensions (ft); ratio	Total Wall Length (ft)	Wall Length per 100 ft^2	Wall Length (ft)	Direction
A1, Jefferson	513	31.7	6.18	3.8	x
width	19			4.1	x
depth	27			3.8	x
aspect	1.42			8.1	y
				8.1	y
				3.8	y

Because the aspect ratio is used to compute the lengths of the various types of perimeter walls, there were occasions that the width and depth were flipped to give a more realistic ratio of exterior to party wall lengths.

Table B-2 summarizes the data. Figure B-5 shows a plot of the data illustrating the relation between the size of the unit and the length of interior walls per unit of area. The table includes the prediction and error from a best fit line for the combined data. The open circles in the figure represent the 11 units originally surveyed for FEMA P-2139-2, and the solid dots represent the 22 units added here. The two sets of data do appear to represent one population; therefore, they are combined for this study. There is one outlier that has been removed for the final best fit line for the combined set; it is the point with a unit area of 960 sf and an amount of interior wall is well above the mean prediction. It is a student housing unit that is particularly densely packed. The outlier is unit 31 in Table B-2 and was removed for the final prediction equation. Table 2-2 includes summary data derived from Table B-2. It will be useful to recall that the mean area of the 33 units is 939 sf, which will sometimes be rounded to 1000 sf in examples presented in this appendix.

Table B-2 Summary of Interior Wall Survey

Unit	Area, sf	LF/100 sf	prediction	error
1	795	6.67	6.33	0.34
2	789	5.45	6.31	-0.86
3	826	5.45	6.45	-1.00
4	914	6.24	6.77	-0.53
5	1048	6.39	7.27	-0.88
6	1148	7.93	7.64	0.29
7	1181	8.04	7.76	0.28
8	1297	7.73	8.19	-0.46
9	1448	7.87	8.75	-0.88
10	1265	7.11	8.07	-0.96
11	1005	7.21	7.11	0.10
12	513	6.18	5.29	0.89
13	632	5.56	5.73	-0.17
14	872	7.44	6.62	0.82
15	1045	8.38	7.26	1.12
16	512	3.71	5.28	-1.57
17	624	5.08	5.70	-0.62
18	544	6.1	5.40	0.70
19	720	6.33	6.05	0.28
20	1080	9.27	7.39	1.88
21	616	5.39	5.67	-0.28
22	384	3.44	4.81	-1.37
23	828	6.07	6.45	-0.38
24	1292	8.47	8.17	0.30
25	1518	8.11	9.01	-0.90
26	1409	8.45	8.60	-0.15
27	1442	7.54	8.73	-1.19
28	1451	8.72	8.76	-0.04
29	448	4.46	5.05	-0.59
30	616	6.61	5.67	0.94
31	960	11.25	6.94	4.31
32	1006	6.79	7.11	-0.32
33	767	5.46	6.23	-0.77

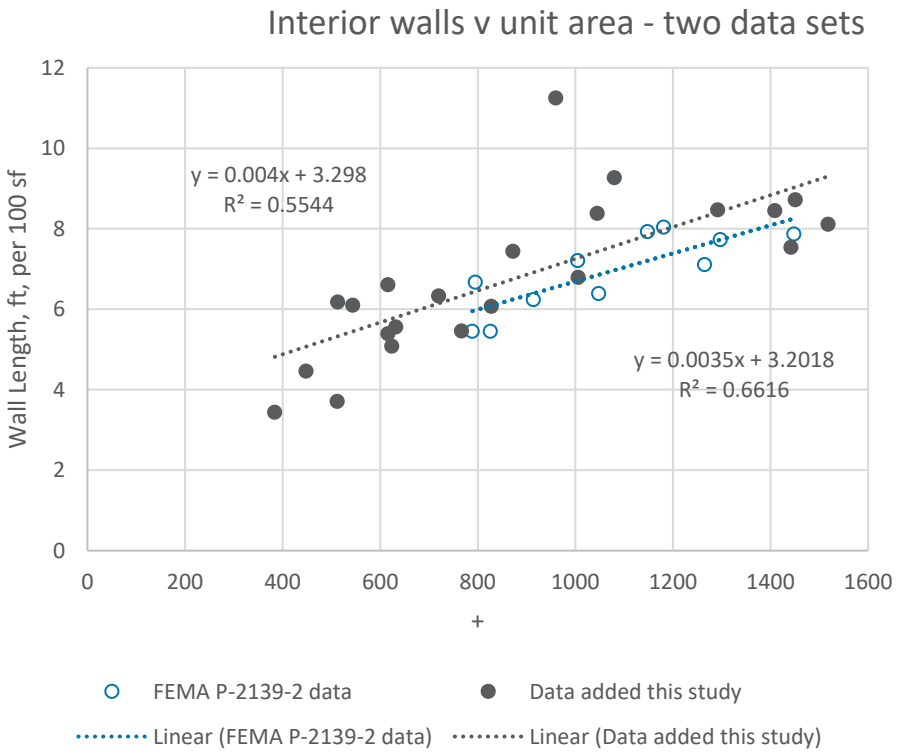

Figure B-5 Plot of length of interior walls per unit area versus the area of the unit.

The final set of data along with 15 percent error bands are shown in Figure B-6. The strength of sheathing on interior walls is based upon 1/2" GWB on each face, and as explained in Section 2.3.2, 90 percent of that strength is used for addition to the capacity of the SFRS. That amounts to 360 pounds per lineal foot of an interior wall. The most convenient way to express the combination of strengths is to express the strength as a resistance per unit floor area. The overstrength computed from interior walls must be divided between the two principal directions of the building; as explained in Section 2.3.2, no basis for a bias in direction was found, so the total strength is divided in half to represent strength available in one direction. Figure B-7 shows the overstrength from sheathing on interior walls in wood light-frame apartment buildings, expressed in pounds per square foot of floor area, including the central trend with ranges 15 percent above and below.

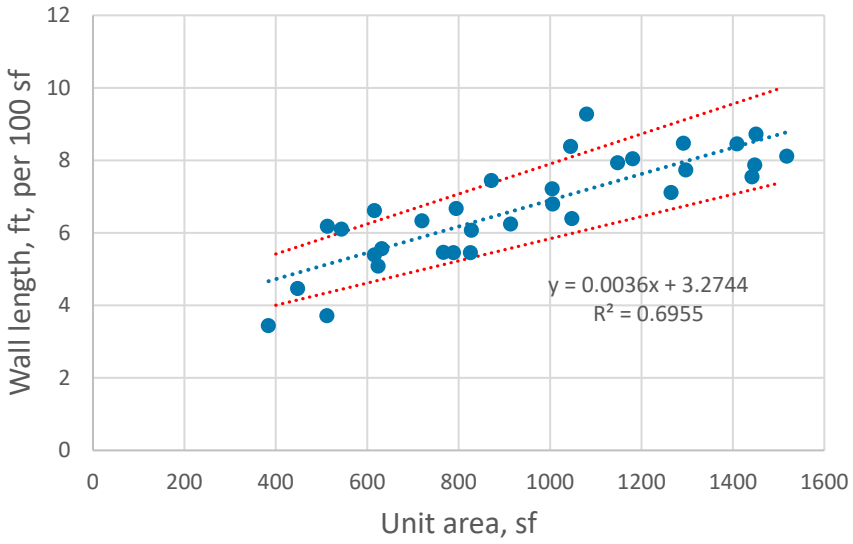

Figure B-6 **Final data for relation between unit area and length of interior walls, with regression line and 15 percent error bands.**

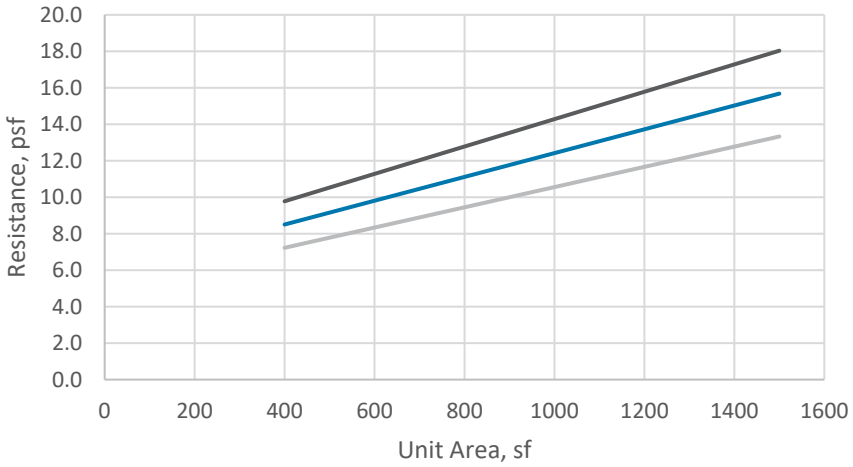

Figure B-7 **Strength from interior walls; central trend with upper and lower ranges.**

B.2.3 Non-SFRS Overstrength from Perimeter Walls

Perimeter walls include unit demising walls (party walls), corridor walls, and exterior walls. Each type has a different strength. The total length of perimeter walls is a function of the unit area and the unit aspect ratio. Figure 2-8 is a plot of the aspect ratio for the units surveyed—the mean value is 1.3, with a range from 0.7 to 2.1. Table B-3 shows the length of exterior walls as a function of unit area and unit aspect ratio.

Table B-3 Lineal Feet of Perimeter Wall Per 100 sf of Unit Area

Unit area	Aspect ratio			
sf	0.9	1	1.3	1.7
400	20.0	20.0	20.2	20.7
500	17.9	17.9	18.0	18.5
600	16.4	16.3	16.5	16.9
700	15.1	15.1	15.2	15.7
800	14.2	14.1	14.3	14.6
900	13.4	13.3	13.4	13.8
1000	12.7	12.6	12.8	13.1
1100	12.1	12.1	12.2	12.5
1200	11.6	11.5	11.6	12.0
1300	11.1	11.1	11.2	11.5
1400	10.7	10.7	10.8	11.1
1500	10.3	10.3	10.4	10.7

The three types of perimeter walls have different strengths, and it is necessary to work with archetype building plans (not unit plans) to allocate the total perimeter to each of the three types. The most common plan is a double-loaded corridor, and a simplified and doubly symmetric version of that is adopted for the archetype configuration. A plan for an eight-unit floor plan is shown in Figure 2-7. The analysis has considered plans ranging from four to 24 units on a floor. Table B-4 shows the fraction of total perimeter belonging to each class of wall as a function of the number of units and the unit aspect ratio, using the same aspect ratio of all units on a floor. The values shaded beige are used for the central trend, the values shaded in green are used for the upper range, and the values shaded in blue are used for the lower range.

Table B-4 Share of Total Perimeter for Each Type of Perimeter Wall for Various Plan Sizes and Unit Aspect Ratios

Plan	Wall	Unit aspect ratio							
Size	Type	0.7	0.9	1	1.1	1.3	1.5	1.7	2
4 units	ext	0.500	0.500	0.500	0.500	0.500	0.500	0.500	0.500
	cor	0.294	0.263	0.250	0.238	0.217	0.200	0.185	0.167
	dem	0.206	0.237	0.250	0.262	0.283	0.300	0.315	0.333
	sum	1.000	1.000	1.000	1.000	1.000	1.000	1.000	1.000
8 units	ext	0.397	0.382	0.375	0.369	0.359	0.350	0.343	0.333
	cor	0.294	0.263	0.250	0.238	0.217	0.200	0.185	0.167
	dem	0.309	0.355	0.375	0.393	0.424	0.450	0.472	0.500
	sum	1.000	1.000	1.000	1.000	1.000	1.000	1.000	1.000
12 units	ext	0.363	0.342	0.333	0.325	0.312	0.300	0.290	0.278
	cor	0.294	0.263	0.250	0.238	0.217	0.200	0.185	0.167
	dem	0.343	0.395	0.417	0.437	0.471	0.500	0.525	0.556
	sum	1.000	1.000	1.000	1.000	1.000	1.000	1.000	1.000
16 units	ext	0.346	0.322	0.313	0.304	0.288	0.275	0.264	0.250
	cor	0.294	0.263	0.250	0.238	0.217	0.200	0.185	0.167
	dem	0.360	0.414	0.438	0.458	0.495	0.525	0.551	0.583
	sum	1.000	1.000	1.000	1.000	1.000	1.000	1.000	1.000
20 units	ext	0.335	0.311	0.300	0.290	0.274	0.260	0.248	0.233
	cor	0.294	0.263	0.250	0.238	0.217	0.200	0.185	0.167
	dem	0.371	0.426	0.450	0.471	0.509	0.540	0.567	0.600
	sum	1.000	1.000	1.000	1.000	1.000	1.000	1.000	1.000
24 units	ext	0.328	0.303	0.292	0.282	0.264	0.250	0.238	0.222
	cor	0.294	0.263	0.250	0.238	0.217	0.200	0.185	0.167
	dem	0.377	0.434	0.458	0.480	0.518	0.550	0.577	0.611
	sum	1.000	1.000	1.000	1.000	1.000	1.000	1.000	1.000

No attempt at a statistical analysis of this data is made; the trends are selected as follow. The central values are selected for the 12-unit building with the mean aspect ratio of 1.3, which is the mean aspect ratio. The central values are highlighted in beige in Table B-4. The low and high range for the values are highlighted in blue and green, respectively. The extremes of reported aspect ratios were not used; 0.9 and 1.7 are slightly more extreme than one standard deviation each way from the mean aspect ratio from the survey data. Extending the number of units per story beyond 24 does not result in much difference in the results. Table B-5 summarizes these values.

Table B-5 Share of Perimeter Length for Each Wall Type

	Central	Low	High
Exterior	0.312	0.238	0.500
Corridor	0.217	0.185	0.263
Demising	0.471	0.237	0.577

The unit strength of the corridor walls is based upon one layer of 5/8" GWB directly attached to one face and two layers of 5/8" attached to the opposite face with acoustic isolation clips (commonly called a resilient channel, although the shape is not actually a channel), a common detail to provide both required fire resistance and acoustic isolation. The strength of a single layer of 5/8" GWB is 250 plf. There is little data available for the strength provided by sheathing attached via the resilient channel, and it is common practice in design to ignore any resistance provided by that detail. However, at least one set of non-public tests indicates that the resistance of the double layer on resilient channels over cold-formed steel studs is equivalent to a single layer directly attached to cold-formed steel studs. For the purpose of this study, that approximation is used, even though the framing material is different. (For minimal fastening, the limit state is the fastener cutting through the GWB, so not much difference is expected.) Thus, the basic strength used here is 500 plf. This is reduced by the peak shaving factor of 0.9 and the bi-directional factor of 0.5. One further reduction is to subtract a four-foot length for access into the apartment unit. This last factor obviously depends on the unit size and the aspect ratio. In order to avoid unjustified complexity, one factor for this reduction is selected, based upon the mean area of 939 sf and the mean aspect ratio of 1.3. That yields a length of corridor wall of 26.9 feet and subtracting a four-foot opening produces a further reduction factor of 0.85. The net result is that the strength of the corridor wall is 191.5 plf in each direction.

The unit strength of the party wall is simpler. There are no openings. The walls can be constructed the same as the corridor wall, but there are two more common details: parallel walls separated by an inch, with no sheathing in the interstitial space, and a single wall on a wide plate with the studs staggered so that each stud has sheathing on only one face. All three options give the same result a single layer of 5/8" GWB effective for the unit on one side of the wall. Beginning with the 250 plf basic strength, the result is 112.5 plf in each direction.

The exterior wall construction used in this analysis includes 5/8" GWB (250 plf) on the interior face of the wall, 7/16" OSB with minimum nailing (600 plf basic strength) on the exterior face, and an exterior finish. The strength varies significantly based upon the exterior finish material. Given its preponderance in current construction, stucco is selected as the base case, and straight board siding is included as an alternate, with basic strengths of 1000 plf and 200 plf, respectively.

It is important to consider the effect of openings in the exterior walls. Two buildings were examined carefully to form a basis for this effect. Figure B-8 and Figure B-9 show one elevation for each building.

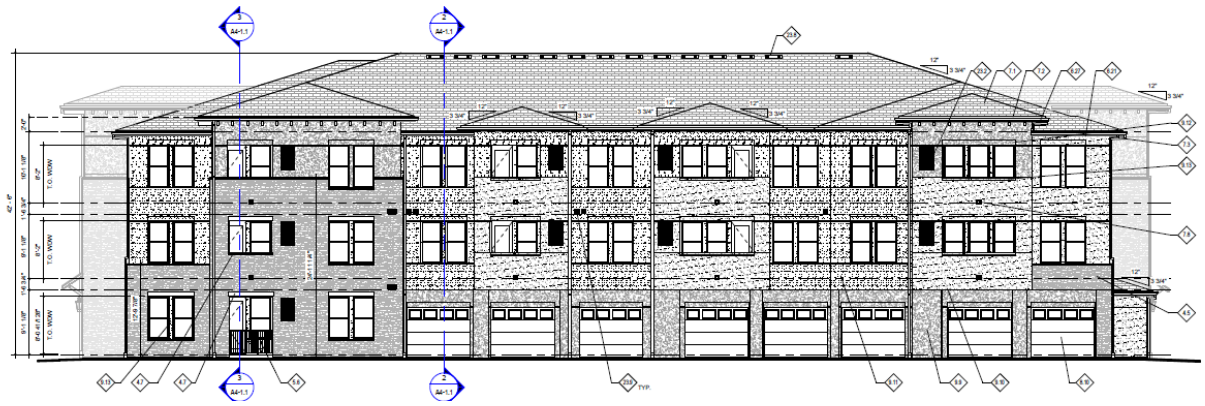

Figure B-8 Elevation of apartment with first-floor parking.

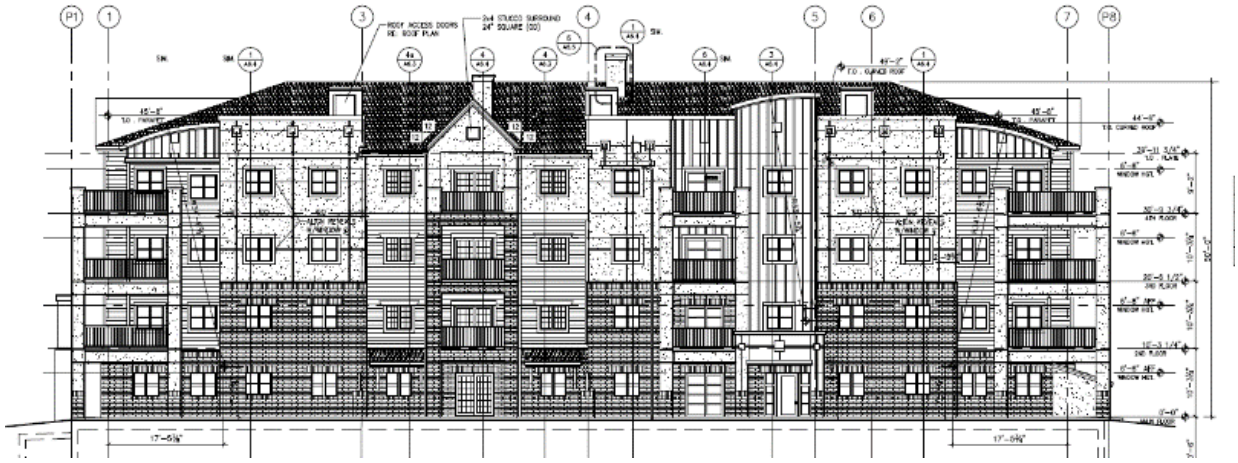

Figure B-9 Elevation of condominium with small windows.

Even though the garage door openings appear to dominate the building shown in Figure B-8, the upper stories have nearly as much openings in the exterior walls, in part because the garage doors exist only on one face of the building. The totals are 52 percent open at the first story and 50 percent open at the typical story. (The one face with the garage doors is 62 percent open.) The openings in the building shown in Figure B-9 comprise 31 percent of the exterior perimeter. For this study a range of openings in the exterior wall from 30 percent to 70 percent is used, with 50 percent

open as the central trend. The basic unit strength for the stucco-covered exterior wall is 0.9 × 1000 + 600 + 0.9 × 250 = 1725 plf, which is reduced to 431 plf considering the two-way factor and the 50 percent open factor.

The central trend for strength contributed from the unit perimeter walls is derived thus:

1. Total perimeter for A = 900 sf and aspect ratio = 1.3 from Table B-3 is 13.4*900/100 = 121 lf
2. Shares for exterior, corridor, and party walls for a 12 unit building with unit aspect ratio = 1.3 from Table B-4 are 0.312, 0.217, and 0.471, respectively
3. Strength from exterior wall = 121 × 0.312 × 431 / 900 = 18.1 psf
4. Strength from corridor wall = 121 × 0.217 × 191 / 900 = 5.6 psf
5. Strength from party walls = 121 × 0.417 × 112 / 900 = 7.1 psf

The total strength from the perimeter walls for the stated conditions is 30.8 psf. For the same size unit, the strength from the interior walls is 11.8 psf, thus the total strength from non-SFRS wall is 42.6 psf.

Figure B-5 through Figure B-7 show that the length of interior wall per unit area goes up as the unit size increases. Table B-3 shows that the length of perimeter wall per unit area goes down as the unit size increases. To an extent these trends offset each other, as shown in Figure 2-9.

The number of units per story and the unit aspect ratio are important parameters in the development of the non-SFRS overstrength, but variations in their values do not have a particularly significant impact on the final strength, as shown in Figure 2-10 and Figure 2-11. The fraction of openings in the exterior wall is a significant variable, as shown in Figure 2-12 and Figure 2-13.

B.2.4 Total Overstrength for Wood-Frame Apartment Buildings

As shown in Section 2.3.1, the overstrength ratio for the SFRS alone is independent of design ground motion (see Figure 2-3). All the non-SFRS strength is essentially independent of the design ground motion level, which means that the total overstrength ratio decreases as the design ground motion increases. Furthermore, the overstrength ratio decreases as the number of stories increases. Figure 2-14 through Figure 2-16 show the variation in the overstrength ratio for the wood apartment buildings with the numbers of stories and the level of short-period spectral acceleration.

B.2.5 Overstrength for Wood-Frame Commercial Buildings

Two-to-four story wood-frame commercial buildings are idealized in this study as multi-tenant office buildings. That allows the same form of archetype floor plan as used for apartment buildings. The significant differences are:

- Average unit size is 2000 sf,
- Average unit aspect ratio is 1.0,

- Either four or eight units per story, and
- Partitions interior to the unit do not connect to the structure above.

The similarities are that the exterior, corridor, and party walls are the same as developed for the apartment building. Therefore, the strengths of the perimeter walls are the same as developed in Section B2.4. The larger unit size leads to a smaller length of perimeter wall per square foot. When combined with the lack of strength from interior partitions, the non-SFRS strength for average conditions is 25 psf, as opposed to 40 psf used for the average apartment building. Figure 2-17 shows the variation with number of stories and ground motion level, and Figure 2-18 shows the range of values for a three-story building.

One-story commercial buildings can serve a wide variation of occupancies, and the architectural layouts vary much more than the common apartment buildings. Therefore, the assumed non-SFRS contribution is small, but because the only mass contributing to the design demand is from the roof, the overstrength ratio is still fairly high, as shown in Figure 2-19.

B.2.6 Drift for Wood-Frame Shear Walls

The majority of wood light frame buildings are under five stories. ASCE/SEI 7 limits the computed drift ratio for buildings up through four stories to 2.5 percent of the height, given the design ground motion and the specified allowance for inelastic response. At five stories, the ASCE/SEI 7 limit drops to 2 percent. The methodology for computation of drift for wood-frame shear walls is specified in the SPDWS. It requires inclusion of deformation at the nail connection of panel to framing (referred to as nail slip), the in-plane shear deformation of the panel itself, the flexural deformation from strain in the vertical boundary members of the shear wall, and an allowance for deformation at the connection of the shear wall to its base (either the foundation or the story below). SPDWS tabulates a stiffness value for the first two components in the same table that defines the nominal strength of wood shear walls for various panel materials and thicknesses and nail sizes and spacing. Table B-6 is an extract of those values, plus the drift computed applying a deflection amplification factor of 4 for walls loaded to their capacity.

Table B-6 Nail Slip and In-Plane Shear Drift of Wood Shear Walls

Panel Thickness (in.)	Size of Nail (common)	Spacing of Nails (in.)	Nominal Shear (lb./ft)	Shear Stiffness (kips/inch)		Drift Ratio, including C_d = 4 and φ = 0.5	
				OSB	Plywood	OSB	Plywood
7/16	8	6	670	15	11	0.7%	1.0%
7/16	8	4	980	22	14	0.7%	1.2%
7/16	8	2	1540	42	21	0.6%	1.2%
15/32	10	6	870	22	14	0.7%	1.0%
19/32	10	6	950	19	13	0.8%	1.2%
19/32	10	4	1430	26	16	0.9%	1.5%
19/32	10	2	2430	48	22	0.8%	1.8%

The table shows that heavily loaded plywood walls come close to the drift limit for five story buildings, but oriented-strand board (OSB) walls do not.

The flexural contribution to drift is generally less than the nail slip and shear contribution, but it does depend on the height-to-length ratio of the panel. If one assumes the stress due to the design seismic load in the end posts at the first story of a five story building is 500 psi and use a modulus of 1600 ksi, the strain will be 0.000313. Applying the C_d of 4, the additional drift is 0.5%, 0.25%, and 0.125% for walls with height-to-length ratios of 2, 1, and 0.5, respectively. If one uses an allowance of 1/4" for anchorage device deformation, the added drift also depends on the height-to-length ratio of the panel, and it amounts to 0.4%, 0.2%, and 0.1% for the same aspect ratios.

All told, the drift ratio for a heavily loaded plywood wall can exceed the 2 percent limit, but the drift ratio for a heavily loaded OSB wall will not exceed the 2 percent limit until the panel height-to-length ratio exceeds 2, below which SDPWS provisions for derating the usable capacity of the wall kick in, to account for that flexibility. Therefore, the overstrength computations for this study do not have a component for additional strength due to drift control in the design of tall (five stories) wood light-frame buildings. There are two circumstances in practice where designs are likely controlled by drift: the use of heavily loaded plywood shear panels, and the use of continuous steel rods for the tension chord in multi-story rods.

B.3 Wind Load Effect on Overstrength

Wind loading, if it's greater than the design seismic loading, can be a potential source of overstrength. This issue was investigated for sites in California in an unpublished study by Magnusson Klemencic Associates, and it was shown through two independent studies not to be the case for very high seismic locations. The first study was conducted for buildings with varying:

- Seismic-force-resisting systems (*R* factors),
- Building plan dimensions,
- Building heights,
- Building density, and
- Building location.

Figure B-10 highlights the results of one of the 48 scenarios studied, confirming that wind loading doesn't contribute more overstrength than seismic design loading. Blue dots indicate the ratio of $C_{s,wind}/C_{s,seismic}$ is less than 1.0, signifying that seismic demands govern the design at that location. This figure shows all locations are governed by seismic demands for the given scenario. The same was true for all other scenarios studied in the locations of very high seismic demand. Red dots indicate specific cities for reference.

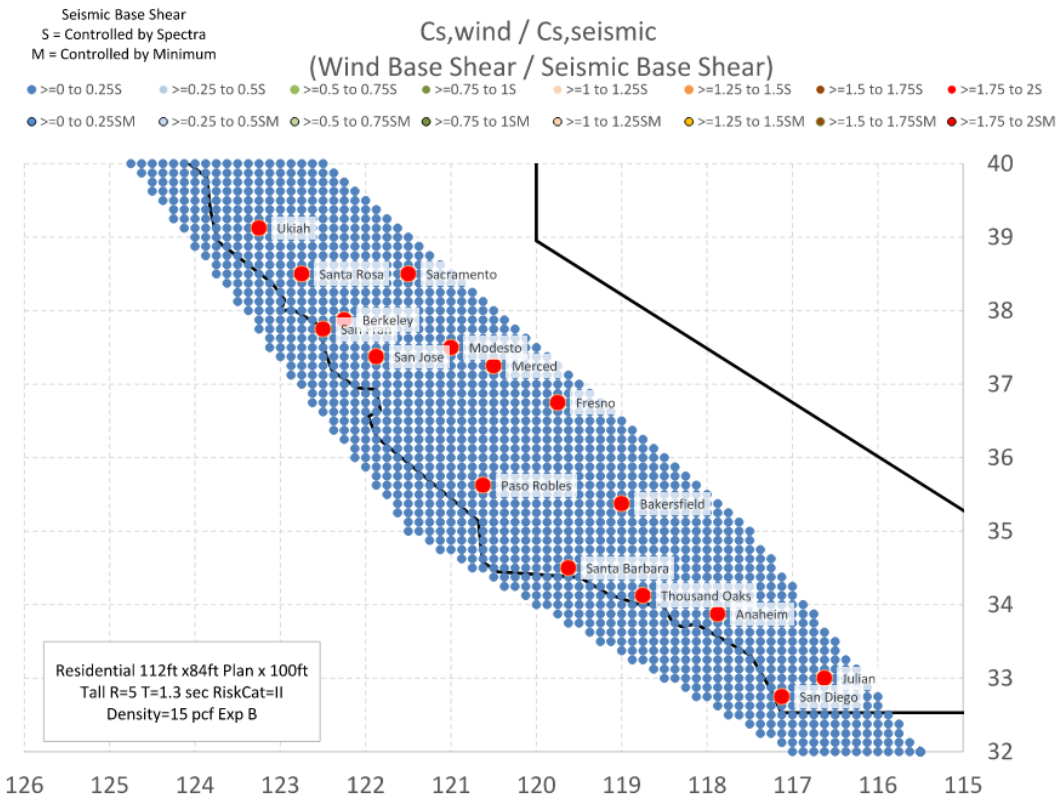

Figure B-10 Ratio of $C_{s,wind}/C_{s,seismic}$ for California (figure credit: Magnusson Klemencic Associates.)

The second study developed a spreadsheet that showed the resulting controlling *R* factor from a variety of user inputs similar to those listed above. These results also confirmed that wind loading doesn't contribute overstrength more than the seismic design loading.

B.4 Minimum Base Shear Effect on Overstrength

When either of the two ASCE/SEI 7 minimum base shear equations (Eq. 12.8-6 or Eq. 12.8-7) control the design of the SFRS, the resulting design has an overstrength that exceeds the overstrength resulting from a design that is governed by the design response spectrum equations (Eq. 12.8-1 to Eq. 12.8-5).

In very high seismic regions, the minimum base shear equations govern the seismic design when the periods are large, which results in increased SFRS overstrength relative to designs governed by Equation 12.8-1 to Equation 12.8-5.

For Site Class D sites, using the ASCE/SEI 7-16 formulation of the equations, the period for which Eq. 12.8-7 governs over Equation 12.8-4 is given by:

$$T = 4/3(F_v)$$

where F_v is the long-period site coefficient. However, F_v is no longer used in ASCE/SEI 7-22. In ASCE/SEI 7-16, F_v is given as 1.7. However, this value cannot be used directly. A 1.5 penalty factor is assigned to a design that does not incorporate a site-specific ground motion hazard analysis, resulting in an effective F_v of 2.55. In ASCE/SEI 7-16 Section 21.3, F_v is given as 2.5.

For a sample site in Millbrae, California, ASCE/SEI 7-22 gives an S_{M1} of 2.79 and an S_1 of 1.02, which results in an effective F_v of 2.73. These values will vary by location. An estimated value for an effective F_v of 2.5 is used to determine the period, *T*, for which Equation 12.8-7 controls:

$$T = 4/3(F_v) = 4/3(2.5) = 3.3\text{s}$$

The period, *T*, for which Equation 12.8-6 governs is more complicated. *T* is a function of the values of S_s and S_1 for a site and the building *R* factor. For Site Class D sites and using an effective F_v of 2.5 as described above, *T* is given as:

$$T = 56.8 \times S_1/(S_s \times R)$$

For typical ratios of S_s/S_1 and values of *R*, this equation results in the ranges of *T* shown in Table B-7.

Table B-7 Controlling Period, *T*, Based on ASCE/SEI 7-22 Equation 12.8-7

S_s/S_1	$R = 5$	$R = 6$	$R = 8$
2.25	5.0	4.2	3.2
2.5	4.5	3.8	2.8
2.75	4.1	3.4	2.6
3	3.8	3.2	2.4

For periods greater than approximately 2.5 s and an *R* of 8 design, the seismic design will be controlled by the Equation 12.8-6. For periods greater than 3.2 s and an *R* of 5 or 6 design, the seismic design will be controlled by Equation 12.8-6. Both period values are less than the period of 3.3 s associated with Equation 12.8-7. For this study only archetypes with periods less than these values were evaluated.

Appendix C: Numerical Modeling Process

C.1 Introduction

In Chapter 4 and Chapter 5, results from a series of analyses using numerical models for wood and non-wood systems are presented. Chapter 3 explains the underlying engineering those analyses were based upon, as well as how the results are then processed. Specifically, Chapter 3 provides a description of each of the components of those analyses: the collapse surfaces generated from incremental dynamic analyses, the resulting *ACMR*, and probability of collapse conditioned on S_{MT}. This appendix summarizes the process for generating *ACMR* and probability of collapse in a step-by-step manner.

C.2 Analytical Modeling Process

C.2.1 Collapse Surface Development

1. Develop a family of backbone curves, or capacity boundaries as shown for example in Figure C-1. These represent the same archetype (type of seismic-force-resisting system and number of stories) at various normalized strengths (V_{max}/W). For wood systems characterized using a multiple-degree-of-freedom model, the Equivalent Lateral Force (ELF) procedure of ASCE/SEI 7 is used to distribute the normalized peak base shear (V_{max}/W) vertically to individual stories. For non-wood systems characterized using an equivalent single-degree-of-freedom (eSDOF) model, the V_{max}/W is assigned directly as the lateral strength of the eSDOF model.

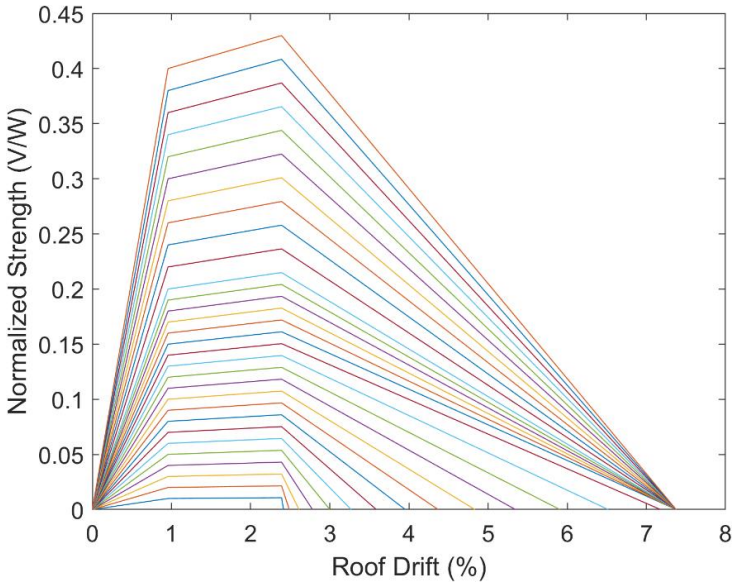

Figure C-1 Example of a backbone family for a 9-story steel SMF archetype.

2. Perform an incremental dynamic analysis (IDA) for each of the backbones in a given family.
3. Adjust the IDAs such that the individual ground motion curves are monotonically increasing. This step ensures that there is a unique value of spectral acceleration, S_a, at a given drift level. An example adjusted set of IDA curves are shown in Figure C-2.
4. Interrogate the IDA at discrete drift ratios (*DR*'s) to get non-simulated collapse spectral accelerations at the archetype's ASCE/SEI 7 design period, S_{CT}, from each of the 44 ground motions. These points are shown as black dots in Figure C-2.
5. Determine collapse spectral acceleration at the incipient collapse drift level, DR_{IC}. DR_{IC} is defined as the peak drift ratio (*DR*) at which either the IDA flattens, the analysis ceased to converge (typically at very large drifts), or a maximum drift value was reached. These points are shown as open circles in Figure C-2. The median DR_{IC}, $\widehat{DR}_{IC}$, is the median value for the 44 FEMA P-695 ground motions.

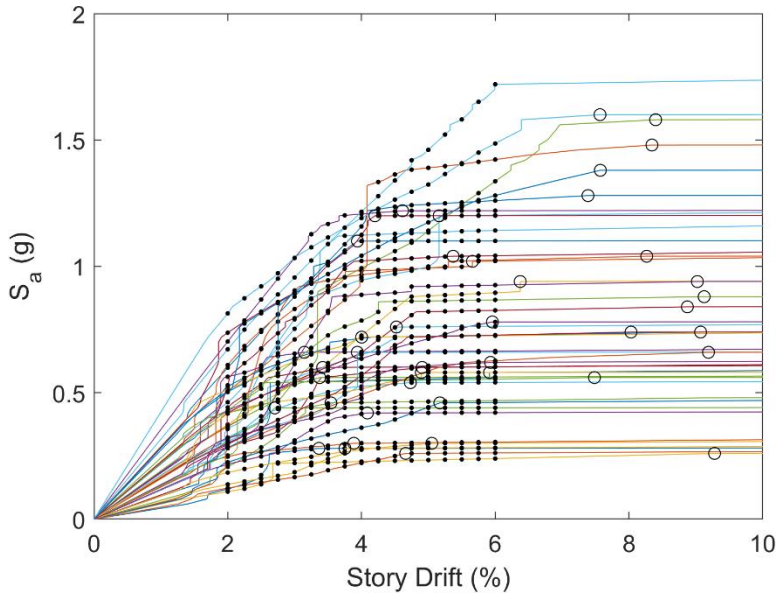

Figure C-2 Example of IDA results for a 9-story steel SMF archetype with normalized strength $V_{max}/W = 0.12$.

6. Calculate the median of the 44 S_{CT} values, $\hat{S}_{CT}$, at each of the discrete values of V_{max}/W in the family of backbones at each *DR* from step 4.
7. Fit a surface with independent variables V_{max}/W and *DR* and dependent variable $\hat{S}_{CT}$ with a polynomial of the form:

   $$\hat{S}_{CT} = A \times (V_{max}/W) + B \times (V_{max}/W)^2 + C \times DR + D \times DR^2 + E \times (V_{max}/W) \times DR + F \times (V_{max}/W)^2 \times DR + G \times (V_{max}/W) \times DR^2 + H \times (V_{max}/W)^2 \times DR^2 + I$$

8. Enforce a plateau if the surface dips at high V_{max}/W and *DR*.

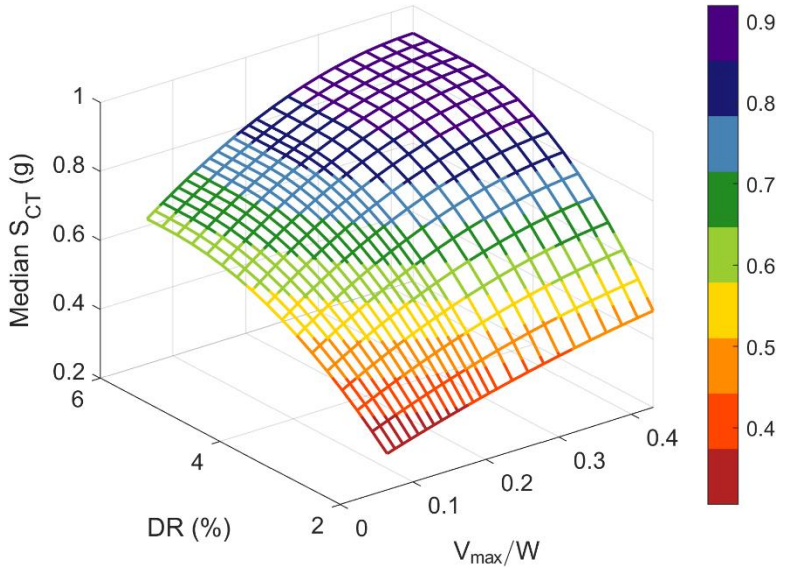

Figure C-3 Example of a collapse surface from a 9-story steel SMF archetype with a plateau.

C.2.2 Adjusted Collapse Margin Ratio and Probability of Collapse

1. Choose discrete values of S_{MT}, the spectral acceleration at the ASCE/SEI 7 design period, $T = C_u T_a$, due to MCE_R shaking.

2. Calculate V_{max}/W for each value of S_{MT} for a given risk category and overstrength with Equation 3-8:

$$\frac{V_{max}}{W} = \frac{\frac{2}{3} S_{MT} \Omega}{R / I_e}$$

3. Determine a relationship between median DR_{IC}, DR_{IC}, and V_{max}/W. For wood systems, an exponential fit was used. For non-wood systems, a linear fit was used.

4. Calculate the ductility factor, μ_T, from Equation 3-3 using the calculated DR_{IC} from step 3 and $\delta_{y,eff}$ as defined in Chapter 3 and in FEMA P-695:

$$\mu_T = \frac{DR_{IC}}{\delta_{y,eff}}$$

5. Calculate spectrum shape factor (*SSF*) using the ASCE/SEI 7 design period and ductility factor, μ_T, by interpolating in Table 3-2 or Table 3-3 for Far-Field or Near-Field record sets, respectively.

6. Use the collapse surface to calculate $\hat{S}_{CT}$ at chosen discrete *DR*'s and calculated V_{max}/W values form step 2.

7. Calculate collapse margin ratio (*CMR*) using Equation 3-5 for each $\hat{S}_{CT}$ from step 6 (at each V_{max}/W and *DR* pair):

$$CMR = \frac{\hat{S}_{CT}}{S_{MT}}$$

8. Calculate *ACMR* using Equation 3-6:

$$ACMR = SSF \times CMR$$

9. Find acceptable *ACMR* for each chosen discrete *DR* using interpolation within Table 3-1 and the β value prescribed in Table 3-6. Consider only the 10% collapse probabilities for Risk Category II and 2.5% collapse probability for Risk Category IV.

10. Calculate probability of collapse conditioned on S_{MT} using a cumulative normal probability distribution for a fragility curve normalized by S_{MT} with a median of *ACMR* and a distribution of β using Equation 3-7:

$$P[Col \mid S_{MT}] = \Phi\left[\frac{\ln(1) - \ln(ACMR)}{\beta}\right]$$

Generic fragility curves, one as a function of S_a and one as a function of S_a normalized by S_{MT}, are presented in Figure C-4 to show the relationship between the key parameters.

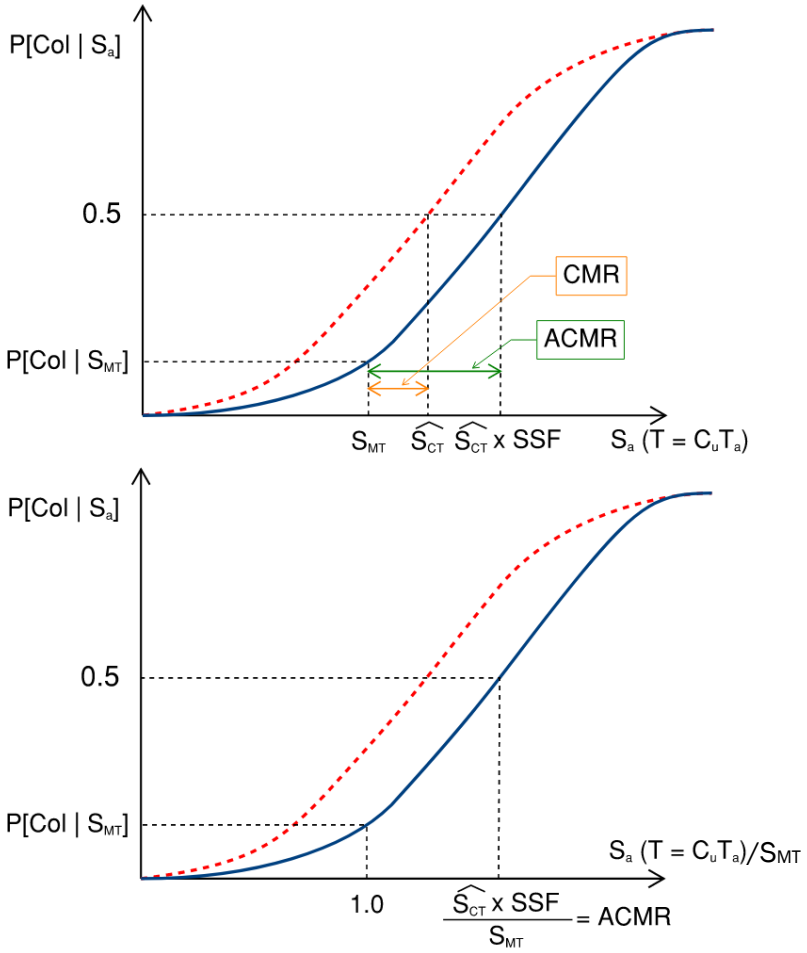

Figure C-4 **Example fragility curves derived from the calculated values of $\hat{S}_{CT}$ and *ACMR*, where the top figure is a function of S_a and the bottom figure is a function of S_a normalized by S_{MT}.**

Appendix D: Multiple-Degree-of-Freedom Wood Models Development

D.1 Numerical Model Development

In FEMA P-2139-2, detailed three-dimensional (3D) computer models were developed using the *Timber3D* analysis program (Pang et al., 2012) to evaluate the seismic response behavior and seismic collapse performance of wood light-frame archetypes. The *Timber3D* program was developed specifically for modeling the nonlinear dynamic response and collapse mechanisms of 3D wood light-frame buildings under earthquake shaking.

Figure D-1 shows an example 3D wood light-frame model developed for the 4-story multi-family dwelling archetype in FEMA P2139-2 (MFD3B). The framing members (i.e., sawn lumber) of vertical walls and floor and roof diaphragms were modeled using two-node and 12 degree-of-freedom (DOF) elastic frame elements with co-rotational formulation which account for geometric nonlinearity (i.e., P-delta effects). A database of 4-foot by 10-foot wall and 8-foot by 10-foot wall building blocks was utilized to explicitly model each of the perimeter and interior walls. A wall building block consisted of end studs modeled using two-node 12 degrees-of-freedom (DOFs) frame elements. The end studs were connected to top and bottom plates (12-DOF frame elements) via 6-DOF frame-to-frame (F2F) link elements representing the end connections. The lateral response (restoring force versus displacement) of a wood light-frame wall sheathed with structural panels or nonstructural finish material was modeled using F2F link element with a nonlinear hysteresis spring defined for the DOF parallel to the in-plane direction of the wall.

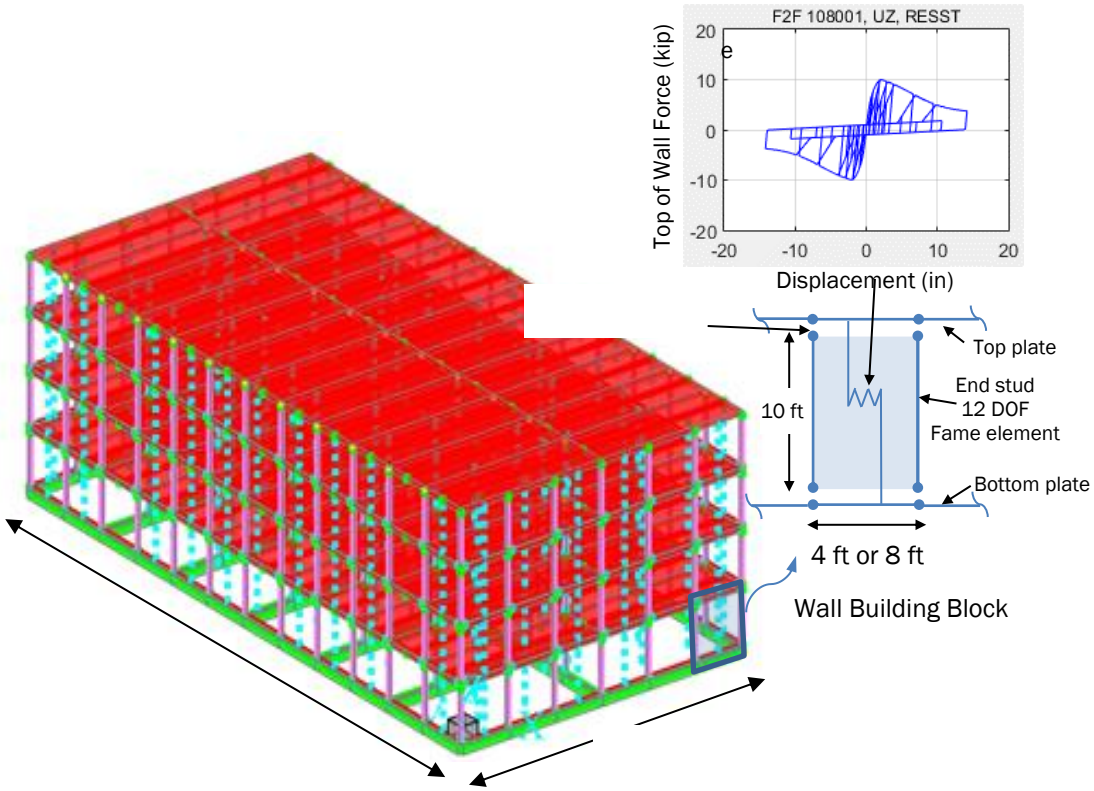

Figure D-1 FEMA P-2139-2 3D wood light-frame building model for 4-story multi-family dwelling archetype (MFD3B).

While the detailed 3D models developed in FEMA P-2139-2 were able to simulate the seismic response and collapse behavior of wood light-frame buildings more accurately when compared to prior models (e.g., the zero-height pancake model used in FEMA P-695), the effort required for an analyst to construct each detailed 3D model and the computation demand in terms of the total run-time required to conduct a nonlinear time history analysis were relatively high. To be able to evaluate and quantify the additional collapse risk associated with a portfolio of wood light-frame buildings covering all possible design spaces in regions of very high seismicity, simplified models with better computation efficiency are required.

In this study, two modeling approaches were developed for wood light-frame buildings: (1) a two-dimensional (2D) multiple-degree-of-freedom (MDOF) model, and (2) an equivalent single-degree-of-freedom (eSDOF) model (Figure D-2).

To develop the simplified 2D MDOF model, the behavior of the 3D model in one of the two lateral directions is modeled by assigning a lumped mass (weight) at each floor (or roof) diaphragm and, at each story, a pair of nonlinear hysteresis springs, one representing the collective contribution of structural shear walls and the other representing the combined contribution of nonstructural walls and finish materials. The 2D MDOF model was further simplified into an eSDOF model with an equivalent seismic weight (W_e), an equivalent height (H_e), and a single nonlinear spring representing

the force versus displacement hysteresis relationship at the effective height. Note that the eSDOF model can also be developed directly using responses of a detailed 3D model.

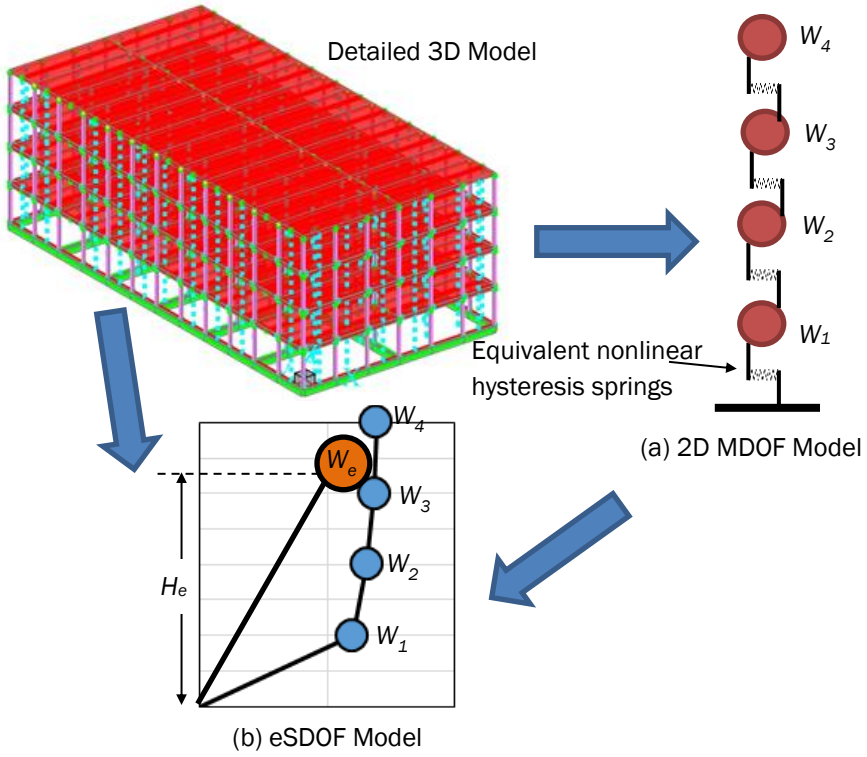

Figure D-2 Simplification of a detailed 3D model into a 2D MDOF model and an eSDOF model.

While the eSDOF model is more efficient than the 2D MDOF model in terms of computation time, the use of an eSDOF model does not allow explicit consideration of the influences of nonstructural finish material and the vertical distribution of shear strengths on the collapse performance of wood light-frame buildings. For this reason, the 2D MDOF model was selected as the primary modeling approach over the eSDOF model to study the additional collapse risk of wood light-frame buildings in regions of very high seismicity. The details of the development of eSDOF models may be found in Appendix E. The development of 2D MDOF models is summarized in the sections that follow.

D.1.1 2D MDOF Model

The 2D MDOF model consists of (1) stacked rigid pin-pin frames modeled using 2-node 12-DOF frame elements, and (2) two nonlinear shear springs in each story modeled using F2F elements to account for the shear contributions from the seismic-force-resisting system (SFRS) and the nonstructural finish materials (Figure D-3). The story height is 10 feet and the width of the 2D model is 8 feet. The rigid pin-pin frames represent the gravity load carrying capacity of studs and floor/roof diaphragms. Without the nonlinear F2F shear springs, the pin-pin frames are unstable laterally. Half of the story weight is assigned to each of the top node of the two studs in each story.

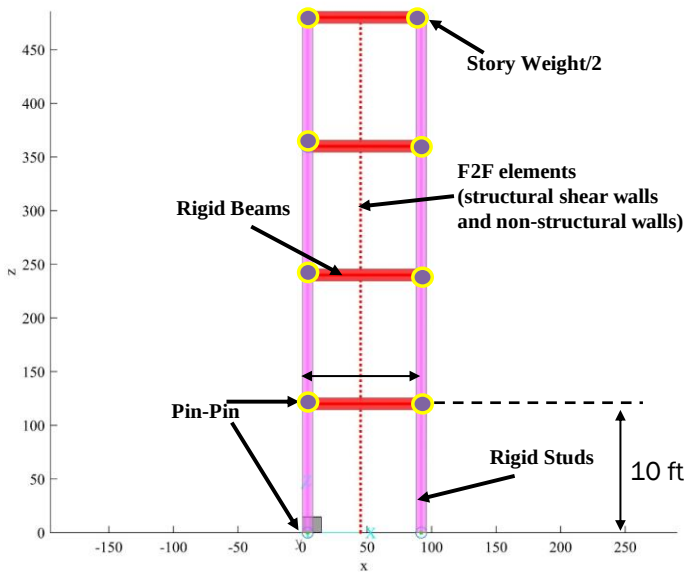

Figure D-3 Schematic illustration of the 2D MDOF model.

The detailed 3D model developed for the four-story multi-family dwelling archetype (MFD3B) in FEMA P-2139-2 is used to illustrate the process of creating a simplified 2D MDOF model. The detailed 3D model consists of 588 wall building blocks per story in the two lateral directions (Figure D-1). The cyclic responses of structural and nonstructural walls are described in the next section.

D.1.2 Normalized Nonlinear Cyclic Wall Responses

The cyclic response of walls was characterized using the Residual Strength (RESST) hysteresis model developed in FEMA P-2139-2. The RESST model was modified from the Consortium of Universities for Research in Earthquake Engineering (CUREE) hysteresis model (Folz and Filiatrault, 2001). The ascending branch of the RESST model is identical to that of the CUREE model, which follows a nonlinear exponential monotonic envelope curve (Figure D-4). However, the post-peak branch of the backbone curve is updated with a reversed S-curve anchored at an inflection point (D_x) and converging to a post-peak residual strength ratio (f_3) to characterize post-capping strength and stiffness degradations. The hysteretic rule of the RESST model is completely determined by 12 physically identifiably parameters as shown in Figure D-4 and defined in Table D-1. The peak strength (F_u) and displacement at peak strength (D_u) are not input parameters for the RESST model as the values can be obtained by locating the interception point between the ascending and descending backbone curves.

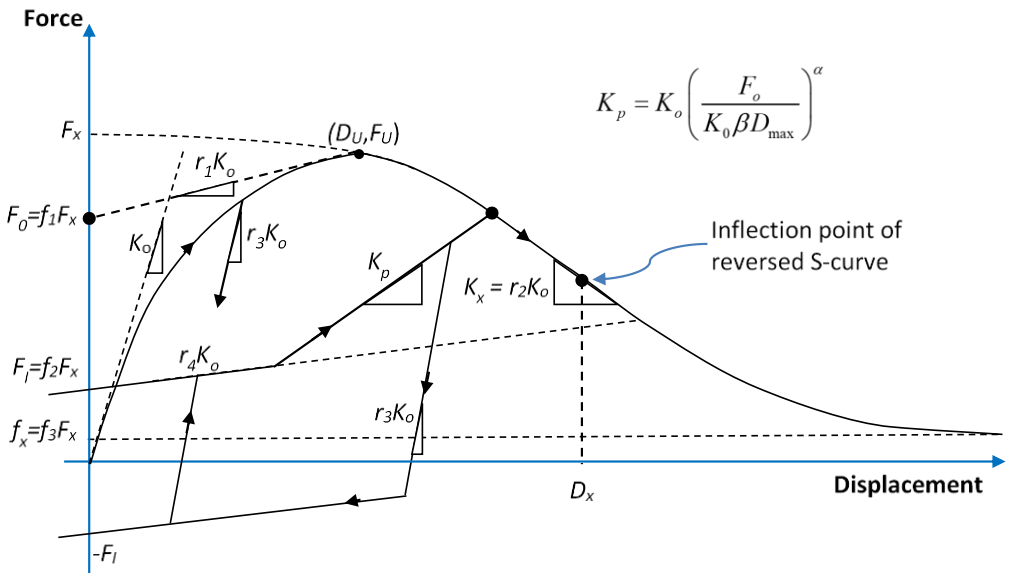

Figure D-4 Residual strength (RESST) hysteresis model.

Table D-1 Parameters of the RESST Hysteresis Model

Parameter	Unit	Description
K_o	Force/Displacement	Initial stiffness
r_1	Unitless	Asymptotic stiffness ratio on the ascending branch of backbone curve ($0 < r_1 < 1$)
r_2	Unitless	Stiffness ratio at the inflection point on the post-peak descending branch of backbone curve ($r_2 < 0$)
r_3	Unitless	Unloading stiffness ratio ($r_3 \geq 1$)
r_4	Unitless	Asymptotic peak force of the descending branch of the backbone curve (when displacement = 0)
F_x	Force	Asymptotic peak force of the descending branch of the backbone curve (when displacement = 0)
f_1	Unitless	Normalized force intercept (i.e., displacement = 0) of the asymptotic line on the ascending branch of the backbone curve ($0 \leq f_1 \leq 1$)
f_2	Unitless	Normalized zero-displacement force intercept of the pinched lines ($0 \leq f_2 \leq 1$)
f_3	Unitless	Post-peak residual strength to asymptotic peak strength ratio ($0 \leq f_3 \leq 1$)
D_x	Displacement	Displacement at the inflection point on the post-peak descending branch of the backbone curve
α	Unitless	Hysteretic parameter for stiffness degradation
β	Unitless	Hysteretic parameter for stiffness degradation

The database of wall building blocks in FEMA P-2139-2 consists of fourteen different 4-foot or 8-foot wide by 10-foot tall individual wall building blocks. These wall building blocks represent walls sheathed with structural panels or finish materials that are commonly specified in new wood light-frame construction (Table D-2).

Figure D-5 shows the backbone curves of the fourteen wall building blocks that were derived from the data of full-scale walls tested prior to 2008 and fitted to the RESST hysteresis model. The fitted RESST parameters for 8-foot and 4-foot wide walls are shown in Table D-3. The design strengths specified in the 2015 version of *National Design Specification for Wood Construction* (NDS, 2015), which were used to design the SFRSs of wood archetypes in FEMA P-2139-2, are shown in the last column of Table D-2. The ultimate or peak strength (F_u) for each of the wall building blocks are listed in the second-to-last column of Table D-3 and shown graphically in Figure D-5.

Table D-2 Description of Wall Building Blocks and Design Strength (FEMA P-2139-2)

Building Block ID	Description	Design Strength (plf)
OSB-Low	7/16-inch OSB sheathing on Douglas-Fir framing, single row of 8d common nails at 6 inches on-center along all panel edges.	520
OSB-Medium	7/16-inch OSB sheathing on Douglas-Fir framing, single row of 8d common nails at 3 inches on-center along all panel edges.	980
OSB-High	19/32-inch OSB sheathing on Douglas-Fir framing, single row (staggered) of 10d common nails at 2 inches on-center along all panel edges.	1740
OSB-Nonstruc	Same as OSB-Low but with minimum nailing.	N/A
Min-Gyp	1/2-inch gypsum wallboard on unblocked studs at 16 inches on-center, 5d cooler nails at 7 inches on-center along all panel edges.	200
Max-Gyp	5/8-inch gypsum wallboard on unblocked studs at 16 inches on-center, 6d cooler nails at 4 inches on-center along all panel edges.	350
Nonstruc-Gyp	Same as Min-Gyp, but with floating corner construction.	N/A
Stucco	New stucco construction.	N/A
Siding	Horizontal wood siding.	N/A

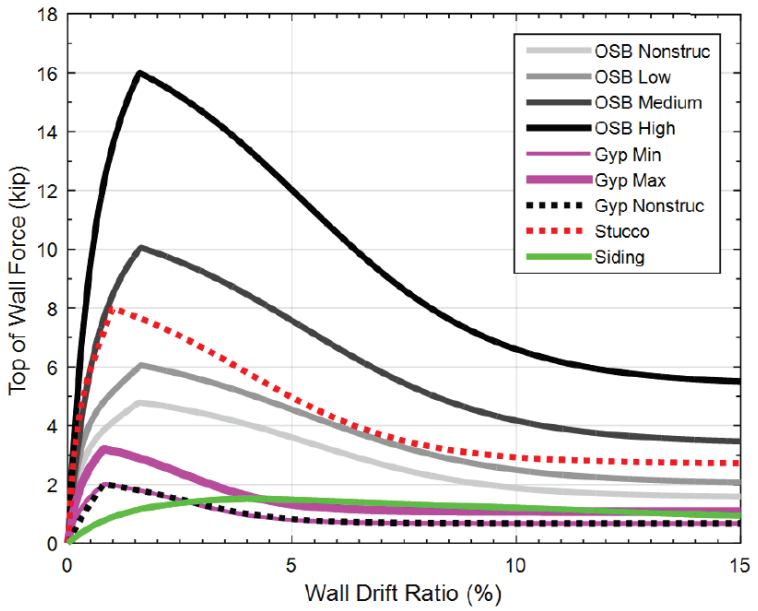

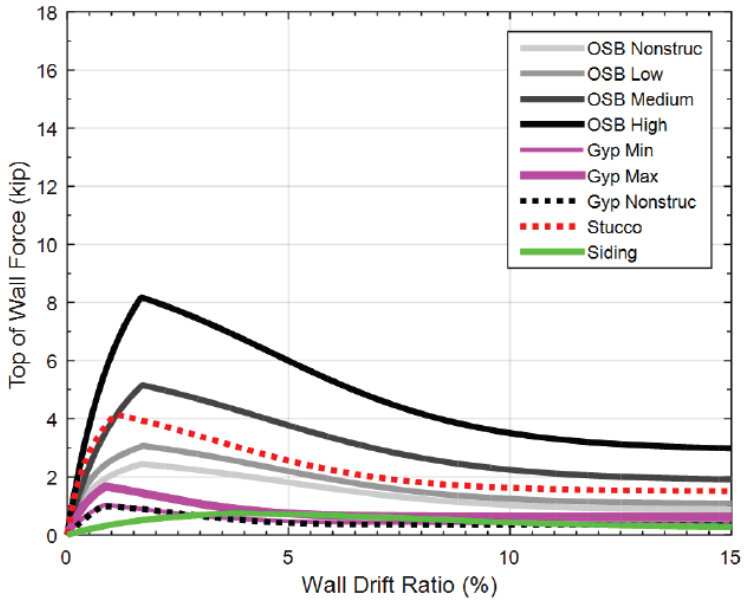

Figure D-5 Backbone curves for wall building blocks, (top) 8-ft wide and 10-ft tall wall, and (bottom) 8-ft wide and 10-ft tall wall (FEMA P-2139-2).

In FEMA P-2139-2, detailed archetypes were designed with configurations of shear walls and partition walls (sheathing types, nail sizes, nailing schedules and wall lengths) specified from the list of wall building blocks. In this study, the main objective is to evaluate the seismic collapse performance of code-compliant wood buildings in very high seismic regions. Since the force-based design procedure specifies the seismic demand in terms of force or required base shear, instead of explicitly determining the wall configurations, all the wall building block backbone curves were normalized to have a peak force of 1 kip.

To normalize the wall building blocks, the initial stiffness (K_o) and asymptotic peak force (F_x) parameters were divided by the peak force (F_u) shown in Table D-3. The resulting normalized RESST parameters by peak force are shown in Table D-4. Note that the F_u is equal to unity for all normalized backbone curves. Plotting the backbone curves of wood structural panel walls (OSB-low, OSB-medium and OSB-high) and nonstructural OSB walls (OSB-Nonstruc) revealed that the normalized backbone curves are nearly identical in shape (Figure D-6). Similarly, it was observed that the shapes of the normalized backbone curves for the three types of gypsum walls (Min-Gyp, Max-Gyp and Nonstruc-Gyp) are similar. Further normalizations were performed by generating an average backbone curve for the (1) OSB and (2) gypsum walls (Figure D-5).

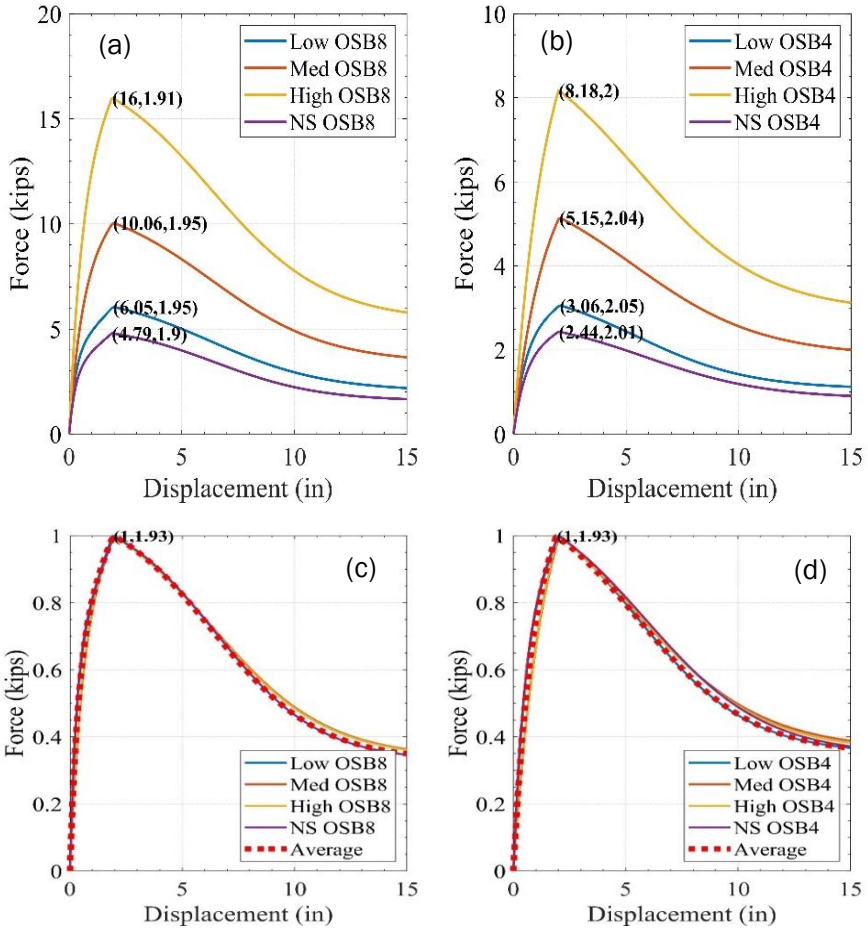

Figure D-6 Normalization of the FEMA P-2139-2 backbone curves of wall building blocks by force: actual backbone curves for (a) 8-ft wide and (b) 4-ft wide walls, normalized backbone curves for (c) 8-ft wide and (d) 4-ft wide walls.

Stucco is typically used for the exterior face of perimeter walls and gypsum is used to finish the interior face of perimeter walls and both faces of interior walls. The actual backbone shape depends on the relative amounts or lengths of stucco and gypsum walls in a building. While the backbone curve shapes of walls sheathed with stucco and gypsum are not identical, especially in the post-peak region, both stucco and gypsum walls have similar pre-peak behaviors and reach their peak strength at approximately the same displacement. To further simplify the model to utilize only one backbone curve to represent the contribution of all nonstructural elements (i.e., stucco and gypsum in this case), an average backbone curve for gypsum and stucco is developed (Figure D-7). The final 2D MDOF model uses only two normalized wall hysteresis models, where one represents the contribution of structural walls and the other represents the combined contribution of nonstructural finish materials, namely gypsum and stucco (Table D-5).

Table D-3 RESST Hysteresis Parameters For 8-feet Wide by 10-feet Tall Wall Building Blocks

Wall Type	K_o (kip/in)	r_1	r_2	r_3	r_4	F_x (kip)	f_1	f_2	f_3	D_x (in)	α	β	F_u (kip)	D_u (in)
8-feet by 10-feet														
OSB-Low	15.00	0.08	-0.03	1.01	0.01	6.79	0.57	0.13	0.30	6.30	0.75	1.05	6.05	1.95
OSB-Medium	15.00	0.08	-0.05	1.06	0.01	11.29	0.72	0.09	0.30	6.30	0.75	1.04	10.06	1.95
OSB-High	24.00	0.08	-0.05	1.02	0.01	17.92	0.73	0.13	0.30	6.30	0.77	1.15	16.00	1.91
OSB-Nonstruc	12.00	0.08	-0.03	1.01	0.01	5.24	0.59	0.13	0.30	6.50	0.75	1.05	4.79	1.90
Min-Gyp	5.20	0.17	-0.06	1.45	0.01	2.26	0.53	0.09	0.30	3.00	0.38	1.09	2.02	0.97
Max-Gyp	9.10	0.15	-0.05	1.45	0.01	3.62	0.54	0.09	0.30	3.10	0.38	1.09	3.21	0.96
Nonstruc-Gyp	5.00	0.46	-0.12	1.45	0.01	2.26	0.56	0.09	0.30	3.10	0.38	1.09	2.23	0.55
Stucco	50.00	0.13	-0.03	1.45	0.01	9.04	0.44	0.09	0.30	4.70	0.38	1.09	8.88	0.73
4-feet by 10-feet														
OSB-Low	5.00	0.08	-0.05	1.01	0.01	3.57	0.65	0.12	0.30	5.50	0.75	1.05	3.06	2.05
OSB-Medium	5.00	0.09	-0.08	1.06	0.01	6.20	0.80	0.12	0.30	5.30	0.75	1.04	5.15	2.04
OSB-High	8.00	0.09	-0.08	1.02	0.01	9.68	0.82	0.12	0.30	5.50	0.77	1.15	8.18	2.00
OSB-Nonstruc	4.00	0.08	-0.05	1.01	0.01	2.81	0.66	0.12	0.30	5.90	0.75	1.05	2.44	2.01
Min-Gyp	1.73	0.09	-0.09	1.45	0.01	1.35	0.88	0.07	0.30	2.10	0.38	1.09	1.04	1.01
Max-Gyp	3.03	0.09	-0.08	1.45	0.01	2.08	0.82	0.08	0.30	2.40	0.38	1.09	1.67	1.03
Nonstruc-Gyp	2.50	0.46	-0.12	1.45	0.01	1.13	0.56	0.09	0.30	3.10	0.38	1.09	1.11	0.55
Stucco	16.67	0.16	-0.04	1.45	0.01	5.00	0.51	0.11	0.30	4.00	0.38	1.09	4.76	0.87

Table D-4 Normalized RESST Hysteresis Parameters For 4-feet Wide by 10-feet Tall Wall Building Blocks

Wall Type	K_o (kip/in)	r_1	r_2	r_3	r_4	F_x (kip)	f_1	f_2	f_3	D_x (in)	α	β	F_u (kip)	D_u (in)
8-feet by 10-feet														
OSB-Low	2.48	0.08	-0.03	1.01	0.01	1.12	0.57	0.13	0.30	6.30	0.75	1.05	1.00	1.95
OSB-Medium	1.49	0.08	-0.05	1.06	0.01	1.12	0.72	0.09	0.30	6.30	0.75	1.04	1.00	1.95
OSB-High	1.50	0.08	-0.05	1.02	0.01	1.12	0.73	0.13	0.30	6.30	0.77	1.15	1.00	1.91
OSB-Nonstruc	2.50	0.08	-0.03	1.01	0.01	1.09	0.59	0.13	0.30	6.50	0.75	1.05	1.00	1.90
Min-Gyp	2.58	0.17	-0.06	1.45	0.01	1.12	0.53	0.09	0.30	3.00	0.38	1.09	1.00	0.97
Max-Gyp	2.83	0.15	-0.05	1.45	0.01	1.13	0.54	0.09	0.30	3.10	0.38	1.09	1.00	0.96
Nonstruc-Gyp	2.25	0.46	-0.12	1.45	0.01	1.01	0.56	0.09	0.30	3.10	0.38	1.09	1.00	0.55
Stucco	5.63	0.13	-0.03	1.45	0.01	1.02	0.44	0.09	0.30	4.70	0.38	1.09	1.00	0.73
4-feet by 10-feet														
OSB-Low	1.63	0.08	-0.05	1.01	0.01	1.16	0.65	0.12	0.30	5.50	0.75	1.05	1.00	2.05
OSB-Medium	0.97	0.09	-0.08	1.06	0.01	1.20	0.80	0.12	0.30	5.30	0.75	1.04	1.00	2.04
OSB-High	0.98	0.09	-0.08	1.02	0.01	1.18	0.82	0.12	0.30	5.50	0.77	1.15	1.00	2.00
OSB-Nonstruc	1.64	0.08	-0.05	1.01	0.01	1.15	0.66	0.12	0.30	5.90	0.75	1.05	1.00	2.01
Min-Gyp	1.67	0.09	-0.09	1.45	0.01	1.30	0.88	0.07	0.30	2.10	0.38	1.09	1.00	1.01
Max-Gyp	1.82	0.09	-0.08	1.45	0.01	1.25	0.82	0.08	0.30	2.40	0.38	1.09	1.00	1.03
Nonstruc-Gyp	2.25	0.46	-0.12	1.45	0.01	1.01	0.56	0.09	0.30	3.10	0.38	1.09	1.00	0.55
Stucco	3.50	0.16	-0.04	1.45	0.01	1.05	0.51	0.11	0.30	4.00	0.38	1.09	1.00	0.87

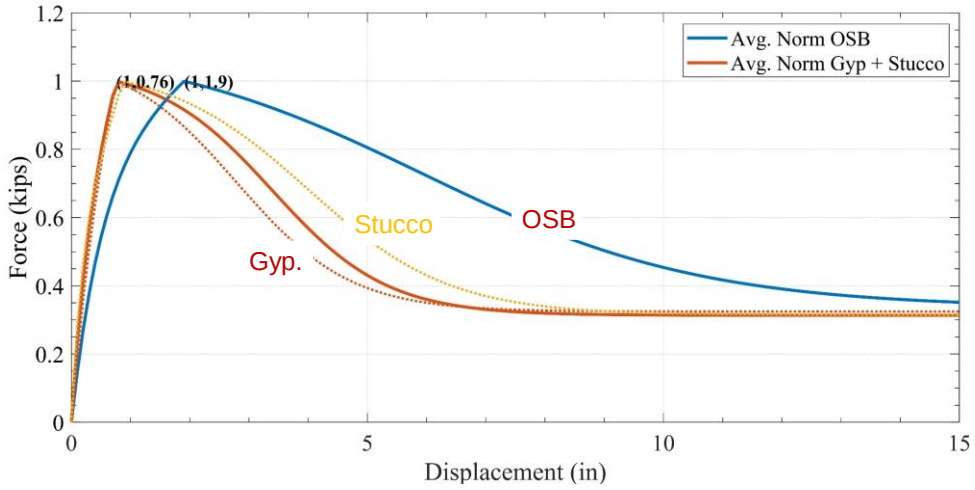

Figure D-7 **Average normalized backbone curves: the blue curve represents the average of normalized OSB low, medium, high, and nonstructural walls, the red solid curve represents the average of the stucco and gypsum backbone curves.**

Table D-5 **Normalized RESST Hysteretic Parameters for 2D MDOF Model of FEMA P-2139-2 Archetypes**

Wall Type	K_o (kip/in)	r_1	r_2	r_3	r_4	F_x (kip)	f_1	f_2	f_3	D_x (in)	α	β	F_u (kip)	D_u (in)
OSB	1.72	0.08	-0.05	1.02	0.01	1.13	0.66	0.12	0.30	6.00	0.75	1.07	1.00	2.00
Gyp. and Stucco	2.73	0.23	-0.07	1.45	0.01	1.04	0.57	0.10	0.30	3.41	0.38	1.09	1.00	2.01

D.2 Model Validation 1: 2D MDOF vs. FEMA P-2139-2 MFD3B

The simplified modeling approach presented in Section D.1.1 and the normalized backbone curves developed in Section D.1.2 were used to model the longitudinal direction of the 4-story multi-family dwelling archetype (MFD3B) of FEMA P-2139-2. The MFD3B archetype was designed following ASCE/SEI 7-10 for SDC D_{max} locations, corresponding to a short-period design response acceleration parameter (S_{DS}) of 1.00g and maximum considered earthquake (MCE_R) ground motion spectral acceleration (S_{MS}) of 1.5g. More details about the modeling and design can be found in FEMA P-2139-2.

The backbone curves of all the structural walls in the longitudinal direction in each story were combined to obtain the inter-story force versus displacement response. The peak forces for each story are presented in Table D-6. The process was repeated by removing the structural walls and leaving only the nonstructural walls sheathed either with gypsum or stucco in the MFD3B archetype.

Note that the peak story strengths from nonstructural finish materials are the same for all four stories since the floor plans are identical for all floors.

Table D-6 Peak Forces of Nonlinear Hysteresis Springs for Structural and Nonstructural Walls

	Peak Force (kips)	
Story	**Structural**	**Nonstructural**
1	239.4	153.0
2	219.7	153.0
3	168.0	153.0
4	134.3	153.0

The parameters of the two nonlinear hysteretic springs for each story, one to account for structural and the other for nonstructural walls, were determined by multiplying the stiffness (K_o) and asymptotic peak force (F_x) parameters of the corresponding normalized RESST hysteretic model shown in Table D-5 with the peak forces shown in Table D-6. The hysteresis loops of the structural and nonstructural walls scaled to the peak strengths of the detailed FEMA P-2139-2 MFD3B archetype are shown graphically in Figure D-8.

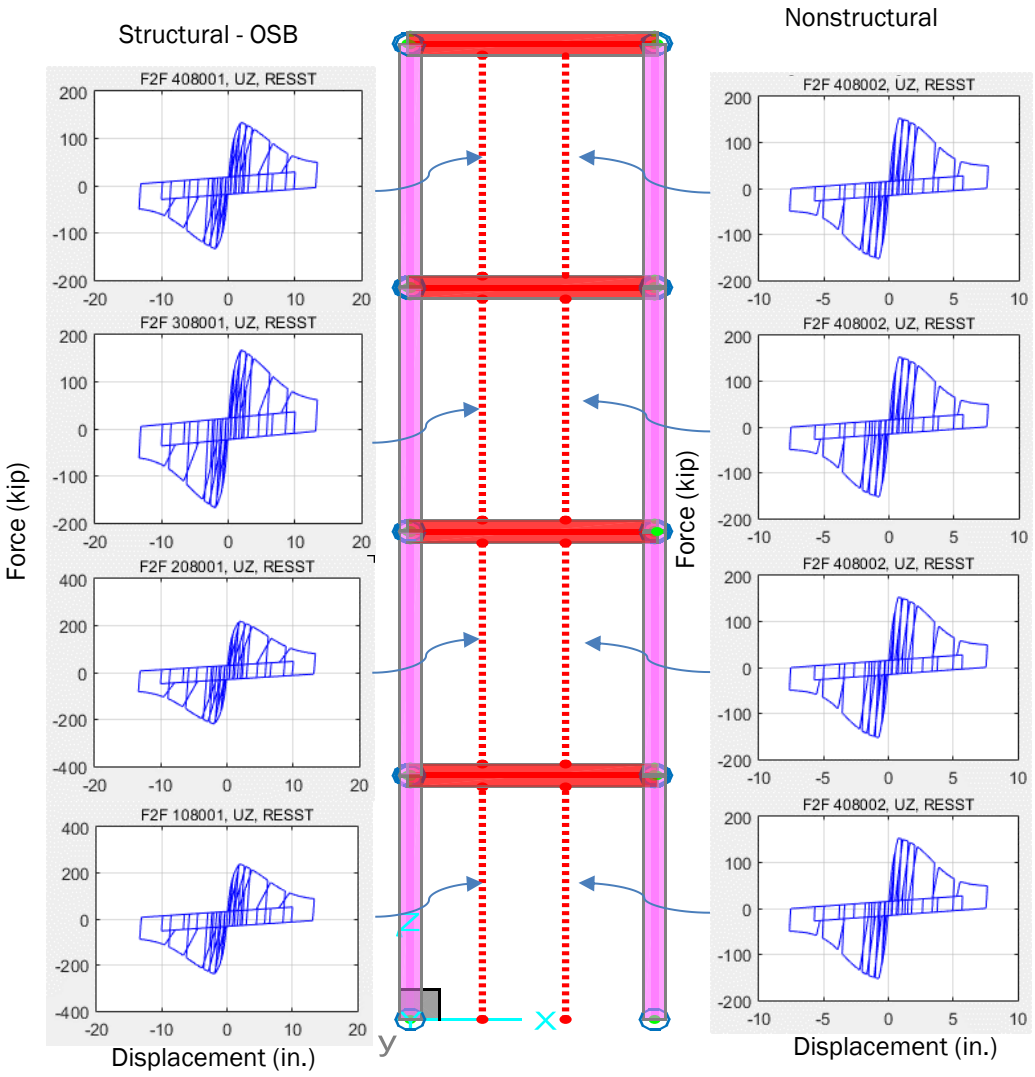

Figure D-8 Simplified 2D MDOF model for the longitudinal direction of the FEMA P-2139-2 four-story multi-family dwelling (MFD3B) archetype with two nonlinear hysteretic springs per story.

Table D-7 summarizes the key parameters for the two models, namely the simplified 2D MDOF and the detailed 3D MFD3B model. To validate the simplified 2D MDOF model against the detailed model of FEMA P-2139-2, the following three analyses were performed:

- Modal analyses to evaluate elastic natural periods and mode shapes,
- Nonlinear static pushover analyses, and
- Nonlinear incremental dynamic analyses (IDAs) in accordance with the FEMA P-695 methodology.

Table D-7 Key Modeling Parameters for the 2D MDOF and Detailed 3D MFD3B Models for Validation 1

Parameter	Description
Number of Stories	4
Story Weights	As-designed by practitioners (FEMA P-2139-2)
Story Height	10 feet
OSB Backbone Model	Based on shear walls tested up to 2008 (Line et al., 2008)
Vertical distribution of Shear Strength	As-designed by practitioners (FEMA P-2139-2)
Damping	0% Rayleigh Damping assigned to modes 1 and 2
IDA analysis	Apply 44 ground motions along the longitudinal direction only
	Ground motions scaled to the median spectra at a period of 0.25 seconds.
	Simulated and non-simulated collapses were considered
Number of Nonlinear Springs	588 springs in each story for the 3D model 2 springs per floor for the 2D MDOF
Residual Strength Ratio	30% for each wall component. The combined building-level residual strength may vary

D.2.1 Modal and Nonlinear Static Pushover Analyses

Modal analyses were performed by solving the eigenvectors for the mode shapes and eigenvalues for the fundamental periods for the 2D and 3D models. The fundamental periods of the 3D MFD3B model (drift in the longitudinal direction) and the 2D MDOF model were 0.506 seconds and 0.495 seconds, respectively. The slight difference between the two fundamental periods was mainly attributed to the differences that arose from the use of two nonlinear springs in the simplified 2D model to represent the more than 500 wall segments in the detailed 3D model.

A modal pushover analysis was performed along the longitudinal direction of the 3D model and the in-plane direction of the 2D model using the respective fundamental mode to determine the effective lateral forces. Figure D-9 shows the pushover curves in terms of base shear versus roof displacement for the two models. As can be seen, the pushover curve of the simplified 2D model is nearly identical to that of the detailed 3D model. P-delta effects were taken into consideration resulting in the post-peak residual plateau force dropped to zero at roof displacement of about 16 inches.

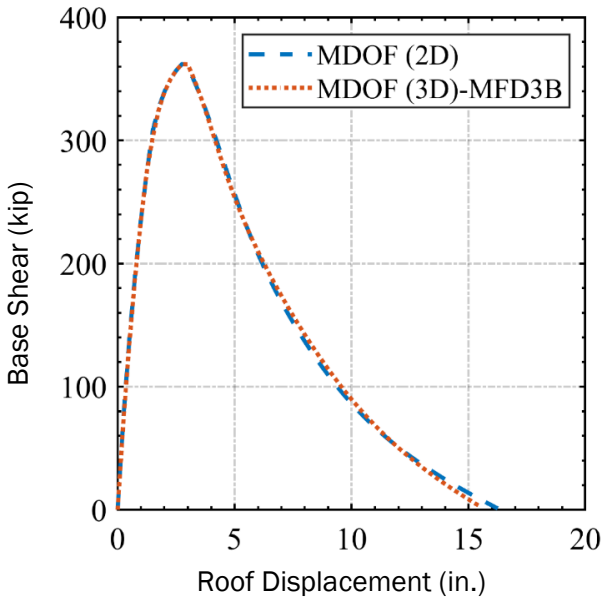

Figure D-9 Pushover curves for the longitudinal direction of the detailed FEMA P-2139-2 3D MFD3B and 2D MDOF models.

D.2.2 Nonlinear Incremental Dynamic Analysis

Timber3D was used to perform IDAs in accordance with the FEMA P-695 methodology. The 44 FEMA P-695 far-field ground motions were used for the IDAs. The 44 ground motions were scaled as a group such that the median acceleration response spectrum of the ground motion ensemble at a period of 0.25 seconds matched the prescribed intensity level (FEMA P-2139-2). The intensity levels were increased with a 0.05g increment, up to an intensity level for which all ground motions caused collapse of the model.

To make the IDA results comparable between the 2D and 3D models, the 44 ground motions were applied as individual uni-axial ground motions along the longitudinal direction of the 3D model (i.e., no ground motions were assigned in the transverse direction). P-delta effects were included by performing gravity load analysis prior to each nonlinear time history analysis. The Rayleigh damping model was used. However, to be consistent with the assumption used in FEMA P-2139-2, a zero damping was assigned to the first two modes for both the 2D and 3D models.

In FEMA P-2139-2, collapse was explicitly simulated using *Timber3D* by tracking the vertical drop of a control node on the roof of the building model. The model was deemed collapsed when the vertical drop of the roof control node exceeded a prescribed value. In this validation study, a *simulated collapse* flag was triggered, and the time history analysis was terminated when the vertical drop of the control node exceeded 80% of the inter-story height.

Figure D-10 shows the IDA curves for the simplified 2D MDOF model. Solid blue markers on the IDA curves indicate points of incipient collapse (IC) (i.e., the last survival intensity levels for the 44 ground motions). Also shown in the figure are the fitted lognormal probability density functions of

peak inter-story drift ratios (*DR*s) and spectral acceleration (S_a) values at incipient collapse. The median peak inter-story drift and spectral acceleration at incipient collapse were 6.4% and 1.94g, respectively.

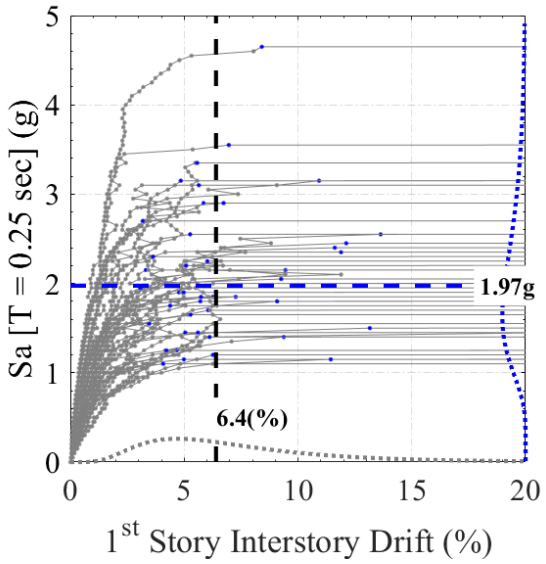

Figure D-10 IDA curves and probability density functions of peak inter-story drifts and spectral accelerations at incipient collapse for the 2D MDOF model.

In addition to simulated collapse, a *non-simulated collapse* criterion based on *DR* limit was defined. A non-simulated collapse occurred when the peak inter-story *DR* exceeded a prescribed *DR* limit. Prior to recording the non-simulated collapse data, the raw IDA curves shown in Figure D-10 were converted into monotonically increasing IDA curves (Figure D-11). In general, the peak inter-story DR is expected to increase as the shaking intensity, S_a, increases. However, it is not uncommon to observe peak DR to temporarily reduce when a particular ground motion is scaled up to a higher intensity in IDA. To alleviate this issue, a monotonically increasing IDA curve was derived for each ground motion by recording the maximum *DR* at, and lower than, the intensity being considered.

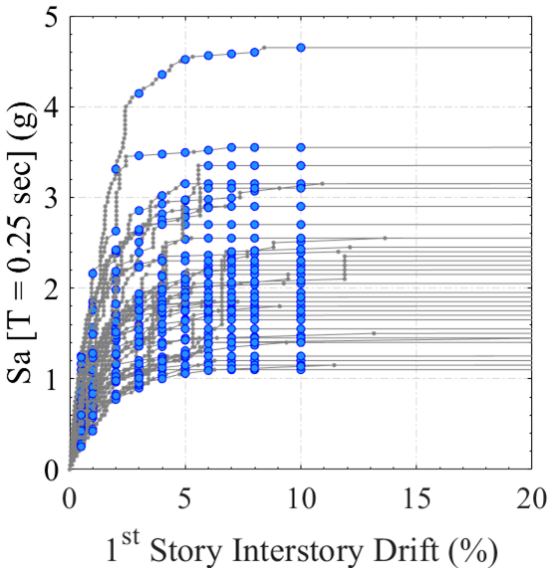

Figure D-11 Monotonically increasing IDA curves and probability density functions of peak inter-story drifts and spectral accelerations at incipient collapse for the 2D MDOF model.

In Figure D-11, each group of circular blue markers aligned vertically represent the non-simulated collapse spectral accelerations of the 44 ground motions for a given *DR* limit. A series of non-simulated collapse *DR* limits, beginning with *DR* of 0.5% and increasing with increments of 0.5%, up to the median incipient collapse *DR* determined using the simulated collapse criterion, was used to record the non-simulated collapse S_a values. A median collapse spectral acceleration, S_{CT}, was then computed for each of the non-simulated collapse *DR* limits.

The same criterion used to determine the incipient collapse points shown in Figure D-10 for the 2D model was also applied to determine the incipient collapse spectral accelerations of the detailed 3D model. Figure D-12 shows the ground motion-to-ground motion comparison of incipient collapse S_a of the 2D and 3D models. In general, the incipient collapse S_a of the 2D model matches that of the detailed 3D model reasonably well.

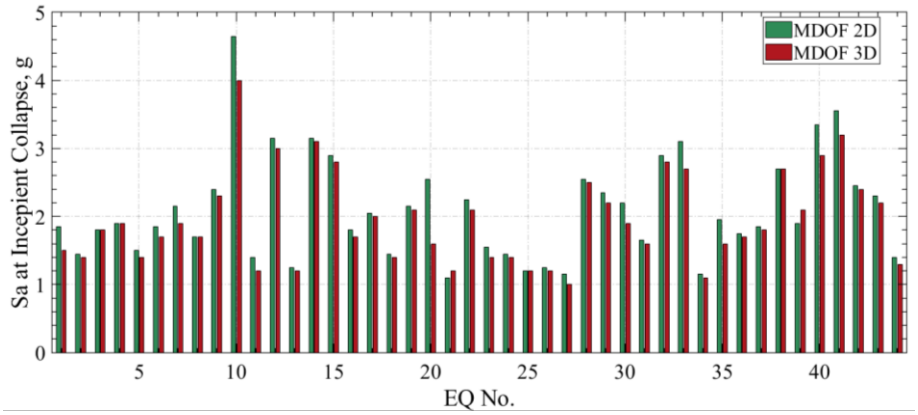

Figure D-12 Earthquake to earthquake spectral acceleration at incipient collapse for 2D MDOF and 3D MDOF.

The FEMA P-695 methodology was applied to create the collapse fragility curves and to compute the MCE_R collapse probabilities of the 2D MDOF and detailed 3D models. Table D-8 summarizes the raw S_{CT} values and the FEMA P-695 MCE_R collapse probabilities of the two models.

The collapse S_{CT} was taken as the median incipient collapse S_a plus the increment of the IDA. Take the 2D MDOF model as an example: the median incipient collapse S_a was 1.97g (Figure D-10) and the IDA increment was 0.04g, resulting in a simulated collapse $\hat{S}_{CT}$ of 2.01g (Table D-8). The collapse margin ratio (*CMR*) was computed as the ratio of the median 5%-damped spectral acceleration of the collapse level ground motions ($\hat{S}_{CT}$) to the 5%-damped spectral acceleration of the MCE_R ground motions (S_{MT} = 1.5g), *CMR* = 2.01g/1.5g = 1.35. Per FEMA P-695, the adjusted collapse margin ratio (*ACMR*) must be computed by multiplying the *CMR* by the ductility based spectral shape factor (*SSF*). For a typical wood light-frame building with significant ductility (μ_T > 8), *SSF* = 1.33 (from Table 7-1b of FEMA P-695). Thus, *ACMR* = *CMR* × *SSF* = 1.80. The probability of collapse as a function of ground motion intensity (at the period, *T*) is assumed to be lognormally distributed with an adjusted median (i.e., *ACMR* × S_{MT}) and a lognormal standard deviation, β_{TOT}. β_{TOT} accounts for total collapse uncertainty related to: (1) record-to-record variability; (2) design requirements (for the SFRS of interest); (3) test data (used to establish nonlinear properties); and (4) modeling methods, as described in Section 7.3 of FEMA P-695. To be consistent with FEMA P-2139-2, β_{TOT} = 0.50 was used to compute the MCE_R collapse probability.

$$P[\text{col} \mid MCE_R] = \Phi\left(\frac{LN(1/ACMR)}{\beta_{TOT}}\right)$$

Where, $\Phi(.)$ is the standard normal cumulative distribution function. The raw collapse rates and FEMA P-695 collapse fragility curves derived from the simulated collapse data are shown in Figure D-13. Table D-8 shows that the MCE_R collapse probabilities obtained using the 2D MDOF and the detailed 3D models were 12.04% and 14.39%, respectively. The values in brackets in Table D-8

represent the ratio of the 2D MDOF model predicted results to the benchmark results of the detailed 3D model.

Table D-8 FEMA P-695 MCE_R Collapse Probabilities of the 2D MDOF and Detailed 3D Models

Model	*DR* (%)	Raw	FEMA P-695: *SSF* = 1.33 and β_{tot} = 0.5		*CMR*	*ACMR*
		$\hat{S}_{CT}$ (g)	$\hat{S}_{CT}$ × *SSF* (g), (2D/3D)	P(COL|MCE_R) %, (2D/3D)		
2D MDOF	Simulated	2.01	2.67 (1.05)	12.04 (0.84)	1.35	1.80
	0.50	0.57	0.76 (0.99)	91.34 (1.00)	0.38	0.51
	1.00	0.94	1.25 (1.01)	64.42 (1.00)	0.62	0.83
	2.00	1.41	1.88 (1.01)	32.74 (0.99)	0.94	1.25
	3.00	1.63	2.17 (1.02)	23.03 (0.95)	1.09	1.45
	4.00	1.80	2.34 (1.00)	17.43 (0.94)	1.20	1.60
	5.00	1.89	2.51 (1.02)	15.08 (0.93)	1.26	1.68
Detailed 3D	Simulated	1.91	2.54	14.39	1.28	1.70
	0.50	0.58	0.77	91.07	0.38	0.51
	1.00	0.94	1.24	64.53	0.62	0.83
	2.00	1.40	1.86	33.22	0.93	1.24
	3.00	1.60	2.13	24.13	1.07	1.42
	4.00	1.77	2.35	18.49	1.18	1.57
	5.00	1.85	2.46	16.20	1.23	1.64

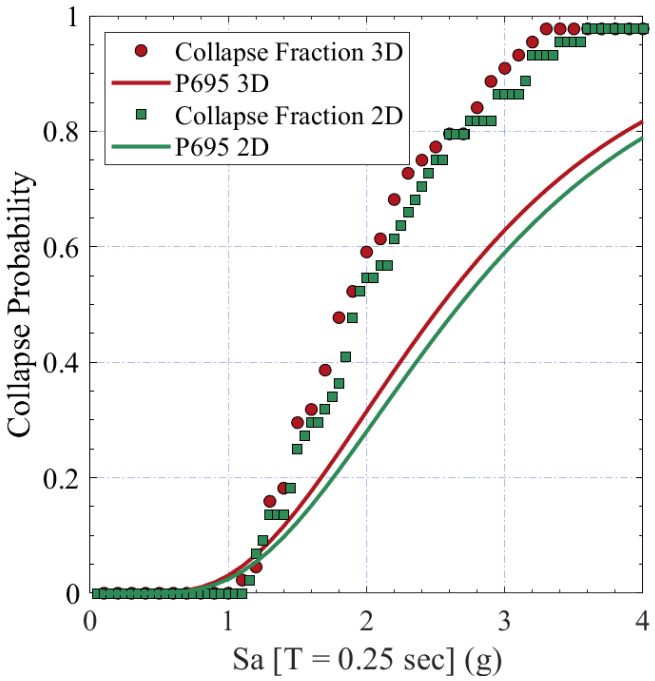

Figure D-13 Collapse rates from IDA and FEMA P-695 collapse fragility curves for 2D MDOF and detailed 3D models using simulated collapse criterion.

Figure D-14 presents the non-simulated collapse rates for 2D MDOF and detailed 3D models. From Table D-8, the collapse rates of the simplified 2D model are within 5% difference of that estimated from the detailed 3D model. The results of collapse analysis for both simulated and non-simulated collapse are tabulated in Table D-8. From the table, it can be seen that the 2D model predicted the median collapse S_{CT} values to within a 5% difference and the probabilities of collapse to within a maximum of 16% difference (as shown in the table 2D/3D ratios).

The IDA for the simplified 2D MDOF model took about 2 hours to perform, whereas the detailed 3D model took approximately 5 days. The close match between the median S_{CT} values determined using the 2D MDOF and detailed 3D models shows that the more computational efficient 2D MDOF model may be used in lieu of the detailed 3D model to evaluate seismic performance of wood light-frame buildings.

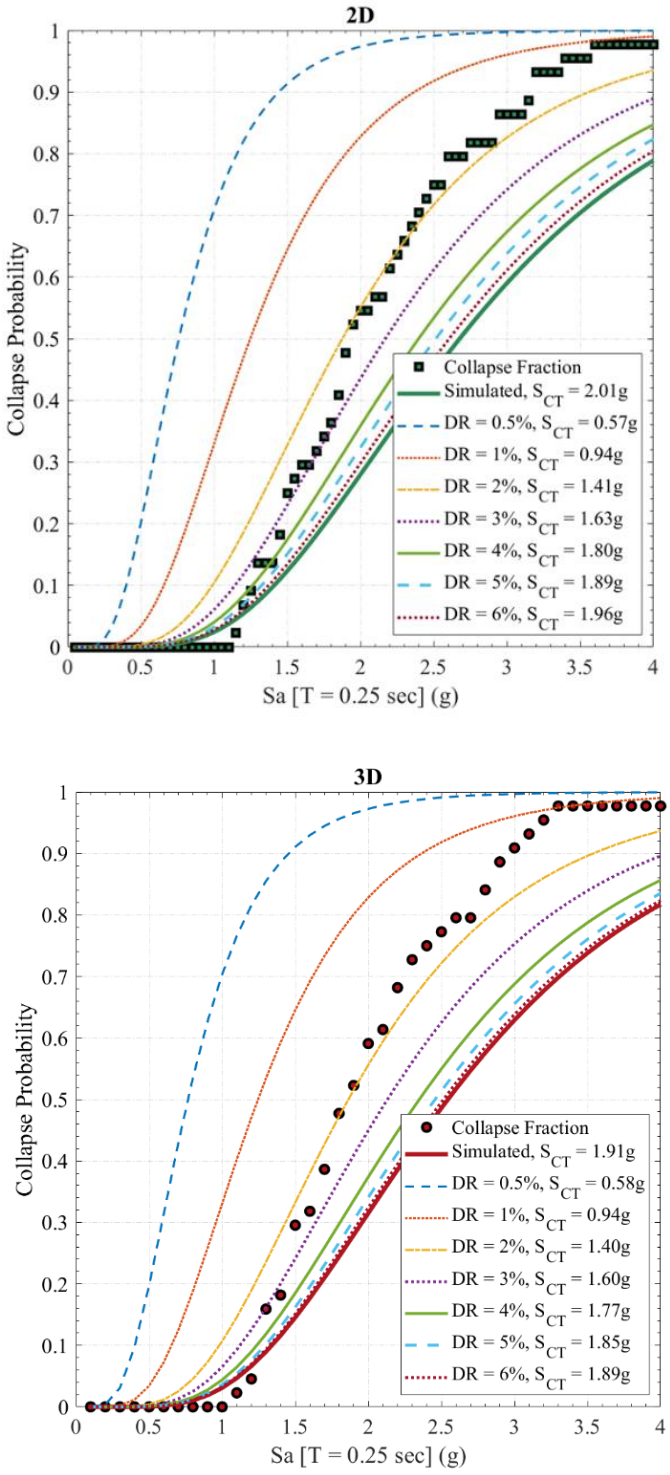

Figure D-14 Collapse rates from IDA and FEMA P-695 collapse fragility curves for 2D MDOF (top) and detailed 3D (bottom) models using non-simulated collapse criterion.

D.3 Hysteresis Model for Wood Structural Panel Shear Walls with Continuous Tie-down Rod System

The normalized structural OSB backbone curve parameters presented in Table D-5 were derived from the baseline backbone curves of FEMA P-2139-2, which were based on the shear walls tested prior to 2008 (Line et al., 2008). These shear walls were installed with hold-downs at the lower corners of end studs to resist overturning forces. In recent years, continuous rod tie-down system is being widely used in multi-story wood light-frame construction. The anchorage mechanism and boundary condition of a continuous rod tie-down system are different from that of conventional hold-downs. The hold-down relies on wood end studs to resist tension force, whereas in continuous rod tie-down system, the metal rods resist the overturning tension force.

A series of wood light-frame shear walls anchored with continuous tie-down rod systems were tested in 2019 (Line et al., 2019). The following two test groups from Line et al. (2019) were utilized to develop normalized wood structural panel hysteresis parameters that are more representative of modern wood light-frame construction with continuous tie-down rod systems.

1. **Test Group H (H01, H02):** Single-sided wall sheathed with 19/32" OSB attached with 10d common nails subjected to cyclic loading.
2. **Test Group G (G01, G02):** Single-sided wall sheathed with 19/32" OSB attached with 10d common nails subjected to monotonic loading.

Figure D-15 shows the monotonic and cyclic wall test data for wood shear walls with hold-downs (Line et al., 2008) and a continuous tie-down rod system (Line et al., 2019). Also shown in the figure are three normalized wood structural backbone curves: (1) FEMA P2139-2 OSB-High baseline backbone curve, (2) FEMA P-2139-2 R2 backbone curve, and (3) the new fitted RESST OSB backbone curve with a residual strength of 30% developed in this study and fitted to the data from Line et al. (2019). The FEMA P-2139-2 baseline backbone curve has a lower peak displacement and shallower post-peak displacement compared to the R2 and RESST models.

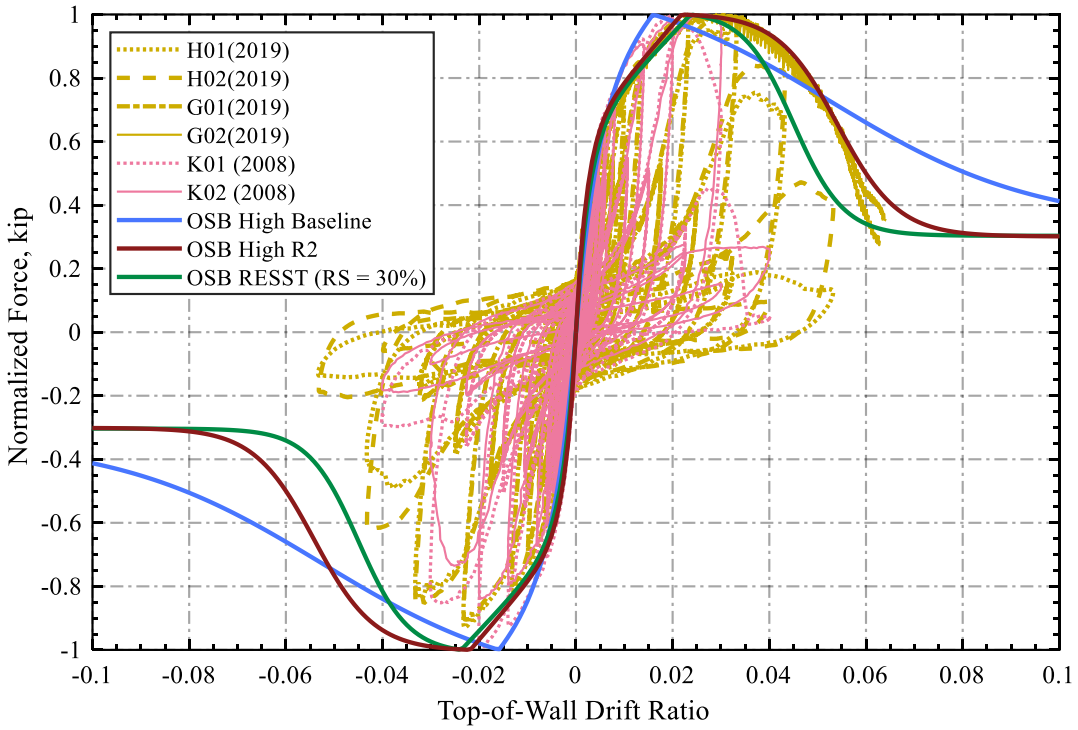

Figure D-15 Normalized structural OSB wall test data and fitted backbone curve model for 10-ft high walls with a 30 percent residual strength (peak forces are normalized to 1 kip).

The prior FEMA P-2139 studies on wood light-frame buildings revealed that the seismic performance was mainly governed by two factors, namely strength and displacement capacity. Strength was quantified in terms of normalized base shear (V_{max}/W) and displacement capacity was considered by varying the post-peak residual strength. To consider displacement capacity, in this study, the normalized OSB RESST hysteresis parameters for a continuous tie-down rod system were fitted to seven different residual strength (*RS*): 0%, 10%, 20%, 30%, 45%, 60%, and 75% of the peak strength. Figure D-16 presents the RESST backbone curves with these *RS* ratios. Table D-7 lists the new fitted RESST backbone parameters.

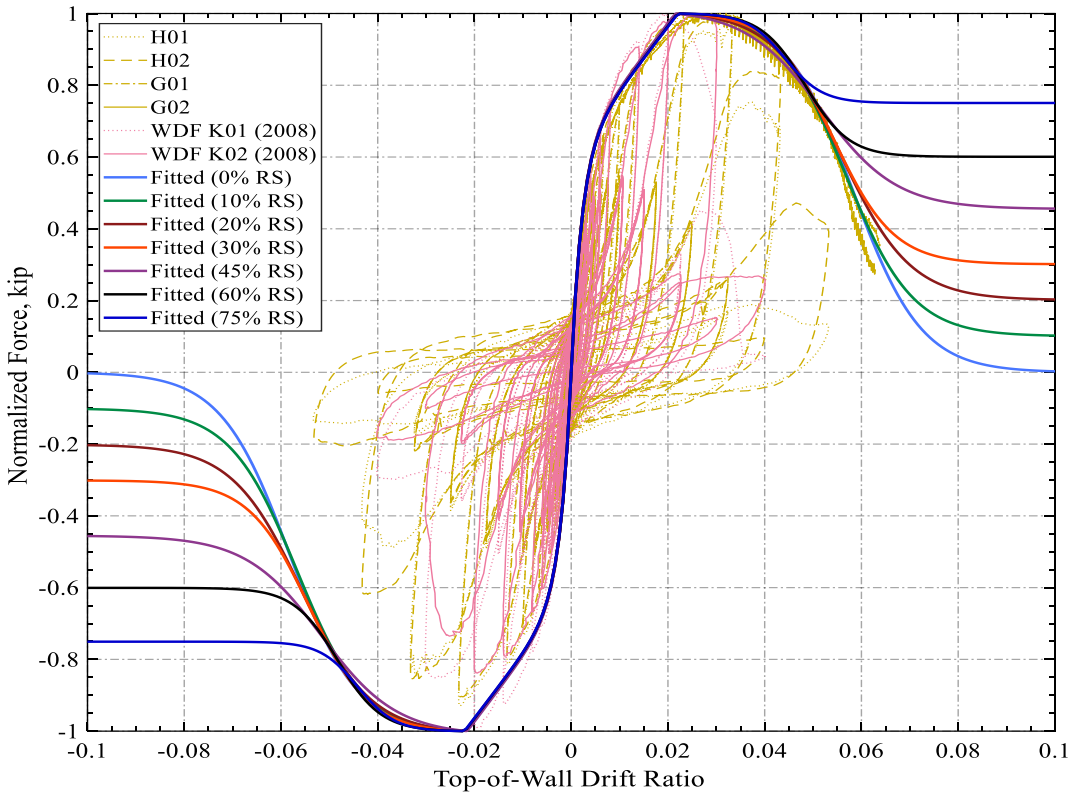

Figure D-16 **Fitted RESST Backbone curve models for 8-ft wide by 10-ft high OSB-High building blocks with 10%, 20%, 30%, 45%, 60%, 75% residual strength.**

Table D-9 **Normalized Wood Structural Panel RESST Hysteresis Parameters for OSB Walls Anchored with a Continuous Tie-down Rod System with Residual Strength Ratios of 0%, 10%, 20%, 30%, 45%, 60% and 75%**

Wall Type	*RS*	K_o (kip/in)	r_1	r_2	r_3	r_4	F_x (kip)	f_1	f_2	f_3	D_x (in)	α	β	F_u (kip)	D_u (in)	$f_3^* = F_x f_3 / F_{max}$
Structural OSB Continuous Tie-down Rod System	0.0	2.47	0.06	-0.12	1.01	0.01	1.006	0.61	0.16	0.00	7.00	0.60	1.15	1.0	2.6	0.00
	0.1	2.46	0.06	-0.11	1.01	0.01	1.006	0.61	0.16	0.10	6.80	0.60	1.15	1.0	2.6	0.10
	0.2	2.46	0.06	-0.10	1.01	0.01	1.007	0.61	0.16	0.20	6.70	0.60	1.15	1.0	2.6	0.20
	0.3	2.46	0.06	-0.10	1.01	0.01	1.004	0.61	0.16	0.30	6.50	0.60	1.15	1.0	2.6	0.30
	0.5	2.46	0.06	-0.08	1.01	0.01	1.003	0.61	0.16	0.45	6.20	0.60	1.15	1.0	2.6	0.45
	0.6	2.46	0.06	-0.08	1.01	0.01	1.001	0.61	0.16	0.60	5.80	0.60	1.15	1.0	2.6	0.60
	0.8	2.45	0.06	-0.06	1.01	0.01	1.001	0.61	0.16	0.75	5.30	0.60	1.15	1.0	2.6	0.75

D.4 Model Validation 2: FEMA P-2139-2 Baseline Models

The modeling approach discussed in Section 4.6 utilizing the ELF method to distribute the strengths of SFRS vertically was used to generate a series of new 2D MDOF models that represent the FEMA P-2139-2 baseline models.

The main difference between Validation 2 and Validation 1 (discussed in Section D.2) is that the 2D MDOF used in Validation 1 was designed to follow the FEMA P-2139-2 models as shown in Table D-7. However, in Validation 2, the 2D MDOF match only the following three primary building response properties:

- Peak base shear including both structural and nonstructural elements, V_{max}/W,
- Residual Strength Ratio, and
- Peak base structural strength, V_{STR}/W.

Other new and improved modeling assumptions of this study are retained in these new models (e.g., backbone curve shape for continuous tie-down rod system, vertical distribution of shear strengths). Table D-10 lists the differences between the FEMA P-2139-2 baseline models and Validation 2 models.

Table D-10 Comparison Between FEMA P-2139-2 Models and Validation 2 Models

	FEMA P-2139-2 Baseline Models	2D MDOF Models
Model type	Detailed 3D	Simplified 2D
OSB Backbone Model	Line et al., 2008	Line et al., 2019 (more representative of new multi-story construction)
Vertical distribution of Shear Strength	As-designed by practitioners	Code based ELF (optimal distribution)
Normalized Strength (V_{max}/W)	Two V_{max}/W were obtained by performing a pushover analysis in each of the two lateral directions	Assigned to match the average V_{max}/W of the responding FEMA P-2139-2 models
Story Weights	As-designed by practitioners	100 kips for each floor, except for roof = 60 kips.
Residual Strength Ratio	30% for each wall component. The combined building level residual strength may vary	Assigned to match the corresponding FEMA P-2139-2 models
Damping	0	0.01

Modal and static pushover analyses discussed in Section D.2.1 and incremental dynamic analyses discussed in Section D.2.2 were performed for each of the Validation 2 models presented in Table D-11. The median collapse acceleration ($\hat{S}_{CT}$) is used as the performance metric to compare between the results of FEMA P-2139-2 and Validation 2 models. The last column of Table D-11 shows that the differences between the predicted median S_{CT} values of the FEMA P-2139-2 and simplified 2D MDOF models are approximately within +/- 10%.

Table D-11 Summary of Median Collapse Acceleration and Median Peak Drift Ratio at Incipient Collapse for FEMA P-2139-2 and New 2D MDOF Models

No. of Stories	FEMA P-2139-2					New 2D MDOF				Percent Difference in $\hat{S}_{CT}$
	Model ID	V_{max}/W[b]	$\hat{S}_{CT}$[a] (g)	*DR*[d] (%)	*RS* actual	Model ID[c]	V_{max}/W[b]	$\hat{S}_{CT}$[e] (g)	*DR* (%)	
Commercial Buildings										
1-Story	COM1B	0.56	2.33	8.2%	0.35	1C-057-032-035	0.55	2.16	8.0%	-7.3%
	COM4B	0.67	2.60	8.8%	0.34	1C-068-043-034	0.66	2.52	9.0%	-3.0%
2-Story	COM2B	0.48	1.96	6.7%	0.35	2C-049-024-035	0.48	2.06	6.5%	4.9%
	COM5B	0.56	2.21	7.4%	0.34	2C-058-031-034	0.56	2.35	7.5%	6.5%
4-Story	COM3B	0.31	1.75	4.6%	0.38	4C-033-020-038	0.31	1.84	4.5%	5.2%
	COM6B	0.44	2.31	5.8%	0.35	4C-046-033-035	0.44	2.45	6.0%	6.2%
Multi-family Dwellings										
1-Story	MFD1B	1.30	3.64	7.1%	0.34	1M-131-028-034	1.30	3.30	7.0%	-9.4%
	MFD4B	1.41	4.15	10.1%	0.34	1M-142-043-034	1.41	3.91	10.0%	-5.8%
2-Story	MFD2B	0.68	2.50	9.0%	0.35	2M-069-025-035	0.68	2.75	9.0%	9.9%
	MFD5B	0.73	2.77	9.9%	0.36	2M-074-033-036	0.73	3.05	10.0%	10.2%
4-Story	MFD3B	0.37	1.81	5.2%	0.37	4M-038-023-037	0.36	1.76	5.0%	-2.7%
	MFD6B	0.44	2.31	5.4%	0.36	4M-045-031-036	0.43	2.35	5.5%	1.8%

[a] The median collapse acceleration values are obtained from FEMA P-2139-2 Table 5-2 with the spectral shape factor (*SSF*) removed. The median S_{CT} values include the 3D factor of 1.2.

[b] The normalized peak strengths (V_{max}/W) are the average values for each FEMA P-2139-2 3D model obtained from pushover analyses with P-Delta in two lateral directions. The V_{max}/W values for the two lateral directions are from FEMA P-2139-2 Table 5-1.

[c] See Section 4.6.5 Model ID and Nomenclature.

[d] The median peak drift ratios at incipient collapse in the first-story are obtained from FEMA P-2139-2 Table 5-3.

[e] The median collapse acceleration is taken at the peak first-story drift ratio of the corresponding FEMA P-2139-2 model (rounded to 0.5%).

Figure D-17 shows the correlation between the median S_{CT} of the Validation 2 models and the FEMA P-2139-2 COM and MFD models. The median S_{CT} data points fall along the one-to-one relationship line and have a very high correlation (correlation coefficient = 96.5%). Thus, the new 2D MDOF modeling approach is validated by comparison to the FEMA P-2139-2 models. This shows that the more efficient 2D MDOF models may be used in lieu of detailed 3D models to evaluate trends in collapse performance of wood light-frame buildings in very high seismic regions.

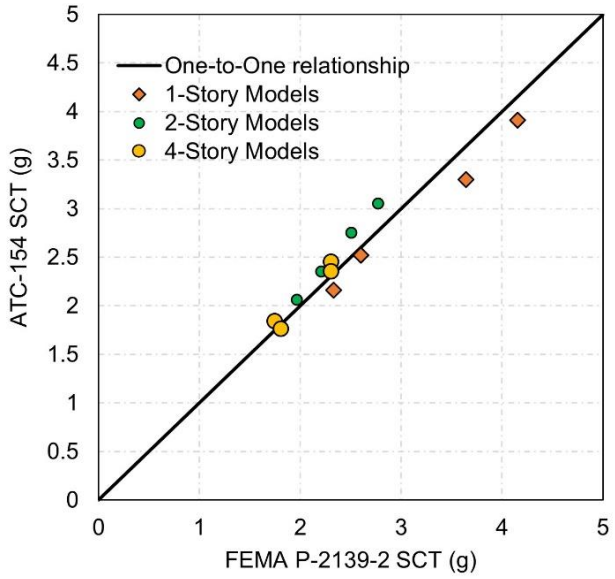

Figure D-17 Correlation between the median collapse accelerations predicted using the new 2D MDOF models (vertical axis) and FEMA P-2139-2 models (horizontal axis).

Appendix E: Equivalent Single - Degree-of-Freedom Non-Wood Models Development

E.1 Introduction

This appendix describes an approach for deriving equivalent single-degree-of-freedom (eSDOF) models from more complex 2D (or 3D) MDOF models. The application of the eSDOF concept to wood light-frame structures is considered first, followed by their application to the three non-wood systems investigated in Chapter 5.

E.2 Conceptual Approach of Developing eSDOF

E.2.1 Introduction

Deriving an eSDOF model from a complex MDOF nonlinear model requires consideration of three important and related nonlinear dynamic response issues: (1) shrinking the multiple degrees of freedom of the MDOF model into a single mode of vibration, (2) incorporating the amplitude-dependent response characteristics of the nonlinear MDOF model into this single mode of vibration, and (3) expressing response in terms of spectral acceleration and spectral displacement (e.g., rather than in terms of normalized pushover force and roof displacement). The Equivalent Lateral Force (ELF) procedure of Chapter 18 (and commentary) of ASCE/SEI 7-16 for the design of structures with a damping system provides all of the requisite terms and equations for developing a response in the "effective fundamental mode" (i.e., where "effective" implies the structure is implicitly nonlinear) and also in terms of a "residual mode of vibration" that accounts for combined dynamic response of all higher modes. The residual mode may not be required for collapse evaluation but provides a measure of the forces and displacements not captured by the effective fundamental mode.

In Chapter 18 of ASCE/SEI 7-16, amplitude-dependent response properties of the effective fundamental mode are evaluated at MCE_R and Design (2/3 of MCE_R) response levels (i.e., for the design of a building with a damping system). This Note uses the same methods as those of Chapter 18 to derive an eSDOF model from a 2D (or 3D) MDOF model but suggests evaluating nonlinear response at or beyond full yield (maximum strength) of the MDOF model to better reflect the displaced shape of the MDOF model at or near collapse displacements. For example, the displaced shape of an eSDOF model of either 2-story or 4-story models of wood light-frame archetypes of FEMA P-2139-2 would reflect the large nonlinear 1st-story displacements at a full yield of those models.

The amplitude-dependent response properties defined by Chapter 18 of ASCE/SEI 7-16 include the "effective seismic weight," recognizing that not all of the seismic weight (W) of the MDOF model

should be used to determine peak response of the effective fundamental mode (i.e., in contrast to the ELF formulas of Chapter 12 that assume 100 percent of the seismic weight acts in the 1st-mode). Likewise, the effective seismic weight would be used to evaluate the peak response of the eSDOF model. The amplitude-dependent response properties of Chapter 18 are defined in terms of "spectral response coordinates", recognizing that earthquake ground motion response spectra define peak response at the center of gravity of the effective fundamental mode of the MDOF. Likewise, response spectral displacement would be used to define peak displacement at the center of gravity of the eSDOF model (which is typically less than the peak roof displacement of the MDOF model).

Consideration of the effective seismic weight (and spectral response coordinates) can have a significant influence on the calculation of peak earthquake displacement and collapse performance of the equivalent 2D SDOF model. A notable exception would be those SFRSs, such as the wood light-frame SFRS, which fail at relatively large 1st-story drift ratios (i.e., SFRS models that have similar peak displacements at all stories). For those systems, the effective seismic weight of the eSDOF model is approximately the same as the seismic weight of the MDOF model, the peak displacement of the eSDOF model (i.e., a center of gravity) is about the same as the 1st-story displacement of the MDOF (and other stories of the MDOF), and additional displacement in the residual mode is negligible.

E.2.2 Steps for Developing eSDOF from MDOF

1. Perform the nonlinear pushover analysis of the MDOF with a lateral load distribution based on the first mode vector. Then, define the effective mass, W_p, and the effective height, H_p, for the first mode that is the mass and height of the proposed SDOF system using Equations E-1, E-2, and E-3.

$$W_p = \frac{\left(\sum w_i \phi_i\right)^2}{\sum w_i \phi_i^2} \tag{E-1}$$

$$\Gamma_p = \frac{W_p}{\sum w_i \phi_i} \tag{E-2}$$

$$H_p = \frac{H}{\Gamma_p} \tag{E-3}$$

   Where w_i is the weight of the ith story, ϕ_i is the pushover nonlinear mode shape of the *i*th story, and Γ_p is the modal participation factor.

2. Define the shear force, V_b, versus story drift, D, curve of each story using the pushover result in Step (1).

3. Determine the spectral acceleration and displacement (S_a–S_d) curve using the base shear force versus roof drift ratio curve using the pushover analysis result in Step (1) using Equations E-4, and Equation E-5:

$$F^* = \frac{V_b}{\Gamma_p} \tag{E-4}$$

$$delta^* = \frac{D}{\Gamma_p} \tag{E-5}$$

4. Determine the backbone curve of the inelastic spring equivalent to the MDOF using the base shear force versus roof drift ratio curve and mode vectors obtained from the pushover analysis result in Step (1).

5. Generate the proposed eSDOF model using the effective mass, effective height, and inelastic springs with the backbone curves determined in Step (4). Then perform nonlinear dynamic analysis of the proposed eSDOF system to evaluate the drift $\bar{\delta}$ of the eSDOF, then the relative displacement Δ_i of the *i*th story of the MDOF can be expressed by Equation E-6:

$$\Delta_i = \phi_i \Gamma_p \bar{\delta} \tag{E-6}$$

The story drift δ_i can be expressed by Equation E-7:

$$\delta_i = (\phi_i - \phi_{i-1}) \Gamma_p \bar{\delta} \tag{E-7}$$

E.2.3 Consideration of P-delta Effect

Approximate the reduction in pushover (backbone curve) strength due to P-delta effects of the eSDOF to represent those of the corresponding MDOF model.

Terms

W_P = effective weight of the eSDOF model at incipient collapse

D_P = displacement of the eSDOF model at incipient collapse

H_P = effective height of the eSDOF model at incipient collapse

DR_P= drift ratio of the eSDOF model at incipient collapse (D_P/H_P)

DR_{GS} = drift ratio of the story governing collapse of the MDOF model at incipient collapse

W = weight of the MDOF model

W_{GS}= weight of the MDOF model above the story governing collapse (i.e., $W_{GS} = W$ where the 1st-story govern collapse)

V_{PD} = partial P-delta force of the eSDOF model at incipient collapse

V_{PD}' = full P-delta force of the eSDOF model at incipient collapse

F_{DR} = factor used to increase P-delta force of the eSDOF model at incipient collapse to account for differences in story drift (pushover mode shape) of the MDOF at incipient collapse

$F_{DR} = DR_{GS}/D_{RP}$

F_W = factor used to increase/decrease P-delta force of the eSDOF model to account for the weight of the model above the governing story of the MDOF model

$F_W = W_{GS}/W_P$

METHODS OF P-DELTA CONSIDERATION:

Method 1: Indirect Calculation of ESDOF Pushover Curve with Full P-delta Effect (Implicit P-delta)

1. Calculate cyclic pushover curves of the MDOF model with and without P-delta.
2. Find the modal participation factor at certain D_p (for example at $0.5V_{max}$) using Equation E-2. Then, transform the cyclic pushover of MDOF based on the effective weight (Equation E-1), and effective height (Equation E-3).
3. Model the SDOF spring by finding the linear and nonlinear backbone parameters that fit the transformed MDOF cyclic pushover response.
4. Run nonlinear time history analysis without the P-delta effect because it is implicitly considered in the backbone curve.

Method 2: Direct Calculation of eSDOF Pushover Curve with Full P-delta Effect (Explicit P-delta)

1. Calculate modal pushover curves of the MDOF model with and without P-delta.
2. Find the modal participation factor at certain D_p (for example at $0.5V_{max}$) using Equation E-2. Then, transform the cyclic pushover of MDOF based on the effective weight (Equation E-1), and effective height (Equation E-3).
3. Model the SDOF spring by finding the hysteresis loop backbone parameters which fit the transformed MDOF cyclic pushover response without P-delta.
4. Calculate pushover curve the eSDOF model with full P-delta by modifying the amount of vertical load, P', used to evaluate P-delta:

$$P' = F_{DR} \times F_W \times W_p$$

5. Run nonlinear time history analysis with P-delta effect.

Method 3: Indirect Calculation of eSDOF Pushover Curve with Full P-delta Effect by Adding a P-delta Spring (Implicit P-delta)

1. Run modal and cyclic pushover analysis of the MDOF with and without P-delta effect.
2. Find the modal participation factor at certain D_p (for example at $0.5V_{max}$) using Equation E-2. Then, transform the cyclic pushover of MDOF based on the effective weight (Equation E-1), and effective height (Equation E-3).
3. Model the SDOF spring by finding the linear and nonlinear backbone parameters which fit the transformed MDOF cyclic pushover response without P-delta.
4. Create a P-delta nonlinear elastic spring that imposes a force equal to the force difference between MDOF with P-delta and MDOF without P-delta.
5. Run time history analyses using the fitted hysteresis parameters without P-delta effect because it is considered implicitly using the P-delta spring.

E.3 Model Development

In this section, the eSDOF is developed for the simplified 2D MDOF from Chapter 4, which was based on a selected model of FEMA P-2139-2.

E.3.1 Selected P-2139-2 3D Model and the Simplified MDOF (2D)

The selected 3D model for validation is a 4-story multifamily dwelling model designed following ASCE/SEI 7-10 for SDC D_{max} locations, corresponding to a short-period design response acceleration parameter (S_{DS}) of 1.00g and maximum considered earthquake (MCE_R) ground motion spectral acceleration (S_{MS}) of 1.5g. This is the same 3D model from FEMA P-2139-2 that was used for validation in Appendix D. A simplified 2D MDOF model was developed and shown in Appendix D to have substantially equivalent collapse performance. That 2D MDOF model is used here for comparison to the eSDOF model. More details about the 3D MDOF modeling and design can be found in FEMA P-2139-2.

E.3.2 eSDOF 3D Model

The eSDOF model is a frame with rigid studs and rigid beams with pin-pin boundary conditions. Therefore, without the spring, the model is unstable. Each node at the top of the stud carries half of the effective weight (W_p). The springs are modeled to include all structural and nonstructural wall elements. The eSDOF is modeled using the *Timber3D* program. The height is equal to the effective height (H_p). Figure E-1 presents a schematic illustration of the eSDOF in *Timber3D*.

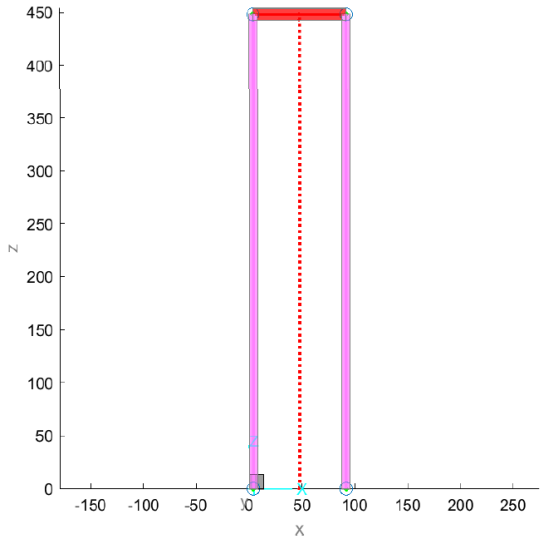

Figure E-1 Schematic illustration of the eSDOF *Timber3D* model.

E.3.3 Steps of eSDOF Development

1. Run 2D MDOF modal and cyclic pushover analysis based on Mode1, with and without P-delta effects. Figure E-2 shows the cyclic pushover analysis without P-delta consideration and modal pushover analysis with and without P-delta influence. The negative P-delta force is the difference between the base shear (BS) with P-delta and without P-delta (pink line).

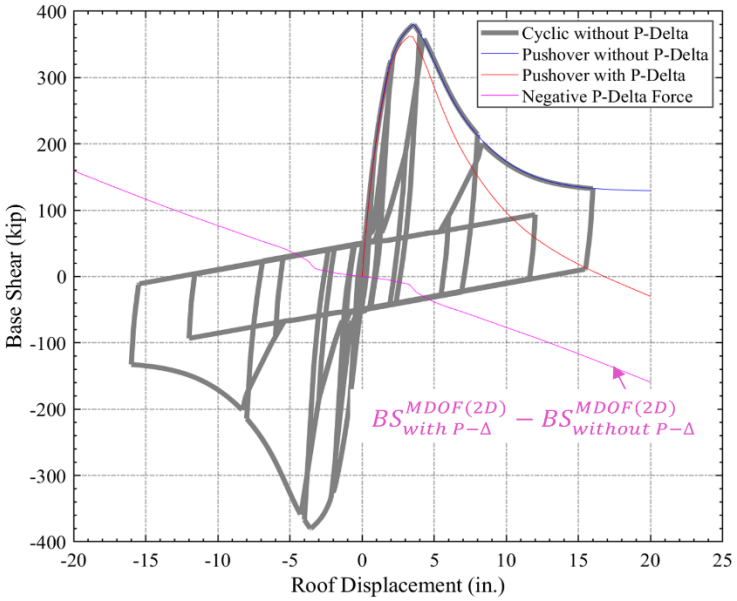

Figure E-2 Cyclic and modal pushover analysis for the 2D MDOF.

2. Derive the drift profile of the MDOF modal pushover with P-delta at $0.5V_{max}$ (See Figure E-3)

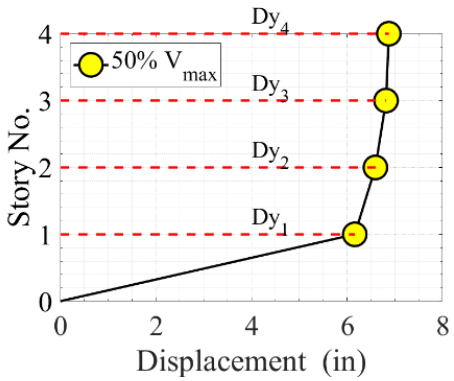

Figure E-3 Drift profile of the MDOF modal pushover analysis with P-delta at 0.5V_{max}.

3. Derive the eSDOF parameters according to equations mentioned in Section E.2.2.

$$W_p = \frac{\left(\sum w_i \phi_i\right)^2}{\sum w_i \phi_i^2} = 966.4 \text{ kips}$$

$$\Gamma_p = \frac{W_p}{\sum w_i \phi_i} = 1.07$$

$$H_p = \frac{H}{\Gamma_p} = 37.35 \text{ft}$$

4. Fit the linear and nonlinear hysteresis parameter to the cyclic pushover analysis without the P-delta effect (see Figure E-4).

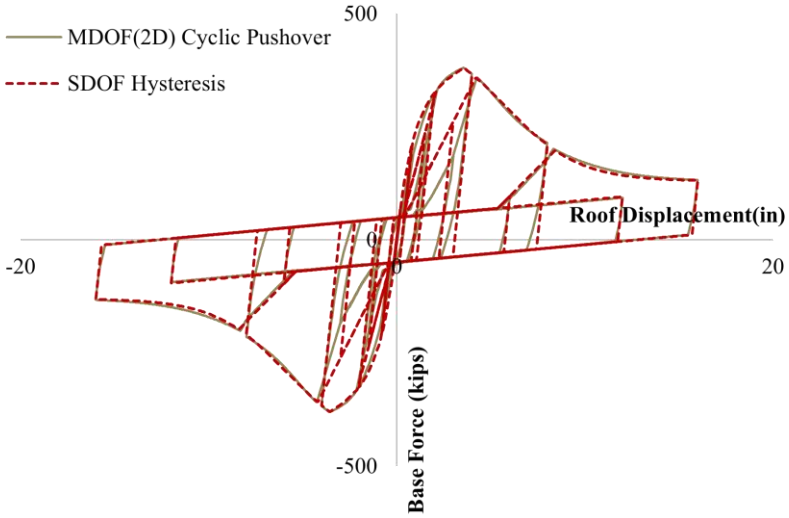

Figure E-4 2D MDOF cyclic pushover analysis and the fitted RESST parameters for the eSDOF.

5. To consider the P-delta effect for the eSDOF, Method 3 is followed. Therefore, a linear P-delta spring was added with a force-displacement relationship equal to the negative P-delta force from the 2D MDOF model as shown in Figure E-5.

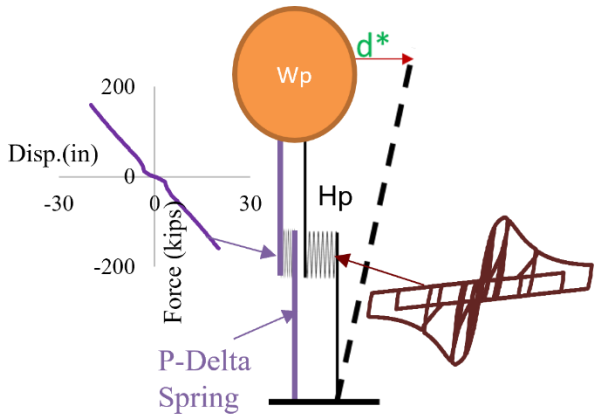

Figure E-5 A linear P-delta spring with a force-displacement relationship equal to the negative P-delta force from the 2D MDOF model was used for the eSDOF model.

E.4 eSODF Validation

The eSDOF model was validated by comparison of dynamic properties and collapse results of with 2D MDOF. To validate the eSDOF model, the following analysis methods are conducted:

- Free vibration analyses to evaluate elastic natural periods and mode shapes,
- Nonlinear static pushover analyses, and
- Nonlinear IDAs per FEMA P-695 methodology.

E.4.1 Free Vibration Analysis and Nonlinear Static Pushover Analysis

Eigenvector analysis was performed to evaluate the fundamental period for the eSDOF and 2D MDOF models. The fundamental period of 2D MDOF was 0.49 sec, and that of the eSDOF was 0.50 sec, showing a close match.

The pushover analysis was conducted along the longitudinal direction of the eSDOF and the 2D MDOF models to extract the overall backbone base shear versus roof displacement response.

The pushover curves for the eSDOF, 2D MDOF, and 3D MDOF models are shown in Figure E-6. The eSDOF model has the same normalized peak pushover strength and same overall backbone base shear versus roof displacement response.

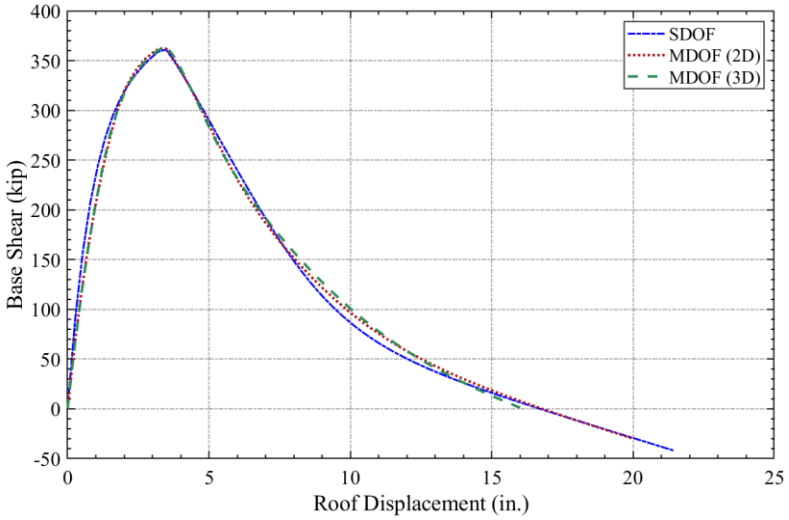

Figure E-6 Pushover curves for the eSDOF, 2D MDOF, and 3D MDOF models.

E.4.2 Nonlinear Incremental Dynamic Analysis

Timber3D was used to perform the nonlinear IDAs according to FEMA P-695 methodology. The 44 FEMA P-695 Far-Field ground motions are used for the IDAs. The records were scaled to the median spectra at the period of 0.25 seconds as per P-2139-2. The IDA analysis was conducted at a specific level of ground motion intensity. The intensity levels are increased with a 0.05g increment, up to an intensity level for which the ground motion caused the model to collapse. At each intensity level, for the three-dimensional model, the 44 ground motions are applied in one orthogonal orientation (longitudinal direction)—which is not the case for the 3D models in P-2139-2—to obtain a comparable response to the 2D MDOF model. The P-delta effect was included. A zero inherent viscous damping is assumed for the eSDOF, 2D MDOF, and 3D MDOF models.

In FEMA P-2139-2, the collapse was explicitly simulated using *Timber3D*. Collapse was defined as when the control node on the roof of the building model achieved a vertical displacement equal to the story height. In this study, collapse is evaluated using simulated collapse and non-simulated collapse.

Figure E-7 shows IDA results for the eSDOF. Peak roof drift was selected as the parameter used to quantify the displacement capacity; the first story drift ratio is calculated using Equation E-6. The blue markers in the figure indicate points of incipient collapse. Also shown in the figure, the fitted lognormal probability density functions of peak roof drift and median spectral acceleration (S_{MT}) at incipient collapse. To compare the 2D MDOF and eSDOF IDAs, the earthquake-to-earthquake spectral acceleration at incipient collapse is plotted in Figure E-8. This figure shows that the S_a at incipient collapse of the eSDOF model had a good match with the 2D MDOF model. The relationship between the incipient collapse S_a between the 2D MDOF and eSDOF is plotted in Figure E-9. The values of S_a at incipient collapse are scattered around the one-to-one line (45-degree line). The median of the ratio of eSDOF S_a at incipient collapse to the 2D MDOF is 0.95, and the dispersion is

0.18. Nonlinear response under two earthquakes at incipient collapse were studied to further investigate the difference between the nonlinear behavior of eSDOF versus the 2D MDOF. The first earthquake is earthquake number 10 (EQ#10: ARC000 and ARC090, FEMA P-695 TableA-4). This earthquake resulted in the same S_a at incipient collapse (right on the one-to-one line, Figure E-9). The second earthquake is earthquake number 4 (EQ#4: HEC000 and HEC090, FEMA P-695 TableA-4), which was one of the furthest points from the one-to-one line (Figure E-9).

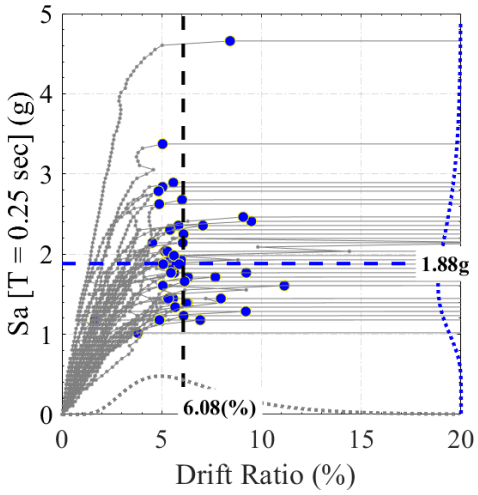

Figure E-7 **IDA curves and probability density functions of peak roof drift and median spectral acceleration at incipient collapse for the eSDOF.**

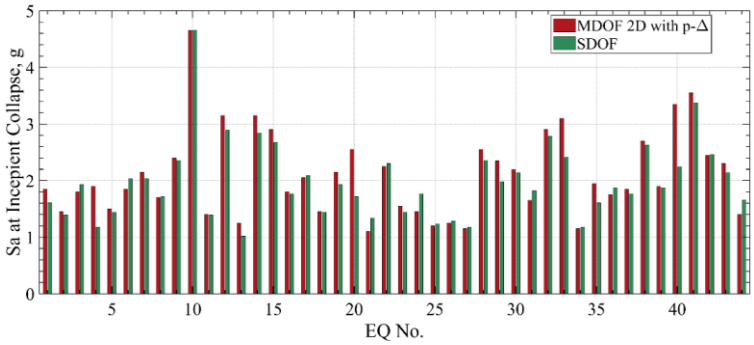

Figure E-8 **Earthquake-to-earthquake spectral acceleration at incipient collapse for 2D MDOF and eSDOF.**

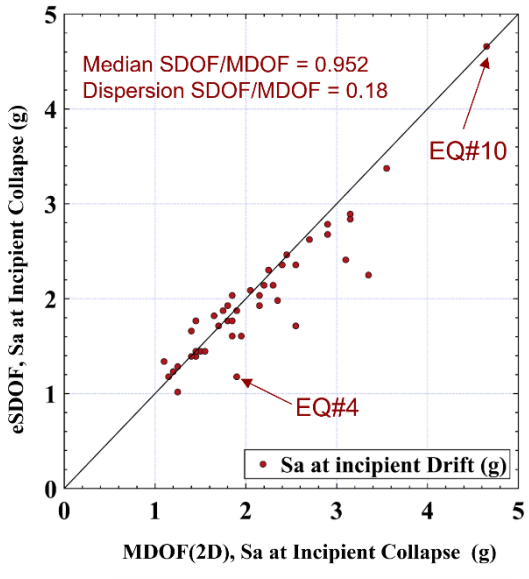

Figure E-9 Earthquake-to-earthquake spectral acceleration statistics at incipient collapse for 2D MDOF and eSDOF.

Example 1: the time history response of EQ#10 at S_a level of 4.65g (incipient collapse level). The time history response of 2D MDOF is like that of eSDOF (refer Figure E-10). The drift profile of the maximum and minimum points of the time history is plotted in Figure E-11. The original drift profile of SDOF (green lines of Figure E-11) is transformed to 2D MDOF shape using Equation E-6 (yellow lines of Figure E-11). The transformed eSDOF profile depends on the model shape ϕ_i. In this appendix, the mode shape used for the analysis is the normalized pushover drift profile at $0.5V_{max}$ (Figure E-3). Under EQ#10, the eSDOF and 2D MDOF models had similar drift profile with higher first story drifts, which is why the eSDOF and 2D MDOF models had the same peak nonlinear response under this earthquake.

Example 2: the time history response of EQ#4 at S_a level of 1.2g (incipient collapse level). The time history response of MDOF and eSDOF is similar as shown in Figure E-12. The drift profile of the maximum and minimum points in the time history is plotted in Figure E-12. The original drift profile of eSDOF (green lines of Figure E-12) is transformed to the 2D MDOF shape using Equation E-6 (yellow lines of Figure E-12). The transformed eSDOF profile depends on the model shape ϕ_i. In this appendix the mode shape used for the analysis is the normalized pushover drift profile at $0.5V_{max}$ (Figure E-3). Under EQ#4, the eSDOF and 2D MDOF had different drift profiles. While the eSDOF follows the $0.5V_{max}$ drift profile, the 2D MDOF response was almost linear, which is why the eSDOF and 2D MDOF models had different nonlinear peak responses under this earthquake.

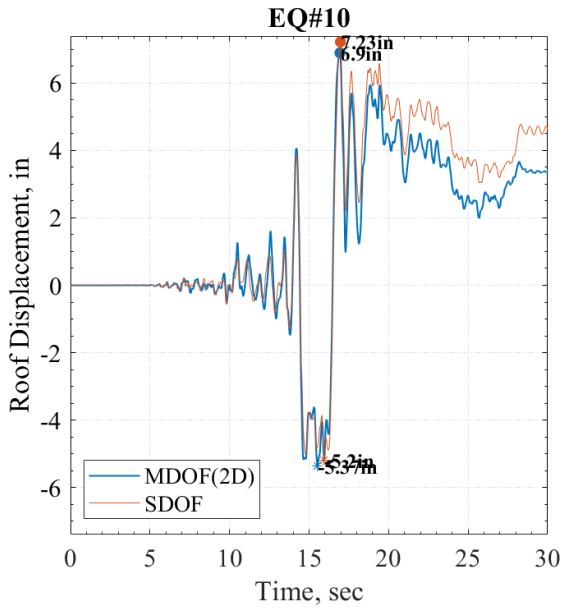

Figure E-10 **Time history responses of EQ#10 at intensity level of 4.65g for 2D MDOF and eSDOF models.**

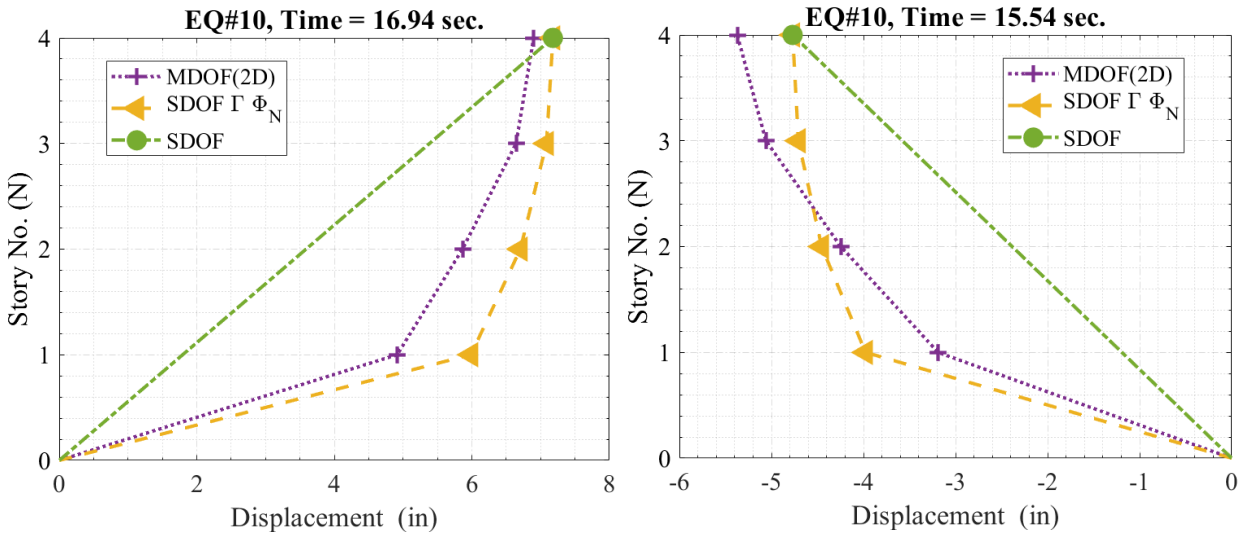

Figure E-11 **Nonlinear drift profiles at the maximum and minimum points of the incipient collapse time history of EQ#10.**

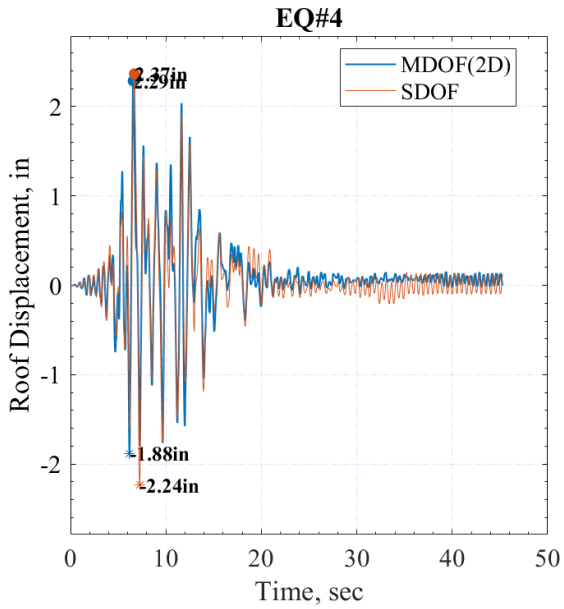

Figure E-12 Time history responses of EQ#4 at intensity level of 1.2g for 2D MDOF and eSDOF models.

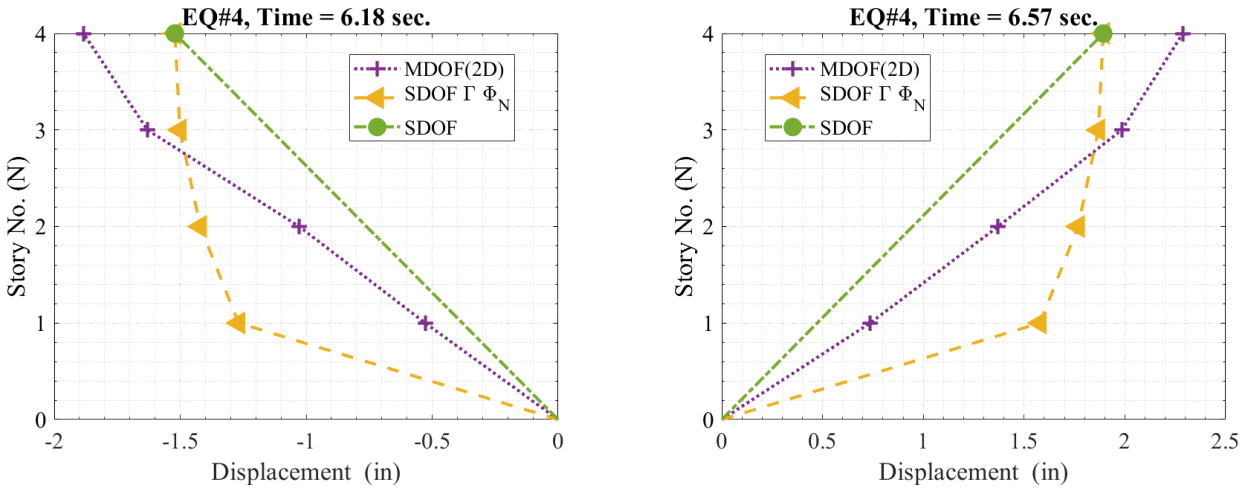

Figure E-13 Nonlinear drift profiles at the maximum and minimum points of the incipient collapse time history of EQ#4.

FEMA P-695 analysis methods are used for calculating the collapse probability for the validation study. Figure E-14 presents the simulated collapse rates for the eSDOF, 2D MDOF, and 3D MDOF models. Collapse rates are within a 2.5% difference. Also, the figure shows the FEMA P-695 collapse probabilities fitted to lognormal distributions with a dispersion of 0.5. Median collapse values ($\hat{S}_{CT}$) are shown in Table E-1.

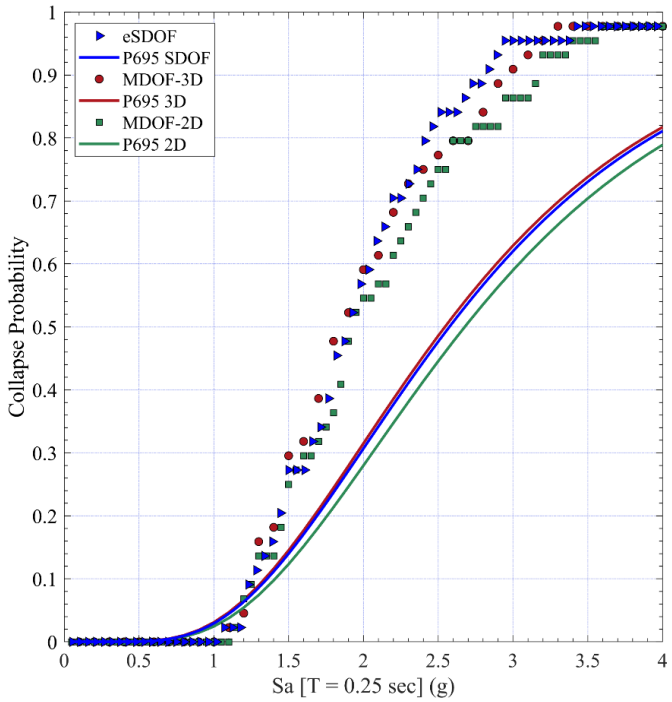

Figure E-14 **Collapse rates from IDA and FEMA P-695 collapse fragility curves for eSDOF, 2D MDOF, and 3D MDOF models.**

Table E-1 **Median Collapse Values from eSDOF, 2D MDOF, and 3D MDOF Models**

Model	$\hat{S}_{CT}$ (g)
2D MDOF	2.01
3D MODF	1.91
eSDOF	1.96

E.5 Development and Validation of eSDOFs for Other Systems

The use of eSDOFs was extended to three other seismic-force-resisting systems to enable the studies described in Chapter 5. The selected systems included steel buckling restrained braced frames (BRBFs), special steel moment resisting frames (SMFs), and ductile coupled reinforced concrete shear walls (DCWs).

E.5.1 Buckling Restrained Braced Frames

Ochoa (2017) developed a series of models for various BRBF designs. The intent of that study was to study the impact of using the ASCE/SEI 7 stability coefficient in the designing the BRBFs. While the

purpose of the current study differs, the archetype designs, many of which reflect current practice, detailed models and results in Ochoa (2017) are useful for developing and validating the eSDOF approach for simulating BRBFs.

The archetype building layout and frame elevations (east-west) from Ochoa are shown in Figure E-15. As shown, 4, 9, and 15 story frames were designed and analyzed. The buildings were designed for ASCE/SEI 7-10, AISC 360-10, and AISC 341-10. Notably, there was only BRBF on each face of the building requiring the use of the redundancy factor, ρ, equal to 1.3 in the designs. The buildings were designed for Seattle, Washington on Site Class C. Both ELF and Modal Response Spectrum Analysis (MRSA) designs were developed and a 15% reduction in ELF base shear was allowed, per ASCE/SEI 7-10, when computing MRSA forces.

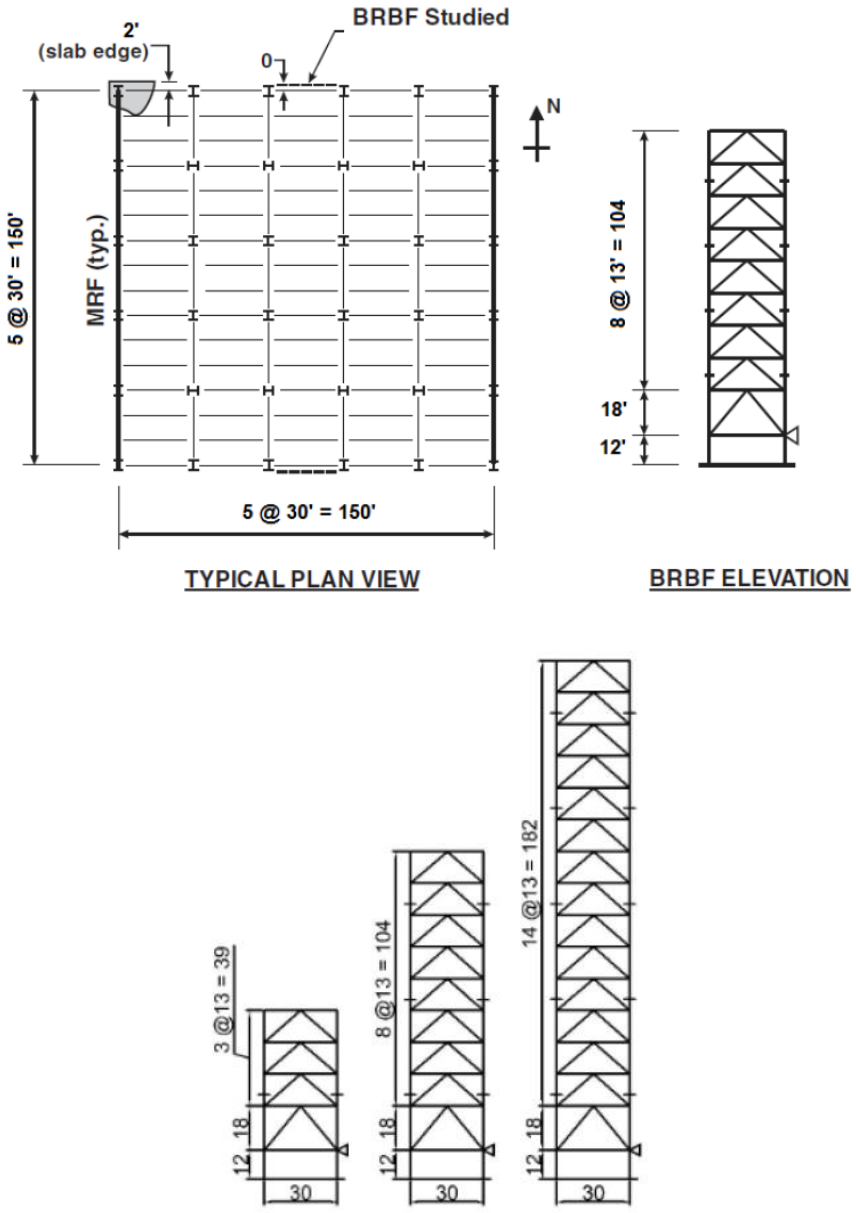

Figure E-15 BRBF archetype plan and elevations (Ochoa, 2017).

There were several design approaches studied by Ochoa (2017), one of the main points being the use of the stability requirements of AISC 360-10, where the lateral force used for design should be multiplied by the factor B_2 to account for second order effects. In general, it is shown in the study that including that stability factor in design improves the behavior of the BRBF and helps it pass FEMA P-695 criteria for the seismic force modification factor of 8. Sections sizes for BRBF members and gravity frame columns are available for each design in Ochoa (2017).

While there are certainly differences between the designs developed by Ochoa (2017) with ASCE/SEI 7-10 and what one would obtain with ASCE/SEI 7-16, including changes to the seismic

hazard, soil coefficients, and rules for using MRSA, the designs developed appear reasonable. Table E-2 summarizes the key design variables for the archetypes that will be used here to validate the eSDOF procedure.

Table E-2 BRBF Archetype Characteristics from Ochoa (2017)

Archetype Name	No. Stories	Roof Height (ft)	Seismic Weight (kips)	C_uT_a (sec)	C_s	V_{ELF} (kips)	V_{MRSA} (kips)
BRBF4-2	4	57	9514	0.87	0.066	625	531
BRBF9-2	9	122	21780	1.54	0.040	982	741
BRBF15-2	15	200	36500	2.23	0.040	1461	1242

Ochoa (2017) developed complex models of the BRBFs that were designed. A schematic of the modeling approach is shown in Figure E-16. Importantly, all columns were included in the analysis, including the gravity frame columns, which were modeled using the same lumped plasticity approach as shown for the columns in the BRBFs. The following summarizes considerations for the detailed models in Ochoa:

1. Beams and columns were modeled using a lumped plasticity approach where zero length springs at the ends of the elements accounted for their deterioration using the modified Ibarra-Medina_Krawinkler (IMK) model available in *OpenSees*. Column flexural strength was reduced for axial loads from gravity loading. Note that the axial loads in BRBF columns may be large and may reduce the flexural strength of the columns. Hence, the contribution of the columns in strong-axis bending may be overstated in the models.
2. Corotational truss elements were used to model the BRBs. The elements used the Steel04 material model in *OpenSees* and their behavior was calibrated to an extensive test database of BRBs. BRB fracture was simulated using a low cycle fatigue model and Minor's Rule for accumulating low cycle fatigue damage.
3. Gusset plates were not explicitly modeled, but their impact on the location of frame plastic hinging was by rigid zones to push beam and column hinging to the ends of the gusset plates.
4. Gravity loads were applied consistent with the recommendations of FEMA P-695.

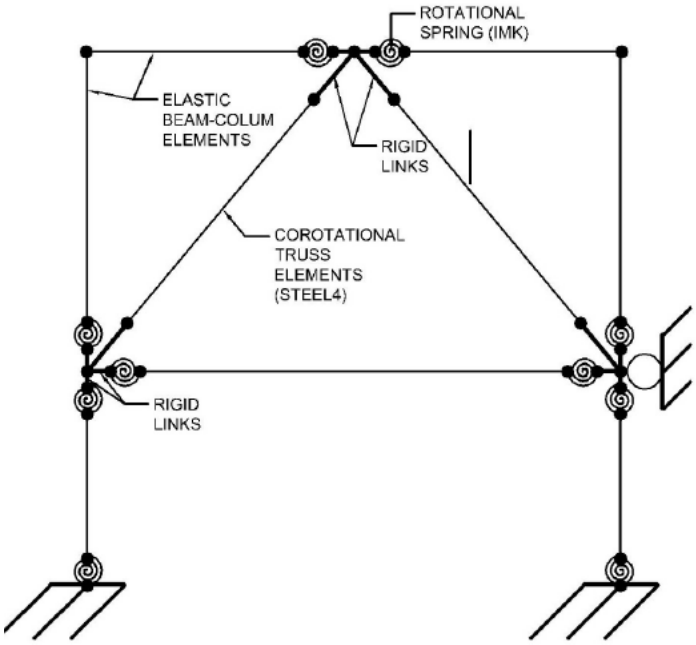

Figure E-16 Schematic of BRBF model (Ochoa, 2017).

The FEMA P-695 Far-Field ground motions were used to assess the collapse performance of the designs. Two potential collapse criteria were considered: (i) the incremental dynamic analysis curve flattens or there is an analysis convergence failure (which was verified to occur at instances of BRBF fracture from low cycle fatigue) and (ii) an approximate 4% story drift non-simulated collapse mode, which is due to BRBs reaching a monotonic ductility limit of 30. The authors note that testing has demonstrated that BRBF gusset and frame connections suffer severe damage at this drift as well.

For archetypes and detailed models shown in Table E-2, eSDOFs were developed. First, the pushover mode shapes for the archetypes were identified. In this case, the pushover modes were based on the story drift profiles from pushover analysis at δ_u as defined in FEMA P-695 and provided in Ochoa (2017). The resulting pushover mode shapes are shown in Figure E-17. For the four-story model, δ_u was 3.33% roof drift, for the nine-story model it was 2.12% roof drift, and for the 15-story model it was 1.99% roof drift.

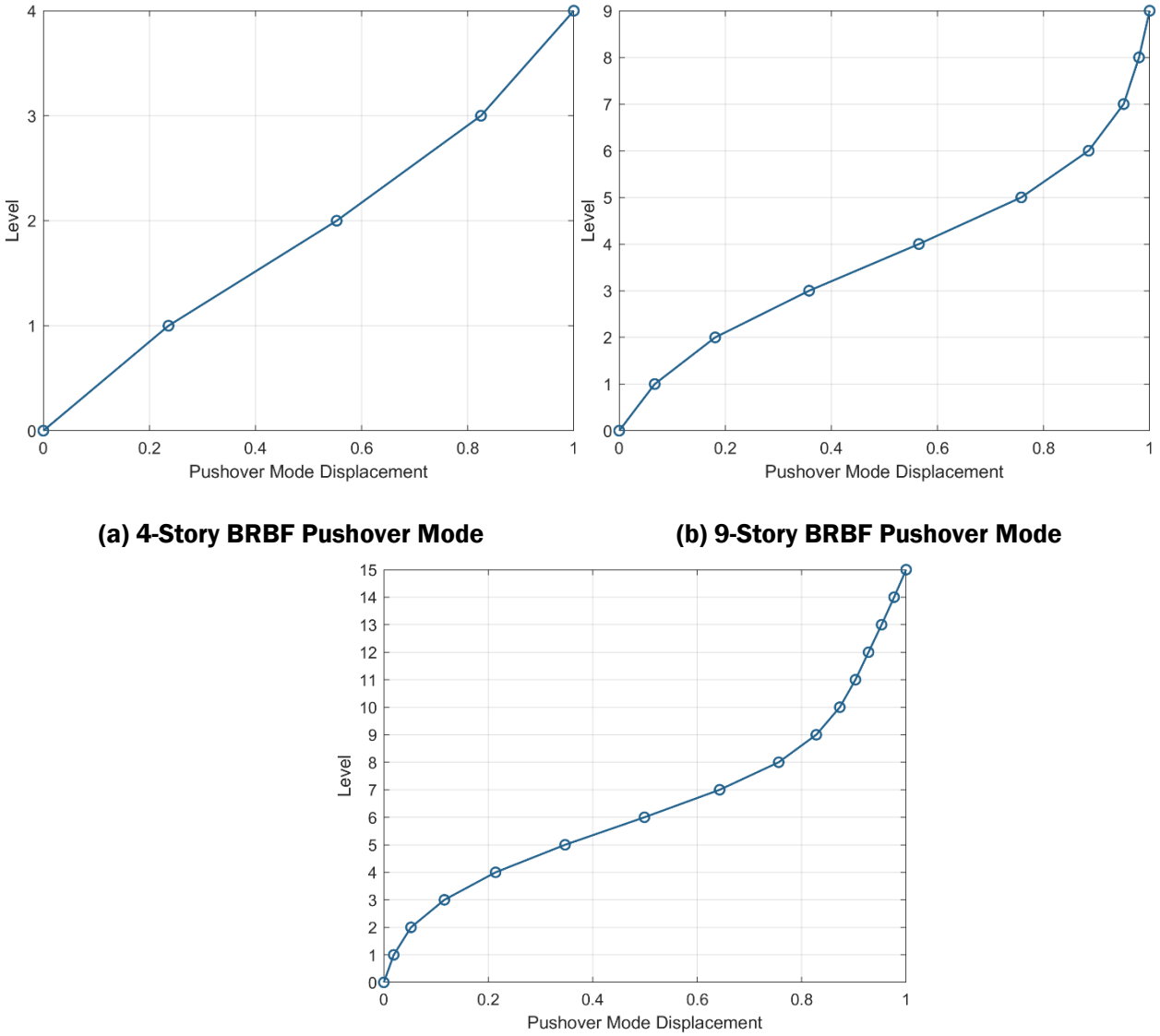

(a) 4-Story BRBF Pushover Mode

(b) 9-Story BRBF Pushover Mode

(c) 15-Story BRBF Pushover Mode

Figure E-17 Pushover mode shapes scaled to estimated maximum roof displacement of the MDOF models compared with the eSDOF models showing the effective height of the SDOF models.

The backbone behavior was then derived for each BRBF model using the nonlinear static analysis results from Ochoa (2017). A trilinear estimation of the nonlinear static response was used as the IMK model in *OpenSees* for the eSDOF behavior. Figure 5-1 shows the generic backbone trilinear curve. Figure E-18 shows the backbone response from Ochoa (2017) compared to the trilinear fit for each building height.

Cyclic deterioration for the eSDOF models must also be defined. Figure E-19 shows the IMK model, which is capable of modeling several types of deterioration (e.g., strength, stiffness, reloading stiffness), used to represent the BRBFs. For the BRBFs, the vast majority of the system's lateral strength is derived from the BRBs, which have very little strength deterioration prior to fracture. After

BRB fracture, P-delta controls, and a mechanism forms at the levels where brace fracture occurred, resulting in the significant negative slope observed in the nonlinear static response. Therefore, cyclic deterioration is not considered, and the backbone is used to generate the necessary negative stiffness at large drifts.

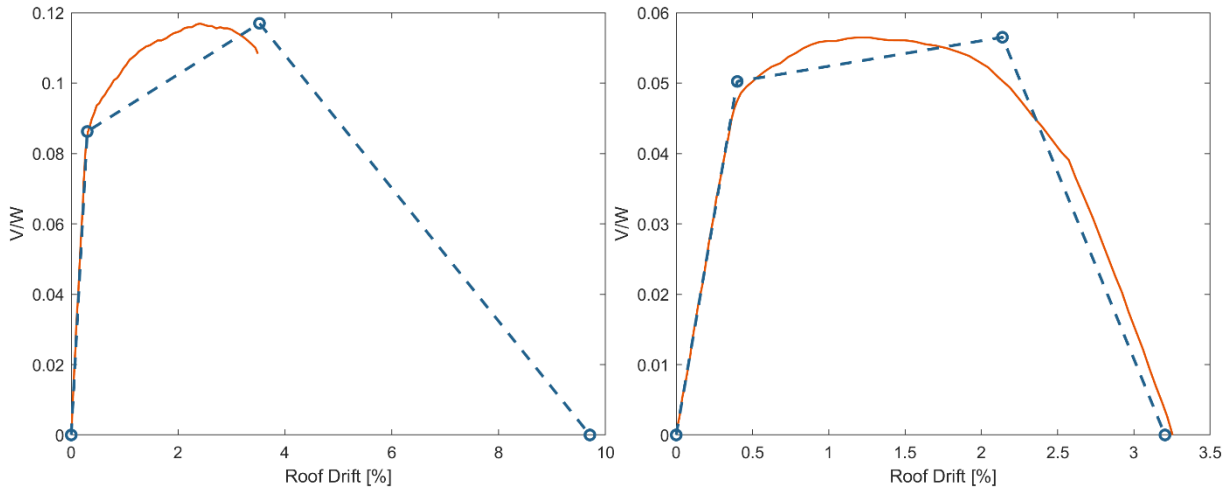

(a) 4-Story BRBF **(b) 9-Story BRBF**

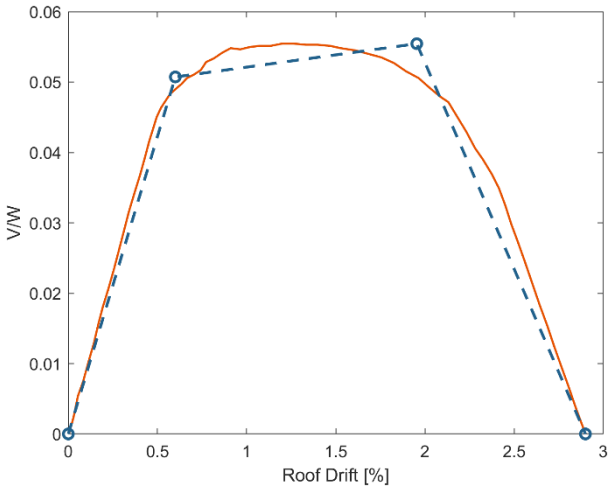

(c) 15-Story BRBF

Figure E-18 Pushover curves and trilinear approximated backbones. The data for the 4-story BRBF MDOF model is only available to the drift shown.

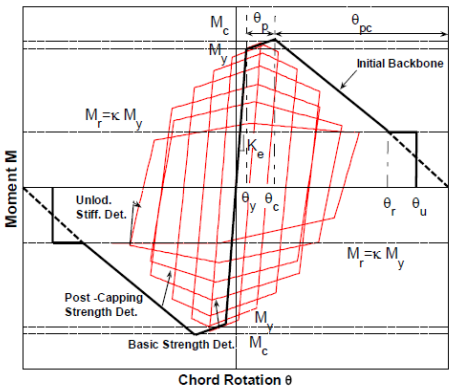

- Effective yield strength and rotation (M_y and θ_y)
- Effective stiffness $K_e=M_y/\theta_y$
- Capping strength and associated rotation for monotonic loading (M_c and θ_c)
- Pre-capping rotation capacity for monotonic loading θ_p
- Post-capping rotation capacity θ_{pc}
- Residual strength $M_r = \kappa M_y$
- Ultimate rotation capacity θ_u

Figure E-19 Modified IMK material model in *OpenSees* (Ibarra and Krawinkler, 2005). Note for eSDOF models of BRBFs, cyclic deterioration was not used.

After developing the pushover modes, backbone response, and cyclic behavior, the eSDOF was created by transforming the backbone response using the modal equations presented in Section E.2.2. The FEMA P-695 Far-Field record set was used to conduct incremental dynamic analysis. The results were then converted back into base shear and roof drift. After conversion, both collapse criteria in the Ochoa (2017) study were included. These included: (1) a maximum interstory drift of 4% to represent a monotonic ductility limit for the BRBs, and a limit for damage to the surrounding frame, and (2) a cumulative ductility/low cycle fatigue limit that was in the material of the BRBs in Ochoa (2017) but was post processed for the eSDOFs. The low cycle fatigue limit was applied by computing the maximum interstory drift at each time step using the pushover mode, then rainflow counting to determine the number of cycles at each drift level, converting that to BRB strain using the brace dimensions from Ochoa (2017) and plugging the resulting approximate cumulative BRB strain into the Coffin-Manson LCF curve used by Ochoa (2017).

Table E-3 compares the median collapse spectral accelerations from Ochoa (2017) to those obtained from the eSDOF analyses. As shown, there is good agreement indicating that the eSDOF approach should be useful for approximating the median collapse spectral acceleration for BRBFs. Notably the results for the 15-story model are the farthest from the results reported by Ochoa. This is likely due to the presence of higher modes in the response and indicates that 15 stories is perhaps the upper limit for using a calibrated eSDOF model to estimate BRBF collapse.

Table E-3 Comparison of Median Collapse Spectral Acceleration for BRBFs from Ochoa (2017) and from eSDOF Analysis

Archetype	Median $S_c(T)$ from Ochoa (2017) (g)	Median $S_c(T)$ from eSDOF (g)
4-Story (BRBF4-2 in Ochoa 2017)	1.22	1.19
9-Story (BRBF9-2 in Ochoa 2017)	0.65	0.63
15-Story (BRBF15-2 in Ochoa 2017)	0.52	0.44

E.5.2 Steel Special Moment Resisting Frames

Steel special moment resisting frames (SMFs) were selected for the development of collapse surfaces as they are notably common in regions of very high seismicity. The data needed for calibration and validation of the eSDOF models required the use of studies that performed FEMA P-695 analyses on a modern code-compliant SMF and had the deformed shape at large drifts available. One such study was found to be the work documented in FEMA P-2012 (FEMA, 2018). That work was focused on the impacts of configuration irregularities on seismic performance and studied a range of systems. As part of that work, a series of regular and code-compliant SMF designs were developed to serve as baseline models irregularity study. These baseline regular designs and their numerical models and simulation results provide the necessary data for testing the use of eSDOFs to represent SMF systems and estimate their median collapse capacity.

The SMFs of interest from FEMA P-2012 are the 3- and 9- story baseline models designed for the maximum spectral accelerations for SDC D_{max}. The frames were designed using ASCE/SEI 7-16 and AISC 341-10 and the MRSA procedure. The building geometries were identical to those developed for the SAC Steel Project and are shown below in Figure E-20.

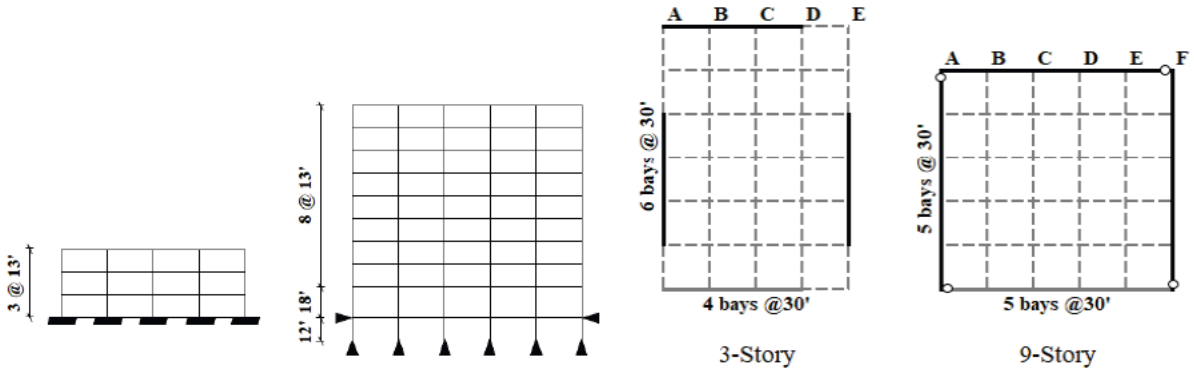

Figure E-20 Archetype SMF building geometries from FEMA P-2012.

The designs for SDC D_{max} were developed for the criteria shown in Table E-4. Drifts were then checked using the ELF demands and the elements were revised to meet a 2% story drift criteria. The 3-story archetype selected for comparison with eSDOF analysis was V0300203(1), while the 9-story

was V0900201(1). FEMA P-2012 Appendix C contains the complete details on the archetype designs, including member sizes.

Table E-4 SMF Archetype Characteristics from FEMA P-2012

Archetype Name	No. Stories	Roof Height (ft)	Seismic Weight (kips)	C_uT_a (sec)	Design Base Shear (MRSA) (kips)
V0300203(1)	3	57	6781	0.735	679
V0900201(1)	9	122	20311	1.83	1341

Detailed nonlinear models were developed and used in the FEMA P-2012 work to establish the collapse capacity of the archetypes. The modeling approach is illustrated in Figure E-21. Lumped plasticity models were used to represent the beam and columns, where the nonlinear behavior was specified with the modified IMK model in *OpenSees*. Nonlinear behavior of the panel zones was also simulated using a 2D joint element in *OpenSees* developed by Altoontash (2004). Generally, the recommendations of NIST GCR 17-917-46v2 were used for modeling the nonlinear behavior of the beams and columns. Composite action for the beams was considered in the development of their behavior.

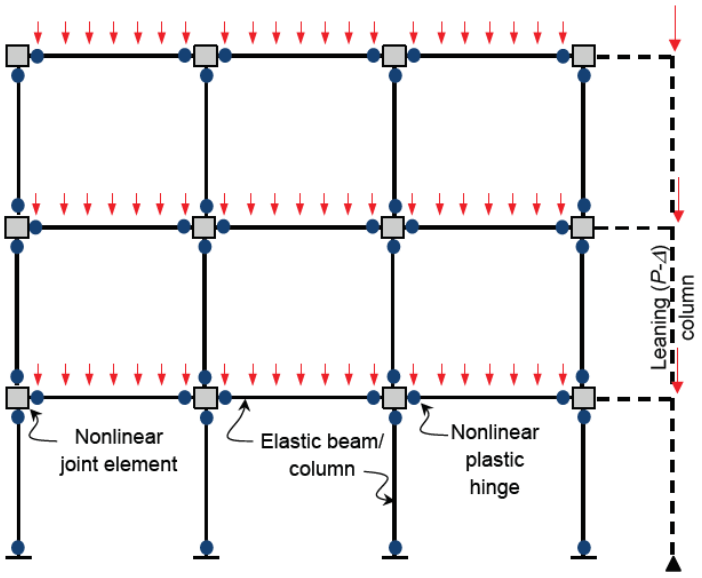

Figure E-21 SMF model schematic from FEMA P-2012.

Pushover modes shapes were developed from the median interstory drift profile near collapse from IDA analysis. This data was reported by the lead analysis team of the SMF study for FEMA P-2012 in private communication. Figure E-22 shows the pushover mode shapes for the two SMFs. As shown, the drift distribution for the 3-story frame is fairly uniform while the 9-story has some drift concentration on lower stories.

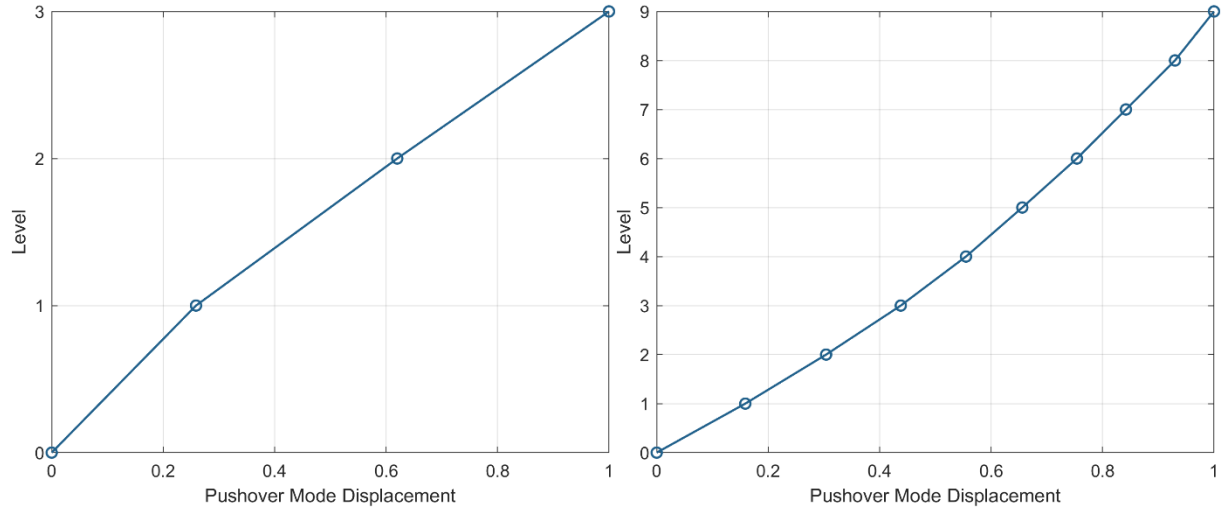

(a) 3-Story SMF **(b) 9-Story SMF**

Figure E-22 Pushover mode shapes for SMF archetypes.

Figure E-23 shows the trilinear backbone fit to the SMF pushover curves from FEMA P-2012. Note that because the pushover analyses reported by the FEMA P-2012 analysis team were terminated at 7.5% and 3.5% roof drift, respectively, for the 3- and 9-story frames, the post-peak slope, K_{pc}, was fit to the descending branches of the pushover curves and continue to zero capacity.

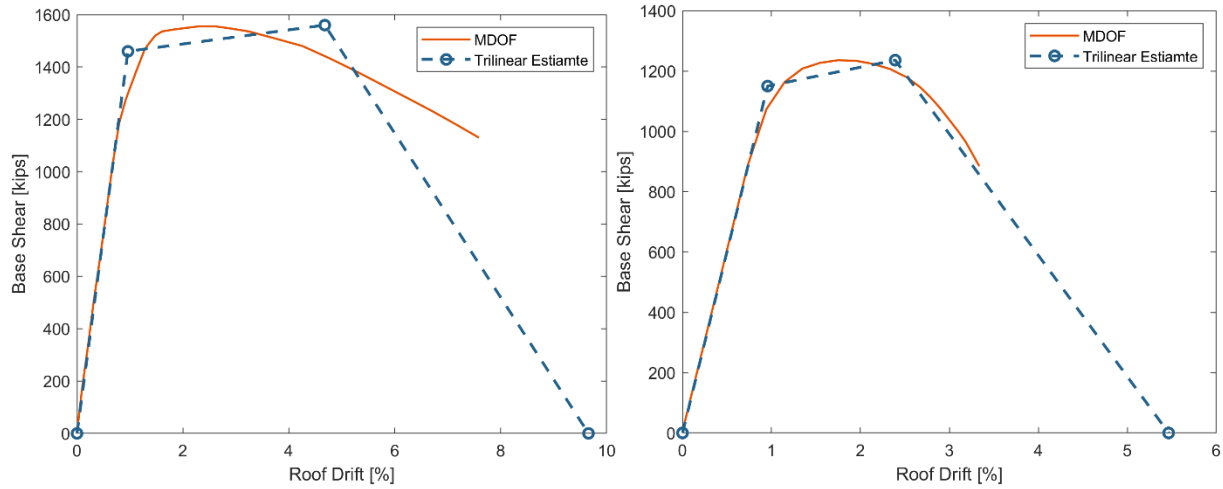

(a) 3-Story SMF **(b) 9-Story SMF**

Figure E-23 Trilinear backbone fit to SMF pushover curves.

Cyclic behavior for SMF eSDOF models was developed using the database by Lignos (http://resslabtools.epfl.ch/) and was selected to correspond to the girders at the stories with peak story drift. This behavior is critical in SMFs because of degradation from local buckling of beams, column, and panel zones. Figure E-24 shows the resulting hysteretic behavior with cyclic deterioration. Where the girders changed sizes over the stories of interest, the value of the deterioration parameter, λ, was taken as the average for the girders on those stories.

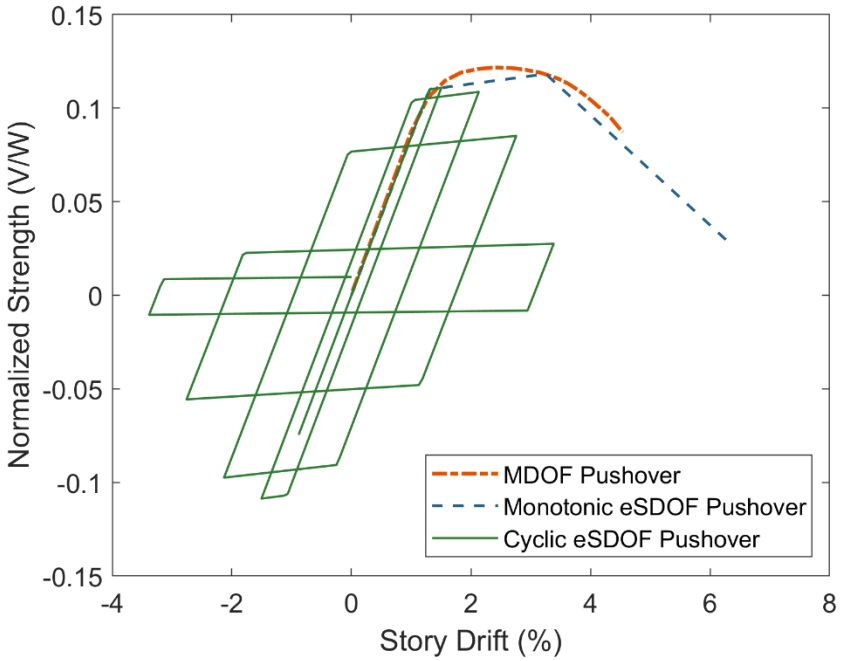

Figure E-24 Cyclic behavior of the eSDOF simulating the 9-Story SMF.

The backbone behaviors of the eSDOF models were transformed using the method described in Section E.2.2. Incremental dynamic analysis was then conducted on the eSODF models. In FEMA P-2012, no additional collapse criteria were used beyond analysis convergence failure and the IDA curves becoming flat. Table E-5 compares the median collapse spectral acceleration results for the detailed models as reported in FEMA P-2012 with those estimated using the eSODF models. Again, the eSDOF analysis results for median collapse spectral acceleration are in good agreement with the results from the more detailed analysis.

Table E-5 Comparison of Median Collapse Spectral Acceleration for SMFs from FEMA P-2012 and from eSDOF Analysis

Archetype	Median $S_c(T)$ from FEMA P-2012 (g)	Median $S_c(T)$ from eSDOF (g)
3-Story SMF V0300203(1)	2.59	2.39
9-Story SMF V0900201(1)	0.74	0.73

E.5.3 Ductile Coupled RC Walls

Ductile coupled reinforced concrete shear walls (DCWs) were selected as the third non-wood lateral system. The system was recently evaluated in a study by Tauberg, Kolozvari, and Wallace (2019) using the FEMA P-695 procedures to establish a new *R* value of 8 for inclusion in ASCE/SEI 7-22. Reinforced concrete shear walls are common in regions of very high seismicity and the recent study provides exceptional data for calibration of eSDOF models, making the use of ductile couple wall systems in this study feasible.

Tauberg et al. (2019) developed many DCW archetypes. The archetypes selected for the eSDOF development were those deemed to be typical in terms of shear wall geometry, coupling beam reinforcement, and number of stories. Importantly, none of the selected archetypes were governed by minimum base shear for design, and the height ranged from 8 to 18 stories. All archetypes selected were designed according to ASCE/SEI 7-16 for the maximum demands for SDC D_{max} using response spectrum analysis subject to scaling the base shear to 100% of the Equivalent Lateral Force base shear with a seismic force modification factor, *R*, of 8. Table E-6 lists the archetypes, referencing the archetype names in Tauberg et al. (2019). Figure E-25 shows the archetype geometry for each building height. For additional details on the designs, including wall and coupling beam dimensions and reinforcement details, refer to Tauberg et al. (2019).

Table E-6 DCW Archetype Characteristics from Tauberg et al. (2019)

Archetype Name	No. Stories	Roof Height (ft)	Seismic Weight (kips)	C_uT_a (sec)	Design Base Shear (ELF) (kips)
8H-DR-3	8	80	12010	0.749	1,201
12H-DR-3	12	120	18378	1.015	1360
18H-DR-3	18	180	27,330	1.376	1490

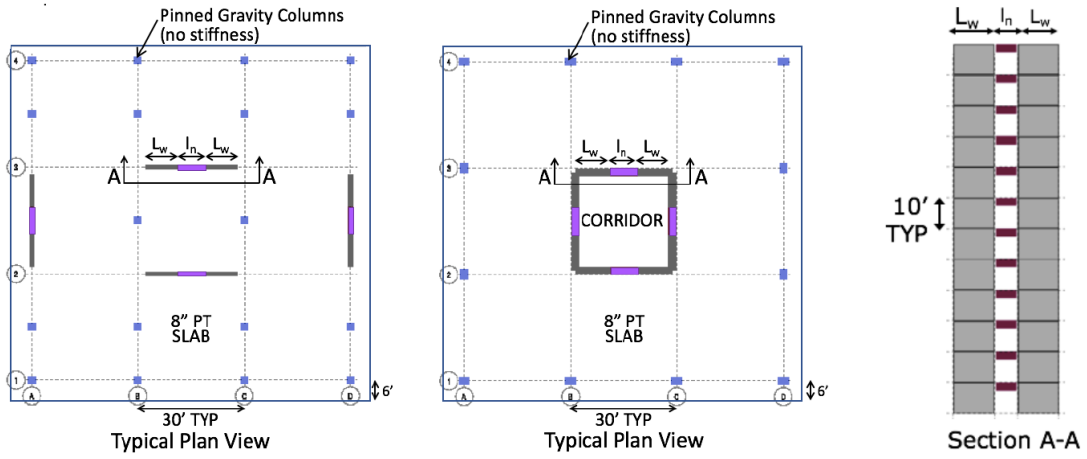

(a) **(b)** **(c)**

Figure E-25 DCW archetype building geometries from Tauberg et al. (2019).

The models used for collapse analysis of the DCW archetypes in Tauberg et al. (2019) are complex. Figure E-26 shows a schematic of their modeling approach. The models are 2D and consisted of only the walls. Mass was distributed at the centerline of each wall pier. A P-delta column is included that had negligible lateral stiffness. The wall piers are connected by rigid coupling beams from the centerline of the wall to the edge of the wall pier. Elastic coupling beam response that considers

both shear and flexural deformations are used for the coupling beams between the wall edges and a nonlinear shear hinge is used at the midpoint of the coupling for representing nonlinear response. The wall pier shear response is simulated with a linear elastic shear spring, and the wall pier axial and flexural response is simulated using the Multiple-Vertical-Line-Element-Model (MVLEM) in *OpenSees,* which was developed and validated by Orakcal et al. (2004), Orakcal and Wallace (2006), and Kolozvari et al. (2015). This complete model for coupled shear walls was validated in Tauberg et al. (2019) against several experiments, and complete details including specified material behaviors are available there.

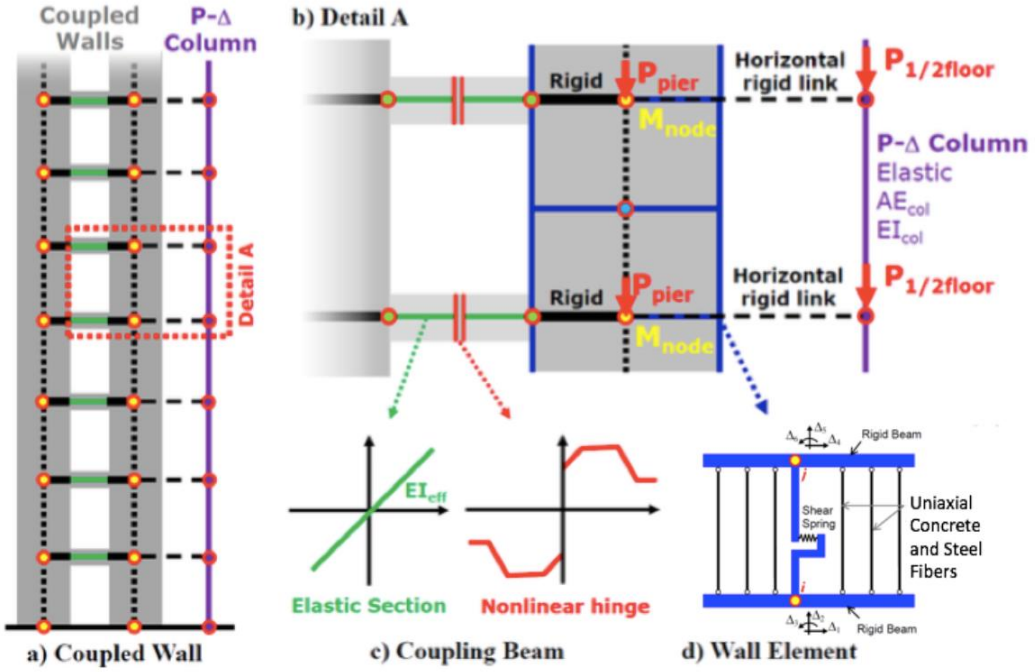

Figure E-26 DCW modeling approach from Tauberg et al. (2019) and Kolozvari et al. (2018).

The archetype models were analyzed for collapse capacity by Tauberg et al. (2019) using the FEMA P-695 procedures and the accompanying standard suite of 22 2-component Far-Field ground motion records (44 total analyses). The archetypes selected here all met the shear requirements of ACI 318-19. Failure was largely due to flexural failure in the wall piers, which was instituted with a non-simulated collapse mode. Previous research by Wallace and Abdullah (2019) was used to establish a roof drift limit at collapse as a function of the instantaneous compression zone dimensions and the wall properties as shown in Figure E-27. As shown, the limit was calibrated against numerous shear wall tests. The roof drift limit was updated at each time step for the current compression zone size. Both shear and axial failure modes were also checked but found not to govern for a majority of ground motions and archetypes. The conclusion of the study was that a seismic force modification factor of 8 was appropriate for such structures.

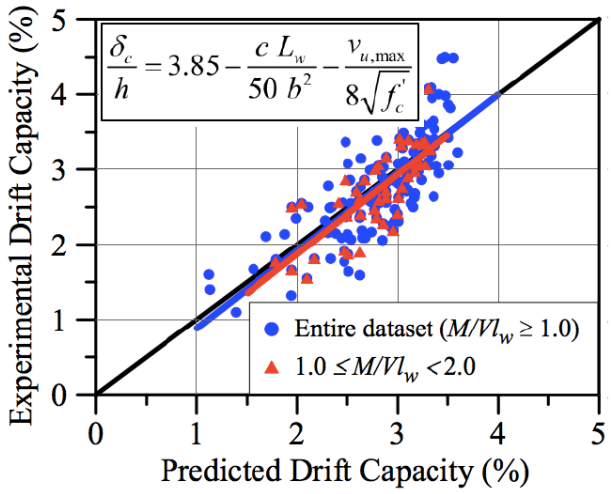

Figure E-27 Roof drift capacity model from Tauberg et al. (2019) and Wallace and Abdullah (2019).

To develop eSDOF models of the selected DCW archetypes a process similar to that used for the BRBF and SMF eSDOF models was followed. In this case, the available data for deriving pushover modes was limited. The report by Tauberg et al. (2019) provided drift distribution "at collapse" (i.e., when the roof drift limit was reached) for only the 12-story archetype. For the 8-story it provided the average drift distribution for MCE_R level shaking, and for the 18-story it provided the average drift distribution at design level shaking. Since the roof drift at flexural failure was considerably smaller than the collapse drift for the other structural systems considered (i.e., 3.5% roof drift maximum from Figure E-27), the drift distributions provided in the report by Tauberg et al. (2019) were deemed acceptable for derivation of the pushover mode shapes. The pushover modes obtained are shown in Figure E-28 for the 8-, 12-, and 18- story DCWs.

Pushover curves available in Tauberg et al. (2019) for the archetypes were used to fit backbone curves for the eSDOF models. Figure E-29 shows the pushover curves, digitized from the report, and the corresponding trilinear backbone curves. As shown, the pushover data in the report was terminated just after the roof drift limit for flexural failure was obtained. For the eSDOF models, a descending branch (i.e., K_{pc}) was added, although a non-simulated collapse mode was typically applied prior to reaching that descending branch.

The cyclic behavior for reinforced concrete shear wall is slightly pinched and follows a peak-oriented behavior after crossing zero force following unloading. Thus, the peak-oriented IMK model available in *OpenSees* was used to represent the cyclic response. This behavior is illustrated in Figure E-30. Cyclic deterioration was neglected for the DCW systems as the roof drift limit would likely minimize the impacts of such deterioration.

For the eSDOF models developed, the FEMA P-695 ground motion set was used to perform incremental dynamic analysis. A roof drift limit near 3.25% was applied for the 8-story wall, 3% for the 12-story wall, and 2.9% for the 18-story wall, consistent with observation that the limit decreases with wall height. The median collapse spectral accelerations for the eSDOF models are compared

with the results from Tauberg et al. (2019) in Table E-7. As shown, the agreement is within 10% for all archetypes.

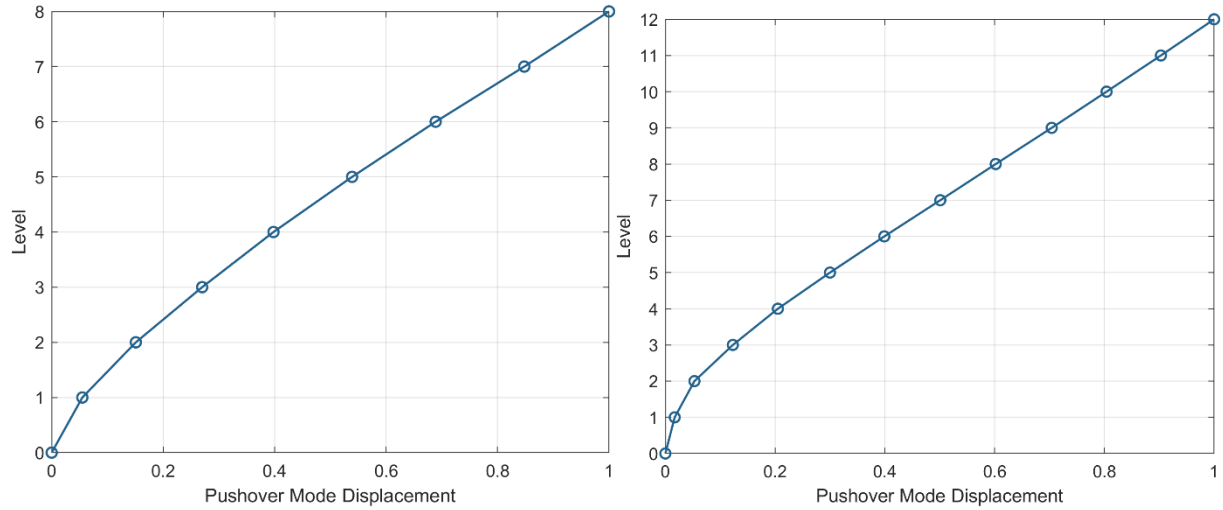

(a) 8-Story **(b) 12-Story**

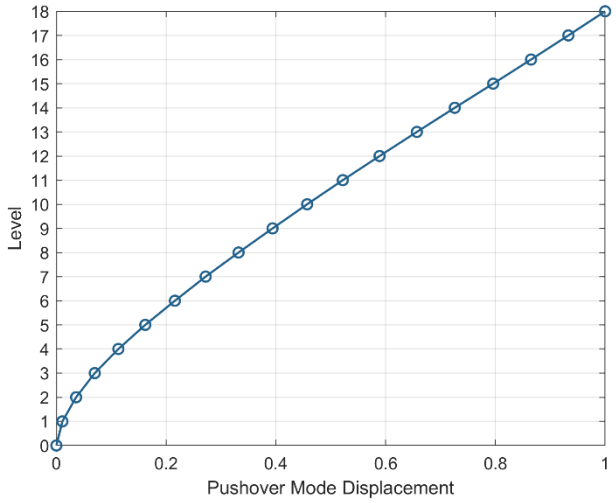

(b) 18-Story

Figure E-28 Pushover mode shapes for DCW archetypes.

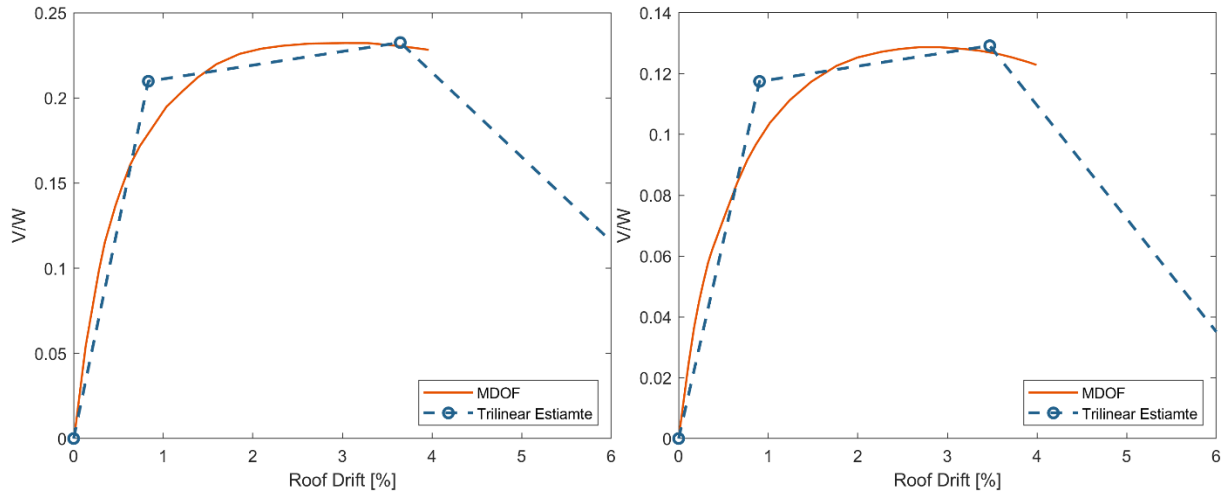

(a) 8-Story DCW **(b) 12-Story DCW**

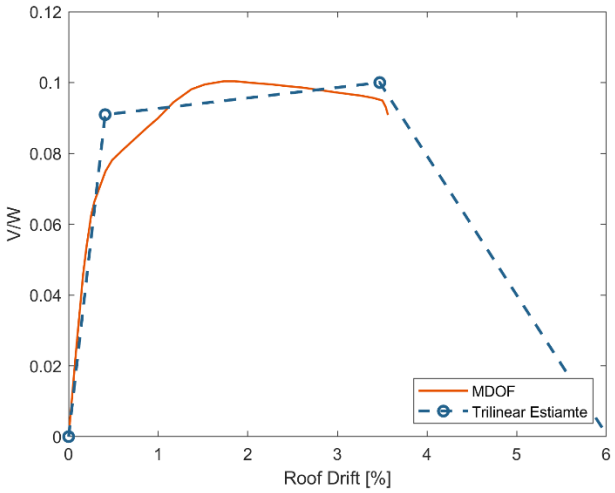

(c) 12-Story DCW

Figure E-29 Trilinear backbone fit to DCW pushover curves.

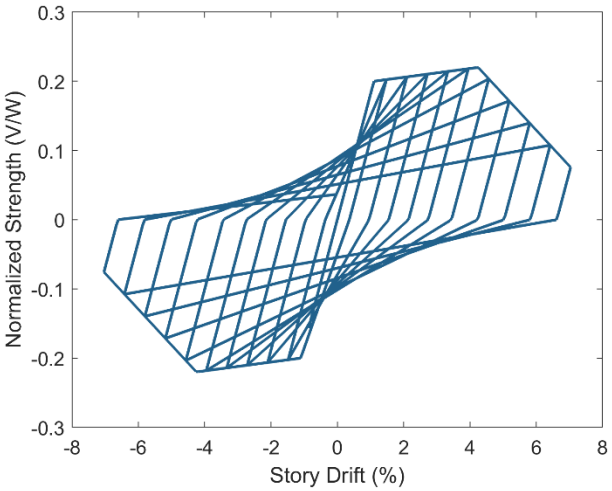

Figure E-30 Cyclic behavior for DCW eSDOFs.

Table E-7 Comparison of Median Collapse Spectral Acceleration for DCWs from Tauberg et al. (2019) and from eSDOF Analysis

Archetype	Median $S_c(T)$ from Tauberg et al. (2019) (g)	Median $S_c(T)$ from eSDOF (g)
8-Story	1.95	1.77
12-Story	1.39	1.42
18-Story	1.02	1.09

Appendix F: Steel Special Moment Resisting Frame Modeling

F.1 Introduction

This appendix presents archetype designs, nonlinear modeling details, and collapse analysis results for three steel special moment resisting frame (SMF) archetypes and the results of nonlinear static analyses of a fourth archetype. The purpose of this portion of the study is to provide additional validation for the trends observed from the eSDOF analyses in Section 5. As such, SMFs were designed for three Risk Category II archetypes at different seismic hazard levels and one Risk Category IV archetype. Nonlinear plane-frame models were developed that utilized current state-of-that-art recommendations for the nonlinear behavior of key SMF components, including the reduced-beam section (RBS) connections, column plastic hinge zones, SMF column panel zones, and gravity frame connections and columns. Nonlinear static analyses were conducted on all four frames, and incremental dynamic analyses through collapse following the analysis procedures of FEMA P-695 were conducted on the three Risk Category II archetype models. To illustrate the behavior of the models, nonlinear dynamic analysis results are also shown for a selected single ground motion at two different scale factors for each of the Risk Category II archetypes. Finally, the results of the detailed SMF modeling are used to construct eSDOF models of the SMFs using the same processes described in Chapter 5 and Appendix E. Incremental dynamic analysis is performed on the eSDOF models consistent with the procedures used in Chapter 5, and the results are compared to the results of the analyses of the detailed SMF models.

F.2 Archetype Designs

Three archetype designs were prepared for a 9-story Risk Category (RC) II office building for seismic hazard levels corresponding to High D (SDC D_{max}, where S_{DS} = 1.0 and S_{D1} = 0.6), Very High Seismic (S_{DS} = 1.5 and S_{D1} = 1.2), and Ultra High Seismic (S_{DS} =2.0 and S_{D1} = 1.8). The relative increases between seismic hazard levels for S_{DS} and S_{D1} are nonuniform due to differences in the spectral shape at default site conditions in ASCE/SEI 7-22. For example, S_{DS} increases by 50% between High D and Very High Seismic, but S_{D1} increases by 100%. The High D hazard level is the highest required by FEMA P-695. The other two hazard levels were selected to explore collapse performance in regions of very high seismicity that are significantly larger than High D but still lower than the highest values determined by the U.S. Geological Survey for ASCE/SEI 7-22 (see Appendix A). In addition to the RC II designs, a 9-story RC IV healthcare building was designed for the High D hazard level.

F.2.1 Building Schematic and Gravity System Design

The 9-story office building archetype is shown in Figures F-1, F-2, and F-3. The floor system consists of 3-1/4" light-weight concrete on 2" metal deck supported on steel beam and girders. The beams and girders are supported on steel columns, which are supported on spread footings in the interior

and a basement wall around the perimeter. The floor system was designed for the following loads and targeted floor vibration levels consistent with office use:

- Dead Load = self weight
- Superimposed Dead Load = 15 psf
- Live Load = 50 psf
- Partition Load = 15 psf
- Cladding Load = 20 psf (ext. area)

For the 9-story RC IV healthcare building, the floor system was designed for the following loads and target floor vibration levels consistent with healthcare use:

- Dead Load = Self weight
- Superimposed Dead Load = 30 psf
- Live Load = 40 psf
- Partition Load = 20 psf
- Cladding Load = 20 psf (ext. area)

The design of gravity system (floor framing and columns) utilized wide-flange sections consistent with the requirements of AISC 341-22 and AISC 360-22. ASTM A992 Gr50 steel was assumed. Floor framing connections consisted of 3- or 4-bolt single shear tabs depending on the depth of the members.

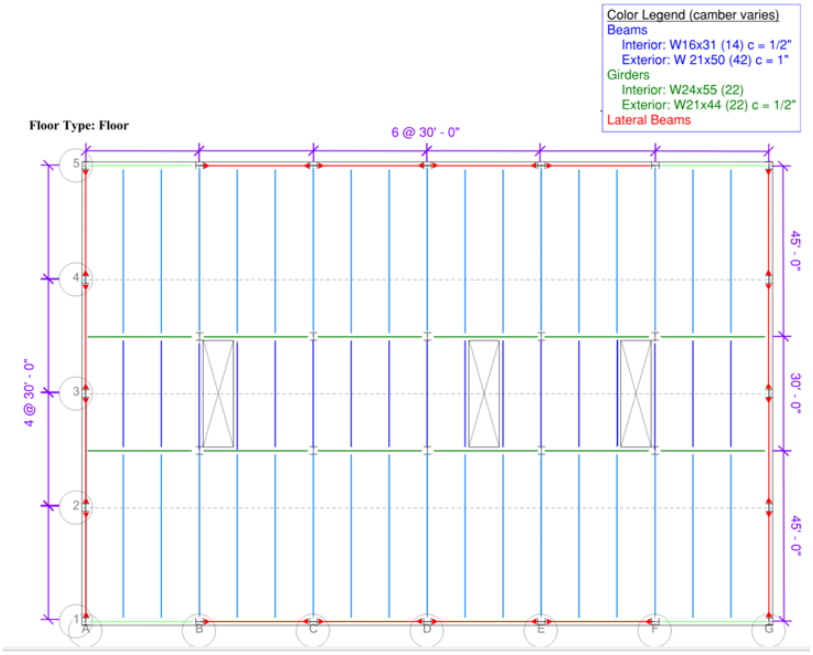

Figure F-1 9-story office building archetype floor framing plan.

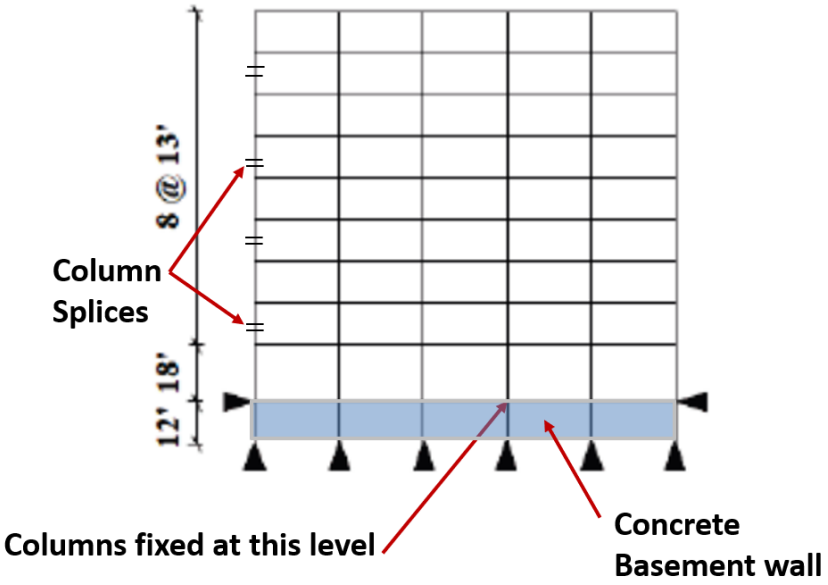

Figure F-2 Generic 9-story archetype frame elevation.

F.2.2 Seismic Design Criteria

The three RC II office archetypes were designed for the three seismic design levels shown in Table F-1. Consistent with RC II requirements, the allowable story drift was limited to 0.02h per ASCE/SEI 7-22 Table 12.12-1. The RC IV healthcare archetype was designed for the High D seismic

design level. Consistent with RC IV requirements, the allowable story drift was limited to 0.01*h* per ASCE/SEI 7-22 Table 12.12-1.

Table F-1 Seismic Design Parameters Used in the Archetype Designs

Design Level	S_{MS} (g)	S_{DS} (g)	S_{M1} (g)	S_{D1} (g)	S_1 (g)	T (sec)	S_{MT} (g)
High D	1.5	1.0	0.9	0.6	0.47	1.83	0.49
Very High Seismic	2.25	1.5	1.8	1.2	0.72	1.83	0.98
Ultra High Seismic	3.0	2.0	2.7	1.8	1.07	1.52	1.78

Note that the periods listed in Table F-1 are the design periods per ASCE/SEI 7, which correspond to $C_u T_a$ for the High D and Very High Seismic designs and the calculated first mode period from modal analysis for the Ultra High design. The value of S_{MT} is the value of the MCE_R spectrum at the design period.

F.2.3 SMF Design, Sections Sizes, Connections

The seismic design for the steel SMF was per AISC 341-22 and AISC 358-22 with the following limitations:

- Column sizes were limited to W14 sections,
- Beam sizes were limited to up to W36 sections, and
- Connections were limited to reduced beam section (RBS).

For both the RC II and RC IV designs, the seismic-force-resisting system consists of perimeter steel SMFs. As shown in Figure F-3, the SMF consists of four moment-frame bays so as to eliminate weak axis MF column connections, which are not prequalified in AISC 358.

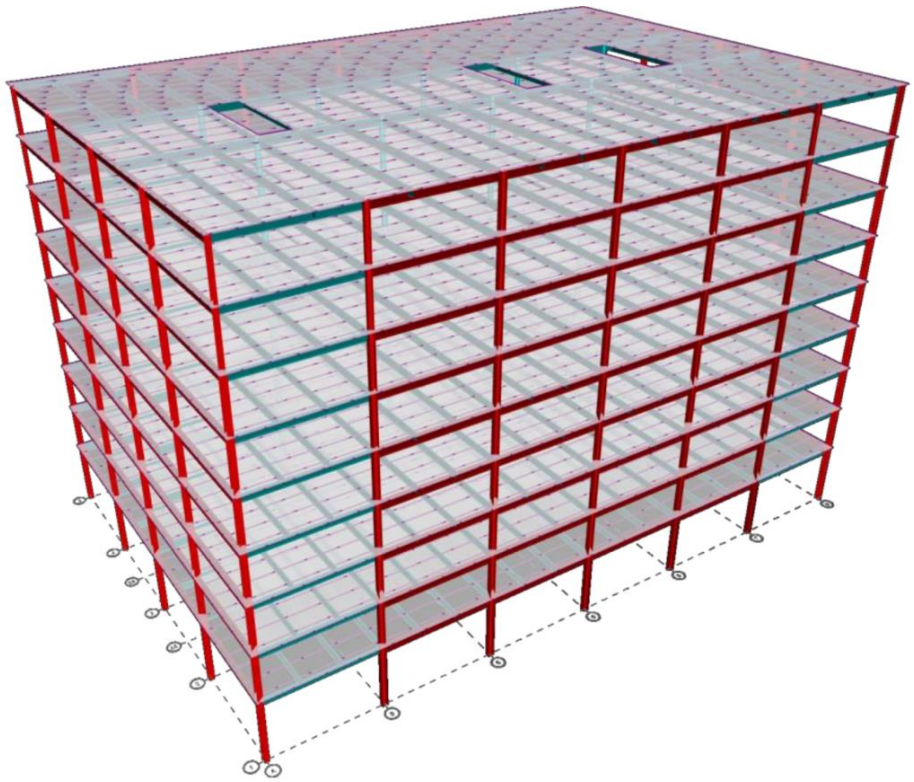

Figure F-3 3D rendering of the 9-story office building archetype.

The steel SMF seismic design reports, prepared by the AISC Steel Solutions Center, are available at https://femap2343.atcouncil.org. As expected, the higher hazard designs employ larger members. One point of interest is that the periods of vibration for the higher hazard designs are less than for the High D design, and because the drift is checked at the computed period, the spectral accelerations for the drift check increase by a greater amount than direct proportion to the design parameter S_{D1}. Since the system is typically controlled by drift, the member moments of inertia increase by more than a simple pro-rata to the ground motions.

F.3 Nonlinear Model Description

F.3.1 Overview

The nonlinear SMF models are developed in *OpenSeesPy*, the python scripting version of *OpenSees*. The models are developed in 2D and represent one of the SMFs in the building and the gravity framing that would be tributary to that SMF. Nonlinear behavior of beams, columns, and panel zones in the SMF are considered as described below. In the gravity framing, the nonlinear behavior of the beam-to-column connections and the columns are considered as described below. Figure F-4 shows a general model schematic with associated labels and column line references that correspond to the plan layout in Figure F-1.

As shown, the model includes one moment frame in the East-West direction (Lines B-1 through F-1) of the archetype and one line of gravity framing (Lines B2.5 through F2.5), which is all of the gravity framing tributary to one moment frame. Also included are two columns (A-1 and G-1) from the moment frame resisting loads in the North-South direction. Those columns are assigned weak axis properties without considering the effects of bi-directional loading. It is assumed that including one weak-axis column from each of the North-South SMFs, while neglecting bi-directional loading effects on their behavior, is a reasonable approximation of the contribution of the N-S SMF to the collapse performance on the building in the E-W direction. A single additional "dummy" column that has pin ends at every level and large axial stiffness is included to place seismic weight that is tributary to the SMF but not included in the tributary area for the columns included in the model.

SMF columns are assumed to be embedded into basement walls. Gravity frame columns are assumed to extend into a 14-foot-tall basement level and are therefore modeled with a linear rotational spring at their base that represents the stiffness of basement level column assuming a pin end condition at the basement floor.

Gravity Loads and Seismic Mass

Gravity loads that are applied for analysis that are consistent with the requirements for FEMA P-695, i.e., $1.05D+0.25L$, where D is nominal dead load and L is the nominal unreduced live load. Gravity loads are applied as point loads on columns at each story and calculated using the column tributary areas. Gravity load tributary to the SMF for P-delta effects but not accounted for in the tributary area of the modeled columns is placed on the dummy column. This load is from a small rectangular area spanning between Lines 1.5 and 3 and from Lines A to midway to B in the plan view in Figure F-1 and the mirror image of that on the East end of the building. Seismic mass is applied as lumped mass at the column nodes at each story and corresponds to 1.0 times the dead load converted to mass.

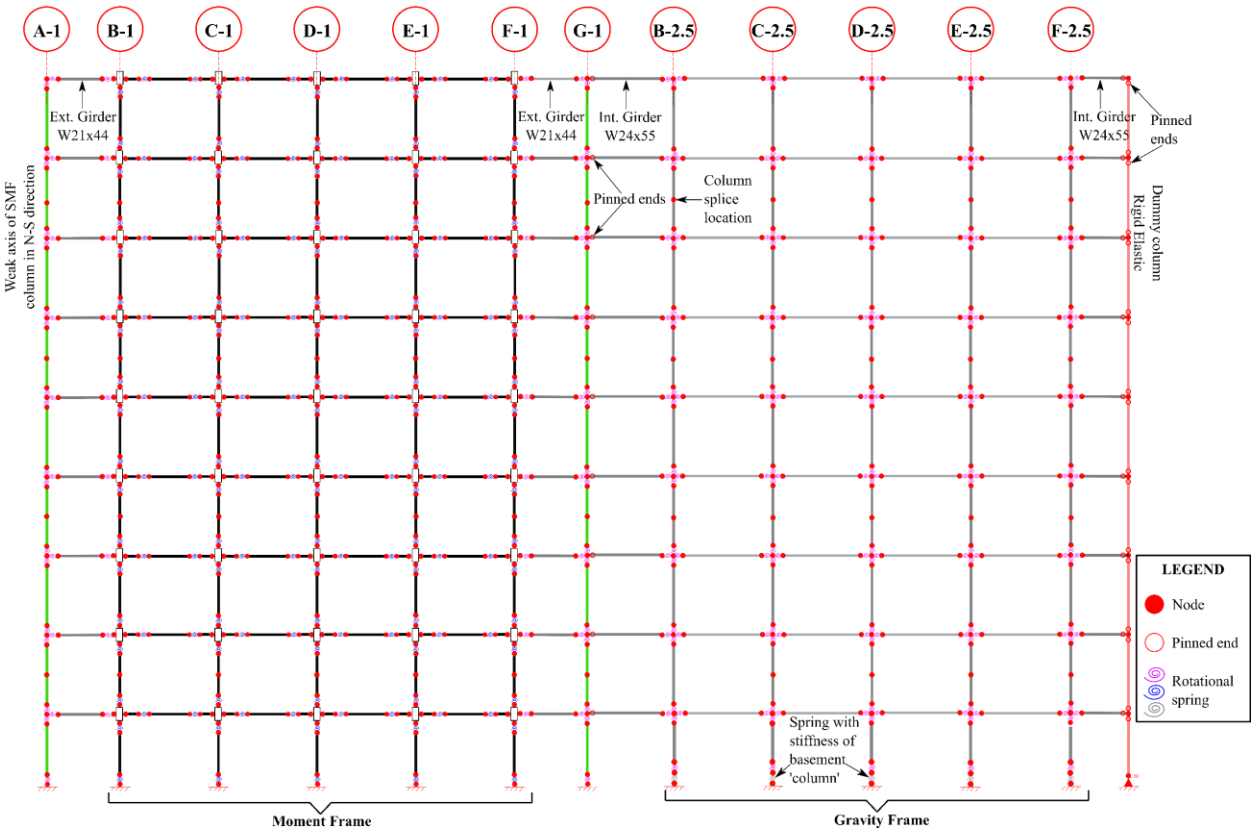

Figure F-4 Schematic of a detailed steel SMF numerical model.

Damping

Stiffness and mass proportional Raleigh damping is applied targeting 2.5% damping for the first and n^{th} modes (where the *n*th mode is at least the 5^{th} mode and is larger if necessary to ensure it corresponds to 90% mass participation). The stiffness proportional damping is computed using the committed stiffness of each analysis step to avoid spurious damping forces. Modal damping does not provide substantial improvements over Raleigh damping for lumped plasticity models (Chopra and McKenna, 2016) and can increase analysis time in *OpenSees*.

Nonlinear Geometric Effect

The beams and columns in both the SMF and gravity frames are modeled with P-delta element transformations in *OpenSeesPy* to account for nonlinear geometric effects. Since lumped plasticity modeling with zero-length spring elements is used there is little benefit in using a more complex and computationally demanding corotational formulation.

F.3.2 SMF Modeling

The SMF is modeled using elastic beam-column elements with lumped plasticity, zero-length nonlinear rotational springs near their ends to model the inelastic flexural behavior. A nonlinear

model for the panel zones is included as well. The SMF columns are fixed at their base consistent with the embedded column base connections specified in the archetype designs.

Beams

Elastic beam-column elements are used to represent the beam with zero-length rotational springs at the locations of assumed nonlinearity. The beams have been designed with RBS beam-to-column connections and the assumed nonlinear flexural response is lumped at the middle of the RBS region. Figure F-5 shows a schematic of the model near the beam end. The behavior of the rotational spring at the middle of the RBS is based on previous work by Lignos and Krawinkler (2011) and uses the bilinear hysteretic material with modified Ibarra-Medina-Krawinkler (IMK) deterioration (Ibarra et al., 2005), denoted IMKBilin in *OpenSees*. Note that the elastic stiffness of the beam-column element is adjusted such that the stiffness of the beam-column element and two rotational springs is equal to the expected elastic stiffness of a beam in double curvature as recommended in NIST (2017b).

Figure F-6 shows the basic hysteretic response of the IMK bilinear material that represents the inelastic behavior of the RBS. Backbone parameters for each section are computed from the equations in NIST (2017b) based on work by Hartloper and Lignos (2016) and Lignos and Krawinkler (2011) and are modified for composite behavior as described below. Note that Figure F-6 denotes the maximum moment as M_c whereas NIST (2017b) uses M_u, but in both cases this is the maximum moment strength considering cyclic hardening. The deterioration parameter, λ_c, is computed from the work by Lignos and Krawinkler (2011) with updated values from the online database available at http://resslabtools.epfl.ch/component/.

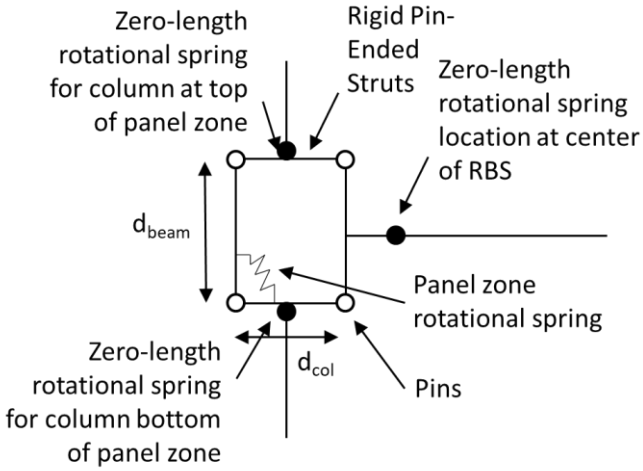

Figure F-5 SMF beam-to-column connection region model schematic.

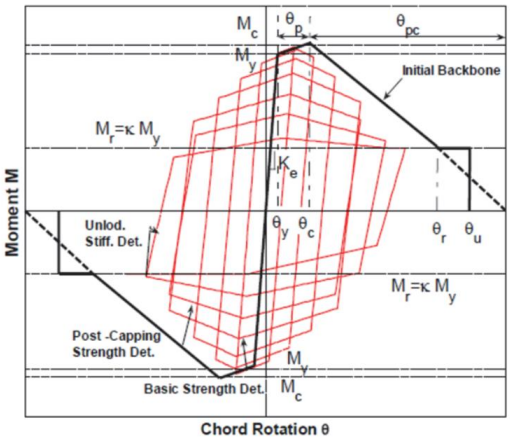

Figure F-6 General moment-rotation behavior of beam and column lumped plasticity zero-length springs, IMKBilin in *OpenSeesPy* (Ibarra et al., 2005).

The impact of composite action on the response of the RBS beam section is included as recommended by Elkady and Lignos (2014), who found a potential 30% increase in collapse capacity (the median spectral acceleration at collapse resulting from incremental dynamic analysis) for SMFs when composite action was considered. Figure F-7 shows an example from Elkady and Lignos (2014) of a zero-length rotational spring before and after modifying for composite behavior and compared with experimental results from Ricles et al. (2004). The figure shows the computed backbone using equations similar to those in NIST (2017b) as the bold black curve, the implemented IMK model with deterioration in red, and experimental results in blue. To develop recommended parameters for the modification of IMK model parameters for RBS composite behavior Elkady and Lignos (2014) studied data from 22 experiments on RBS beams with composite slabs and beam depths ranging from W21 to W36, with more than two thirds of the compiled tests using W36 beams. After fitting IMK models to the behaviors, they reported parameters that can be used to modify the IMKBilin behavior to account for composite behavior as the mean parameter values for the entire data set. Those parameters are used here directly and are given in Table F-1, which shows the mean ratios of key parameters defining the backbone response for the RBS beams with composite action to those without. Notably, using these composite parameters for all cross sections in the current study is a simplification. However, the slab dimensions and beam sizes for the archetypes here are all similar to those in the experiments used to generate the parameters recommended by Elkady and Lignos (2014). Further, the compression force in the slab resulting from application of the parameters in Table F-2 is generally limited to less than $3b_f t_s f'_c$, where b_f is the beam flange width, t_s is the slab thickness, and f'_c is the concrete strength. This limit corresponds to crushing of the concrete against the column flange.

Table F-3 lists the resulting composite beam RBS backbone parameters for the beams in the archetype SMF. Note that the Risk Category IV model parameters are not shown because they are similar section sizes as used for the Very High Seismic design. The ultimate rotation, θ_u, is taken as 0.08 rads as recommended by NIST (2017b) and Hartloper and Lignos (2016). This limit represents the upper bound limit of rotation achieved under cyclic loading in laboratory tests of RBS

connections prior to flange fracture. Figure F-8 shows the implementation of the composite RBS rotational spring model for this project for a W27×94 beam with the composite slab and RBS connection as designed for the SDC D_{max} archetype. Importantly, the analyses did not consider the impact of system level slab restraint in limiting the shortening of the compression zone in the connections, which can provide additional protection against local buckling deterioration.

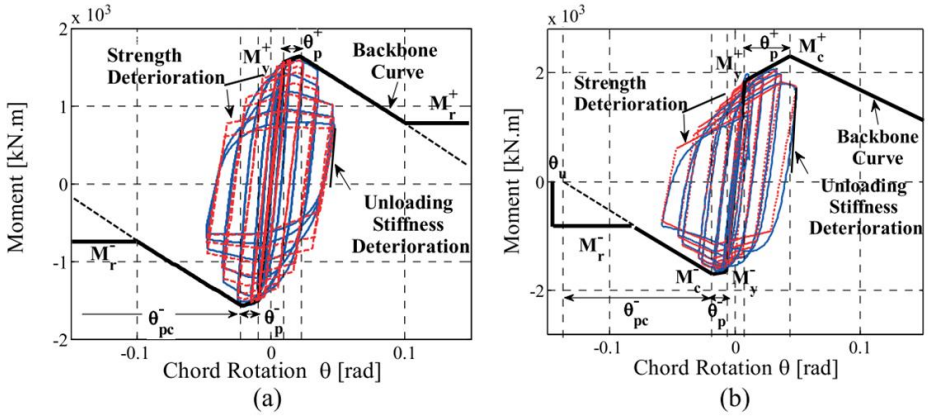

Figure F-7 **Comparison of bare steel (a) and composite RBS (b) response including experimental data (blue), numerical model (blue), and IMKBilin backbone (black) (Elkady and Lignos, 2014).**

Table F-2 **Ratios of Composite RBS IMKBilin Model Parameters to Noncomposite Parameters (Elkady and Lignos, 2014)**

I_c/I_s	M_y^+/M_y	M_y^-/M_y	M_c^+/M_y	M_c^-/M_y	M_r^+/M_y	M_r^-/M_y	θ_p^+/θ_p	θ_p^-/θ_p	$\theta_{pc}^+/\theta_{pc}$	$\theta_{pc}^-/\theta_{pc}$	λ_c/λ_s	D^+	D^-
1.4	1.35	1.25	1.30	1.05	0.3	0.2	1.80	0.95	1.35	0.95	1.0	1.15	1.0

Table F-3 IMKBilin Parameters for Composite RBS Connections in Archetype SMF Models

Section	M_y^+ (kip-in)	M_y^- (kip-in)	M_c^+ (kip-in)	M_c^- (kip-in)	M_r^+ (kip-in)	M_r^- (kip-in)	θ_p^+ (rads)	θ_p^- (rads)	θ_{pc}^+ (rads)	θ_{pc}^- (rads)	θ_u (rads)	λ_c
High D Archetype												
W24×62	9,434	8,735	13,490	10,089	2,096	1,509	0.050	0.026	0.248	0.175	0.08	0.727
W24×84	13,160	12,185	18,819	14,074	2,924	2,106	0.051	0.027	0.264	0.186	0.08	0.850
W27×84	14,480	13,407	20,706	15,485	3,218	2,317	0.043	0.023	0.191	0.134	0.08	0.620
W27×94	16,340	15,129	23,366	17,474	3,631	2,614	0.044	0.023	0.225	0.158	0.08	0.728
Very High Seismic Archetype												
W30×116	22,272	20,623	31,850	23,819	4,949	3,564	0.041	0.022	0.247	0.174	0.08	0.798
W30×132	25,521	23,631	36,496	27,294	5,671	4,083	0.042	0.022	0.297	0.209	0.08	0.968
W30×191	37,922	35,113	54,228	40,555	8,427	6,067	0.043	0.023	0.271	0.191	0.08	1.124
W30×211	42,204	39,077	60,351	45,134	9,379	6,753	0.044	0.023	0.310	0.218	0.08	1.327
Ultra High Seismic Archetype												
W33×130	28,009	25,935	40,053	29,955	6,224	4,482	0.036	0.019	0.219	0.154	0.08	0.698
W36×232	54,807	50,747	78,374	58,613	12,179	8,769	0.038	0.020	0.426	0.300	0.08	1.427
W36×282	66,440	61,519	95,010	71,054	14,764	10,630	0.037	0.020	0.326	0.229	0.08	1.347
W36×361	86,715	80,291	124,002	92,737	19,270	13,874	0.040	0.021	0.455	0.320	0.08	2.062

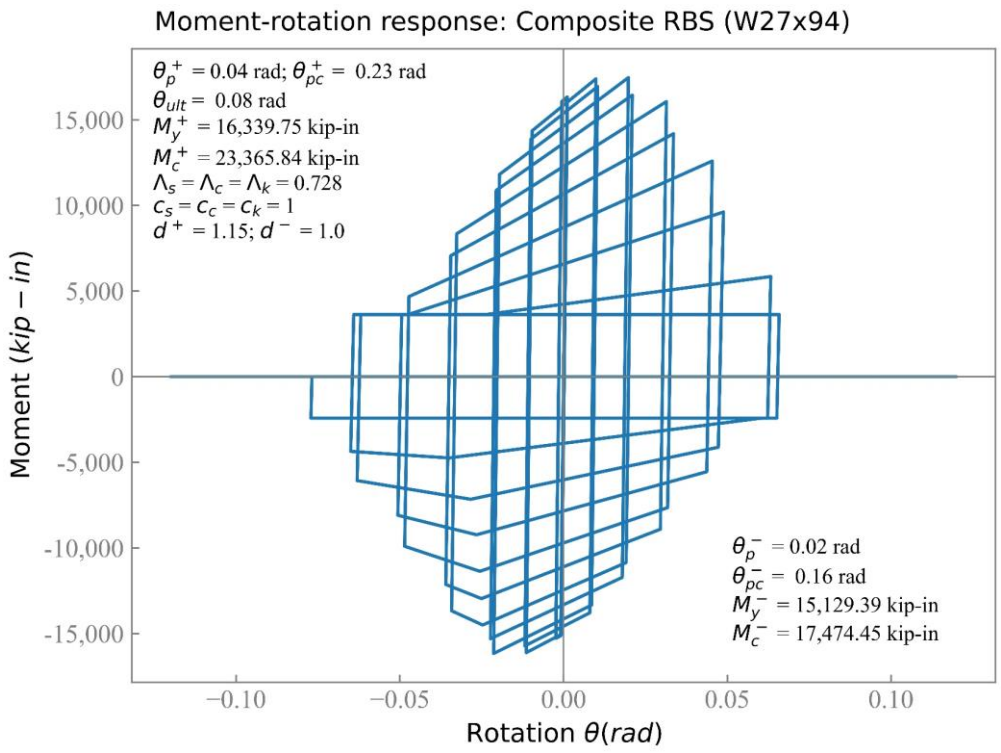

Figure F-8 **Example cyclic moment-rotation behavior for a W27×94 beam with RBS design parameters and slab dimensions per the High D archetype. Note there are two cycles at each rotation step.**

Columns

Columns in the SMF are also modeled with elastic beam-column elements with zero-length rotational springs (hinges) at their ends to model their inelastic flexural behavior. The hinges are located just below or above the beam-to-column connection as appropriate. The same IMKBilin material behavior with modified Ibarra-Medina-Krawinkler deterioration that is used for the beams is also used for the columns but without considerations of composite behavior. Thus, the behavior is symmetric as shown in Figure F-6. The hysteretic behavior for the columns is modified to account for axial load as recommended in Section 4.3.1 in NIST (2017a). Those modifications involve reducing the moments and rotations that define the monotonic backbone as a function of the axial load on the columns due to gravity loading. Table F-4a and Table F-4b list the component model parameters used for each exterior and interior column at each level in the SMF models (the levels with a 0.5 increment are locations where a column splice occurs). The column sections are stocky with low values of both h/t_w and L_b/r_y resulting in large values of both θ_p and θ_{pc}. The practical implication of these large values of the rotations that define the backbone curve is that the behavior of the columns under flexure is essentially bilinear, with full hysteresis and no deterioration until the ultimate rotation, θ_u, is reached. Notably, NIST (2017a) recommends an upper bound value for θ_u of 0.15 rads. However, inspection of the literature on testing of large W14 columns under cyclic axial and flexural demands, which largely is limited to tests by Newell and Uang (2006), reveals that there were no tests that achieved

rotations exceeding 0.1 rads prior to flange fracture. With these test results as the justification—and because all columns in all archetype SMFs and gravity frames are stocky W14 sections that have little deterioration and likely have flange fracture at large rotations as their governing failure mode—θ_u of 0.1 rads is applied to all column sections.

Table F-4a IMKBilin Parameters for Exterior SMF Columns in Archetype SMF Models

Level	Section	P_g/P_y	M_y (kip-in)	M_c (kip-in)	M_r (kip-in)	θ_p (rads)	θ_{pc} (rads)	θ_u (rads)	λ_c
	High D Archetype								
1	W14×211	0.21	21,994	28,593	9,172	0.19	0.30	0.10	6.901
1.5	W14×211	0.18	20,131	26,171	8,585	0.20	0.30	0.10	6.901
2	W14×211	0.18	20,131	26,171	8,585	0.20	0.30	0.10	6.901
3	W14×211	0.16	20,701	26,911	9,019	0.20	0.30	0.10	6.901
3.5	W14×211	0.14	21,270	27,651	9,463	0.20	0.30	0.10	6.901
4	W14×176	0.16	16,903	21,974	7,337	0.20	0.30	0.10	5.005
5	W14×176	0.14	17,462	22,701	7,773	0.20	0.30	0.10	5.005
5.5	W14×176	0.11	18,021	23,428	8,221	0.20	0.30	0.10	5.005
6	W14×159	0.12	15,946	20,729	7,197	0.18	0.30	0.10	4.088
7	W14×159	0.09	16,502	21,453	7,651	0.19	0.30	0.10	4.088
7.5	W14×159	0.06	17,058	22,176	8,118	0.20	0.30	0.10	4.088
8	W14×82	0.12	7,760	9,453	3,516	0.07	0.20	0.10	2.603
9	W14×82	0.06	8,284	10,359	3,951	0.07	0.23	0.10	2.603
	Very High Seismic Archetype								
1	W14×500	0.10	59,733	77,653	27,464	0.20	0.30	0.10	31.209
1.5	W14×500	0.09	60,489	78,636	28,087	0.20	0.30	0.10	31.209
2	W14×500	0.09	60,489	78,636	28,087	0.20	0.30	0.10	31.209
3	W14×500	0.08	61,232	79,602	28,706	0.20	0.30	0.10	31.209
3.5	W14×500	0.07	61,975	80,568	29,331	0.20	0.30	0.10	31.209
4	W14×426	0.08	50,646	65,839	23,731	0.20	0.30	0.10	23.575
5	W14×426	0.07	51,369	66,779	24,340	0.20	0.30	0.10	23.575

Level	Section	P_g/P_y	M_y (kip-in)	M_c (kip-in)	M_r (kip-in)	θ_p (rads)	θ_{pc} (rads)	θ_u (rads)	λ_c
5.5	W14×426	0.05	52,092	67,719	24,957	0.20	0.30	0.10	23.575
6	W14×370	0.06	43,762	56,891	20,832	0.20	0.30	0.10	18.566
7	W14×370	0.04	44,464	57,804	21,435	0.20	0.30	0.10	18.566
7.5	W14×370	0.03	45,167	58,717	22,046	0.20	0.30	0.10	18.566
8	W14×211	0.05	23,377	30,390	11,199	0.20	0.30	0.10	6.901
9	W14×211	0.03	24,031	31,241	11,768	0.20	0.30	0.10	6.901
	Ultra High Seismic Archetype								
1	W14×665	0.08	85,768	111,499	40,010	0.20	0.30	0.10	40.340
1.5	W14×665	0.07	86,654	112,651	40,752	0.20	0.30	0.10	40.340
2	W14×665	0.07	86,654	112,651	40,752	0.20	0.30	0.10	40.340
3	W14×665	0.06	87,526	113,784	41,488	0.20	0.30	0.10	40.340
3.5	W14×665	0.06	88,399	114,918	42,231	0.20	0.30	0.10	40.340
4	W14×550	0.07	69,608	90,490	32,929	0.20	0.30	0.10	36.567
5	W14×550	0.06	70,449	91,584	33,644	0.20	0.30	0.10	36.567
5.5	W14×550	0.04	71,291	92,678	34,368	0.20	0.30	0.10	36.567
6	W14×426	0.06	51,772	67,304	24,684	0.20	0.30	0.10	23.575
7	W14×426	0.04	52,575	68,348	25,374	0.20	0.30	0.10	23.575
7.5	W14×426	0.03	53,378	69,392	26,073	0.20	0.30	0.10	23.575
8	W14×257	0.05	29,333	38,133	14,107	0.20	0.30	0.10	9.744
9	W14×257	0.02	30,077	39,101	14,755	0.20	0.30	0.10	9.744

Table F-4b IMKBilin Parameters for Interior SMF Columns in Archetype SMF Models

Level	Section	P_g/P_y	M_y (kip-in)	M_c (kip-in)	M_r (kip-in)	θ_p (rads)	θ_{pc} (rads)	θ_u (rads)	λ_c
	High D Archetype								
1	W14×257	0.17	25,563	33,231	11,042	0.20	0.30	0.10	9.744
1.5	W14×257	0.15	26,157	34,004	11,501	0.20	0.30	0.10	9.744
2	W14×257	0.15	26,157	34,004	11,501	0.20	0.30	0.10	9.744
3	W14×257	0.13	26,740	34,762	11,959	0.20	0.30	0.10	9.744
3.5	W14×257	0.11	27,323	35,520	12,427	0.20	0.30	0.10	9.744
4	W14×211	0.14	21,270	27,651	9,463	0.20	0.30	0.10	6.901
5	W14×211	0.11	21,839	28,391	9,918	0.20	0.30	0.10	6.901
5.5	W14×211	0.09	22,409	29,131	10,383	0.20	0.30	0.10	6.901
6	W14×176	0.11	18,021	23,428	8,221	0.20	0.30	0.10	5.005
7	W14×176	0.08	18,581	24,155	8,681	0.20	0.30	0.10	5.005
7.5	W14×176	0.05	19,140	24,882	9,154	0.20	0.30	0.10	5.005
8	W14×159	0.06	17,058	22,176	8,118	0.20	0.30	0.10	4.088
9	W14×159	0.03	17,614	22,899	8,598	0.20	0.30	0.10	4.088
	Very High Seismic Archetype								
1	W14×605	0.08	76,556	99,522	35,734	0.20	0.30	0.10	42.943
1.5	W14×605	0.07	77,340	100,543	36,392	0.20	0.30	0.10	42.943
2	W14×605	0.07	77,340	100,543	36,392	0.20	0.30	0.10	42.943
3	W14×605	0.06	78,112	101,545	37,043	0.20	0.30	0.10	42.943
3.5	W14×605	0.06	78,883	102,548	37,701	0.20	0.30	0.10	42.943
4	W14×500	0.07	61,975	80,568	29,331	0.20	0.30	0.10	31.209
5	W14×500	0.06	62,718	81,534	29,964	0.20	0.30	0.10	31.209
5.5	W14×500	0.04	63,461	82,500	30,603	0.20	0.30	0.10	31.209
6	W14×455	0.05	56,316	73,211	27,060	0.20	0.30	0.10	26.707
7	W14×455	0.04	57,042	74,155	27,689	0.20	0.30	0.10	26.707

Level	Section	P_g/P_y	M_y (kip-in)	M_c (kip-in)	M_r (kip-in)	θ_p (rads)	θ_{pc} (rads)	θ_u (rads)	λ_c
7.5	W14×455	0.02	57,769	75,100	28,325	0.20	0.30	0.10	26.707
8	W14×342	0.03	41,139	53,481	20,041	0.20	0.30	0.10	16.197
9	W14×342	0.02	41,831	54,381	20,651	0.20	0.30	0.10	16.197
	Ultra High Seismic Archetype								
1	W14×873	0.06	120,195	156,253	57,026	0.20	0.30	0.10	59.922
1.5	W14×873	0.06	121,121	157,458	57,815	0.20	0.30	0.10	59.922
2	W14×873	0.06	121,121	157,458	57,815	0.20	0.30	0.10	59.922
3	W14×873	0.05	122,034	158,644	58,598	0.20	0.30	0.10	59.922
3.5	W14×873	0.04	122,946	159,830	59,385	0.20	0.30	0.10	59.922
4	W14×730	0.05	99,666	129,566	47,810	0.20	0.30	0.10	46.515
5	W14×730	0.04	100,558	130,726	48,579	0.20	0.30	0.10	46.515
5.5	W14×730	0.03	101,450	131,885	49,355	0.20	0.30	0.10	46.515
6	W14×605	0.04	80,085	104,111	38,736	0.20	0.30	0.10	42.943
7	W14×605	0.03	80,942	105,224	39,483	0.20	0.30	0.10	42.943
7.5	W14×605	0.02	81,798	106,338	40,236	0.20	0.30	0.10	42.943
8	W14×398	0.03	49,102	63,832	23,945	0.20	0.30	0.10	21.061
9	W14×398	0.02	49,892	64,860	24,642	0.20	0.30	0.10	21.061

Figure F-9 shows the moment versus rotation (shown as drift) for a W14×233 with a 30% axial load ratio with the moment rotation behavior for the model as described above. The figure shows a comparison of the behavior with the results of a test from Newell and Uang (2006) for a W14×233 column with approximately the same axial load. As shown, deterioration is minimal prior to fracture of the column. The most significant difference in the response is the lack of Bauschinger effect in the model, which results from using the IMK model but does not affect the behavior at collapse. Note that the moment story drift in the experiment includes the elastic flexural response of the column where the model is only the plastic hinge response.

The columns on Frame Lines A-1 and G-1 are included in the model as described above. These columns belong to the SMF oriented in the N-S direction of the building and thus are modeled with their weak-axis properties. They are included to represent the contribution of the N-S moment frames

to E-W lateral load resistance, in addition so that the shear connections for the gravity girders on Line 1 can be included. Only a single column from each N-S SMF in the E-W model is included because the sections are under biaxial loading and the complete hysteretic behavior is unknown. It is assumed that a reasonable approximation is to include one column from each N-S moment, to neglect biaxial loading, and to model that column with its full weak-axis properties. The columns are modeled again as elastic beam-column elements with rotational springs at their ends at each level to simulate the inelastic behavior.

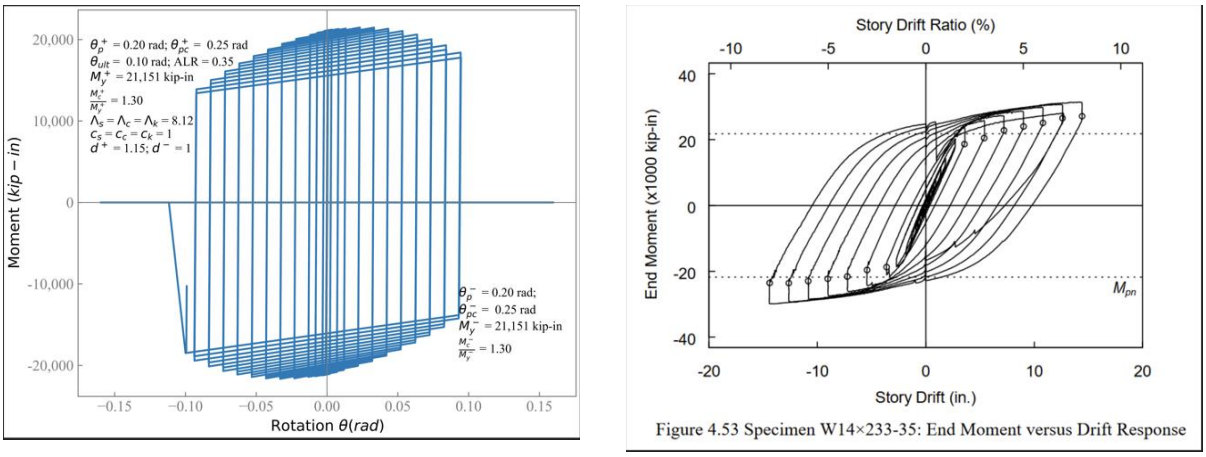

Figure F-9 Example cyclic moment-rotation behavior for a W14×233 column with 30% axial load ratio and IMK behavior as prescribed compared with a similar test from Newell and Uang (2006).

An IMK model is used to represent their nonlinear behavior where backbone moment strength parameters are calculated per NIST (2017a) with weak axis section properties used. For θ_p and θ_{pc}, upper bound values given in NIST (2017a) of 0.2 rads and 0.3 rads respectively are used. As noted above, this represents stocky sections with little web or lateral torsional buckling, which is consistent with the expected weak-axis response of the stocky W14 columns. An upper bound value of θ_u equal to 0.1 rads is used because it is anticipated that outer fiber strains would be large enough to initiate fracture at this rotation level. The cyclic deterioration parameter, λ_c, was set to 300 to essentially eliminate deterioration. Thus, the weak-axis flexural properties of the columns on Lines A-1 and G-1 have essentially bilinear behavior with a moment capacity reduced for axial load, no deterioration up to a rotation capacity of 0.1 rads, after which they deteriorate to near-zero strength.

Panel Zones

Panel zones are modeled with the Krawinkler panel zone model as illustrated in Figure F-5. The model uses rigid pin-ended struts in the boundary of the panel zone and a rotational spring at one corner that controls the nonlinear behavior of the panel zone. The panel zone shear force versus shear rotation backbone is as shown in Figure F-10, which is from NIST (2017a). The panel zone strengths and shear deformations are calculated as recommended by Kim et al. (2015), which considers the contribution of the column flanges and has been shown to agree well with

experimental results. The cyclic response of the panel zone is assumed to have kinematic hardening, and panel zone deterioration is not modeled. Table F-5 shows the panel zone backbone properties for the SMF columns in each archetype model.

Importantly, the panel zones in the archetype models were not designed considering the composite strength of the RBS connections. For all archetypes, it was found during preliminary nonlinear static analyses that the panel zones were controlling the behavior of the frame, yielding before the RBS beams and columns and preventing the RBS beams from yielding at all. Because this is inconsistent with the intention of AISC 341 where only limited panel zone yielding is permitted, the yield strength of the panel zones in the models were increased while the stiffness was left as designed. An increase of 50% in the yield strength of the panel zones in the models was found to be adequate as it produced largely RBS yielding behavior with some limited panel zone yielding concentrated in the upper stories where the column sections were smaller. Considering the composite strength of moment frame beams when designing panel zones may be appropriate, especially when W14 columns are used.

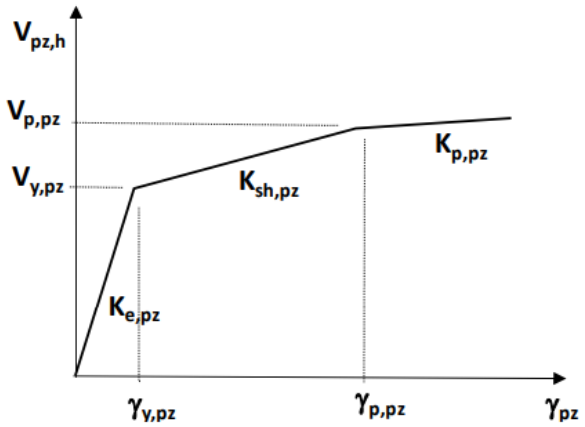

Figure F-10 Backbone shear force versus shear rotation behavior for the panel zone (NIST, 2017b).

Table F-5 Panel Zone Model Parameters Calculated per Kim et al. (2015)

Level	Section	$V_{y,pz}$ (kips)	$V_{p,pz}$ (kips)	$\gamma_{y,pz}$ (rads)	$\gamma_{p,pz}$ (rads)	$K_{e,pz}$ (kips/rad)	$K_{sh,pz}$ (kips/rad)	$K_{p,pz}$ (kips/rad)
High D Archetype								
1	W14×257	1,621	1,956	0.0054	0.0237	302,603	18,244	8,795
2	W14×257	1,621	1,956	0.0054	0.0237	302,603	18,244	8,795
3	W14×257	1,621	1,956	0.0054	0.0237	302,603	18,244	8,795
4	W14×211	1,576	1,900	0.0054	0.0286	294,269	13,945	8,670

Level	Section	$V_{y,pz}$ (kips)	$V_{p,pz}$ (kips)	$\gamma_{y,pz}$ (rads)	$\gamma_{p,pz}$ (rads)	$K_{e,pz}$ (kips/rad)	$K_{sh,pz}$ (kips/rad)	$K_{p,pz}$ (kips/rad)
5	W14×211	1,353	1,647	0.0054	0.0284	252,585	12,771	7,417
6	W14×176	1,459	1,758	0.0054	0.0304	272,341	11,927	8,054
7	W14×176	1,459	1,758	0.0054	0.0304	272,341	11,927	8,054
8	W14×159	1,080	1,327	0.0054	0.0329	201,689	8,948	5,961
9	W14×159	1,080	1,327	0.0054	0.0329	201,689	8,948	5,961
Very High Seismic Archetype								
1	W14×605	1,762	2,128	0.0027	0.0065	657,669	96,837	17,345
2	W14×605	1,762	2,128	0.0027	0.0065	657,669	96,837	17,345
3	W14×605	1,762	2,128	0.0027	0.0065	657,669	96,837	17,345
4	W14×500	1,351	1,647	0.0027	0.0075	504,363	61,353	13,701
5	W14×500	1,351	1,647	0.0027	0.0075	504,363	61,353	13,701
6	W14×455	1,194	1,461	0.0027	0.0080	445,877	49,765	12,251
7	W14×455	1,194	1,461	0.0027	0.0080	445,877	49,765	12,251
8	W14×342	814	1,008	0.0027	0.0102	304,022	25,877	8,602
9	W14×342	814	1,008	0.0027	0.0102	304,022	25,877	8,602
Ultra High Seismic Archetype								
1	W14×873	3,000	3,542	0.0027	0.0061	1,120,083	160,413	29,680
2	W14×873	3,000	3,542	0.0027	0.0061	1,120,083	160,413	29,680
3	W14×873	3,000	3,542	0.0027	0.0061	1,120,083	160,413	29,680
4	W14×730	2,210	2,658	0.0027	0.0066	825,150	115,409	21,951
5	W14×730	2,210	2,658	0.0027	0.0066	825,150	115,409	21,951
6	W14×605	1,699	2,062	0.0027	0.0076	634,333	73,501	17,345
7	W14×605	1,699	2,062	0.0027	0.0076	634,333	73,501	17,345
8	W14×398	982	1,211	0.0027	0.0098	366,658	32,357	10,339
9	W14×398	982	1,211	0.0027	0.0098	366,658	32,357	10,339

F.3.3 Gravity Frame Modeling

As discussed above, the gravity framing that is tributary to the SMF, i.e., half of the gravity framing in the archetype building, is modeled in plane with the SMF. All gravity columns are present and modeled with elastic-beam column elements with the section properties of the gravity frame columns. At each end of the columns at each level a zero-length rotational spring is used to simulate the inelastic flexural behavior of the columns using the same approach detailed above for the SMF columns (i.e., the strength and rotations for the component backbone curves are modified for the axial force from gravity loading), Table F-6 lists the component model parameters used for each column at each level in the gravity framing. Because the gravity columns are reasonably large and stocky W14 shapes, an upper bound on the ultimate rotation, θ_u, or 0.1 rads is again imposed consistent with test results from Newell and Uang (2006). The splices in the gravity columns are modeled as pins.

Table F-6 IMKBilin Parameters for Gravity Frame Columns in Archetype SMF Models

Level	Section	P_g/P_y	M_y (kip-in)	M_c (kip-in)	M_r (kip-in)	θ_p (rads)	θ_{pc} (rads)	θ_u (rads)	λ_c
	High D, Very High Seismic, and Ultra High Seismic Archetypes								
1	W14×132	0.45	9,086	11,305	2,892	0.062	0.101	0.10	3.189
1.5	W14×132	0.40	9,926	12,796	3,360	0.072	0.126	0.10	3.189
2	W14×99	0.54	5,682	6,214	1,617	0.029	0.052	0.10	1.861
3	W14×99	0.47	6,510	7,518	2,028	0.036	0.074	0.10	1.861
3.5	W14×99	0.40	7,339	8,891	2,484	0.044	0.099	0.10	1.861
4	W14×82	0.49	5,048	5,048	1,535	0.028	0.051	0.10	2.603
5	W14×82	0.41	5,855	6,079	1,972	0.035	0.073	0.10	2.603
5.5	W14×82	0.33	6,662	7,284	2,461	0.044	0.101	0.10	2.603
6	W14×61	0.44	4,081	4,081	1,326	0.019	0.050	0.10	1.473
7	W14×61	0.33	4,875	4,985	1,798	0.026	0.078	0.10	1.473
7.5	W14×61	0.22	5,670	6,157	2,338	0.033	0.114	0.10	1.473
8	W14×43	0.31	3,413	3,413	1,282	0.016	0.057	0.10	1.134
9	W14×43	0.16	3,718	3,718	1,628	0.022	0.095	0.10	1.134

The gravity columns are connected to each other and to the SMF with elastic beam-column elements representing the gravity frame beams. At each end of the beams are zero-length rotational springs

that represent the shear beam-to-column connections. The connections are modeled as suggested in NIST (2017a) with the behavior shown in Figure F-11. The model parameters are computed per NIST (2017a), which are largely derived from Liu and Astaneh-Asl (2004). The pinching4 material is used in *OpenSees* to simulate the cyclic response and deterioration of the connection, returning the cyclic behavior shown in Figure F-11. Figure F-12 shows the implementation of this model for a 4-bolt gravity connection from the archetype SMF described above. Table F-7 lists the key component backbone parameter values for each gravity frame connection in the model of each archetype.

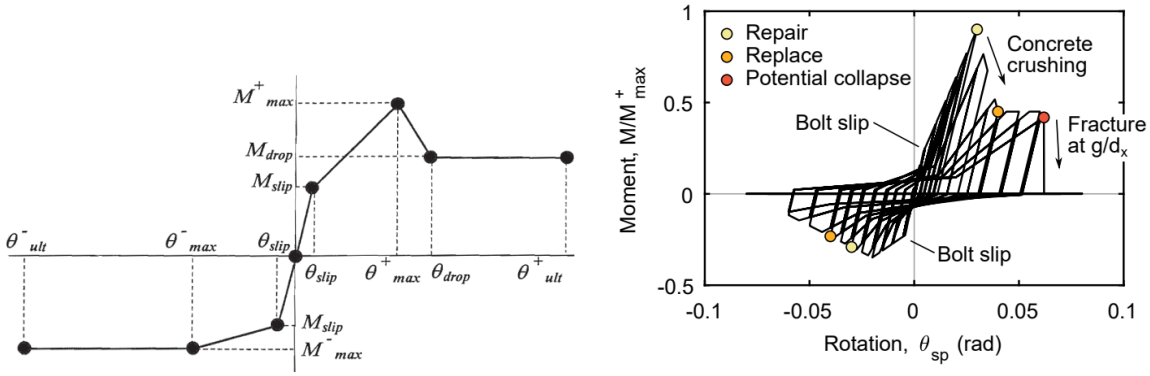

Figure F-11 Backbone and cyclic moment versus rotation behavior for the gravity frame connections (from NIST, 2017b, and Sen et al., 2020).

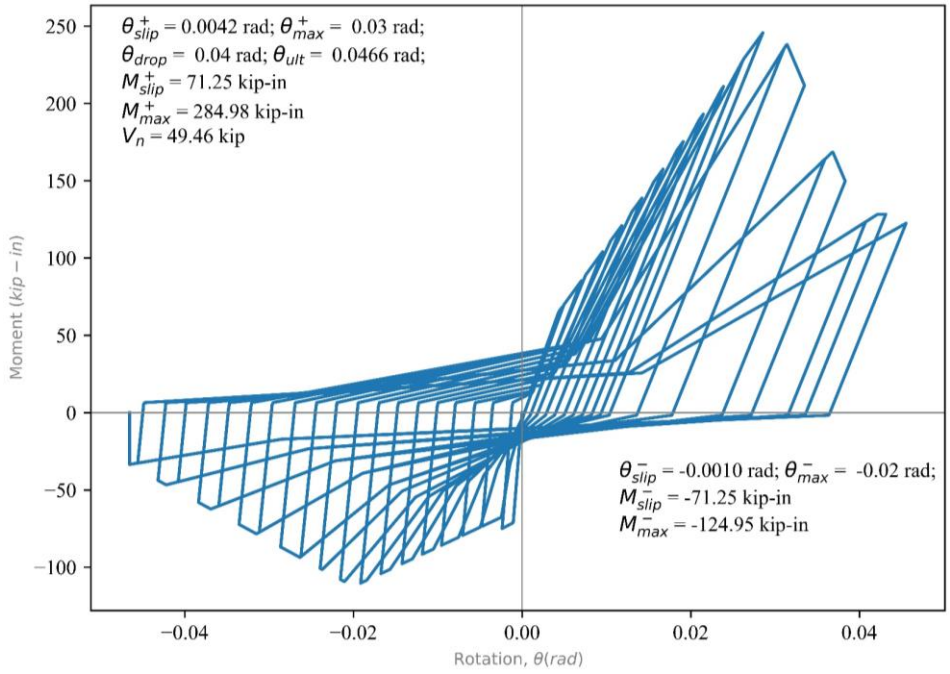

Figure F-12 Implemented 4-Bolt gravity connection moment-rotation behavior.

Table F-7 Backbone Parameters for Gravity Frame Beam-to-Column Connection Models

Connection Type	M_{slip} (kip-in)	M_{max}^+ (kip-in)	M_{drop} (kip-in)	M_{max}^- (kip-in)	θ_{slip} (rads)	θ_{max}^+ (rads)	θ_{drop} (rads)	θ_{ult}^+ (rads)	θ_{max}^- (rads)	θ_{ult}^- (rads)
All Archetypes										
Ext. Girder - Flange	72	288	144	113	0.0042	0.03	0.04	0.057	0.02	0.057
Ext. Girder - Web	72	286	143	113	0.0042	0.03	0.04	0.057	0.02	0.057
Int. Girder	72	287	144	113	0.0042	0.03	0.04	0.047	0.02	0.047

F.4 Modal Analysis

Modal analysis was conducted on the three models. The results for the first three modes for each model are shown in Table F-8. Also shown are the results of the modal analysis conducted by the AISC Steel Solutions Center using a linear centerline model in *ETABS*. As shown, the modal response indicates that the *OpenSees* models are consistently stiffer than the *ETABS* results. This is reasonable since the *OpenSees* models include the gravity frames and include the panel region which shortens the beam and column spans.

Of particular importance is the difference in periods for the three designs. The High Seismic design has a long period of more than 3 seconds. The Very High Seismic design has a period near the ASCE/SEI 7 C_uT_a period of 1.83 seconds, and the Ultra High Seismic design has a period considerably less than the ASCE/SEI 7 C_uT_a period.

Table F-8 Modal Analysis Results

Mode	High D		Very High Seismic		Ultra High Seismic	
	AISC (seconds)	*OpenSees* (seconds)	AISC (seconds)	*OpenSees* (seconds)	AISC (seconds)	*OpenSees* (seconds)
1	3.674	3.15	2.10	1.92	1.52	1.37
2		1.01		0.68		0.53
3		0.46		0.37		0.32

F.5 Nonlinear Static Response

Nonlinear static analysis was performed on each model. The analyses were conducted as prescribed in FEMA P-695 using the first mode equivalent force distribution as the load pattern. The models were loaded until convergence failure occurred. Convergence failure was investigated in all cases and found to correspond to the point where ultimate (i.e., failure) rotations were achieved in the first floor RBS connections and the first-floor columns. In all cases, this corresponds to a drift on the first story of approximately 9%. Figure F-13 shows the resulting pushover curves in terms of base shear versus roof drift, where the base shear is normalized by the tributary seismic weight for the modeled framing (i.e., half of the building).

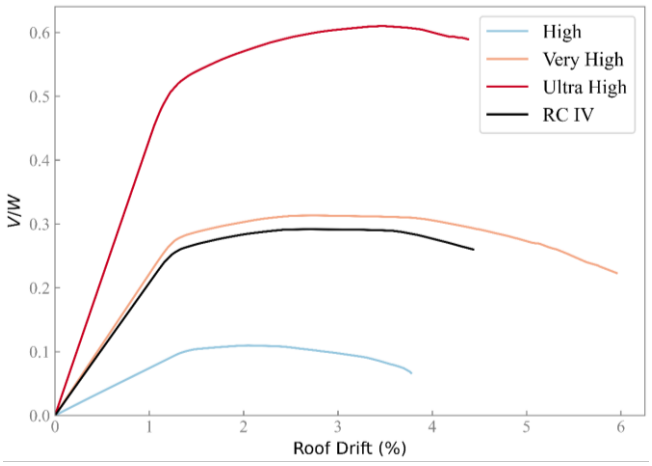

Figure F-13 Pushover Curves for the SMF Designs.

Figure F-14 shows the story drift profile at different values of roof drift for the three designs, where the largest drift corresponds to incipient collapse in the nonlinear static analysis. As shown, all three designs that concentrated drift at the lower stories. Figures F-15 through Figure F-17 show the moment-rotation behaviors for the second-story interior RBS beams (i.e., the beams supporting the first level above the ground), ground-level columns and second-story gravity connections obtained from the nonlinear static analysis. For the beam responses, the plots show the response from the hinges at the left and right beam ends. For the columns, the plots show the response of hinges at the bottom and top of the column on level 1. Each analysis failed to continue to converge as the number of elements reaching zero capacity increased although the exact point of nonconvergence was different for each model. In general, nonconvergence occurred when with both ends of the RBS beams supporting the second level reached zero capacity and/or a first level column reached zero capacity at its base. The figures show, for example, the RBS hinges reaching their ultimate rotation capacity of 0.08 rads and then dropping to zero strength for several of the models. They show similar behavior for the hinges at the base of the columns and the springs representing the shear tab connections in the gravity framing. Note that the nonlinear static analysis was performed with loading from “left to right” in Figure F-4, resulting in positive moment at the left ends of beams and negative moment at the right ends.

The primary observation from the nonlinear static analyses is that all designs have similar collapse modes, where drifts are concentrated on the lower two-to-three levels. In all cases, the distribution of story drift is fairly uniform at 1.5% roof drift. By 3.5% roof drift, the story drift demands are largely concentrated on the lower two or three levels. When story drifts of near 10% are reached at the first level, the column hinges at the base have reached their rotation capacity of 0.1 rads, and the structure is unstable. In some cases, this point of instability is reached slightly before reaching 10% story drift because multiple RBS beam hinges have instead reached their rotation capacity. Importantly, the Very High Seismic design has three stories with large drifts at large roof drift, perhaps indicating that this design is somewhat more effective at spreading the drift demand between stories. Note that the drift at incipient collapse, DR_{IC}, used in Chapter 5 is not found from nonlinear static analyses but instead from incremental dynamic analysis. That means that the story drifts shown in Figure F-14 will not directly correspond to those values. However, the drift profiles from pushover provide insight into the dominant mode of collapse for the structure.

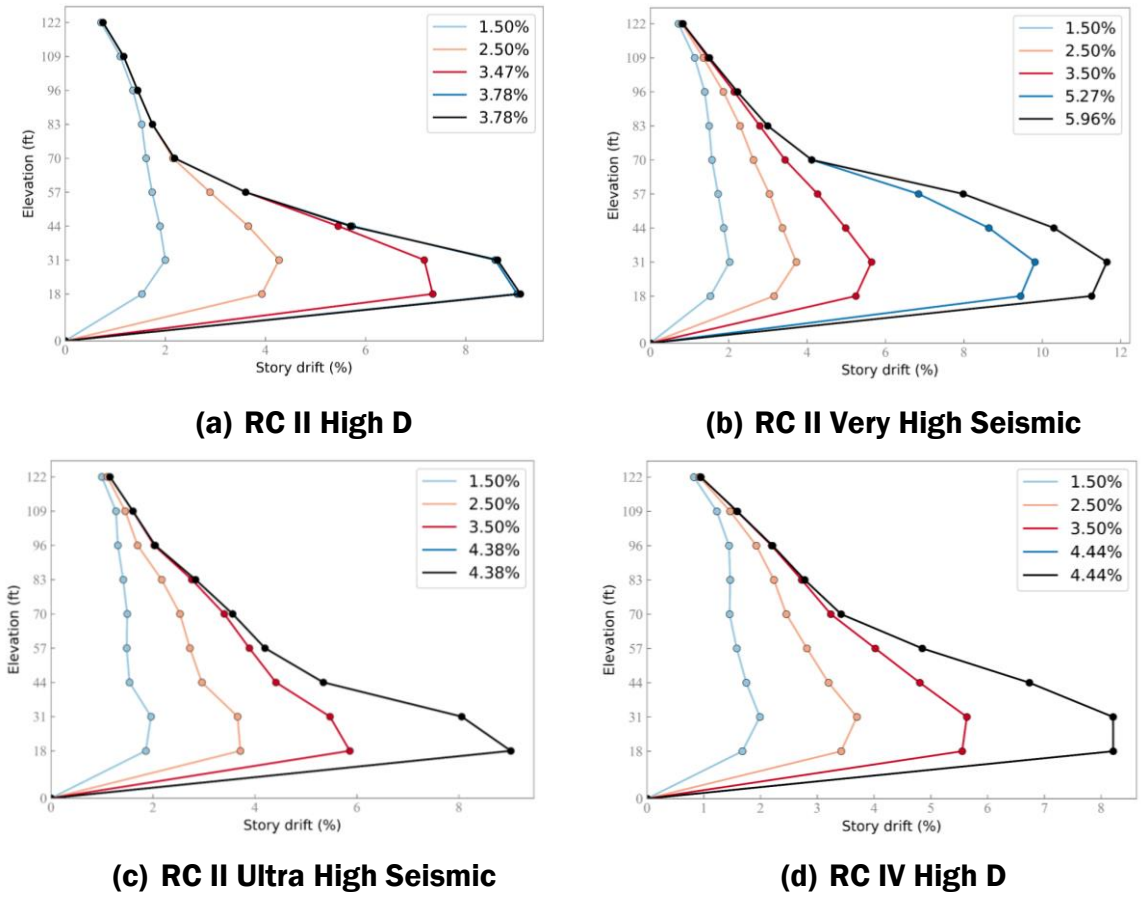

Figure F-14 Story drift profiles from nonlinear static analysis at different roof drift levels, where roof drifts are indicated in the legends.

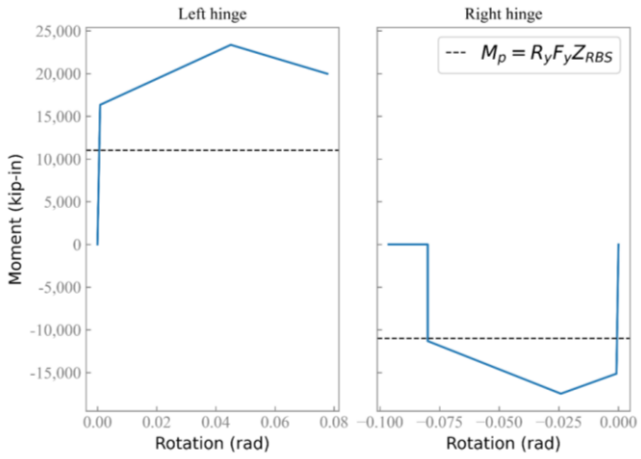

(a) 2nd Floor RBS beam hinge behavior

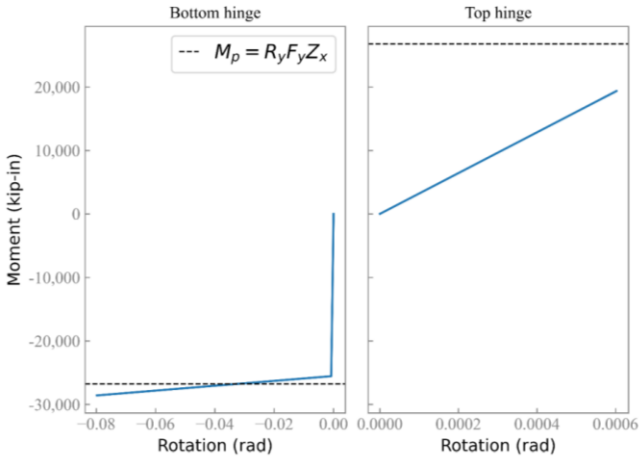

(b) Level 1 column hinge behavior

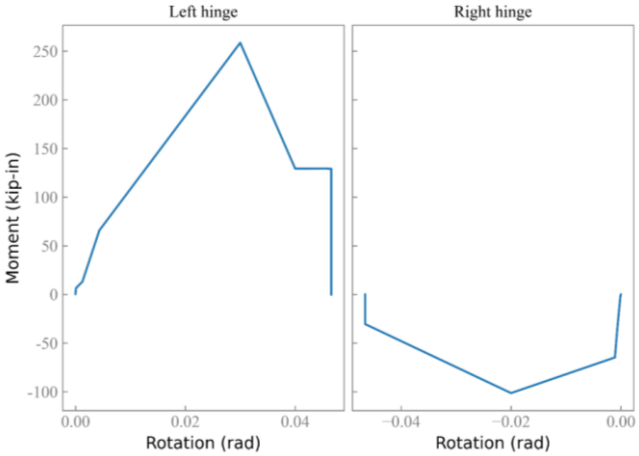

(c) 2nd floor gravity beam hinge behavior

Figure F-15 Nonlinear static analysis component results for the High D Model.

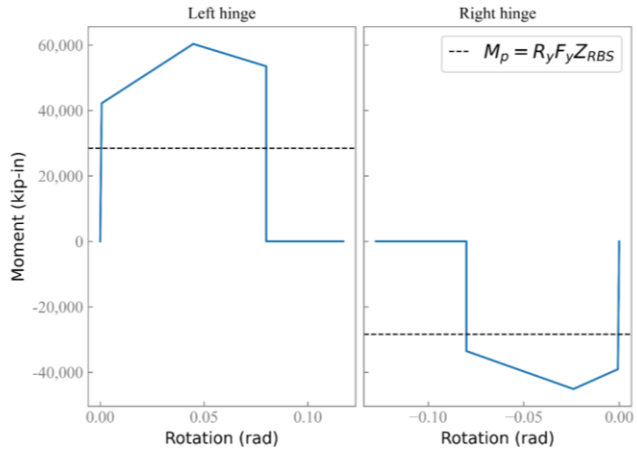

(a) 2nd Floor RBS beam hinge behavior

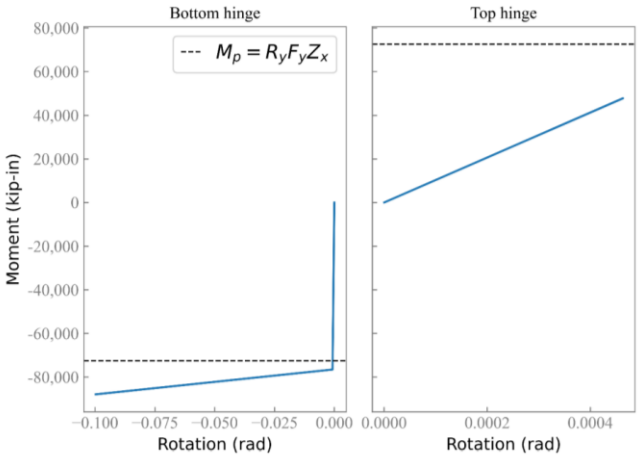

(b) Ground floor column hinge behavior

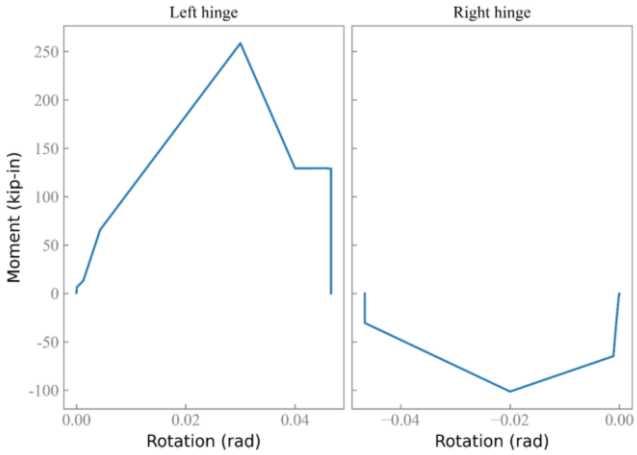

(c) 2nd floor gravity beam hinge behavior

Figure F-16 Nonlinear static analysis component results for the Very High Seismic model.

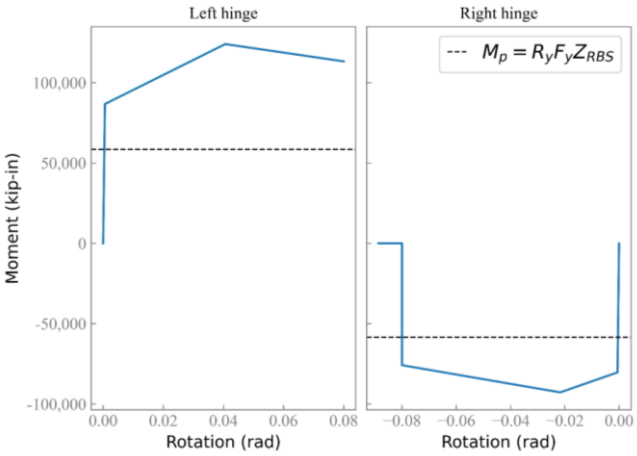

(a) 2nd floor RBS beam hinge behavior

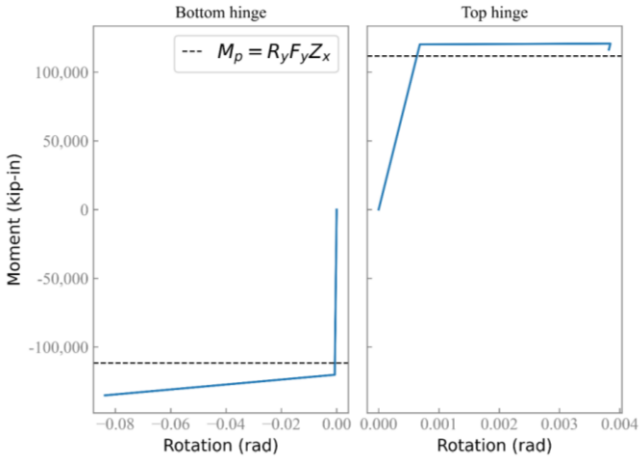

(b) Ground floor column hinge behavior

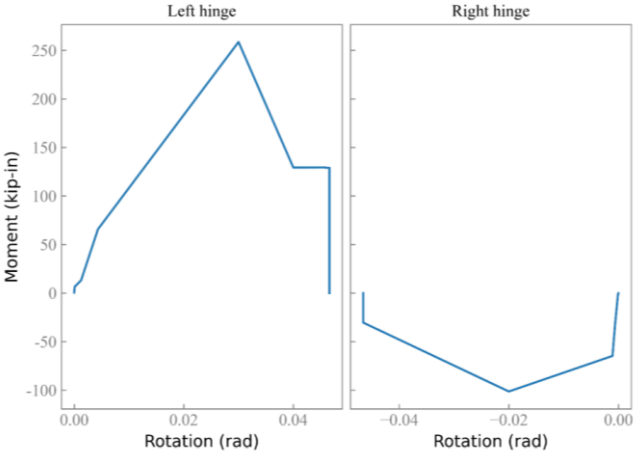

(c) 2nd floor gravity beam hinge behavior

Figure F-17 Nonlinear static analysis component results for the Ultra High Seismic model.

F.6 Nonlinear Dynamic Response

Preliminary nonlinear response history analyses were conducted to check the model response to ground motions. A single ground motion from the FEMA P-695 suite was selected for use. The ground motion was scaled to the MCE_R spectral acceleration at the ASCE/SEI 7 period (1.83 seconds for the High D and Very High Seismic designs and 1.52 seconds for the Ultra High Seismic design) where the MCE_R are given in Table F-1. The same motion was scaled to 2.0 times the MCE_R spectral acceleration at the ASCE/SEI 7 period and run again. This was done to provide an opportunity to investigate the model behavior for a ground motion that causes nonlinear behavior but not collapse and one that causes collapse. Figure F-18 shows the MCE_R spectra used for design of the High D, Very High Seismic, and Ultra High Seismic SMF archetypes and two times those spectra. Figure F-18 also shows the scaled FEMA P-695 ground motion, as described above. These analyses are not intended to provide insight into the SMF collapse performance, which is addressed via incremental

dynamic analysis below, but instead to illustrate the behavior of the components under two different levels of ground motion.

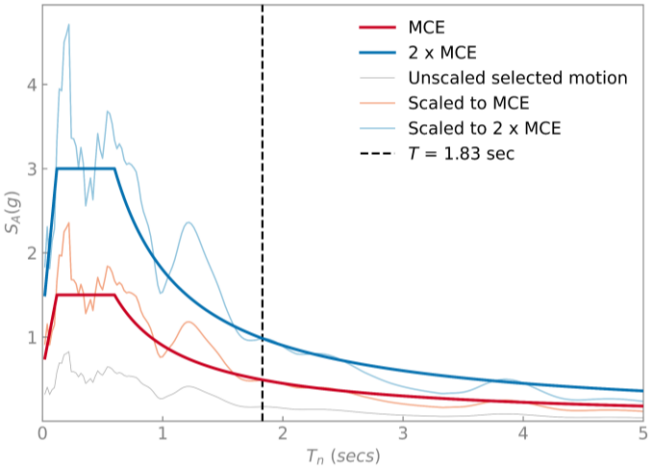

(a) MCE_R spectra and selected ground motion spectra for High D

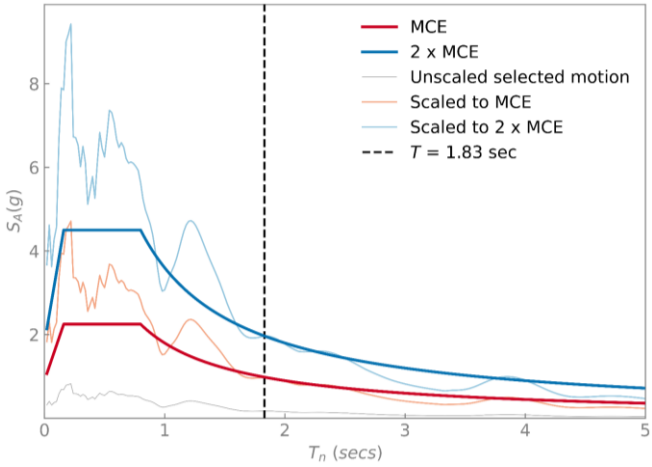

(b) MCE_R spectra and selected ground motion spectra for Very High Seismic

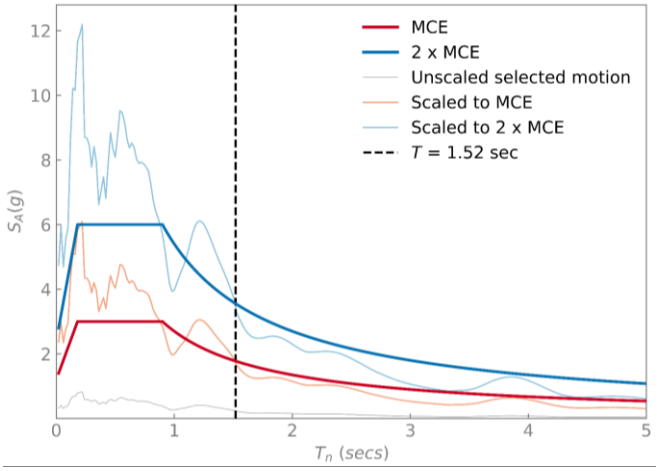

(c) MCE_R spectra and selected ground motion spectra for Ultra High Seismic

Figure F-18 Comparison of the design and amplified design spectra to the selected and amplified ground motion spectra based on MCE_R.

For each nonlinear response analysis, the following data are presented in the following figures:

- Base shear and roof drift response histories,
- Envelope of peak story drift,
- Drift profile at peak roof drift,

- Example 1st floor beam RBS hinge results,
- Example ground floor column hinge results, and
- 1st floor beam gravity beam connection results.

Note that the panel zones remained essentially elastic and thus their behaviors are not shown.

The data are presented in the following order: High D, Very High Seismic, and Ultra High Seismic. Note that for the 2.0MCE_R ground motions, all three models suffered convergence failure, and the ground motions did not complete. As shown, at the time of convergence failure, the RBS connections for the beams supporting the 2nd floor had reached zero capacity, the gravity connections had reached zero capacity and the columns were just reaching their ultimate rotation capacity. In other words, at this instance the fames had essentially zero lateral capacity and the point at which the analyses failed is collapse. Note that the Very High and Ultra High models produced results to very large displacements prior to suffering convergence failure due to dynamic instability. For those cases, results are shown up to a time just before dynamic instability to make sure results are shown for converged analyses.

Note that all frames exhibited ratcheting behavior prior to collapse or even at just large displacements. This ratcheting behavior results in only a few complete cycles of loading for most of the hinges and thus there is very little cyclic deterioration. This is true for the RBS hinges and the column hinges. Additionally, because the RBS hinges consider composite action, one end of the beam generally has considerably larger strength.

Finally, it is important to reiterate that these results are for single ground motion, scaled to two different levels. The maximum story drift from these analyses that would be used to compute DR_{IC}, assuming these were the first motions to cause collapse in an IDA, would be the maximum story drift that occurred during the analysis at any time and at any story. It is clear from the drift profiles below for the three models that the drift profile at collapse is concentrated at the lower one-to-three levels at the exact profile at collapse is slightly different from that obtained from nonlinear static analysis.

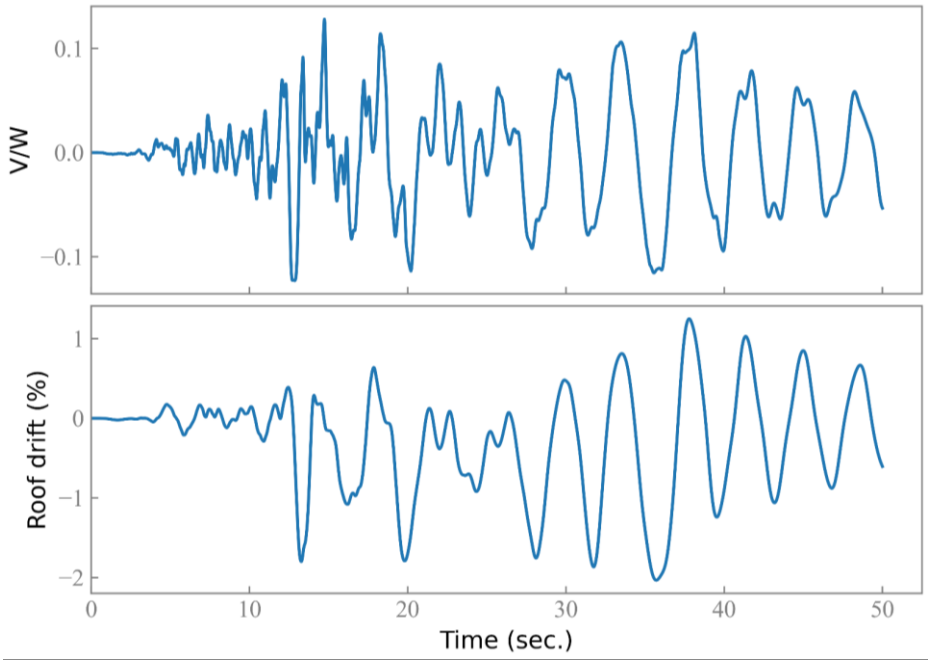

(a) Ground motion scaled to MCE_R

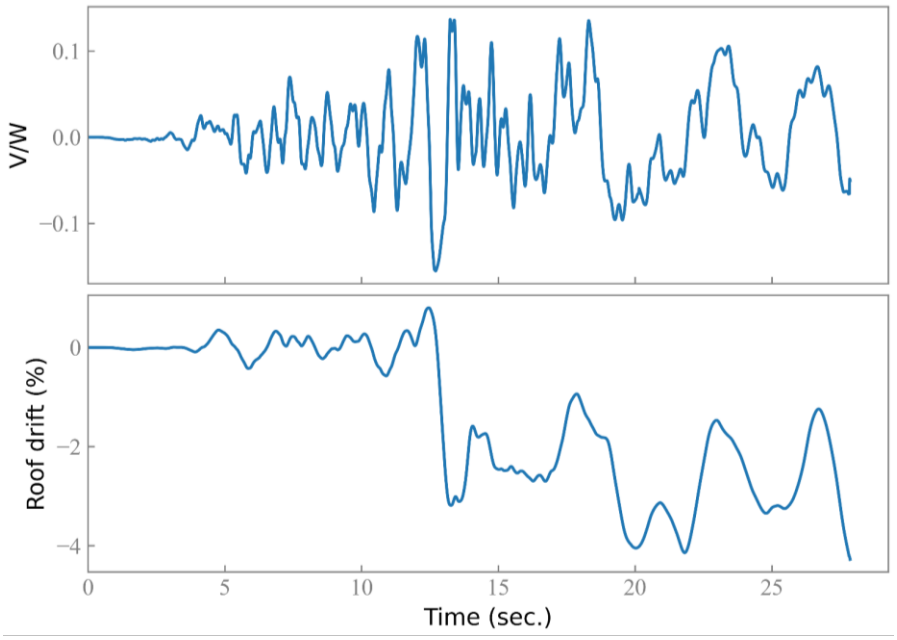

(b) Ground motion scaled to $2.0MCE_R$

Figure F-19 Base shear and roof drift response histories for the High D model.

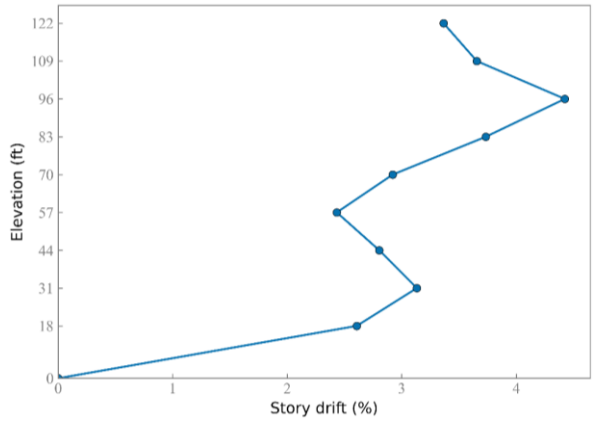

(a) Story drift envelope, ground motion scaled to MCE_R

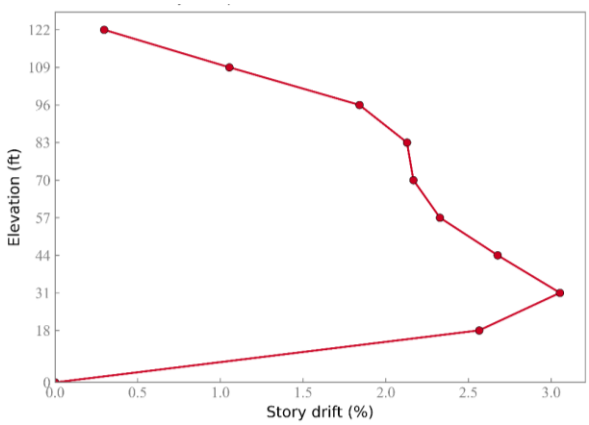

(b) Story drift profile at peak roof drift, ground motion scaled to MCE_R

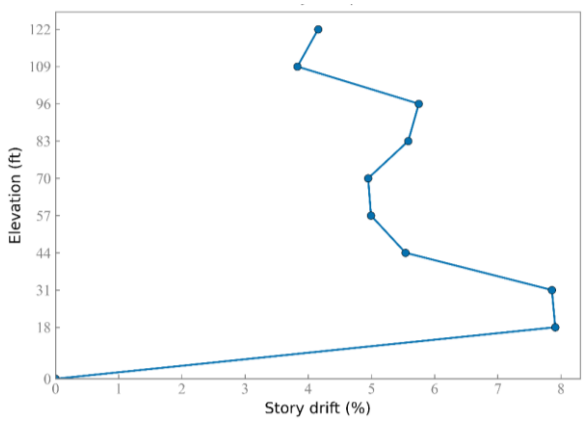

(a) Story drift envelope, ground motion scaled to $2.0MCE_R$

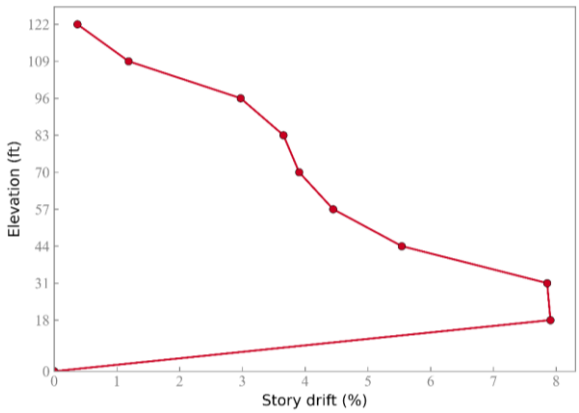

(b) Story drift profile at peak roof drift, ground motion scaled to $2.0MCE_R$

Figure F-20 Drift profiles for the High Seismic model.

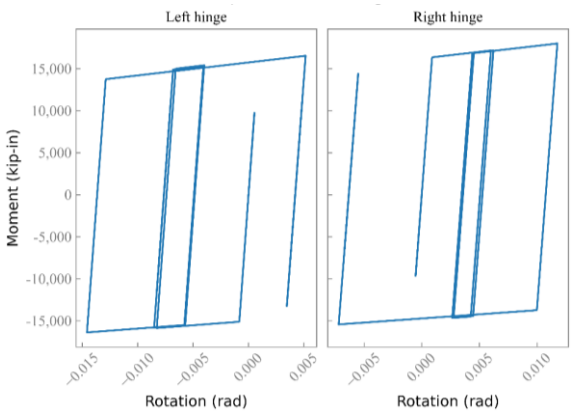

(a) 2nd floor RBS beam response, ground motion scaled to MCE_R

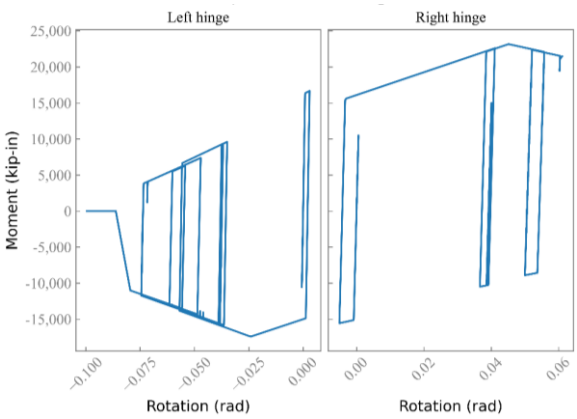

(b) 2nd floor RBS beam response, ground motion scaled to $2.0MCE_R$

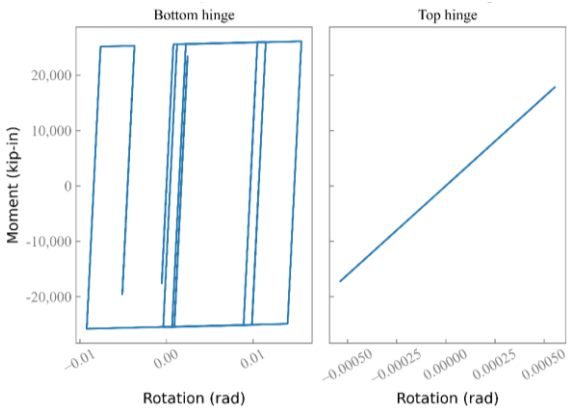

(c) Level 1 column response, ground motion scaled to MCE_R

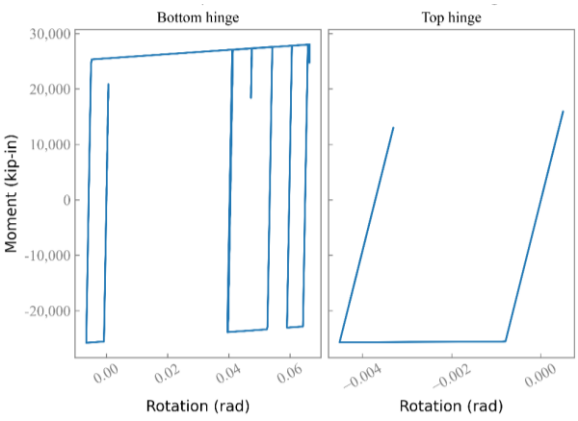

(d) Level 1 column response, ground motion scaled to $2.0MCE_R$

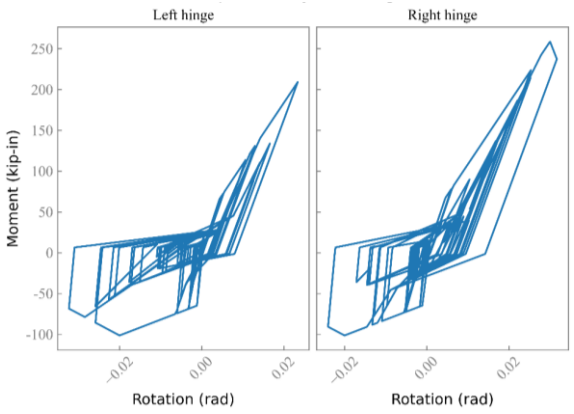

(e) 2nd floor gravity beam connection response, ground motion scaled to MCE_R

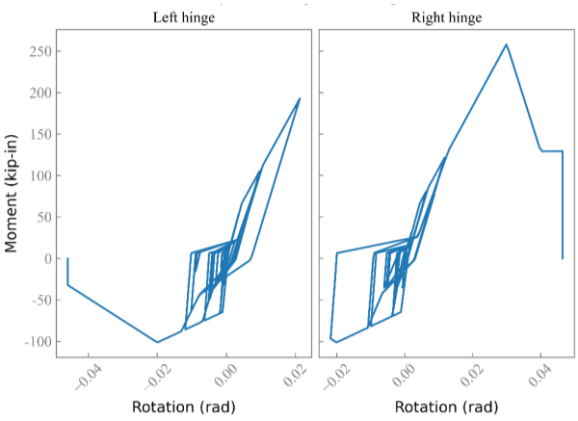

(f) 2nd floor gravity beam connection response, ground motion scaled to $2.0MCE_R$

Figure F-21 Example nonlinear response history component response for the High Seismic model.

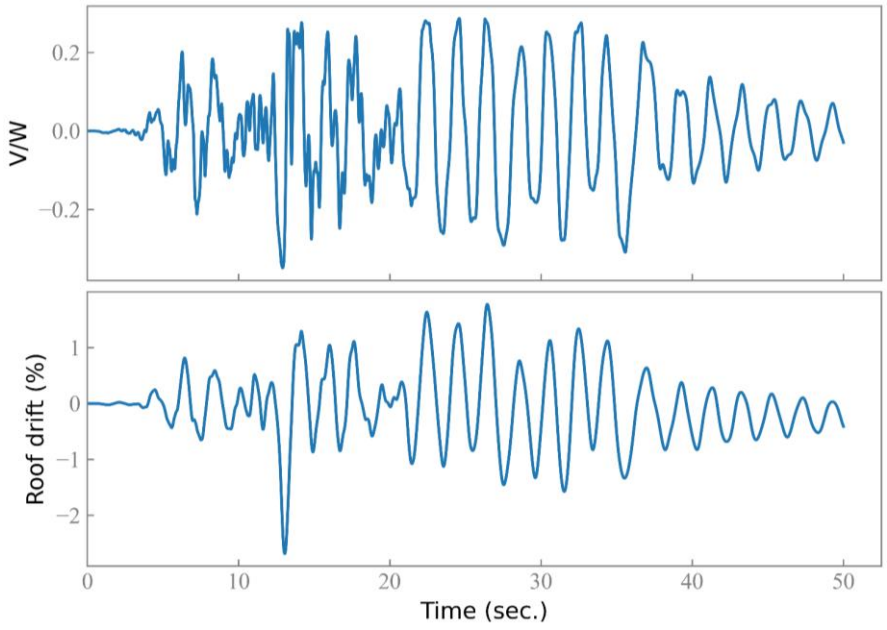

(a) Ground motion scaled to MCE_R

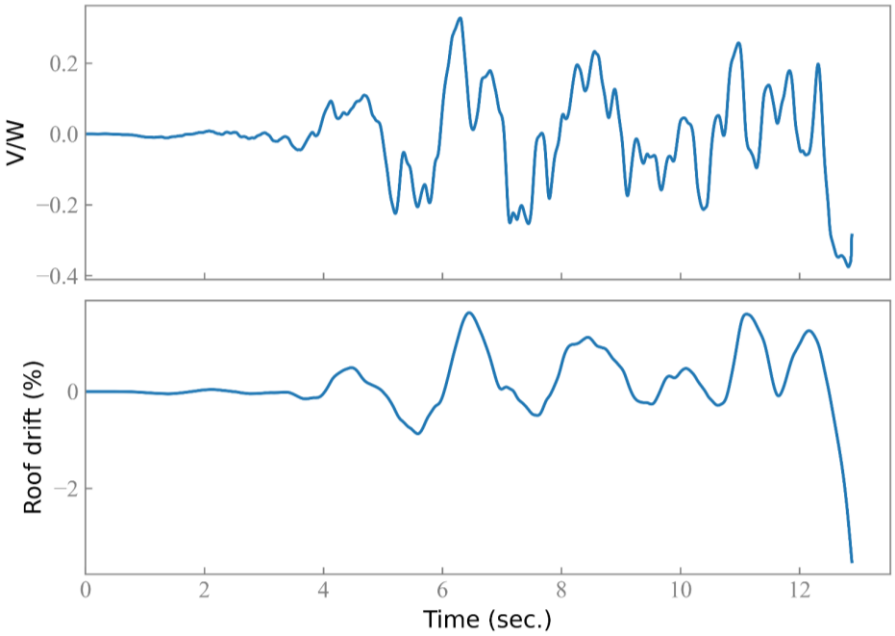

(b) Ground motion scaled to $2.0MCE_R$

Figure F-22 Base shear and roof drift response histories for the Very High Seismic model.

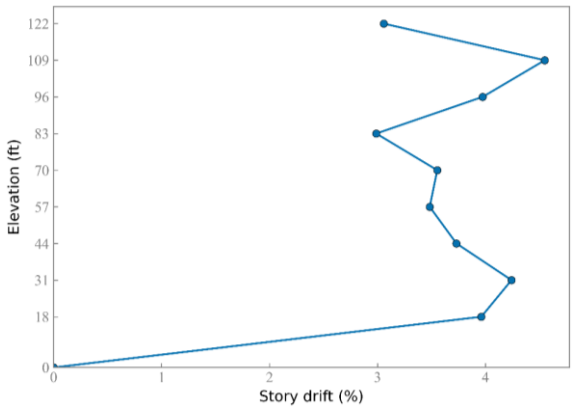

(a) Story drift envelope, ground motion scaled to MCE_R

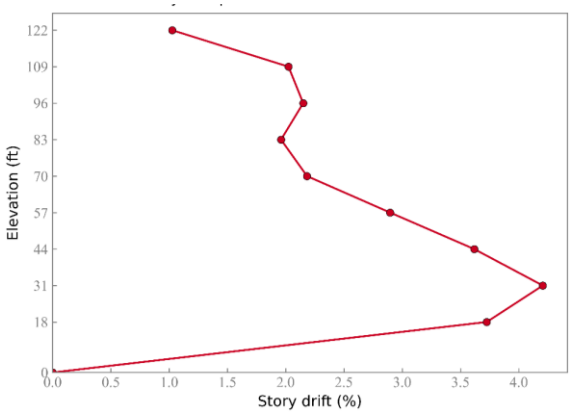

(b) Story drift profile at peak roof drift, ground motion scaled to MCE_R

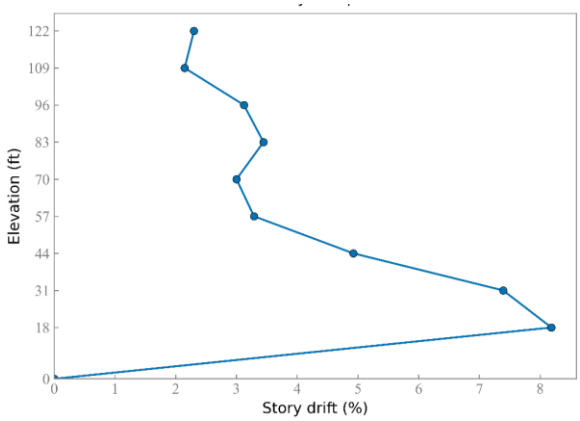

(c) Story drift envelope, ground motion scaled to 2.0MCE_R

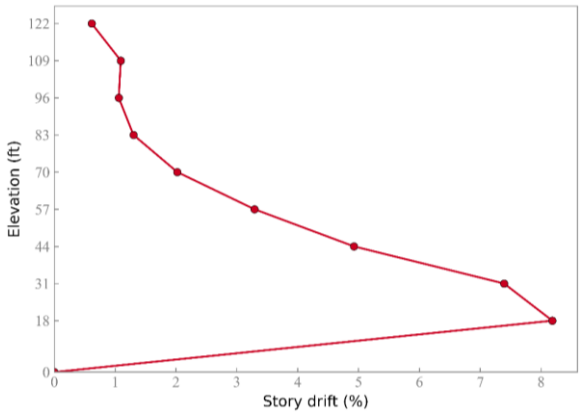

(d) Story drift profile at peak roof drift, ground motion scaled to 2.0MCE_R

Figure F-23 Drift profiles for the Very High Seismic model, where the 2.0 MCE_R results are pulled from a time step prior to collapse (approximately 12.5 seconds).

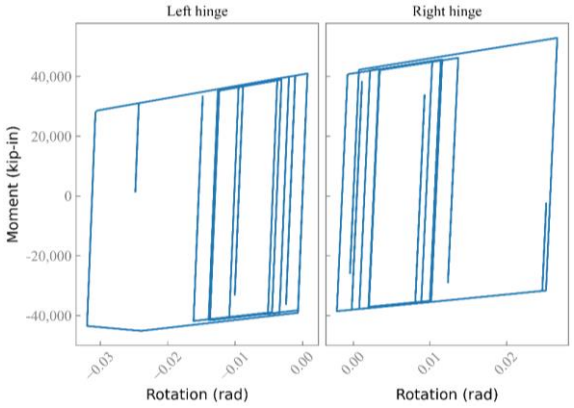

(a) 2nd floor RBS beam response, ground motion scaled to MCE_R

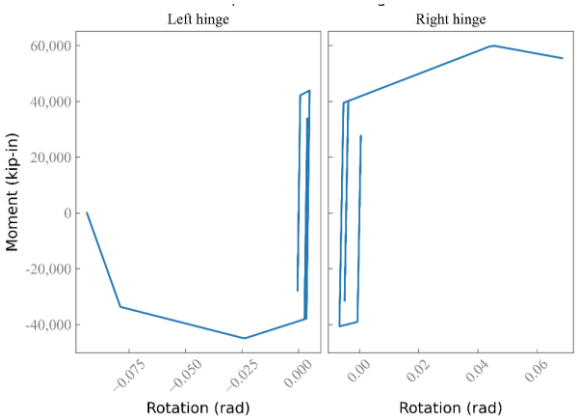

(b) 2nd floor RBS beam response, ground motion scaled to $2.0MCE_R$

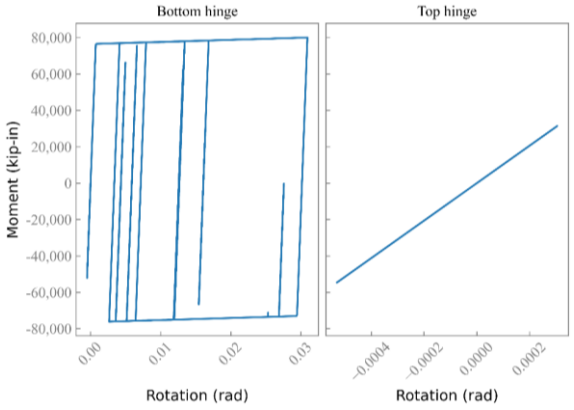

(c) Level 1 column response, ground motion scaled to MCE_R

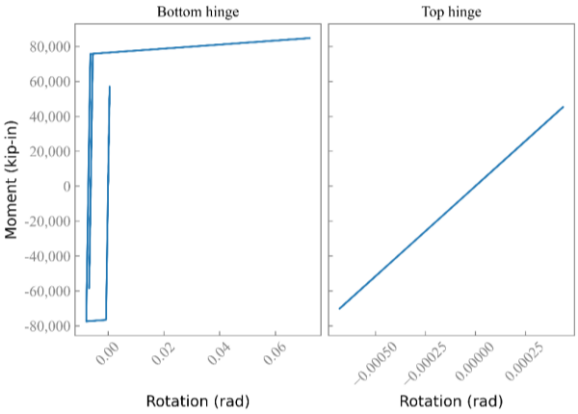

(d) Level 1 column response, ground motion scaled to $2.0MCE_R$

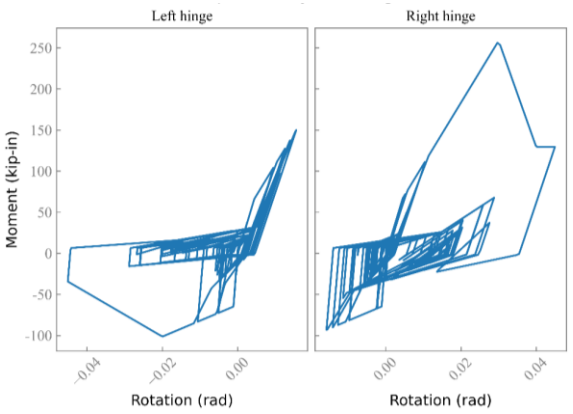

(e) 2nd floor gravity beam connection response, ground motion scaled to MCE_R

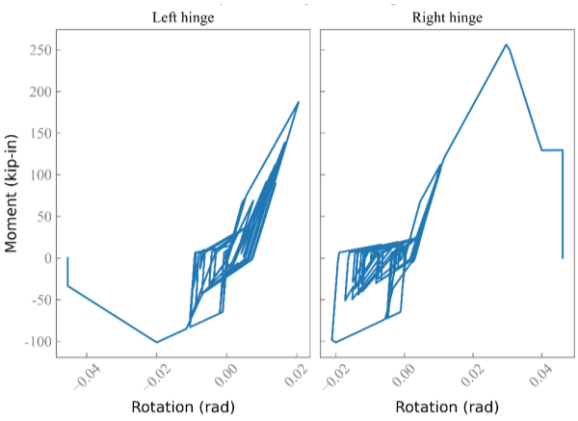

(f) 2nd floor gravity beam connection response, ground motion scaled to $2.0MCE_R$

Figure F-24 Example nonlinear response history component response for the Very High Seismic model, where the 2.0 MCE_R results are shown through a time step prior to collapse (approximately 12.5 seconds).

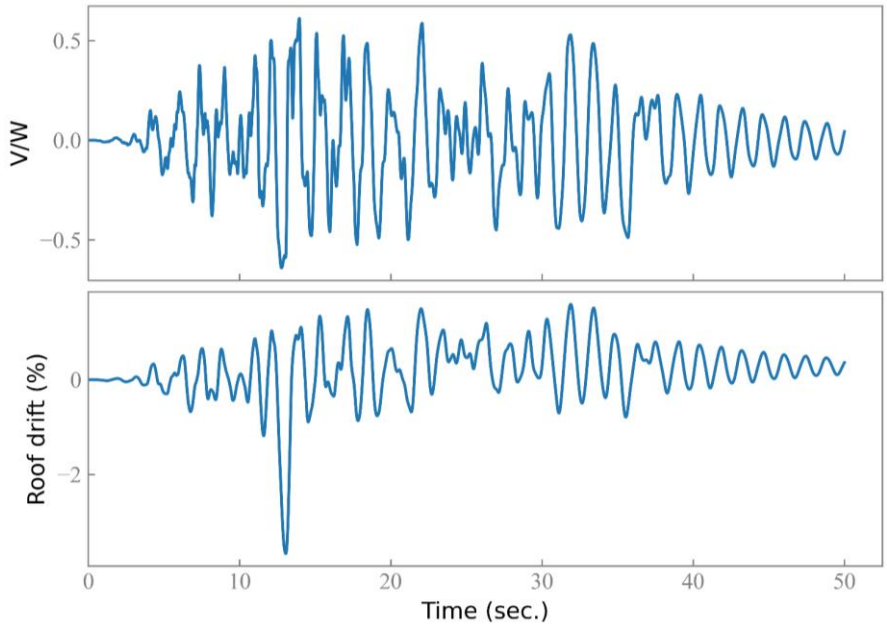

(a) Ground motion scaled to MCE_R

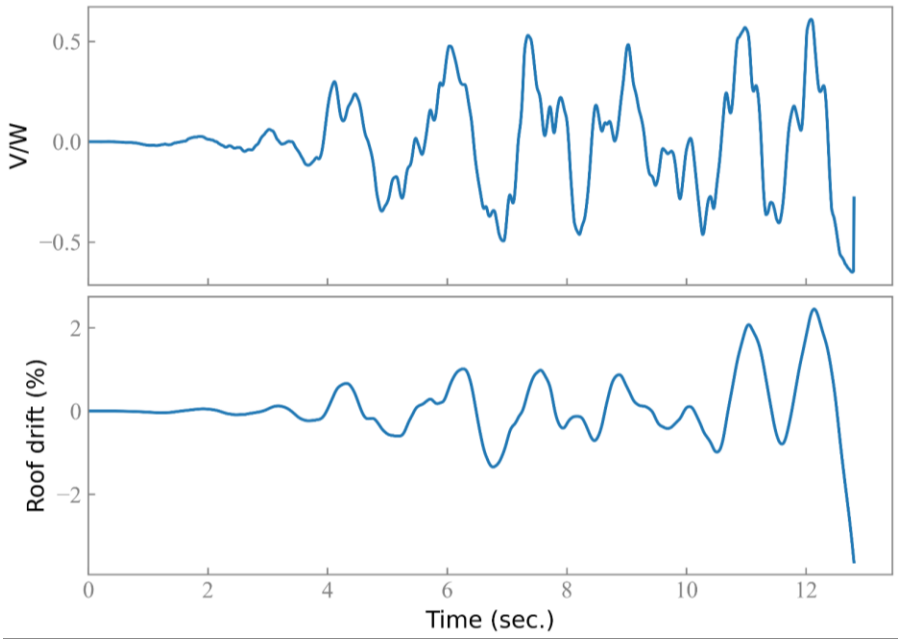

(b) Ground motion scaled to $2.0MCE_R$

Figure F-25 Base shear and roof drift response histories for the Ultra High Seismic model.

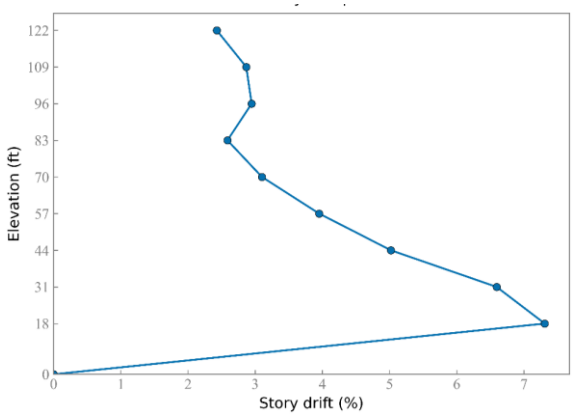

(a) Story drift envelope, ground motion scaled to MCE_R

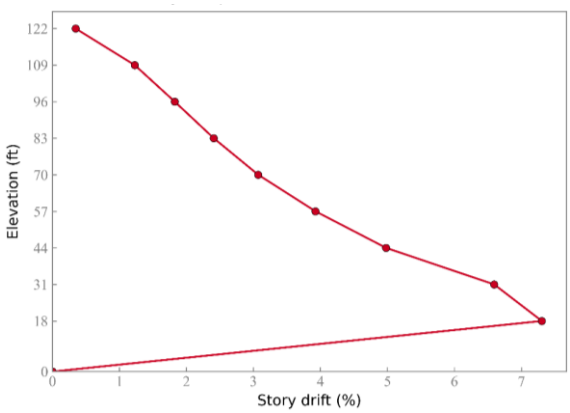

(b) Story drift profile at peak roof drift, ground motion scaled to MCE_R

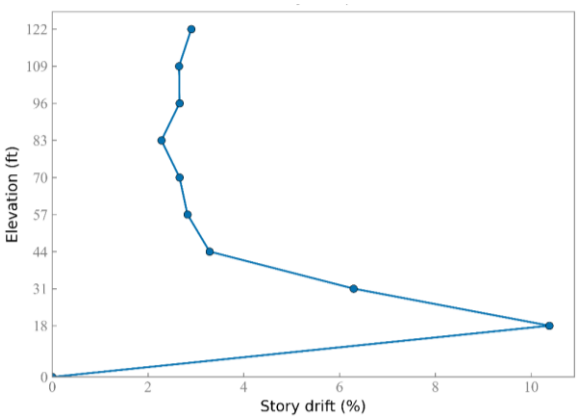

(c) Story drift envelope, ground motion scaled to 2.0MCE_R

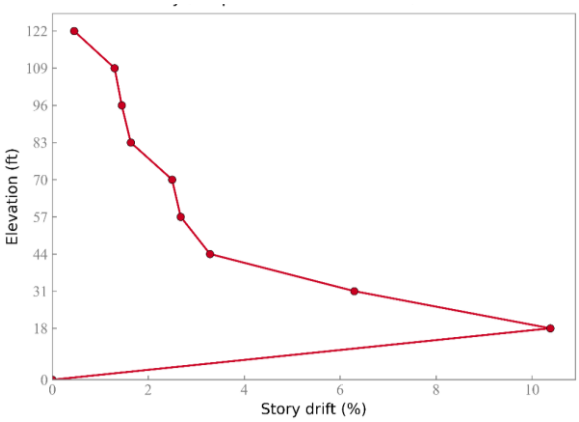

(d) Story drift profile at peak roof drift, ground motion scaled to 2.0MCE_R

Figure F-26 Drift profiles for the Ultra High Seismic model, where the 2.0 MCE_R results are pulled from a time step prior to collapse (approximately 12.5 seconds).

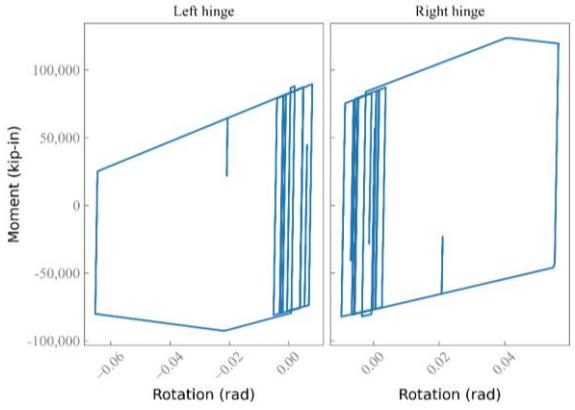

(a) 2nd floor RBS beam response, ground motion scaled to MCE_R

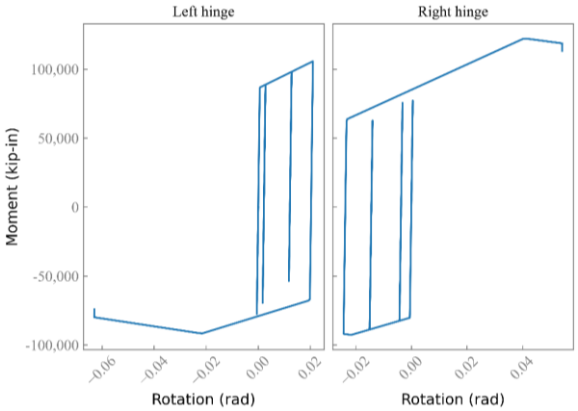

(b) 2nd floor RBS beam response, ground motion scaled to $2.0MCE_R$

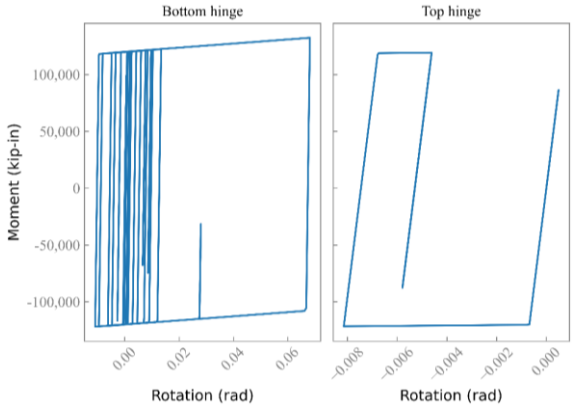

(c) Level 1 column response, ground motion scaled to MCE_R

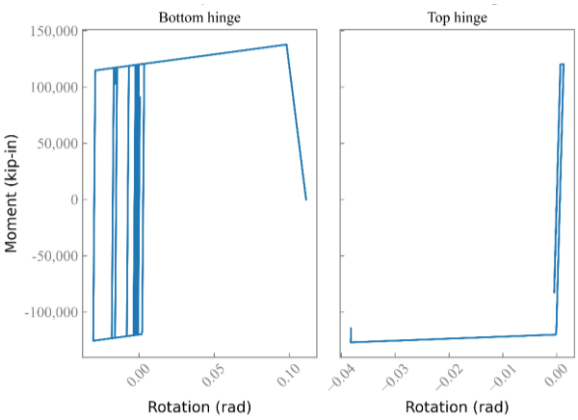

(d) Level 1 column response, ground motion scaled to $2.0MCE_R$

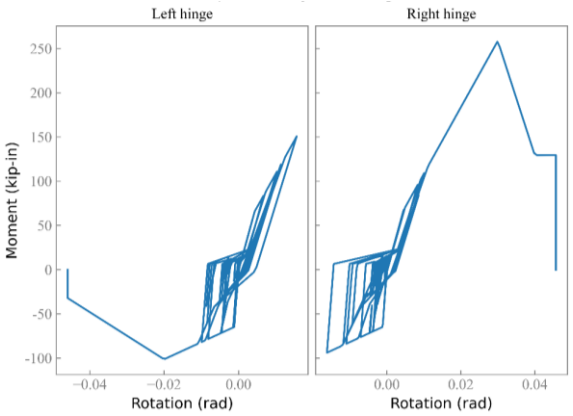

(e) 2nd floor gravity beam connection response, ground motion scaled to MCE_R

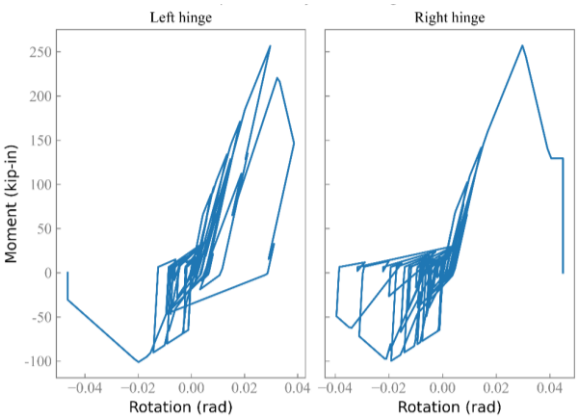

(f) 2nd floor gravity beam connection response, ground motion scaled to $2.0MCE_R$

Figure F-27 Example nonlinear response history component response for the Ultra High Seismic model, where the 2.0 MCE_R results are shown through a time step prior to collapse (approximately 12.5 seconds).

Examining the dynamic results indicates that the component models are stable and producing expected results. It is also clear that the model is capable of executing dynamic analyses through collapse as the Very High and Ultra High models, which are collapsing in the 2.0MCE_R analyses. In those cases, RBS beams fracture, gravity beam connections fracture, and ground floor columns are also fracturing (where fracturing indicates that they are reaching their ultimate rotation capacity and degrading to zero flexural strength).

The drift profile near or at collapse approaches a concentrated ground floor drift, which is where column failures occur. Importantly, the maximum drift at MCE_R is lowest for the High Seismic design (4.5% at the top story) and for the Very High Seismic design (4.25% at the 1st story) and increases significantly for the Ultra High Seismic design (7.25% at the ground floor). The behavior of the Ultra High Seismic design appears closer to collapse at MCE_R for this example ground motion than the Very High and High Seismic designs. It also appears that peak story drift is distributed more uniformly up the height of the building at MCE_R for the High and Very High Seismic designs. For the Ultra High Seismic design, the peak drift is concentrated at the base. For all designs, as the ground motion intensity is increased, the peak story drifts begin to concentrate at the lower stories.

F.7 Incremental Dynamic Analysis

Incremental dynamic analysis was conducted using the FEMA P-695 Far-Field ground motion set (44 individual ground motion components) for the High Seismic, Very High Seismic, and Ultra High Seismic models. For each ground motion, the analyses were conducted using an increment in the median spectral acceleration of 0.05g increments until collapse was observed. The increment was then reduced around the collapse point to provide better resolution on the drift at incipient collapse. Figure F-28 through Figure F-30 show resulting IDA curves. The figures also indicate the median spectral acceleration at collapse, $\hat{S}_{CT}$ of the ground motion set at the building's design period ($C_u T_a$ for the High and Very High Seismic designs, and the first mode computed period for the Ultra High Seismic design) and the median of the story drifts at incipient collapse, DR_{IC}.

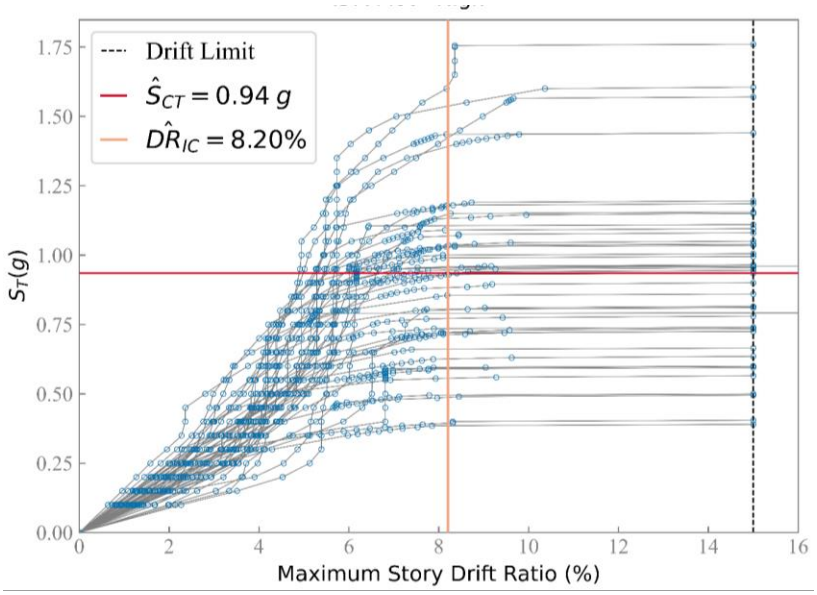

Figure F-28 IDA results for the High D model.

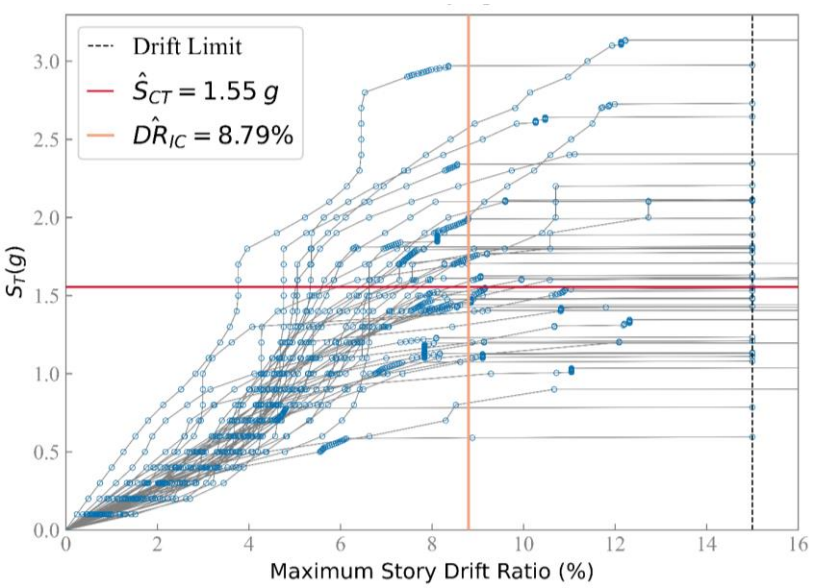

Figure F-29 IDA results for the Very High Seismic model.

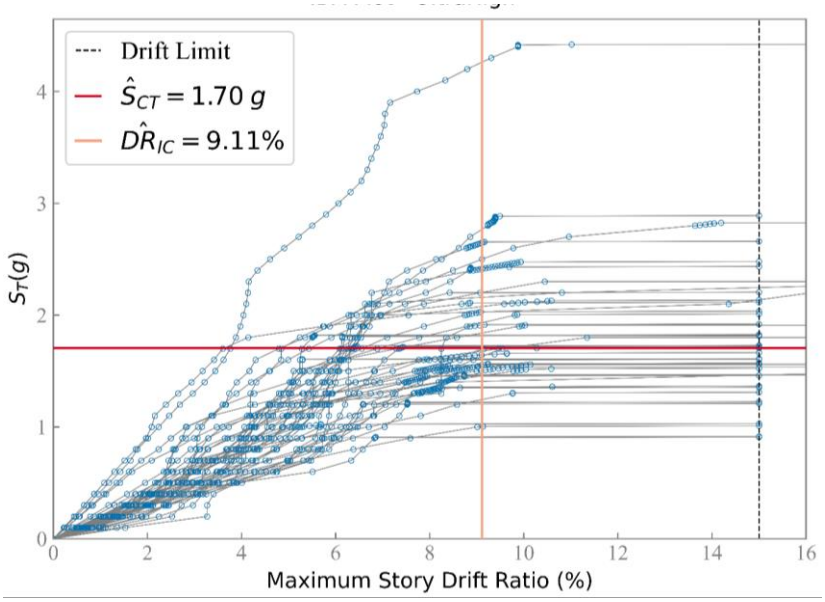

Figure F-30 IDA results for the Ultra High Seismic model.

Figure F-28 to Figure F-30 show that there is a significant increase in $\hat{S}_{CT}$ for the Very High Seismic design relative to the High D design. However, $\hat{S}_{CT}$ for the Ultra High Seismic design is not substantially larger than that for the Very High Seismic design. That trend is similar for DR_{IC}. It is important to note that, as with all IDAs, the $\hat{S}_{CT}$ obtained is the median elastic spectral acceleration of the ground motion set for 5% damping. As such, the forces developed in the system are much lower than the value of $\hat{S}_{CT}$ times the weight of the structure because the structure is responding nonlinearly. This is important in considering the forces that a foundation system must be able to deliver.

Table F-9 summarizes the results of the IDA analyses, including the results of the computation of probability of collapse at MCE_R for the High D, Very High Seismic, and Ultra High Seismic designs. Probability of collapse is shown for values of β equal to 0.5 and 0.6. Note that the eSDOF analysis in Chapter 5 used β equal to 0.6. The calculation of overstrength, spectral shape factor, collapse margin ratio (*CMR*), and adjusted collapse margin ratio (*ACMR*) were carried out in accordance with FEMA P-695, and the MCE_R collapse probabilities were computed as described in Chapter 3. As shown, the probability of collapse at MCE_R increases with increasing S_{MT} used for design.

Table F-9 also shows the median roof drift at collapse, which can be compared to the maximum roof drift from the pushover analyses presented previously. The roof drift at collapse is consistent with the roof drift at the point of non-convergence in the nonlinear static analyses, indicating that the structure losses stability at that roof drift and that the nonlinear static analyses generally predict the proper collapse mode.

Table F-9 Summary of IDA Results and Probability of Collapse at MCE_R Calculations

Arch.	S_{MT} (g)	Period Used for IDA Scaling (sec)	V_{max}/W	Ω	DR_{IC} (%)	Median Roof Drift at Collapse (%)	$\hat{S}_{CT}$ (g)	*SSF*	*ACMR*	P[coll | S_{MT}] (β = 0.5) (%)	P[coll | S_{MT}] (β = 0.6) (%)
High D	0.49	1.83	0.11	2.49	8.20	4.02	0.94	1.35	2.60	2.8	5.6
Very High	0.98	1.83	0.31	3.82	8.79	4.82	1.55	1.47	2.32	4.6	8.1
Ultra High	1.78	1.52	0.61	4.11	9.11	4.42	1.70	1.26	1.20	35.8	38.1

As shown in Table F-9, the overstrength increases with increasing design spectral acceleration. This is an important factor that helps to mitigate the increase in collapse probability with increasing design spectral acceleration. Additionally, there is a small increase in DR_{IC} with increasing design demand that also helps mitigate the increase in collapse probability with increasing design spectral acceleration. When comparing the High D design's performance with that of the Very High Seismic design's performance, the *ACMR* and collapse probabilities are similar due to a substantial increase in overstrength. However, when comparing the Very High Seismic design to the Ultra High Seismic design, the overstrength is similar and collapse probability for the Ultra High Seismic design is substantially larger and greatly exceeds the target 10%. The increase in overstrength can be largely attributed to increases in section sizes to meet drift limits, the inclusion of composite action in the RBS connections that is not considered in design, and perhaps most importantly the use of only W14 columns, which requires significant increases in section size to satisfy strong-column weak beam requirements.

In summary, IDA of the detailed models of the SMF archetypes developed here shows that collapse probability increases with increasing design spectral acceleration. However, there are mitigating factors, such as the increase in overstrength that appears to be largely due to increases in section size in order to meet drift requirements.

F.8 Development and Analysis of eSDOF Models of the Archetype SMFs

The process described in Appendix E was used to develop eSDOF models of the three Risk Category II archetype SMF models for which incremental dynamic analyses were conducted and described in the previous section. Incremental dynamic analysis was then conducted on the eSDOF models using the same set of 44 FEMA P-695 Far-Field ground motions such that the prediction of collapse

spectral acceleration could be compared with that from the detailed SMF models described above. The process included the following steps:

1. Fit trilinear backbones to the nonlinear static analysis results for use in representing the full system response with an IMK model in *OpenSees*. See Figure F-31.

2. Transform the trilinear pushover response to modal space using the pushover mode, which is the normalized deformed shape of the structure near collapse from nonlinear static analysis. This includes calculating an effective seismic weight that becomes the mass of the eSDOF model. See Appendix E for details on this process. For this process, the normalized deformed shape of the MDOF model at maximum strength in Figure F-31 was used.

3. Run incremental dynamic analyses on the eSDOF models.

4. Transform the results back to "real" space using the pushover mode and corresponding participation factor.

5. Compute the $\hat{S}_{CT}$, DR_{IC}, *ACMR*, and probability of collapse at S_{MT} from the incremental dynamic analyses of the eSDOF models, and compare those results with those from the detailed models.

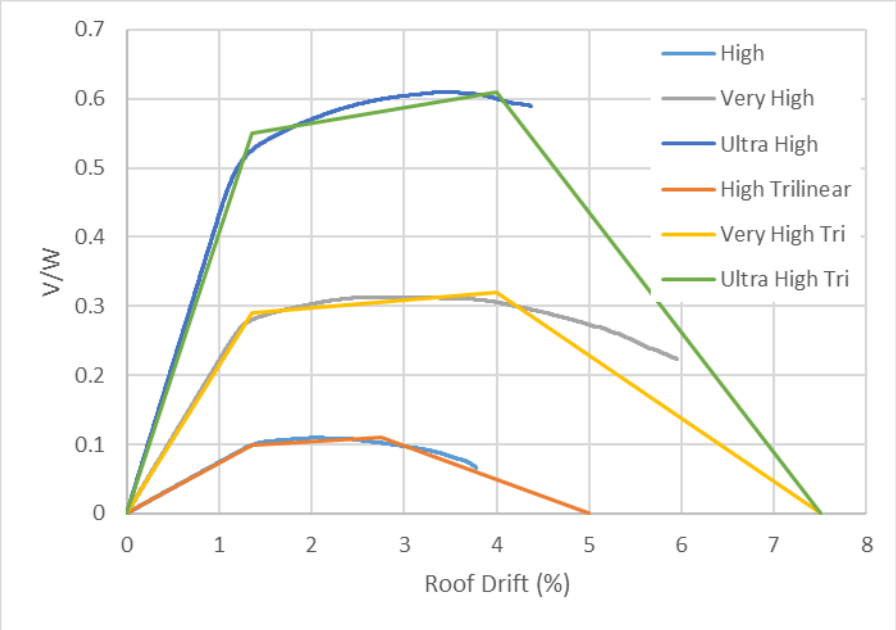

Figure F-31 Trilinear backbone curve fits to pushover curves for the three SMF RC II designs.

Table F-10 shows the results of incremental dynamic analysis of the eSDOF models developed from the backbones of Figure F-31 and the corresponding pushover mode shapes. The table compares the results of analyzing the eSDOF models with the results from analyzing the detailed models. As shown in the table and described above, the eSDOF models have the same strengths and

overstrengths as the detailed models, trilinear responses fit to the nonlinear static responses of the detailed models, and pushover mode shapes derived from the nonlinear static response drift profiles of the detailed models at the points of maximum strengths.

As Table F-10 shows, using the established approach for eSDOF development and analysis yields eSDOF models that are able to predict the $\hat{S}_{CT}$ for the FEMA P-695 Far-Field ground motion set quite closely. Both the eSDOF predicted $\hat{S}_{CT}$ for the High D and the Very High Seismic designs are within 10% of the $\hat{S}_{CT}$ found using the corresponding detailed models. In turn, the probabilities of collapse at MCE_R generated from the eSDOF analyses for those archetypes are close to the results from the detailed MDOF models.

The prediction of $\hat{S}_{CT}$ for the Ultra High Seismic design is 21% larger for the eSDOF analysis than the detailed analysis. This overprediction of $\hat{S}_{CT}$ from the eSDOF model for the Ultra High Seismic design could be due to the deterioration assumed after the detailed model fails to converge in the nonlinear static analysis, as shown in Figure F-31. It could be that in the nonlinear dynamic analyses of the detailed MDOF model, the loss of column hinge strength at the first level is causing a more rapid deterioration of strength than assumed by the descending branch of the trilinear curve in Figure F-31. This could also explain the larger DR_{IC} for the detailed Ultra High Seismic model, which could be generated by a rapidly increasing story drift at the lower level. In fact, the single ground motion results show in Figure F-26 supports this notion, where it is evident that the increase in drift concentration at the lower level at large roof drifts is most severe for the Ultra High Seismic model. Near collapse, a small increase in roof drift appears to cause a very large increase in drift at the first level for the detailed MDOF model of the Ultra High Seismic design. It is possible that this behavior is occurring in many ground motions in the IDA for the detailed model (i.e., the drift concentration at the lower level in the Ultra High Seismic design is increasing very quickly after peak strength). However, in the eSDOF model, the pushover mode shape used for the eSDOF is derived from the deformed shape at peak strength and thus does not quite capture the more extreme concentrated drift profile. This results in an underestimation of DR_{IC} and an overestimation of $\hat{S}_{CT}$ relative to the detailed MDOF model.

In summary, the analysis of eSDOF models of the archetype SMFs shows that the eSDOF analyses are able to produce similar median collapse spectral accelerations, *ACMR*s, and probabilities of collapse at S_{MT} to those from the detailed SMF models. These results show that eSDOF models can be used to study trends in collapse performance when calibrated to the pushover curves, cyclic deterioration characteristics, and pushover mode shapes of detailed models.

Table F-10 Comparison of Collapse Analysis Results for the Detailed SMF Models and eSDOF Models Developed from the Detailed SMF Models.

Arch.	S_{MT} (g)	V_{max}/W	Ω	DR_{IC} (%)	$\hat{S}_{CT}$ (g)	*CMR*	*SSF*	*ACMR*	P[coll|S_{MT}] (β = 0.6) (%)
Detailed MDOF SMF Results									
High D	0.49	0.11	2.49	8.20	0.94	1.92	1.35	2.60	5.6
Very High	0.98	0.31	3.82	8.79	1.55	1.58	1.47	2.32	8.1
Ultra High	1.78	0.61	4.11	9.11	1.70	0.96	1.26	1.26	38.1
eSDOF SMF Results: Models Calibrated to Detailed SMF Model Results from This Study									
High D	0.40	0.12	2.49	8.66	1.00	2.04	1.35	2.76	4.5
Very High	0.98	0.31	3.82	8.13	1.60	1.63	1.47	2.39	7.3
Ultra High	1.78	0.61	4.11	8.44	2.06	1.16	1.26	1.45	26.7

F.9 Comparison with eSDOF Model Results Derived from FEMA P-2012 and Discussion

Table F-11 compares the collapse results for the 9-story eSDOF SMF models in Chapter 5 with those results above from the detailed models described in this appendix. Recall that the SMF eSDOF models in Chapter 5 were developed using the pushover response and pushover mode shape from the results of FEMA P-2012, which is a different building with different moment frame layout, floor weights, and deterioration. For this comparison, eSDOF models from the SMF-9B family described in Chapter 5 have been selected such that they have S_{MT} values close to those corresponding to High D, Very High Seismic, and Ultra High Seismic designs. The SMF-9B family was selected because it was developed from the 9-story SMF in FEMA P-2012 and was developed to approximately consider the impact of the gravity framing on the system's collapse behavior as described in Chapter 5.

As shown in Table F-11, the eSDOF results are pessimistic relative to the results for the detailed models here. In particular, the values of DR_{IC} for the eSDOF models derived from the FEMA P-2012 results are considerably lower than those found from analysis of the MDOF models presented above. The table indicates that the overstrength is somewhat similar for the Chapter 5 eSDOF models and the detailed MDOF models described above, with the exception of the model designed for a demand

at the SDC D_{max} boundary. For that model, the eSDOF model has a considerably larger overstrength than the corresponding MDOF model. Finally, $\hat{S}_{CT}$ is consistently lower for the Chapter 5 eSDOF models relative to the detailed MDOF models described above, which leads to smaller *ACMR* and larger probability of collapse at S_{MT}. The potential causes of these differences are as follows:

1. The median story drift at incipient collapse, DR_{IC}, is larger in the detailed models. This is a direct result of allowing the hinge models for the columns and the RBS connections to reach values of ultimate rotation capacity that are larger than those used in the FEMA P-2012 study that was the basis for the development of the eSDOF models. The actual rotation capacity of the large column sections and composite RBS connections (0.1 rads and 0.08 rads respectively for the detailed models as described above) is a point of considerable uncertainty and is important for interpreting the results of the analyses. For the eSDOF analyses, a 5% story drift was used as a proxy for loss of capacity in the beams and columns as described in Chapter 5. The impact of more available deformation capacity in the detailed models is clear when comparing the results as it results in much larger values of DR_{IC}. It is possible that the actual rotation capacity lies between the values used in these different models.
2. The deterioration parameter, λ, for the Bilinear IMK model used to represent the full building response in the eSODF analyses was 76 and was based on the average of the deterioration parameter for the beams and columns at the critical stories from the FEMA P-2012 archetypes. For the MDOF models described above, the deterioration parameter is substantially larger than this value for the columns in the Very High and Ultra High Seismic designs, meaning that the columns in the detailed models have less cyclic deterioration. This works to increase DR_{IC} and increase $\hat{S}_{CT}$.
3. Perhaps most importantly, the detailed SMF models showed that the displacement at peak system strength (denoted the capping displacement) was larger for the Very High and Ultra High designs relative to the High D design. This implies that drift capacity can increase with increasing S_{MT}. The eSDOF SMF models presented in Section 5.2 through Section 5.7 all have the same displacement at peak system strength for a given building height.

In summary, the trend of increasing collapse probability with increasing design spectral acceleration appears in both the eSDOF analyses and in the results of analyses of the more detailed SMF models. Some mitigating factors slow the trend but do not eliminate it. The most important factors are an increase in overstrength with increasing design spectral acceleration, an increase in DR_{IC} with increasing S_{MT}, and an increase in the displacement at peak system strength with increasing S_{MT}. The detailed models show that when design spectral accelerations are large: (1) collapse probabilities well above the ASCE/SEI 7 maximum values can occur, and (2) those values are substantially larger than those for structures designed for the SDC D upper boundary.

Table F-11 Comparison of Collapse Analysis Results for the Detailed SMF Models and eSDOF Models Developed from the FEMA P-2012 Models and Used for the eSDOF Analysis in Chapter 5

Arch.	S_{MT} (g)	V_{max}/W	Ω	DR_{IC} (%)	$\hat{S}_{CT}$ (g)	*CMR*	*SSF*	*ACMR*	P[coll|S_{MT}] (β = 0.6) (%)
Detailed MDOF SMF Results									
High D	0.49	0.11	2.49	8.20	0.94	1.92	1.35	2.60	5.6
Very High	0.98	0.31	3.82	8.79	1.55	1.58	1.47	2.32	8.1
Ultra High	1.78	0.61	4.11	9.11	1.70	0.96	1.26	1.26	38.1
eSDOF SMF Results from Chapter 5									
High D	0.50	0.12	3.70	4.59	0.70	1.40	1.43	2.01	12.0
Very High	1.00	0.31	3.70	4.59	0.86	0.86	1.43	1.23	36.3
Ultra High	1.80	0.62	4.20	4.59	0.91	0.49	1.43	0.72	70.8

Appendix G: Capacity Spectrum Method Background and Examples

G.1 Introduction

This appendix provides background and examples of the capacity-spectrum method (CSM) used in Section 6.2 to calculate values of the VHS Load Amplifier (i.e., *ACMR10%/ACMR*) and to explain graphically the relationship of collapse trends to the shape of the response spectrum and the effective period of response at incipient collapse. Background on the CSM is provided in Section G.2, adaptation of the CSM to collapse evaluation is described in Section G.3, and topical CSM examples are provided in Sections G.4, G.5, and G.6.

The CSM example of Section G.4 calculates values of the VHS Load Amplifier illustrating collapse trends of three hypothetical archetypes with extremely different effective periods using a demand spectrum characterized by the traditional three domains of idealized response: (1) the domain of constant acceleration, (2) the domain of constant velocity, or (3) the domain of constant displacement. This example establishes conceptual bounds on the value of the VHS Load Amplifier.

The CSM example of Section G.5 calculates values of the VHS Load Amplifier illustrating collapse trends of a hypothetical mid-rise (T = 0.75 s) archetype using demand spectra representing the shape (frequency content) of deterministic MCE_R (scenario) ground motions assuming one of three different site (source) conditions: (1) Site Class C (M6.0), (2) Site Class CD (M7.0) or (3) Site Class D (M8.0). This example illustrates the importance of spectrum shape on collapse trends.

The CSM example of Section G.6 investigates the collapse performance of the 4-story BRBF archetype of Chapter 6 and compares collapse results from CSM analysis with those of Chapter 6 that are based on IDA. The same Far-Field ground motions are used for this comparison, where the median response spectrum of Far-Field record set is used for CSM analysis and the corresponding individual records of the Far-Field record set are used for IDA. This example illustrates that CSM analysis can reliably replicate collapse performance of the same archetype evaluated using IDA.

G.2 Background and Applications of the CSM

The underlying concept of the capacity-spectrum method (CSM) dates to the 1970s (Freeman et al., 1975; Freeman, 2004), and the original performance-based design methods of the ATC-40 Project, SSC 96-01 (CSSC, 1996) and the ATC-33 Project, FEMA 273 (FEMA, 1997) for seismic retrofit of existing buildings, the latter of which may now be found in ASCE/SEI 41.

The CSM was adapted, enhanced, and incorporated into the HAZUS technology for estimating earthquake damage and loss to buildings (FEMA, 1996; FEMA, 2002). The State of California adopted the CSM of the HAZUS technology for evaluating and ranking the collapse vulnerability of older hospital buildings (OSHPD, 2007; Tokas and Lobo, 2009). Among other applications, the CSM

of the HAZUS technology also provided the technical basis of the third-edition update of FEMA P-154 for rapid visual screening of seismic hazards (FEMA, 2015).

The CSM relies on the concept of effective period and the associated concept of effective damping, which were originally proposed for equivalent lateral force (ELF) design of the isolation system of a base-isolated structure (SEAONC, 1986; SEAOC, 1990; UBC, 1991) incorporated into the 1991 UBC (ICBO, 1991) and that may now be found in Chapter 17 of ASCE/SEI 7-22. The ELF procedures required for design of base-isolated structures have been shown to provide accurate, slightly conservative, estimates of the mean peak displacement calculated using nonlinear response history analysis (NRHA) (Lashkari and Kircher, 1993; Constantinou et al., 1993). Advantages of the CSM include relative simplicity of calculation of peak response and graphical visualization of demand (i.e., median response spectra) relative to capacity (i.e., strength characterized by pushover/backbone curves), where both are plotted in terms of response spectral acceleration versus response spectral displacement, so-called ADRS plots. Disadvantages include the inherent limitation of median (only) estimates of peak response or failure and the necessity of simplified nonlinear models that may not capture all modes of failure, such as those that might be found from more detailed nonlinear models evaluated using NHRA (e.g., IDA of FEMA P-695).

G.3 Adaptation of CSM to Collapse Evaluation

G.3.1 Overview

The capacity-spectrum method (CSM) is a graphical representation of the "equivalent" secant linearization of a nonlinear system (Christopoulos and Filiatraut, 2022). Seismic demand spectra are plotted in an acceleration-displacement response spectra (ADRS) format for different values of equivalent viscous damping and compared, on the same plot, to the pushover (backbone) capacity curve of the structure of interest. The pushover curve of an MDOF model of the structure, defined in terms of base shear (V_b) and roof displacement (D) is transformed to equivalent SDOF (eSDOF) spectral values using the effective weight (W_p) and participation factor (Γ_p) of the nonlinear pushover mode at incipient collapse:

$$W_p = \frac{\left(\sum w_i \varnothing_i\right)^2}{\sum w_i \varnothing_i^2} \tag{G-1}$$

$$\Gamma_p = \frac{W_P}{\sum w_i \varnothing_i} \tag{G-2}$$

Where w_i is the weight of the ith story and $\varnothing_i$ is the nonlinear pushover mode shape (normalized to unity at the roof). Conversion of the roof displacement, D, and base shear, V_b, to the equivalent eSDOF spectral acceleration, SA, and spectral displacement, SD, of the capacity curve are calculated using the following formulas:

$$SA = \frac{V_b}{W_p} \tag{G-3}$$

$$SD = \frac{D}{\Gamma_p} \tag{G-4}$$

The CSM is illustrated in Figure G-1. Intersection of the capacity curve with the demand spectrum represents maximum nonlinear response of the structure with respect to displacements and accelerations. When the demand spectrum is scaled to intersect the capacity curve at the spectral displacement corresponding to incipient collapse (SD_{IC}), the scaled demand spectrum represents ground motions strong enough to affect median collapse, analogous to the scaling of individual earthquake records used by the IDA methods of FEMA P-695 to determine the median collapse acceleration, $\hat{S}_{CT}$. The eSDOF displacemnt at collapse, SD_{IC}, is derived from the drift ratio at incipient collapse, DR_{IC}, of the story govering collapse (i.e., of the corresponding MDOF system) based on governing story and roof heights, pushover mode shape at incipient colapse and Equation G-4.

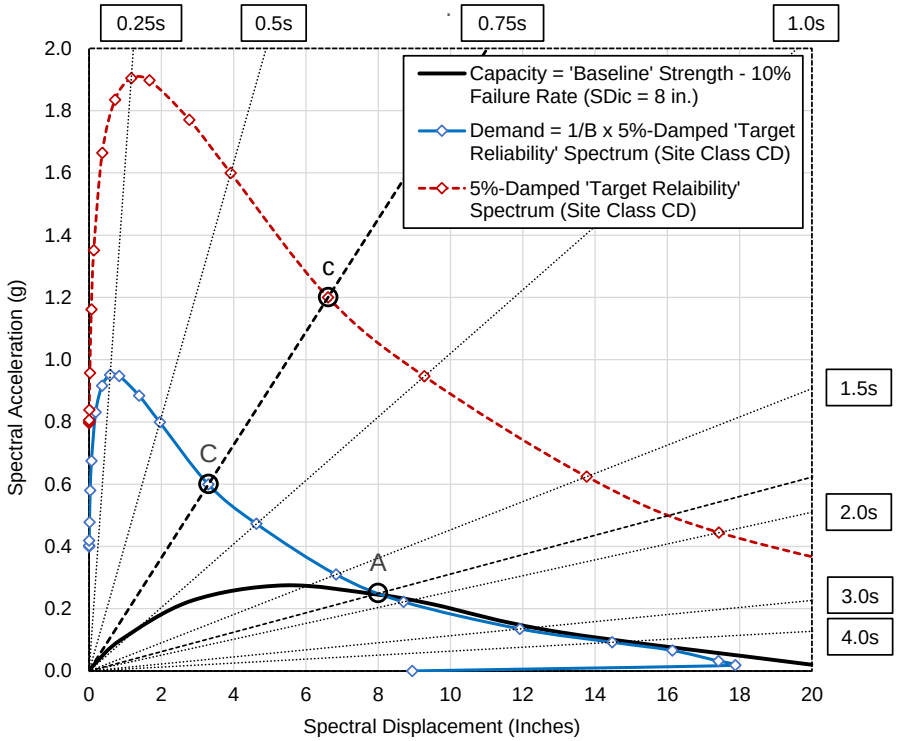

Figure G-1 **Illustration of the CSM showing a hypothetical capacity curve of "Baseline" strength, presumed to achieve target reliability (10% failure rate), the β_{eff}-damped "Target Reliability" demand spectrum scaled to match the capacity curve at incipient collapse displacement, SD_{IC} = 8 inches (Point A) and the corresponding 5%-damped "Target Reliability" response spectrum representing Site Class CD response, where the β_{eff}-damped demand spectrum is equal to the 5%-damped spectrum factored by $1/B$, representing response reduction corresponding to the effective damping (β_{eff}) of the capacity curve at incipient collapse.**

Although hypothetical, the strength of the Baseline capacity curve of Figure G-1 is typical of a high ductility (R = 8) system designed for S_{MT} = 1.0 × SDC D_{max} ground motions (i.e., VHS boundary, Figure 6-1). There is nothing unique about this capacity curve and other curves with different pushover (backbone) properties could have been used to illustrate the CSM. Likewise, there is nothing unique to the demand spectrum and other demand spectra with different shapes (e.g., representing different site conditions) could have been used to illustrate the CSM. For this example, the 5%-damped response spectrum was calculated using the PEER NGA West-2 Excel spreadsheet (PEER, 2014) assuming median response of a Site Class CD site located 8 km from fault rupture of a magnitude M7.0 earthquake. These values of earthquake magnitude and site distance are representative of those of MCE_R (scenario earthquake) ground motions at the VHS boundary.

The shape of the β_{eff}-damped demand spectrum is assumed to be the same as that of the 5%-damped response spectrum over response periods of interest. Periods of interest range from the elastic design period, T, to the effective period, T_{eff}. Since the demand spectrum is scaled to incipient collapse (Point A), only the shape of the demand spectrum matters to the CSM. The intersection point (Point A) represents spectral acceleration at an effective period, $T_{eff,A}$, and level of effective damping, β_{eff}, that correspond to peak nonlinear response at incpient collapse, in contrast to linear elastic response at design period, T, and the nominal 5%-damping level of the median collapse parameter, $\hat{S}_{CT}$, of FEMA P-695.

The reduction of the 5%-damped response spectrum for a higher level of effective damping, β_{eff}, represents the nonlinear inelastic dynamic response effects of the capacity curve, and is conceptually, the same as the effective damping and associated damping factors of ASCE/SEI 7-22 specified for ELF design of a seismically isolated or damped structure with a higher level of effective damping (e.g., B factors of Table 18.7-1, ASCE/SEI 7-22). In this example, the value of the damping factor, B = 2.0, which corresponds to effective damping of about β_{eff} = 38%. As shown in Figure G-1 at the elastic design period, T = 0.75 s, the value of β_{eff}–damped spectral acceleration is SA(C) = 0.6 g (Point C) and the corresponding value of 5%-damped spectral acceleration is SA(c) = 1.2 g (Point c), where 5%-damped spectral acceleration at Point c represents the CSM estimate of the median collapse parametereter, $\hat{S}_{CT}$.

Building upon the CSM example and concepts discussed above, a CSM example with two hypothetical capacity curves is shown in Figure G-2, one with Baseline strength and the other with 2.0 × Baseline strength. The key feature of these two capacity curves is that they are both based on the same pushover (backbone) properties, since they characterize the nonlinear behavior of the same archetype with different model strengths. Two β_{eff}-damped demand spectra with the same shape (e.g., same Site Class CD site conditions) are shown in Figure G-2. The first “Target Reliability” demand spectrum is scaled to the capacity curve with Baseline strength (Point A), which is presumed to achieve the 10% failure rate at the VHS boundary. The second, stronger demand spectrum is scaled to the capacity curve with two times Baseline strength (Point B). Conceptually, the stronger demand curve represents site-specific MCE_R ground motions which are, in this example, the ratio of SA(D)/SA(C) stronger than those of the Target Reliability demand spectrum (VHS boundary). The

intersection points of Figure G-2 (i.e., Points A, A', B, C and D representing β_{eff}-damped response and Points a, a', b, c and d, representing the corresponding values of 5%-damped response) are used in Section G.3.3 to develop equations for CSM-based calculation of the VHS Load Amplifier (*ACMR10%/ACMR*).

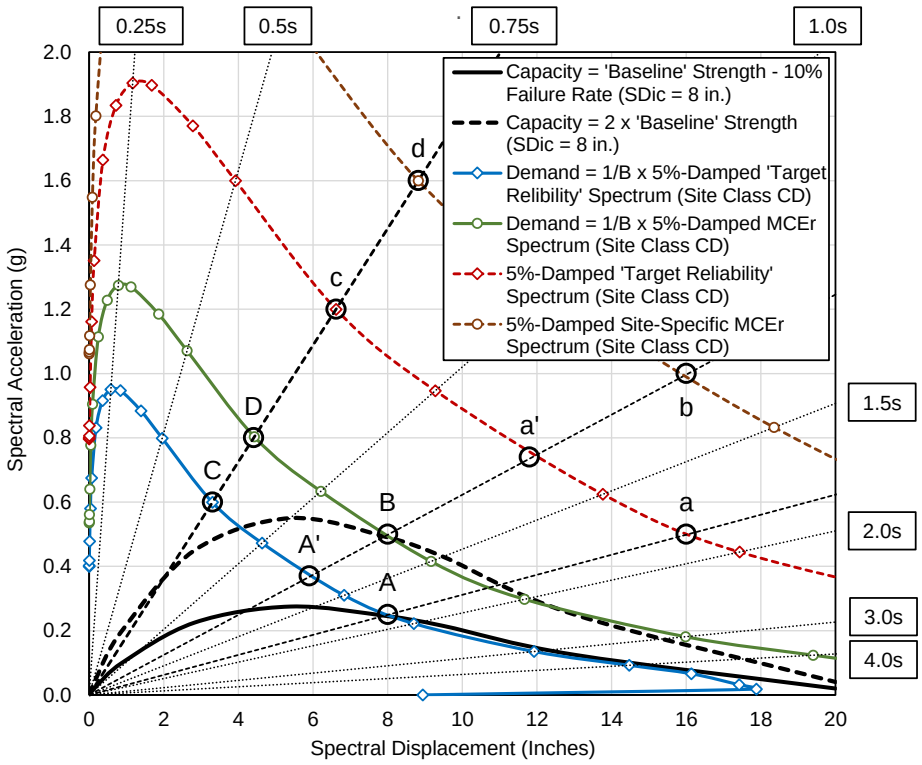

Figure G-2 Plots of two hypothetical capacity curves (i.e., "Baseline" strength and 2.0 x "Baseline" strength) and demand spectra of the same shape (e.g., same Site Class CD site conditions) scaled to Baseline strength (Point A) and two times Baseline strength (Point B) at incipient collapse (SD_{IC} = 8 inches), where demand spectra define values of β_{eff}-damped spectral acceleration at the elastic design period, *T* (Points C and D). Also shown are the two 5%-damped response spectra corresponding to the two β_{eff}-damped demand spectra.

In the ADRS format, lines of constant period are represented by "spokes" from the origin. In Figure G-2, spokes indentify the elastic design period, *T* (i.e., *T* = 0.75 s in this example), as well as the effective period, $T_{eff,A}$, at incipient collapse of the capacity curve with Baseline strength (Point A) and the effective period, $T_{eff,B}$, at incipient collapse of the capacity curve with two times Baseline stength (Point B). Median collapse spectral accelerations conditioned on the response at the elastic design period, *T*, are shown in Figure G-2 for the demand spectrum scaled to Baseline capacity (Point C) and for the demand spectrum scaled to two times Baseline strength (Point D). These median values of spectral accelerations (i.e., Points C and D) represent β_{eff}-damped response of the demand spectra. Methods and equations used to determine values of effective period and effective

damping and example values of these parameters for the CSM example of Figure G-2 are described in the Section G.3.2.

G.3.2 Effective Stiffness and Damping

The efective period, T_{eff}, is based on the secant stiffness, k_{eff}, corresponding to the values of spectral acceleration, SA_{IC}, and spectral displacemt, SD_{IC}, at incipient collapse, as defined by Equation G-5:

$$T_{eff}(\mathrm{s}) = \sqrt{\frac{4\pi^2}{g}}\sqrt{\frac{SD_{IC}}{SA_{IC}}} \tag{G-5}$$

For example, values of the effecitve period at Points A and B (Figure G-2) are calculated:

$$T_{eff,A} = 0.32\sqrt{\frac{8.0(\mathrm{in.})}{0.25(\mathrm{g})}} = 1.81\,\mathrm{s}$$

$$T_{eff,B} = 0.32\sqrt{\frac{8.0(\mathrm{in.})}{0.5(\mathrm{g})}} = 1.28\,\mathrm{s}$$

Where the constant 0.32 (in units of $\mathrm{s(g/in.)}^{0.5}$) = $\mathrm{sqrt}(4\pi^2/\mathrm{g}) = \mathrm{sqrt}(4(3.142)^2/386.4\ \mathrm{in/s^2/g})$

Demand spectra represent nonlinear response at a level of effective damping that corresponds to the hysteretic energy disspiated through dynamic response, where the amount of effective damping, β_{eff}, at incipient collapse, adapted from Eq. 17.8-2 of ASCE/SEI 7-22, is defined by Equation G-6:

$$\beta_{eff} = \left(\frac{2}{\pi}\right)\frac{E_{loop}}{k_{eff}\left(2SD_{IC}\right)^2} = 0.637\frac{E_{loop}}{4\left(SA_{IC}\right)\left(SD_{IC}\right)} \tag{G-6}$$

The symbol, E_{loop}, defines the area enclosed by the hysteresis loop during a full cycle of response at peak displacements of +/- SD_{IC}. The area under the hysteresis loop is esitmated from the capacity curve assuming symetrical response and monotonically increasing force-deflection behavior (i.e., the undelying assuption of Eq. 17.8-2 of ASCE/SEI 7-22). Effective damping is defined in terms of spectral acceleration, rather than the forces associated with spectral acceleration, by omitting seismic weight (mass) from both the numerator and the denominator of Equation G-6.

For those capacity curves that are (or can be) characterized by bilinear behavior with spectral displacement, SD_Y, and spectral acceleration, SA_Y, at yield (e.g., typical of the non-wood archetype models of this project up to peak strength), effective damping can be calculated by Equation G-6a:

$$\beta_{eff} = 0.637\,\frac{\left(SA_Y\,SD_{IC} - SD_Y\,SA_{IC}\right)}{SA_{IC}\,SD_{IC}} \tag{G-6a}$$

For those capacity curves that are (or can be) characterized by elasto-plastic behavior, effective damping can be calculated by Equation G-6b:

$$\beta_{eff} = 0.637 \frac{\left(SD_{IC} - SD_{Y}\right)}{SD_{IC}} \quad \text{(G-6b)}$$

Where an equivalent elasto-plastic curve is used to approximate the area of the hysteresis loop by assuming plastic behavior at spectral accelerations from SD_Y to SA_{IC}.

For example, values of effecitve damping of the capacity curves anchored to Points A and B (Figure G-2) are calculated:

$$\beta_{eff,A} = 0.637 \frac{\left(8 \text{ in.} - 3.2 \text{ in.}\right)}{8 \text{ in.}} = 0.38$$

$$\beta_{eff,B} = 0.637 \frac{\left(8 \text{ in.} - 3.2 \text{ in.}\right)}{8 \text{ in.}} = 0.38$$

Where a yield displacement of SD_Y = 3.2 inches was selected to approximate the area of the hysteresis loop.

It is important to note that the yield level and the associated value of effective damping (β_{eff} = 38%) are same for both Baseline strength and two times Baseline strength (and presumably other strength levels) since the basic shape of the capacity curve is the same. Although not always exactly the same, the pushover (backbone) curves of a given archetype are typically very similar for different model strengths of that archetype. This is the case for both wood light-frame and non-wood archetypes investigated by this study, and the associated small differences in effective damping (e.g., between Baseline and two times Baseline strength) have neglibile influence on collapse trends (i.e., values of the VHS Load Amplifier).

G.3.3 Calculation of the VHS Load Amplifier

In Chapter 6, collapse trends are characterized by the VHS Load Amplifier (i.e., the ratio of *ACMR10%/ACMR*) as a function of normalized demand (S_{MT}/S_{MT} = SDC D_{max}), where values of the VHS Load Amplifier are developed using the CSM characterization of demand and capacity and the intersection Points A, A', B, C and D shown in Figure G-2, representing 5%-damped response reduced by the damping factor, *B*.

In terms of 5%-damped response, the VHS Load Amplifier (ratio of *ACMR10%/ACMR*) is defined by the equation:

$$\text{VHS Load Amplifier} = \frac{ACMR10\%}{ACMR} \cong \frac{\left(\frac{S_{CT,c}}{S_{MT,a}}\right)}{\left(\frac{S_{CT,d}}{S_{MT,b}}\right)} = \left(\frac{S_{MT,b}}{S_{MT,a}}\right) \times \left(\frac{S_{CT,c}}{S_{CT,d}}\right) \tag{G-7}$$

Where $S_{CT,c}$ and $S_{CT,d}$ are the 5%-damped values of $\hat{S}_{CT}$ at Points c and d, as shown in Figure G-2 and $S_{MT,a}$ and $S_{MT,b}$ are the 5%-damped values of MCE_R design spectral acceleration of Baseline capacity and $(V_{max}/W)_B/(V_{max}/W)_A$ times Baseline capacity curves. In the calculation of the VHS Load Amplifier, the value of the spectrum shape factor, *SSF*, is implicitly assumed to be the same for the target value of *ACMR10%* and the calculated value of *ACMR* (i.e., *ACMR* = *SSF* × *CMR*). The *SSF* is defined in terms of period-based ductility, μ_T, as described in Appendix B of FEMA P-695. The value of the *SSF* is the same for archetypes with large displacement capacity at incipient collapse, typical of the SFRSs of this study, and decreases systematically to *SSF* = 1.0 at μ_T = 1.0 (i.e., linear response, $T_{eff} = T$).

The first expression of Equation G-7 is defined in terms of β_{eff}-damped response at Points A and B:

$$\frac{S_{MT,b}}{S_{MT,a}} = \frac{S_{MT,B}}{S_{MT,A}} \times \frac{B(B)}{B(A)}$$

$$= \frac{1.5\left(R/I_e\right)\left(V_{max}/W\right)_B / \Omega_B}{1.5\left(R/I_e\right)\left(V_{max}/W\right)_A / \Omega_A} \times \frac{B(B)}{B(A)}$$

$$= \frac{SA(B)}{SA(A)} \times \frac{\Omega(A)}{\Omega(B)} \times \frac{B(B)}{B(A)} \tag{G-8}$$

The terms Ω(A) and Ω(B) are the respective values of overstrength, Ω, of capacity curves representing Baseline strength, i.e., S_{MT} = 1.0 x SDC D_{max}, (Point A) and design for a stronger intensity of MCE_R ground motions, assumed to be S_{MT} = 2.0 x Ω(A)/Ω(B) x SDC D_{max} in Figure G-2 (Point B). The terms *B*(A) and *B*(B) are the respective values of the damping factor (*B*) corresponding to the effective damping (β_{eff}) level of the demand spectra scaled to incipient collapse of the capacity curves representing Baseline strength (Point A) and design for a stronger intensity of MCE_R ground motions (Point B).

The second expression of Equation G-7 is defined in terms of β_{eff}-damped response at Points C and D:

$$\frac{S_{CT,c}}{S_{CT,d}} = \frac{SA(C)}{SA(D)} \times \frac{B(C)}{B(D)} \tag{G-9}$$

Where the terms $B(C)$ and $B(D)$ are the respective values of the damping factor (B) corresponding to the effective damping (β_{eff}) level of the demand spectra at the design period, T.

It may be noted that 1.5 (R/I_e) appears in both the numerator and denominator of Equation G-8, such that the value of R/I_e could be adjusted to achieve target performance without affecting the ratio of *ACMR10%/ACMR*, if for example the current value of the R factor specified in Table 12.2-1 does not achieve the target reliability (10% failure rate) for capacity based on Baseline strength (i.e., S_{MT} = 1.0 x SDC D_{max}). There would be a negligible change to the ratio of $SA(C)/SA(D)$, where the respective capacity curves are both made stronger (or weaker) to achieve the 10% failure rate due to the associated change in the values of effective period (i.e., $T_{eff,C}$ and $T_{eff,D}$).

Combining Equation G-8 and Equation G-9, the VHS Load Amplifier is defined in terms of β_{eff}-damped response at Points A, B, C and D of Figure G-2:

$$\text{VHS Load Amplifier} = \frac{ACMR10\%}{ACMR} \cong \left\{ \frac{SA(B)}{SA(A)} \times \frac{\Omega(A)}{\Omega(B)} \times \frac{B(B)}{B(A)} \right\} \times \left\{ \frac{SA(C)}{SA(D)} \times \frac{B(C)}{B(D)} \right\} \tag{G-10}$$

The overstrength and damping factor terms are included in Equation G-10 for completeness, although the overstrength ratio is typically, $\Omega(A)/\Omega(B) \approx 1.0$ for most archetype models with certain notable exceptions (e.g., the three models of the 9-story archetype of the special study of Section 5.8). As discussed in the previous section, the ratio of damping factor ratios, $B(A)/B(B)$ and $B(C)/B(D)$ is approximately 1.0, in all practical cases. Equation G-10 may be simplified by assuming that both the amount of effective damping and the amount of overstrength remain constant with change in the normalized pushover strength, V_{max}/W, of the archetype model:

$$\text{VHS Load Amplifier} = \frac{ACMR10\%}{ACMR} \cong \frac{SA(B)}{SA(A)} \times \frac{SA(C)}{SA(D)} \tag{G-11}$$

Or, equivalently:

$$\text{VHS Load Amplifier} = \frac{ACMR10\%}{ACMR} \cong \frac{SA(A')}{SA(A)} \tag{G-11a}$$

The ratio of $SA(A')/SA(A)$, is a simple and informative characterization of the relationship of the value of VHS Load Amplifier (*ACMR10%/ACMR*) and the shape (slope) of the demand spectrum. If the demand spectrum is approximately horizontal at incipient collapse, i.e., $SA(A') \approx SA(A)$, (e.g., when the effective period, T_{eff}, is in the acceleration domain), then the value of the VHS Load Amplifier ≈ 1.0, indicating no appreciable additional collapse risk with increase in normalized demand. Conversely, if the slope of demand spectrum is nearly vertical at incipient collapse, i.e., $SA(A') \approx SA(B)$, (e.g., when the effective period, T_{eff}, is approaching the displacement domain), then the value of the VHS Load Amplifier, and the additional collapse risk, increases roughly in proportion to the increase in normalized demand.

Finally, for applications where earthquake ground motions are defined by 5%-damped response spectral acceleration (i.e., MCE_R ground motions), Equation G-10 may simplified and ratios of β_{eff}-damped spectral acceleration expressed in terms of ratios of 5%-damped spectral acceleration:

$$\text{VHS Load Amplifier} = \frac{ACMR10\%}{ACMR} \cong \frac{SA(\text{b})}{SA(\text{a})} \times \frac{SA(\text{c})}{SA(\text{d})} \tag{G-12}$$

Or, equivalently:

$$\text{VHS Load Amplifier} = \frac{ACMR10\%}{ACMR} \cong \frac{SA(\text{a}')}{SA(\text{a})} \tag{G-12a}$$

The above equations are valid since the ratios of 5%-damped spectral acceleration of Equation G-12 and Equation G-12a have the same value as the corresponding ratios of Equation G-11 and Equation G-11a. That is, $SA(\text{b})/SA(\text{a}) = SA(\text{B})/SA(\text{A})$ and $SA(\text{c})/SA(\text{d}) = SA(\text{C})/SA(\text{D})$. While ratios of 5%-damped accelerations response may be used in Equation G-12 and Equation G-12a to estimate values of the VHS Load Amplifier ($ACMR10\%/ACMR$), individual values of 5%-damped response are not, in general, valid representations of peak nonlinear response, as characterized by the CSM and the values of T_{eff} and β_{eff} at incipient collapse.

G.4 Response Domain Example

G.4.1 Introduction

The CSM example of this section calculates values of the VHS Load Amplifier of three hypothetical archetypes with extremely different effective periods using a demand spectrum characterized by the traditional three domains of idealized response (1) the domain of constant acceleration, (2) the domain of constant velocity or (3) the domain of constant displacement. This example establishes conceptual bounds on the value of the VHS Load Amplifier.

G.4.2 Scope and Approach

Values of the VHS Load Amplifier are calculated using idealized demand spectra defined by (1) a constant spectral acceleration at response periods, $T \leq 0.6$ s, (2) a constant spectral velocity at response periods, $0.6 \text{ s} < T < 6.0$ s, and (3) a constant spectral displacement at response periods, $T \geq 6.0$ s. These three idealized domains of response are the same as those of the two-period design response spectrum of Figure 11.4-1 of ASCE/SEI 7-22 (and prior editions of ASCE/SEI 7), where the "short-period" transition period, $T_S = 0.6$ s, typical of default site conditions and the "long-period" transition period, $T_L = 6$ s. A value of $T_L = 6$ s is only applicable to sites whose hazard is governed by smaller-magnitude earthquakes, but is selected for this example, since sites governed by large-magnitude earthquakes, which have longer transition periods (e.g., $T_L = 12$ s for sites governed by M8.0 events) are not relevant for seismic design of buildings.

Three notional building archetypes (i.e., one for each response domain) are defined in terms of their elastic design periods (1) a *Very Short* building archetype with an elastic design period, T = 0.15 s, (2) a *Mid-Rise* building archetype with an elastic design period, T = 1.0 s, and (3) a *Very Tall* building archetype with an elastic design period, T = 6.0s. For simplicity, notional building archetypes are modeled as elasto-plastic, single-degree-of-freedom (SDOF) systems, where each of the archetypes are modeled with two pushover strengths representing (1) Baseline capacity, presumed to comply with target reliability (i.e., 10% failure rate) and (2) pushover strength equal to two times Baseline capacity. Normalized pushover strength (V_{max}/W) and other key properties of archetype models are summarized along with collapse results in Table G-1. The pushover strengths of the three different notional building archetypes reflect the very significant differences in base shears required for design of archetypes that have very different elastic design periods.

Collapse performance of each of the six archetype models (i.e., three archetypes x two model strengths each) is evaluated graphically using the CSM to determine the spectral accelerations at the four intersection points (i.e., Points A, B, C and D of Figure G-2) required by Equation G-11 for calculation of the VHS Load Amplifier. Graphical solutions of intersection points are shown in Figure G-3 (linear axes) and Figure G-4 (log axes) for the *Mid-Rise* building archetype whose response is in the velocity domain, and in Figure G-5 (log axes) for the *Very Short* building archetype whose response is in the acceleration domain and in Figures G-6 (log axes) for the *Very Tall* building archetype whose response is in the displacement domain. Plots of capacity curves and demand spectra are shown in Figures G-4, G-5, and G-6 with log axes to better illustrate the three idealized domains of constant acceleration, velocity and displacement on the same figure.

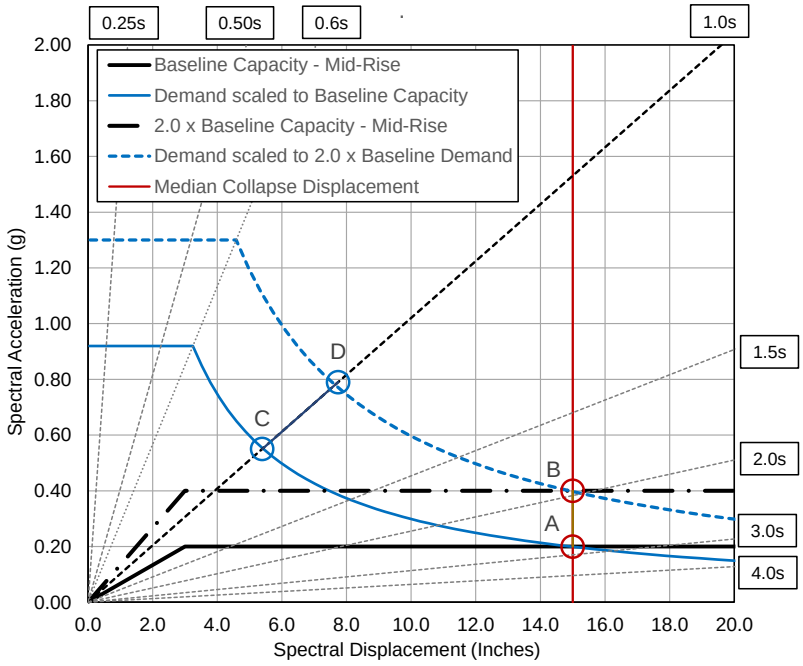

Figure G-3 Example CSM collapse evaluation of a notional *Mid-Rise* building archetype governed by nonlinear response in the idealized domain of constant velocity.

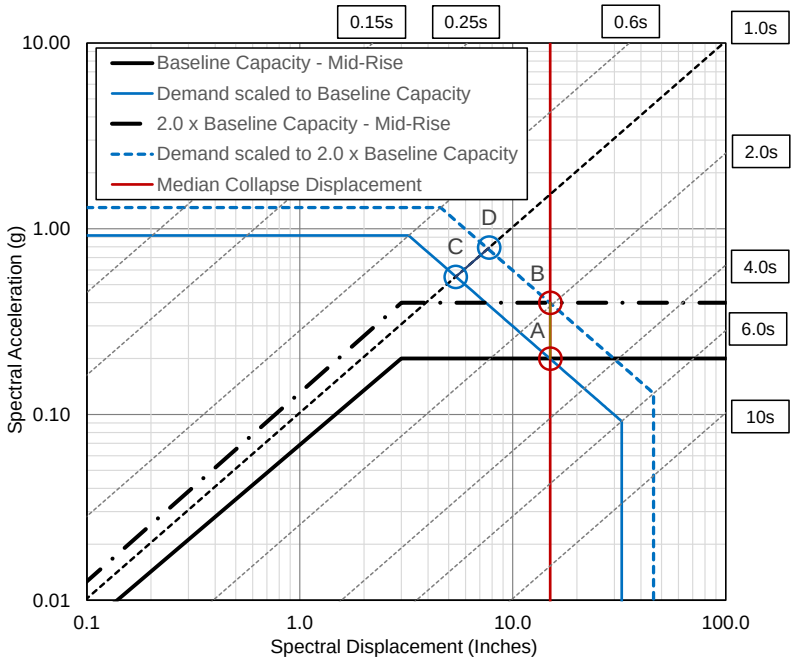

Figure G-4 Example CSM collapse evaluation of a notional *Mid-Rise* building archetype governed by nonlinear response in the idealized domain of constant velocity.

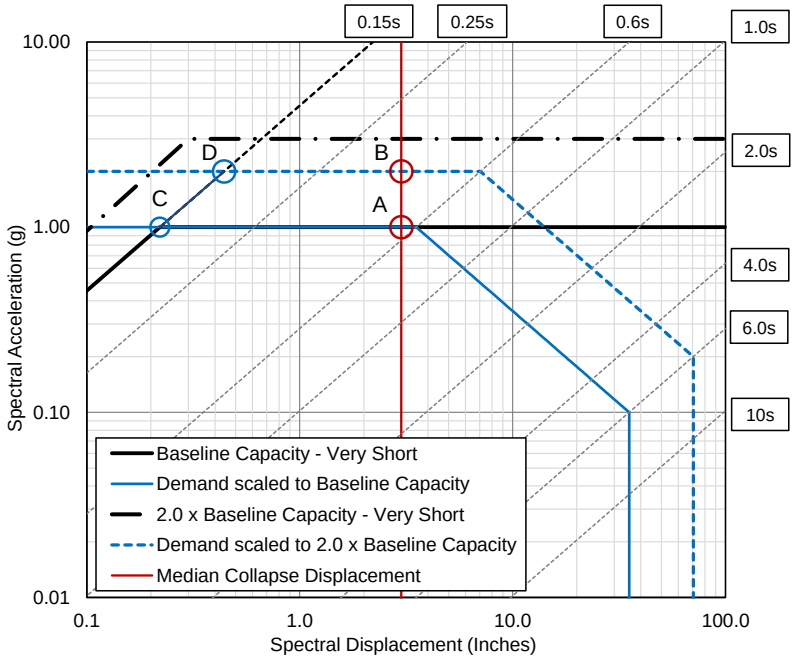

Figure G-5 Example CSM collapse evaluation of a notional *Very Short* building archetype governed by nonlinear response in the idealized domain of constant acceleration.

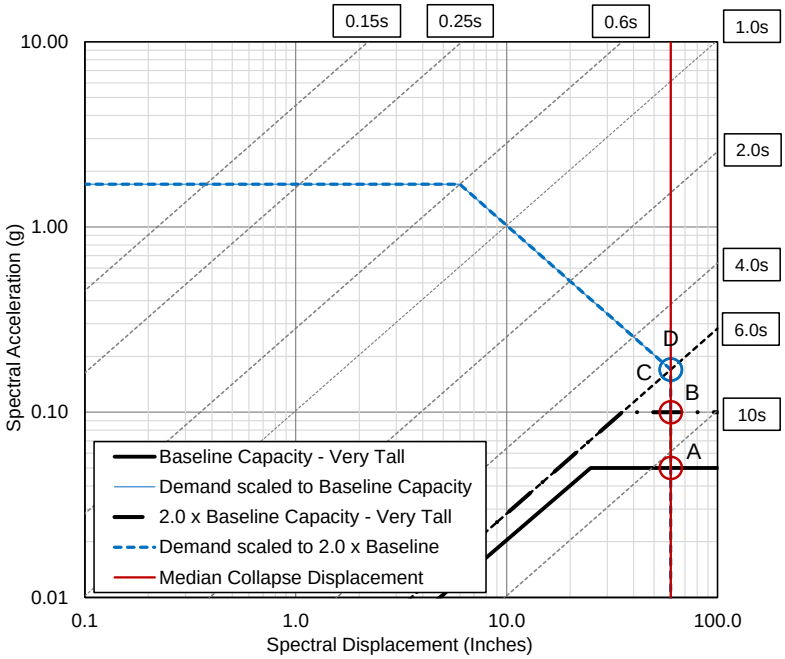

Figure G-6 Example CSM collapse evaluation of a notional *Very Tall* building archetype governed by nonlinear response in the idealized domain of constant displacement.

G.4.3 Collapse Evaluation Results

A summary of key response properties and collapse performance metrics, including the values of spectral acceleration at Points A, B, C and D of Figures G-3 through G-6, are summarized in Table G-1 for Baseline capacity and two times Baseline capacity models of each of the three notional building archetypes. Also included in Table G-1 are values of the VHS Load Amplifier, calculated using Equation G-11 and the spectral accelerations of Points A, B, C and D.

Table G-1 Summary of Response Properties, Collapse Performance Metrics and Values of the VHS Load Amplifier of Baseline Capacity and 2 x Baseline Capacity Models of Three Notional Building (*Very Short*, *Mid-Rise* and *Very Tall*) Archetypes Evaluated for Demand Spectra with Idealized Domains of Constant Acceleration, Constant Velocity and Constant Displacement

Notional Building Archetypes and Response Domains			
Archetype	Very Short	Mid-Rise	Very Tall
Domain	Acceleration	Velocity	Displacement
Parameters and Results - Baseline Capacity Models			
T (s)	0.15	1.00	6.00
V_{max}/W (g)	1.00	0.20	0.05
SD_y (in.)	0.22	3.00	25.0
SD_{IC} (in.)	3.0	15.0	60.0
SA_{IC} (g) – Point A	1.00	0.20	0.050
T_{eff} (s)	0.55	2.77	11.09
$S_{CT,\beta eff}$ (g) – Point C	1.00	0.557	0.170
Parameters and Results - Two × Baseline Capacity Models			
T (s)	0.15	1.00	6.00
V_{max}/W (g)	2.00	0.40	0.10
SD_y (in.)	0.30	3.00	35.3
SD_{IC} (in.)	3.0	15.0	60.0
SA_{IC} (g) – Point B	2.00	0.40	0.100
T_{eff} (s)	0.39	1.96	7.84
$S_{CT,\beta eff}$ (g) – Point D	2.00	0.788	0.170
VHS Load Amplifier, Equation G-11			
SA(B)/SA(A)	2.00	2.00	2.00
SA(C)/SA(D)	0.50	0.71	1.00
VHS Load Amplifier	1.00	1.41	2.00

G.4.4 Summary and Generalization of Findings

The rate of increase in the collapse risk with increase in the ground motions is intrinsically lower for buildings with shorter effective periods at incipient collapse (all else equal) as shown by the very different values of the VHS Load Amplifier of Table G-1. There is no additional collapse risk with increase in the value of S_{MT} for the *Very Short* building archetype, whose effective period at incipient collapse (e.g., T_{eff} = 0.55 s at 1 × Baseline capacity) is in the idealized domain of constant acceleration; whereas, the collapse risk of the *Very Tall* building archetype, whose effective period at incipient collapse (e.g., T_{eff} = 7.84 s at 2 × Baseline capacity) is in the idealized domain of constant displacement, increases in proportion to the increase in the value of S_{MT}.

Collapse results are generalized to define upper-bound and lower-bound limits of the value of the VHS Load Amplifier as a function of normalized demand, as illustrated in Figure G-7. In contrast to the idealized response domains of this example, the more realistic multi-period response spectra of ASCE/SEI 7-22 transition gradually from the acceleration domain to the displacement domain and likewise values of the VHS Load Amplifier at a given level of MCE_R ground motions would be expected to also gradually increase as the effective period of the model of the building archetype increases. That is, taller structures are expected to have larger values of the VHS Load Amplifier than shorter structures, all else equal, as illustrated notionally on the right-hand side of Figure G-7.

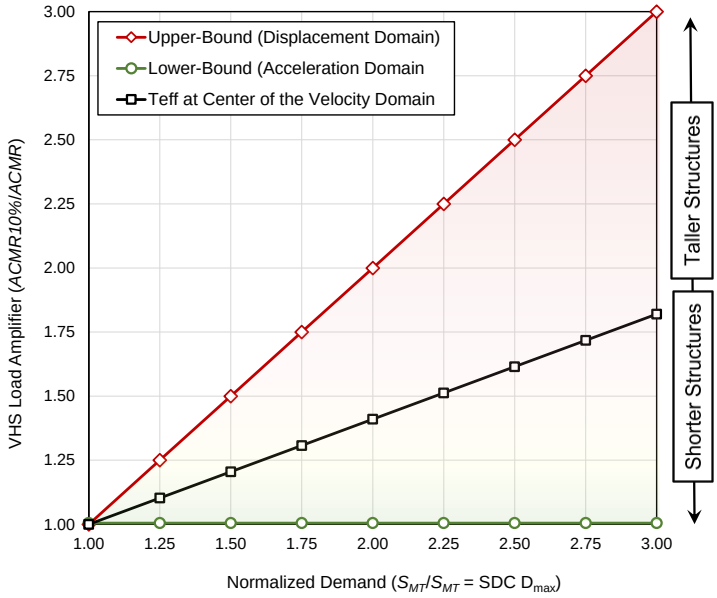

Figure G-7 **Notional collapse trends of the VHS Load Amplifier derived from CSM examples illustrating the importance of period range of interest on collapse performance. Collapse trends include (1) the theoretical upper-bound on collapse performance when peak nonlinear response is in the idealized domain of constant displacement (steep trend line shown with red diamonds) and (2) the theoretical lower-bound on collapse performance when peak nonlinear response is in the idealized domain of constant acceleration (flat trend line shown with green circles).**

G.5 Spectrum Shape Example

G.5.1 Introduction

The CSM example of this section calculates values of the VHS Load Amplifier of a hypothetical *Mid-Rise* (T = 0.75 s) building archetype designed and evaluated for demand spectra with different shapes (frequency contents) of MCE_R ground motions with different site (source) conditions: (1) Site Class C (magnitude M6.0), (2) Site Class CD (magnitude M7.0) and (3) Site Class D (magnitude M8.0) ground motions. This example illustrates the influence of spectrum shape and, in particular, site class on the value of the VHS Load Amplifier.

G.5.2 Scope and Approach

Values of the VHS Load Amplifier are calculated using multi-period response spectra representing scenario MCE_R ground motions of (1) a Site Class C site, 3 km from a magnitude M6.0 earthquake, (2) a Site Class CD site, 8.0 km from a magnitude M7.0 earthquake and (3) a Site Class D site, 12.5 km from a magnitude M8.0 earthquake. A magnitude M8.0 earthquake at 12.5 km scenario earthquake (Site Class D) corresponds to the magnitude and distance of the Deterministic Lower Limit of ASCE/SEI 7-22. For Site Class C and CD scenarios, magnitudes and distances are selected to generate ground motions comparable to the short periods of the Site Class D scenario. Median response spectra were calculated for each of the three site class scenarios using the PEER NGA West-2 spreadsheet (Seyhan, 2014). Spectral shape is based on median, rather than 84th percentile, response for consistency with the spectral shape concepts of Appendix B of FEMA P-695, although the difference in spectral shape of median versus 84th percentile response is negligible, as compared to differences in spectral shape due to site class.

Response spectra of the three site class scenarios are plotted in Figure G-8 (linear axes) and in Figure G-9 (log axes), where log axes provide a better illustration of response at long periods, as well as at short periods. Differences in the frequency content (shape) of the spectra due to site class are apparent where Site Class D response is about twice that of Site Class C at the elastic design period, T = 0.75 s, of the *Mid-Rise* building archetype, and about four times greater at a response period of T = 2 seconds. At long periods (i.e., T ≥ 3 s), differences in the earthquake magnitudes of the Site Class C (M6.0), Site Class CD (M7.0) and Site Class D (M8.0) scenarios significantly affect the shape and transition from the velocity domain to the displacement domain of the demand spectra, although at response periods typically longer than the effective periods of Mid-Rise building archetype. Also shown in Figure G-8 and Figure G-9 is the median response spectrum of the Far-Field record set scaled by 2.0/1.5, where 2.0 is the approximate factor required by Table A-3 of FEMA P-695 for scaling median spectral acceleration of the Far-Field record set to SDC D_{max} spectral acceleration at short periods, and 1.5 is the factor of ASCE/SEI 7-22 used to reduce MCE_R spectral acceleration to design earthquake spectral acceleration. As shown in these figures, the frequency content of the scaled median spectrum of the Far-Field record set best represents the frequency content of the Site Class CD spectrum, although the slope is somewhat steeper (and hence similar to that of the Site Class C spectrum).

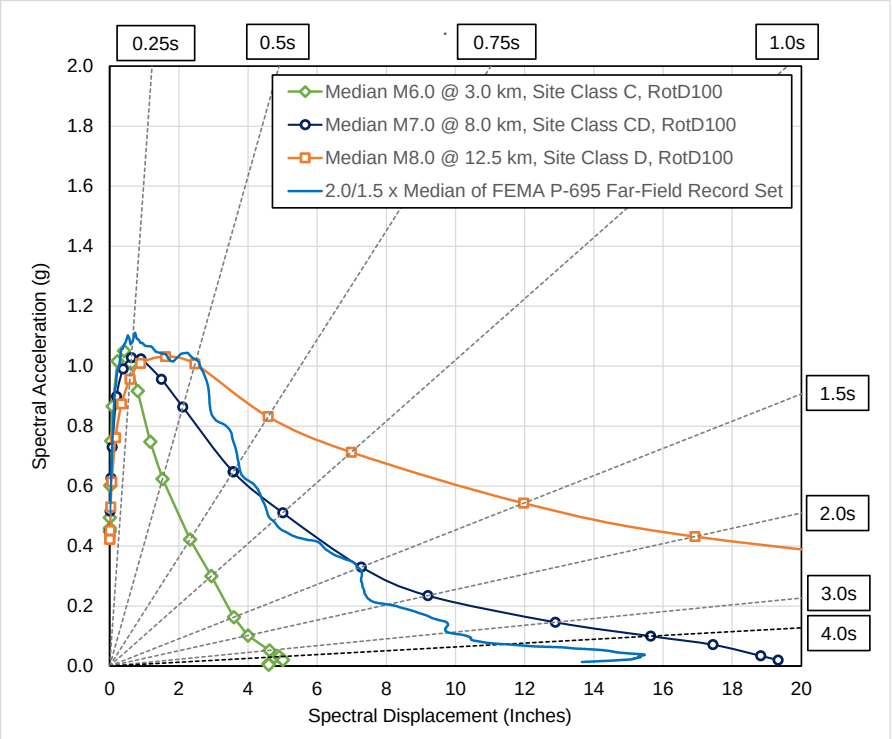

Figure G-8 **Median response spectra of Site Class C (M6.0), Site Class CD (M7.0) and Site Class D (M8.0) ground motions and the Far-Field record set (factored by 2.0/1.5).**

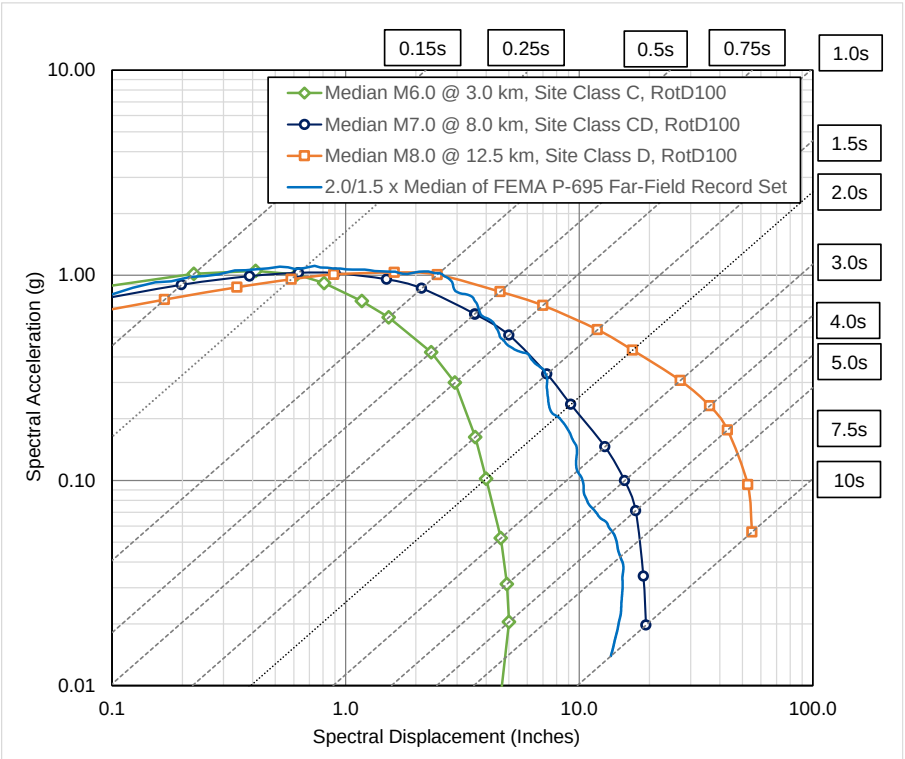

Figure G-9 **Median response spectra of Site Class C (M6.0), Site Class CD (M7.0) and Site Class D (M8.0) ground motions and the Far-Field record set (factored by 2.0/1.5).**

Values of the VHS Load Amplifier are calculated for a hypothetical *Mid-Rise* building archetype with an elastic design period, T = 0.75 s. This archetype is modeled with two different pushover strengths, one representing (1) Baseline capacity, presumed to comply with target reliability (i.e., 10% failure rate) and (2) the other with pushover strength equal to two times Baseline capacity. The hypothetical *Mid-Rise* building archetype is same for each the three site classes; however, models of the archetype have different Baseline and two times Baseline strengths corresponding to differences in design spectral acceleration of Site Class C, CD and D response spectra at the elastic design period, T = 0.75 s. For example, the Baseline strength, V_{max}/W = 0.38g, of the model representing Site Class D design, is twice that of the Baseline strength, V_{max}/W = 0.19g, of the model representing Site Class C design. In all cases, capacity curves have the same failure displacement, SD_{IC} = 8 inches, and essentially the same backbone curve shape (e.g., peak strength at about SD = 5 inches. Normalized pushover strength (V_{max}/W) and other key properties of each of the models of the hypothetical *Mid-Rise* building archetype are summarized in Table G-2, along with collapse results.

Collapse performance of each of the six models of the hypothetical *Mid-Rise* building archetype (i.e., three scenario site classes x two model strengths each) is evaluated graphically using the CSM to determine the spectral accelerations at the four intersection points (i.e., Points A, B, C and D of Figure G-2) required by Equation G-11 for calculation of the VHS Load Amplifier. Graphical solutions of intersection points are shown in Figure G-10 (linear axes) and Figure G-11 (log axes) for collapse evaluation using Site Class C demand spectra, in Figure G-12 (linear axes) and Figure G-13 (log axes) for collapse evaluation using Site Class CD demand spectra, and in Figure G-14 (linear axes) and Figure G-15 (log axes) for collapse evaluation using Site Class D demand spectra.

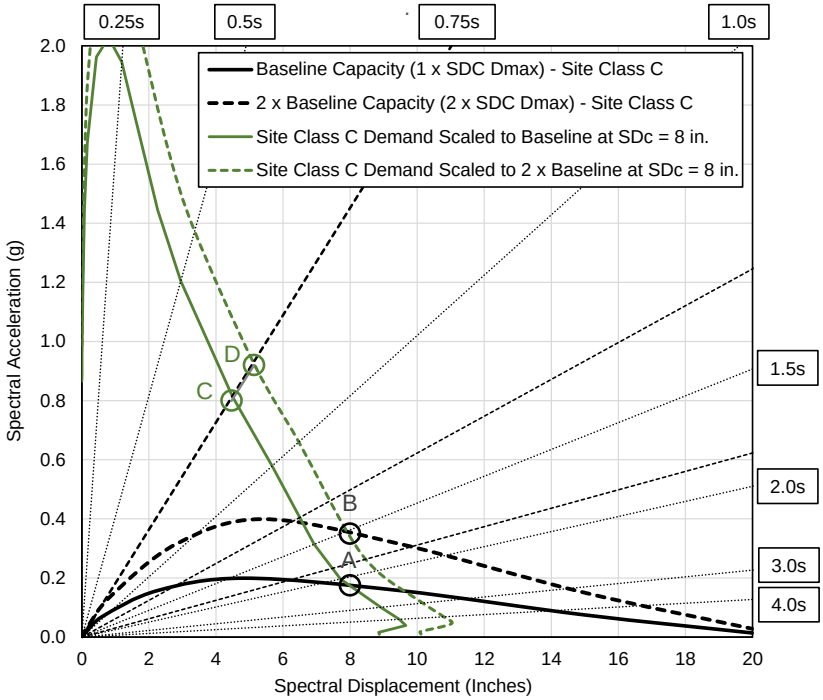

Figure G-10 Example CSM collapse evaluation of a hypothetical *Mid-Rise* building archetype using Site Class C (M6.0) demand spectra.

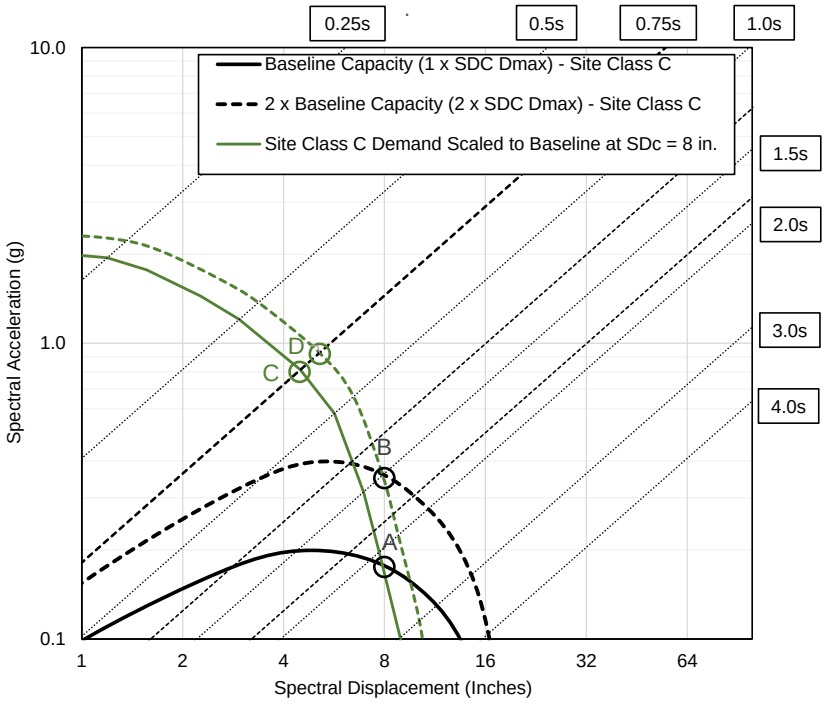

Figure G-11 Example CSM collapse evaluation of a hypothetical *Mid-Rise* building archetype using Site Class C (M6.0) demand spectra.

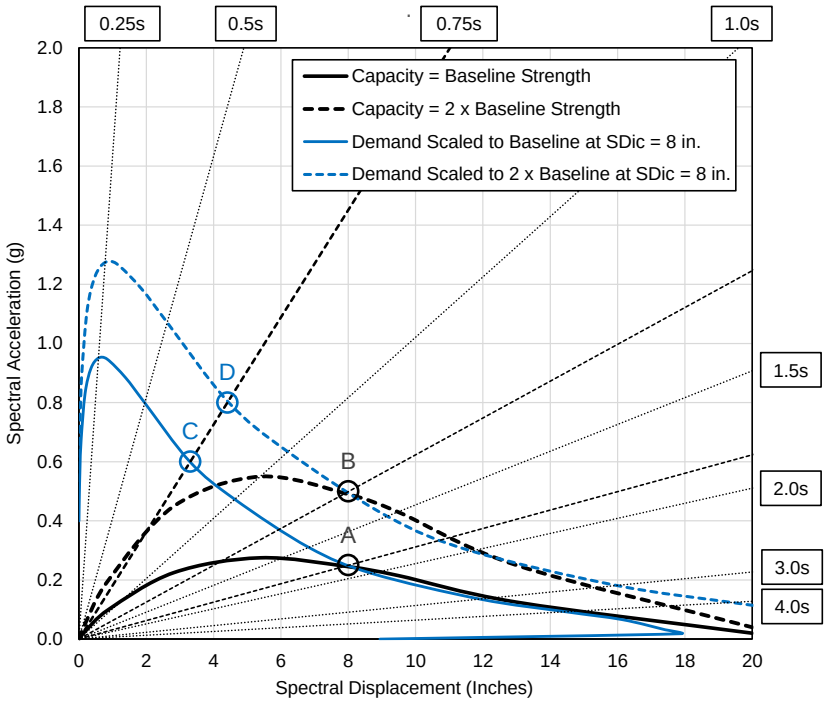

Figure G-12 Example CSM collapse evaluation of a hypothetical *Mid-Rise* building archetype using Site Class CD (M7.0) demand spectra.

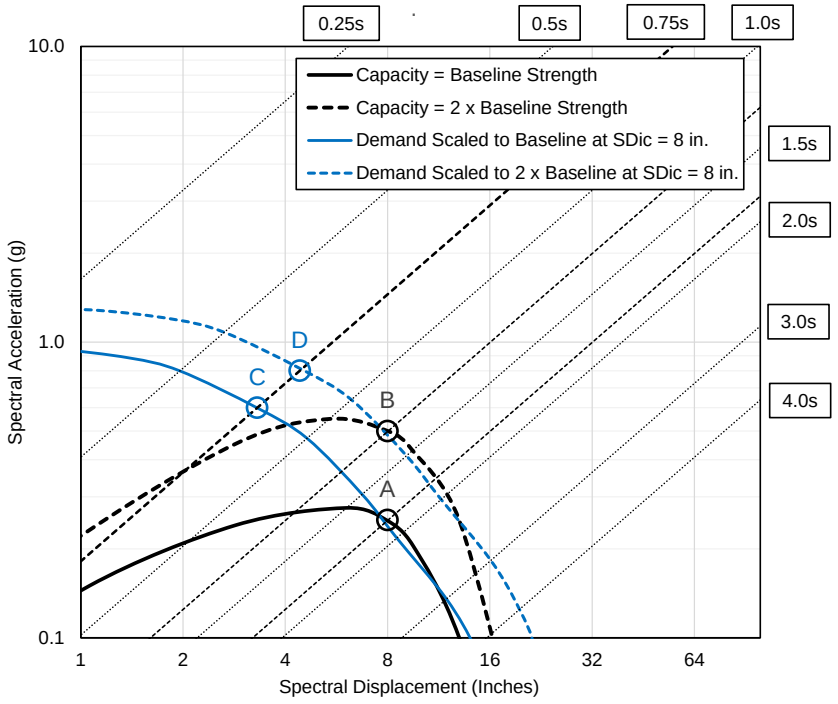

Figure G-13 Example CSM collapse evaluation of a hypothetical *Mid-Rise* building archetype using Site Class CD (M7.0) demand spectra.

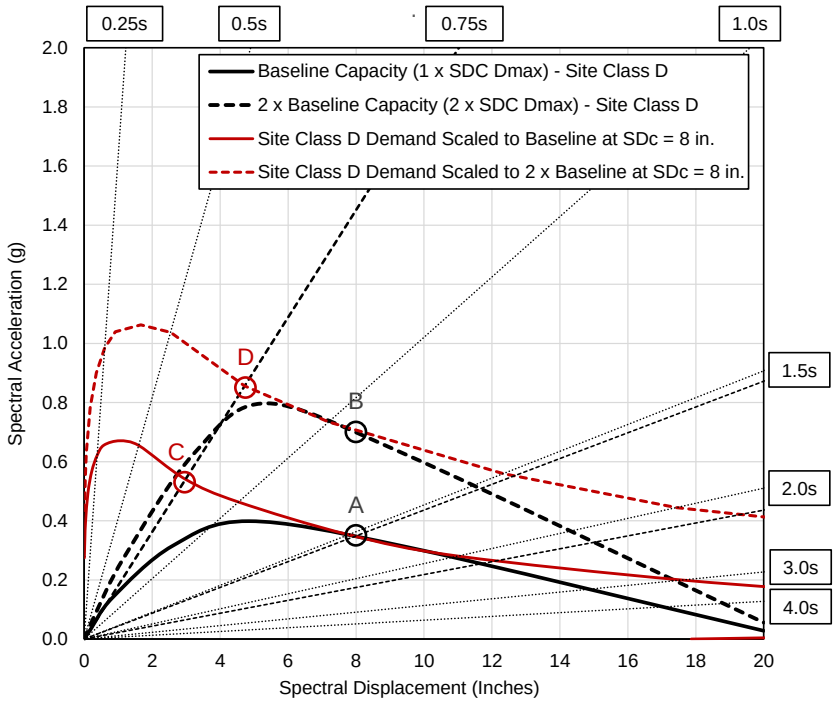

Figure G-14 **Example CSM collapse evaluation of a hypothetical *Mid-Rise* building archetype using Site Class D (M8.0) demand spectra.**

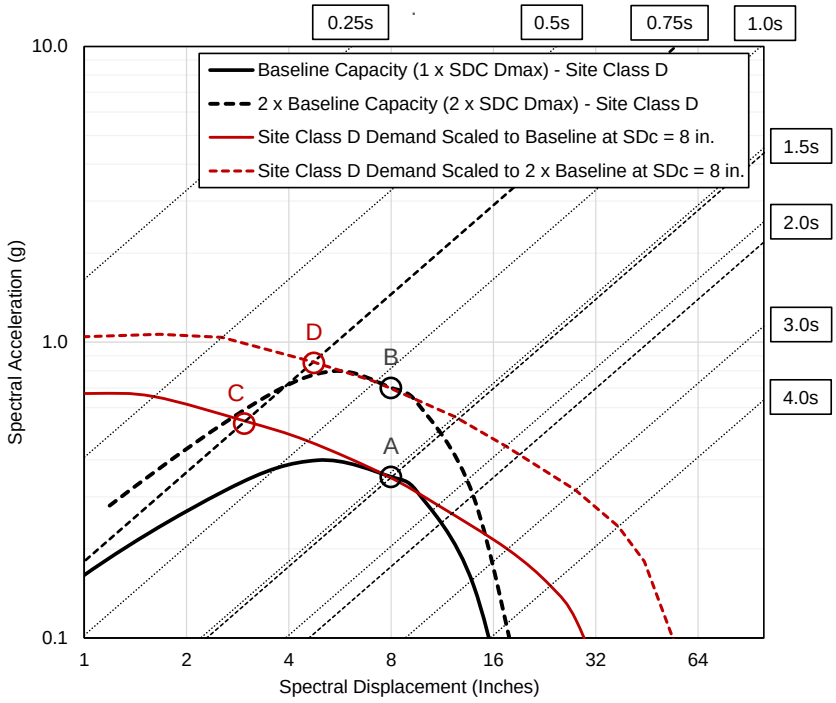

Figure G-15 **Example CSM collapse evaluation of a hypothetical *Mid-Rise* building archetype using Site Class D (M8.0) demand spectra.**

G.5.3 Collapse Evaluation Results

A summary of key response properties and collapse performance metrics, including values of spectral acceleration at Points A, B, C and D of Figures G-10 through G-15, are summarized in Table G-2 for the Baseline capacity model and the two times Baseline capacity model of the hypothetical *Mid-Rise* building archetype designed and evaluated for each of the three scenario site class response spectra. Also included in Table G-2 are values of the VHS Load Amplifier, calculated using Equation G-11 and the spectral accelerations of Points A, B, C and D.

Table G-2 Summary of the Properties, Collapse Performance Metrics and Values of the VHS Load Amplifier of Baseline and 2 × Baseline Capacity Models of a Hypothetical *Mid-Rise* Building Archetype Designed and Evaluated for Three Scenario Response Spectrum Shapes Representing (1) Site Class C (M6.0), (2) Site class CD (M7.0), and (3) Site Class D (M8.0) MCE_R Ground Motions

Three Response Spectrum Shapes			
Magnitude	M6.0	M7.0	M8.0
Distance	3 km	8 km	12.5 km
Site Class	C	CD	D
Parameters and Results - Baseline Capacity Models			
T (s)	0.75	0.75	0.75
V_{max}/W (g)	0.200	0.280	0.400
SD_{IC} (in.)	8.0	8.0	8.0
SA_{IC} (g) – Point A	0.18	0.25	0.35
T_{eff} (s)	2.16	1.81	1.53
B	2.0	2.0	2.0
$S_{CT,\beta eff}$ (g) – Point C	0.81	0.600	0.530

Table G-2 Summary of the Properties, Collapse Performance Metrics and Values of the VHS Load Amplifier of Baseline and 2 × Baseline Capacity Models of a Hypothetical *Mid-Rise* Building Archetype Designed and Evaluated for Three Scenario Response Spectrum Shapes Representing (1) Site Class C (M6.0), (2) Site class CD (M7.0), and (3) Site Class D (M8.0) MCE_R Ground Motions (continued)

Three Response Spectrum Shapes			
Magnitude	M6.0	M7.0	M8.0
Distance	3 km	8 km	12.5 km
Site Class	C	CD	D
Parameters and Results - Two × Baseline Capacity Models			
T (s)	0.75	0.75	0.75
V_{max}/W (g)	0.40	0.56	0.80
SD_{IC} (in.)	8.0	8.0	8.0
SA_{IC} (g) – Point B	0.35	0.50	0.70
T_{eff} (s)	1.53	1.28	1.08
B	2.0	2.0	2.0
$S_{CT,\beta eff}$ (g) – Point D	0.92	0.80	0.85
VHS Load Amplifier, Equation G-11			
SA(B)/SA(A)	2.00	2.00	2.00
SA(C)/SA(D)	0.88	0.75	0.63
VHS Load Amplifier	1.75	1.50	1.25

G.5.4 Summary and Generalization of Findings

The rate of increase in the collapse risk with increase in the ground motions is significantly influenced by the shape of the demand spectrum, as shown by comparison of the values of the VHS Load Amplifier of Table G-2 for Site Class C, CD and D demand spectra. The values of the VHS Load Amplifier are directly related to the slope of the demand spectrum at incipient collapse (Points A and B), as illustrated in Figures G-10 through G-15. For Site Class C demand spectra, which are relatively steep at incipient collapse (Figure G-10), the value of VHS Load Amplifier is 1.75; whereas, for site Class D demand spectra, which are relatively flat at incipient collapse (Figure G-14), the value of VHS Load Amplifier is 1.25. For Class CD demand spectra that are approximately proportional to $1/T$ at incipient collapse (i.e., Site Class CD demand spectra are roughly at right angles to period spokes in Figure G-13), the value of VHS Load Amplifier is 1.50, which is similar to the theoretically value of 1.41 for response in the idealized domain of constant velocity (Table G-1).

Collapse results of Table G-2 and are generalized in Figure G-16 to show notional values of the VHS Load Amplifier as a function of normalized demand, where stiffer sites are expected to have larger values of the VHS Load Amplifier than softer sites, all else equal. VHS Load Amplifier trends shown in Figure G-16 are influenced by the value of effective period, as well as site class, and would necessarily change if values of the effective period were significantly shorter or significantly longer, than those of the models of the hypothetical *Mid-Rise* building archetype of this example.

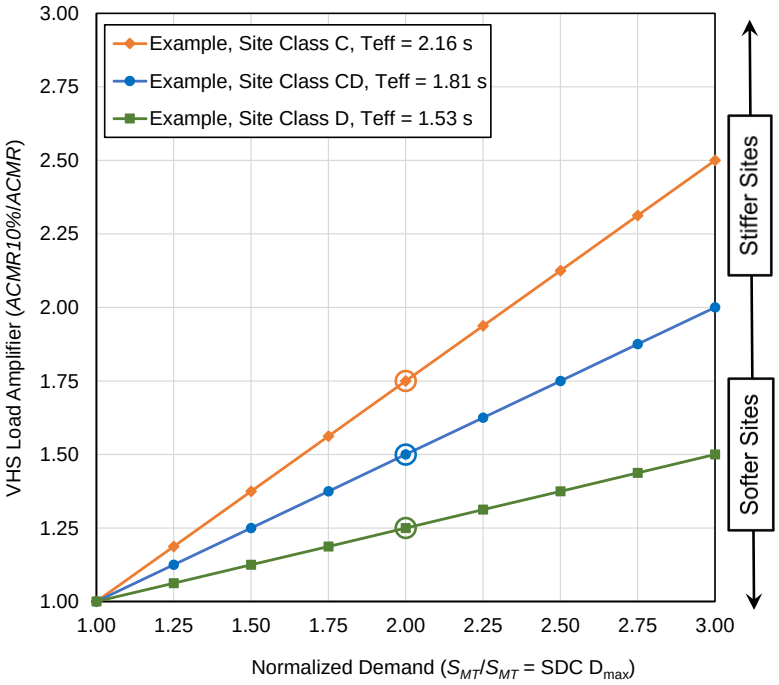

Figure G-16 Notional collapse trends of the VHS Load Amplifier derived from CSM examples illustrating the importance of spectrum shape (site class) on collapse performance.

G.6 BRBF Example

This section provides an example illustration of the capacity-spectrum method (CSM) used to estimate values of median collapse acceleration, $\hat{S}_{CT}$, of the 4-story BRBF archetype (BRBF4A) of Chapter 5. Collapse results from the CSM analyses are compared with those of Chapter 5 that are based on IDA. There is nothing unique about the choice of BRBF4A archetype and other archetypes could have been used equally well for this example. The same Far-Field ground motions are used for this comparison, where the median response spectrum of Far-Field record set is used for CSM analysis and the corresponding individual records of the Far-Field record set are used for IDA. This example illustrates that CSM analysis can reliably replicate collapse performance of the same archetype evaluated using IDA (i.e., when CSM and IDA models are based on the same nonlinear hysteretic properties of the archetype).

Values of $\hat{S}_{CT}$ are calculated for three models of the BRBF4A archetype with different strengths by scaling the median spectrum of the Far-Field record set to intersect model pushover strength at the collapse displacement capacity of the model. In this sense, values of $\hat{S}_{CT}$ are calculated directly from the median Far-Field spectrum, whereas, in Chapter 5 values of $\hat{S}_{CT}$ are calculated as the median of results of IDA of individual Far-Field earthquake records (of the same Far-Field spectrum). The three model strengths of this example are (1) "Baseline" strength corresponding to design at VHS boundary (i.e., 1.0 × SDC D_{max} of FEMA P-695), (2) 2 × Baseline strength and (3) ½ × Baseline strength.

The CSM example illustrates the relationship between $\hat{S}_{CT}$ and the shape of the median Far-Field spectrum, which shows that doubling (or halving) the design strength does not double (or halve) the value of $\hat{S}_{CT}$. Values of *ACMR* are derived from the calculated values of $\hat{S}_{CT}$ for each of three models and shown to be essentially the same as those of Chapter 5 (as summarized in Table 6-2 of Chapter 6), confirming the similar trends in collapse performance from the two different methods of analysis (i.e., IDA and CSM).

The BRBF4A archetype has a roof height of 57 feet and a corresponding design period, T = 0.87 s. The Baseline model has a maximum strength, V_{max}/W = 0.23g, corresponding to Risk Category II design (i.e., R/I_e = 8/1.0) of the BRBF4A archetype for $S_{MT} = S_{M1}/T$ = 0.9g / 0.87 s = 1.03g, corresponding to the VHS boundary (i.e., 1.0 x SDC D_{max} of FEMA P-695). Backbone curves (incorporating P-delta effects) and other properties of the three strength models are taken from Chapter 5 (e.g., Figure 5-6(a)). Backbone curves are converted to eSDOF modal pushover curves (i.e., nonlinear model strength expressed as a function of spectral acceleration, SA, and spectral displacement, SD) using the same pushover mode assumptions as those of Chapter 5. The pushover curves of the three strength models of the BRBF4A archetype are shown in Figure G-17. Backbone curve and pushover properties are summarized in Table G-3. Table G-3 also provides notes, definitions and sources of these and other parameters to support the CSM example.

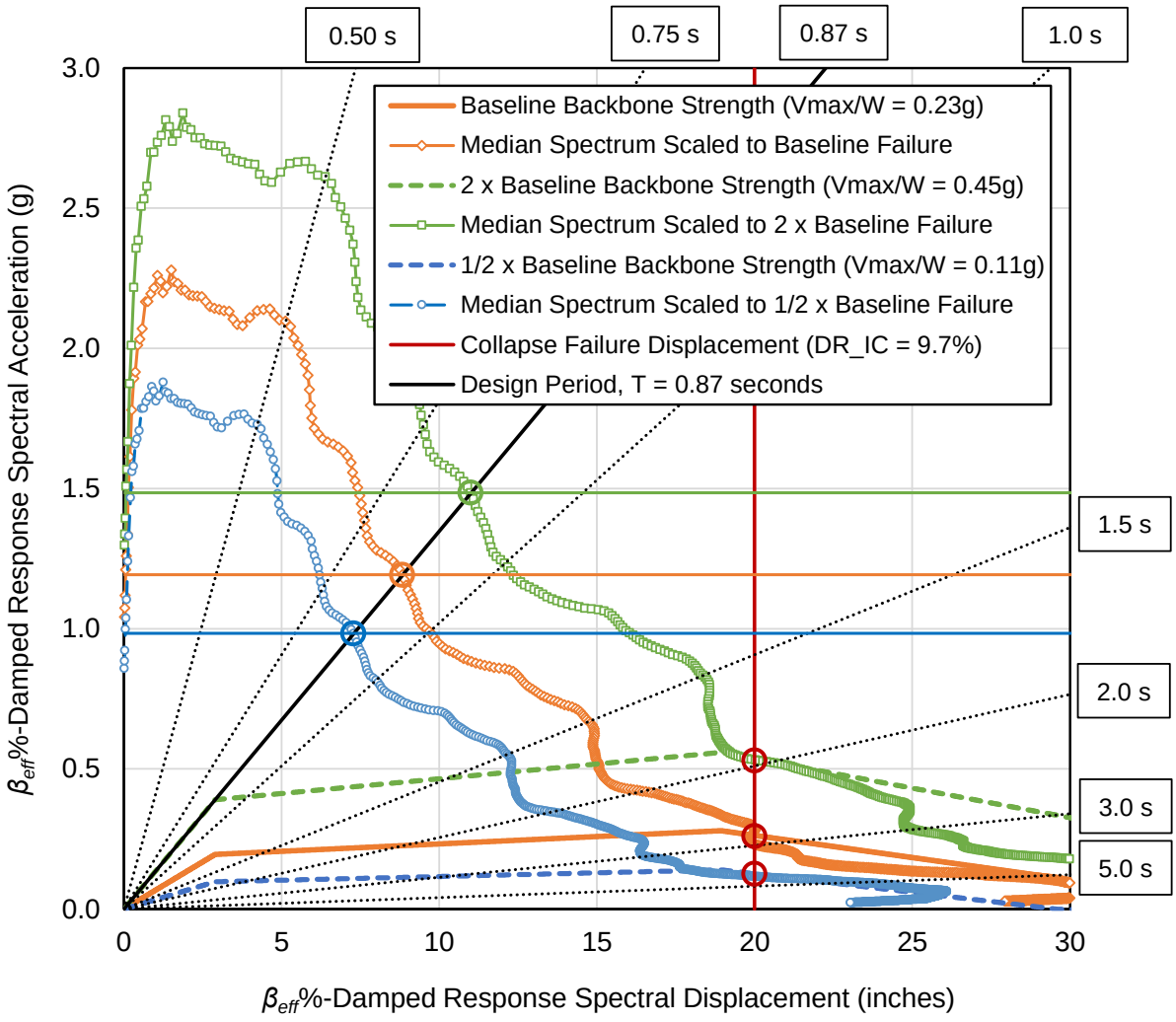

Figure G-17 **Example CSM illustration of the variation in collapse performance as a function of model strength using three model strengths (Baseline strength, 2 × Baseline strength and ½ × Baseline model strength) of the four-story BRBF4A archetype of Chapter 5.**

Table G-3 Summary of the Nonlinear Properties and CSM Parameters of the Three BRBF4A Archetype Models Used to Illustrate the Variation in Collapse Performance as a Function of Model Strength in Figure G-17

Parameter	Baseline Strength	2 × Baseline	1/2 × Baseline	Notes
Archetype Model Properties (from Chapter 5 adapted from Ochoa, 2017)				
N	4	4	4	Number of Stories
h (in.)	684	684	684	Height = 57 ft = 18 ft (1st story) + 3 × 13 ft
T (s)	0.87	0.87	0.87	Design Period, $T = C_u T_a$, FEMA P-695
Backbone Curve Properties (selected from curves of Figure 5-6(a))				
T_1 (s)	1.23	0.87	1.74	$T_1 \approx T$ = 0.87s for 2 × Baseline strength
V_y/W	0.15	0.3	0.075	Baseline strength corresponds to S_{M1} = 0.9 g
Roof DR_y	0.30%	0.30%	0.30%	Roof drift at yield strength is constant
Roof D_y (in.)	2.1	2.1	2.1	Roof drift at yield strength times height
V_{max}/W	0.23	0.45	0.11	Baseline strength corresponds to S_{M1} = 0.9 g
Roof DR_{max}	3.6%	3.6%	3.6%	Roof drift at maximum strength is constant
Roof D_{max} (in.)	24.3	24.3	24.3	Roof drift at maximum strength times height
eSDOF Pushover Properties (from Chapter 5 and Appendix I)				
W_P / W	0.85	0.85	0.85	Effective weight, Equation (G-1)
Γ_P	0.78	0.78	0.78	Participation Factor, Equation (G-2)
SA_y (g)	0.18	0.35	0.09	Spectral acceleration at yield, Equation (G-3)
SD_y (in.)	2.62	2.62	2.62	Spectral displacement at yield, Equation (G-4)
SA_{max} (g)	0.26	0.53	0.13	Spectral accel. at maximum strength, Eq. (G-3)
SD_{max} (in.)	19.0	19.0	19.0	Spectral displ. at maximum strength, Eq. (G-4)

Table G-3 Summary of the Nonlinear Properties and CSM Parameters of the Three BRBF4A Archetype Models Used to Illustrate the Variation in Collapse Performance as a Function of Model Strength in Figure G-17 (continued)

Parameter	Baseline Strength	2 × Baseline	1/2 × Baseline	Notes
Capacity-Spectrum Analysis (median spectrum of the Far-Field record set, Table A-3, FEMA P-695)				
Median DR_{IC}	9.7%	9.7%	9.7%	Drift ratio at incipient collapse (Table I-1)
SD_C (in.)	20.0	20.0	20.0	Collapse displacement of eSDOF model at DR_{IC}
Scale Factor	2.85	3.55	2.35	Median spectrum scaled to SD_C
SA_C (g)	0.26	0.51	0.13	Spectral acceleration at collapse displacement
T_{eff} (s)	2.8	2.0	4.0	Effective period at incipient collapse, Eq. (G-5)
S_{CT} [$\beta = \beta_{eff}$] (g)	1.19	1.49	0.98	Collapse acceleration at T, damping = β_{eff}
β_{eff} (% critical)	38%	38%	38%	Effective damping, Equation (G-6)
B Factor	2.0	2.0	2.0	Damping Coefficient, e.g., T18.7-1, ASCE 7-22
S_{CT} [$\beta = 5\%$] (g)	2.39	2.97	1.97	S_{CT} [$\beta = 5\%$] = $B \times S_{CT}$ [$\beta = \beta_{eff}$]
Calculation of *ACMR* from Capacity-Spectrum Analysis and comparison with *ACMR* of IDA (Chapter 5)				
S_{MT} (g)	1.03	2.07	0.52	Baseline $S_{MT} = S_{M1}/ T$ = 0.9g / 0.87s
CMR	2.31	1.44	3.81	S_{CT} [$\beta = 5\%$] / S_{MT}
SSF	1.43	1.43	1.43	from Table 3-2 (Table I-3)
ACMR	3.30	2.06	5.44	*ACMR* = *SSF* x *CMR*
ACMR (IDA)	3.36	2.17	5.54	from Table 6-3 (Table I-3)

The spectral displacement collapse capacity of the BRBF4A archetype is SD_C = 20 inches, corresponding to a median DR_{IC} of 9.7%. This limit is shown by a (solid red) vertical line in Figure G-14. It may be noted that this failure displacement occurs just beyond the spectral displacement of SD_{max} = 19 inches at the maximum strength of the models, which is the same for each BRBF4A model, as discussed in Chapter 5. Collapse performance is determined for each model by scaling the median Far-Field spectrum to intersect the respective pushover curve at the collapse displacement, SD_C = 20 inches. Intersection points are shown in Figure G-14 by (red) circles. The intersection points correspond to effective periods (T_{eff}) at collapse that are about 2.3 times the elastic period (T_1) of each model, i.e., T_{eff} = 2.8 s for the Baseline model, T_{eff} = 2.0 s for the 2 × Baseline strength model and T_{eff} = 4.0 s for the ½ × Baseline strength model. Lines of constant period are shown as "spokes"

from the origin in Figure G-17, which are related to spectral acceleration (SA) and spectral displacement (SD) by the formula: T (spoke) = sqrt[$(g/4\pi^2)(SD/SA)$], where g is the gravity constant.

The median Far-Field spectrum scaled to the collapse displacement of the model represents response at the "effective" damping level of the model, where effective damping is defined in terms of the equivalent energy dissipated by hysteretic response. In Chapter 5, BRBF archetypes are assumed to not degrade during cyclic-load response and thus the full area of the hysteresis loop is used to estimate the effective damping of the three models, which is approximately, β_{eff} = 38% (e.g., Equation 17.8-1 of ASCE/SEI 7-22). This relatively high level of effective damping would be substantially lower for archetype models with hysteretic properties that degrade during cyclic-load response (e.g., wood archetypes of Chapter 4) and thus would not have the benefit of the full area of the hysteresis loop. The ratio of 5%-damped response (nominal damping level of the median collapse acceleration parameter, $\hat{S}_{CT}$) to β_{eff}-damped response is estimated using the B factors of Table 18-7-1 of ASCE/SEI 7-22, which is approximately B = 2.0 for β_{eff} = 38%.

The three median Far-Field spectra scaled to collapse failure at SD_C = 20 inches, intersect the design-period "spoke" of 0.87s at 1.19 g (Baseline strength), 1.49 g (2 × Baseline strength) and 0.98 g (½ × Baseline strength), as shown by circles in Figure G-17. These intersection points represent collapse spectral accelerations, conditioned on the design period (T) at the effective damping level of β_{eff} = 38%. In terms of 5%-damped response, these intersection points correspond to $\hat{S}_{CT}$ = 2.39 g = B x S_{CT} = 2.0 x 1.19 g (Baseline strength), $\hat{S}_{CT}$ = 2.97 g = 2.0 × 1.49 g (2 × Baseline strength) and $\hat{S}_{CT}$ = 1.97 g = 2.0 × 0.98 g (½ × times Baseline strength). The important take away from the intersection points shown in Figure G-17 is that the range of values of $\hat{S}_{CT}$ (i.e., about 1.5 = 2.97g/1.97g) is much less than the factor of four range of model strengths, indicating that median collapse acceleration, and hence collapse performance, does not scale in proportion with model strength. The difference in the range of $\hat{S}_{CT}$ values and model strengths is typical of the collapse results of Chapter 4 and Chapter 5, and related to the shape of median Far-Field response spectrum scaled to a common collapse displacement (i.e., SD_C = 20 inches).

The elastic design period (T) is the conditioning period required by the FEMA P-695 methodology for IDA and collapse evaluation that defines both MCE_R spectral acceleration (S_{MT}) and median collapse acceleration ($\hat{S}_{CT}$). In general, the value of the first-mode period of the model (T_1) is different from that of design period (T). Collapse performance evaluated using T_1, in lieu of T, would be essentially the same, provided MCE_R spectral acceleration and median collapse acceleration are both defined in terms of T_1. Conceptually, this would be a different design-period "spoke" in Figure G-14 (e.g., at T_1 = 1.23 s for the model with Baseline strength), representing archetypes designed for MCE_R spectral acceleration at T_1. The value of the median collapse acceleration ($\hat{S}_{CT1}$) at T_1 would be different, but likewise the value of S_{MT1} would also be different, and the collapse margin ratio (CMR) would be the same, $CMR = \hat{S}_{CT1}/S_{MT1} = \hat{S}_{CT}/S_{MT}$).

Values of *ACMR* derived from the calculated values of $\hat{S}_{CT}$ are shown in Table G-3 and compared with the values of *ACMR* of Chapter 5 for each of the three strength models. The values of *ACMR* based on the CSM analysis are similar to those of the IDA of Chapter 5. The important take away is that the ratio of the *ACMR* of the baseline strength model to the *ACMR* of the 2.0 $\times$ baseline strength model (i.e., 3.30/2.06 = 1.6) supports the collapse trends shown in Figure 6-11 of Chapter 6 for the BRBF4A.

References

ASCE, 2005, *Minimum Design Loads for Buildings and Other Structures*, ASCE/SEI 7-05, American Society of Civil Engineers, Reston, Virginia.

ASCE, 2016, *Minimum Design Loads and Associated Criteria for Buildings and Other Structures*, ASCE/SEI 7-16, American Society of Civil Engineers, Reston, Virginia.

ASCE, 2022, *Minimum Design Loads and Associated Criteria for Buildings and Other Structures*, ASCE/SEI 7-22, American Society of Civil Engineers, Reston, Virginia.

ASCE, 2023. *Seismic Evaluation and Retrofit of Existing Buildings*, ASCE/SEI 41-23, American Society of Civil Engineers, Reston, Virginia.

ATC, 2013, *Evaluation of Seismic Performance Assessment Methodologies & Building Seismic Performance*, ATC-63-2/3, Applied Technology Council, Redwood City, California. Unpublished Manuscript.

Charney, F. A., 1991, "Correlation of the analytical and experimental inelastic seismic response of a 1/5-scale seven-story reinforced concrete frame-wall structure," ACI Special Publication SP-127, *Earthquake-Resistant Concrete Structures—Inelastic Response and Design*, American Concrete Institute, Farmington Hills, Michigan.

Constantinou, M.C., Winters, C.W., and Theodossiou, D., 1993, "Evaluation of SEAOC and UBC analysis procedures, Part 2: flexible superstructure," *Proceedings of a Seminar on Seismic Isolation, Passive Energy Dissipation and Active Control*, ATC-17-1, Applied Technology Council, Redwood City, California.

CSSC, 1996, *Seismic Evaluation and Retrofit of Concrete Buildings, Volume 1*, ATC-40/SSC 96-01, prepared by the Applied Technology Council for the California Seismic Safety Commission, Sacramento, California.

Elkady, A. and Lignos, D.G., 2014a, "Effect of gravity framing on the overstrength and collapse capacity of steel frame buildings with perimeter special moment frames," *Earthquake Engineering & Structural Dynamics*, Vol. 44, pp. 1289–1307.

Elkady, A. and Lignos, D.G., 2014b, "Modeling of the composite action in fully restrained beam-to-column connections: implications in the seismic design and collapse capacity of steel special moment frames," *Earthquake Engineering & Structural Dynamics*, Vol. 43, pp. 1935–1954.

Elkady, A. and Lignos, D.G., 2015, "Effect of gravity framing on the overstrength and collapse capacity of steel frame buildings with perimeter special moment frames," *Earthquake Engineering & Structural Dynamics*, Vol. 44, pp. 1289–1307.

Fahnestock, L. A., Sause, R., and Ricles, J. M., 2007, "Seismic response and performance of buckling-restrained braced frames," *Journal of Structural Engineering*, Vol. 133, No. 9, pp. 1195–1204.

FEMA, 1996, *HAZUS Earthquake Model Technical Manual*, Federal Emergency Management Agency, Washington, D.C.

FEMA, 1997, *NEHRP Guidelines for the Seismic Rehabilitation of Buildings*, FEMA 273, prepared by the Applied *Technology* Council for the Building Seismic Safety Council and the Federal Emergency Management Agency, Washington, D.C.

FEMA, 2000, *State of the Art Report on Systems Performance of Steel Moment Frames Subject to Earthquake Ground Shaking*, FEMA-355C, prepared by the SAC Joint Venture, a partnership of the Structural Engineers Association of California, the Applied Technology Council, and the California Universities for Research in Earthquake Engineering, for the Federal Emergency Management Agency, Washington, D.C.

FEMA, 2002, *HAZUS Advanced Engineering Building Module, Technical and User's Manual,* Federal Emergency Management Agency, Washington, D.C.

FEMA, 2009a, *NEHRP Recommended Seismic Provisions for New Buildings and Other Structures*, FEMA P-750, prepared by the Building Seismic Safety Council of the National Institute of Building Sciences for the Federal Emergency Management Agency, Washington, D.C.

FEMA, 2009b, *Quantification of Building Seismic Performance Factors*, FEMA P-695, prepared by the Applied Technology Council for the Federal Emergency Management Agency, Washington, D.C.

FEMA, 2009c, *Effects of Strength and Stiffness Degradation on Seismic Response*, FEMA P440a, prepared by the Applied Technology Council for the Federal Emergency Management Agency, Washington, D.C.

FEMA, 2015, *Rapid Visual Screening of Buildings for Potential Seismic Hazards: A Handbook, Third Edition,* FEMA P-154, prepared by the Applied Technology Council for the Federal Emergency Management Agency, Washington, D.C.

FEMA, 2018, *Assessing Seismic Performance of Buildings with Configuration Irregularities,* FEMA P-2012, prepared by the Applied Technology Council for the Federal Emergency Management Agency, Washington, D.C.

FEMA, 2020, *Short-Period Building Collapse Performance and Recommendations for Improving Seismic Design, Volumes 1-4*, FEMA P-2139, prepared by the Applied Technology Council for the Federal Emergency Management Agency, Washington, D.C.

FEMA, 2022, *Hazus Inventory Technical Manual, Hazus 6.0*, Federal Emergency Management Agency, Washington, D.C.

Flores, F, Charney, F.A., and Lopez-Garcia, D., 2014, "Influence of gravity framing system on the collapse performance of special steel moment frames," *Journal of Constructional Steel Research*, Vol. 101, pp. 351–362.

Freeman, S.A., Nicoletti, J.P., and Tyrell, J.V., 1975, "Evaluations of existing buildings for seismic risk—a case study of Puget Sound Naval Shipyard, Bremerton, Washington," *Proceedings of the 1st National Conference in Earthquake Engineering*, pp. 113–122.

Freeman, S.A, 2004, "Review of the development of the capacity spectrum method," *ISET Journal of Earthquake Technology*, Paper No. 438, Vol. 41, No. 1, pp. 1–13.

Ibarra L.F., Medina, R.A., and Krawinkler, H., 2005a, "Hysteretic models that incorporate strength and stiffness deterioration," *Earthquake Engineering & Structural Dynamics*, Vol. 34, No. 12, pp. 1489–1511.

Ibarra, L.F., and Krawinkler, H., 2005b, *Global Collapse of Frame Structures Under Seismic Excitation*, Report No. 152, John A. Blume Earthquake Engineering Center, Stanford University, Stanford, California.

ICBO, 1991, *Uniform* Building *Code*, *1991 Edition*, International Conference of Building Officials, Whittier, California.

ICC, 2018, *International Building Code*, *2018 Edition*, International Code Council, Country Club Hills, Illinois.

ICC-ES, 2022, *Qualification of Building Seismic Performance of Alternative Seismic Force-Resisting Systems*, AC494, International Code Council Evaluation Service, LLC, Brea, California.

Kim, T. and Han, S.W., 2020, "Seismic collapse performance of steel special moment frames designed using different analysis methods," *Earthquake Spectra*, Vol. 37, No. 2, pp. 988–1012.

Lashkari, B. and Kircher, C.A., 1993. "Evaluation of SEAOC & UBC analysis procedures, Part 1: stiff superstructure," *Proceedings of a Seminar on Seismic Isolation, Passive Energy Dissipation and Active Control*, ATC-17-1, Applied Technology Council, Redwood City, California.

Lignos, D., and Krawinkler, H., 2011, "Deterioration modeling of steel components in support of collapse prediction of steel moment frames under earthquake loading," *Journal of Structural Engineering*, Vol. 137, No. 11, pp. 1291–1302.

Line, P., Hohbach, D., and Waltz, N., 2019, "In-plane racking strength tests of wood-frame wood structural panel shear walls with 2-inch panel edge nail spacing and representative multi-story details," *Proceedings of the 2019 SEAOC Convention*, Squaw Creek, California.

Luco, N., Rezaeian, S., Rukstales, K.S., Powers, P.M., Shumway, A.M., Martinez, E.M., and Smoczyk, G.M., 2021, *Gridded Earthquake Ground Motions for the 2020 NEHRP Recommended Seismic Provisions and 2022 ASCE/SEI 7 Standard*, U.S. Geological Survey data release, https://link.edgepilot.com/s/6a11f25b/mijWKuNl806zfSdDD131DQ?u=https://doi.org/10.5066/P9I0R4O6.

National Geophysical Data Center / World Data Service (NGDC/WDS). 2012: NCEI/WDS Natural Hazards Image Database. First. https://doi.org/10.7289/V5154F01. Accessed August 9, 2022.

NIST, 2010, *Evaluation of the FEMA P-695 Methodology for Quantification of Building Seismic Performance Factors*, NIST GCR 10-917-8, prepared by the NEHRP Consultants Joint Venture, a partnership of the Applied Technology Council and the Consortium for Universities for Research in Earthquake Engineering, for the National Institute of Standards and Technology, Gaithersburg, Maryland.

NIST, 2017a, *Guidelines for Nonlinear Structural Analysis for Design of Buildings: Part I—General*, NIST GCR 17-917- 46v1, prepared by the Applied Technology Council for the National Institute of Standards and Technology, Gaithersburg, Maryland

NIST, 2017b, *Guidelines for Nonlinear Structural Analysis for Design of Buildings: Part IIa*—Steel Moment Frames, NIST GCR 17-917- 46v2, prepared by the Applied Technology Council for the National Institute of Standards and Technology, Gaithersburg, Maryland

Ochoa, S.R., 2017, *Seismic Stability of Buckling-Restrained Braced Frames*, Master's Thesis, University of Illinois at Urbana-Champaign, Urbana, Illinois.

OSHPD, 2007, "Express terms for proposed building standards of the Office of Statewide Health Planning and Development regarding proposed changes to 2007 California Building Code Standards Administrative Code, California Code of Regulations, Title 24, Part 1, Chapter 6 – HAZUS," California Office of Statewide Health Planning and Development, Sacramento, California.

SEAOC, 1990, "Tentative general requirements for the design and construction of seismic isolated structures," Appendix 1L, *Recommended Lateral Force Requirements and Commentary*, Seismology Committee, Structural Engineers Association of California, Sacramento, California.

SEAONC, 1986, "Tentative General Requirements for the Design and Construction of Seismic Isolated Structures," Seismology Committee, Structural Engineers Association of Northern California, San Francisco, California.

Seyhan, E., 2014, "Weighted Average of 2014 NGA West-2 GMPEs," PEER NGA West-2 spreadsheet, Pacific Earthquake Engineering Research Center, University of California, Berkeley, Berkeley, California.

Tauberg, N., Kolozvari, K, and Wallace, J., 2019, *Ductile Reinforced Concrete Coupled Walls: FEMA P695 Study*, UCLA SEERL 2019/01, UCLA Structural/Earthquake Engineering Research Laboratory, University of California, Los Angeles, Los Angeles, California.

Tokas, C.V. and Lobo, R.F., 2009, "Risk based seismic evaluation of Pre-1973 hospital buildings using the HAZUS methodology," *Proceedings of the 2009 ATC & SEI Conference on Improving the Seismic Performance of Existing Buildings and Other Structures*, San Francisco, California.

Yamaguchi, N. and Yamazaki, F., 2000, "Fragility curves for buildings in Japan based on damage surveys after the 1995 Kobe Earthquake," Paper No. 2451, *Proceedings of the 12th World Conference on Earthquake Engineering*, Auckland, New Zealand.

Yamazaki, F. and Murao, O., 2000, "Vulnerability functions for Japanese buildings based on damage data due to the 1995 Kobe Earthquake," *Implications of Recent Earthquakes on Seismic Risk*, Series on Innovation in Structures and Construction, Vol. 2., Imperial College Press, London, United Kingdom.

Zaruma, S. and Fahnestock, L., 2018, "Assessment of design parameters influencing seismic collapse performance of buckling-restrained braced frames," *Soil Dynamics and Earthquake Engineering*, Vol. 113, pp. 35–46.

Zhu, M., McKenna, F., and Scott, M.H., 2018, "OpenSeesPy: python library for OpenSees finite element framework," *SoftwareX*, Vol. 7, pp. 6–11.

Project Participants

Federal Emergency Management Agency

Mai (Mike) Tong (Project Officer)
Federal Emergency Management Agency
400 C Street, SW, 6th Floor
Washington, DC 20472

Robert D. Hanson (Technical Advisor)
Federal Emergency Management Agency
5885 Dunabbey Loop
Dublin, Ohio 43017

Applied Technology Councils

Jon A. Heintz (Project Executive)
Applied Technology Council
201 Redwood Shores Parkway, Suite 240
Redwood City, California 94065

Justin Moresco (Project Manager)
Applied Technology Council
201 Redwood Shores Parkway, Suite 240
Redwood City, California 94065

Project Technical Committee

Charles A. Kircher (Project Technical Director)
Kircher & Associates
1121 San Antonio Road, Suite D-202
Palo Alto, California 94303

John Hooper
Magnusson Klemencic Associates
1301 Fifth Avenue, Suite 3200
Seattle, Washington 98101-2699

Jeffrey W. Berman
University of Washington
Dept. of Civil & Environmental Engineering
201 More Hall, Box 352700
Seattle, Washington 98195

Weichiang Pang
Clemson University
Glenn Department of Civil Engineering
312 Lowry Hall
Clemson, South Carolina 29634

James R. Harris
J. R. Harris & Company
1175 Sherman Street, Suite 2000
Denver, Colorado 80203

Project Review Panel

Russell Berkowitz
Forell/Elsesser Engineers, Inc.
160 Pine Street, 6th Floor
San Francisco, California 94111

Kelly Cobeen
Wiss, Janney, Elstner Associates
2000 Powell Street, Suite 1650
Emeryville, California 94608

Gregory Deierlein
Stanford University
Dept. of Civil & Environmental Engineering
Blume Earthquake Engineering Center, MC 3037
Stanford, California 94305

Andre Filiatrault (Emeritus Professor)
University at Buffalo
Department of Civil, Structural and
Environmental Engineering
134 Ketter Hall
Buffalo, New York 14260

Emily Guglielmo
Martin/Martin Consulting Engineers
700 Larkspur Landing Circle, Suite 155
Larkspur, California 94939

Devin Huber
American Institute of Steel Construction
130 East Randolph, Suite 2000
Chicago, Illinois 60601

Phil Line
American Wood Council
222 Catoctin Circle SE, Suite 201
Leesburg, Virginia 20175

James O. Malley
Degenkolb Engineers
375 Beale Street, Suite 500
San Francisco, California 94105

Bob Pekelnicky
Degenkolb Engineers
375 Beale Street, Suite 500
San Francisco, California 94105

Working Group Members

Bibek Bhardwaj
Clemson University
Glenn Department of Civil Engineering
312 Lowry Hall
Clemson, South Carolina 29634

Addie Lederman
University of Washington
Dept. of Civil & Environmental Engineering
201 More Hall, Box 352700
Seattle, Washington 98195

Dimitrios Lignos
École Polytechnique Fédérale de Lausanne
Lausanne, Vaud
Switzerland

Sereen Majdalaweyh
Clemson University
Glenn Department of Civil Engineering
312 Lowry Hall
Clemson, South Carolina 29634

Uzochukwu D. Uwaoma
University of Washington
Dept. of Civil & Environmental Engineering
201 More Hall, Box 352700
Seattle, Washington 98195

Workshop Participants

Russell Berkowitz
Forell/Elsesser Engineers

Jeffrey W. Berman
University of Washington

Finley Charney
Virginia Tech

Kelly Cobeen
Wiss, Janney, Elstner Associates

Greg Deierlein
Stanford State University

Dan Dolan
Washington State University

John Hooper
Magnusson Klemencic Associates

Larry Fahnestock
Washington State University

Andre Filiatrault
University at Buffalo

Emily Guglielmo
Martin/Martin Consulting Engineers

Robert Hanson
FEMA

James Harris
J.R. Harris & Company

Sandy Hohener
Degenkolb Engineers

Bob Pekelnicky
Degenkolb Engineers

Devin Huber
American Institute of Steel Construction

Charlie Kircher
Kircher & Associates

Addie Lederman
University of Washington

Phil Line
American Wood Council

Bret Lizundia
Rutherford & Chekene

Nicolas Luco
USGS

Bonnie Manley
American Iron and Steel Institute

Adolfo Matamoros
University of Texas at San Antonio

Silvia Mazzoni
University of California, Los Angeles

Justin Moresco
Applied Technology Council

Weichiang Pang
Clemson University

Rafael Sabelli
Walter P Moore

Tom Sabol
Englekirk Structural Engineers

Siamak Sattar
NIST

Gwenyth Searer
Wiss, Janney, Elstner Associates

Andrew Sen
Marquette University

Barbara Simpson
Oregon State University

Mai (Mike) Tong
FEMA

Reid Zimmerman
KPFF

Mike Mahoney
FEMA

Francisco Flores
American Wood Council

FEMA

FEMA P-2343